

NOTE TO USERS

Page(s) missing in number only; text follows. Page(s) were scanned as received.

211

This reproduction is the best copy available.

UMI[®]

UNIVERSITY OF OKLAHOMA

GRADUATE COLLEGE

AN EXPERIMENTAL AND NUMERICAL STUDY OF
DIFFUSION FLAMES IN CROSS-FLOW AND
QUIESCENT ENVIRONMENT
AT SMOKE POINT CONDITION

A Dissertation

SUBMITTED TO THE GRADUATE FACULTY

in partial fulfillment of the requirements for the

degree of

Doctor of Philosophy

By

Sien Fong Goh
Norman, Oklahoma
2003

UMI Number: 3096336

UMI[®]

UMI Microform 3096336

Copyright 2003 by ProQuest Information and Learning Company.

All rights reserved. This microform edition is protected against
unauthorized copying under Title 17, United States Code.

ProQuest Information and Learning Company
300 North Zeeb Road
P.O. Box 1346
Ann Arbor, MI 48106-1346

© Copyright by Sien Fong Goh 2003

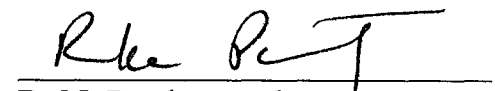
All Rights Reserved.

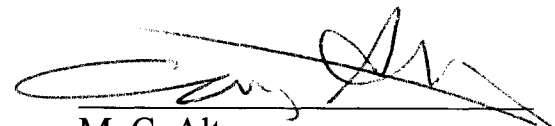
AN EXPERIMENTAL AND NUMERICAL STUDY OF
DIFFUSION FLAMES IN CROSS-FLOW AND QUIESCENT
ENVIRONMENT AT SMOKE POINT CONDITION

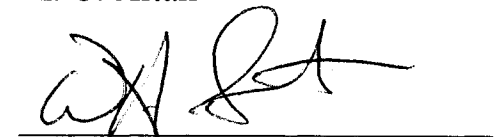
A DISSERTATION APPROVED FOR THE
THE SCHOOL OF AEROSPACE AND MECHANICAL ENGINEERING


By


S. R. Gollahalli (Chairman)


R. N. Parthasarathy


M. C. Altan


W. H. Sutton


R. G. Mallinson

Acknowledgement

Trust in the LORD with all your heart and lean not on your own understanding; in all your ways acknowledge him, and he will make your paths straight. (Proverb 3: 5-6)

First, I would like to thank God for all that He has done in my life. He has led me in all the aspects of my life. I would not have made it so far without Him. May all the glory be unto Him.

I thank my wife, Ming May, who has been very patient through the last two years of my academic career. I am very grateful for her support, understanding, and love, which has provided me strength to finish this dissertation. I would like to thank my parents for their long years of support in my study, both in financial and spiritual matters. I would like to thank them for their love and encouragement. They brought me up well. I would also like to thank my brother and sisters at home for their support.

Dr. Gollahalli has been a great mentor to me for the last six years. Since I was an undergraduate research assistant in the Combustion Laboratory, he has been very supportive to me. He was not only showing concern for my research progress but also other aspects of my life. I am very grateful for all his encouragement and coaching. I am thankful for he has brought out the best of me in my academic life.

I would like to thank Dr. Parthasarathy, Dr. Altan, Dr. Sutton and Dr. Malinson for their service as my committee members. Furthermore, I appreciate the great deal of time that Dr. Chang spent coaching me during my preparation for the qualifying exam. Without friendship, the research in the laboratory would have been monotonous. I specially want to thank Mr. Benjamin Baird for his help, suggestions, and friendship for the last five years. I am also thankful for the help from Sathish, Chendhill, and Praveen.

My life in Norman has been much better because of my brothers and sisters in Christ in Southern Oklahoma Chinese Baptist Church; especially, Pastor Tony, Esther and their family, who have provided me their love and support during my stay in Norman. They will always be parts of my family in my heart. I would like to thank Pastor Morris for his painstaking effort in editing my thesis. His effort was far beyond my expectation. Finally, I am grateful for the love, prayer support and the partnership in the Lord with these wonderful brothers and sisters in the church. I will surely treasure these friendships from the bottom of my heart.

I would like to dedicate this dissertation to my wife, Ming-May Koo.

Table of Contents

Acknowledgement	iv
Tables of Contents	vi
List of Tables	xi
List of Figures	xii
Abstract	xxii
Chapter I Introduction and Objective	1
Chapter II Literature Review	4
2.1 Introduction	4
2.2 Smoke Point	4
2.3 Soot Formation Process	9
2.4 Soot Oxidation Process	13
2.5 Soot Formation Investigation	16
2.6 Soot Primary Size Measurement	17
2.7 Purpose of LIF Measurement	18
Chapter III Flame Structure of Diffusion Flame at Smoke Point in Quiescent and	
Cross-Flow Environment	20
3.1 Introduction and Overview	21
3.2 Experimental Facilities, Instrumentation and Procedures	22
3.2.1 Smoke Point Determination	22
3.2.2 Experimental Facilities	26
3.2.3 Experimental Instrumentation	28

3.3 Experimental Results and Discussion	33
3.3.1 Critical Fuel Mass Flow Rate and Inert Gas Mass Flow Rate at Smoke Point	33
3.3.2 Temperature profiles	42
3.3.3 Global Emissions	47
3.3.4 In-Flame Concentration Profiles	51
3.3.5 Flame Height and Flame Length	60
3.3.6 Velocity Profiles	62
3.3.7 Flame Radiation	64
3.4 Summary and Conclusions	65
Chapter IV Laser Induced Incandescence Measurement	156
4.1 Literature Survey on LII	158
4.1.1 Introduction	158
4.1.2 Theoretical development	161
4.2 Experimental Techniques	167
4.2.1 Laser Fluence or Irradiance	167
4.2.2 Detection Gate and Timing	169
4.2.3 Laser and Detection Wavelength	173
4.2.4 Calibration Method	174
4.3 Experimental Setup	174
4.3.1 Calibration	176
4.3.2 Signal Correction	177

4.4 Results and Discussion	180
4.4.1 Quiescent Condition	180
4.4.2 Cross-Flow Condition	183
4.5 Conclusion	189
Chapter V Laser Induced Fluorescence Measurement	219
5.1 Introduction	220
5.2 Experimental Techniques	221
5.2.1 OH Quantification	224
5.2.2 Spectroscopic Modeling	225
5.3 Results and Discussions	229
Chapter IV Computational Analysis	260
6.1 Introduction	261
6.2 Continuity and Momentum Equations	262
6.2.1 The Standard k- ϵ Model	262
6.2.2 Transport Equations for the Standard k- ϵ Model	262
6.2.3 Effects of Buoyancy on Turbulence in the k- ϵ Models	263
6.2.4 Modeling the Turbulent Viscosity	264
6.3 Energy Equation	265
6.4 Equilibrium Mixture Fraction/PDF Model	266
6.4.1 Advantages of the Non-Premixed Approach	266
6.4.2 Definition of the Mixture Fraction	266
6.4.3 Transport Equations for the Mixture Fraction	267
6.5 Equilibrium Model	268

6.5.1 Derivation of Mean Scalar Values from the Instantaneous Mixture Fraction	269
6.6 Computational Facility	270
6.7 Boundary Conditions	270
6.8 Grid Generation and Validation	271
6.9 Converging Criterion	272
6.9.1 Definition of Residuals	272
6.10 2-D Modeling	
6.11 Results and Discussion	273
6.11.1 Quiescent Condition Flame	274
6.11.2 Cross-Flow Condition Flame	276
6.12 Conclusion	281
Chapter VII Overall Discussion, Conclusions and Recommendations	323
7.1 Chemical and Momentum Effect	323
7.2 Cross-Flow Effect	324
7.2.1 Momentum-Dominated Region Flame (60% and 100% CFMFR Flame)	325
7.2.2 Transition Region Flame (20% CFMFR Flames for 2 and 3 m/s Cross-Flow and 30% CFMFR for 4 m/s Cross-Flow)	326
7.2.3 Chemical-Dominated Region (10% CFMFR Flame)	328
7.3 Computation Modeling	329
7.4 Experimental Recommendations	331

References	333
Appendix I	344
Appendix II	346
Appendix III	348

List of Tables

Chapter III

3.1a Test Matrix for Quiescent Condition	25
3.1b Test Matrix for Cross-Flow Condition	25
3.2 Gas Composition	32
3.3 Experimental Uncertainties	32
3.4 Nominal Condition and Experimental Parameters	32
3.5 Specific Heat for Tested Inert Gases	35
3.6 Ranges of Momentum and Chemical Dominated Regions and Transition Regions for All the Cross-Flow Conditions	41
3.7a Quiescent Experimental Conditions	68
3.7b Cross-Flow Experimental Conditions	68

Chapter IV

4.1 Literatures of Application of LII for Soot Concentration Measurement	191
--	-----

Chapter V

5.1 OH Collisional Quenching Parameters	240
5.2 Summery of Soot Oxidant Dominance	241

Chapter VI

6.1 Grid Information for Different Grid Configuration	284
6.2 Grid Information for Different Grid Configuration with Different Temperature Gradients	286
6.3 Converging Criteria	287
6.4 Numerical Flame Length	287

List of Figures

Chapter I

3.1	Combustion Chamber, Smoke Point Detection and Soot Volume Fraction Measurement Setup	69
3.2	Flame Emission and Radiation Measurement, and Flame Imaging Setup	70
3.3	In-Flame Gas Sampling and Temperature Measurements Setup	71
3.4	Schematic Diagram of the Combustion Wind Tunnel and Smoke Point Detection	72
3.5	Coordinate System of the Wind Tunnel	73
3.6a	Velocity Profile of the Middle of the test section at 3.4 m/s in X direction	74
3.6b	Velocity Profile of the Middle of the test section at 3.4 m/s in Y direction	74
3.6c	Velocity Profile Along the Z axis at the Center of the Test Section At 3.5 m/s	75
3.7a	Inert Gases Mass Flow Rate Comparison at Smoke Point	76
3.7b	Inert Gases Volume Flow Rate Comparison at Smoke Point	76
3.8	Jet Reynolds Number Comparison for Different Inert Gases at Smoke Point	77
3.9	Nitrogen Mass Flow Rate Comparison for Single Burner and Co-annular Burner at Smoke Point	78
3.10	Jet Reynolds Number Comparison for Single Burner and Co-annular Burner at Smoke Point for Nitrogen Dilution for Single Burner Study	78
3.11	Hydrogen Mass and Volume Flow Rate for Each Fuel Mass and Volume Flow Rate at Smoke Point for Nitrogen Dilution for Single Burner Study	79
3.12	Hydrogen Mass and Volume Flow Rate for Each Fuel Mass and Volume Flow Rate at Smoke Point for Nitrogen Dilution for Goh (1999) Co-Annular Burner Study	79
3.13	Smoke Point Results for Different Cross Flow Conditions	80
3.14	Jet Reynolds Number at Smoke Point for Different Cross Flow Conditions	80
3.15	Relation of CFMFR with Cross-Flow Velocity	81
3.16	Momentum Flux Ratio at Smoke Point for Different Cross Flow Conditions	81
3.17	Comparison of Current Upright Wind Tunnel Nitrogen Mass Flow Rate at 4.0 m/s to Horizontal Wind Tunnel Nitrogen Mass Flow Rate at 4.02 m/s	82
3.18	Comparison of Current Upright Wind Tunnel Fuel Jet Reynolds Numbers at 4.0 m/s to Horizontal Wind Tunnel Fuel Jet Reynolds Numbers at 4.02 m/s	82
3.19	Comparison of Current Upright Wind Tunnel Momentum Flux Ratio at 4.0 m/s to Horizontal Wind Tunnel Momentum Flux Ratio at 4.02 m/s	83
3.20a	The Calculated Froude Number for the Flame and the Cross-Flow for Different Percentage CFMFR for 2m/s Cross-Flow Condition.	83
3.20b	The Calculated Froude Number for the Flame and the Cross-Flow for Different Percentage CFMFR for 3m/s Cross-Flow Condition	84
3.20c	The Calculated Froude Number for the Flame and the Cross-Flow for Different Percentage CFMFR for 4m/s Cross-Flow Condition	84
3.21	Mole Fraction of Jet Gas Mixture for Nitrogen Dilution Study in Quiescent Condition	85
3.22a	Mole Fraction of Jet Gas Mixture at Smoke Point at 2 m/s Cross-Flow	85

3.22b	Mole Fraction of Jet Gas Mixture at Smoke Point at 2.5 m/s Cross-Flow	86
3.22c	Mole Fraction of Jet Gas Mixture at Smoke Point at 3.0 m/s Cross-Flow	86
3.22d	Mole Fraction of Jet Gas Mixture at Smoke Point at 3.5 m/s Cross-Flow	87
3.22e	Mole Fraction of Jet Gas Mixture at Smoke Point at 4.0 m/s Cross-Flow	87
3.22f	Mass Fraction of Jet Gas Mixture at Smoke Point in Quiescent Condition	88
3.22g	Mass Fraction of Jet Gas Mixture at Smoke Point at 2 m/s Cross-Flow	88
3.22h	Mass Fraction of Jet Gas Mixture at Smoke Point at 2.5 m/s Cross-Flow	89
3.22i	Mass Fraction of Jet Gas Mixture at Smoke Point at 3 m/s Cross-Flow	89
3.22j	Mass Fraction of Jet Gas Mixture at Smoke Point at 3.5 m/s Cross-Flow	90
3.22k	Mass Fraction of Jet Gas Mixture at Smoke Point at 4 m/s Cross-Flow	90
3.23	Schematic Diagram Showing the Vortex System of a Jet in Cross-Flow	91
3.24a	Radial Temperature Profiles at 100% CFMFR for Three Flame Heights	92
3.24b	Radial Temperature Profiles at 60% CFMFR for Three Flame Heights	92
3.24c	Radial Temperature Profiles at 30 % CFMFR for Three Flame Heights	93
3.24d	Radial Temperature Profiles at 10 % CFMFR for Three Flame Heights	93
3.25a	Temperature Profiles in X direction for 100% CFMFR at 2 m/s Cross-flow at Three Different Locations	94
3.25b	Temperature Profiles in X direction for 60% CFMFR at 2 m/s Cross-flow at Three Different Locations	94
3.25c	Temperature Profiles in X direction for 20% CFMFR at 2 m/s Cross-flow at Three Different Locations	95
3.25d	Temperature Profiles in X direction for 20% CFMFR at 2 m/s Cross-flow at Three Different Locations	95
3.26a	Temperature Profiles in X direction for 100% CFMFR at 3 m/s Cross-flow at Three Different Locations	96
3.26b	Temperature Profiles in X direction for 60% CFMFR at 3 m/s Cross-flow at Three Different Locations	96
3.26c	Temperature Profiles in X direction for 20% CFMFR at 3 m/s Cross-flow at Three Different Locations	97
3.26d	Temperature Profiles in X direction for 20% CFMFR at 3 m/s Cross-flow at Three Different Locations	97
3.27a	Temperature Profiles in X direction for 100% CFMFR at 4 m/s Cross-flow at Three Different Locations	98
3.27b	Temperature Profiles in X direction for 60% CFMFR at 4 m/s Cross-flow at Three Different Locations	98
3.27c	Temperature Profiles in X direction for 30% CFMFR at 4 m/s Cross-flow at Three Different Locations	99
3.27d	Temperature Profiles in X direction for 10% CFMFR at 4 m/s Cross-flow at Three Different Locations	99
3.28	Emission Index of NO, NO _x and CO for CFMFR and Fuel-Nitrogen Mixture at Smoke Point	100
3.29	Global CO ₂ and O ₂ Concentrations for CFMFR and Fuel-Nitrogen Mixture at Smoke Point	100
3.30a	Radial NO Concentration Profiles at CFMFR	101
3.30b	Radial NO Concentration Profiles at 60% CFMFR	101
3.30c	Radial NO Concentration Profiles at 30% CFMFR	102

3.30d	Radial NO Concentration Profiles at 10% CFMFR	102
3.31a	Radial CO Concentration Profiles at CFMFR	103
3.31b	Radial CO Concentration Profiles at 60% CFMFR	103
3.31c	Radial CO Concentration Profiles at 30% CFMFR	104
3.31d	Radial CO Concentration Profiles at 10% CFMFR	104
3.32a	Radial CO ₂ Concentration Profiles at CFMFR	105
3.32b	Radial CO ₂ Concentration Profiles at 60%CFMFR	105
3.32c	Radial CO ₂ Concentration Profiles at 30% CFMFR	106
3.32d	Radial CO ₂ Concentration Profiles at 10% CFMFR	106
3.33a	Radial O ₂ Concentration Profiles at CFMFR	107
3.33b	Radial O ₂ Concentration Profiles at 60% CFMFR	107
3.33c	Radial O ₂ Concentration Profiles at 30% CFMFR	108
3.33d	Radial O ₂ Concentration Profiles at 10% CFMFR	108
3.34a	Radial Soot Concentration Profiles at 100% CFMFR	109
3.34b	Radial Soot Concentration Profiles at 60% CFMFR	109
3.34c	Radial Soot Concentration Profiles at 30% CFMFR	110
3.34d	Radial Soot Concentration Profiles at 10% CFMFR	110
3.35a	Emission Index for CO, NO and NO _x at 2m/s Cross-Flow	111
3.35b	Global Emission for CO ₂ and O ₂ Concentration at 2 m/s Cross-Flow	111
3.36a	Emission Index for CO, NO and NO _x at 2.5 m/s Cross-Flow	112
3.36b	Global Emission for CO ₂ and O ₂ Concentration at 2.5 m/s Cross-Flow	112
3.37a	Emission Index for CO, NO and NO _x at 3 m/s Cross-Flow	113
3.37b	Global Emission for CO ₂ and O ₂ Concentration at 3 m/s Cross-Flow	113
3.38a	Emission Index for CO, NO and NO _x at 3.5 m/s Cross-Flow	114
3.38b	Global Emission for CO ₂ and O ₂ Concentration at 3.5 m/s Cross-Flow	114
3.39a	Emission Index for CO, NO and NO _x at 4 m/s Cross-Flow	115
3.39b	Global Emission for CO ₂ and O ₂ Concentration at 4 m/s Cross-Flow	115
3.40a	Radial NO Concentration Profiles on X Axis at Three Locations at 100% CFMFR at 2 m/s Cross-Flow	116
3.40b	Radial NO Concentration Profiles on X Axis at Three Locations at 60% CFMFR at 2 m/s Cross-Flow	116
3.40c	Radial NO Concentration Profiles on X Axis at Three Locations at 20% CFMFR at 2 m/s Cross-Flow	117
3.40d	Radial NO Concentration Profiles on X Axis at Three Locations at 10% CFMFR at 2 m/s Cross-Flow	117
3.41a	Radial CO Concentration Profiles on X Axis at Three Locations at 100% CFMFR at 2 m/s Cross-Flow	118
3.41b	Radial CO Concentration Profiles on X Axis at Three Locations at 60% CFMFR at 2 m/s Cross-Flow	118
3.41c	Radial CO Concentration Profiles on X Axis at Three Locations at 20% CFMFR at 2 m/s Cross-Flow	119
3.41d	Radial CO Concentration Profiles on X Axis at Three Locations at 10% CFMFR at 2 m/s Cross-Flow	119
3.42a	Radial CO ₂ Concentration Profiles on X Axis at Three Locations at 100% CFMFR at 2 m/s Cross-Flow	120

3.42b	Radial CO ₂ Concentration Profiles on X Axis at Three Locations at 60% CFMFR at 2 m/s Cross-Flow	120
3.42c	Radial CO ₂ Concentration Profiles on X Axis at Three Locations at 20% CFMFR at 2 m/s Cross-Flow	121
3.42d	Radial CO ₂ Concentration Profiles on X Axis at Three Locations at 10% CFMFR at 2 m/s Cross-Flow	121
3.43a	Radial O ₂ Concentration Profiles on X Axis at Three Locations at 100% CFMFR at 2 m/s Cross-Flow	122
3.43b	Radial O ₂ Concentration Profiles on X Axis at Three Locations at 60% CFMFR at 2 m/s Cross-Flow	122
3.43c	Radial O ₂ Concentration Profiles on X Axis at Three Locations at 20% CFMFR at 2 m/s Cross-Flow	123
3.43d	Radial O ₂ Concentration Profiles on X Axis at Three Locations at 10% CFMFR at 2 m/s Cross-Flow	123
3.44a	Radial NO Concentration Profiles on X Axis at Three Locations at 100% CFMFR at 3 m/s Cross-Flow	124
3.44b	Radial NO Concentration Profiles on X Axis at Three Locations at 60% CFMFR at 3 m/s Cross-Flow	124
3.44c	Radial NO Concentration Profiles on X Axis at Three Locations at 20% CFMFR at 3 m/s Cross-Flow	125
3.44d	Radial NO Concentration Profiles on X Axis at Three Locations at 10% CFMFR at 3 m/s Cross-Flow	125
3.45a	Radial CO Concentration Profiles on X Axis at Three Locations at 100% CFMFR at 3 m/s Cross-Flow	126
3.45b	Radial CO Concentration Profiles on X Axis at Three Locations at 60% CFMFR at 3 m/s Cross-Flow	126
3.45c	Radial CO Concentration Profiles on X Axis at Three Locations at 20% CFMFR at 3 m/s Cross-Flow	127
3.45d	Radial CO Concentration Profiles on X Axis at Three Locations at 10% CFMFR at 3 m/s Cross-Flow	127
3.46a	Radial CO ₂ Concentration Profiles on X Axis at Three Locations at 100% CFMFR at 3 m/s Cross-Flow	128
3.46b	Radial CO ₂ Concentration Profiles on X Axis at Three Locations at 60% CFMFR at 3 m/s Cross-Flow	128
3.46c	Radial CO ₂ Concentration Profiles on X Axis at Three Locations at 20% CFMFR at 3 m/s Cross-Flow	129
3.46d	Radial CO ₂ Concentration Profiles on X Axis at Three Locations at 10% CFMFR at 3 m/s Cross-Flow	129
3.47a	Radial O ₂ Concentration Profiles on X Axis at Three Locations at 100% CFMFR at 3 m/s Cross-Flow	130
3.47b	Radial O ₂ Concentration Profiles on X Axis at Three Locations at 60% CFMFR at 3 m/s Cross-Flow	130
3.47c	Radial O ₂ Concentration Profiles on X Axis at Three Locations at 20% CFMFR at 3 m/s Cross-Flow	131
3.47d	Radial O ₂ Concentration Profiles on X Axis at Three Locations at 10% CFMFR at 3 m/s Cross-Flow	131

3.48a	Radial NO Concentration Profiles on X Axis at Three Locations at 100% CFMFR at 4 m/s Cross-Flow	132
3.48b	Radial NO Concentration Profiles on X Axis at Three Locations at 60% CFMFR at 4 m/s Cross-Flow	132
3.48c	Radial NO Concentration Profiles on X Axis at Three Locations at 30% CFMFR at 4 m/s Cross-Flow	133
3.48d	Radial NO Concentration Profiles on X Axis at Three Locations at 10% CFMFR at 4 m/s Cross-Flow	133
3.49a	Radial CO Concentration Profiles on X Axis at Three Locations at 100% CFMFR at 4 m/s Cross-Flow	134
3.49b	Radial CO Concentration Profiles on X Axis at Three Locations at 60% CFMFR at 4 m/s Cross-Flow	134
3.49c	Radial CO Concentration Profiles on X Axis at Three Locations at 30% CFMFR at 4 m/s Cross-Flow	135
3.49d	Radial CO Concentration Profiles on X Axis at Three Locations at 10% CFMFR at 4 m/s Cross-Flow	135
3.50a	Radial CO ₂ Concentration Profiles on X Axis at Three Locations at 100% CFMFR at 4 m/s Cross-Flow	136
3.50b	Radial CO ₂ Concentration Profiles on X Axis at Three Locations at 60% CFMFR at 4 m/s Cross-Flow	136
3.50c	Radial CO ₂ Concentration Profiles on X Axis at Three Locations at 30% CFMFR at 4 m/s Cross-Flow	137
3.50d	Radial CO ₂ Concentration Profiles on X Axis at Three Locations at 10% CFMFR at 4 m/s Cross-Flow	137
3.51a	Radial O ₂ Concentration Profiles on X Axis at Three Locations at 100% CFMFR at 4 m/s Cross-Flow	138
3.51b	Radial O ₂ Concentration Profiles on X Axis at Three Locations at 60% CFMFR at 4 m/s Cross-Flow	138
3.51c	Radial O ₂ Concentration Profiles on X Axis at Three Locations at 30% CFMFR at 4 m/s Cross-Flow	139
3.51d	Radial O ₂ Concentration Profiles on X Axis at Three Locations at 10% CFMFR at 4 m/s Cross-Flow	139
3.52	Flame Radiation for Different Inert Gases at Smoke Point	140
3.53	Flame Radiation Fraction for Different Inert Gases at Smoke Point	140
3.54a	Flame Height for Different Inert Gases at Smoke Point	141
3.54b	Flame Length for Different Cross-Flow Speed at Smoke Point	141
3.55	Definitions of Flame Height in Quiescent Environment and Flame Length and Width in Cross-Flow	142
3.56a	100% CFMFR Flame and Nitrogen Inert Gas Dilution Flames Images	143
3.56b	Argon Inert Gas Dilution Flames Images	143
3.56c	Carbon Dioxide Inert Gas Dilution Flames Images	144
3.56d	Helium Inert Gas Dilution Flames Images	144
3.57a	2 m/s Cross-Flow Condition Flames Images for Different CFMFR with Nitrogen Dilution	145
3.57b	2.5 m/s Cross-Flow Condition Flames Images for Different CFMFR with Nitrogen Dilution	145

3.57c	3.0 m/s Cross-Flow Condition Flames Images for Different CFMFR with Nitrogen Dilution	146
3.57d	3.5 m/s Cross-Flow Condition Flames Images for Different CFMFR with Nitrogen Dilution	146
3.57e	4.0m/s Cross-Flow Condition Flames Images for Different CFMFR with Nitrogen Dilution	147
3.58	Flame Shape Comparison of Horizontal (at CFMFR and 4.02 m/s Cross-Flow) and Vertical (at CFMFR and 4.0 m/s Cross-Flow) Cross-Flow Flame	147
3.59a	Radial Velocity Profiles at 100% CFMFR for Three Flame Heights	148
3.59b	Radial Velocity Profiles at 60 % CFMFR for Three Flame Heights	148
3.59c	Radial Velocity Profiles at 30 % CFMFR for Three Flame Heights	149
3.59d	Radial Velocity Profiles at 10 % CFMFR for Three Flame Heights	149
3.60a	Z Velocity Profiles in X direction at 100% CFMFR at 2 m/s Cross-flow at Three Different Locations	150
3.60b	Z Velocity Profiles in X direction at 60% CFMFR at 2 m/s Cross-flow at Three Different Locations	150
3.60c	Z Velocity Profiles in X direction at 20% CFMFR at 2 m/s Cross-flow at Three Different Locations	151
3.60d	Z Velocity Profiles in X direction at 10% CFMFR at 2 m/s Cross-flow at Three Different Locations	151
3.61a	Z Velocity Profiles in X direction at 100% CFMFR at 3 m/s Cross-flow at Three Different Locations	152
3.61b	Z Velocity Profiles in X direction at 60% CFMFR at 3 m/s Cross-flow at Three Different Locations	152
3.61c	Z Velocity Profiles in X direction at 20% CFMFR at 3 m/s Cross-flow at Three Different Locations	153
3.61d	Z Velocity Profiles in X direction at 10% CFMFR at 3 m/s Cross-flow at Three Different Locations	153
3.62a	Z Velocity Profiles in X direction for 100% CFMFR at 4 m/s Cross-flow at Three Different Locations	154
3.62b	Z Velocity Profiles in X direction for 60% CFMFR at 4 m/s Cross-flow at Three Different Locations	154
3.62c	Z Velocity Profiles in X direction for 30% CFMFR at 4 m/s Cross-flow at Three Different Locations	155
3.62d	Z Velocity Profiles in X direction for 10% CFMFR at 4 m/s Cross-flow at Three Different Locations	155

Chapter IV

4.1	Effect of Laser Fluence on LII Signal	172
4.2	Comparison of Relative Heat Transfer of a Laser Heated Soot Particle Through Various Heat Transfer Paths	172
4.3	Experimental Setup for LII Measurement at Quiescent Condition	194
4.4	Schematic of LII Measurement Setup for Cross-flow Condition	195
4.5	Timing of Laser and Camera Chronological Chart	196
4.6	Geometry of the Tomographic Correction	197

4.7	Flow Chart for Signal Correction	198
4.8	Propane Calibration Flame	200
4.9	Corrected and Uncorrected Result and Shaddix and Symth Results	200
4.10	Corrected and Uncorrected Result for Quiescent Result at 100% CFMFR at 30cm HAB	201
4.11	The Difference in Percentage of Corrected and Uncorrected Result for Quiescent Result at 100% CFMFR at 30cm Flame Height	201
4.12	Schematic Diagram Showing the Slice of measurement Take at Three Flame Locations in Cross-Flow	202
4.13	2-D View of Soot Concentration Profile	203
4.14a	Tomographic Soot Concentration at Three Flame Locations for 10% CFMFR Flame at 2.0 m/s Cross-Flow	204
4.14b	Tomographic Soot Concentration at Three Flame Locations for 20% CFMFR Flame at 2.0 m/s Cross-Flow	204
4.14c	Tomographic Soot Concentration at Three Flame Locations for 60% CFMFR Flame at 2.0 m/s Cross-Flow	205
4.14d	Tomographic Soot Concentration at Three Flame Locations for 100% CFMFR Flame at 2.0 m/s Cross-Flow	206
4.15a	Tomographic Soot Concentration at Three Flame Locations for 10% CFMFR Flame at 3.0 m/s Cross-Flow	207
4.15b	Tomographic Soot Concentration at Three Flame Locations for 20% CFMFR Flame at 3.0 m/s Cross-Flow	207
4.15c	Tomographic Soot Concentration at Three Flame Locations for 60% CFMFR Flame at 3.0 m/s Cross-Flow	208
4.15d	Tomographic Soot Concentration at Three Flame Locations for 100% CFMFR Flame at 3.0 m/s Cross-Flow	209
4.16a	Tomographic Soot Concentration at Three Flame Locations for 10% CFMFR Flame at 4.0 m/s Cross-Flow	210
4.16b	Tomographic Soot Concentration at Three Flame Locations for 30% CFMFR Flame at 4.0 m/s Cross-Flow	210
4.16c	Tomographic Soot Concentration at Three Flame Locations for 60% CFMFR Flame at 4.0 m/s Cross-Flow	212
4.16d	Tomographic Soot Concentration at Three Flame Locations for 100% CFMFR Flame at 4.0 m/s Cross-Flow	212
4.17a	PLII for 10% CFMFR Flame at 2 m/s Cross-Flow in x-z Plane	213
4.17b	PLII for 20% CFMFR Flame at 2 m/s Cross-Flow in x-z Plane	213
4.17c	PLII for 60% CFMFR Flame at 2 m/s Cross-Flow in x-z Plane	214
4.17d	PLII for 100% CFMFR Flame at 2 m/s Cross-Flow in x-z Plane	214
4.18a	PLII for 10% CFMFR Flame at 3 m/s Cross-Flow in x-z Plane	215
4.18b	PLII for 20% CFMFR Flame at 3 m/s Cross-Flow in x-z Plane	215
4.18c	PLII for 60% CFMFR Flame at 3 m/s Cross-Flow in x-z Plane	216
4.18d	PLII for 100% CFMFR Flame at 3 m/s Cross-Flow in x-z Plane	216
4.19a	PLII for 10% CFMFR Flame at 4 m/s Cross-Flow in x-z Plane	217
4.19b	PLII for 30% CFMFR Flame at 4 m/s Cross-Flow in x-z Plane	217
4.19c	PLII for 60% CFMFR Flame at 4 m/s Cross-Flow in x-z Plane	218
4.19d	PLII for 100% CFMFR Flame at 42 m/s Cross-Flow in x-z Plane	218

Chapter V

5.1	Quantum Excitation	241
5.2	Schematic of LIF and PLIF Measurement Setup	242
5.3	Comparison of LIF Signal and Off-Resonance Signal	243
5.4	OH Concentration of Quiescent Condition Flames at Four Different CFMFR	244
5.5a	Radial Soot and OH Concentration Profiles for 10% CFMFR Flames at 25% Flame Length	245
5.5b	Radial Soot and OH Concentration Profiles for 10% CFMFR Flames at 50% Flame Length	245
5.6a	Radial Soot and OH Concentration Profiles for 60% CFMFR Flames at 25% Flame Length	246
5.6b	Radial Soot and OH Concentration Profiles for 60% CFMFR Flames at 50% Flame Length	246
5.6c	Radial Soot and O ₂ Concentration Profiles for 60% CFMFR Flames at 50% Flame Length	247
5.7	X-Y Plane OH Molar Concentration at 25% Flame Length in 2 m/s Cross-Flow for 10%, 20%, 60% and 100% CFMFR	248
5.8	OH Molar Concentration Cross Section at 25% Flame Length for 3 m/s Cross-Flow at 10%, 20%, 60% and 100% CFMFR	249
5.9	OH Molar Concentration Cross Section at 25% Flame Length for 4 m/s Cross-Flow at 10%, 20%, 60% and 100% CFMFR	250
5.10a	Soot and OH Concentration Profiles for 10% CFMFR Flame in 2m/s Cross-Flow at 25% Flame Length	251
5.10b	Soot and OH Concentration Profiles for 60% CFMFR Flame in 2m/s Cross-Flow at 25% Flame Length	251
5.11a	Soot and OH Concentration Profiles for 10% CFMFR Flame in 3m/s Cross-Flow at 25% Flame Length	252
5.11b	Soot and OH Concentration Profiles for 60% CFMFR Flame in 3m/s Cross-Flow at 25% Flame Length	252
5.12a	Soot and OH Concentration Profiles for 10% CFMFR Flame in 4m/s Cross-Flow at 25% Flame Length	253
5.12b	Soot and OH Concentration Profiles for 60% CFMFR Flame in 4m/s Cross-Flow at 25% Flame Length	253
5.13a	OH PLIF Image for 10% CFMFR at 2 m/s cross-flow	254
5.13b	OH PLIF Image for 20% CFMFR at 2 m/s cross-flow	254
5.13c	OH PLIF Image for 60% CFMFR at 2 m/s cross-flow	255
5.13d	OH PLIF Image for 100% CFMFR at 2 m/s cross-flow	255
5.14a	OH PLIF Image for 10% CFMFR at 3 m/s cross-flow	256
5.14b	OH PLIF Image for 20% CFMFR at 3 m/s cross-flow	256
5.14c	OH PLIF Image for 60% CFMFR at 3 m/s cross-flow	257
5.14d	OH PLIF Image for 100% CFMFR at 3 m/s cross-flow	257
5.15a	OH PLIF Image for 10% CFMFR at 4 m/s cross-flow	258
5.15b	OH PLIF Image for 30% CFMFR at 4 m/s cross-flow	258
5.15c	OH PLIF Image for 60% CFMFR at 4 m/s cross-flow	259
5.15d	OH PLIF Image for 100% CFMFR at 4 m/s cross-flow	259

Chapter VI

6.1a	Temperature Results Comparison of Different Grid Sizes for a Benchmark Solution at a Line at Symmetry Plane	284
6.1b	Comparison of Benchmark Problem and Solution From the Model	285
6.2	Temperature Results Comparison for Different Grid Sizes After Grid Adaptation with Different Temperature Gradients for a Benchmark Solution at a Line On Symmetry Plane	286
6.3a	Boundary Conditions and Dimensions of the Domain	288
6.3b	Initial Before Grid Adaptation for All Cases (a), and Grid for 100% CFMFR After grid Adaptation at the Symmetry Plane	289
6.4	After Adaptation Grid for 100% CFMFR Quiescent Flame Study in 2-D	290
6.5a	Comparison Results of Flame Temperature for Both Numerical and Experimental for 100% CFMFR Flame in Quiescent Condition at Three Flame Locations	291
6.5b	Comparison Results of Flame Temperature for Both Numerical and Experimental for 60% CFMFR Flame in Quiescent Condition at Three Flame Locations	292
6.5c	Comparison Results of Flame Temperature for Both Numerical and Experimental for 30% CFMFR Flame in Quiescent Condition at Three Flame Locations	293
6.5d	Comparison Results of Flame Temperature for Both Numerical and Experimental for 10% CFMFR Flame in Quiescent Condition at Three Flame Locations	294
6.6a	Comparison Results of Flame O ₂ Volumetric Concentration for both Numerical and Experimental in (A) 100% and (B) 60% CFMFR Flame in Quiescent Condition	295
6.6b	Comparison Results of Flame O ₂ Volumetric Concentration for both Numerical and Experimental in (C) 30% and (D) 10% CFMFR Flame in Quiescent Condition	296
6.7a	Comparison Results of Flame CO ₂ Volumetric Concentration for both Numerical and Experimental in (A) 100% and (B) 60% CFMFR Flame in Quiescent Condition	297
6.7b	Comparison Results of Flame CO ₂ Volumetric Concentration for both Numerical and Experimental in (C) 30% and (D) 10% CFMFR Flame in Quiescent Condition	298
6.8a	Comparison Results of Flame CO Volumetric Concentration for both Numerical and Experimental in (A) 100% and (B) 60% CFMFR Flame in Quiescent Condition	299
6.8b	Comparison Results of Flame CO Volumetric Concentration for both Numerical and Experimental in (C) 30% and (D) 10% CFMFR Flame in Quiescent Condition	300
6.9a	X-Z Plane Temperature Profile at 2 m/s Cross-Flow Condition	301
6.9b	X-Z Plane Temperature Profile at 2.5 m/s Cross-Flow Condition	301
6.9c	X-Z Plane Temperature Profile at 3 m/s Cross-Flow Condition	302
6.9d	X-Z Plane Temperature Profile at 3.5 m/s Cross-Flow Condition	302
6.9e	X-Z Plane Temperature Profile at 4 m/s Cross-Flow Condition	303
6.10	Comparison of In-Flame Temperature for Model and Experimental Results At 2.0m/s Cross-Flow at the Three Flame Locations	304

6.11	Comparison of In-Flame Temperature for Model and Experimental Results At 3.0m/s Cross-Flow at the Three Flame Locations	305
6.12	Comparison of In-Flame Temperature for Model and Experimental Results At 4.0m/s Cross-Flow at the Three Flame Locations	306
6.13	Comparison of In-Flame O ₂ Concentration for Model and Experimental Results At 2.0m/s Cross-Flow at the Three Flame Locations	307
6.14	Comparison of In-Flame CO ₂ Concentration for Model and Experimental Results At 2.0m/s Cross-Flow at the Three Flame Locations	308
6.15	Comparison of In-Flame CO Concentration for Model and Experimental Results At 2.0m/s Cross-Flow at the Three Flame Locations	309
6.16	Comparison of In-Flame OH Concentration for Model and Experimental Results At 2.0m/s Cross-Flow, 60% CFMFR at 25% of the Flame Length	310
6.17	Comparison of In-Flame O ₂ Concentration for Model and Experimental Results At 3.0m/s Cross-Flow at the Three Flame Locations	311
6.18	Comparison of In-Flame CO ₂ Concentration for Model and Experimental Results At 3.0m/s Cross-Flow at the Three Flame Locations	312
6.19	Comparison of In-Flame CO Concentration for Model and Experimental Results At 3.0m/s Cross-Flow at the Three Flame Locations	313
6.20	Comparison of In-Flame OH Concentration for Model and Experimental Results At 3.0m/s Cross-Flow, 60% CFMFR at 25% of the Flame Length	314
6.21	Comparison of In-Flame O ₂ Concentration for Model and Experimental Results At 4.0m/s Cross-Flow at the Three Flame Locations	315
6.22	Comparison of In-Flame CO ₂ Concentration for Model and Experimental Results At 4.0m/s Cross-Flow at the Three Flame Locations	316
6.23	Comparison of In-Flame CO ₂ Concentration for Model and Experimental Results At 4.0m/s Cross-Flow at the Three Flame Locations	317
6.24	Comparison of In-Flame CO Concentration for Model and Experimental Results At 4.0m/s Cross-Flow, 60% CFMFR at 25% of the Flame Length	318
6.25	3-D Plot of 100% CFMFR Flame at 2 m/s Cross-Flow	319
6.26a	100% CFMFR Flame x-y Plane Temperature Profiles at 2 m/s Cross-Flow for Three Flame Locations	320
6.26b	60% CFMFR Flame x-y Plane Temperature Profiles at 2 m/s Cross-Flow for Three Flame Locations	320
6.27a	100% CFMFR Flame x-y Plane Temperature Profiles at 3 m/s Cross-Flow for Three Flame Locations	321
6.27b	60% CFMFR Flame x-y Plane Temperature Profiles at 3 m/s Cross-Flow for Three Flame Locations	321
6.28a	100% CFMFR Flame x-y Plane Temperature Profiles at 4 m/s Cross-Flow for Three Flame Locations	322
6.28b	60% CFMFR Flame x-y Plane Temperature Profiles at 4 m/s Cross-Flow for Three Flame Locations	322

Abstract

An experimental and numerical study of a turbulent smoke point diffusion flame in a quiescent and cross-flow condition was performed. The fuel mass flow rate of a turbulent smoke point flame was determined at a quiescent condition and in cross-flow with velocity ranging from 2 to 4 m/s. This fuel mass flow rate is defined as the Critical Fuel Mass Flow Rate (CFMFR). The fuel used in this study was propylene and the burner jet diameter of 3.2 mm ID was used. The jet range of Reynolds number for quiescent condition was 2511 to 24981; at 2m/s cross-flow, the Reynolds number and Flame Froude number range was 1136 to 12614, and 3.17 to 2.85; at 3m/s cross-flow, the range was 1032 to 12036 and 3.71 to 3.88; at 4 m/s cross-flow, the range was 760 to 10501 and 2.12 to 4.32. At a fuel mass flow rate below the CFMFR the flame produces smoke. In the dilution study, an amount of inert gas (nitrogen) was added to the fuel stream to achieve the smoke point condition for ten different fractions of CFMFR. From this dilution study, three regions were defined, the chemically-dominated region, transition region, and momentum-dominated region. The first objective of this study was to determine the factors behind the distinction of these three regions. The second objective was to understand the effect of cross-flow velocity on the smoke point flame structure. The flame temperature, radiation, geometrical dimension of flame, velocity, and global emissions and in-flame species concentration were measured. Laser Induced Incandescence (LII) was used to measure the soot concentration and Laser Induced Fluorescence (LIF) was used to measure the OH concentration. The third objective was to study a numerical model that can simulate the turbulent smoke point flame structure. A standard κ - ϵ model was used to calculate the flow characteristics and a mixture-fraction

equilibrium method was used to simulate the chemistry of combustion process. A probability density function was used to compute the interaction of the turbulence and chemistry of the flame.

The dilution study showed that the flames in quiescent condition and in the 3.5 and 4 m/s cross-flow condition had the chemically-dominated region at 5% to 20% CFMFR, the transition region at 20% to 40% CFMFR, and the momentum-dominated region at 40% to 100% CFMFR. On the other hand, the flame in cross-flow of 2 to 3 m/s showed the chemically-dominated region at 5% to 10% CFMFR, the transition region at 10% to 30% CFMFR, and the momentum-dominated region at 30% to 100% CFMFR. The chemically-dominated flame had a sharp dual-peak structure for the flame temperature, CO₂ and NO concentration profiles at 25% and 50% flame length. However, the momentum-dominated region flame exhibited a dual peak structure only at 25% flame length. The decrease of flow rate from 30% to 10% CFMFR showed an increase of flame length. The LII study showed that the soot concentration increased with the decrease of the turbulence intensity in the momentum dominated region (tested on the 100% and 60% CFMFR). On the other hand, from the transition region to the chemically-dominated region, the soot concentration showed a decrease, which exhibited the opposite behavior of the 100% to 60% CFMFR flames. Hence, the jet momentum had the least effect in the chemically-dominated region. The comparison of the OH and soot concentration profiles shows that OH dominates the soot oxidation process for a chemically-dominated region flame. However, the momentum-dominated flame showed that OH dominated the soot oxidation process only in the near-burner region (~25% of the flame length), and most of the flame soot oxidation process was dominated by O₂

concentration. The division of the dominance of OH (whose production is dependent on chemical reaction rate) and O₂ (whose concentration in the flame is mainly dependent on diffusion rate) in oxidizing the soot are the prominent factors behind the distinction of the three regions.

The cross-flow velocity had a non-monotonic effects on the flame. The evidences could be observed from the flame length and the soot concentration results. The flame length showed a decrease when the cross-flow velocity increased from 2 to 3 m/s. However, the flame length increased when the cross-flow velocity was increased from 3.5 to 4 m/s. The flames in cross-flow velocities of 3.5 and 4 m/s behaved like a co-flow flame, which caused the decrease of mixing rate, and the increase of flame length. The overall soot concentration showed a decrease for the flames at 2 m/s to 3 m/s cross-flow velocity. However the flame at 3 to 4 m/s cross-flow showed an increase of overall soot concentration.

The numerical model was fairly adequate in qualitatively predicting a smoke point turbulent diffusion flame structure in a cross-flow and quiescent condition. The model failed in the prediction of a laminar flame. The model showed a good agreement between experimental and numerical results for O₂ concentration and flame temperature. The numerical CO₂ concentration results showed a good agreement with the experimental results for most of the cases. However, CO concentration was over predicted in the high equivalence ratio region because of the presence of soot in the experimental flame (which was not considered in the numerical model) and the inadequacy of the equilibrium model in predicting CO.

Chapter I

Introduction and Objectives

The main purpose of this study was to investigate the reason behind the distinctions of the momentum and chemically dominated regions of turbulent flames near smoke point. The study was approached through conventional experimental methods and laser diagnostics. Furthermore, a computational model was also used to numerically study the flames in quiescent and cross-flow conditions at smoke point condition. This thesis consists of seven chapters and three appendices.

Chapter II contains the literature review of the pertinent topics. The definition of smoke point, the momentum and chemically dominated regions are explained in this chapter. The soot formation and oxidation processes, and a brief explanation of the methodology used to investigate the processes are also discussed in this chapter.

In Chapter III, the critical fuel mass flow rate (CFMFR) at the smoke point of the flame is first defined. The results of the CFMFR for all the experimental conditions are presented. Then, the results of nitrogen gas dilution study on propylene flames at the different fractions of CFMFR are presented. From the dilution study result, the chemical-dominated, momentum-dominated and transition regions are defined. A series of conventional analytical methods were used to characterize the smoke point flame. The results include the temperature, global and in-flame species concentrations (O_2 , CO , CO_2 , NO , and NO_x), soot concentration, velocity, flame height, and flame radiation. Also, the dilution effect of different inert gases was also investigated.

Chapter IV focuses on the investigation of the soot concentration distribution of the smoke point flame for both in the momentum and chemically dominated regions.

Laser Induced Incandescence (LII) was used for the soot concentration study. A brief introduction of LII modeling is discussed in this chapter to provide an understanding of the soot particle heating process by a laser. Then, a literature review of the LII method is also summarized in a table to show the wide applications of LII method. A review of this literature facilitated the development of an optimized way to apply LII for the soot concentration measurement. Then, the LII signal was calibrated with the known soot concentration results from literature. The soot concentration measurement was performed in quiescent and three selected cross-flow conditions at three flame locations. The results and discussions of the soot concentration distribution provide an understanding of the distinction of the two regions.

The OH concentration measurement with Laser Induced Fluorescence technique (LIF) of the smoke point flame is discussed in Chapter V. The modeling of the OH measurement methodology is first discussed, and then followed by the OH Laser Induced Fluorescence (LIF) signal modeling. The OH and soot concentration results were put together to delineate the dominant soot oxidation mechanism. The discussions provide an understanding of the soot process in the momentum and chemical dominated regions.

The numerical modeling of the smoke point flame is presented in Chapter VI. The flow modeling, the energy equation and the PDF modeling for the combustion process are first discussed. Then, the boundary conditions, the grid generation and validation, and converging criteria for the study are presented. The comparison of the experimental and the numerical results is then presented in a later section. Finally, the effectiveness of the numerical model in modeling the flame is discussed.

The overall discussion and conclusion are presented in Chapter VII. In this chapter, the inferences on the distinction of the momentum and chemically domination are drawn based on the evidence and results provided in the previous chapters. The cross-flow effect on the smoke point flame is also discussed in this chapter. A few recommendations for future numerical and experimental research are presented in the last part of the chapter.

Appendix I is the LII signal correction program. Appendix II shows an example of the uncertainty calculation, and Appendix III shows the sample calculation of some of the important parameters.

Chapter II

Literature Review

2.1 Introduction

Concern about the possible environmental impact caused by flare stacks has initiated much research. A flare produces highly turbulent diffusion flame in cross-flow (TDFCF). Flares are often used in petroleum refineries or chemical plants. Sometimes the flares extend up hundreds of feet during plant shuts down or some other operations. Large amounts of smoke may be released from the flare due to incomplete combustion. It is well known that smoke and soot particles associated with it are hazardous to humans and other living organisms. Death from lung cancer and cardiopulmonary disease are related to air pollution. Small particles with a diameter equal to or smaller than $2.5\text{ }\mu\text{m}$ are a potential risk to health because they are likely to be of higher toxicity than larger particles and they can penetrate deeper into the cardiopulmonary system (Miller et al., 1979). Hence, investigations have to be performed to optimize the combustion process to minimize the emission of pollutants. The combustion characteristics of flare stacks are very complex due to the interaction between an uncontrolled environment (wind or cross-flow) and the varying composition of the hydrocarbon fuel and other gases that leave the stack.

2.2 Smoke Point

Smoke is a cloud of soot particles that escape unburned. A diffusion flame produces smoke over a wide range of fuel flow rates. Above or below this flow rate the

flame does not smoke. A laminar diffusion flame with an initial fuel flow rate that does not produce smoke will eventually emit smoke if the fuel flow rate is increased to a critical point. The increase of fuel flow rate increases its residence time in the flame, which allows a larger concentration of soot. Soot particles will eventually grow by coagulation and some other factors that will be addressed in the following section. The higher soot concentration of the flame increases radiation losses, which leads to a cooler flame (Kent and Wagner 1984). Flame temperature plays a key role in soot production and oxidation process (which will be explained in the soot formation section). Then, a further increase of fuel flow rate will transform the laminar flame to a turbulent flame. Subsequently, the flame stops producing smoke if the flow rate is increased to a certain critical point. Hence, there are two smoke points for a diffusion flame. There has been extensive research on the first smoke point in the laminar flame region, where the flame just starts to smoke, but there are only a few studies on the second smoke point in the turbulent region.

A well-accepted definition of flame smoke point is the condition just before soot escapes unburned from a laminar flame. Alternately, Roper and Smith (1979) define smoke point as the condition at which the soot oxidation would become negligibly small. Due to some complications in the experiment to determine the smoke point (laminar flame) performed by Glassman and Yaccarino (1980), their definition of smoke point was the condition where the ‘wings’ (due to soot breakthrough) reach the same height as the corresponding flame apex. Although there are several methods to determine smoke points of laminar diffusion flames (Kent and Wagner, 1984; Roper, 1984; Glassman and Yaccarino, 1981), there is hardly any literature concerning the method to determine the

turbulent flame smoke point. Hence, the objective of the author and co-workers was to develop a technique to determine the smoke point of turbulent diffusion flames and to characterize the sooting properties of selected hydrocarbon fuels (propylene, ethylene and propane).

The author and collaborators have done an extensive study on turbulent smoke point in quiescent and cross-flow conditions. In previous studies, (Goh, 1999) the relation of the smoke point with the mass flow rate of fuels and the mass flow rate of nitrogen were established for three different fuels, three different burners, and a set of cross-flow conditions. Besides, mass flow rate results (CFMFR and dilution), the total flame radiation, and the profiles of radiation, temperature, soot and pollutants were also obtained.

From the results of the mass flow rate required to attain the smoke point, two distinct regions were discovered. These two regions were labeled Region I and Region II. To provide an understanding of these two regions, let us examine the results of one of the cross-flow smoke point experiments of an ethylene diffusion flame in 2.68 m/s cross-flow in Figure 2.1 (Goh, 1999). The results are presented in the form of the variation of the critical fuel mass flow rate versus the mass flow rate of nitrogen required to be added to the fuel to achieve the smoke point. The critical mass flow rate (CFMFR) is defined as the mass flow rate of the pure hydrocarbon fuel at the smoke point of its attached flame. In fact, all the smoke point results showed similar trends, where the nitrogen flow rate rose from zero at the 100% critical mass flow rate, attained a maximum value at a certain fraction of the critical flow rate, and then decreased to zero at the zero fuel mass flow rate. Smoke emission from diffusion flames basically depends on the soot formation and

burnout processes occurring in the flame. Both these processes are functions of the soot-precursor species concentrations, temperature distribution, soot trajectories, and residence time of the soot particles in the flame field. In a diffusion flame, if soot concentration increases with residence time, the chemical control is more important; on the other hand, if the residence time does not change, diffusion control is more important (Kent and Wagner, 1984). Both these distinct processes were exhibited in all the results. Region I is defined as the region on the right of the maximum value and Region II as that on the left.

In Region I, the amount of nitrogen needed to achieve smoke point increased with decreasing fuel mass flow rate. As the fuel mass flow rate was decreased, the fuel jet velocity and consequently the air entrainment into the flame also decreased, the latter at a higher rate than the former. Thus, in order to meet the smoke point condition, (completely suppress smoke liberation) more nitrogen was needed to intensify the flame turbulence and air-fuel mixing rate. Hence, it can be concluded that this region was fluid-dynamics-controlled or it may be described as a momentum-dominated region. In Region II, the amount of nitrogen supplied decreased with a decrease in fuel mass flow rate. In the study by Glassman and Yaccarino (1980), nitrogen was added to the fuel to alter the flame temperature. They found that increasing nitrogen mass flow rate could reduce flame temperature. The lower the flame temperature, the lower was the flame tendency to smoke. This was because the fuel pyrolysis process was dependent strongly upon the flame temperature; the lower the temperature, the lower the rate of pyrolysis reactions. Hence, Region II was a chemical reaction dominated region. The temperature data of the smoke point study can be found in Kusadome (1999).

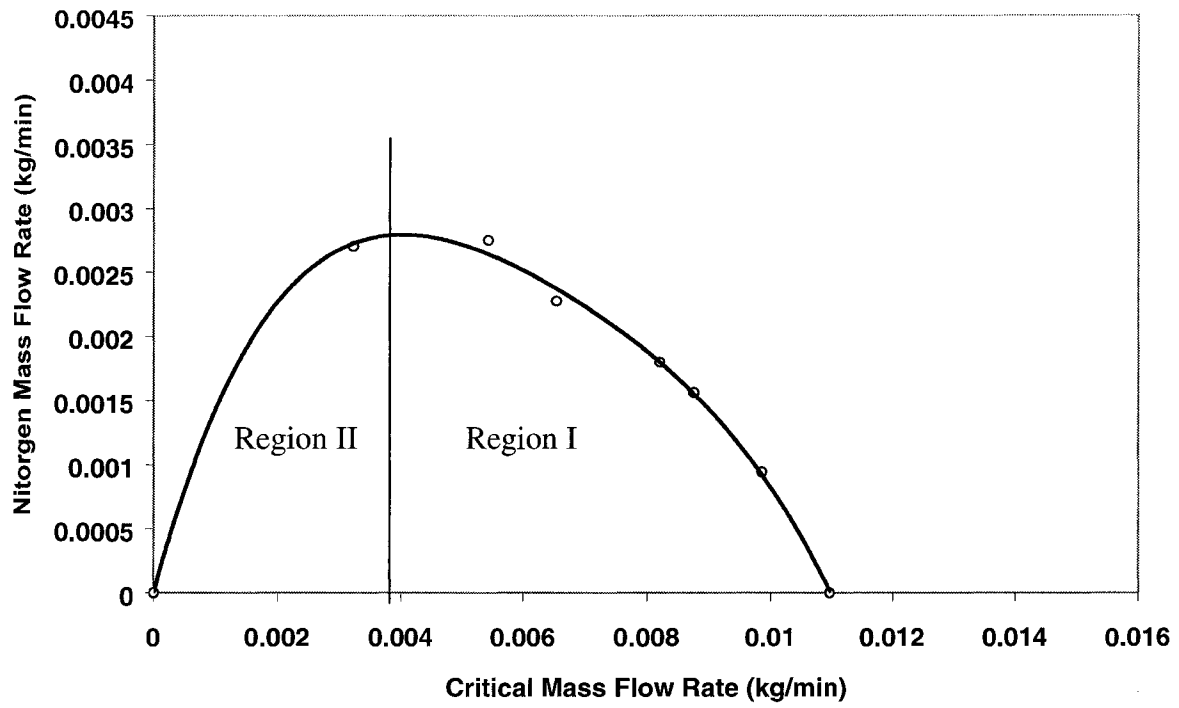


Figure 2.1 Comparison for Critical Fuel Mass Flow Rate Versus Nitrogen Mass Flow Rate in an Ethylene Gas Diffusion Flame at 2.68 m/s Cross-Flow Condition for 3.2 mm ID Burner

2.3 Soot Formation Process

The smoke emission from a diffusion flame depends on the soot formation and its burnout process. The soot formation process has been studied over the years. Due to the complexity of the process, it is still a subject of research. The process depends on the temperature distribution, residence time, species concentration, and soot particle trajectories (Kent and Wagner, 1984). The soot formation process in a diffusion flame can be characterized by four steps. They are the formation of soot precursor species, particle inception, surface growth and particle agglomeration, and particle oxidation. (Turns, 1996)

During the fuel pyrolysis process, various types of small molecular weight hydrocarbons are formed, particularly acetylene (C_2H_2). These small hydrocarbon molecules react with each other and form unsaturated (radicalic) hydrocarbons. When this hydrocarbon, which is known as the precursor, contains a sufficiently large number of carbon atoms, it undergoes cyclization to form an aromatic ring. (Glassman, 1988) The aromatic ring structure grows by the addition of an alkyl group, especially, acetylene. This aromatic ring is commonly known as polycyclic aromatic hydrocarbon (PAH). These PAH are normally the size of 0.5 nm (Bockhorn, 1994) or carry the weight of 500-1000 amu (atomic mass unit) (Richter and Howard 2000).

Ultimately the PAH attains a sufficient size to form nuclei (2000 to 10000 amu) or with an effective diameter of 1.5 nm (Richter and Howard 2000). This condensed phase carbon particle contains a high quantity of hydrogen atoms. Then, at high temperature, the particles dehydrogenate. At the same time, it also goes through a coagulation process by absorbing gaseous hydrocarbon species both physically and

chemically. Then, the particles become carbonaceous soot structure by undergoing chemical reformation (Glassman, 1988). The soot particles continue to be exposed to the species from the pyrolyzing fuel as they travel through the flame, and undergo surface growth and agglomeration. Simultaneously, the particles also experience oxidation from some gaseous product, like OH. In a diffusion flame, most of the oxidation of soot particle proceeds mainly at the region close to the flame tip. The reason is that soot particles normally are formed interior to the reaction zone lower in the flame, and follow the streamlines in the flame which do not cross the reaction zone until the region close to the flame tip (Turns, 1994). However, the chemistry of the soot formation process is similar regardless of the initial condition (fuel types, premixed or diffusion) (Palmer and Cullis, 1965).

In a premixed flame, the precursor formation rate is inversely related to the temperature. The precursor formation process has to compete with the oxidation precursor process mainly by the OH radicals. In the premixed flame study by Milliken (1962), the oxidation rate increases faster than the formation rate of the precursor with the increase of flame temperature. On the other hand, in a diffusion flame, the oxidation attack on the precursor is very small. The higher the temperature the greater is the pyrolysis rate and the precursor formation rate, and this leads to a higher rate of incipient soot formation rate. The radical diffusion process is also important in a diffusion flame, especially the H radical which can accelerate the pyrolysis reaction in a fuel rich region (Glassman, 1988).

In a buoyancy-controlled flame, the residence time of an element is in square root relation with the flame height or volumetric flow rate (Roper, 1977). As a result, the

increase of the volumetric flow rate increases the time for the pyrolysis process and this causes the increase of the flame-sooting tendency. On the other hand, for a momentum-controlled laminar flame, the flame height is directly proportional to the volumetric flow rate or the velocity of the jet. Hence, the sooting tendency for a momentum-controlled flame would be unchanged with the increase of the volumetric flow rate (Glassman 1988).

Generally, soot formation in a diffusion flame happens in the temperature range of $1300\text{ K} < T < 1600\text{ K}$ (Smyth et. al, 1985; Turns, 1996). For all different type of fuels, the initial detection of the soot particle takes place at the centerline of the flame when the flame temperature reaches $1350 \pm 35\text{ K}$ (Glassman, 1988). On the other hand, soot ceases to oxidize at temperatures below 1300 (Kent and Wagner, 1984). Besides the temperature factor, the soot formation and oxidation are also determined by the local effective C/O ratio, the local hydrocarbon concentrations, and the residence time of the particle both in the soot forming region and oxidation region (Wagner, 1978).

Although the sooting characteristics of a diffusion flame are dominated by the chemistry of the fuel pyrolysis and fuel structure, the chemistry of soot formation is independent of the initial condition. This essentially means that the chemistry for soot formation is the same for all fuel and flame conditions (premixed or not), but the reaction rate is dependent on the fuel type and flame condition. The reason is that the rate of formation of an initial aromatic ring structure is dependent on the fuel type. Then, the next step of reaction is the formation of a larger aromatic ring, which leads to soot nuclei. The concentration of incipient soot formation particles determines the total amount of

soot formed in the flame. Hence, the rate of formation of the initial ring controls the overall soot formation rate (Glassman, 1988).

Smyth and Miller (1987) proposed that the fundamental soot precursor formation process consists of these mechanisms: ions (Kern, et. al 1988), ring growth (Crittenden and Long 1973), polyacetylene chains (Homann and Wagner, 1967), and neutral radicals (Benson, 1987) and Glassman (1988) added Diel-Alder reactions. This is a comprehensive mechanism based upon the dependence of soot precursor growth on neutral radicals. There are high and low temperature branches in this general mechanism, so this mechanism can be applied to a wide variety of combustion conditions. In this mechanism, acetylene (C_2H_2) and H play an important role through many of the reaction steps. There are three proposed routes for pyrolysis products to form a benzene molecule. A benzene molecule eventually loses a hydrogen atom and becomes a phenyl radical (C_6H_5), which is the main element to form a precursor. The first route is the reaction of acetylene to the n-butadienyl radical (C_4H_5) to form benzene. The second route is the reaction of vinyl radical added to the vinyl acetylene, which reacts with C_2H_3 to form benzene. The third route is through species allene and its isomer methyl acetylene, which by losing one hydrogen atom reacts with each other to form benzene. There is also another possible reaction step that contributes to the formation of a phenyl radical, which is the reaction of vinyl acetylene radical with acetylene to become a linear C_6H_5 chain. This linear C_6H_5 eventually forms a ring phenyl radical. The phenyl radical reacts with acetylene to form phenyl acetylene. In the latter reaction steps, acetylene continues to contribute to the process until the precursor is formed. The reaction routes are shown in Figure 2.2. In the McKinnon and Howard (1992) study, both experimental and numerical

investigations show that acetylene contributes most of the mass to a soot system through both the formation of PAH and also through direct addition to the soot particle. Acetylene is pyrolysed at a relatively low temperature range, 893-1019 K (Xu and Pacey, 2001). Hence, the role of acetylene and H in soot formation is very critical. After the precursor is formed, it travels along the streamline and continue to react with other PAH until it reaches a sufficient size to become a nucleus (3000 to 1000 atoms). This fundamental unit of the soot nucleus has a spherical shape with diameter of 10-50nm (Walker et al., 1966).

2.4 Soot Oxidation Process

Throughout the streamline, the particle continues the agglomeration process both physically and chemically with other particles or hydrocarbon molecules. The particle also bonds by shared carbon decomposition to form loose particles of 0.1-1 μm size. At the same time, the particle also undergoes an oxidation process. The participants of carbon oxidation are O_2 and the O and OH radicals in the Cavaliere et al. (1994) study. Beside these species, H_2O , CO_2 and NO_2 also oxidize and gasify soot, and other than the radicals O and OH, NO_2 is the most reactive at low temperature (Stanmore et al., 2001). OH radical is a very effective carbon oxidant for a wide range of temperatures. Furthermore, the activation energy with this reagent, which is 11 kJ/mol (Roth et al. 1998), is also very low. However, near the flame axis, the oxidant (O_2 or OH) concentration is low and the soot particle has to compete with other hydrocarbons for the oxidant. At a temperature below 970 K, CO is the primary product from the soot oxidation. Nevertheless, above 970 K CO starts to be oxidized to CO_2 and it reaches the

complete conversion at region 1070 K (Marcucilli et al. 1994). Most oxidation of soot takes place near the flame tip, where the condition is similar to a premixed particle flame (Roper et. al, 1977). The surface oxidation rate of the soot particle in the presence of O₂ is similar to graphite oxidation (Ubhayakar, 1976). The reaction process of O₂ on the carbon can be both absorption and desorption (Stanmore et al. 2001). Desorption reaction is more common than absorption reaction. The activation energy for desorption for the step, which releases CO, is 285 kJ/mol and CO₂ is 335 kJ/mol (Du et al. 1990). Absorption reaction only occupies <5% of the surface sites (De Soete, 1988). Every O₂ absorption step is accompanied by the release of a molecule CO or CO₂, through the reaction $-C+O_2 \rightarrow -C(O) +CO, CO_2$. Many turbulent diffusion flame studies (Magnussen, 1975; Dazell et al., 1970) have found that the soot mass concentration increases along the flame axis, and decreases rapidly by oxidation at a height of 80 to 100 burner diameters from the burner. The soot concentration field in the turbulent flame is basically mixing-controlled (Becker, 1977).

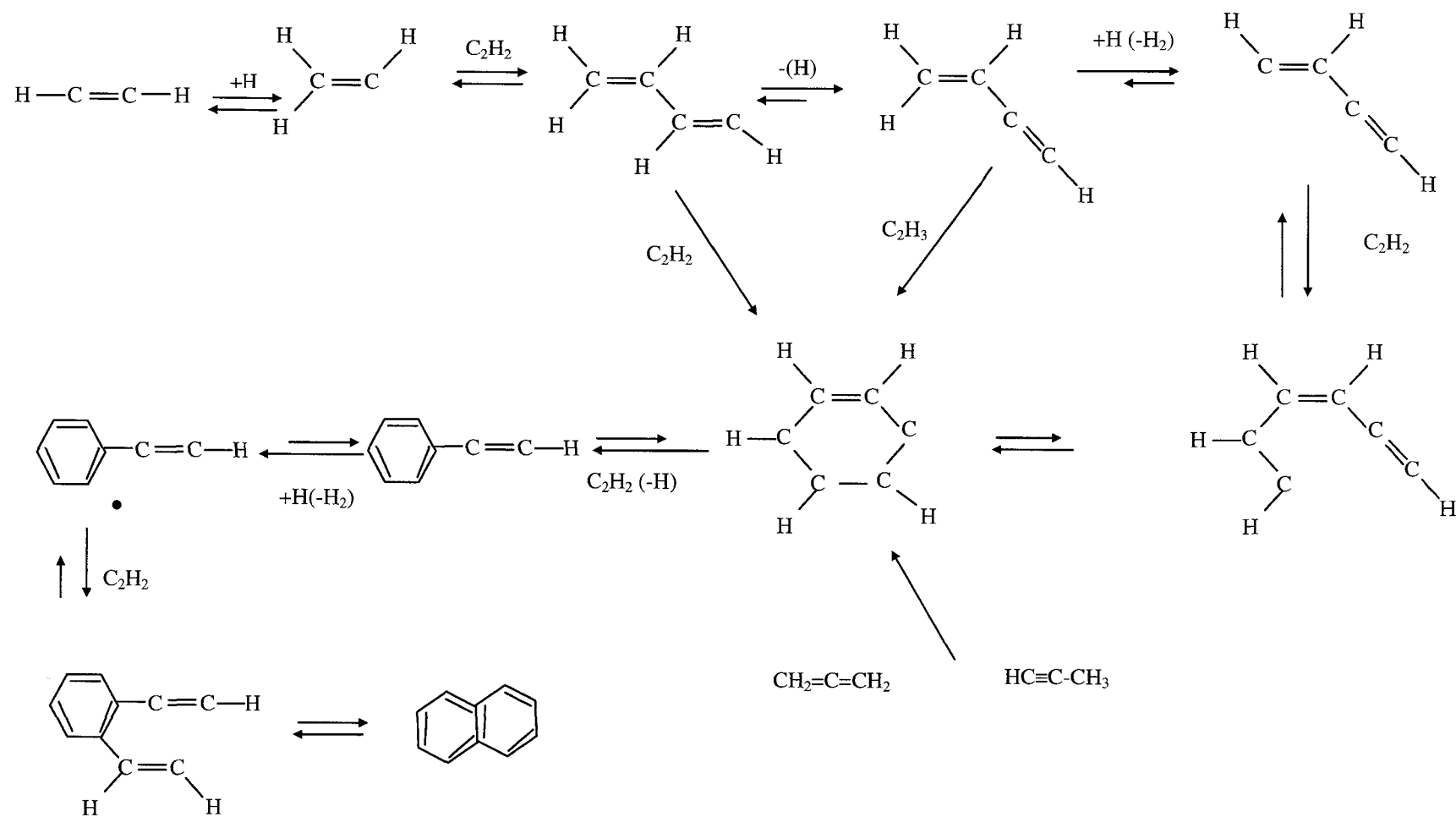


Figure 2.2 General Reaction Route for PAH Ring Formation.

2.5 Soot Formation Investigation

Research on the soot formation process is important because it provides the knowledge of how to control or limit the soot production. The complex nature of soot formation, which depends on the combustion process has made the characterization of a single parameter that defines the amount soot formed per unit mass of fuel impossible.

There is a similar finding between the smoke point research done by Goh et al. (1999) and the soot formation research done by Axelbaum and Law (1990) and Axelbaum et al. (1988). These groups studied the temperature and the dilution effects in co-flow and counter-flow environments respectively. Their studies identified the relative importance of fuel concentration dilution and flame temperature reduction on soot formation when inert gases were added to fuel. They found that temperature effects dominated the soot formation rate when large amounts of inert gases were added into the diffusion flame. At some other conditions, when moderate amounts of inert gases were added into the flame, the temperature reduction was small, but the fuel dilution effect on the soot production was significant. This agrees with Goh's (1999) findings and speculations in the chemically dominated region where the proportion of inert addition was considerably large and in the momentum dominated region where the dilution addition was considerably small. There are two explanations for these phenomena. First, the addition of inert gas may reduce the flame temperature, especially in the near burner region. The reduction of flame temperature will lower the reaction rate (especially fuel pyrolysis) until the reaction ceases, which may result in flame blow-off. The second explanation is that the dilution of inert gas may reduce the possibility for the fuel

molecules to react with oxidation agents until there is an insufficient reaction rate to produce a flame, thus the flame would destabilize.

Axelbaum and Law (1990) have provided a preliminary insight into the soot formation rate of laminar diffusion and counter-flow flames, but presently, there is no published research related to soot formation rate in complex turbulent diffusion flames, particularly a turbulent diffusion flame in cross-flow (TDFCF). Furthermore, the need for verification of the arguments that the author has on the two regions (Region I and Region II) also motivates a further investigation of soot growth rate in cross-flow flames. Hence, the objective of this research is to investigate the soot growth rate in TDFCF, and explore the possibility of developing an empirical relation of soot growth rate with some related parameters, like momentum flux ratio and fuel and diluent mass flow rate. The reason for focusing the study on soot surface growth rate is that soot surface growth, rather than nucleation has been found to dominate soot mass yield (Harris and Weiner, 1984; Megaridis and Dobbins, 1989; Sunderland and Faeth, 1996; Sunderland et al., 1995). Hence, by knowing the surface area of the soot at each location, a model of soot growth rate may be formulated from experimental results. In fact, in many theoretical models that characterize soot growth, the soot surface area growth is an essential parameter. So, soot mass addition rate will depend upon the total surface growth rate in addition to the number of potential reactive sites (Howard, 1990).

2.6 Soot primary size measurement

Sunderland et al. (1995) demonstrated in their experiments with laminar jet diffusion flames, that soot nucleation ceased roughly at an equivalence ratio less than 1.7.

Since a large part of the flame has an equivalence ratio of less than 1.7 (Turns, 1996), soot nucleation dominates only for a small part of the flame. This fact also applies to turbulent diffusion flames because turbulent fuel-air mixing is higher than laminar mixing, leading to an equivalence ratio less than 1.7 in turbulent flames. Therefore, the behavior of soot surface growth rate is important for the study of smoke characteristics in a turbulent diffusion flame.

2.7 Purpose of LIF measurement

In fuel-rich hydrocarbon flames at 1700 to 1800 K, the soot particles are oxidized by OH radicals rather than by the larger concentration of CO₂ or H₂O (Millikan, 1962). This phenomenon has also been observed experimentally by Fenimore and Jones (1967). Hence, monitoring the concentration of OH radicals in a diffusion flame is one of the keys to understanding the soot oxidation process. On the other hand, OH is also a good indicator for the fuel-lean side of the reaction zone in diffusion flames. In many PLIF studies, OH fluorescence appeared as a thin strip, because OH occurs along the stoichiometric region between the fuel and the oxidizer flows. The OH, O₂ and soot concentration can provide valuable information of the influence of the momentum and chemical effect on the soot oxidation process.

Acetylene is considered to be a major soot growth species (Harris et al., 1986). Acetylene is pyrolysed at a relatively low temperature range, 893-1019 K. Most of the acetylene is in the fuel pyrolysis region and the residence time for the pyrolysis is around 23-451 ms (Xu and Pacey, 2001). Hence, in order to understand the formation rate and the destruction rate, the measurement should be done relatively close to the burner

region. In the molecular zone, acetylene can react with some radicals to form PAH or it can react with PAH to form a heavier PAH (Glassman, 1988; Prefferle et al., 1994). Hence, monitoring the acetylene concentration can provide crucial information about the soot formation rate.

As discussed in the previous paragraph, PAH molecules can coagulate and become nuclei for soot particles. PAH is also considered as an important group of species that contributes to increase of soot mass beside acetylene. PAH consists of hydrocarbon in many different type of molecular structure. Normally PAH size is in the range of 250 amu (light PAH) to three rings size or larger (heavy PAH) (McKinnon and Howard, 1992). For instance, some of the commonly known light PAH are naphthalene, acenaphthalene, and cyclpenta[cd]pyrene (Macadam et. al, 1996).

Chapter III

Flame Structure of Diffusion Flames at Smoke Point in Quiescent and Cross-Flow Environments

Nomenclature

$A_{f,frontal}$	Frontal area of the visible flame volume exposed to cross-flow
D_j or D	Jet diameter
Fr_{cf}	Froude number for cross-flow
Fr_f	Froude number for flame
g	Gravitational acceleration
V_f	Visible flame volume
v_j	Jet velocity
v_∞	Cross-flow velocity
ρ_∞	Ambient density
ρ_f	Flame density
ρ_j	Jet gas density

3.1. Introduction and Overview

Although Goh (1999) had performed the smoke point experiments with a burner with the same dimension (3.2 mm ID), the study to determine the smoke point had to be repeated for this project. The reason was the difference in the way hydrogen gas was introduced to attach the flame to the burner rim in the two studies. In the present study, hydrogen gas was mixed with the fuel gas. On the other hand, in Goh's earlier experiments, hydrogen gas was not mixed with fuel. Instead, in that study, a co-annular burner was used, where hydrogen flame supplied from the outer burner acted as a pilot flame to stabilize the hydrocarbon fuel flame. Hence, in the current study, the addition of hydrogen into the fuel increased the total jet momentum.

In this study, the effect of both the quiescent environment and the cross-flow at the smoke point condition were studied. For the establishment of baseline conditions, a study in quiescent conditions was conducted. In the quiescent condition, the smoke point for pure fuel and fuel with nitrogen dilution was studied. Besides nitrogen gas, other inert gases were also studied to compare the effects of the different types of inert gases at the smoke point. These gases were argon, carbon dioxide and helium.

In this study, the flame in a cross-flow was the main focus. In the cross-flow experiment, the smoke point for five different cross-flow conditions was studied. The cross-flow speeds ranged from 2 m/s to 4 m/s with an increment of 0.5 m/s.

In most conditions, the flame radiation and global pollutant emissions were measured. For a few selected conditions, the temperature, the species concentration, and the velocity profiles were also measured.

3.2 Experimental Facilities, Instrumentation and Procedures

3.2.1 Smoke Point Determination

The method of determining the smoke point was the same as employed by Goh (1999) for both the quiescent and the cross-flow conditions. At the quiescent condition, a laser beam was used as a means to determine the smoke point. A 5 mW He-Ne laser was used to generate a beam of 3 mm diameter and wavelength of 633 nm about 5 cm above the flame. The method of determining the smoke point involved observing the visibility of the attenuated laser beam just above the flame. When a flame started to smoke, the laser beam became visible due to the scattered radiation, and the intensity of the illumination of the laser beam was a function of the concentration of smoke. A viewing angle of about 15 degrees from the laser beam in the forward scatter mode was found to yield repeatable and sensitive results. The smoke point of the flame was determined when the laser beam just became visible as a continuous beam. The schematic of the experimental setup is shown in Figure 3.1.

The method of smoke point determination in cross-flow was also similar to the method used in the quiescent experiments as described above. Instead of just one laser beam line, a laser sheet was used. The laser sheet was more appropriate for two main reasons. First, the flame was highly turbulent, so the fluctuation of the flame covered a wide area; as a result, a point detection was not possible. Second, the exhaust gases were well mixed and diluted once they were carried downstream, causing the smoke particles to spread over a wide area. The same He-Ne laser was used in this cross-flow study. The laser beam passed through a cylindrical lens, so that the line beam could be spread into a laser sheet. The laser was mounted on a tripod, which could be moved vertically and

horizontally for the laser sheet to be located at a suitable location for smoke point detection. Similar to the laser beam method for the quiescent condition, the smoke point of the flame in cross-flow was determined when the laser sheet just became visible as a continuous sheet from its forward scattering. The schematic diagram of the setup is shown in Figure 3.4. The measured repeatability of this method is given in Table 3.3.

For both the quiescent and the cross-flow conditions, the CFMFR was first determined. With only the fuel (without the inert gas dilution) and a sufficient amount of hydrogen to attach the flame, the CFMFR was determined with the method mentioned above. Then, the fuel flow rate was set at ten different values. They were 90%, 80%, 70%, 60%, 50%, 40%, 30%, 20%, 10% and 5% of the CFMFR. At each of these fractions, an amount of inert gas was added to achieve the smoke point condition. In the quiescent condition, the comparisons of the amount of addition of different inert gases needed to suppress smoke for each fraction of CFMFR were performed. In the cross-flow condition, the CFMFR at each of the five cross-flow conditions was determined. Then, similar to the quiescent condition study, the ten settings of fuel flow rate were used for the dilution study. Only the nitrogen gas was used as the diluent in the cross-flow experiments.

Different Inert Gases Dilution Studies

The comparison study for the different inert gases at the smoke point condition was done after the CFMFR was determined. Nitrogen, argon, carbon dioxide and helium inert gases were used to compare their mass percentage in fuel diluent mixture needed to suppress smoke. For all the flames with the different inert gas dilution, the global flame

radiation and the flame height were measured. Only in the nitrogen gas diluted flames, the temperature and the in-flame species concentration profiles and the global emission characteristics were measured at the CFMFR and the three different fractions of CFMFR (60%, 30% and 10%). The reason for the selection of these three fractions will be explained in the following section.

Cross-Flow Studies

At each of the five cross-flow conditions, the CFMFR and the percentage of nitrogen dilution of the ten CFMFR fractions were determined. For all the cross-flow conditions and the CFMFR fractions, the global emissions of some pollutants were measured. At the cross-flow condition of 2 m/s, 3 m/s and 4 m/s, and the four selected CFMFR fractions, the temperature, the emission, and the velocity profiles were measured. The test matrix for both the quiescent and the cross-flow conditions is shown in Table 3.1. The reason that some fractions were chosen to do the profiles measurement is explained in this chapter in Section 3.3, the result section.

Table 3.1a Test Matrix for Quiescent Condition

CFMFR	Global Emission	Global Flame Radiation	Temperature Profile	Emission Profile	Soot Concentration Profile	Flame Height	Velocity Profile
100%	✓	✓	✓	✓	✓	✓	✓
90%	✓	✓				✓	
80%	✓	✓				✓	
70%	✓	✓				✓	
60%	✓	✓	✓	✓	✓	✓	✓
50%	✓	✓				✓	
40%	✓	✓				✓	
30%	✓	✓	✓	✓	✓	✓	✓
20%	✓	✓				✓	
10%	✓	✓	✓	✓	✓	✓	✓
5%	✓	✓				✓	

Table 3.1b Test Matrix for Cross-Flow Condition

Cross-Flow	2, 2.5, 3, 3.5, 4 m/s		2 and 3 m/s			4m/s		
CFMFR	Global Emission	Flame Length	Temperature Profile	Emission Profile	Velocity Profile	Temperature Profile	Emission Profile	Velocity Profile
100%	✓	✓	✓	✓	✓	✓	✓	✓
90%	✓	✓						
80%	✓	✓						
70%	✓	✓						
60%	✓	✓	✓	✓	✓	✓	✓	✓
50%	✓	✓						
40%	✓	✓						
30%	✓	✓				✓	✓	✓
20%	✓	✓	✓	✓	✓			
10%	✓	✓	✓	✓	✓	✓	✓	✓
5%	✓	✓						

3.2.2 Experimental Facilities

Combustion Chamber

For this study, a test combustion chamber available in the Combustion and Flame Dynamics Laboratory was used. The combustion chamber is shown in Figures 3.1 to 3.3. The vertical steel combustion chamber of 76 cm \times 76 cm cross-section and 143 cm height housed the burner at the center floor of the chamber. At the bottom of the chamber, a 16 cm diameter opening provided airflow into the chamber. A 36 cm diameter flow diverter plate was installed between the nozzle burner outlet and the base plate opening at a height of 10 cm to diffuse the incoming air flow in order to create almost quiescent air conditions within the chamber. Three of the walls were each fitted with a tempered plate glass window (20 x 145 cm) for optical access (laser and photography). The fourth wall was fitted with a slotted metal sheet for instrument access (quartz probe and thermocouple). The top section of the combustion chamber was opened to the atmospheric pressure through an exhaust duct. The ambient pressure in the laboratory was maintained slightly above the atmospheric pressure. Hence, the positive draft inside the chamber ensured that the combustion products were vented through the exhaust duct. Figure 3.1 also shows the setup for smoke point detection and the soot volume fraction measurement using the extinction/scattering method (Yagi and Iino, 1960). A He-Ne laser was used to determine the smoke point (Goh, 1999) and it was also used for the soot volume fraction measurement.

Wind Tunnel

A schematic of the vertical combustion wind tunnel is shown in Figure 3.4. The test section length was 76 cm and the cross-section was 35.6 cm X 35.6 cm. The coordinate system of the wind tunnel test section is indicated in Figure 3.5. Three side walls were fitted with the tempered glass for optical access, and the fourth was fitted with a slotted metal plate for introducing the probes and the burner. The slotted metal wall was also provided with access for adjusting the equipment or cleaning the windows. The slot was sealed during the experiment. All the three glass windows were cooled using a cooling fan on each side. The coordinate system is defined in Figure 3.5.

Two blowers and a suction fan were used to provide the airflow. The maximum flow in the test section was 4.3 m/s. The flow in the test section was relatively uniform. The velocity profiles at 3.4 m/s in X and Y direction in the cross section at the middle of the test section are shown in Figures 3.6a and 3.6b. There was less than 5 % variation (maximum or minimum to average velocity) at 3.4 m/s flow condition. The variation of the velocity in Z direction was also minor. The variation was approximately 7% (maximum or minimum to average velocity) and is shown in Figure 3.6c at a cross-flow of 3.5 m/s. At the lower velocity condition, the variation was smaller. Two screens were installed at the end of the flow settling section to provide a uniform flow before the air stream entered the turning duct section. This section consists of twenty 7.6 cm round diameter ducts. The turning ducts were used because they were proven to be more effective than the turning vanes. The opening areas of the ducts were adjusted to ensure that the flow at the exit of the ducts was relatively uniform. After the air exited from the

ducts, the flow passed through the another filter. This filter further reduced the flow fluctuation and provided a more uniform flow before the flow entered the contraction.

Fuel Supply Train

A burner diameter of 3.2 mm was used throughout the study. The fuel gas supply train consists of commercial grade propylene, nitrogen, and hydrogen cylinders, the pressure regulators, and a set of calibrated rotameters. Each cylinder was mounted with a multi-stage pressure regulator. Table 3.2 shows the gas composition. A set of two of ball-rotameters was used to measure the fuel and the nitrogen flow rates. These flow meters were calibrated with a wet test meter for each different gas. Before entering the burner, the fuel, the hydrogen and the nitrogen were mixed in a mixing chamber.

3.2.3 Experimental Instrumentation

Conventional Measurements of Pollutant Emission

Figure 3.2 shows the experimental setup for the flame pollutant emission measurements in quiescent conditions. Conventional analytical instrument and measurement methods were used to measure the emissions of NO, NO_x, CO and CO₂, and O₂. The gas sample from the flame products was collected and analyzed with four different analyzers. Two Rosemount Analytical (Model 880A NDIR), nondispersive infrared analyzers were used for the CO and CO₂ emission measurements. Oxygen concentration was measured using a MSA Catalyst Research MiniOX I polarographic sensor. The NO and NO_x concentrations were measured using a Thermo Environmental Instruments Model 42H chemiluminescent analyzer. For the global emission measurement, combustion products were collected through a cone. The gas sample was

collected at the end of the cone using a quartz probe that was connected to the measurement setup. For in-flame species concentration profile measurements, the quartz probe was inserted into the flame. The sampling of gas flow rate was regulated by a rotameter and was sent into the analyzers by an electrical pump. The sample gas was first chilled to remove the moisture and filtered to remove the particulate matter before it was pumped into the analyzers.

Flame Temperature Measurement

A type R (platinum/13% rhodium platinum) in-house-made thermocouple with wire diameter of 0.2 mm and bead diameter of 0.25 mm was used to obtain temperature measurements in the flame. The thermocouple was mounted on a linear traversing mechanism that was driven by a computer-controlled stepper motor. The collection of temperature data and the motion of the stepper motor were controlled by a data acquisition computer using a Strawberry Tree data sampling and QuickLog data acquisition and processing software. Temperature profiles were taken radially at three axial locations, 25%, 50% and 75% of the flame height. The collected thermocouple temperature data were corrected for radiative, convective, and conductive losses. The setup is shown in Figure 3.3.

Flame and Flow Velocity Measurement

The dynamic pressure of the flame and the flow in Z direction were measured using a pitot static tube and a barocel. The barocel reading output was connected to a DAQ system which was connected to a computer. The stepper motor, which drove a

traverse mechanism in X direction, was also connected to the DAQ and the computer. A Strawberry Tree software controlled the stepper motor movement and also collected the data from the barocel. The temperature results were used to correct the gas density with the ideal gas assumption at all the locations before the calculations of the velocity from the dynamic pressure were performed.

Flame Radiation Measurement and Flame Imaging

The flame radiation data were collected using a wide-angle (150 degree viewing angle) highly sensitive pyrhelimeter of absorptivity 0.96. The radiometer was mounted on a tripod at approximately the mid-height of the flame and far enough from it to satisfy the inverse-square law. The radiometer output readings were collected using the data acquisition system described above. The setup is shown in Figure 3.2.

The flame image was captured using a CCD camera with a shutter speed of 1/10000 s. The flame images were grabbed using a Matrox picture grabbing software. Then the flame height measurements were done offline, using Adobe Photoshop software on the captured flame images. The determined flame height for the quiescent condition was the length from the burner tip to the location where the flame appeared in contiguous white color (corresponding to CCD saturation). The cross-flow flame length measurement was similar to the quiescent method. The definition of the flame dimension for the quiescent and the cross-flow flame is shown in Figure 3.55. The flame length for cross-flow flame was measured vertically in Z direction from the tip of the flame where images showed contiguous white to the Z location where the burner was located, which is L_{Fz} in Figure 3.55. Both sides of the flame images from X and Y direction were taken.

All the dimensions illustrated on Figure 3.55 were critical for the calculation of the Froude number. The calculation of the Froude number will be discussed in Section 3.3.1. Three images were collected on each flame and five images were collected on one of the flames for uncertainty analysis. The uncertainty of the flame length and the flame height were shown in Table 3.3. Table 3.4 show the nominal testing condition and the range of the experimental parameters.

Table 3.2 Gas Compositions

Gas composition of vol. %			
	Propylene	Hydrogen	Nitrogen
Propylene	75.958		
Propane	20.518		
Methane	1.672		
Ethane	1.625		
Butane	0.226		
Hydrogen		99	
Nitrogen			99

Table 3.3 Experimental Uncertainties*

CFMFR	0.06 µg/min
N2 Flow rate	0.02 µg/min
Global Emission	
CO ₂	0.06 %
O ₂	0.06 %
Emission Index	
NO	0.057
NO _x	0.054
CO	0.000
Emission Profile	
NO	0.545 PPM
CO	0.080 PPM
CO ₂	0.08 %
O ₂	0.06 %
Temperature	24 K
Soot Concentration	4.09E-07 g/ml
Radiation	0.28 kW
Radiant Fraction	0.04
Flame Height	0.57 cm

*at 95% Confidence

Table 3.4 Nominal Condition and Experimental Parameters

Nominal Condition	
Ambient Air	
Humidity	50%
Temperature	292K
Pressure	100.6kPa
Jet Diameter	3.2mm ID
Quiescent	
Fuel Mass Flow Rate	0.62 - 17.32 g/min
Nitrogen Mass Flow Rate	1.32 - 4.11 g/min
Hydrogen Mass Flow Rate	0.08 - 67 g/min
Jet Velocity	6.92 - 38.15 m/s
Jet Reynolds Number	1265 - 12589
Cross-Flow	
Cross-Flow Velocity	2 - 4m/s
Fuel Mass Flow Rate	0.93 - 8.63g/min
Nitrogen Mass Flow Rate	0.60 - 2.2g/min
Hydrogen Mass Flow Rate	0.042 - 0.939g/min
Jet Velocity	3.68 - 33.98m/s
Jet Reynolds Number	383 - 6357
Jet Froude Number	430.42 - 36785.99
Momentum Flux Ratio	0.35 - 136.66

3.3 Experimental Results and Discussion

3.3.1 Critical Fuel Mass Flow Rate and Inert Gas Mass Flow Rate at Smoke Point

3.3.1a Quiescent Condition

Figure 3.7a shows the relation of the critical fuel mass flow rate and different inert gas flow rates to attain the smoke point for a quiescent condition. All curves show a skewed bell shape profile. All the inert-gas diluted flames had their transition point (from chemically to momentum domination) at around 40% CFMFR, except Ar, which had its transition point (from momentum dominated region to chemically dominated region) at 50% CFMFR. Overall, the comparison shows that the Ar gas had the highest flow rate, followed by CO₂, N₂ and He. This result agrees with the Schug et al. (1980) result. The laminar flame smoke point experiment in their study showed the order as CO₂, N₂, Ar and He in volumetric flow rate, which is in the same order as current study if the results is presented in a volumetric flow rate form (Figure 3.7b). The reason that they gave was that the additive gas participates in the heat transport process, which was a diffusion process with thermal diffusivity and thermal conductivity as the important properties. The additive gas also acted as a heat sink, so the specific heat, C_p of the heat capacity was an important parameter. The exaggerate trends of He may be caused by the high diffusivity (which is about three times higher than other gases, Table 3.5). The high thermal diffusivity caused faster heat transfer from the reaction front into the outside airflow. In Table 3.5, the specific heat of each inert gas is shown. The order of the specific heat of each gas correlates well with the inverse order of the amount of inert gas addition at the smoke point.

In a laminar dilution flame study, Santoro and Richardson (1994) found interdiffusional effects between the inert gas and the fuel. They found that in a N_2 or an Ar diluted diffusion flame, N_2 from the air tends to diffuse into the core of the flame while the fuel tends to diffuse toward the flame front. The dilution affected the concentration of fuel in the flame only in a region very near the burner. At a short height from the burner, the concentration of fuel for the diluted and the undiluted flames were the same. Hence, at the region very near to the burner, where the soot started to form, the reduction of temperature was very critical. In their flame temperature measurement, they found that the diluted flame had a lower temperature than the undiluted flame in the region close to the burner. Schug et al. (1980) laminar diffusion flame study found that the addition of additive Ar, N_2 , and CO_2 (depending of the amount) was able to decrease the gas temperature at jet port from about $600^\circ C$ (pure fuel) to about $200^\circ C$. Further away from the burner, the undiluted flame had a lower temperature for Santoro and Richardson (1994) study. The lower temperature of the undiluted flame in the far burner region was due to the higher radiative heat loss caused by the higher in-flame soot concentration. However, the Schug et al. (1980) smoke point study found that the overall diluted flame had slightly lower temperature than the undiluted. The difference between these two studies is that Schug et al. study maintained the smoke point condition, where fuel flow rate was different for diluted and undiluted flame. Whereas, Santoro and Richardson (1994) study used the same fuel flow rate for both conditions.

The temperature effect explanation alone may be sufficient for laminar flame, but it is more complicate for a turbulent flame. Most of the time the smoke point is due to the combination of many different factors in a turbulent flame. Some factors other than the

temperature that influence the soot production are the concentration (fuel, oxidizer and product gases), the residence time (Santoro and Richardson, 1994) and the turbulence intensity (Goh, 1999).

Table 3.5 Specific Heat for Tested Inert Gases (Wylen, et. al, 1994)

Gas	Specific Heat Cp (kJ/kgK)	Diffusivity cm ² /s
Argon	0.523	0.148
CO ₂	0.846	0.14
N ₂	1.039	0.187
He	5.1926	0.58

Figure 3.8 shows the jet exit Reynolds number at the smoke point for all the flame conditions. They were not significantly different from 5% to 30% CFMFR, but above 30% CFMFR, all the results for different inert gases branch out. Above 30% CFMFR, the CO₂-fuel jet exit Reynolds number was higher than that of the rest of the inert gas-fuel mixtures. It was followed closely by the jet Reynolds number of nitrogen-fuel gas. The helium-fuel jet exit Reynolds number was lower than the rest of the inert gases below 50% CFMFR. However, above 50% CFMFR, the helium-fuel gas mixture jet Reynolds number exceeds argon-fuel gas mixture jet Reynolds number. This was because CO₂ viscosity was the lowest among the inert gases. Argon mass flow rate was the highest. However, because of its high kinematic viscosity, argon-fuel Reynolds number was the lowest in the region higher than 50% CFMFR. Hence, Figure 3.7a and 3.8 show the importance of the role momentum parameters played in the momentum dominated region. In the region lower than 30% CFMFR, the momentum parameters did not play as significant a role as those above 30%. Therefore, this again supports the presence of a chemical dominated region below 30% CFMFR.

As mentioned in the earlier section, this study employed the same diameter burner as Goh (1999). The reason the smoke point experiment was repeated was because the mechanism of attaching the flame to the burner was different in the present and earlier experiments. Figure 3.9 shows the comparison of the results of the current study, which used a single outlet burner, with the results of Goh (1999), who used a co-annular burner. A higher amount of hydrogen was required in the present experiment to attach the flame for the single burner experiment as shown in Figure 3.9. The way that the flame attached was different for both burners. In the co-annular burner, hydrogen delivered from the outer tube created a piloted flame type attachment. On the other hand, in the single burner, hydrogen gas had to mix with the fuel to create a fuel mixture that is sufficient to attach the flame to the burner. Hence, a higher amount of hydrogen was needed in a single burner to attach the flame than in a co-annular burner. As a result, the total jet Reynolds number for the single burner study was higher, which is shown in Figure 3.10. The hydrogen volume and mass flow rates for both burners are shown in Figures 3.11 and 3.12. Both figures show a significant difference in the amount of hydrogen required to attach the flame. Both figures also show that the higher the fuel flow rate, the larger amount of hydrogen was required to attach the flame, which was consistent with Bandaru and Turns (2000) findings. The higher fuel flow rate caused longer lift-off region. Hence, a higher amount of hydrogen was required to reattach the longer lift-off length flame.

3.3.1b Cross-Flow Condition

Figure 3.13 shows the CFMFR and the nitrogen mass flow rate for all tested cross-flow speeds. The relation of the cross-flow speed to the CFMFR is shown in Figure

3.15, which was relatively linear. On the other hand, Goh et al. (2001) showed that the relation of CFMFR with the cross-flow velocity was non-monotonic. The CFMFR decreased from 0.0134 kg/min at 2.68m/s to 0.0129 kg/min at 3.58 m/s and then increased to 0.0156 kg/min at 4.02 m/s (Goh et al. 2001). Although both studies were done with the same diameter burner and with the similar cross-flow conditions, the setup and the burner configuration were different. Goh et al. (2001) study was done in a horizontal wind tunnel, but for this study, the wind tunnel was upright. The burner that Goh et al. (2001) used was a co-annular burner, but for this study a single straight tube burner was used. Due to the limitation of this current wind tunnel (max speed 4.3 m/s), the non-monotonic relation could not be studied at higher cross-flow conditions if it existed. The non-monotonic relation, however, started earlier in the horizontal wind tunnel than in the vertical wind tunnel. Figure 3.17 shows the comparison of both conditions for Goh et al. (2001a) results and the current results for various percentages of CFMFR versus the nitrogen mass flow rate at smoke point. It is to be noted that the Goh et al. (2001) results were not complete; they ranged only from 100% CFMFR to 50% CFMFR. This was because a stable lower CFMFR flame could not be attained with the pilot flame technique (co-annular burner). In the current study, nitrogen mass flow rates are significantly lower than Goh et al. (2001) results. As mentioned previously, in the current study, the hydrogen gas was mixed with the fuel gas. Hence, the amount of nitrogen gas needed was lower than in the experiment of Goh et al. (2001), because the addition of hydrogen gas to the fuel stream provided the extra momentum needed to suppress the smoke. On the other hand, from the comparison of the total jet Reynolds number (Figure 3.18), both results were very close; the similarity was also shown in the

comparison of momentum flux ratio in Figure 3.19. The difference of the wind tunnel setup also contributed to the variation. The buoyancy effect in a horizontal wind tunnel was perpendicular to the cross-flow momentum. The buoyancy effect became significant at far downstream parts of the flame (Brzustowski 1976). In fact, the buoyancy effects in a horizontal cross-flow flame shortened the flame due to the increase of air entrainment. On the other hand, in the current study, the cross-flow and the buoyancy effects were in the same direction. The Froude number of the flame with a constant density, ρ_f defined by Brzustowski (1976) was

$$Fr_f = \frac{v_j^2}{gD_j} \left(\frac{\rho_f}{\rho_\infty - \rho_f} \right)$$

v_j is the jet velocity, g is the gravitational acceleration, D_j is the jet diameter and ρ_∞ is the ambient density.

The Froude number for flame, Fr_f , and cross-flow, Fr_{cf} , defined by Bandaru and Turns (2000) for their vertical cross-flow study was

$$Fr_f = \frac{\rho_j v_j^2 \pi D_j^2}{4(\rho_j - \rho_\infty) V_f g}$$

$$Fr_{cf} = \frac{\rho_\infty v_\infty^2 A_{f,frontal}}{(\rho_j - \rho_\infty) V_f g}$$

$$V_f = \frac{\pi W_x W_z}{12}$$

$$A_f = \frac{W_z L_{fx}}{2}$$

The flame dimensions that Bandaru and Turns (2000) defined for their Froude numbers are shown in Figure 3.55; here, V_f is the visible flame volume, $A_{f,frontal}$ is the frontal area of the visible flame volume exposed to cross-flow, ρ_j is the jet gas density, and v_∞ is the cross-flow velocity.

Figure 3.20a to c shows the calculated Froude number values for both flame and the cross-flow at 2, 3 and 4 m/s. At 2 m/s cross flow condition, the flame Froude number was higher than unity. On the other hand, the cross-flow Froude numbers for 90% and 80% CFMFR were lower than unity; they were 0.956 and 0.934. This, in fact, showed that the buoyancy effects were significant for the flame at low cross-flow conditions with a large flame. At 50% and 60% CFMFR, the Froude number was almost unity (1.08 and 1.06), which meant that both the momentum and the buoyancy were almost equally important. Since the buoyancy effect started at a lower cross-flow velocity in the vertical wind tunnel than in the horizontal wind tunnel, we can conclude that the vertical wind tunnel flame entrains more air into the flame than the latter. Another evidence of this phenomenon can be observed from Figure 3.19, the comparison of momentum flux ratio in a similar experiment but in a different wind tunnel. In this figure, the momentum flux ratio in the wind tunnel was higher than in the vertical wind tunnel. Furthermore the CFMFR of the horizontal wind tunnel studies was twice that in the vertical wind tunnel, but was not in itself a complete proof, because both the burners and the hydrogen supplement method were different in the two studies. However, the significant difference of CFMFR is noteworthy.

In the cold jet studies where an orifice was used instead of a tube, four known vortical structures have been documented. They were the horseshoe vortices, the jet shear

layer, the wake structure and the counter rotating vortex pair (CVP) (Fric and Roshko, 1994; Smith and Mungal, 1998). However, in the tube studies, the wall effect vortices, which are the horseshoe vortices and some wake structures caused by the flow and the wall are not significant. The jet shear layer and the CVP are dominant in the tube studies. Broadwell and Breidenthal (1984) showed that the CVP occurred from the jet momentum normal to the cross-flow. The CVP was initiated very near to the pipe exit by the shear layer. The shear layer was folding and rolling up the jet in the study of Kelso et al. (1996). The CVP expanded and dominated the downstream flow. In horizontal wind tunnel flame experiments, many had observed that the buoyancy effect amplified the CVP in the downstream region of the flame. However, the buoyancy effects in the vertical cross-flow flames were different from those in the horizontal cross-flow flames. The flame image at CFMFR at 4.02 m/s cross-flow showed an increase in width from the burner location to a certain maximum value and then decreased slowly until the end of the visible flame (Goh, 1999). On the other hand, the flame in the current study at CFMFR at 4 m/s showed the increase of width from the burner location and reached a maximum width at the end of the visible flame. Figure 3.58 shows the comparison of both flame images. From the images, the horizontal flame tilted upward due to the buoyancy effect. On the other hand, in the vertical cross-flow flame, the flame did not tilt as much as in the horizontal cross-flow. The flame cross-sectional images in the study of Gollahalli et al. (1975) and Brzustowski et al. (1975) showed that the flame width viewed from the top (-X direction) expanded. Those images also showed that the CVP spread open as it traveled downstream of the flame. From these phenomena, it can be concluded that in the horizontal cross-flow buoyancy force pushes the flame upward and decreases

the flame width (viewing from Y direction) and spreads the flame sideways (viewing from -X direction). However, in the vertical cross-flow, buoyancy force was in the same direction as the cross-flow. The buoyancy force may reinforce the cross-flow in expanding the CVP.

Table 3.6 summarizes the different regions in Figure 3.13 for all the cross-flow conditions. The increase of cross-flow beyond 3 m/s showed a shift of the transition point from 20% CFMFR to 30% CFMFR. This shifting phenomenon has also been observed in Goh's (1999) studies. The increase of cross-flow speed increased the quenching effect on the flame. Hence, a higher fuel flow rate (or more heating energy) was needed to maintain the soot production rate (fuel pyrolysis rate) at the smoke point. Furthermore, higher cross-flow speeds may cause quick dilution of fuel jet mixing, and a higher amount of fuel could escape unburned (Goh et al., 2002). The transition region changed at the higher cross-flow rate.

Table 3.6 Ranges of Momentum and Chemical Dominated Regions and Transition Regions for All the Cross-Flow Conditions

Cross-Flow Speed	Momentum-Dominated Region	Transition Region	Chemical-Dominated Region
2 m/s	100% to 30%	10% to 30%	10% to 5%
2.5 m/s	100% to 30%	10% to 30%	10% to 5%
3 m/s	100% to 30%	10% to 30%	10% to 5%
3.5 m/s	100% to 40%	20% to 40%	20% to 5%
4 m/s	100% to 40%	20% to 40%	20% to 5%

The increase of cross-flow velocity decreased the total jet exit Reynolds number to achieve the smoke point as shown in Figure 3.14. The increase of cross-flow speed increased the overall mixing rate in the flame. Figure 3.16 again shows that the lower the

cross-flow velocity, the higher was the jet momentum required to attain smoke point.

This figure also shows that in the momentum flux ratio, R , which is defined as

$$R = \frac{\rho_j v_j^2}{\rho_\infty v_\infty^2}$$

at the smoke point decreases as the cross-flow increases. The gradient of the curves also decreases from a lower cross-flow speed to a higher cross-flow speed.

All profile measurements were done to cover these three regions, the momentum-dominated regions, the transition region and the chemical-dominated regions. The test matrix to cover all these regions is shown in Table 3.1.

3.3.2 Temperature profiles

3.3.2a Quiescent Condition

The radial temperature profiles in the flames in quiescent conditions are shown in Figures 3.24 a to d. The profiles for all the three flame locations (25% of L_f is in the near-burner region, 50% of L_f is in the mid-flame region and 75% of L_f is in the far-burner region) reveal a trend expected in diffusion flames. Because of the shearing effects with the stagnant surrounding air, the fuel jet expands. As a result, the flame radius increased. This can be observed from the temperature profiles (only fuel and nitrogen-fuel mixed flames temperature were measured) and the flame image pictures in Figures 3.56a to d experiment. In these figures, the radial dimension (r) was normalized with the burner inner diameter, D .

At all four CFMFR values, the temperature profiles had dual peaks in the mid-flame and the near-burner regions. The location of peak temperatures indicated the region

of highest flame oxidation rate where the fuel and the air mixture were close to stoichiometric value. In the far-burner region, all the temperature profiles showed only one peak. Furthermore, the peak temperature in the far-burner region was lower than in the other two locations. This was because the near-burner and mid-flame regions had more gas-phase reactions than the far-burner region. In the far burner region, most of the reactions relate to the oxidization of soot, which were mostly concentrated at the central region near the flame axis. Hence, at the far-burner region, the peak temperature occurred at the center (soot concentration profiles are shown in Figures 3.34a to d for all four percentages of CFMFR).

In a turbulent flame, the surrounding air continued to mix into the flame as gases travel upward. So, further away from the burner, a higher amount of air was entrained into the flame. This phenomenon is evident in Figure 3.33 a to d, where the far-burner region showed a higher O_2 concentration than in the mid-flame region. Also, the mid-flame region showed higher O_2 concentration than the near-burner region. The higher amount of air entrainment could promote oxidation reaction, which increased the local flame temperature. But after a certain point, further introduction of cooler air actually reduced the flame temperature. Hence, due to a larger amount of cooler air entering the flame and the consequent reduction of reaction rate as the gases traveled upward, the overall flame temperature dropped from the mid-flame region to the far-burner region.

The 100% and 60% CFMFR flames had a lower peak temperature compared with the 30% and 10% CFMFR flame. The peak temperatures in flames were around 1650 (all three locations for 60% CFMFR) to 1700 K (all three locations for 100% CFMFR). But for the 30% and 10% CFMFR flames peak temperatures were around 2300 K, which was

very close to the adiabatic temperature of propylene. The reason for the higher flame temperature was because the mole fraction of hydrogen was higher than propylene in the fuel jet gas mixture. Hydrogen gas has the higher adiabatic flame temperature than propylene. Figure 3.21 shows the mixture fraction of propylene, hydrogen and nitrogen mixture. At 40% CFMFR, all the three gases had almost the same mixture fraction (volume). All the mole-fractions of propylene gas above 40% CFMFR were higher than the rest of the gases. Below 40% CFMFR, the propylene gas mole fractions were lower compared to other gases. Secondly, the 10% CFMFR flames appeared laminar and 30% flame was in transition from turbulent to laminar. Figure 3.56a shows 30% CFMFR flame was less turbulent than 60% and 100% flames and about half of the flame appeared relatively smooth.

At 10% CFMFR, the jet exit Reynolds number was 2054 (Figure 3.8), and the flame appeared to be a laminar flame. The factors that influence the soot formation in a laminar flame are the species concentration, the temperature and the residence time (Santoro and Richardson, 1994). In their study, they found that the temperature effect was the most important parameter in soot formation. The dilution was able to reduce the residence time for soot growth by increasing the time for soot particle inception.

3.3.2b Cross-Flow Conditions

Figures 3.25 to 3.27 show the flame temperature profiles in the flame at 2, 3 and 4 m/s cross-flow and for the four different percentages of CFMFR and at the three different flames locations (far-burner, mid-flame and near-burner regions corresponding to 75%, 50% and 25% of flame length, L_{Fz}). The flame temperature profiles at 2 and 3 m/s cross-

flow were measured from the burner exit location on X-axis. In all the temperature profiles, 0 on the X-axis represents the burner exit location. The flame in a cross-flow velocity of 4 m/s bent more along the cross-flow than the other flames; hence the flame measurements started at ten burners diameter from the burner exit. The temperature and the velocity profiles were plotted in this way because from the plots, the location of peaks and the shapes of the flame can be identified.

Most of the temperatures profiles showed double peaks in the mid-flame and the near-burner regions. The flame on the left side or the side that was closer to the burner had a higher flame temperature than the right side. This phenomenon can be explained by observing the velocity profiles in Figure 3.60 to 3.62. The velocity of the gases on the side nearer to the burner was higher than in the flame on the other side in the near-burner and the mid-flame regions. The reasons for the high velocity on the left side are discussed in Section 3.3.6. The higher Z velocity certainly causes the increase of the shearing effect between the flame and the cross-flow. Hence, more air is brought into the flame.

The evidence of the higher air entrainment can also be observed from the concentration profiles in Figures 3.40 to 3.51. Figures 3.43, 3.47 and 3.51 show that the O₂ concentration profile on the left side in the near-burner and mid-flame region has a lower slope compared to that on the right side. This indicates that the O₂ or the air penetrated deeper inside the flame on the left side due to the higher mixing. Furthermore, the CO₂ (Figure 3.42, 3.46, and 3.50) concentration is also higher on the left side. This also indicates that the higher mixing contributes to the higher reaction rate in this region, which leads to the higher flame temperature.

Besides the enhancement of the air entrainment through the interaction between flow and the flame, the buoyancy effect also plays a secondary role in enhancing the air entrainment. The buoyancy effect was important especially in the 2 m/s cross-flow condition, where the Froude number was small or below unity (Figure 3.20a). The buoyancy augments the shearing effects between the flame and the cross-flow.

All the flame temperature profiles in the far-burner region of the 20% and 10% CFMFR flames in the 2 m/s and 3 m/s cross-flow and the 30% and 10% CFMFR flames in the 4 m/s (transition region and chemically dominated regions) show a more conspicuous double peak structure than the other higher CFMFR flames. At a lower momentum flux ratio (30% CFMFR or lower), the flame started to behave like a laminar flame, especially the 10% and 5% CFMFR flames for all cross-flow. From Figure 3.57a to e, the 10% and 5% CFMFR flames appear smoother than at other higher CFMFR flame conditions. Hence, a smaller peak on the right side signifies the lower mixing in the flame at these low percentages CFMFR.

Furthermore, the peak temperatures in the 20% and 10% CFMFR flames in the 2 and 3 m/s cross-flow and in the 30% and 10% CFMFR flames in the 4 m/s cross-flow were higher than at the higher CFMFR flames. In Figures 3.22a to 3.22e, the ratio of the mole fraction between the hydrogen and the fuel were approximately constant. Hence, the explanation that the higher hydrogen concentration in the fuel caused the higher flame temperature as given in the quiescent condition section may not hold. Although all the flame temperature measurements were done at the same three flame locations relative to the flame length (25%, 50% and 75% of L_{fz}), the absolute distances from the burner were different. For the smaller flames, the measurements were done closer to the burner, where

the influence of the hydrogen flames (with higher temperature) was more significant. This was because the hydrogen gas diffuses and reacts faster than the propylene gas. As a result, the smaller flames of 20% and 10% CFMFR in the 2 and 3 m/s cross-flow and 30% and 10% CFMFR in the 4 m/s cross-flow had the higher peak temperature.

A more detail discussion on the cross-flow effect will be presented in Chapter VII. These temperature results will also be applied in the discussion in soot (Chapter IV) and OH (Chapter V) study. The temperature results will also be used to compare with the numerical results in Chapter VI.

3.3.3 Global Emission

3.3.3a Quiescent Conditions

Figures 3.28 and 3.29 show the flame global emission indices for NO, NO_x, CO, CO₂ and O₂ for all the CFMFR at quiescent conditions. The emission indices of NO and NO_x increased slightly from the 100% to 80% CFMFR flames. The peak of NO and NO_x indices at the 30% CFMFR flame were due to low measured values of CO and CO₂ concentration.

The CO emission index at the 30% to 5% CFMFR flame show a decreasing trend. This observable fact is consistent with the Santoro and Richardson (1994) finding for a laminar flame. Figure 3.21 shows that the mole fraction for N₂ gas surpassed propylene gas at 30% and below CFMFR. As explained in section 3.3.1, the inert gas reduces the soot growth residence time by reducing the flame temperature at a location very near to the burner. There is a strong correlation between the soot and the CO emission. Köylü

and Faeth (1991) found that the higher soot emission led to the higher CO emission. In Figures 3.34c and 3.34d, the overall soot concentration in the 30% CFMFR flames was higher than the 10% CFMFR flame. From this fact, it is evident that in the 30% and lower CFMFR flames condition, the chemical reaction effect was more important.

On the other hand, the soot concentration in both 100% and 60% CFMFR flames (Figures 3.34a and 3.34b) does not show a very significant difference within the uncertainty limits. However, the CO emission indices show an increasing trend from 100% CFMFR to 40% CFMFR. The jet Reynolds number results in Figure 3.8 shows the decreasing trend from 100% to 5% CFMFR. Hence, the increase of CO emission indices from 100% to 40% CFMFR was caused by the deficiency of CO oxidation due to the reduction of turbulence mixing. Therefore, from this evidence, 100% to 40% CFMFR region shows the domination of the momentum effect.

As shown in Figure 3.29, the CO₂ concentration exhibits an opposite behavior to the O₂ concentration. The increase of fuel flow rate increased the production of CO₂ and O₂ consumption in the flame. The figure shows the O₂ and the CO₂ concentrations are linearly proportional to the fuel flow rate.

3.3.2b Cross-Flow Global Emission

Figures 3.35 to 3.39 show the global flame emission for NO, NO_x, CO, CO₂ and O₂ for all the cross-flow conditions. The CO, NO and NO_x emission profiles are plotted in log scale. Some of the values are very small due to the heavy dilution by the cross-flow. Especially in the CO concentration measurement, a slight difference in the measurement may cause significant difference in the emission index calculation.

The mole fraction plots for all the cross-flow conditions in Figures 3.22a to 3.22e show that in almost all conditions, the hydrogen mole fractions were higher than the rest of the gases except in a few low CFMFR conditions. Hence, in the cross-flow conditions, the hydrogen gases played an important role in the emission. A higher amount of hydrogen gas was needed in the cross-flow condition compared to the quiescent condition. In fact, from the comparison of the entire hydrogen mole fraction in all the cross-flow conditions, the overall hydrogen mole fractions increase with the cross-flow. The higher the cross-flow, the larger amount of hydrogen is needed to attach the flame. However, the amount of hydrogen by mass added into the flame still a very small amount compare to the other species. Observe Figure 3.22f to k, the hydrogen mass fraction is less than 13% of the total mass.

All the cross-flow global emission indices profiles show an increasing trend for CO as the fuel flow rate decreases. Especially in 30% to 5% CFMFR flames, the increment rates of CO emission indices were escalated. On the contrary, the trends of the CO emission indices are different from the quiescent condition in the 30% to 5% CFMFR flames, where the trend is decreasing. Hence, both the quiescent and the cross-flow at the 30% to 5% CFMFR flames behaved differently. The difference can also be observed in Figures 3.54a and b. The increase of the flame length from the 30% to 20% CFMFR flames is substantial (relatively) compared to the flame height increment in quiescent condition at these CFMFR conditions. The increase of flame length increases the flame soot formation residence time. Hence, in this region, more soot (relative to the fuel flow rate) was formed and oxidized, which in effect brought about the higher CO emission.

Most of the cross-flow emission profiles results show almost the same or slightly lower in-flame CO concentration in the 20% and 10% CFMFR flames in the 2 and 3 m/s cross-flow, and the 30% and 10% CFMFR flames in the 4 m/s compare with 60% and 100% CFMFR. However, the CO global emission indices in the lower CFMFR are still higher than in the higher CFMFR. Consequently, the mixing of the flame with the cross-flow may be important. At lower momentum fluxes, the flame started or behaved like a laminar flame (see Figure 3.57), which in effect reduced the flame mixing with cross-flow. Hence, the lower CO oxidation rate caused higher amount of CO (relative to fuel flow rate) to escape unoxidized. The CO emission index results in cross-flow is also an indication of the transition of momentum-dominated region to chemical dominated region.

The NO and NO_x emission indices stay approximate within a small variation through most of the percentages of CFMFR flames. However, when it comes to a very small fuel flow rate like 20% to 5% CFMFR, the NO and NO_x emission indices escalates. In the gas mixture mole fractions figures (Figures 3.22a to 3.22e), the high hydrogen mole fraction may contribute to this phenomenon. As explained in the flame temperature profiles section, a hydrogen flame has a higher flame adiabatic temperature than a propylene flame. Hence, the higher hydrogen gas mole fraction causes the increase of the overall flame temperature (shown in Figures 3.25 to 3.27). The higher flame temperature may be the main factor for the higher NO and NO_x production, which is according to NO thermal mechanism. This occurrence also can be observed from the NO concentration profiles for all cross-flow conditions. The NO concentration in the 20% and 10% CFMFR flames in the 2 and 3 m/s cross-flow and in the 30% and 10% CFMFR flames in the 4

m/s show a significantly higher value than in the 60% and 100% CFMFR flames. On the other hand, the increments maybe mainly be due to the way that the emissions index was calculated. Part of the denominator of the emission index formula is CO_2 and CO concentrations. The CO_2 and CO concentrations were very small in cross-flow conditions. In some cases CO_2 and CO concentrations were almost undetectable due to strong dilution. Hence, a very small denominator may blow out the emission index results. This is the reason that the CO emission indices at 4 m/s flames global emission result are not presented because they are unreasonably high.

Figures 3.35b to 3.39b show the global emission for CO_2 and O_2 . The trends for both species are the same as in the quiescent condition. The CO_2 concentrations for cross-flow condition were lower compared with the quiescent condition. The reason is that the fuel flow rates for the cross-flow were about half of the quiescent fuel flow rate. Furthermore, the strong dilution on the emission from the cross-flow may reduce the measured values.

3.3.4 In-Flame Concentration Profiles

All the concentration profiles are plotted with respected to the normalized (with burner diameter) diameter. Hence, the concentration profile plots for the cross-flow are not the same as the temperature and the velocity plots. All the concentration profiles are plotted with zero as the center of the flame. On the other hand, the temperature and the velocity profiles for the cross-flow are plotted with respect to the distance from the burner exit location. The reason for they are plotted differently is because the exact shape of the flame can be more easily understood this way. The temperature figures with the

exact location rather than the normalized coordinate system enable the understanding of the shape of the flames at different momentum flux ratio.

3.3.4a Quiescent In-flame Emission Profiles

NO Concentration

The concentration profiles of NO concentration for all the four tested conditions are shown in Figure 3.30a to 3.30d for 100%, 60%, 30% and 10% CFMFR. Thermal NO mechanism explains that the NO production depends on the temperature for a wide range of equivalence ratio. The NO concentration profiles in Figures 3.30 a to d show a resemblance with temperature profiles in Figure 3.24 a to d with the feature of double peaks in the near-burner and the mid-flame regions. The NO productions were higher in the near-burner and the mid-flame regions because of the higher temperature and the higher availability of radicals in these regions.

Overall, the 30% and 10% CFMFR flames had a lower in-flame NO concentration. Although the peak temperatures of the 100% and 60% CFMFR flames were lower than the 30 % and 10% CFMFR flames, the average flame temperatures of 100% and 60% CFMFR were higher because the flames were wider and with more high temperature region than the 30% and 10% CFMFR flames. Hence, this explains why the NO concentration of the 30% and 10% CFMFR flames were lower than the other higher CFMFR flames.

CO Concentration

Figures 3.31 a to d show the CO concentration was higher at the near burner region where the O₂ concentration was low. The CO molecules further oxidize to CO₂ as

they travel along the flame to a region with higher O_2 concentration. The CO concentrations for the 30% and 10% CFMFR flames were lower than the 100% and 60% CFMFR flames. The reason for this lower CO was discussed in the global emission section above. This was mainly because to the addition of inert gas reduces the soot growth residence time, which leads to a low in-flame soot concentration and subsequently reduces the CO formation.

CO₂ concentration

Figures 3.32a to 3.32d show the higher CO_2 concentration in the mid-flame and the far-burner regions. In these two regions, the oxidation of soot particles was higher compared to the near-burner region where the soot particle just nucleated. In fact, in Figures 3.34a to d, the near-burner region has a very low soot particle concentration compared to the mid-flame and the far-burner regions. The near-burner and the mid-flame region CO_2 concentration profiles show a double peak, which is consistent with the CO_2 concentration profiles for a diffusion flame. The peaks were where most oxidation took place, where O_2 from the air diffused into the flame and oxidized with the soot particles and other species, like CO and H_2 . A single peak at the far-burner region was because of the oxidation of the soot particles, which were concentrated at the center of the flame. Furthermore, the gases were well mixed with the O_2 from the air (O_2 concentration in the far-burner region was higher). In the far-burner region, there were enough hot gases that led to the growing importance of buoyancy force. The narrowing of the flame as shown in Figure 3.56a was caused by the acceleration of the buoyancy force.

This is because conservation of mass requires the streamlines to come closer together as the velocity increases (Turns, 1996).

The CO₂ concentrations in the 100% and 60% CFMFR flames were slightly higher (0.5% to 1%) than in the 30% and 10% CFMFR flames. There were two main reasons for this difference. First, the soot production rate for this region was lower for the 30% and 10% CFMFR flames as described previously. Secondly, at a lower jet Reynolds number (Figure 3.8), the flame approached or was at laminar flame condition at the 30% and 10% CFMFR flames. These were the reasons for the lower flame mixing effect, which led to lower CO₂ formation.

O₂ concentration

Figures 3.33a to 3.33d show the in-flame O₂ concentration profiles in at the four percentages of CFMFR. The O₂ concentration profiles are like the inverted profiles for CO₂ concentration. The slopes are steeper in the near-burner and mid-flame regions because the rate of O₂ diffusion rate into the flame was still low. The O₂ concentration in the far-burner region was higher, which is consistent with the explanation in the CO₂ concentration section. The O₂ concentration in the far-burner region was higher because the flame was well mixed with the excess O₂ that was entrained throughout the flame. The 30% and 10% CFMFR flames had higher O₂ concentration in the far-burner region because this region had a low oxidation rate due to the low in-flame soot concentration (as explained in global emission section). The main chemical reaction in the far-burner region was soot oxidation.

Soot Concentration

Figures 3.34a to 3.34d show the in-flame soot concentration profiles for the four percentages of CFMFR. In most cases, the far-burner region had a higher soot concentration than the rest of the regions. Overall, the 100% and 60% CFMFR flames had approximately the same magnitude of peak soot concentration in the far-burner region (within the uncertainty) but the profiles were of different shapes. In the 100% to 60% CFMFR flames, the mid-flame region soot concentration was lower. The reason may be mainly due to the N_2 addition into the flame. From 60% to 30% and 10% CFMFR, the flames showed a significant decrease of soot concentration. The reason for the decrease was that the mole fraction of nitrogen for the 30% and 10% CFMFR flames was higher compared to that in the 100% and 60% CFMFR flames. As discussed in the global emission section, the addition of nitrogen can cause a reduction of the flame temperature at the region very close to the burner. The temperature reduction in this region reduces the soot production rate (Santoro and Richardson, 1994). On the other hand, the reduction of fuel flow rate may also cause the decrease of soot concentration in the flame. The reduction of fuel flow rate, in effect, decreased the total carbon supplied into the flame.

3.3.4b Cross-Flow Emission Profiles

Figures 3.35 to 3.51 show the concentration profiles of NO, CO, CO₂ and O₂ on X-axis in the 2 m/s, 3 m/s and 4 m/s cross-flow flames. In order to cover all regions, the momentum-dominated, the chemically-dominated, and the transition regions, four different CFMFR were selected for the different cross-flow conditions For 2 m/s and 3

m/s cross-flow, the concentration profiles were measured at 100%, 60%, 20% and 10% of CFMFR; for 4 m/s cross-flow, 100%, 60%, 30% and 10% CFMFR flames were measured. The transition region for 2 m/s and 3 m/s cross flow was 20%, and for 4 m/s cross-flow was 30%. The cross-flow flames were not axisymmetric on the axis of measurement; as a result, all the concentration profiles exhibit skew, quiescent diffusion flame like, concentration profiles.

NO Concentration

The NO concentration profiles for the flames in the 2, 3 and 4 m/s cross-flow are shown in Figures 3.40, 3.44 and 3.48 for all the four conditions. Similar to those the in quiescent condition flame, most NO concentration profiles at the mid-flame and the near-burner regions show a dual-peak profile. The NO formation rate depends on temperature according to thermal mechanism for a wide range of equivalence ratios. In most of the cross-flow flames, the NO concentration profiles for the momentum-dominated region to the transition regions (Refer to Table 3.5) show that the near-burner and the mid-flame regions exhibited a dual peak profile. However, almost all the chemically-dominated region flames show that the near-burner and the mid-flame region NO concentration profiles exhibit a dual-peak characteristic. All profiles in the far-burner region had only a single peak. Overall, the 20% and 10% CFMFR flames in the 2 and 3 m/s cross-flow and the 30% and 10% CFMFR flames in the 4 m/s cross-flow had slightly higher NO concentration peaks than in the other higher CFMFR flames. In general, the peak temperature in the 20% and 10% CFMFR flames in the 2 and 3m/s cross-flow and in the 30% and 10% CFMFR flames in the 4 m/s were higher than the other two higher CFMFR

flames. Hence, temperature was the main factor for the NO concentration difference for these two regions.

The NO concentration profiles at the different cross-flow conditions are similar to each other. There are some variations in the peak values, but the trends of the profiles are similar. The only significant variation of the peak values is in the 100% CFMFR flames. The order for the peak NO concentration in 100% CFMFR flames is at 4 m/s cross-flow as the highest, and followed by 3 m/s and 2 m/s velocity cross-flows. For the rest of the percentages of CFMFR flames, the NO peak concentration differences were within the uncertainty limit.

CO Concentration

Figures 3.41, 3.45 and 3.49 are the CO concentration profiles in the flames in the 2, 3 and 4 m/s cross-flow. All the flames had the peak of CO concentration at or close to the center of the flames. The concentration profiles for all CO concentrations are like a bell shape or a slightly skewed bell shape. The near-burner region of all flames had the highest CO concentration followed by the mid-flame region and then the far-burner region. The explanations for the behavior of CO concentration profiles are similar to those in the quiescent condition section, which is mainly determined by to the availability of O₂ in the flame and local soot concentration.

The CO concentration profiles for all the cross-flow conditions had similar profiles; even the magnitudes are surprisingly close in some cases, especially in the far-burner region. More discussion on these results will be presented in the Chapters IV and

V, where these results are discussed along side with the soot and OH concentration results.

CO₂ Concentration

Figures 3.42, 3.46 and 3.50 show the CO₂ concentration profiles for the flames in the 2, 3 and 4 m/s cross-flow. In the momentum-dominated region, the CO₂ concentration in the near-burner region showed dual-peak profiles. In 2 m/s and 4 m/s cross-flow, the mid-flame region also exhibited a double peak character. The peak on the left is higher than the one at the right for all cases, which resembles the trend of the NO concentration profile. In general, in the momentum-dominated region, the CO₂ concentration in the far-burner region was higher than in the mid-flame region, and the near-burner region had the lowest CO₂ concentration.

In the chemically-dominated region, the dual-peak profile in the near-burner region is present in all cross-flow conditions. The dual-peak profile in some of the flames was not as obvious as in the quiescent condition flames. First, the cross-flow flames were better mixed with cross-flow air than the quiescent conditions flames. Secondly, the quiescent fuel flow rates were about double that in the cross-flow condition, which led to a larger flame.

O₂ Concentration

Figures 3.43, 3.47 and 3.51 show the O₂ concentration profiles in the cross-flow of 2, 3 and 4 m/s. All the O₂ concentration profiles were shaped like an inverted skewed bell shaped curve. In fact, they were almost the inversion of CO₂ concentration profiles.

This is a typical O_2 concentration trend for a diffusion flame. The O_2 from the surrounding air was diffused into the flame naturally and by shear with cross-flow. The slopes on the right side of the curves for all conditions were steeper than the ones on the left side. The Z-velocity results in Figures 3.60 to 3.62 show a higher Z-velocity on the left side of the flame. Hence, the higher mixing on the left side of the flame caused the higher mixing rate and deeper penetration of air into the flame. As a result, this caused more influx of air into the left side of the flame and it led to a lower O_2 concentration profile slope. In general, by comparing the O_2 concentration at the three flame locations in the flame, the far-burner region had higher O_2 concentration than the other two flame locations. This was because the air was continuously entrained and was mixed into the flame by the CVP. Furthermore, the oxidation rate in the far-burner region was less compared with that at the other two locations. The flame became narrower and smaller as the fuel flow rate decreased. Furthermore, the slope of O_2 concentration profile on the left side became sharper than in the flame at the higher fuel flow rate. This may indicate that the entrainment or penetration of O_2 into the flame became lower. This was because at the lower fuel flow rate, the lower momentum from the jet and the lower heating from the flame reduced the mixing effects between the flame and the surrounding air. Hence, at the lower CFMFR, the momentum effect on the flame was low, compared with the higher CFMFR flames.

All the O_2 concentrations profiles for all the cross-flow conditions exhibited similar trends. However, the values had a slight difference at some of the flame conditions. Most of the flames in the 2 m/s cross-flow had lower O_2 concentrations than the flames in the 3 and 4 m/s cross-flow. As mentioned earlier, the CO_2 concentration

profile is normally the inverted profile of O_2 concentration. The 3 and 4 m/s cross-flow flames had better mixing than the 2 m/s cross-flow in high CFMFR case, which could bring more O_2 into the flames.

3.3.5 Flame Height or Flame Length

The definition of flame height/length is the distance from the burner to the end of visible luminous zone. Strictly speaking, the actual sense of height has to include the after burning of CO and soot. This small distance of the afterburning of these species that contributed to the flame height is probably the same and small for most fuel conditions (Roper, 1977; Roper and Smith, 1977), and does not cause any serious error in the measurements and results (Schug et al. 1980). The definitions of the flame dimensions in the quiescent and the cross-flow conditions are shown in Figure 3.55.

3.3.5a Flame Height in Quiescent Conditions

Figure 3.54a shows the flame height for all the cases with the inert gases dilution studied and at all the different percentages of CFMFR. The nitrogen gas diluted flames had the higher flame height compared to other inert gas (CO_2 , He, and Ar) diluted flames from CFMFR of 30% to 90%. However, the profile is reversed at conditions below 30% of CFMFR. At 20% and 10% CFMFR, the nitrogen gas diluted flame heights were the lowest. Then, on 5% CFMFR, the nitrogen gas diluted flame height was the second lowest. On the other hand, the argon gas diluted flames were the shortest from 90% to 30% CFMFR, but with 20% CFMFR, the argon-diluted flame was the tallest.

3.3.5b Flames Dimensions in Cross-Flow Conditions

Figure 3.54b shows the flame height in all the cross-flow conditions and at all the percentages of CFMFR studied. The flame length, L_{Fz} was initially reduced with the increase of cross-flow speed from 2 m/s to 3 m/s, but the further increase of the cross-flow speed, 3.5m/s to 4 m/s, increased it. The non-monotonic relation can be explained from the observation of the flame shape. The initial increase of cross-flow momentum (2 m/s to 3m/s) increased the air entrainment into the flame, which in effect shortened the flame length. However, with further increase of cross-flow momentum (3.5 m/s to 4 m/s), up to a certain momentum flux ratio (~ 25), the flames started to bend more along the cross-flow. As a result, the cross-flow effect on the flame was less significant for the higher cross-flow speed than the lower cross-flow speed because of the reduction of the flame frontal area, A_f . Hence, the flame length increased. This non-monotonic relation was also observed by Goh (1999).

For all the cross-flow conditions, there is a dip in flame length profile at 30% CFMFR. Surprisingly, at that point, all the flames for all the cross-flow conditions had somewhat the same length. At 20% CFMFR, the flame length started to increase again at all the cross-flow conditions. From 10% to 5% CFMFR, the flame length decreased again. This phenomenon indicated that the transition of the flames from a fully turbulent flame to a laminar flame. The 30% CFMFR flames were probably in the transition region. From the flame images in Figures 3.57a to 3.57e, the flames at 30% or 20% CFMFR appeared smoother for more than one to two thirds of the flame. The 10% and 5% CFMFR flames appeared laminar. A laminar flame had less air entrainment than a

turbulent flame due to the low mixing. Hence, the lower mixing caused the increase of the flame residence time to oxidize the soot. As a result, the flame in the transition region or the laminar flame appeared longer.

3.3.6 Velocity Profiles

3.3.6a Velocity Profiles in Flame at Quiescent Conditions

Figures 5.59a to 5.59d are the upward axial velocity profiles in all the four percentages CFMFR flames. All these velocity values were calculated from the measured dynamic pressure and the corrected density from the temperature results.

All the flames had the peak velocity on the centerline of the flames. The velocity decreased along the axial direction of the flame. The axial velocities at 60% CFMFR flame in the near-burner and the mid-flame region were lower than in the 100% CFMFR flame because the 60% CFMFR jet momentum was lower (Refer to Figure 3.8 for the exit jet Reynolds number for all percentages of CFMFR). However, the axial velocities in the core of the far-burner region of flame were very close for both conditions, though the 60% CFMFR radials profile was smaller. This was because in the far-burner region, the gas flow was dominated by the buoyancy effect, whereas in the near-burner region, the jet momentum was dominating the flow. The increasing buoyancy effects in the 10% and 30% CFMFR flames can be observed from the change of the velocity profiles. In the 30% CFMFR flame, the overall velocities for all three axial locations were higher than in the 60% CFMFR flame, even though the 30% CFMFR flame jet momentum was lower. The increase of the velocity may indicate that the flame was in transition from a turbulent to a laminar flame, where the buoyancy effect became more significant. In the flame

images (Figure 3.57a), the transition was evident in the 30% and 20% CFMFR flames. The 10% and 5% CFMFR flames were evidently laminar flames. Furthermore, the flame peak temperature of the 30% CFMFR flame was higher than in the 60% CFMFR flames for all three locations. The higher temperature had the effect of increasing the velocity value due to the way that the velocity value was calculated. The density on the velocity term was derived from the temperature results with the assumptions of ideal gas and most of gases were air. The lower density values resulting from the high temperatures led to higher velocities. At 10% CFMFR, the flame appeared to be very narrow and had a higher axial velocity than the other CFMFR flames. The lower fuel flow rate and the strong buoyancy effects caused the flame to become long and narrow. In a laminar flame, the acceleration due to the buoyancy force caused the flame to become narrow at the flame-end. Furthermore, the lack of mixing in a laminar flame caused the increase of residence time, which in effect increased the flame length.

3.3.6b Cross-Flow Velocity Profiles

Figures 3.60 to 3.62 show the Z velocity component results in the flames at 2, 3 and 4 m/s cross-flow for the four different percentages of CFMFR at three different locations, in the far-burner, mid-flame and near-burner regions (75%, 50% and 25% of flame length, L_{Fz}).

As mentioned in the temperature section (3.3.2), the measured Z-velocity component for all cross-flow conditions was higher on the left side than the right side. The better air entrainment at the left side of the flame can be explained by the CVP behavior. The roll up and the folding mechanism due to the interaction of the jet and the

cross-flow developed into CVP downstream. Figure 3.23 provides a schematic diagram of the process.

The point of peak velocity was located very close to the peak temperature region. For instance, in Figure 3.25a, the peak temperature is around the normalized distance of 20 (r/D), but the peak velocity is around 22 (r/D) in Figure 3.60a. There were two reasons for this. First, in the high temperature regions, the gas was accelerating due to the buoyancy effect. Secondly, it was caused by the way that the velocity value was calculated (as mentioned in previous section, 3.3.6a).

3.3.7 Flame Radiation

Figures 3.52 and 3.53 show the results for the total flame radiation and the flame radiation fraction at quiescent flame conditions. The total flame radiation is directly proportional to fuel flow rate. Figure 3.52 shows that the flame radiation increases almost linearly with the fuel flow rate. The comparison of the flame radiation for different inert gases shows that the argon gas diluted flames radiation was slightly lower than the radiation from the other inert gas diluted flames. On the other hand, the helium gas diluted flames radiation was slightly higher than the other inert gases diluted flame radiation at a high fuel flow rates. These phenomena can be explained from Figure 3.7a. The argon mass flow rate was the highest among other inert gases at smoke point condition. The higher argon mass flow rate may have absorbed more radiating heat from the flame than other inert dilution flame. On the other hand, the helium mass flow rate was the lowest among the other inert gases at each of the CFMFR. Thus, the helium gas diluted flame had the highest flame radiation.

However, the variation in radiation among the flames was small. The flame radiation fraction of heat release also showed that the variations in them among the flames was also small. The order (highest to lowest) of the value was about the same as the total flame radiation results. This was because all the flames have the same fuel mass flow rate; in another words, they had the same heating value.

3.4 Summary and Conclusion

All the smoke point results (quiescent and cross-flow conditions) show a skewed bell shape curve for the inert gas addition mass flow rate versus the fuel mass flow rate. From these results, two separate regions were defined as the chemical and momentum dominated regions, which are separated by a transition region. All the flames in quiescent condition and the 3.5 and 4 m/s cross-flow showed the transition region located at 20% to 40% CFMFR. The 2 to 3 m/s cross-flow flames had the transition region located at 10% to 30% CFMFR. This study was different from Goh's (1999) study mainly because the burner and the wind tunnel configurations used in both studies were different. The different burner configuration (introduction of hydrogen gas to attach the flame) caused the difference in the jet exit Reynolds number, which lead to the different smoke point results. The horizontal and the vertical wind tunnel had different flame buoyancy effect, which also lead to dissimilar smoke point results.

The inert gases comparison shows that the increasing rank of the gas effectiveness in suppressing smoke was He, N₂, CO₂ and Ar (mass basis). The main reason for this phenomenon was the heat sink capability of the gas. Hence, the specific heat of the gas becomes an important parameter. Thus, the rank of the effectiveness of the gases in

suppressing the smoke followed the rank of the specific heat of the gases. The comparison of the cross-flow flames showed that the jet Reynolds number and the momentum flux ratio (relative to respective percentage CFMFR) at the smoke point decreased with an increasing cross-flow velocity.

The temperature profiles in the flames at the quiescent condition and two lowest CFMFR show a dual-peak structure in the near-burner and mid-flame regions, because most reactions in this region were gas phase reactions. The far-burner region temperature profile showed a single peak because most of the reactions in this region were heterogeneous kinetic-controlled soot oxidation, as most of the soot particles in this region were concentrated near the flame centerline. The left side of the cross-flow flame had a higher temperature than the right side (x direction). This was mainly due to the mixing effect of the CVP, which caused the increase of the flame oxidation rate on the left side of the flame. The flame buoyancy effect also played an important role in influencing the mixing rate in the higher momentum flux ratio flames.

The global emission index results (quiescent and cross-flow conditions) showed that the momentum-dominated region flame had an increase of CO concentration as the CFMFR decreased. This phenomenon showed that the turbulence intensity (or the momentum effect) was the primary influence of CO oxidation in these flames. However, in the chemically-dominated region of the flame, the CO emission index decreased as the CFMFR decreased. This observation showed the behavior opposite to that in the momentum-dominated region, which signifies the dominance of the chemical effect. The global emission results in both quiescent and cross-flow flames showed that the O₂ and the CO₂ concentrations were in an opposite trend. In the cross-flow flames global

emission results, the NO and NO_x emission indices showed an increasing trend with the decrease of CFMFR. However, NO and NO_x emission indices in quiescent flames show very small discrepancy at different CFMFR.

At quiescent conditions the in-flame concentration profiles showed that the NO concentrations of the 10% and 30% CFMFR flames were higher than in the 60% and 100% CFMFR flames. This was because that the 60% and 100% CFMFR flames had a wider high temperature region than the 10% and 30% CFMFR flames. The CO₂ concentration results exhibited a dual peak at the near-burner and mid-flame regions for all the flames. The explanation for this phenomenon was similar to the one given in the temperature section. The O₂ concentration results showed an inverted behavior as the CO₂ concentration profile, which was expected in a diffusion flame.

In the cross-flow flames, the NO concentration profile was very similar to the temperature profile. Hence, the temperature effect dominated the NO production rate. Almost all of the near-burner and the mid-flame region of the chemically-dominated flames, and most of the momentum-dominated flames showed a dual peak structure. The NO and CO₂ concentration on the left side of the flame were higher than those on the right, which had similar characteristic as the temperature profile. Similar to the NO concentration profile, the CO₂ concentration profile also exhibited a dual-peak structure in the near burner region for all the cross-flow flames. Again, similar to the quiescent condition flame, the O₂ concentration profile of the cross-flow also showed an inverted structure of the CO₂ concentration profile. The gradient of the O₂ concentration on the left of the flame was lower than on the one on right, which indicated that the mixing rate on the left side of the flame was higher than the one on the right (x direction). The cross-

flow flame velocity results also showed a higher mixing rate on the left side of the flame than the one on the right.

The cross-flow flame structure exhibited a non-monotonic relation in the flame length versus the cross-flow velocity results. The flame length decreased with the increase of the cross-flow velocity from 2 to 3 m/s. However, from 3.5 to 4 m/s cross-flow, the flame length started to increase. These higher cross-flow velocity flames (3.5 and 4 m/s, momentum flux ratio, $R \leq 40$) behaved like a co-flow flame, which resulted in a decrease of the mixing rate, and an increase of the residence time and the flame length. All the cross-flow flames show a decrease of flame length from 100% CFMFR to the transition region. However, the flame length result shows an increase from the transition to 10% CFMFR. This was due to the transformation of the flame from turbulence-controlled to a laminar condition.

The flame radiation measurement result of the quiescent condition flames showed that the total flame radiation decreased with the decreased of CFMFR. There was a small variation of the flame radiation for different inert gas dilutions.

Table 3.7a Quiescent Experimental Conditions

% CFMFR	Mass Flow Rate			Jet Vel m/s	Mass Fraction			Jet Reynolds Number
	Propylene (g/min)	Nitrogen (g/min)	Hydrogen (g/min)		Propylene	Nitrogen	Hydrogen	
100%	17.322	0.000	0.671	38.15	0.963	0.000	0.037	12589
90%	15.562	1.324	0.651	37.91	0.887	0.075	0.037	11668
80%	13.802	2.136	0.627	36.63	0.833	0.129	0.038	10630
70%	12.042	2.345	0.573	33.49	0.805	0.157	0.038	9423
60%	10.282	2.942	0.468	29.75	0.751	0.215	0.034	8340
50%	8.522	3.646	0.340	25.63	0.681	0.292	0.027	7301
40%	6.762	4.112	0.340	24.34	0.603	0.367	0.030	6215
30%	5.002	4.034	0.282	20.57	0.537	0.433	0.030	4950
20%	3.242	3.843	0.237	16.94	0.443	0.525	0.032	3666
10%	1.482	2.834	0.110	9.74	0.335	0.640	0.025	2070
5%	0.602	2.243	0.084	6.92	0.205	0.766	0.029	1265
0%	0	0	0	0.00	0.000	0.000	0.000	0

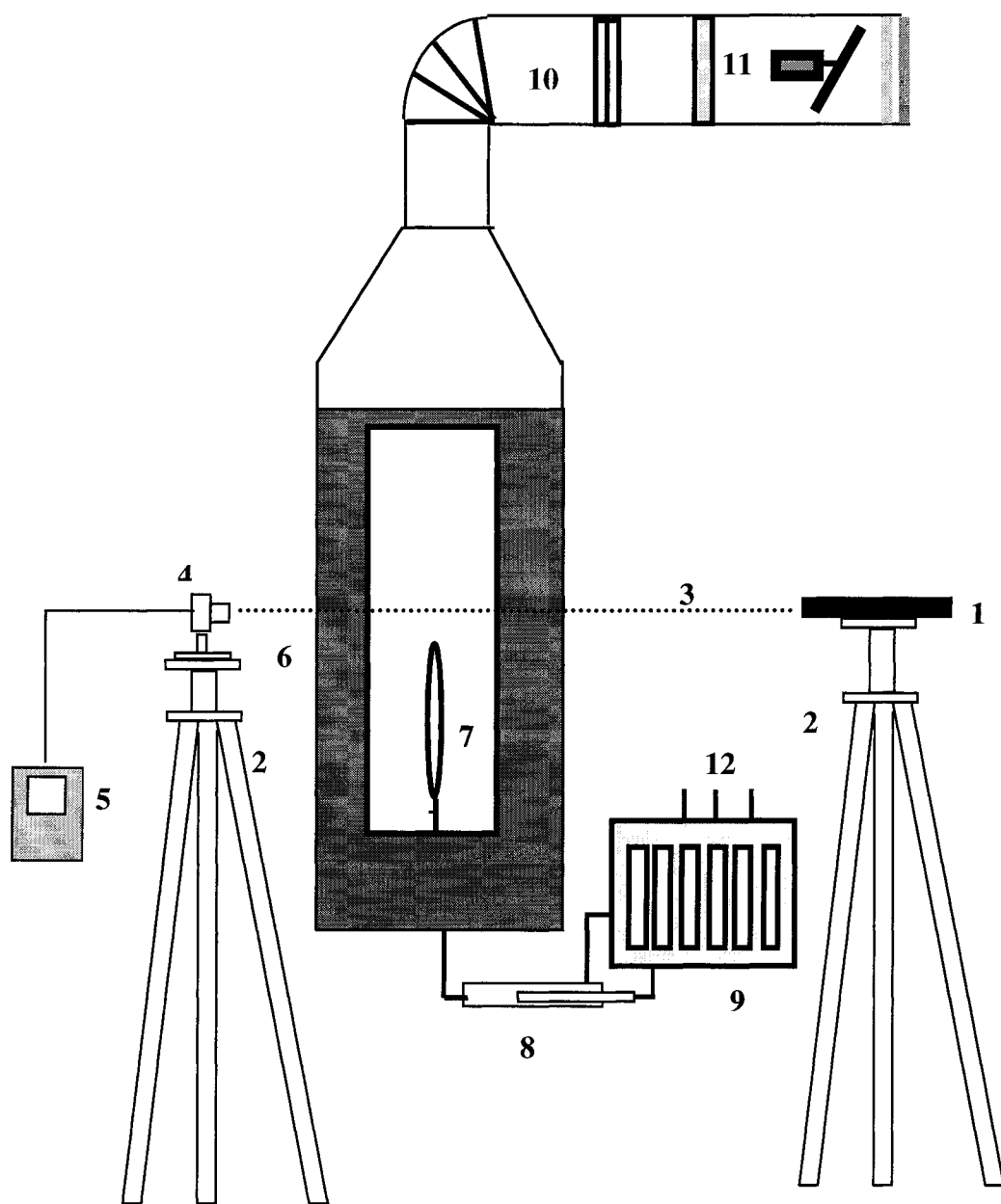
Table 3.7b Cross-Flow Experimental Conditions

Cross-Flow Velocity				2m/s								
Cross-Flow Reynolds number				48767								
% CFMFR	Mass Flow Rate			Jet Vel m/s	Mass Fraction			Momentum Flux Ratio R	Jet Reynolds Number	F _{fr} Froude # Jet	F _{fr} Froude # Flame	F _{fr} Froude # Cross-Flow
	Propylene (g/min)	Nitrogen (g/min)	Hydrogen (g/min)		Propylene	Nitrogen	Hydrogen					
100%	8.629	0.000	0.919	33.98	0.904	0.000	0.096	136.66	6357	36785.99	2.85	1.32
90%	7.738	1.252	0.666	28.71	0.801	0.130	0.069	116.79	6035	26266.27	1.98	0.96
80%	6.847	1.342	0.607	26.33	0.778	0.153	0.069	97.55	5422	22082.83	2.31	0.93
70%	5.956	1.885	0.502	23.57	0.714	0.226	0.060	82.81	4943	17689.84	2.59	1.13
60%	5.066	1.957	0.424	20.66	0.680	0.263	0.057	64.79	4322	13593.08	1.98	1.06
50%	4.175	2.201	0.349	18.15	0.621	0.327	0.052	51.41	3763	10491.79	2.58	1.08
40%	3.284	2.088	0.294	15.49	0.580	0.368	0.052	36.98	3092	7645.27	2.45	1.25
30%	2.394	2.166	0.226	12.83	0.500	0.453	0.047	25.85	2486	5240.39	2.70	1.72
20%	1.503	2.404	0.134	9.86	0.372	0.595	0.033	16.79	1937	3099.64	2.90	1.63
10%	0.612	1.885	0.057	5.91	0.240	0.738	0.022	6.36	1125	1112.57	3.93	2.94
5%	0.167	1.187	0.042	3.74	0.120	0.850	0.030	2.20	573	445.88	3.17	2.26
Cross-Flow Velocity				3m/s								
Cross-Flow Reynolds number				73151								
100%	8.197	0.000	0.939	33.97	0.897	0.000	0.103	58.10	6065	36759.73	3.89	2.80
90%	7.349	0.763	0.739	29.24	0.830	0.086	0.084	48.45	5634	27235.21	3.19	2.31
80%	6.502	1.193	0.640	26.48	0.780	0.143	0.077	41.31	5145	22338.27	2.91	2.17
70%	5.654	1.563	0.584	24.72	0.725	0.200	0.075	36.10	4659	19463.04	2.79	2.11
60%	4.807	1.760	0.522	22.51	0.678	0.248	0.074	29.87	4118	16135.56	3.44	2.34
50%	3.959	1.933	0.442	19.76	0.625	0.305	0.070	23.43	3563	12441.41	3.54	2.67
40%	3.112	2.016	0.371	17.10	0.566	0.367	0.067	17.60	2985	9315.47	3.24	2.54
30%	2.264	1.963	0.275	13.57	0.503	0.436	0.061	11.44	2351	5865.77	2.47	2.28
20%	1.417	2.201	0.160	10.05	0.375	0.583	0.042	7.11	1817	3216.96	3.31	3.84
10%	0.569	1.533	0.090	6.07	0.260	0.699	0.041	2.49	983	1172.64	3.87	4.75
5%	0.145	1.031	0.072	4.20	0.116	0.826	0.057	0.98	520	561.02	3.71	5.29
Cross-Flow Velocity				4m/s								
Cross-Flow Reynolds number				97534								
100%	7.105	0.000	0.889	31.37	0.889	0.000	0.111	26.41	5292	31354.90	4.32	4.74
90%	6.367	0.595	0.787	28.98	0.822	0.077	0.102	23.65	4925	26750.60	3.19	3.18
80%	5.629	1.067	0.670	25.95	0.764	0.145	0.091	20.13	4517	21458.46	4.32	4.21
70%	4.890	1.372	0.566	22.99	0.716	0.201	0.083	16.53	4064	16839.57	3.25	3.15
60%	4.152	1.395	0.512	20.79	0.685	0.230	0.084	13.27	3544	13769.37	3.37	3.41
50%	3.414	1.491	0.395	17.12	0.644	0.281	0.075	9.55	3018	9333.02	3.91	4.79
40%	2.675	1.401	0.319	14.13	0.609	0.319	0.072	6.54	2450	6360.27	2.64	4.31
30%	1.937	2.148	0.279	13.61	0.444	0.492	0.064	6.25	2203	5902.57	3.88	5.86
20%	1.198	2.118	0.194	10.52	0.341	0.603	0.055	3.89	1663	3526.29	3.74	5.19
10%	0.465	1.413	0.092	5.76	0.236	0.717	0.047	1.20	874	1057.16	2.08	5.30
5%	0.093	0.739	0.075	3.68	0.103	0.815	0.082	0.35	383	430.42	2.12	8.22

Cross-Flow Reynolds Number = $\frac{v_{\infty} D_{test}}{v_{\infty}}$ where D_{test} is hydraulic diameter of the test section x-y cross sectional area.

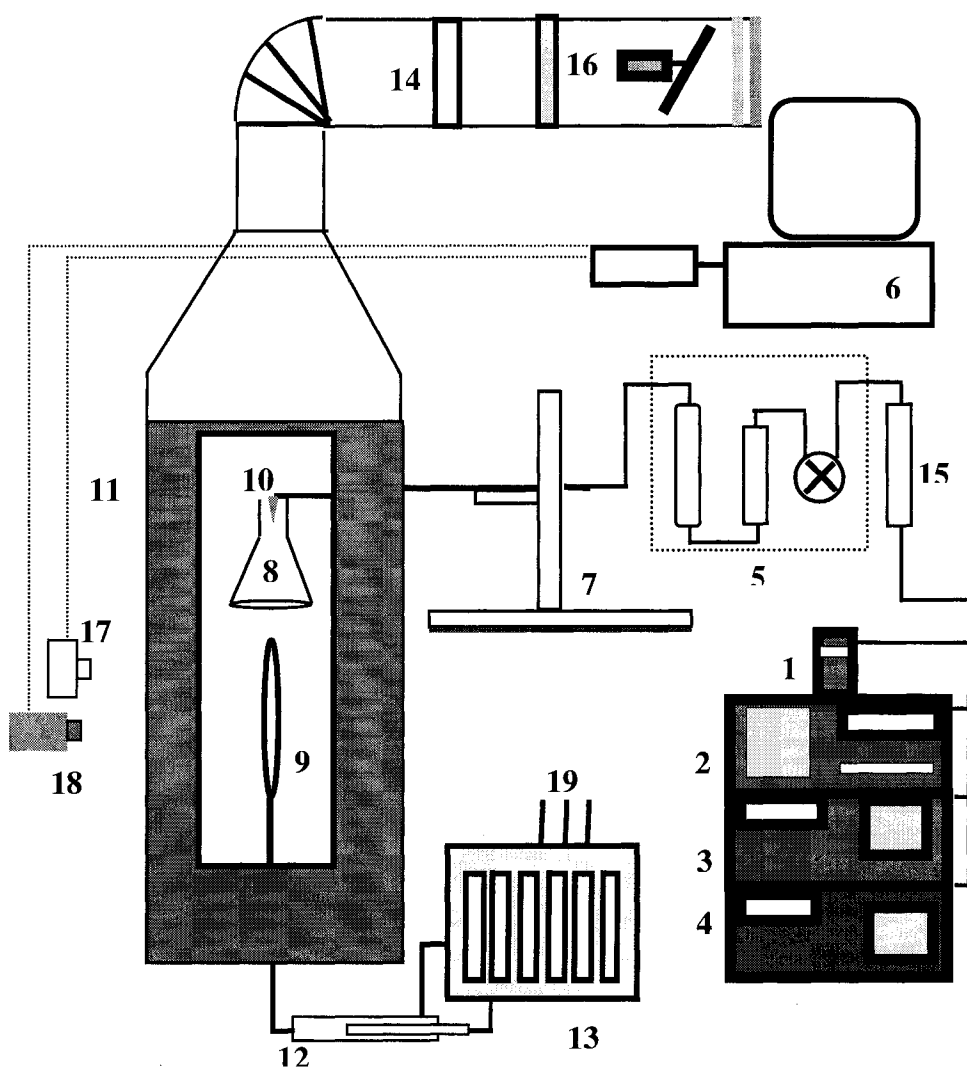
Jet Froude number = $\frac{v_j}{g D_j}$ where g is the gravitational acceleration, D_j is the jet diameter.

Flame and cross-flow Froude number is defined in page 37.



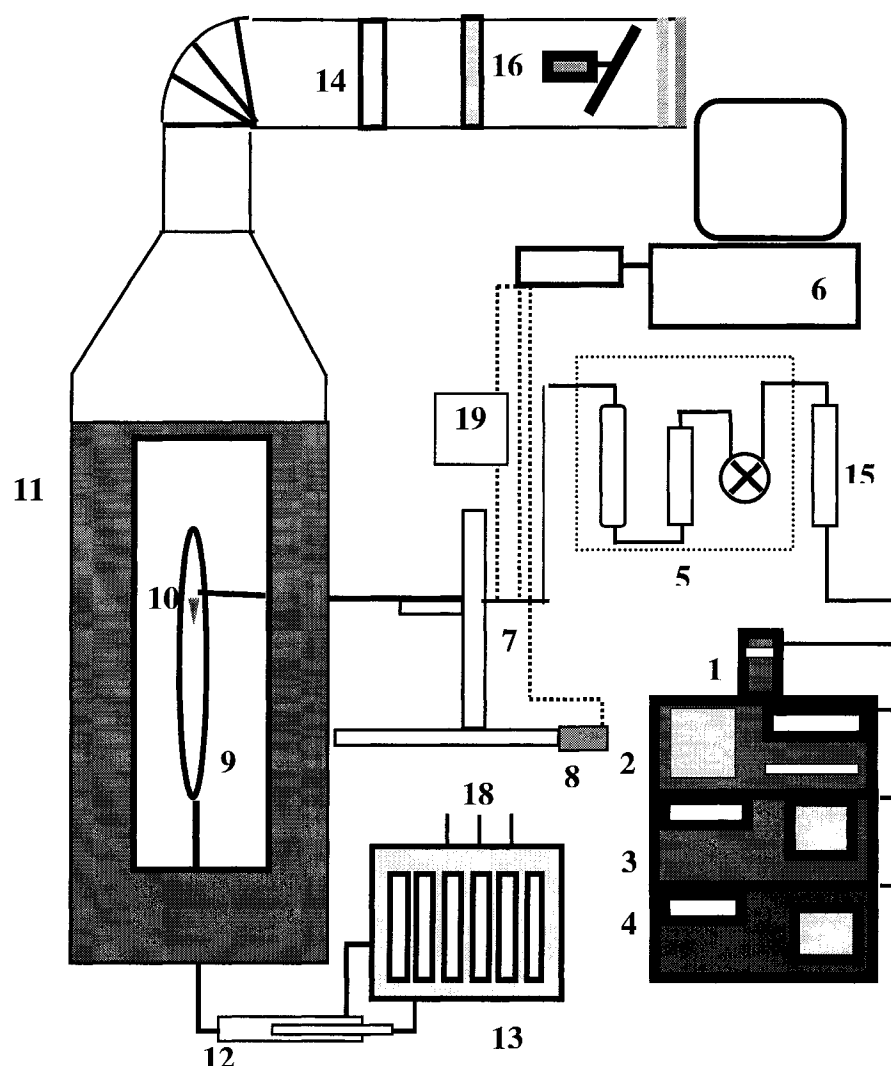
- | | |
|-------------------------|---|
| 1. He-Ne Laser | 7. Flame with Burner |
| 2. Tripod | 8. Mixing Device |
| 3. Laser Beam | 9. Rotameters |
| 4. Laser Power Detector | 10. Damper |
| 5. Display | 11. Relay Valve |
| 6. Combustion Chamber | 12. To Fuel, Hydrogen and Nitrogen Supply |

Figure 3.1 Combustion Chamber, Smoke Point Detection and Soot Volume Fraction Measurement Setup



- | | |
|--|--|
| 1. Oxygen Analyzer | 10. Quartz probe |
| 2. NO-NO _x Analyzer | 11. Combustion Chamber |
| 3. CO ₂ Analyzer | 12. Mixing Device |
| 4. CO Analyzer | 13. Rotameters |
| 5. Exhaust Treatment System:
Particulate Filter, Ice-Bath,
Vacuum Pump | 14. Damper |
| 6. DAS and Computer | 15. Rotameter |
| 7. 2-D Traverse Mechanism | 16. Relay Valve |
| 8. Exhaust Collection Cone | 17. Radiometer |
| 9. Flame with Burner | 18. CCD Camera |
| | 19. To Fuel, Hydrogen and Nitrogen
Supply |

Figure 3.2 Flame Emission and Radiation Measurement, and Flame Imaging Setup



- | | |
|--|---|
| 1. Oxygen Analyzer | 10. Quartz probe or Thermocouple or Pitot Static Tube |
| 2. NO-NO _x Analyzer | 11. Combustion Chamber |
| 3. CO ₂ Analyzer | 12. Mixing Device |
| 4. CO Analyzer | 13. Rotameters |
| 5. Exhaust Treatment System:
Particulate Filter, Ice-Bath,
Vacuum Pump | 14. Damper |
| 6. DAS and Computer | 15. Rotameter |
| 7. 2-D Traverse Mechanism | 16. Relay Valve |
| 8. Stepper Motor | 18. To Fuel, Hydrogen and Nitrogen Supply |
| 9. Flame with Burner | 19. Barocel |

Figure 3.3 In-Flame Gas Sampling and Temperature Measurements Setup

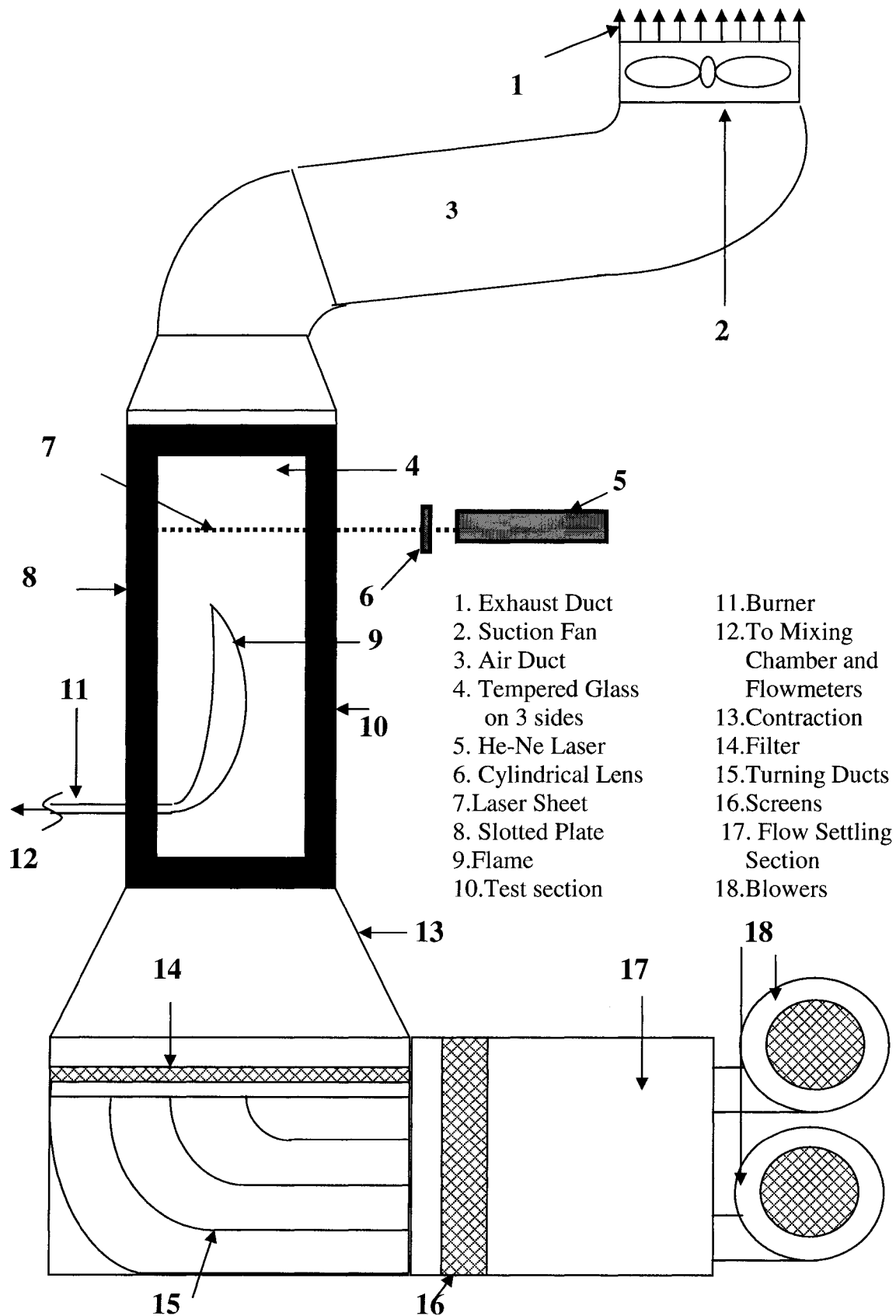


Figure 3.4 Schematic Diagram of the Combustion Wind Tunnel and Smoke Point Detection

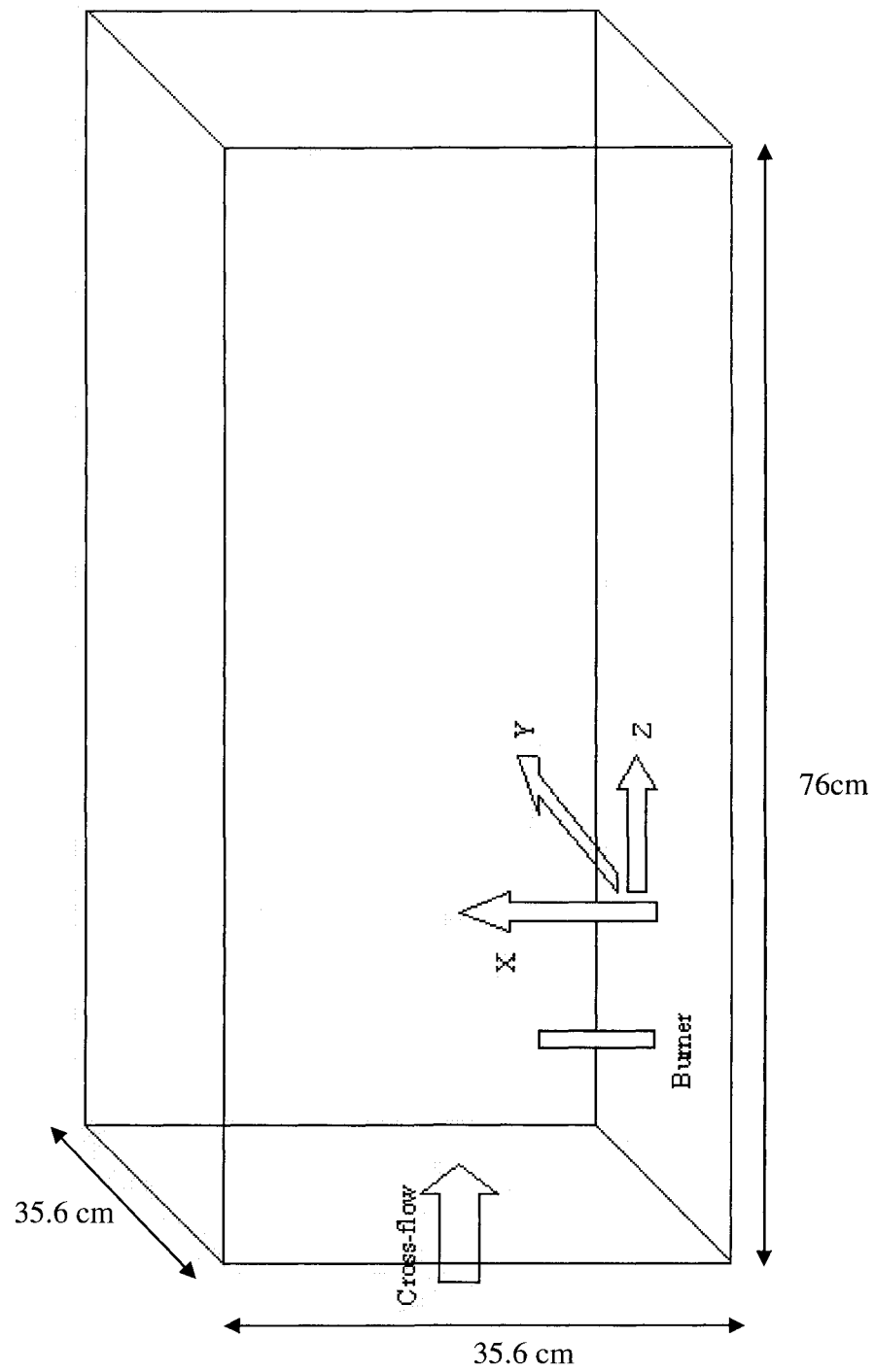


Figure 3.5 Coordinate System of Wind Tunnel.

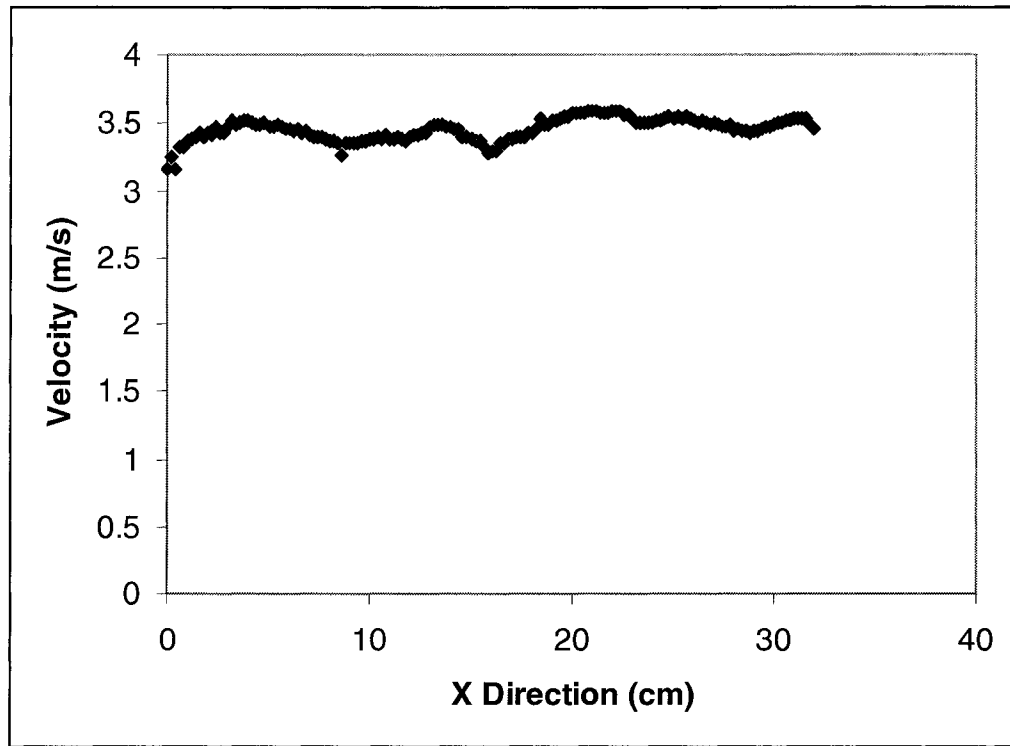


Figure 3.6a Velocity Profile of the Middle of the Test Section at 3.4 m/s in X Direction

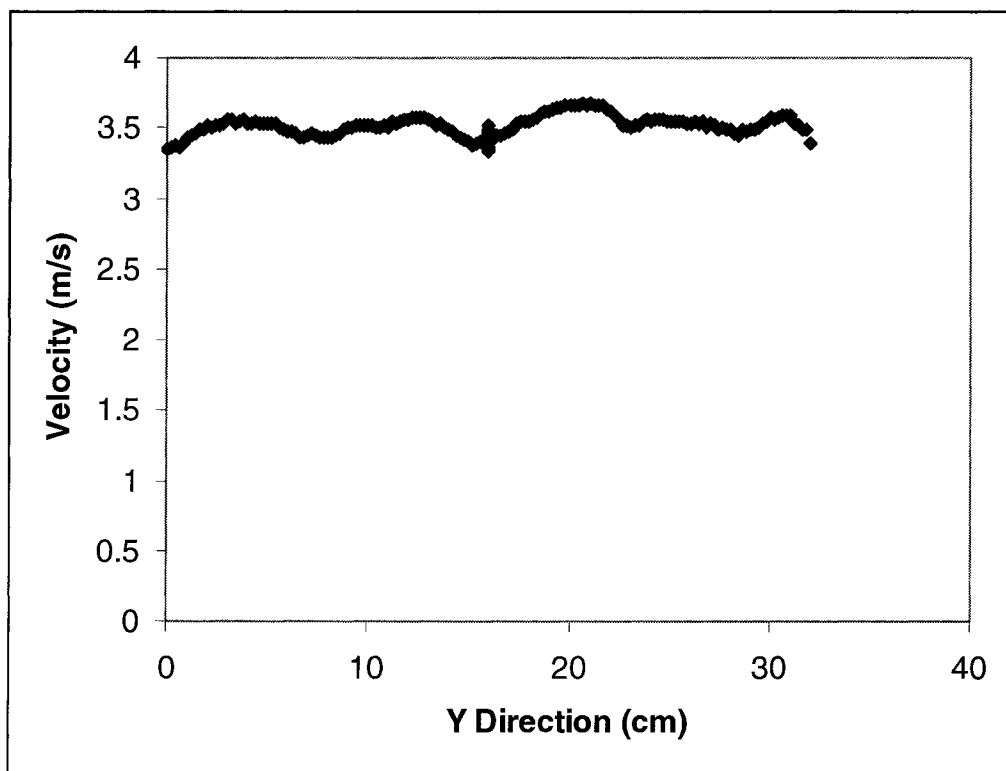


Figure 3.6b Velocity Profile of the Middle of the Test Section at 3.4 m/s in Y Direction

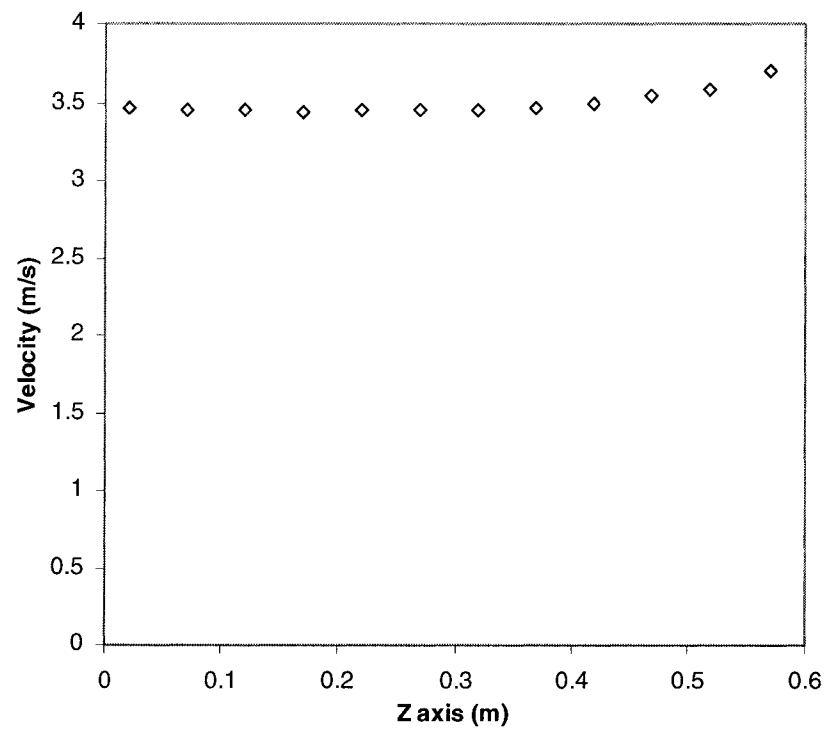


Figure 3.6c Velocity Profile along the Z axis at the Center of the Test Section at 3.5 m/s

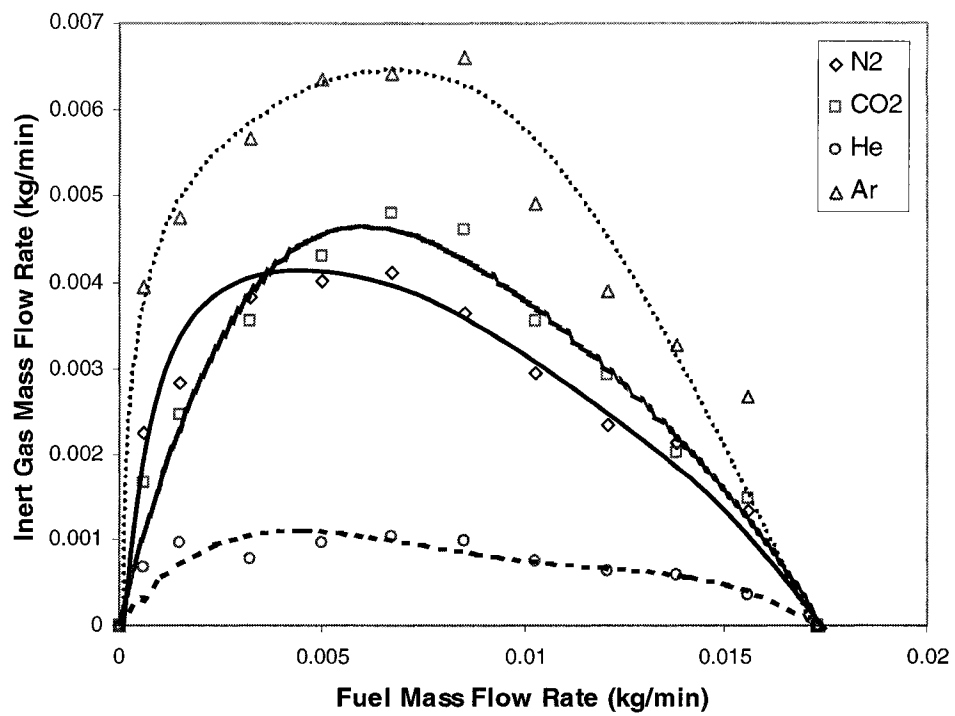


Figure 3.7a Inert Gases Mass Flow Rate Comparison at Smoke Point

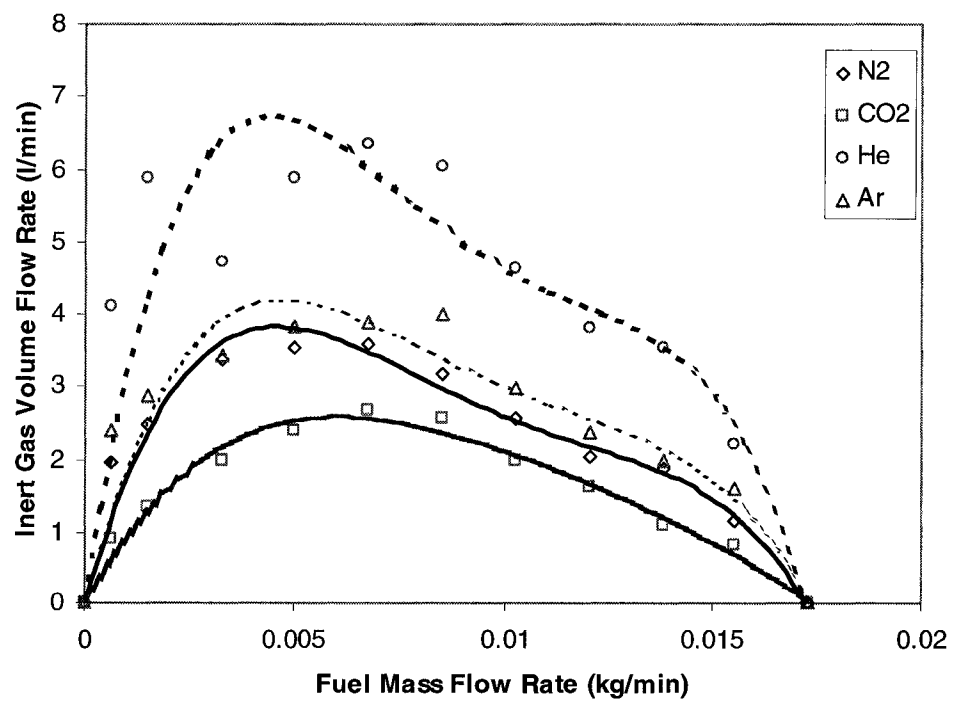


Figure 3.7b Inert Gases Volume Flow Rate Comparison at Smoke Point

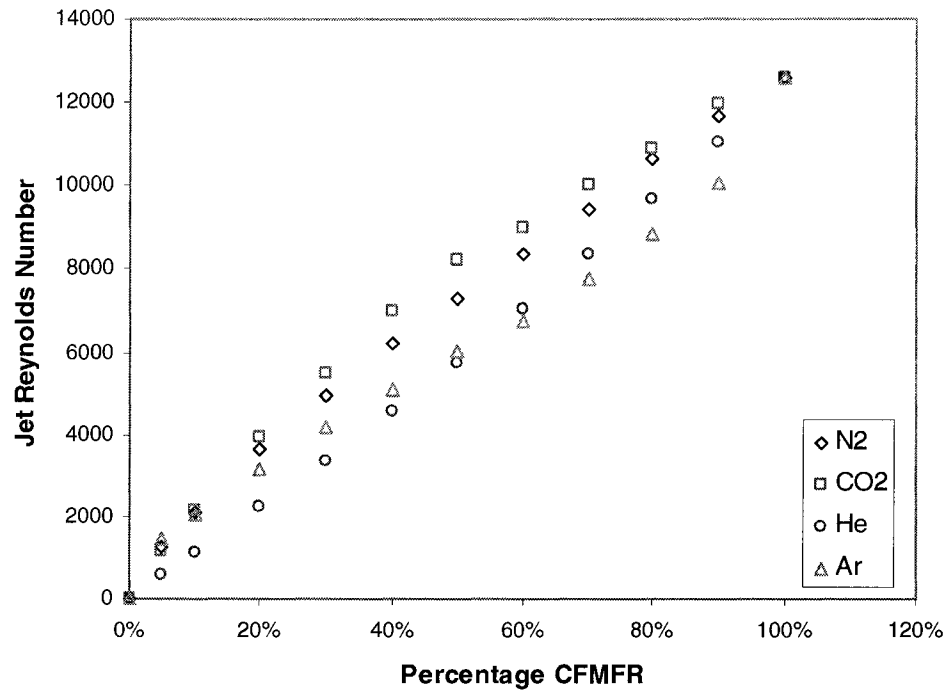


Figure 3.8 Jet Reynolds Number Comparison for Different Inert Gases at Smoke Point

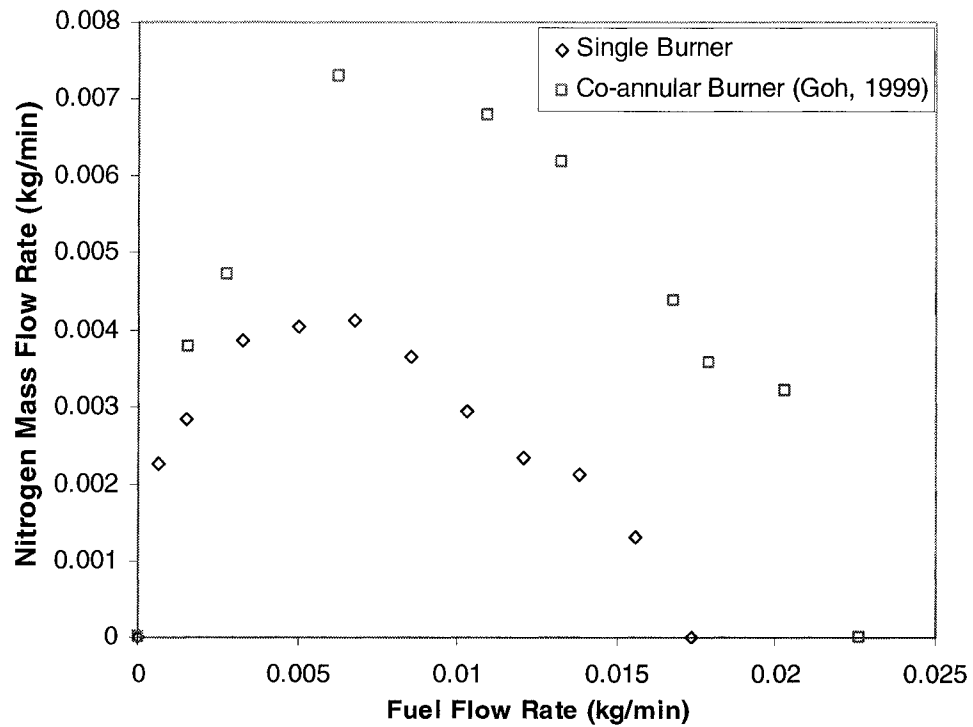


Figure 3.9 Nitrogen Mass Flow Rate Comparison for Single Burner and Co-annular Burner at Smoke Point

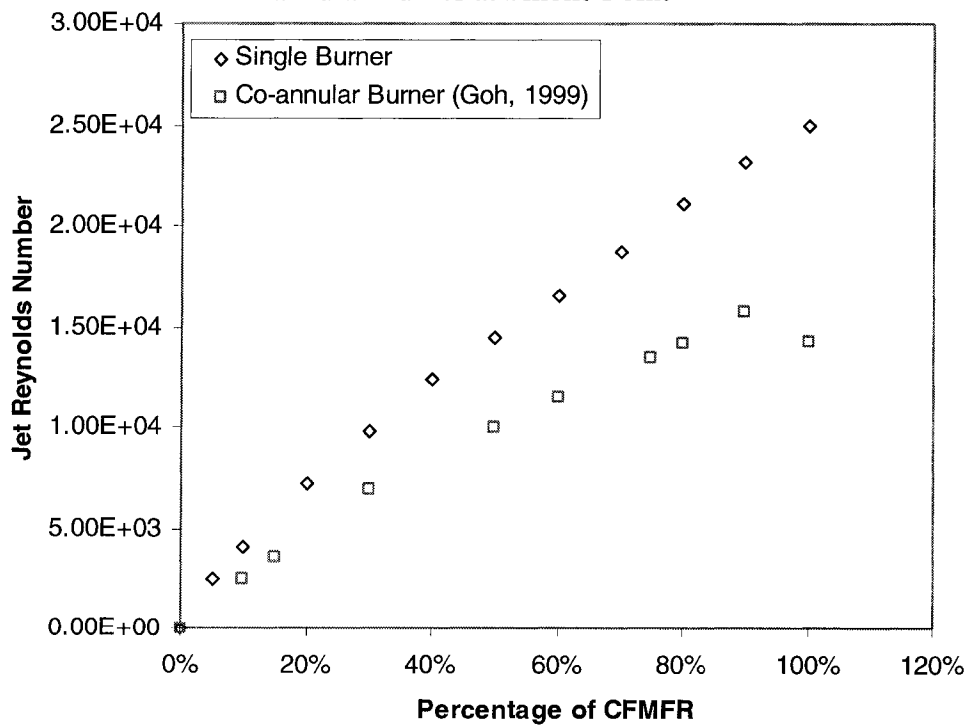


Figure 3.10 Jet Reynolds Number Comparison for Single Burner and Co-annular Burner

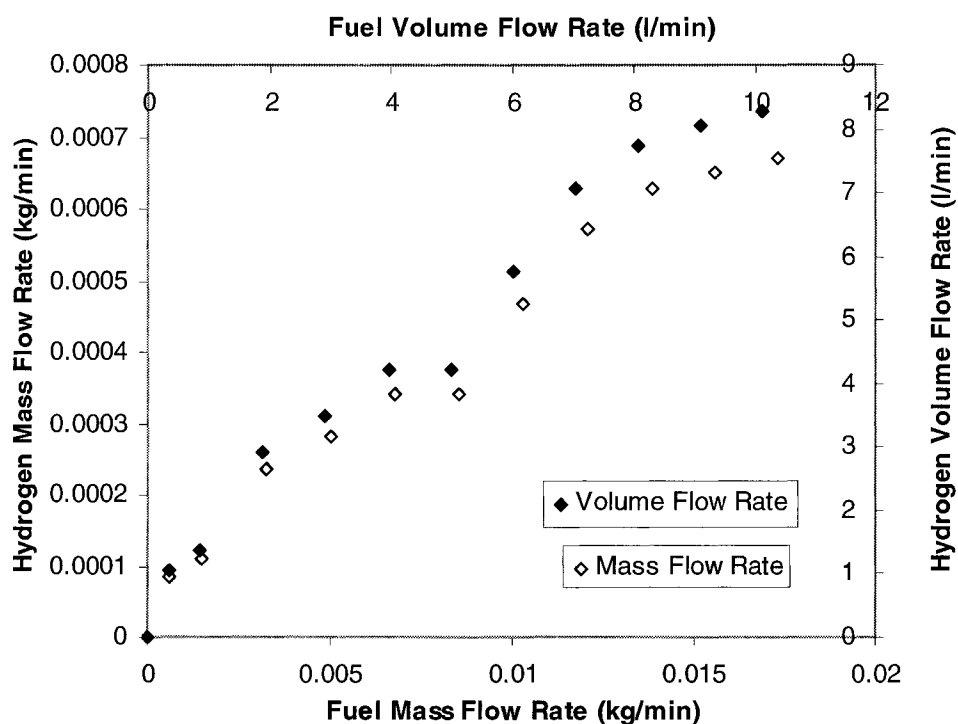


Figure 3.11 Hydrogen Mass and Volume Flow Rate for Each Fuel Mass and Volume Flow Rate at Smoke Point for Nitrogen Dilution for Single Burner Study

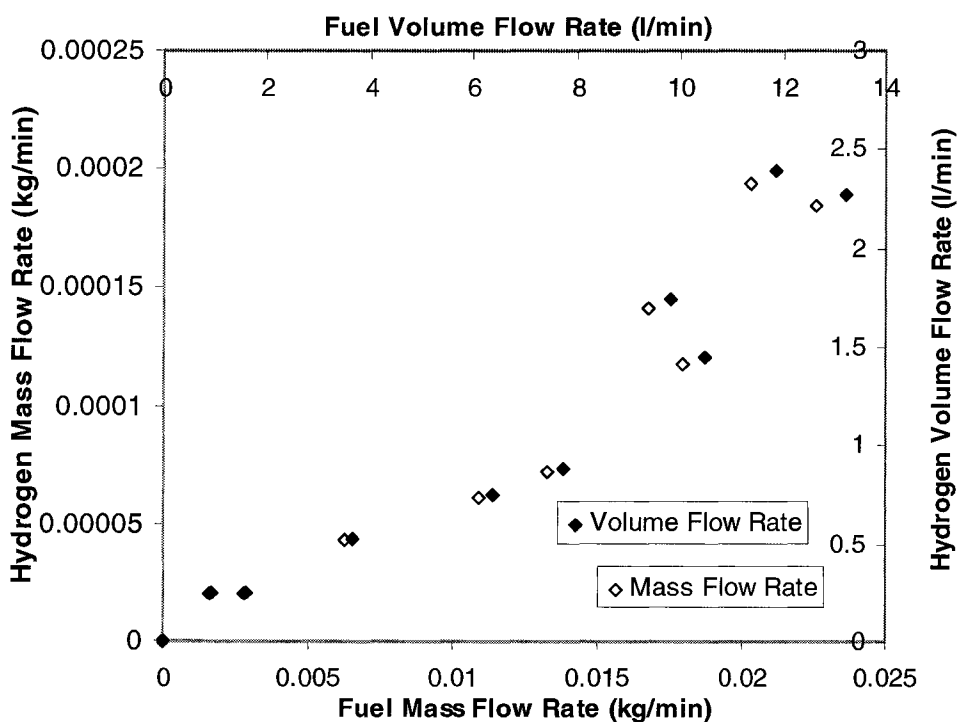


Figure 3.12 Hydrogen Mass and Volume Flow Rate for Each Fuel Mass and Volume Flow Rate at Smoke Point for Nitrogen Dilution for Goh (1999) Co-Annular Burner Study

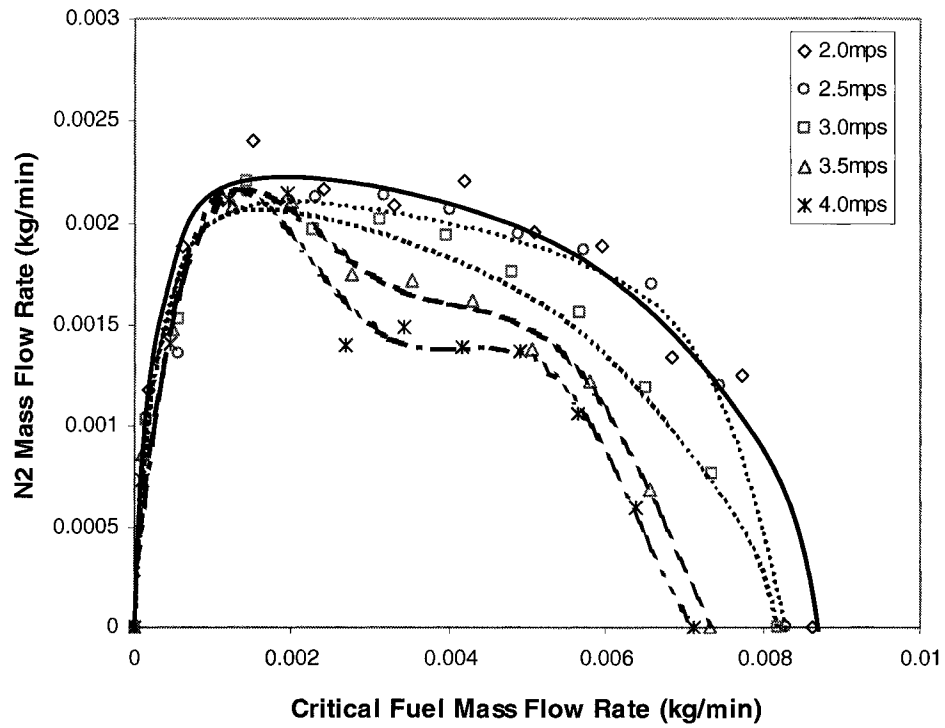


Figure 3.13 Smoke Point Results for Different Cross Flow Conditions

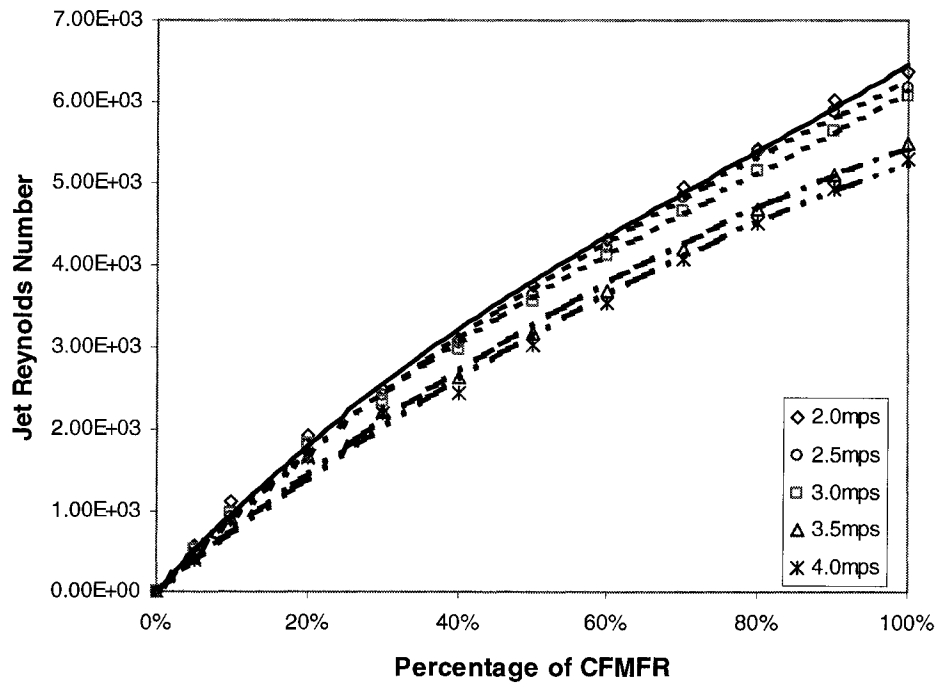


Figure 3.14 Jet Reynolds Number at Smoke Point for Different Cross Flow Conditions

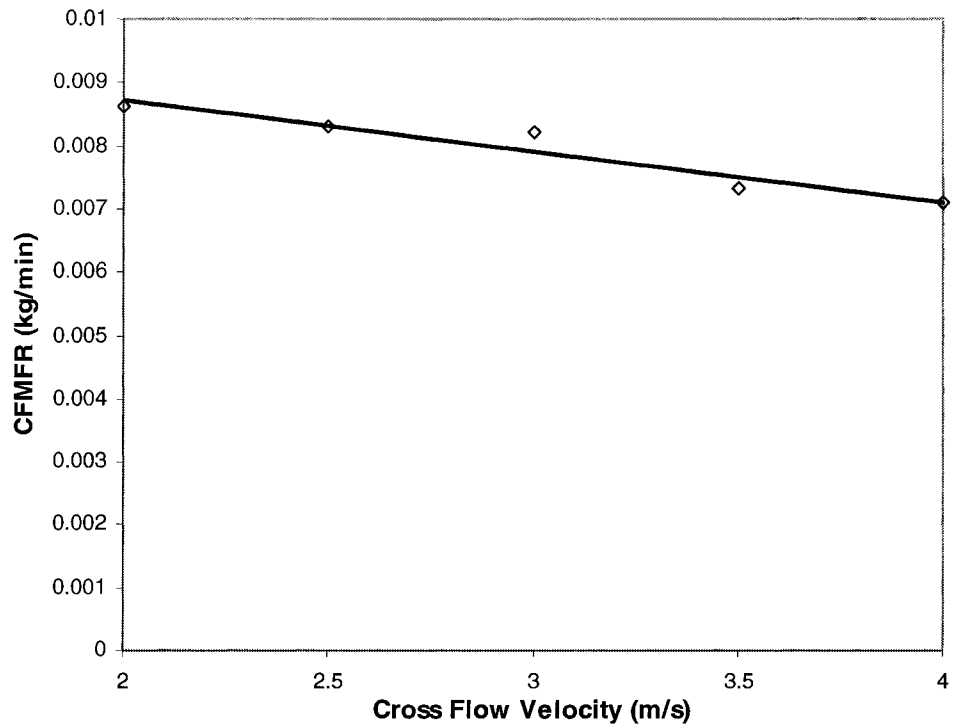


Figure 3.15 Relation of CFMFR with Cross-Flow Velocity

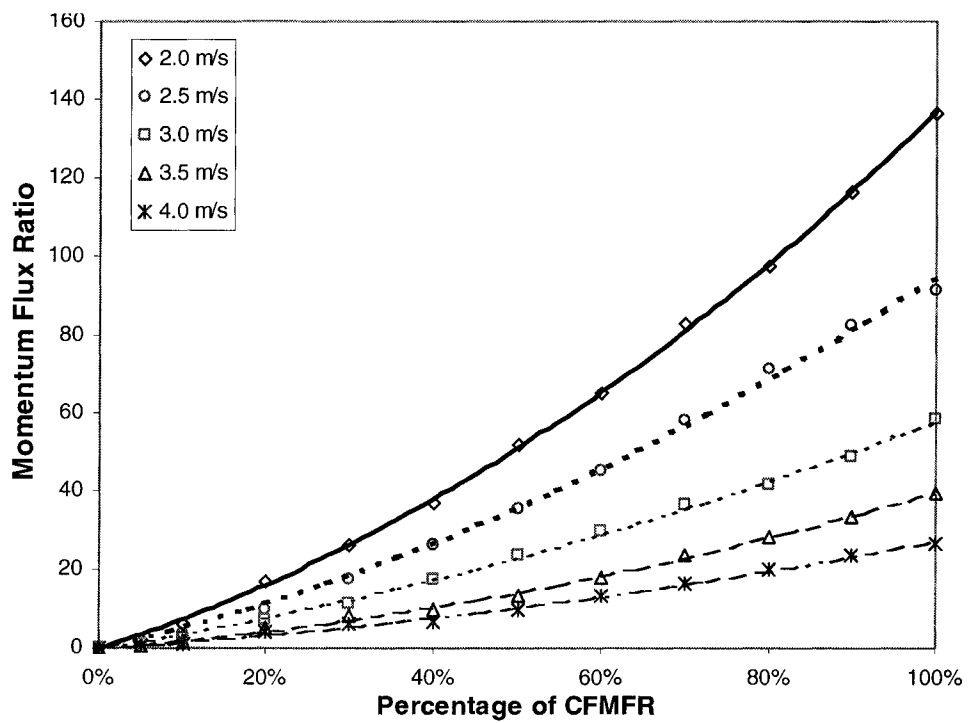


Figure 3.16 Momentum Flux Ratio at Smoke Point for Different Cross Flow Conditions

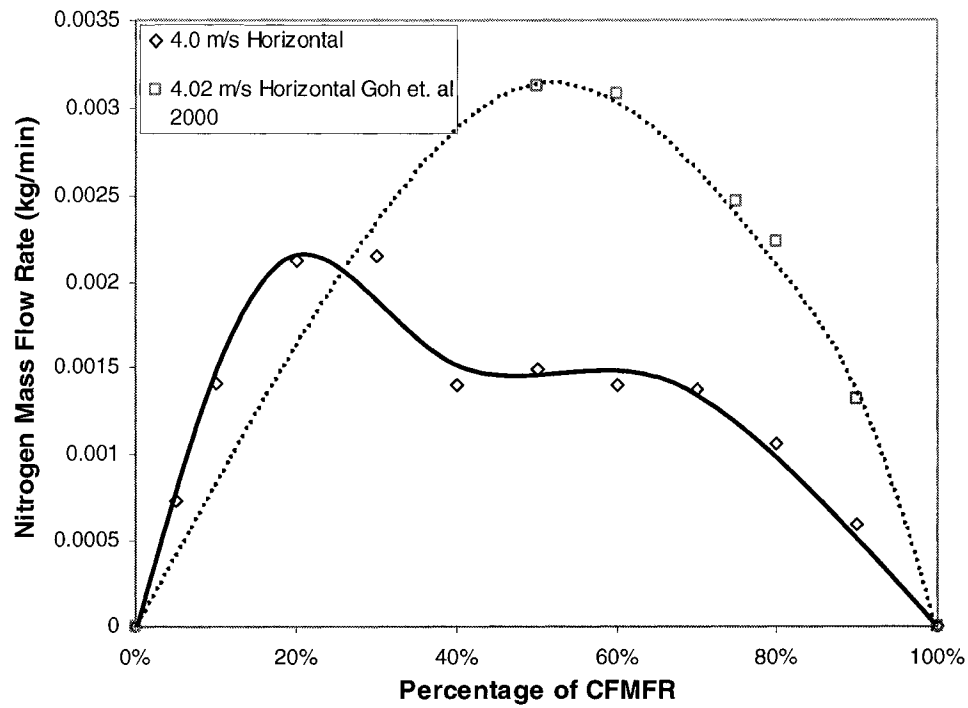


Figure 3.17 Comparison of Current Upright Wind Tunnel Nitrogen Mass Flow Rate at 4.0 m/s to Horizontal Wind Tunnel Nitrogen Mass Flow Rate at 4.02 m/s

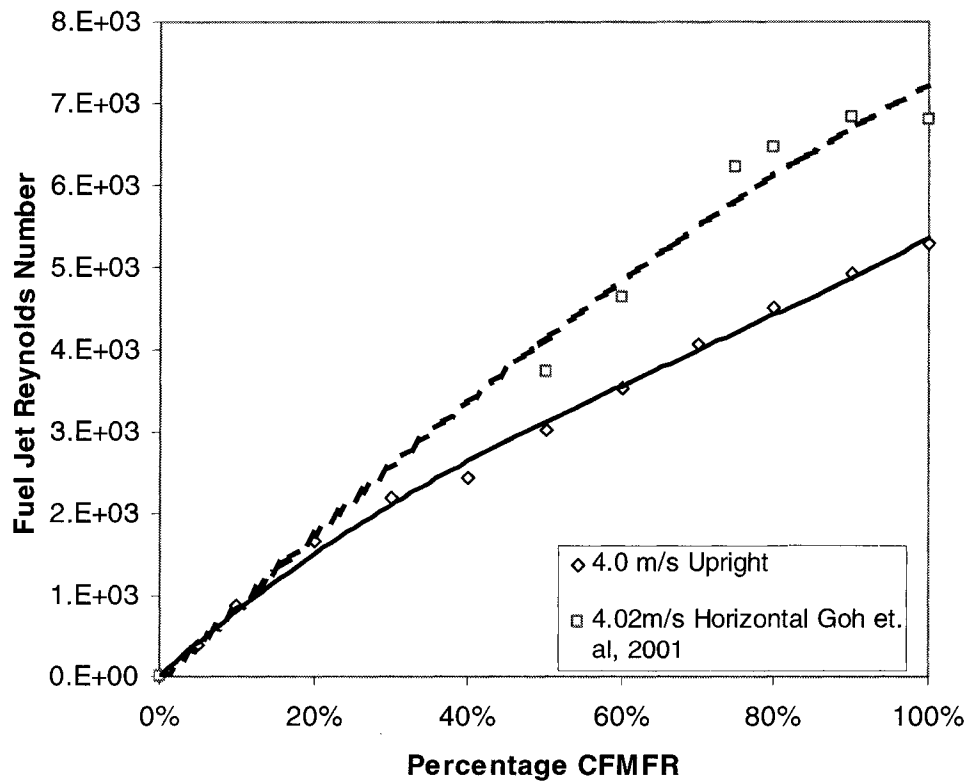


Figure 3.18 Comparison of Current Upright Wind Tunnel Fuel Jet Reynolds Numbers at 4.0 m/s to Horizontal Wind Tunnel Fuel Jet Reynolds Numbers at 4.02 m/s

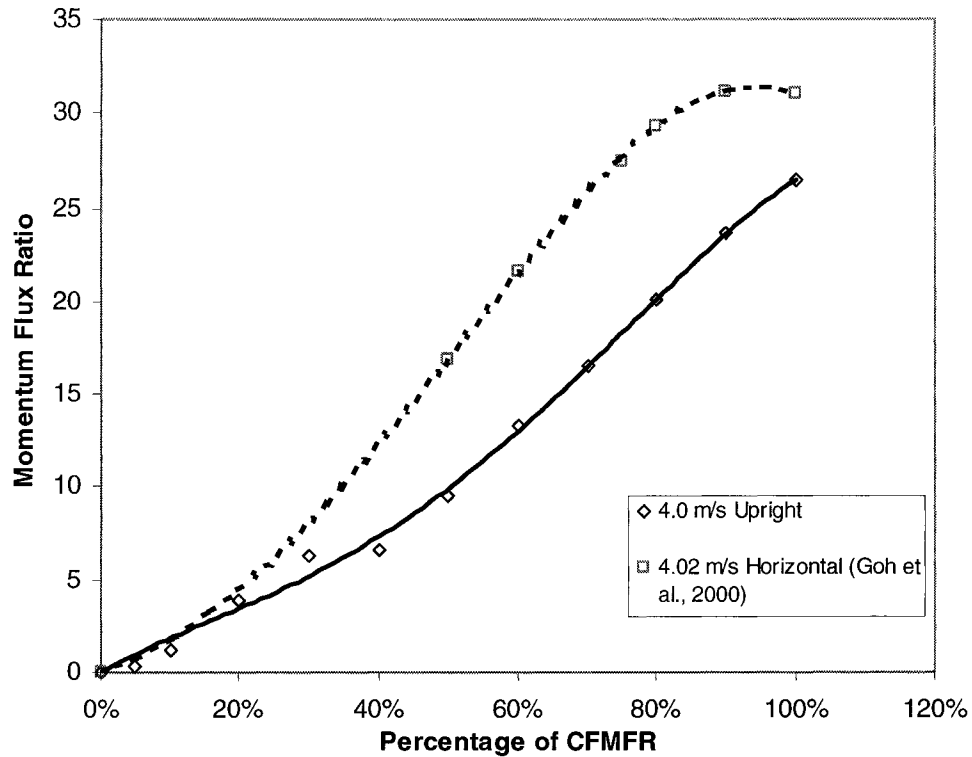


Figure 3.19 Comparison of Current Upright Wind Tunnel Momentum Flux Ratio at 4.0 m/s to Horizontal Wind Tunnel Momentum Flux Ratio at 4.02 m/s Cross-Flow

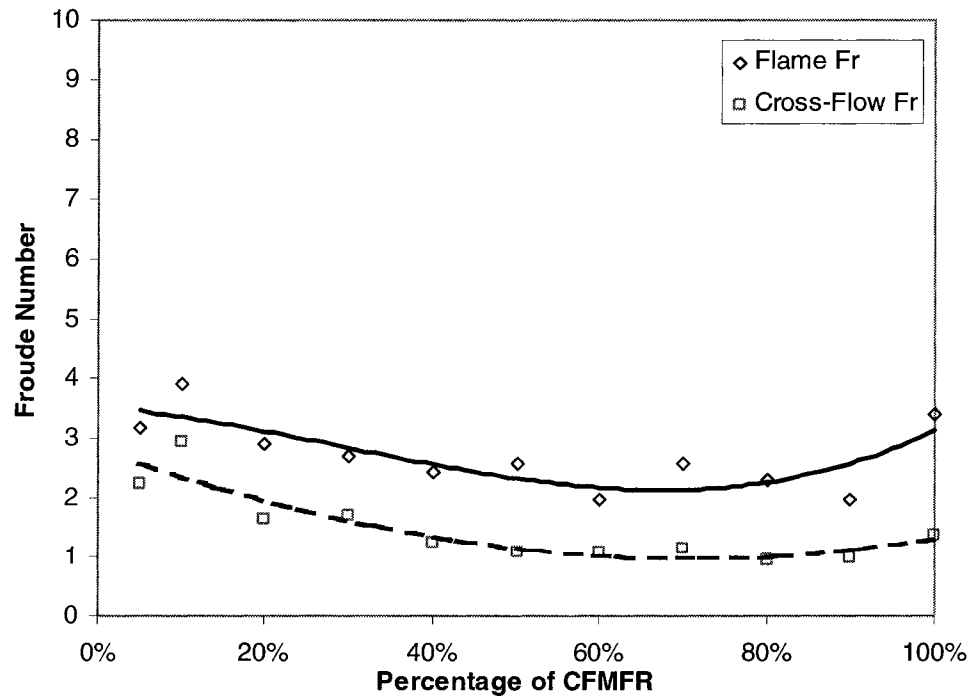


Figure 3.20a The Calculated Froude Number for the Flame and the Cross-Flow for Different Percentages of CFMFR at 2m/s Cross-Flow Condition.

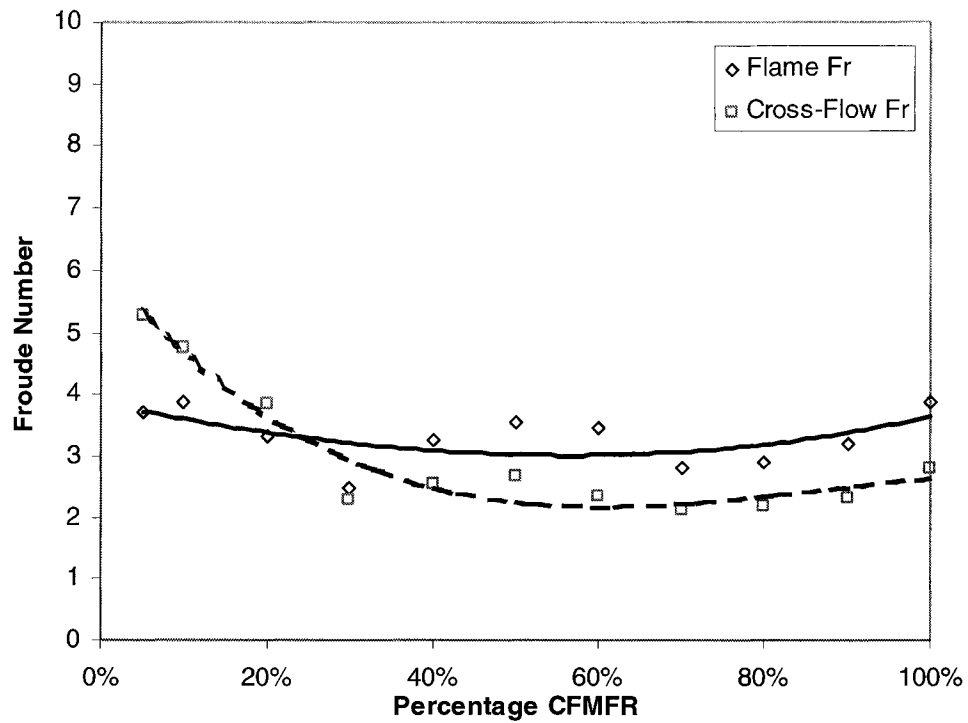


Figure 3.20b The Calculated Froude Number for the Flame and the Cross-Flow for Different Percentages of CFMFR for 3m/s Cross-Flow Condition.

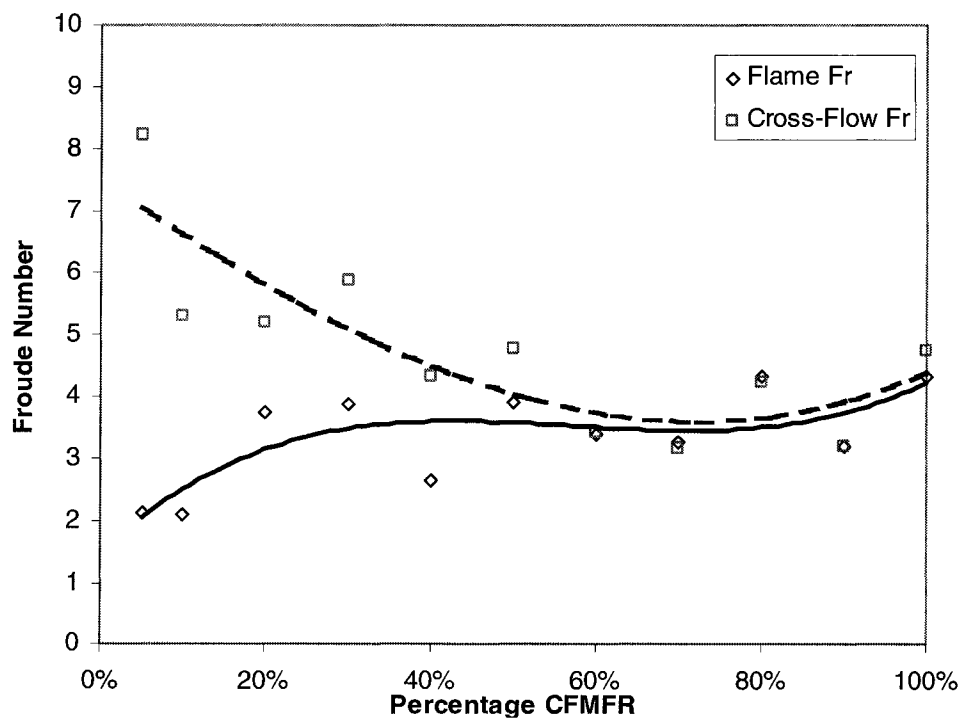


Figure 3.20c The Calculated Froude Number for the Flame and the Cross-Flow for Different Percentages of CFMFR for 4m/s Cross-Flow Condition.

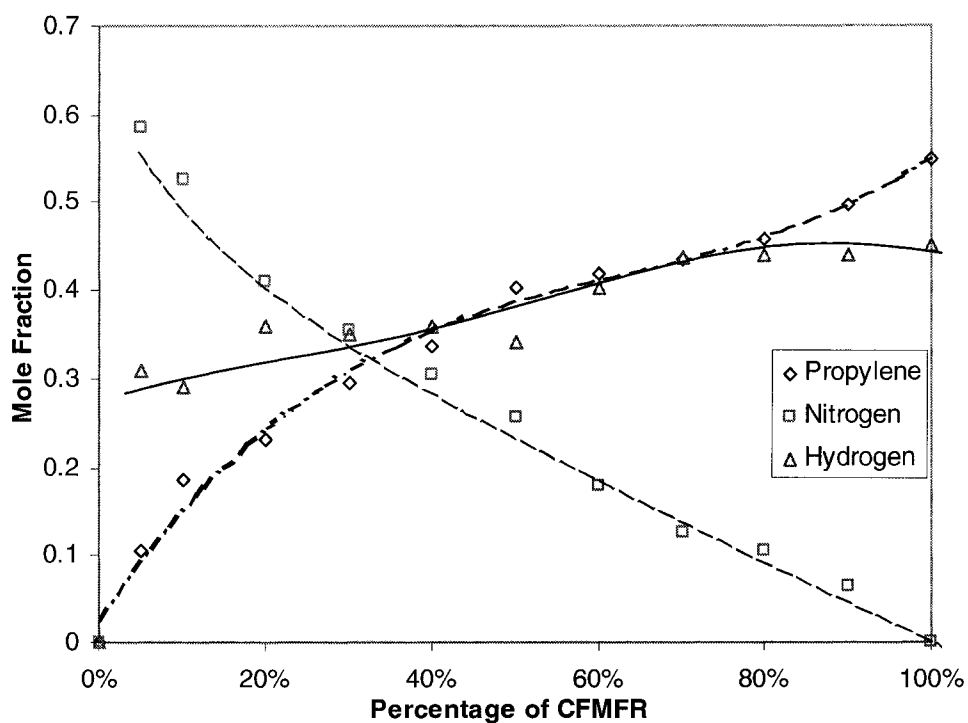


Figure 3.21 Mole Fraction of Jet Gas Mixture for Nitrogen Dilution Study in Quiescent Condition

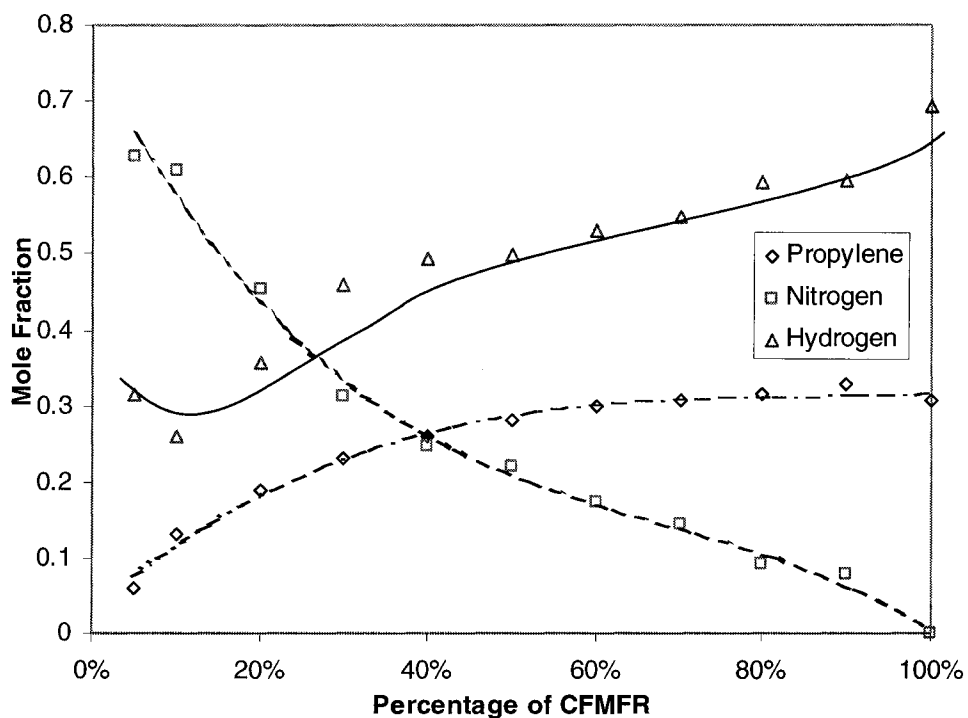


Figure 3.22a Mole Fraction of Jet Gas Mixture at Smoke Point at 2m/s Cross-Flow

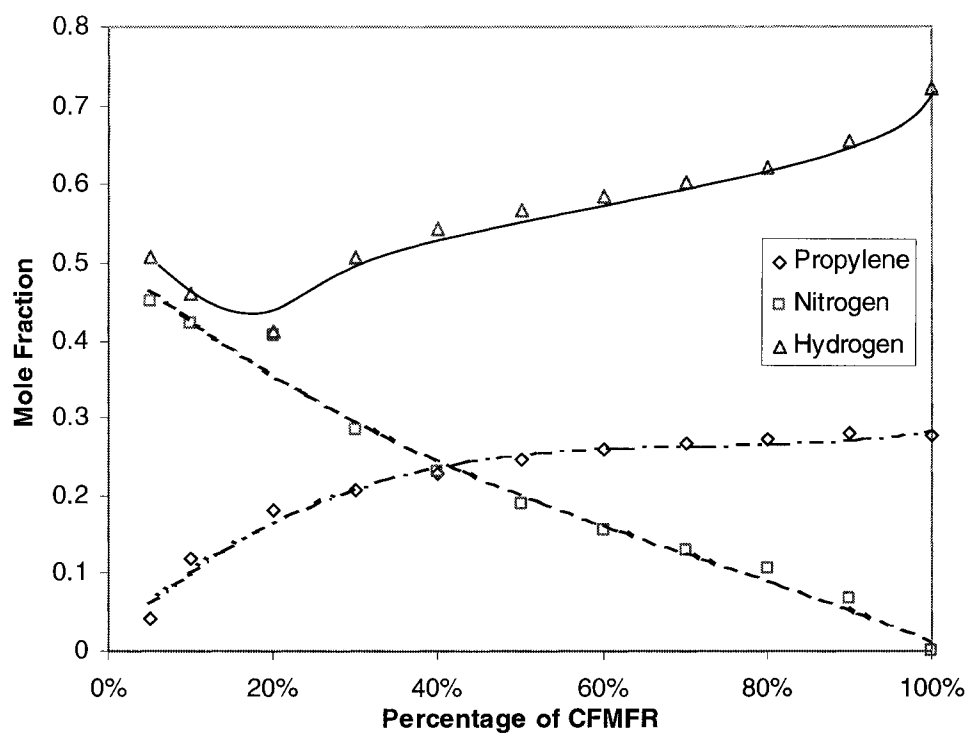


Figure 3.22b Mole Fraction of Jet Gas Mixture at Smoke Point at 2.5 m/s Cross-Flow

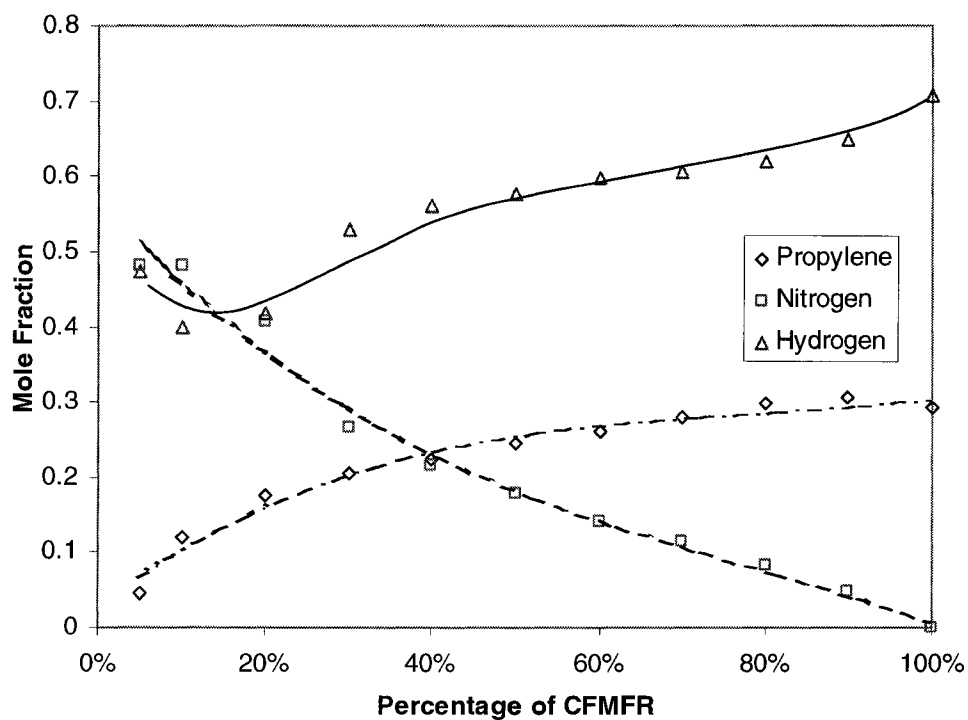


Figure 3.22c Mole Fraction of Jet Gas Mixture at Smoke Point at 3.0 m/s Cross-Flow

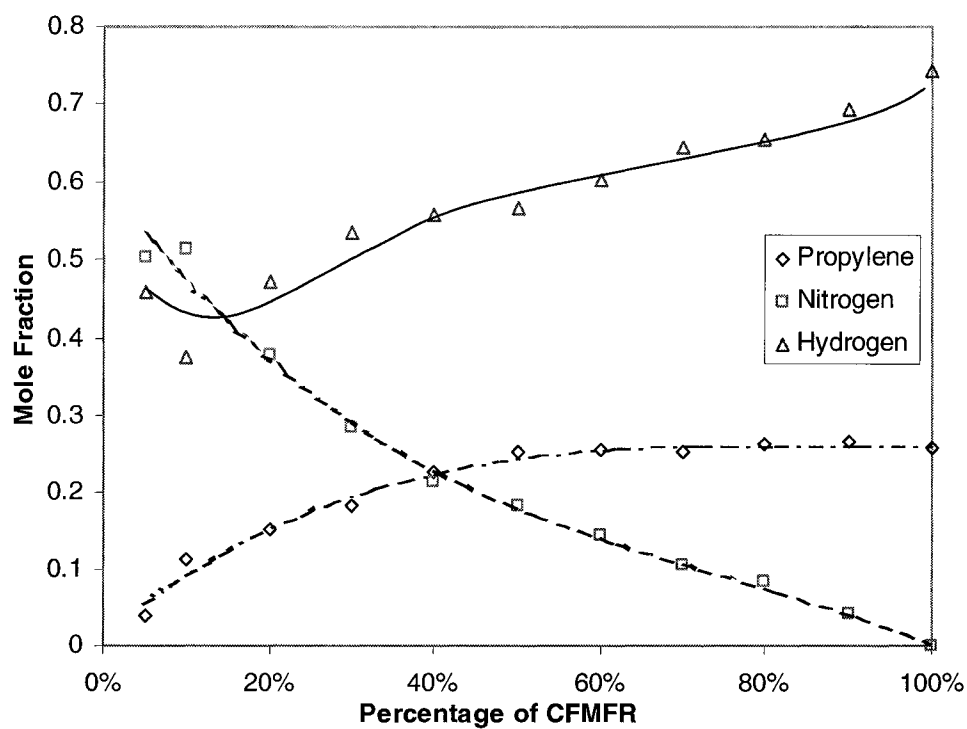


Figure 3.22d Mole Fraction of Jet Gas Mixture at Smoke Point at 3.5 m/s Cross-Flow

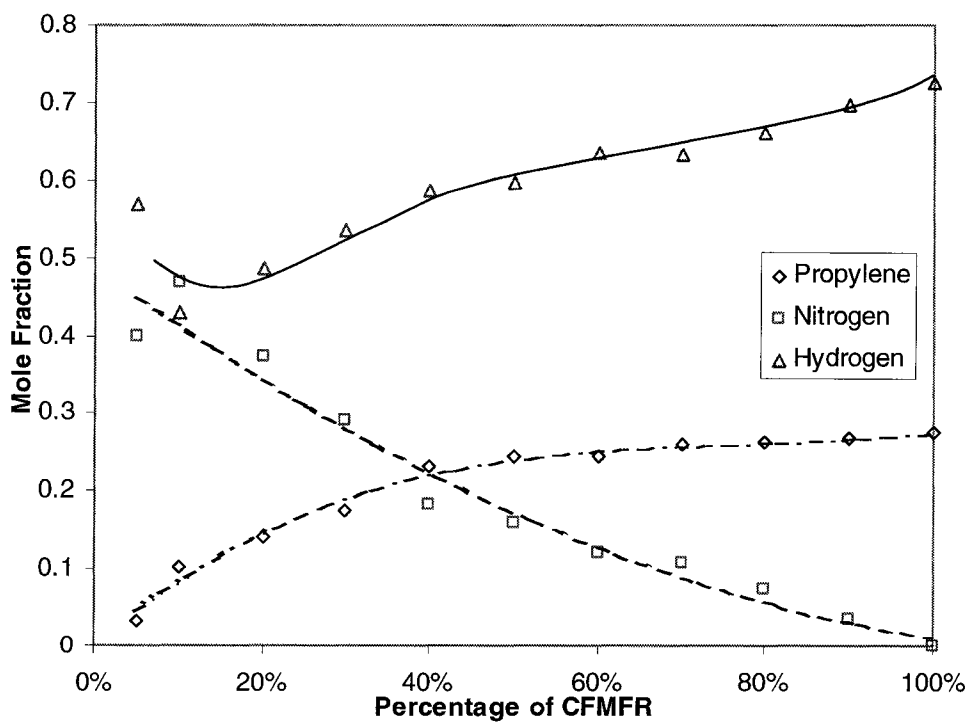


Figure 3.22e Mole Fraction of Jet Gas Mixture at Smoke Point at 4.0 m/s Cross-Flow

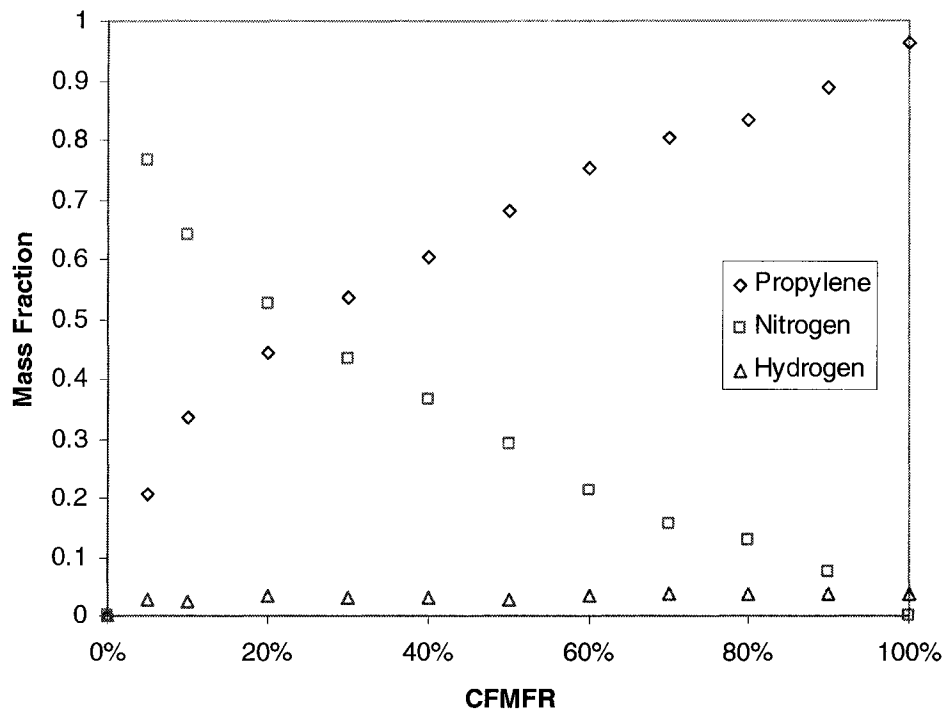


Figure 3.22f Mass Fraction of Jet Gas Mixture at Smoke Point in Quiescent Condition

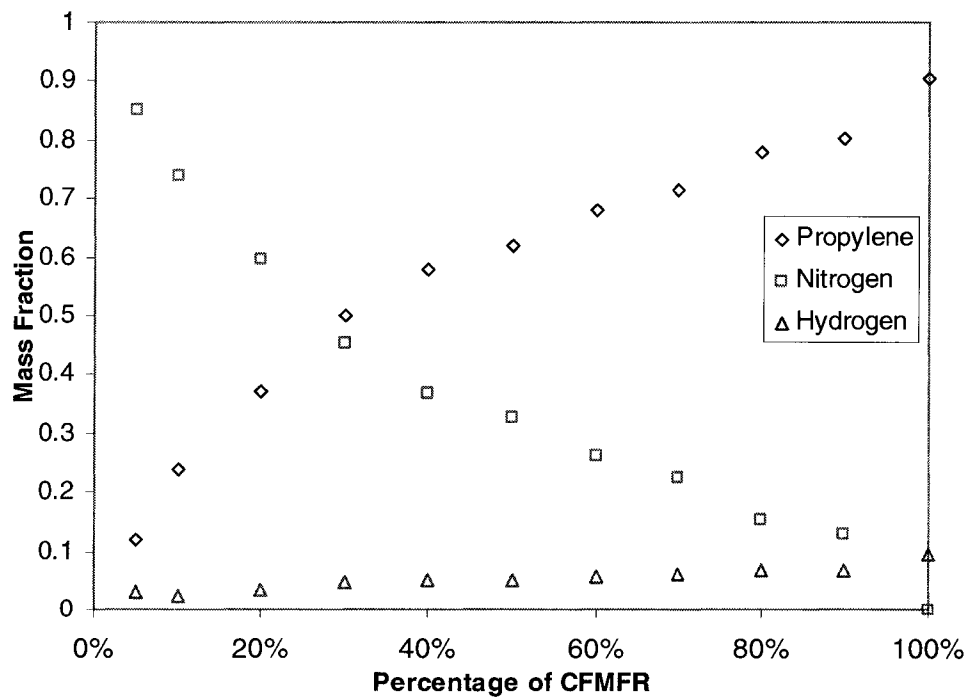


Figure 3.22g Mass Fraction of Jet Gas Mixture at Smoke Point at 2 m/s Cross-Flow

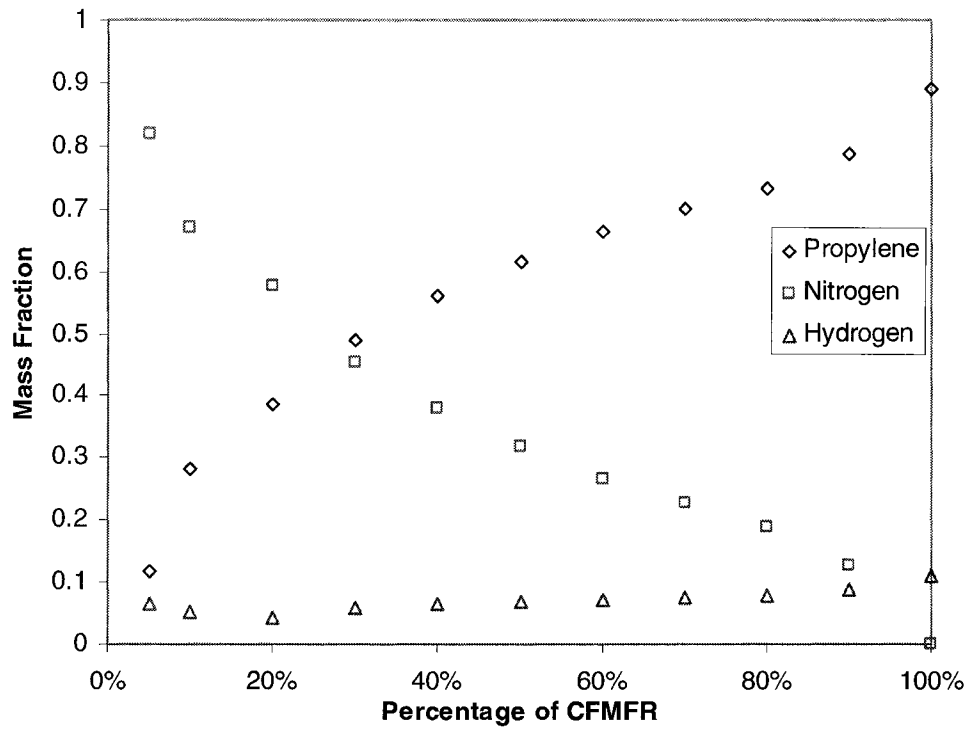


Figure 3.22h Mass Fraction of Jet Gas Mixture at Smoke Point at 2.5 m/s Cross-Flow

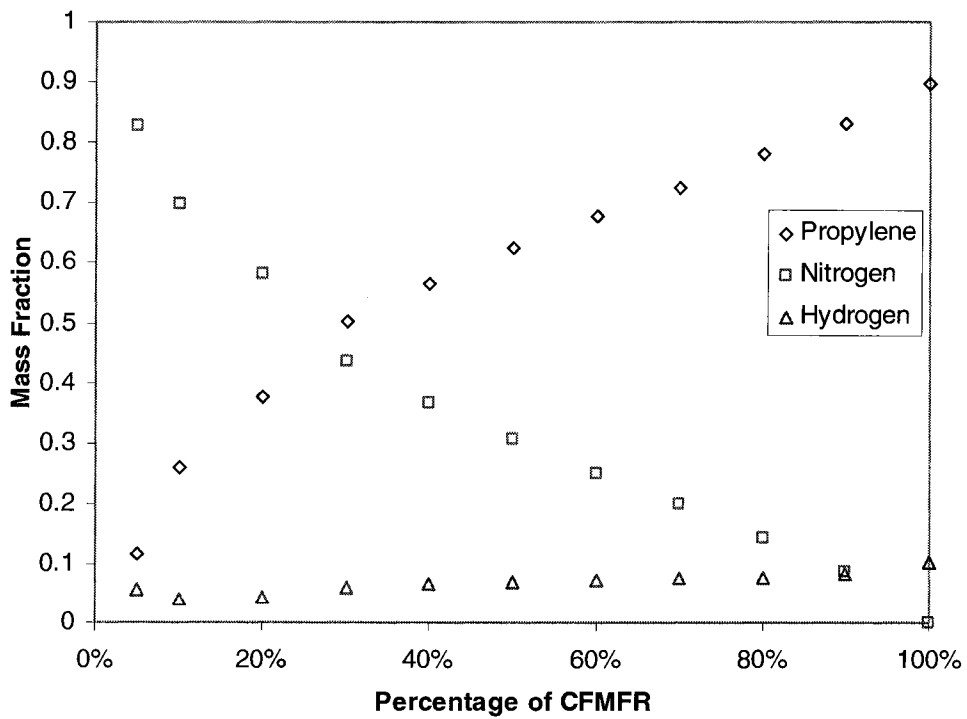


Figure 3.22i Mass Fraction of Jet Gas Mixture at Smoke Point at 3 m/s Cross-Flow

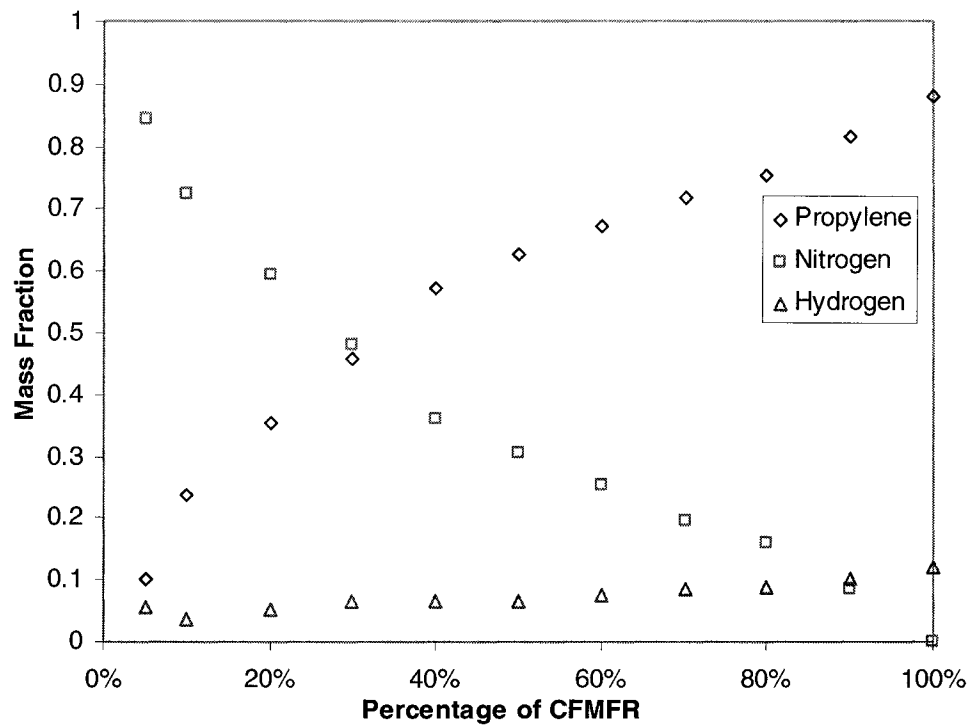


Figure 3.22j Mass Fraction of Jet Gas Mixture at Smoke Point at 3.5 m/s Cross-Flow

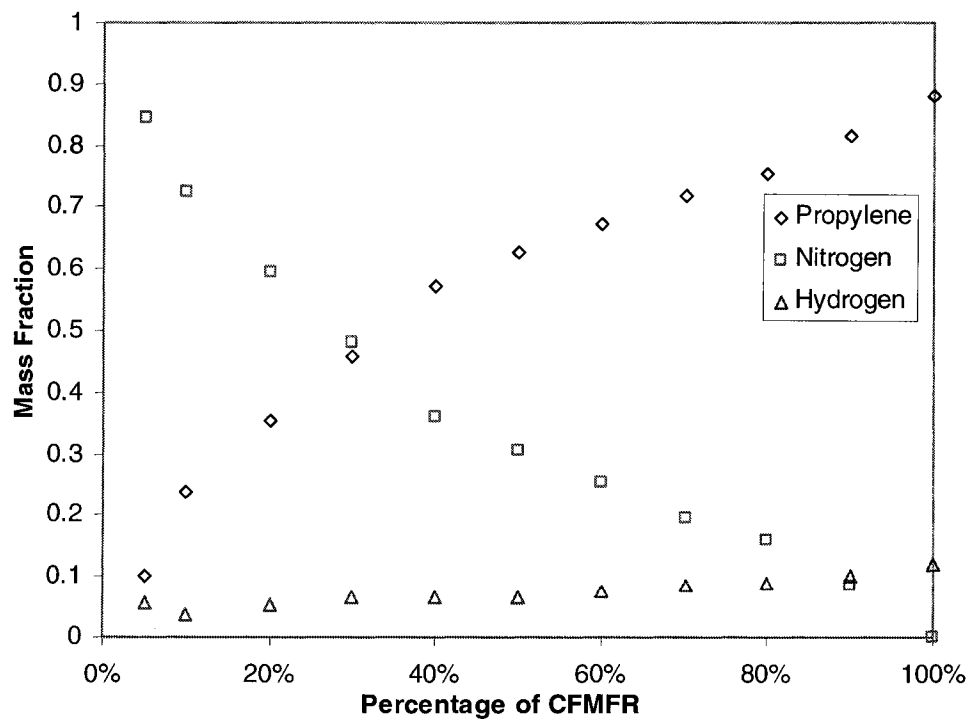


Figure 3.22k Mass Fraction of Jet Gas Mixture at Smoke Point at 4 m/s Cross-Flow

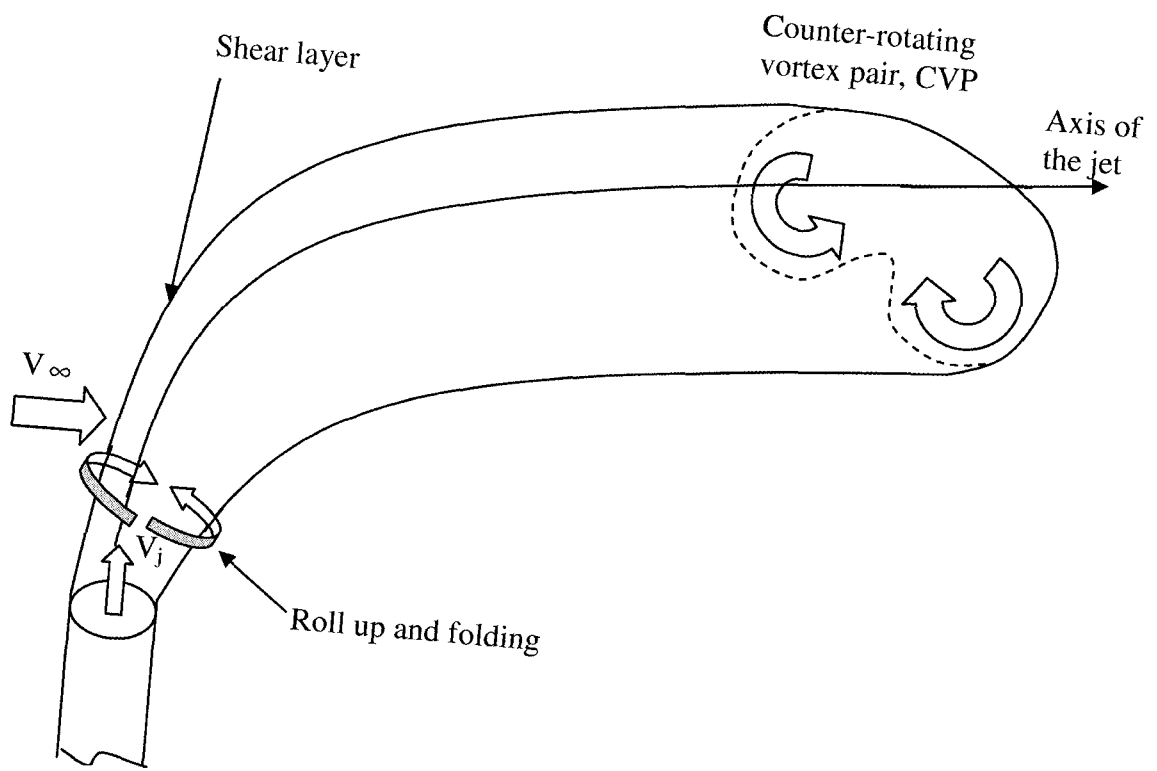


Figure 3.23 Schematic Diagram Showing the Vortex System of a Jet in Cross-Flow

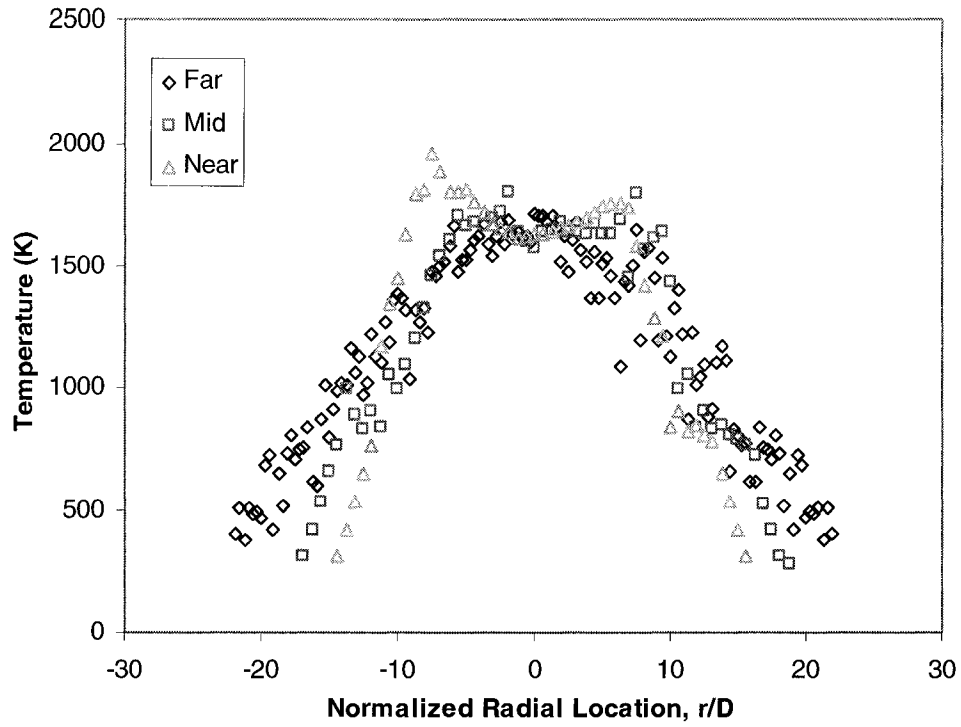


Figure 3.24a Radial Temperature Profiles at 100% CFMFR for Three Flame Heights (Far: 75%, Mid: 50%, Near: 25% Flame Height) (D: Burner Diameter)

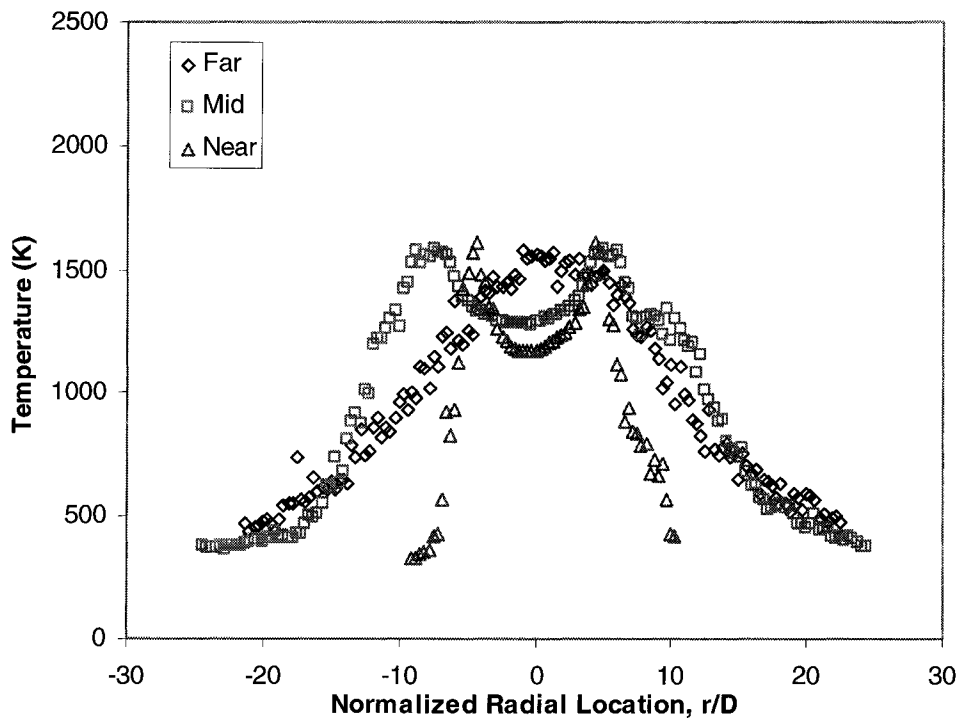


Figure 3.24b Radial Temperature Profiles at 60% CFMFR for Three Flame Heights (Far: 75%, Mid: 50%, Near: 25% Flame Height) (D: Burner Diameter)

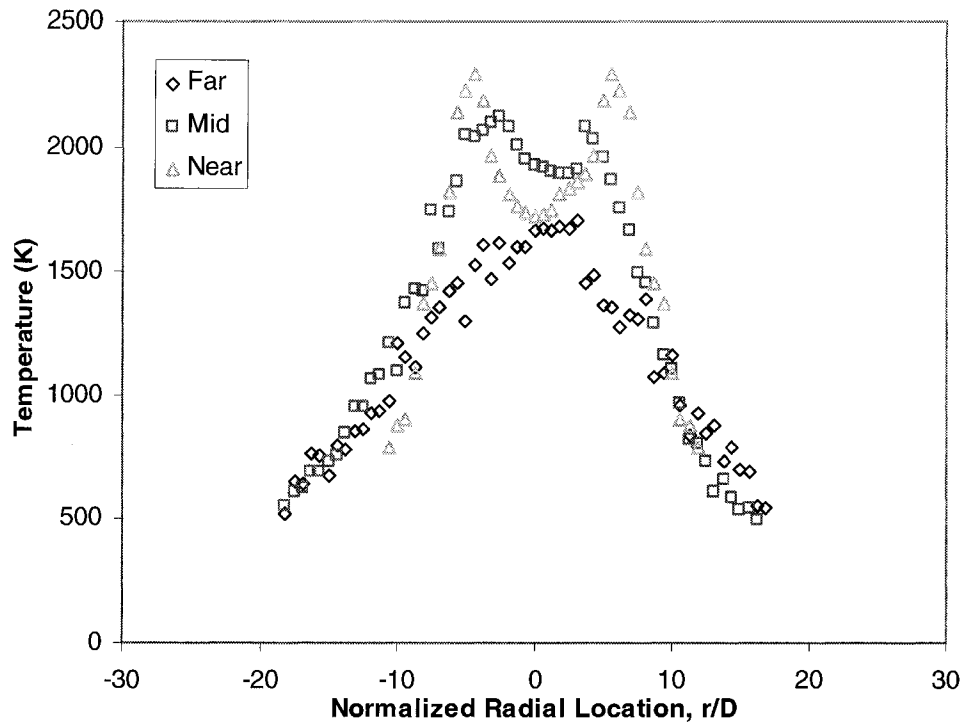


Figure 3.24c Radial Temperature Profiles at 30% CFMFR for Three Flame Heights (Far: 75%, Mid: 50%, Near: 25% Flame Height) (D: Burner Diameter)

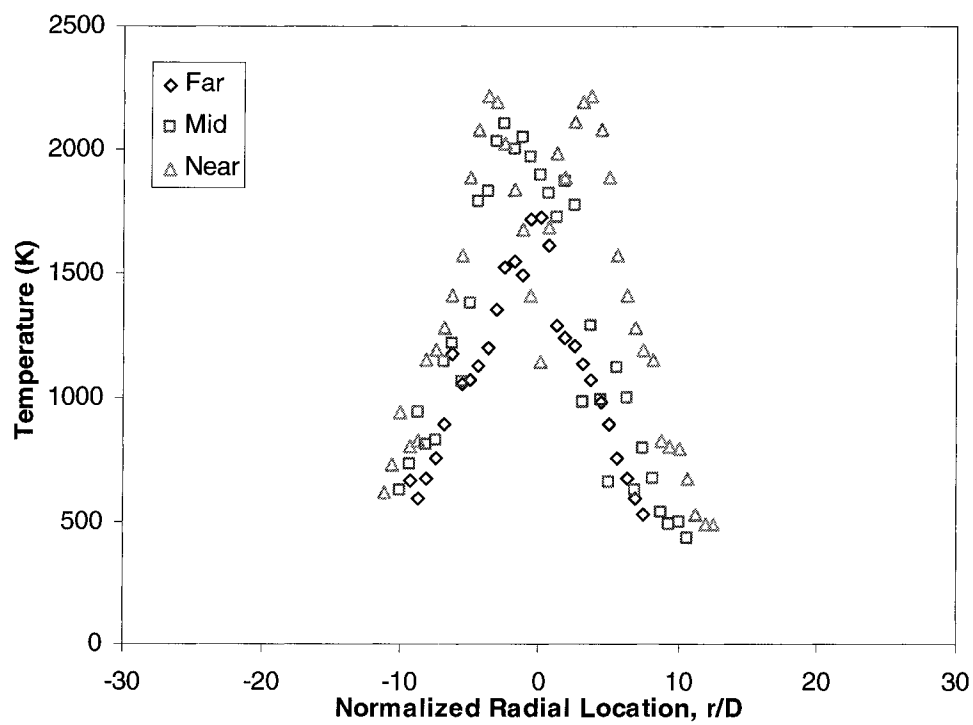


Figure 3.24d Radial Temperature Profiles at 10% CFMFR for Three Flame Heights (Far: 75%, Mid: 50%, Near: 25% Flame Height) (D: Burner Diameter)

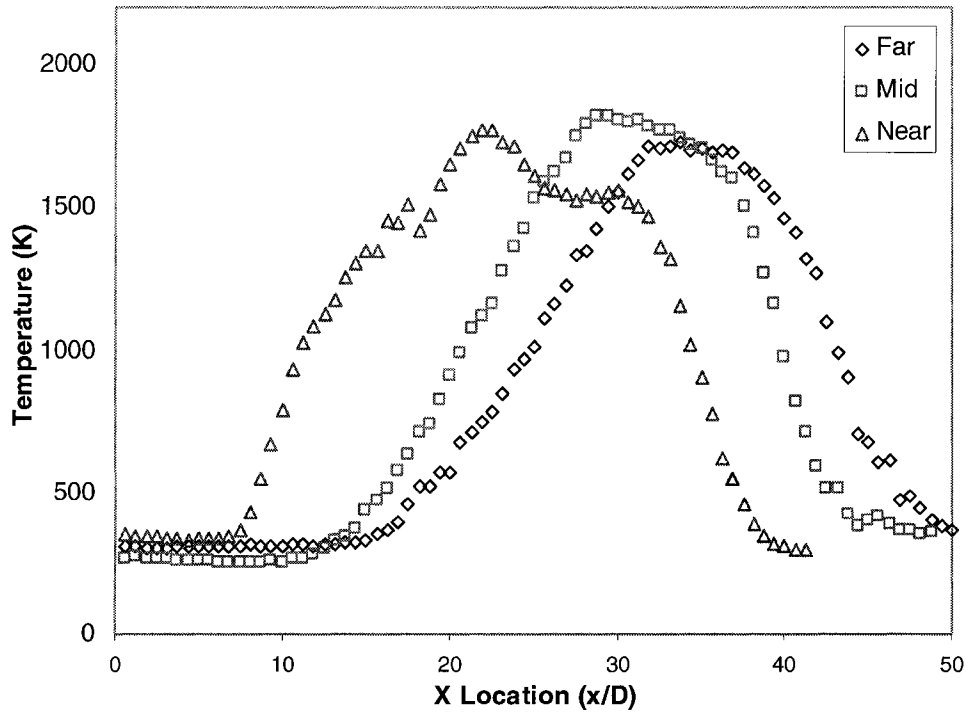


Figure 3.25a Temperature Profiles in X direction at 100% CFMFR at 2 m/s Cross-flow at Three Different Locations (Far 75%, Mid 50% and Near 25% of Flame Length)

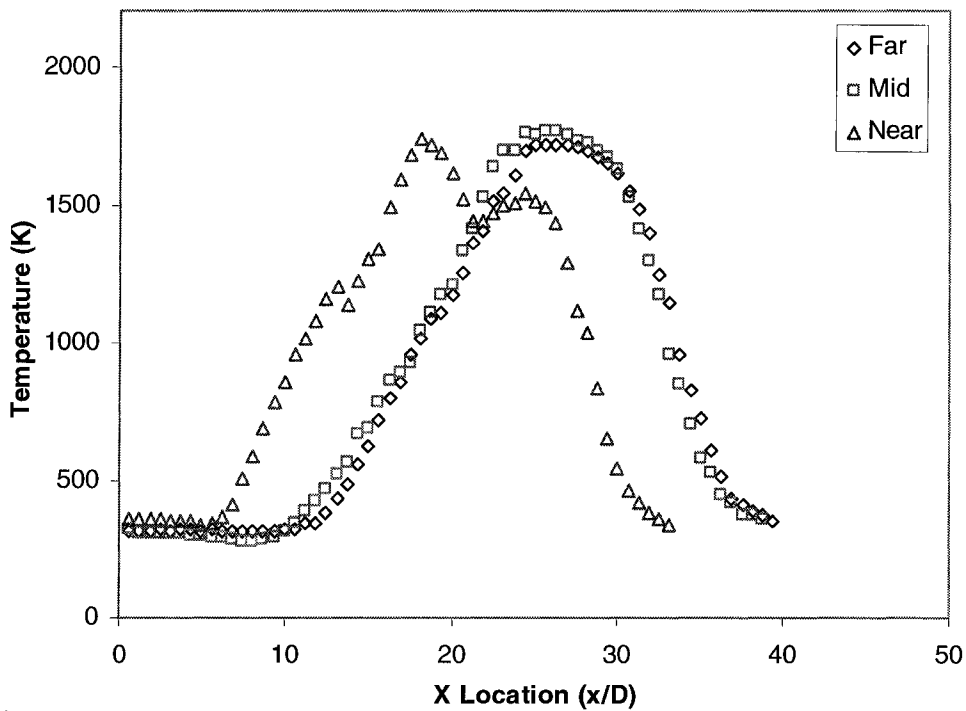


Figure 3.25b Temperature Profiles in X direction at 60% CFMFR at 2 m/s Cross-flow at Three Different Locations (Far 75%, Mid 50% and Near 25% of Flame Length)

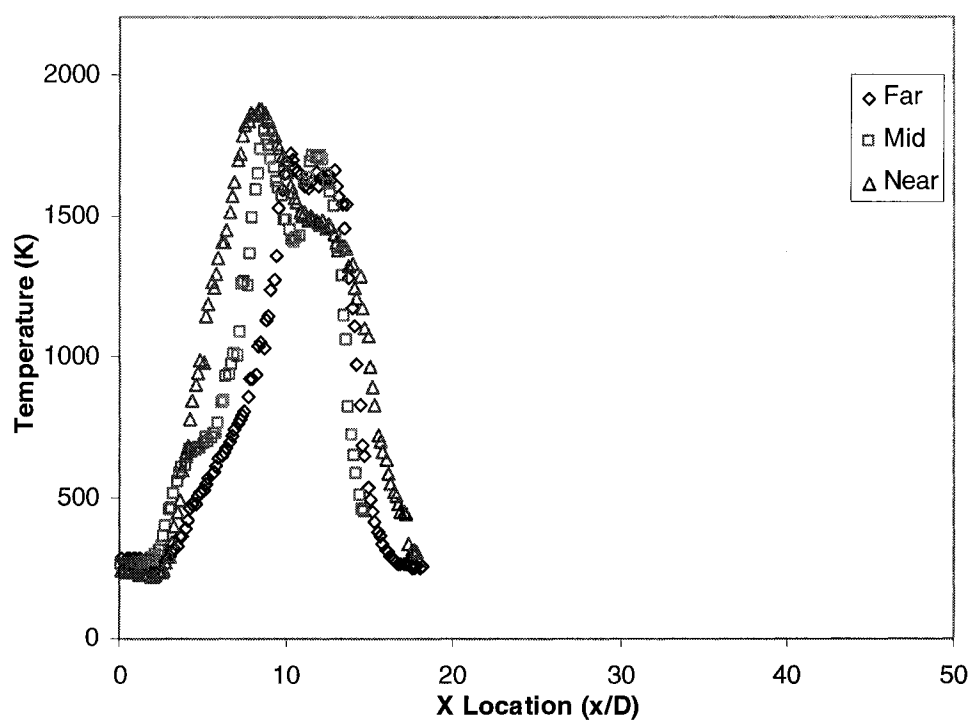


Figure 3.25c Temperature Profiles in X direction at 20% CFMFR at 2 m/s Cross-flow at Three Different Locations (Far 75%, Mid 50% and Near 25% of Flame Length)

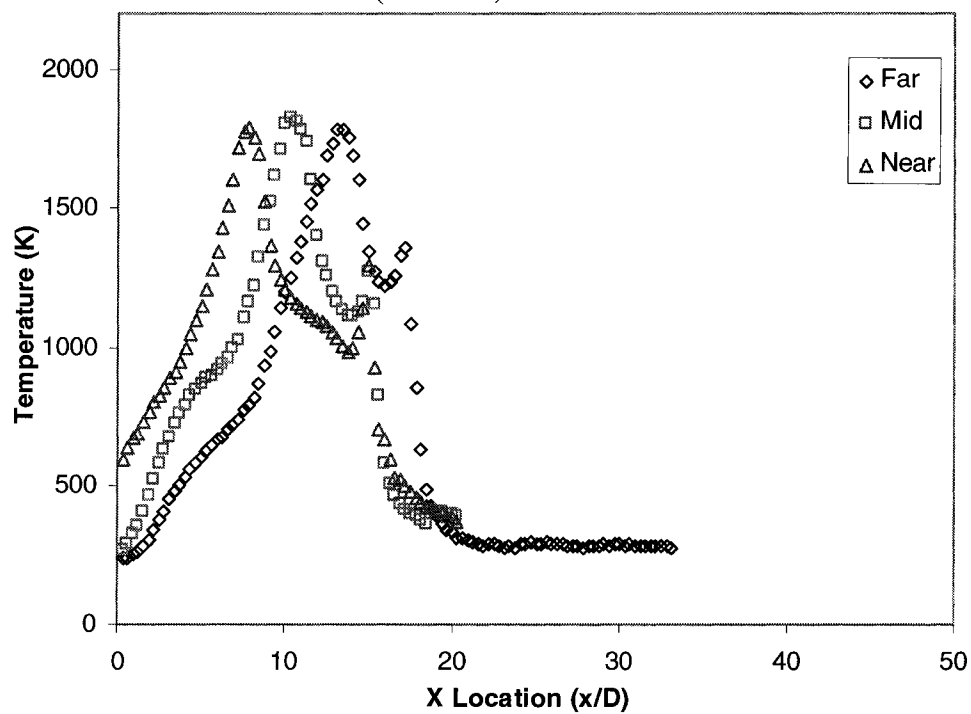


Figure 3.25d Temperature Profiles in X direction at 10% CFMFR at 2 m/s Cross-flow at Three Different Locations (Far 75%, Mid 50% and Near 25% of Flame Length)

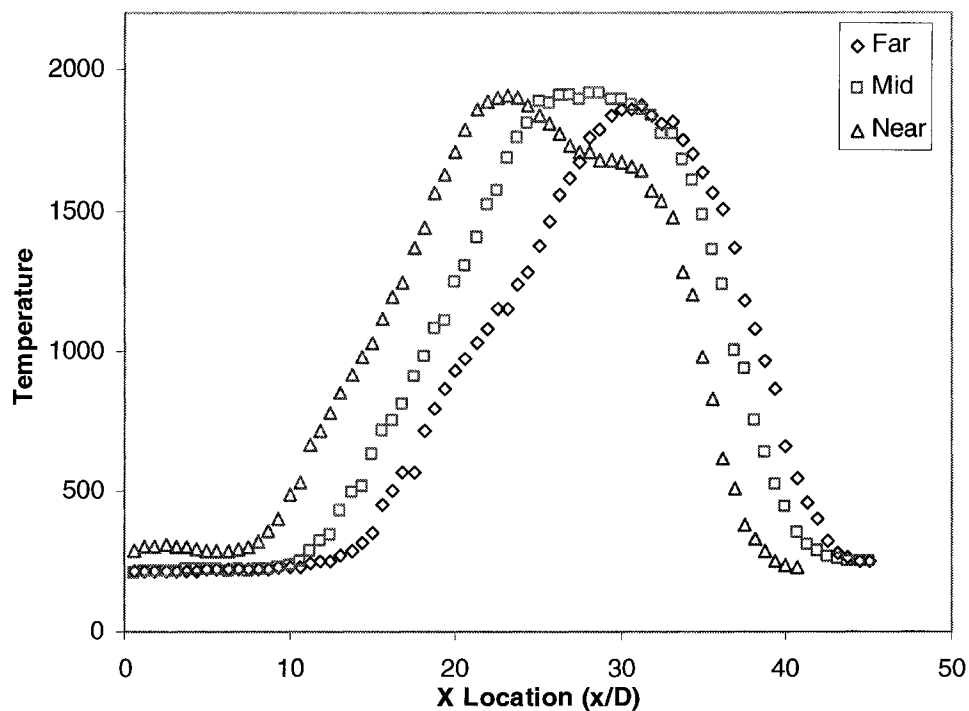


Figure 3.26a Temperature Profiles in X direction at 100% CFMFR at 3 m/s Cross-flow at Three Different Locations (Far 75%, Mid 50% and Near 25% of Flame Length)

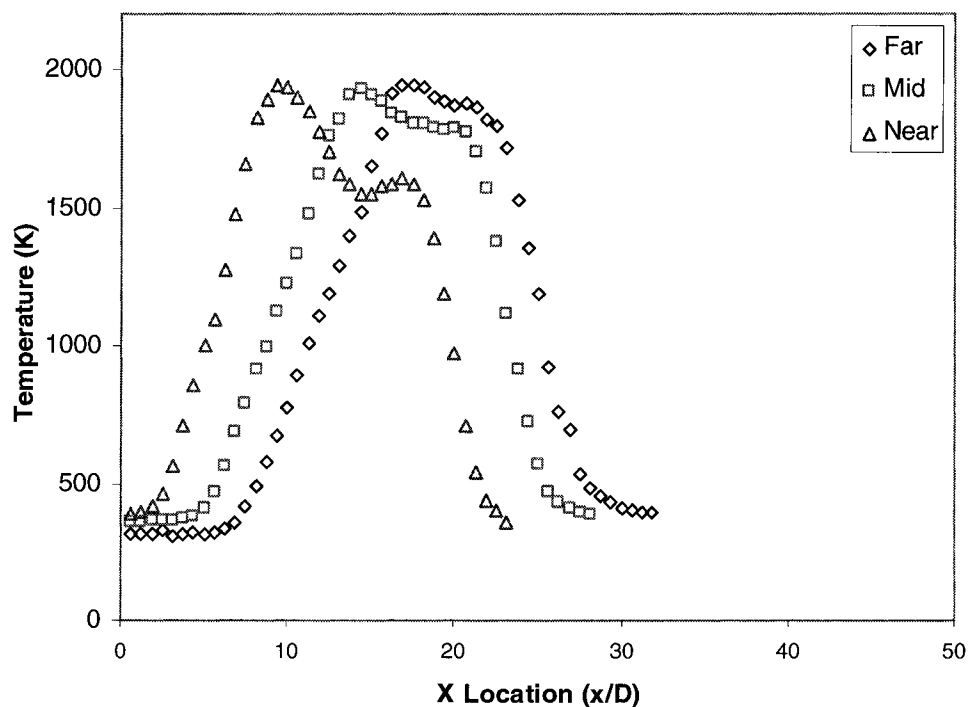


Figure 3.26b Temperature Profiles in X direction at 60% CFMFR at 3 m/s Cross-flow at Three Different Locations (Far 75%, Mid 50% and Near 25% of Flame Length)

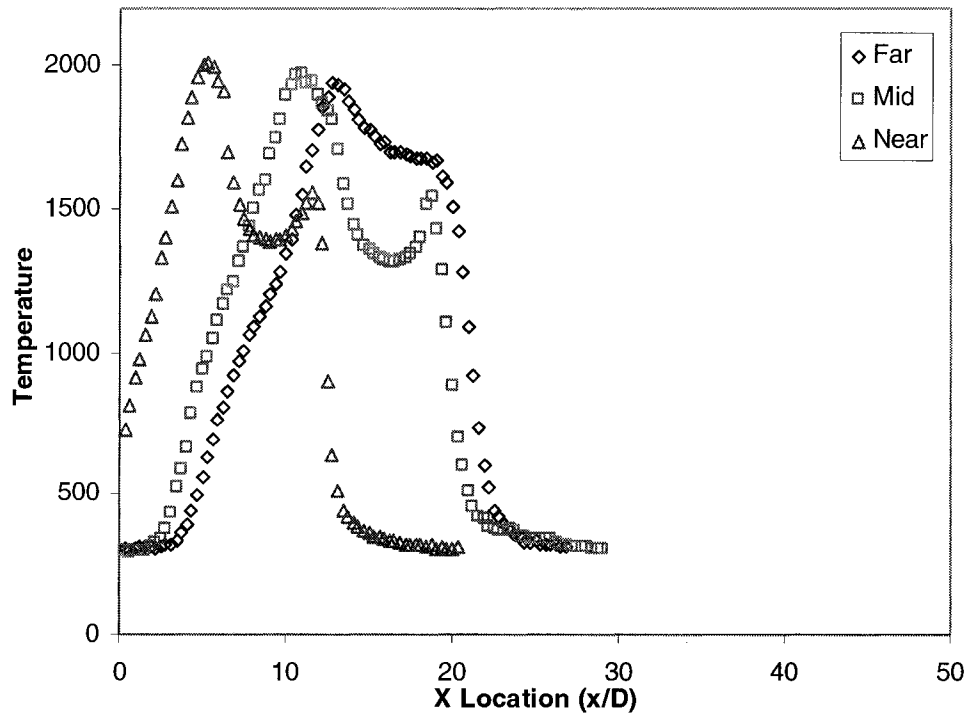


Figure 3.26c Temperature Profiles in X direction at 20% CFMFR at 3 m/s Cross-flow at Three Different Locations (Far 75%, Mid 50% and Near 25% of Flame Length)

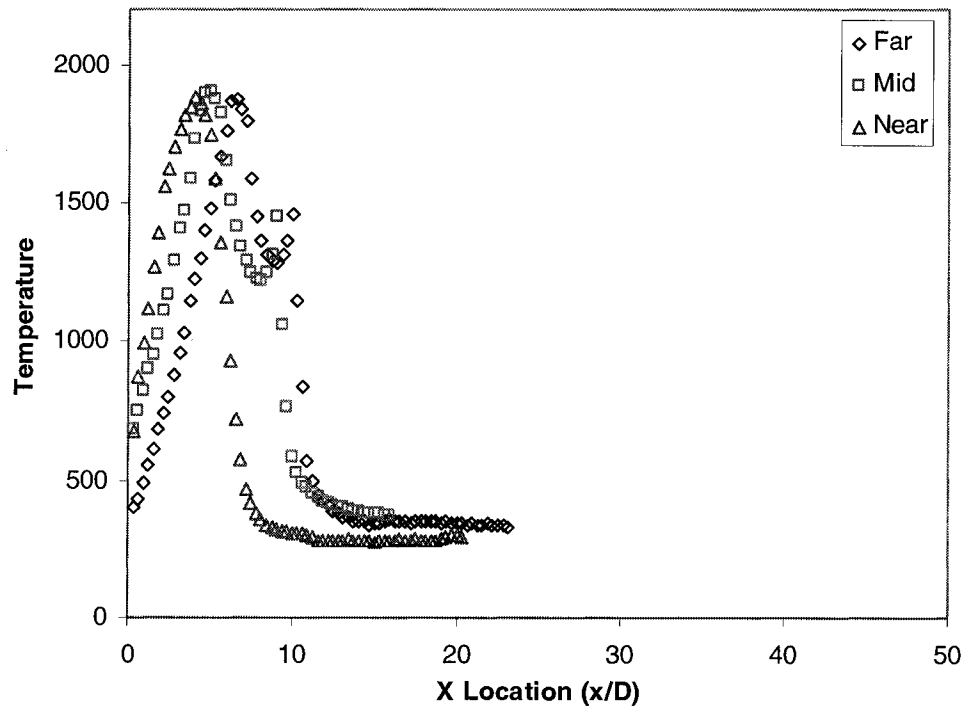


Figure 3.26d Temperature Profiles in X direction at 10% CFMFR at 3 m/s Cross-flow at Three Different Locations (Far 75%, Mid 50% and Near 25% of Flame Length)

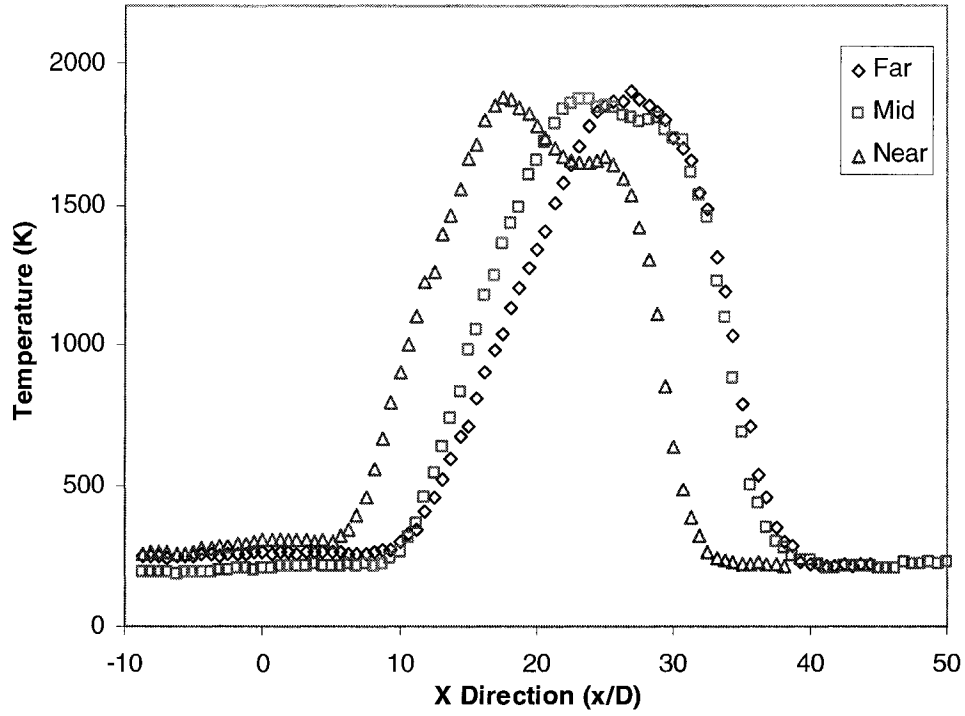


Figure 3.27a Temperature Profiles in X direction at 100% CFMFR at 4 m/s Cross-flow at Three Different Locations (Far 75%, Mid 50% and Near 25% of Flame Length)

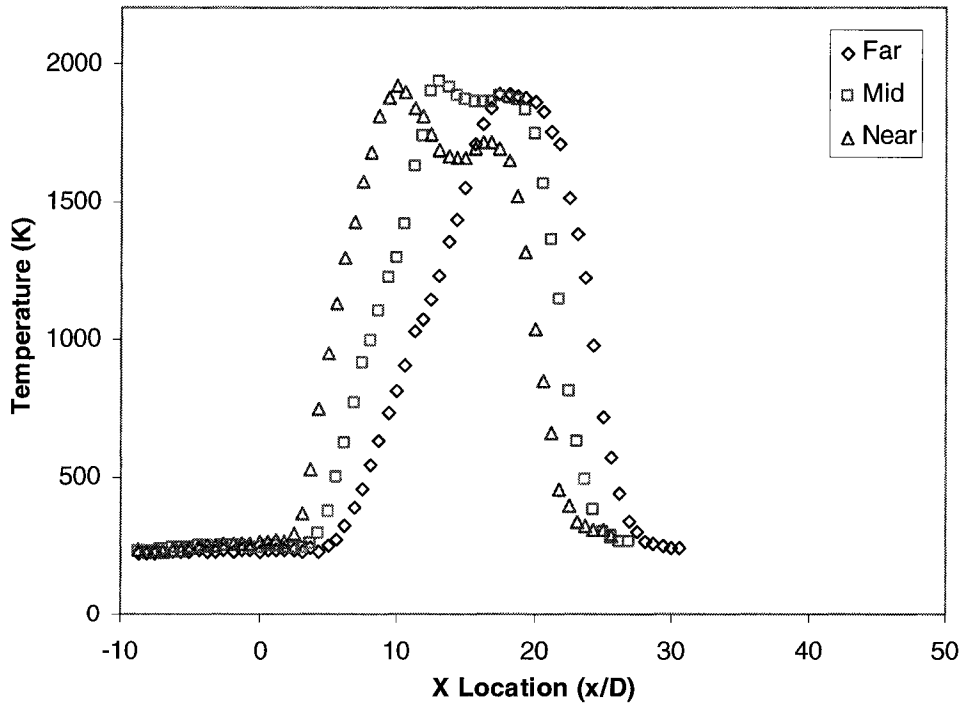


Figure 3.27b Temperature Profiles in X direction at 60% CFMFR at 4 m/s Cross-flow at Three Different Locations (Far 75%, Mid 50% and Near 25% of Flame Length)

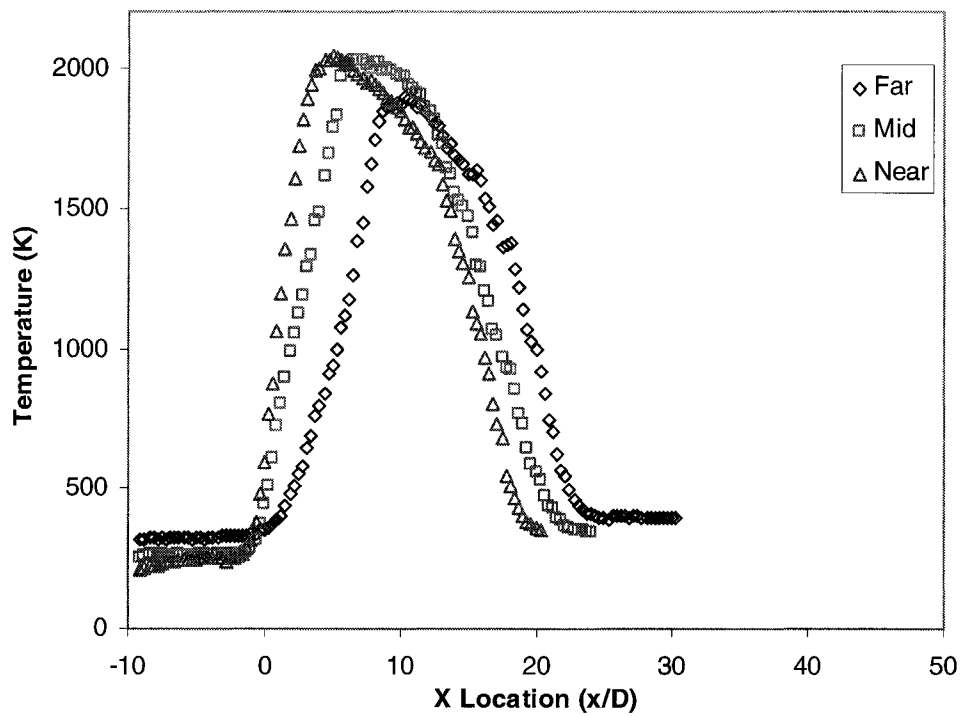


Figure 3.27c Temperature Profiles in X direction at 30% CFMFR at 4 m/s Cross-flow at Three Different Locations (Far 75%, Mid 50% and Near 25% of Flame Length)

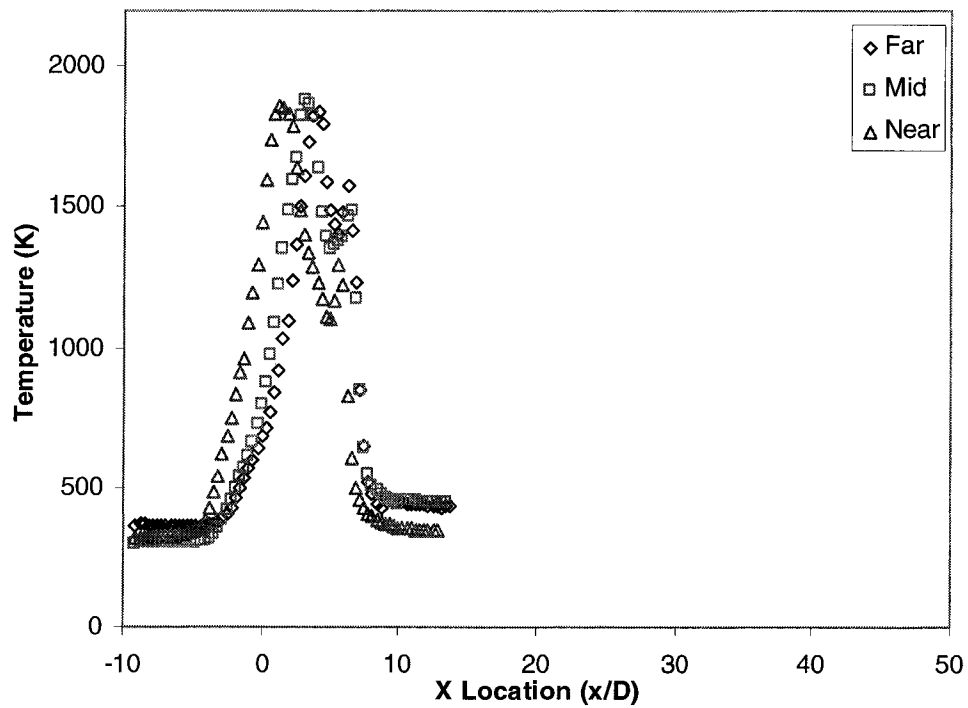


Figure 3.27d Temperature Profiles in X direction at 10% CFMFR at 4 m/s Cross-flow at Three Different Locations (Far 75%, Mid 50% and Near 25% of Flame Length)

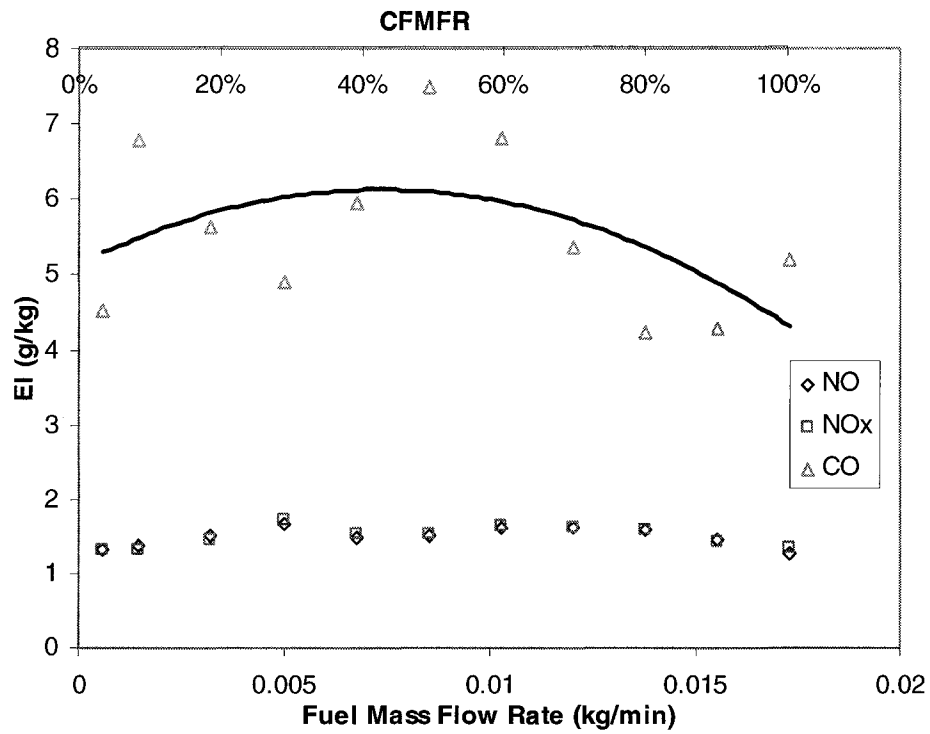


Figure 3.28 Emission Index of NO, NO_x and CO at CFMFR and Fuel-Nitrogen Mixture at Smoke Point

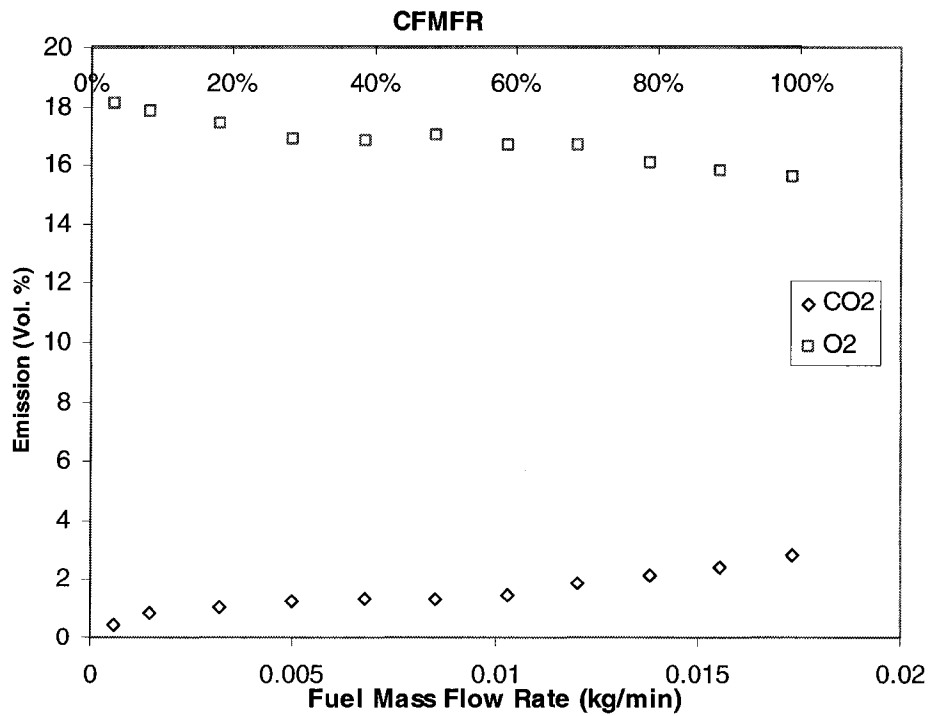


Figure 3.29 Global CO₂ and O₂ Concentrations at CFMFR and Fuel-Nitrogen Mixture at Smoke Point

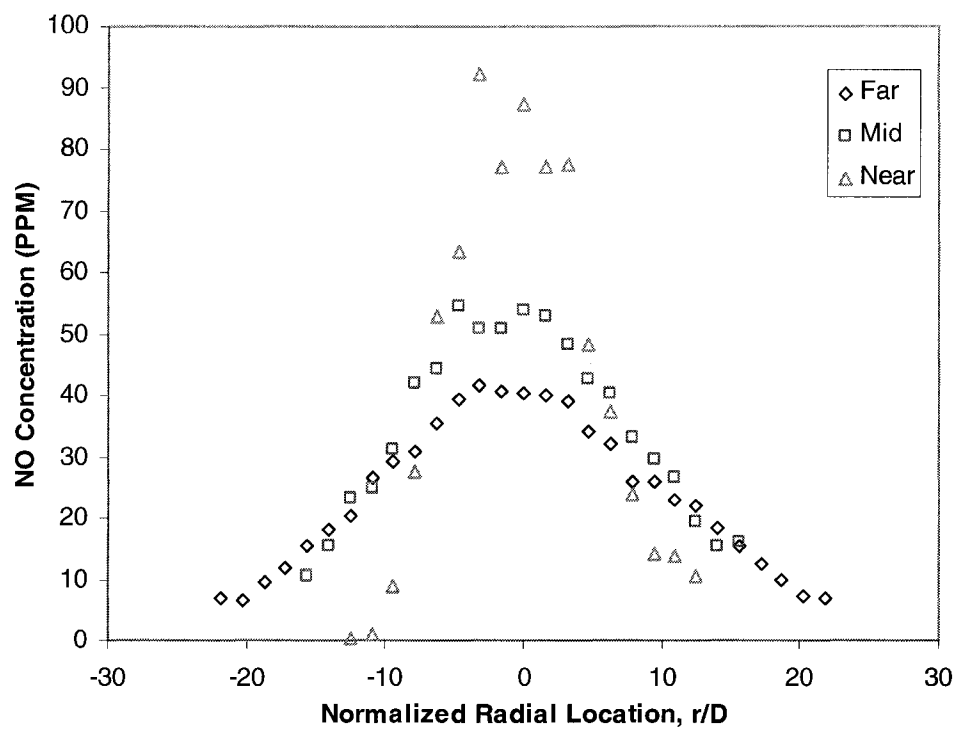


Figure 3.30a Radial NO Concentration Profiles at 100 CFMFR
(Far: 75%, Mid: 50%, Near: 25% Flame Height) (D: Burner Diameter)

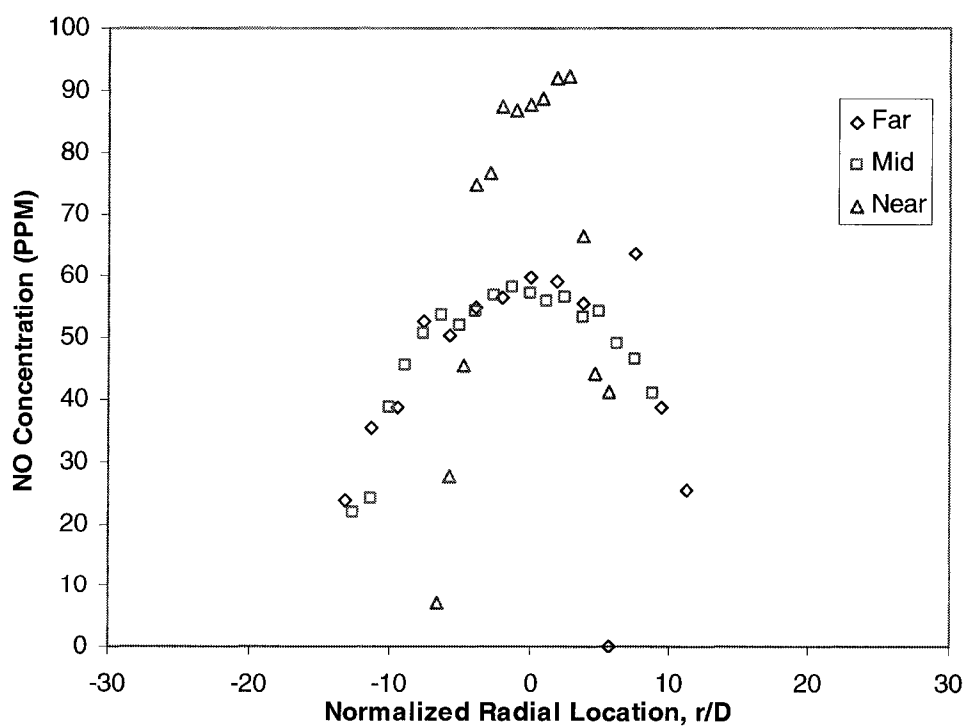


Figure 3.30b Radial NO Concentration Profiles at 60% CFMFR
(Far: 75%, Mid: 50%, Near: 25% Flame Height) (D: Burner Diameter)

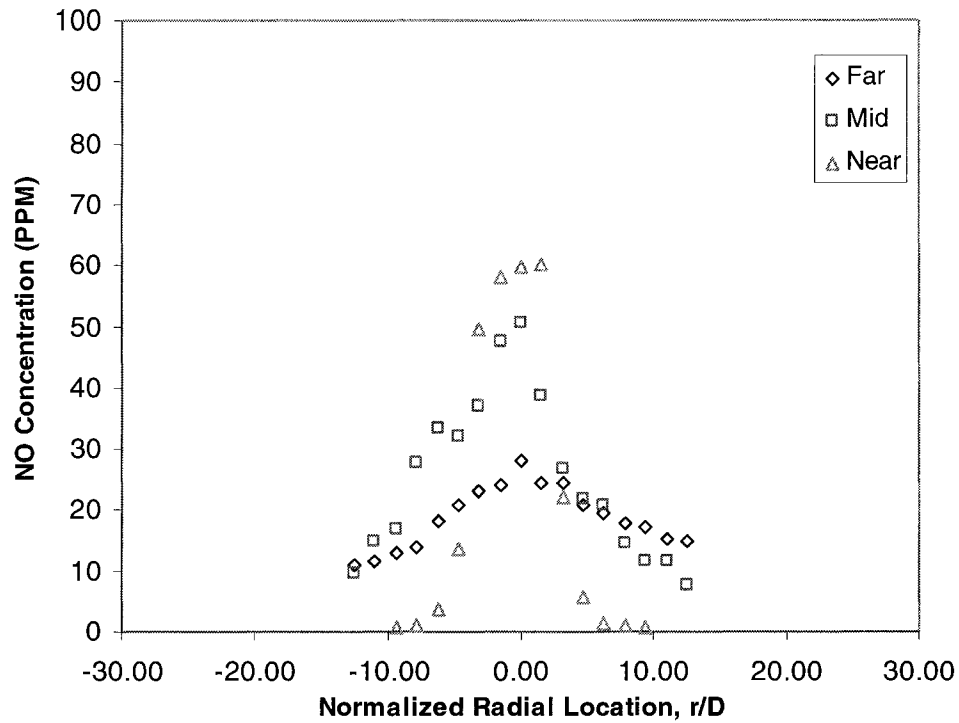


Figure 3.30c Radial NO Concentration Profiles at 30% CFMFR
(Far: 75%, Mid: 50%, Near: 25% Flame Height) (D: Burner Diameter)

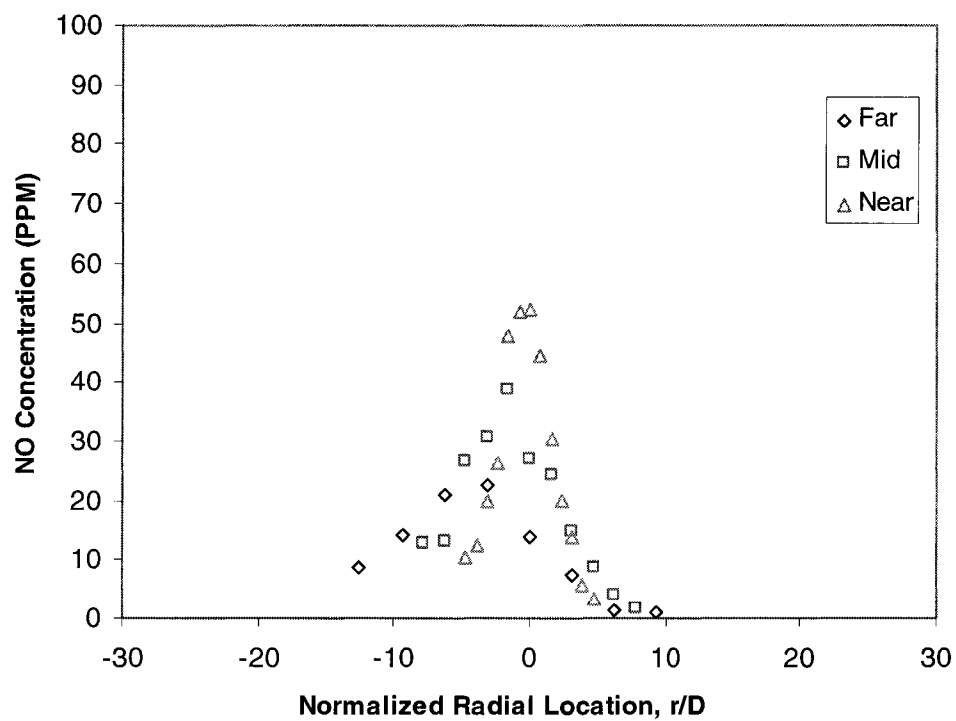


Figure 3.30d Radial NO Concentration Profiles at 10% CFMFR
(Far: 75%, Mid: 50%, Near: 25% Flame Height) (D: Burner Diameter)

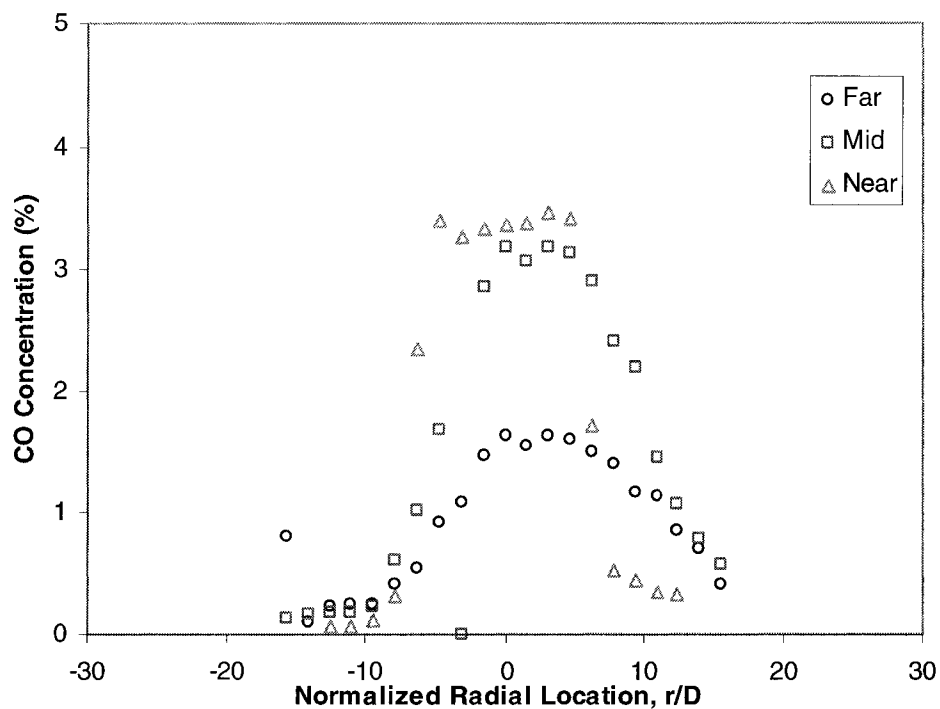


Figure 3.31a Radial CO Concentration Profiles at 100% CFMFR
(Far: 75%, Mid: 50%, Near: 25% Flame Height) (D: Burner Diameter)

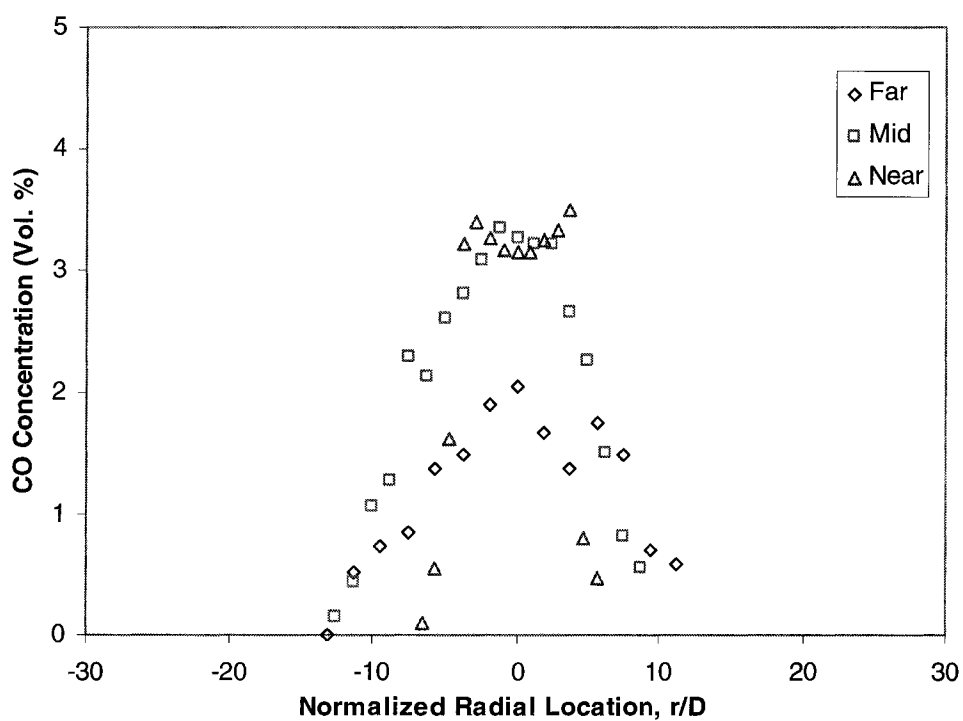


Figure 3.31b Radial CO Concentration Profiles at 60% CFMFR
(Far: 75%, Mid: 50%, Near: 25% Flame Height) (D: Burner Diameter)

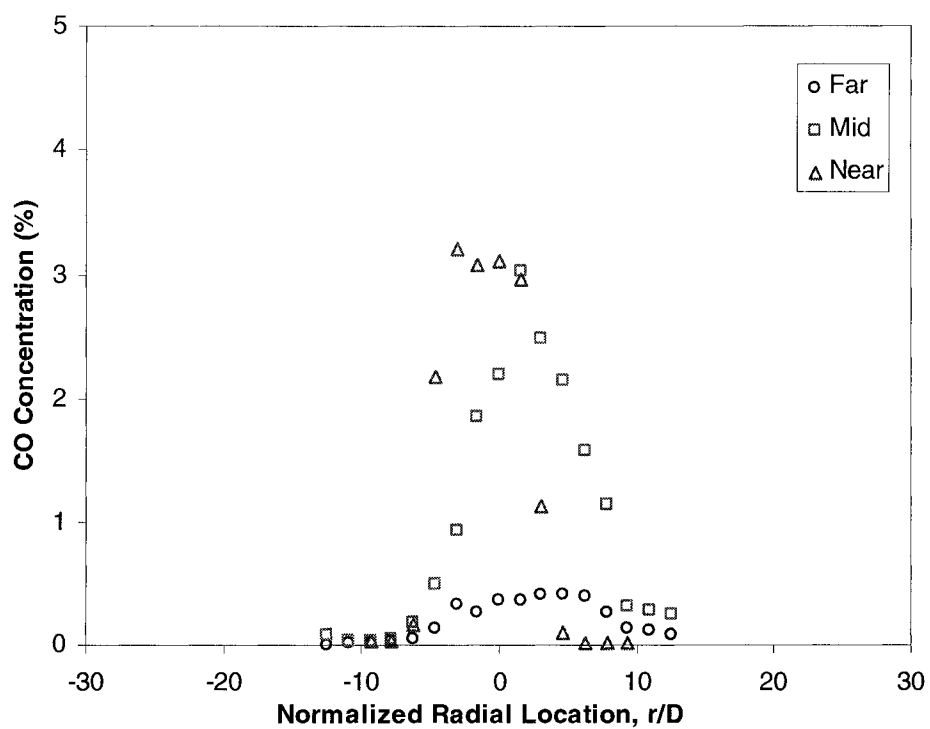


Figure 3.31c Radial CO Concentration Profiles at 30% CFMFR (Far: 75%, Mid: 50%, Near: 25% Flame Height) (D: Burner Diameter)

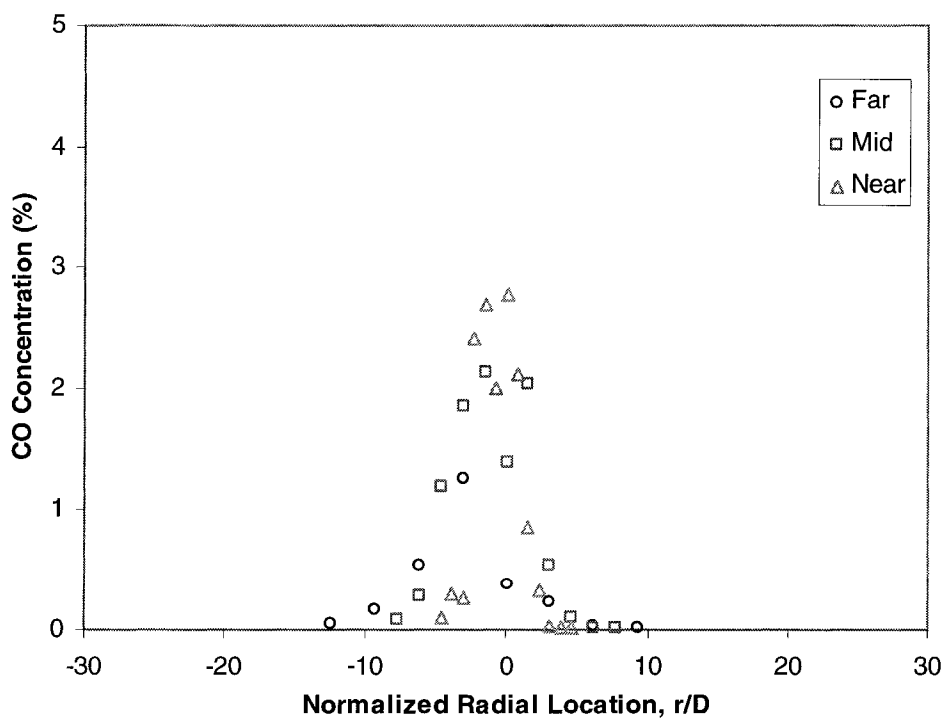


Figure 3.31d Radial CO Concentration Profiles at 10% CFMFR (Far: 75%, Mid: 50%, Near: 25% Flame Height) (D: Burner Diameter)

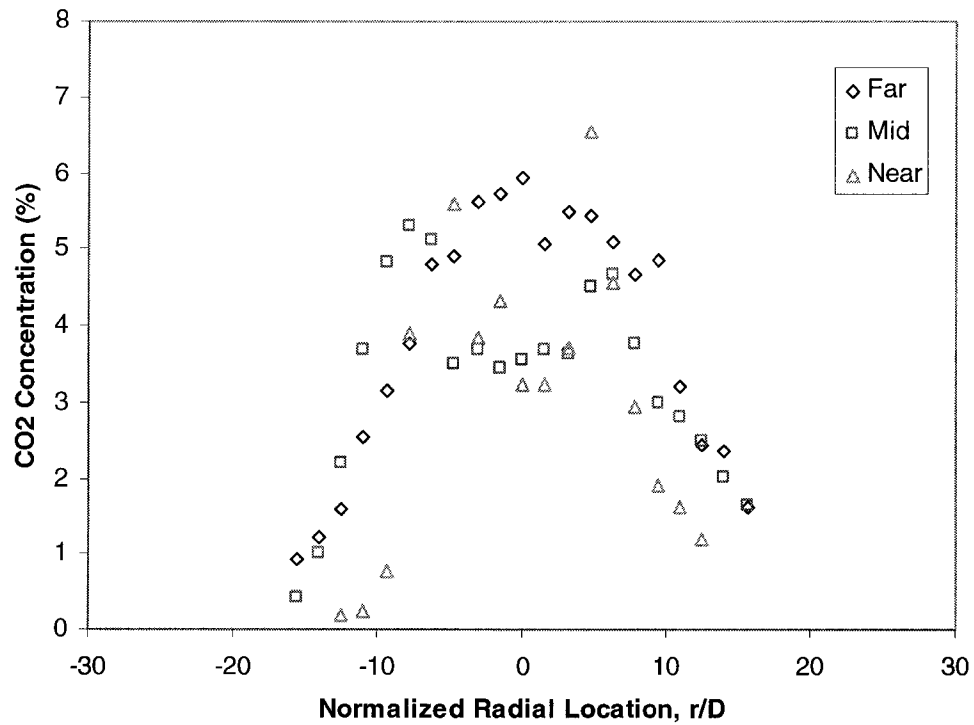


Figure 3.32a Radial CO₂ Concentration Profiles at 100% CFMFR
(Far: 75%, Mid: 50%, Near: 25% Flame Height) (D: Burner Diameter)

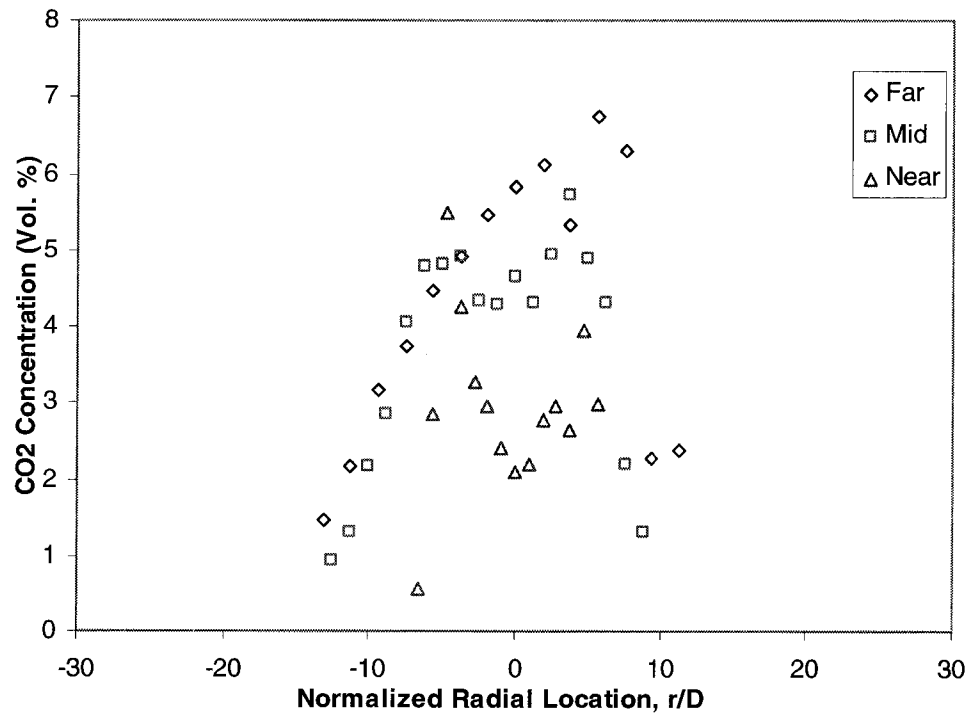


Figure 3.32b Radial CO₂ Concentration Profiles at 60% CFMFR
(Far: 75%, Mid: 50%, Near: 25% Flame Height) (D: Burner Diameter)

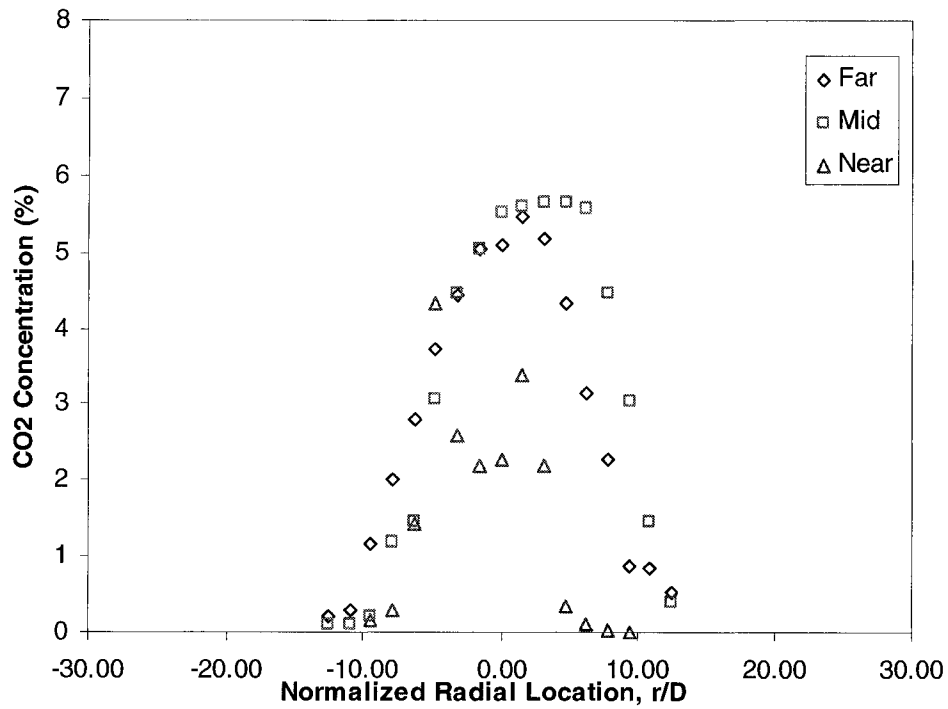


Figure 3.32c Radial CO₂ Concentration Profiles at 30% CFMFR (Far: 75%, Mid: 50%, Near: 25% Flame Height) (D: Burner Diameter)

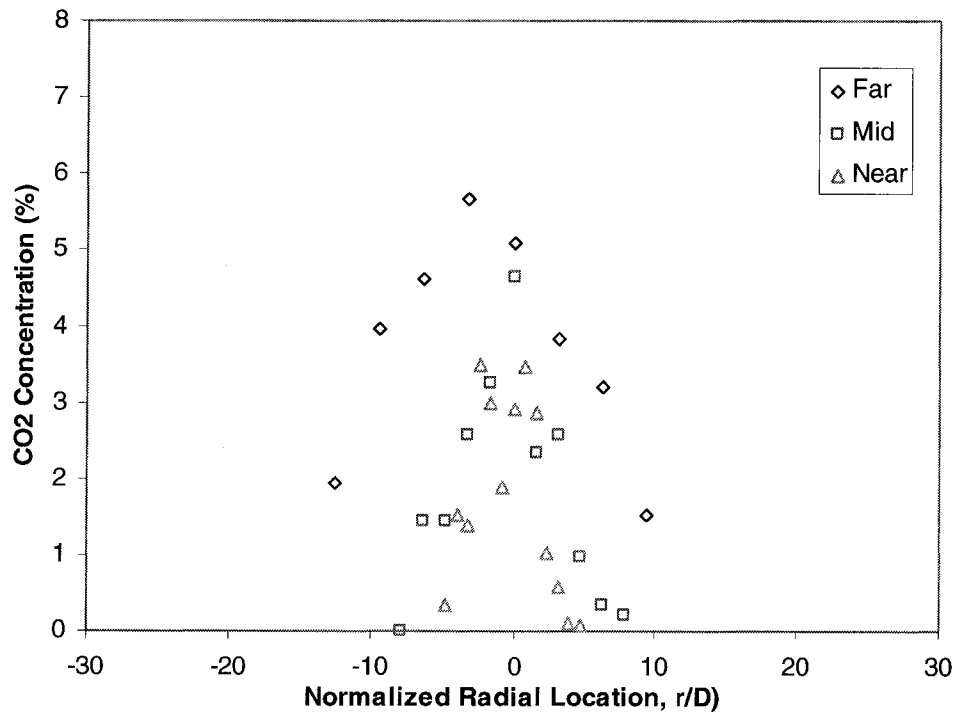


Figure 3.32d Radial CO₂ Concentration Profiles at 10% CFMFR (Far: 75%, Mid: 50%, Near: 25% Flame Height) (D: Burner Diameter)

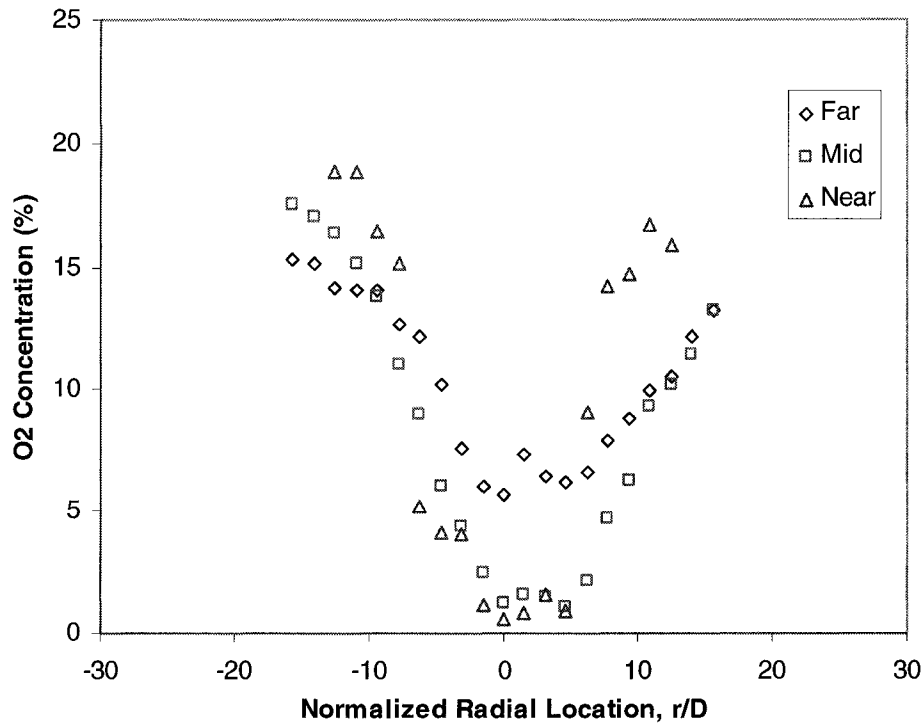


Figure 3.33a Radial O₂ Concentration Profiles at 100% CFMFR
(Far: 75%, Mid: 50%, Near: 25% Flame Height) (D: Burner Diameter)

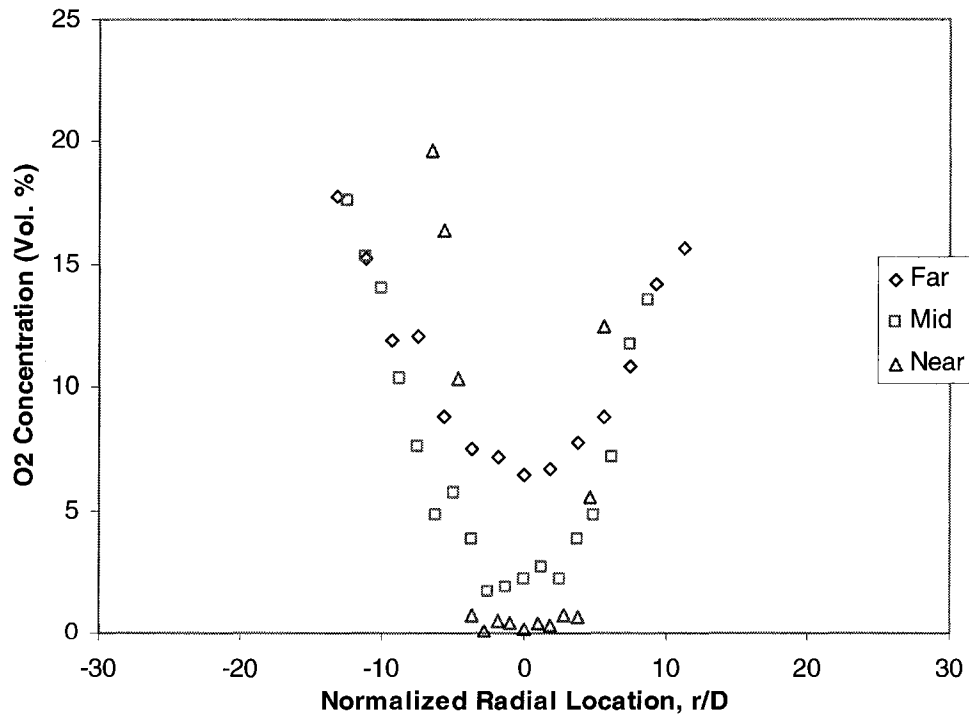


Figure 3.33b Radial O₂ Concentration Profiles at 60% CFMFR
(Far: 75%, Mid: 50%, Near: 25% Flame Height) (D: Burner Diameter)

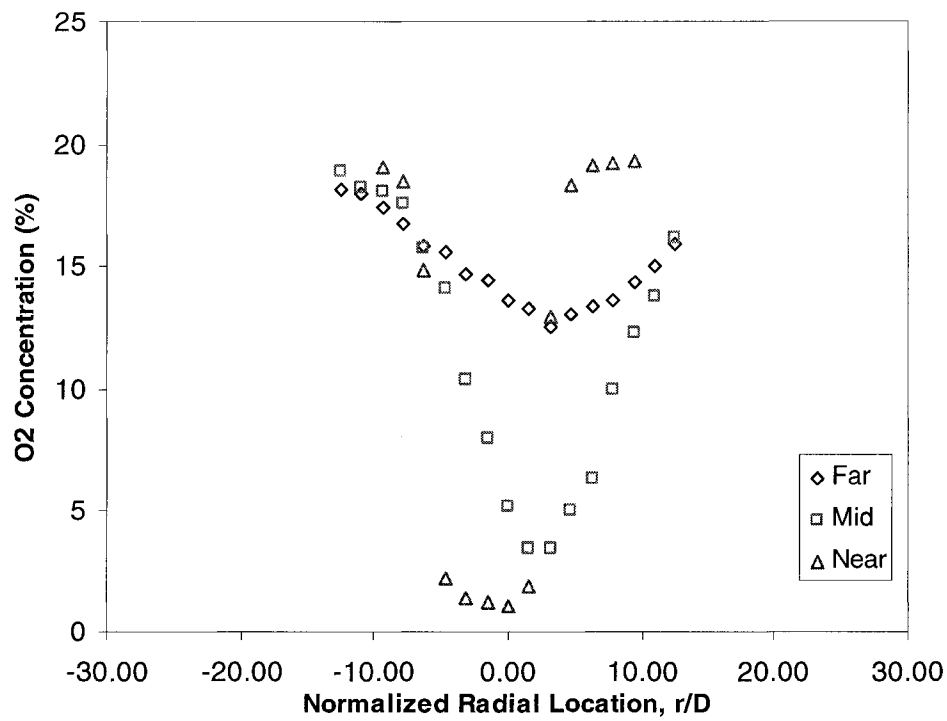


Figure 3.33c Radial O₂ Concentration Profiles at 30% CFMFR
(Far: 75%, Mid: 50%, Near: 25% Flame Height) (D: Burner Diameter)

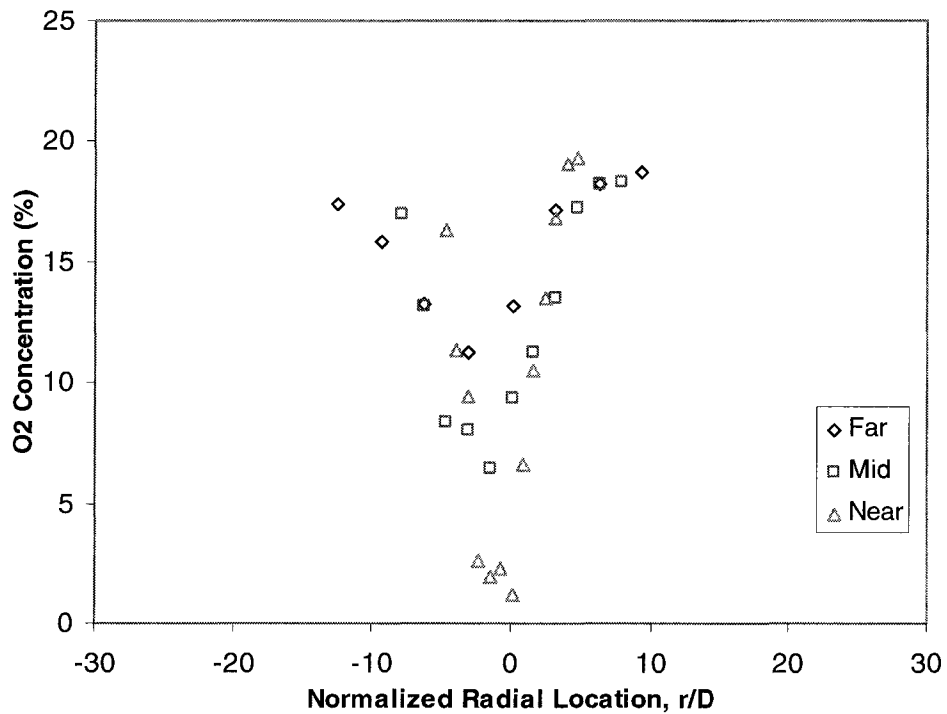


Figure 3.33d Radial O₂ Concentration Profiles at 10% CFMFR
(Far: 75%, Mid: 50%, Near: 25% Flame Height) (D: Burner Diameter)

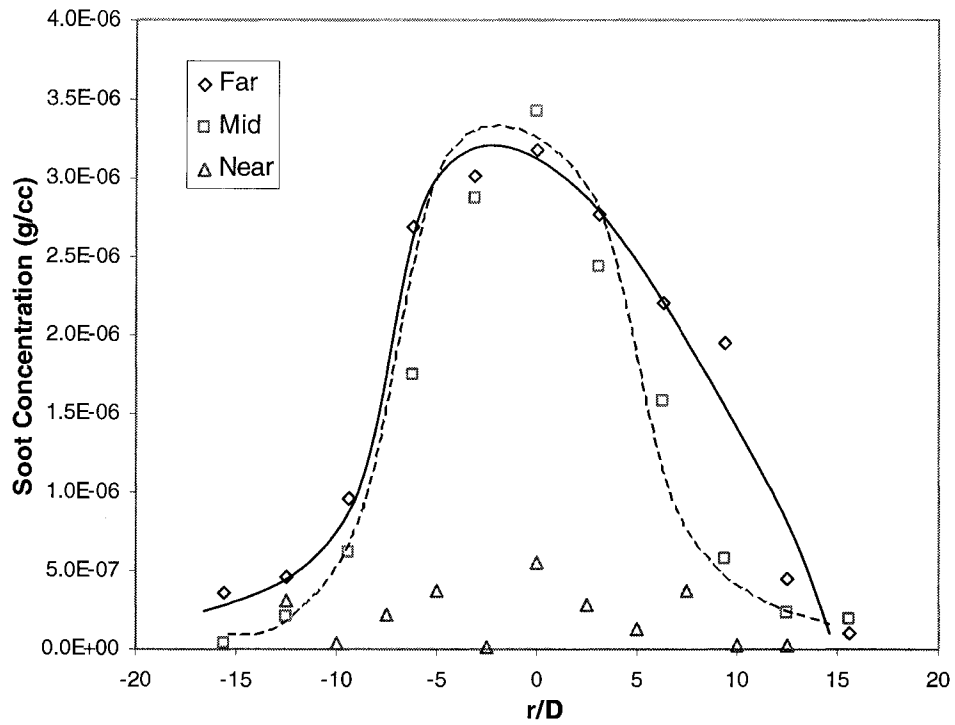


Figure 3.34a Radial Soot Concentration Profiles at 100% CFMFR
(Far: 75%, Mid: 50%, Near: 25% Flame Height) (D: Burner Diameter)

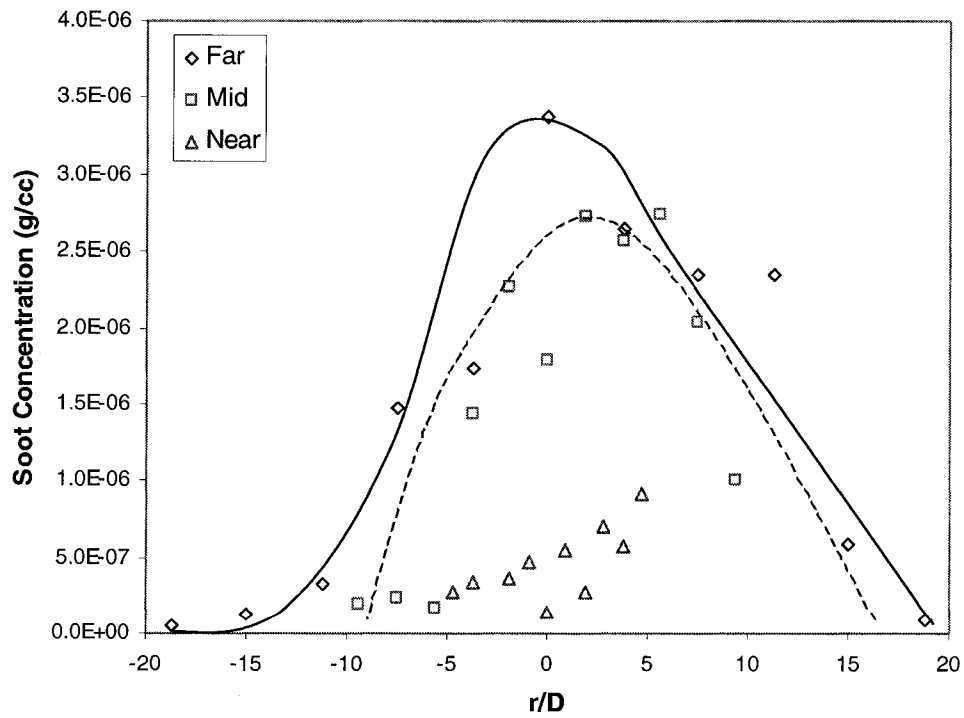


Figure 3.34b Radial Soot Concentration Profiles at 60% CFMFR
(Far: 75%, Mid: 50%, Near: 25% Flame Height) (D: Burner Diameter)

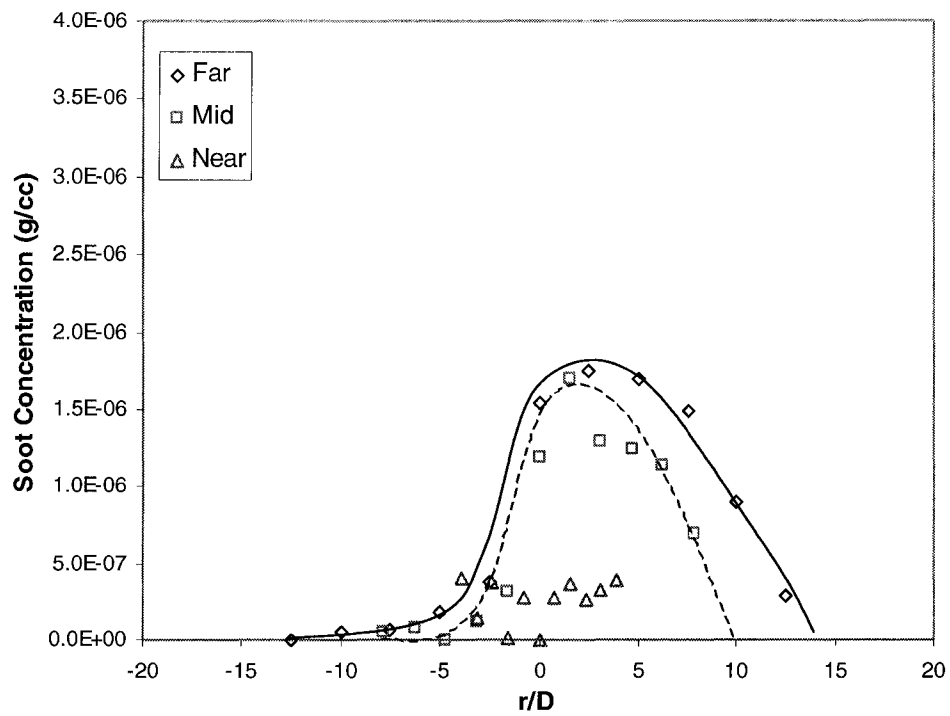


Figure 3.34c Radial Soot Concentration Profiles at 30% CFMFR
(Far: 75%, Mid: 50%, Near: 25% Flame Height) (D: Burner Diameter)

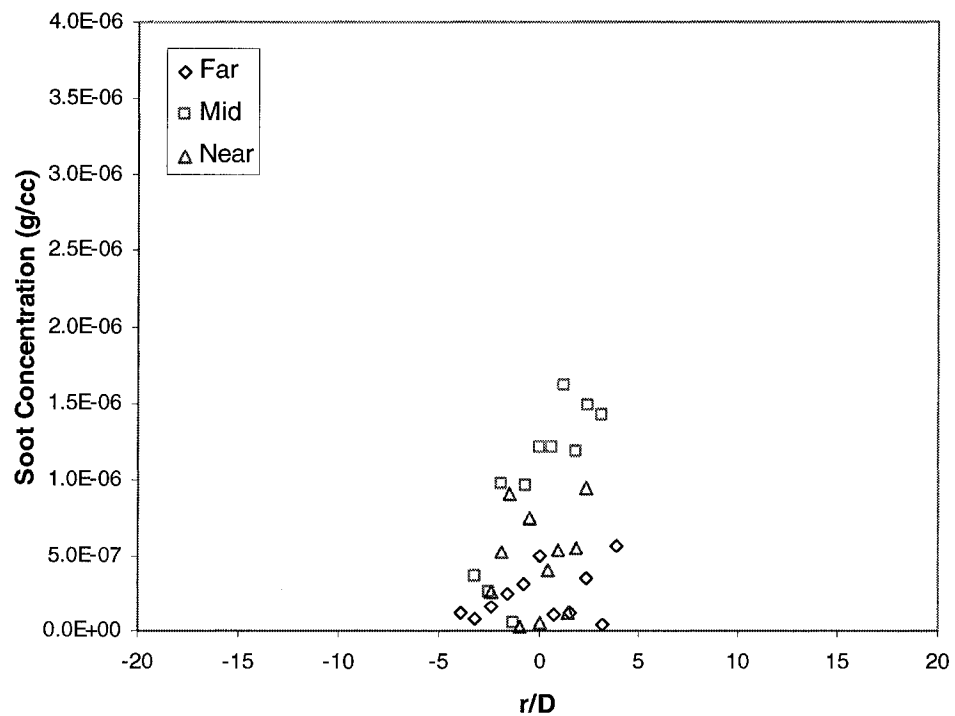


Figure 3.34d Radial Soot Concentration Profiles at 10% CFMFR
(Far: 75%, Mid: 50%, Near: 25% Flame Height) (D: Burner Diameter)

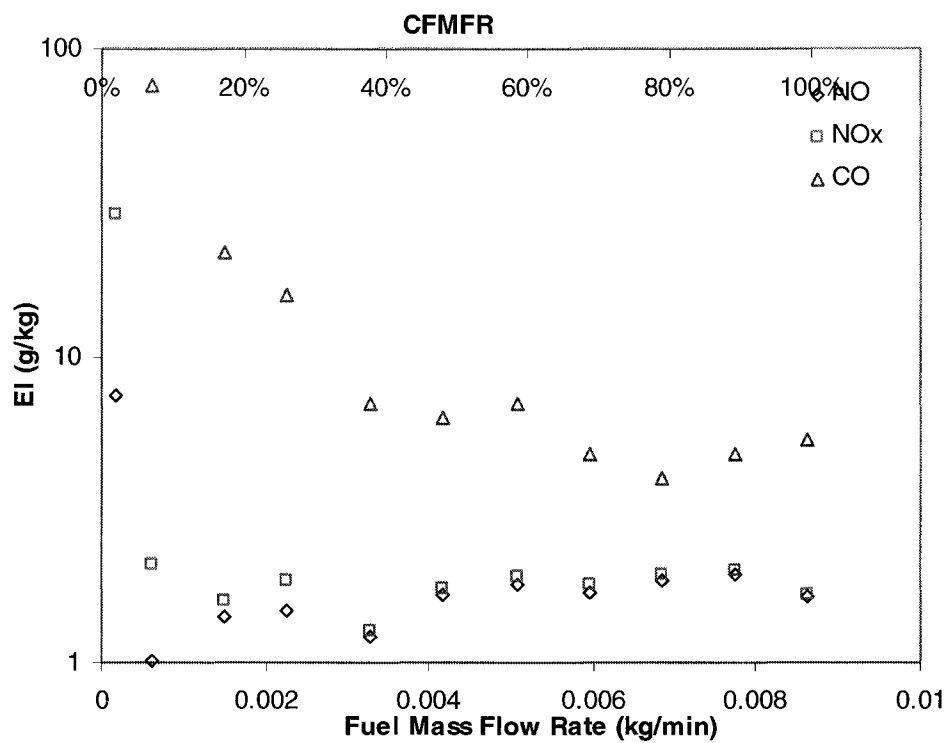


Figure 3.35a Emission Index for CO, NO and NO_x at 2m/s Cross-Flow

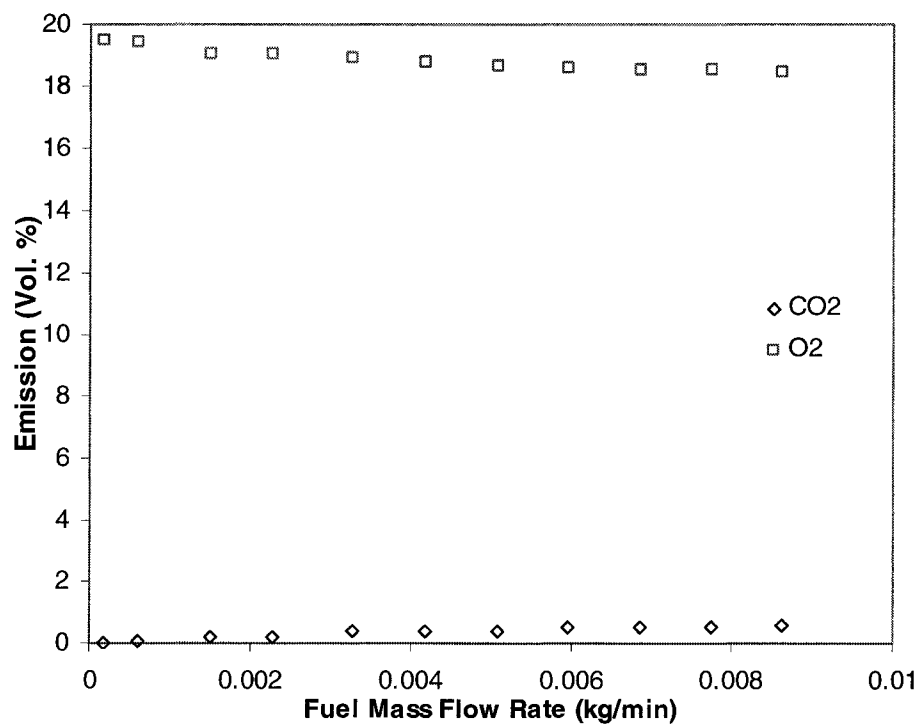


Figure 3.35b Global Emission for CO₂ and O₂ Concentration at 2 m/s Cross-Flow

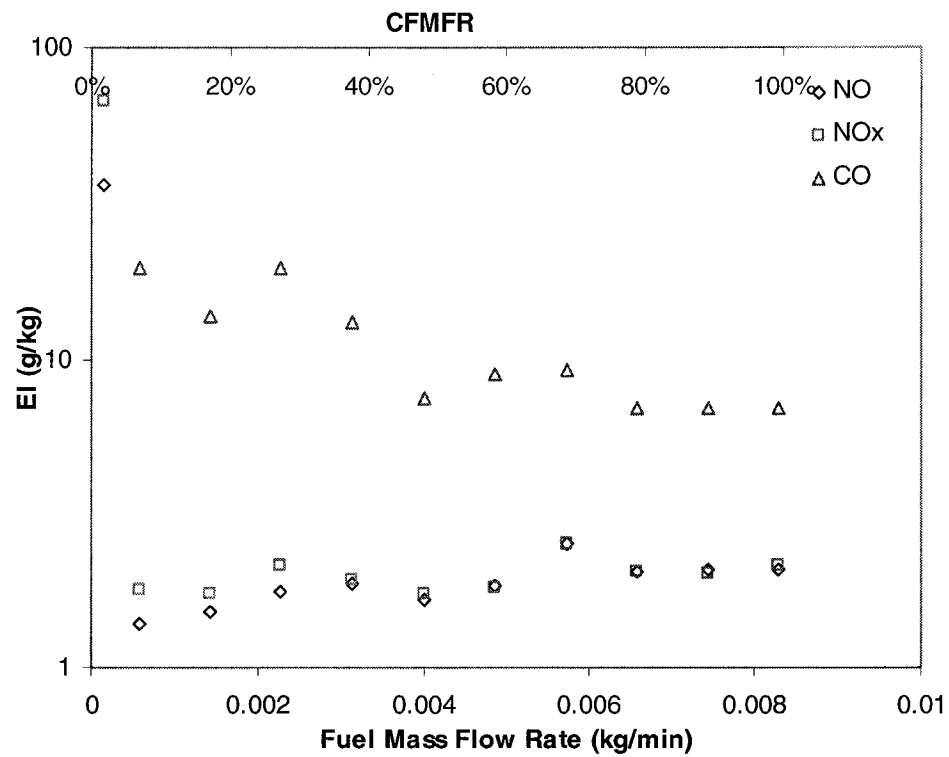


Figure 3.36a Emission Index for CO, NO and NO_x at 2.5 m/s Cross-Flow

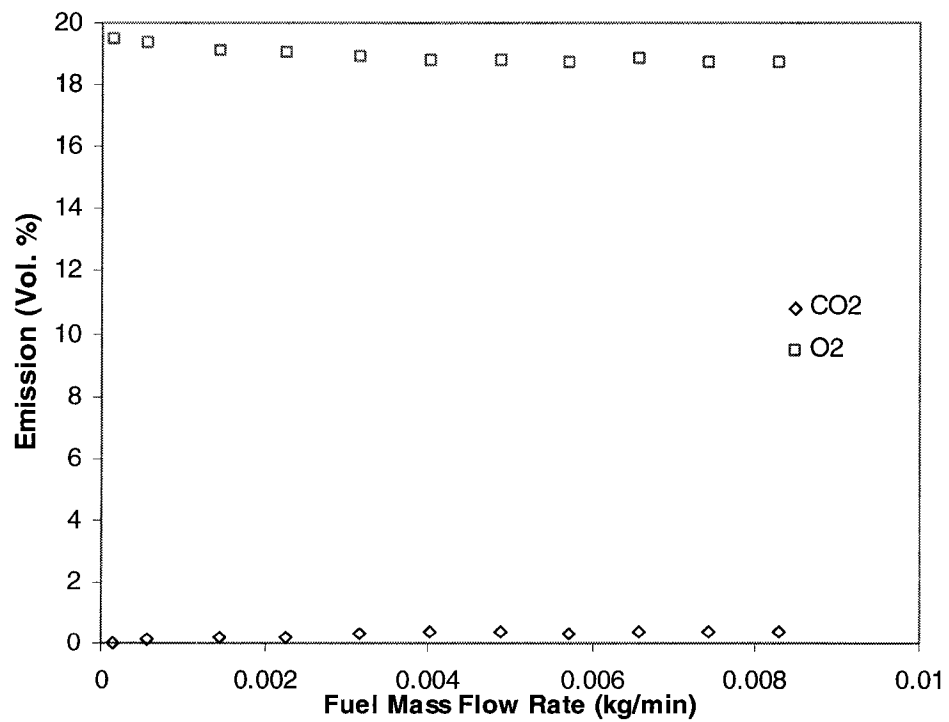


Figure 3.36b Global Emission for CO₂ and O₂ Concentration at 2.5 m/s Cross-Flow

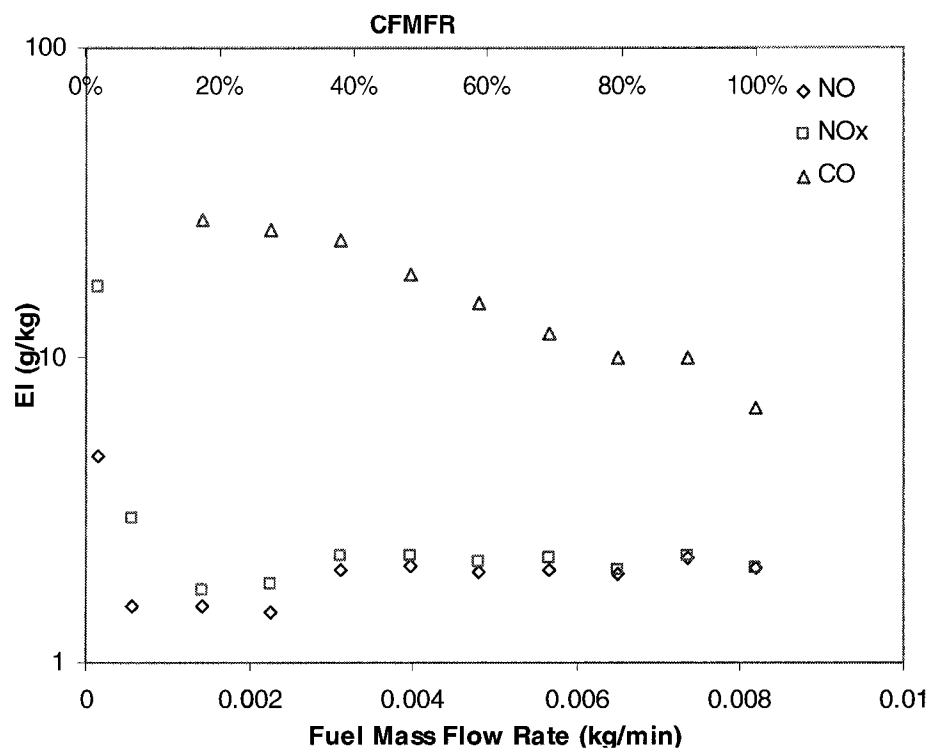


Figure 3.37a Emission Index for CO, NO and NO_x at 3 m/s Cross-Flow

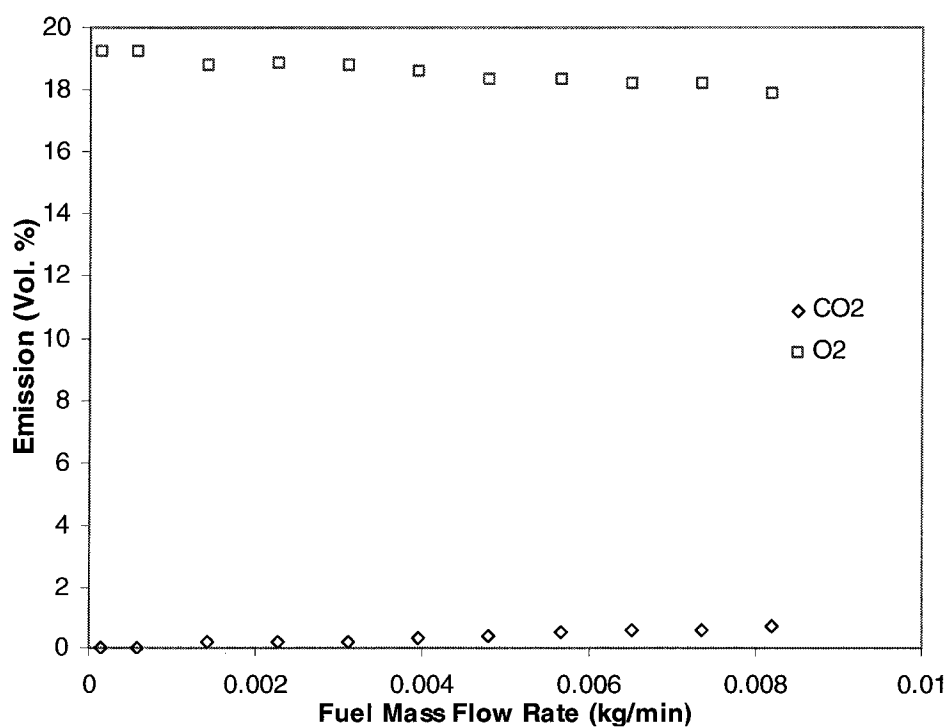


Figure 3.37b Global Emission for CO₂ and O₂ Concentration at 3 m/s Cross-Flow

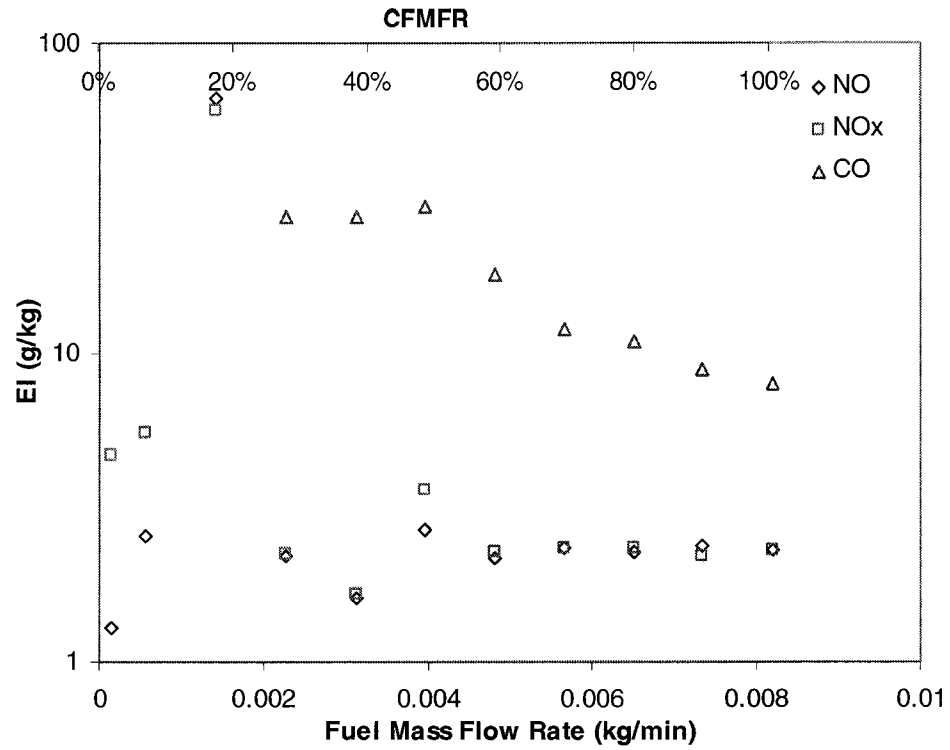


Figure 3.38a Emission Index for CO, NO and NO_x at 3.5 m/s Cross-Flow

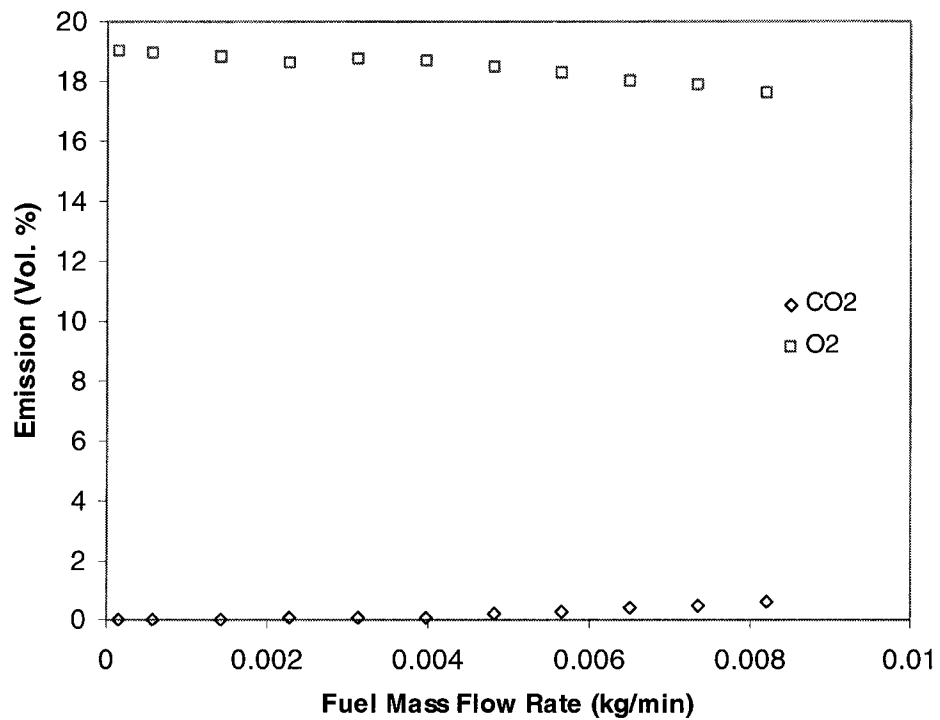


Figure 3.38b Global Emission for CO₂ and O₂ Concentration at 3.5 m/s Cross-Flow

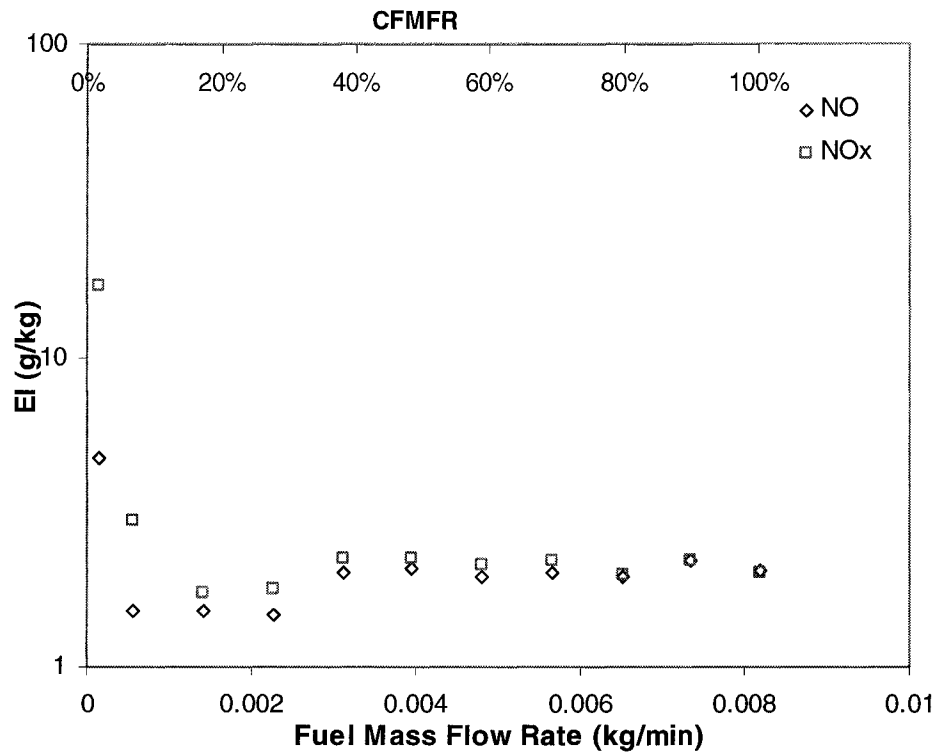


Figure 3.39a Emission Index for NO and NO_x at 4 m/s Cross-Flow

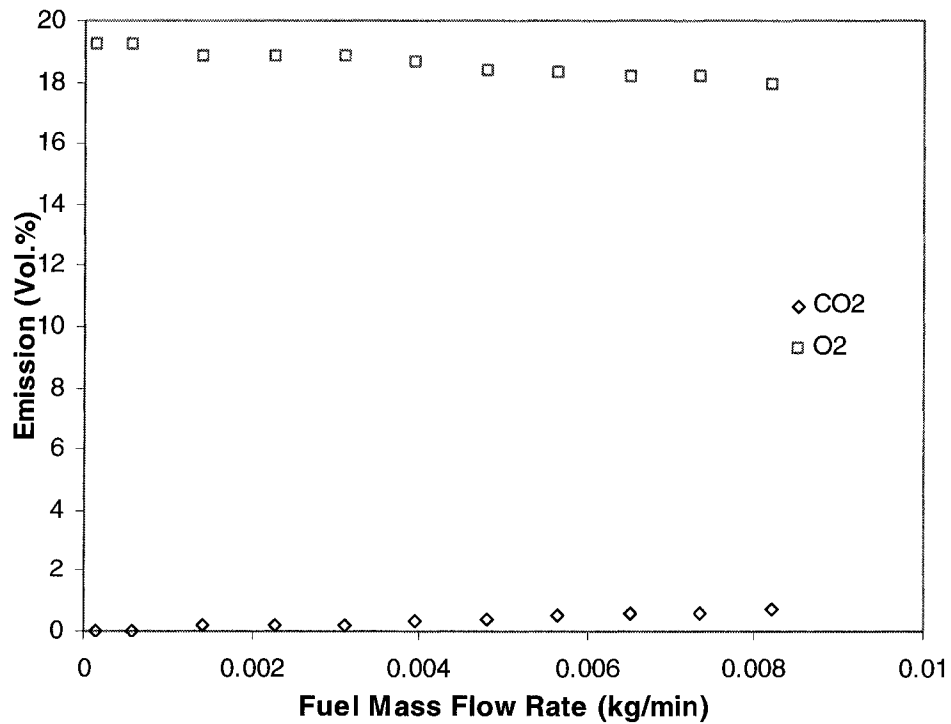


Figure 3.39b Global Emission for CO₂ and O₂ Concentration at 4 m/s Cross-Flow

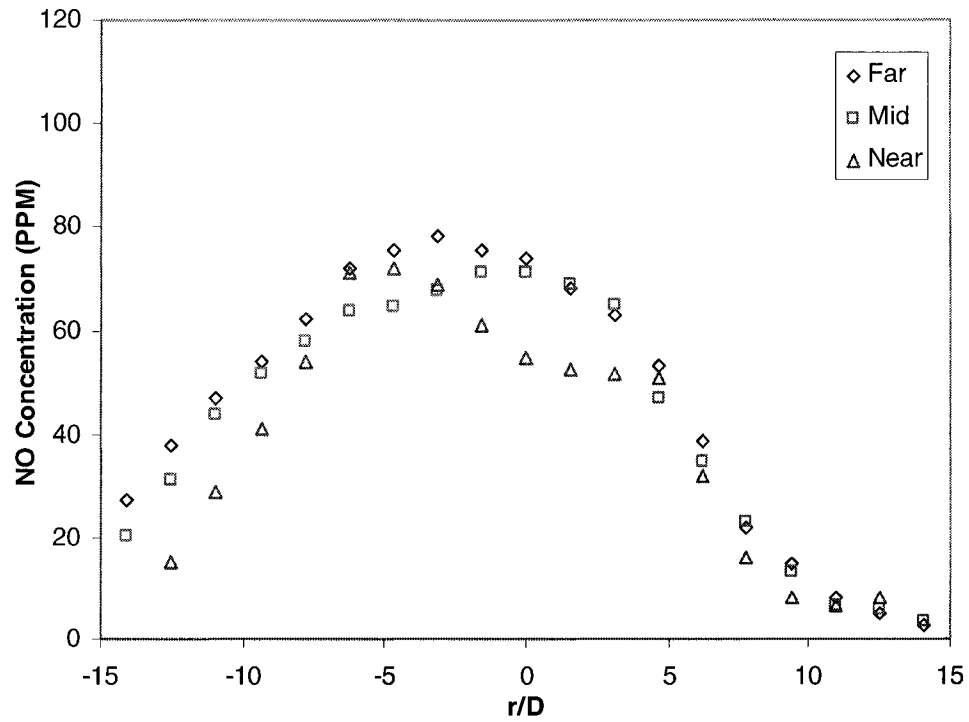


Figure 3.40a Radial NO Concentration Profiles on X Axis at Three Locations at 100% CFMFR at 2 m/s Cross-Flow. (Far: 75%, Mid: 50%, Near: 25% Flame Length) (D: Burner Diameter)

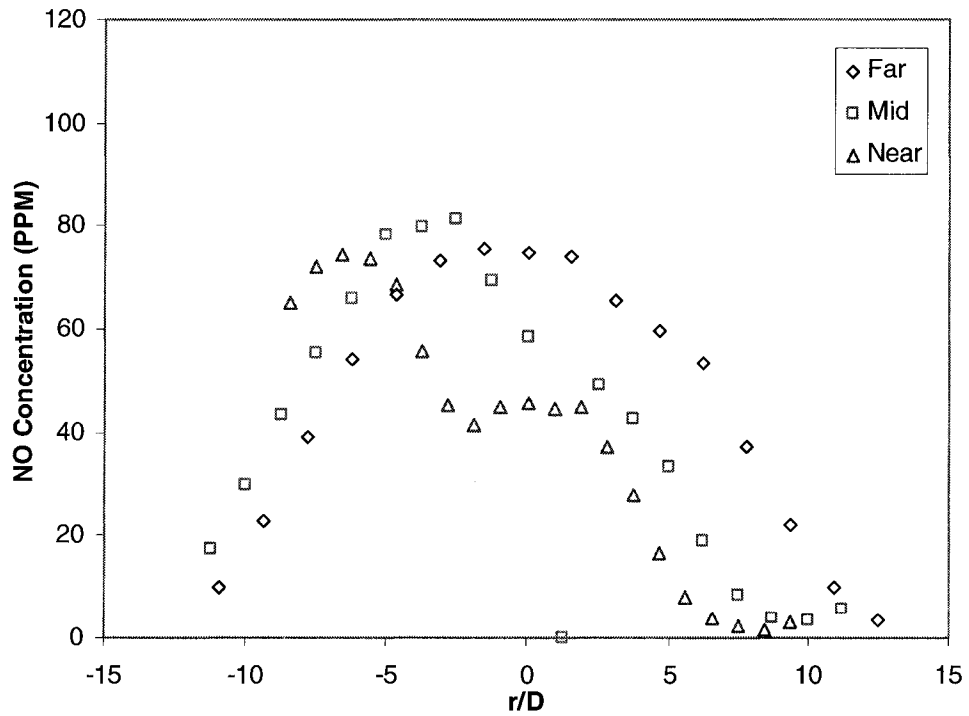


Figure 3.40b Radial NO Concentration Profiles on X Axis at Three Locations at 60% CFMFR at 2 m/s Cross-Flow. (Far: 75%, Mid: 50%, Near: 25% Flame Length) (D: Burner Diameter)

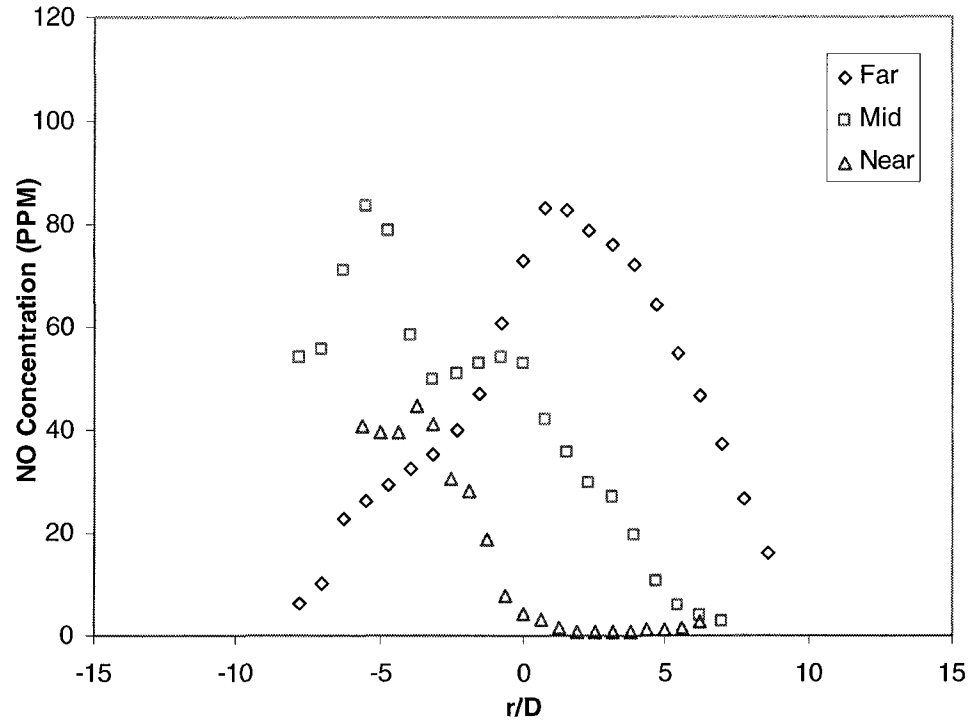


Figure 3.40c Radial NO Concentration Profiles on X Axis at Three Locations at 20% CFMFR at 2 m/s Cross-Flow. (Far: 75%, Mid: 50%, Near: 25% Flame Length) (D: Burner Diameter)

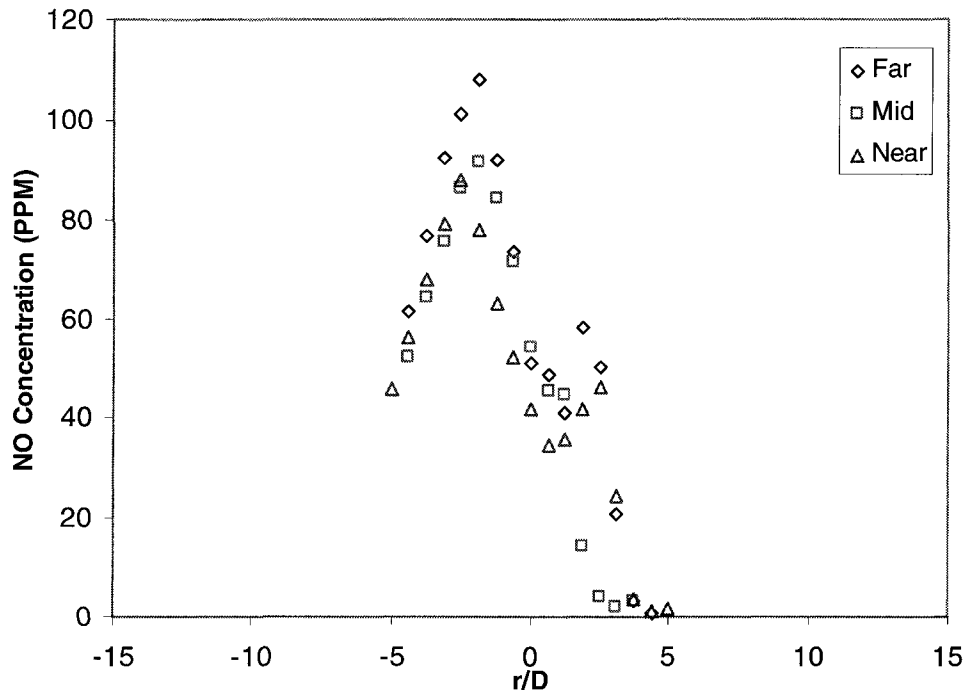


Figure 3.40d Radial NO Concentration Profiles on X Axis at Three Locations at 10% CFMFR at 2 m/s Cross-Flow. (Far: 75%, Mid: 50%, Near: 25% Flame Length) (D: Burner Diameter)

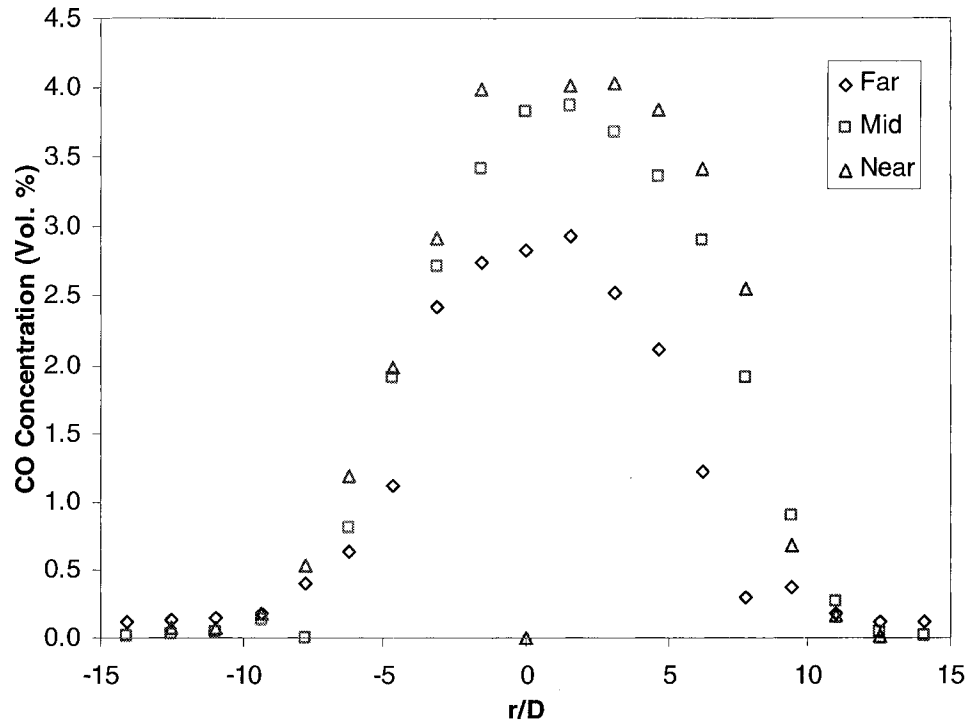


Figure 3.41a Radial CO Concentration Profiles on X Axis at Three Locations at 100% CFMFR at 2 m/s Cross-Flow. (Far: 75%, Mid: 50%, Near: 25% Flame Length) (D: Burner Diameter)

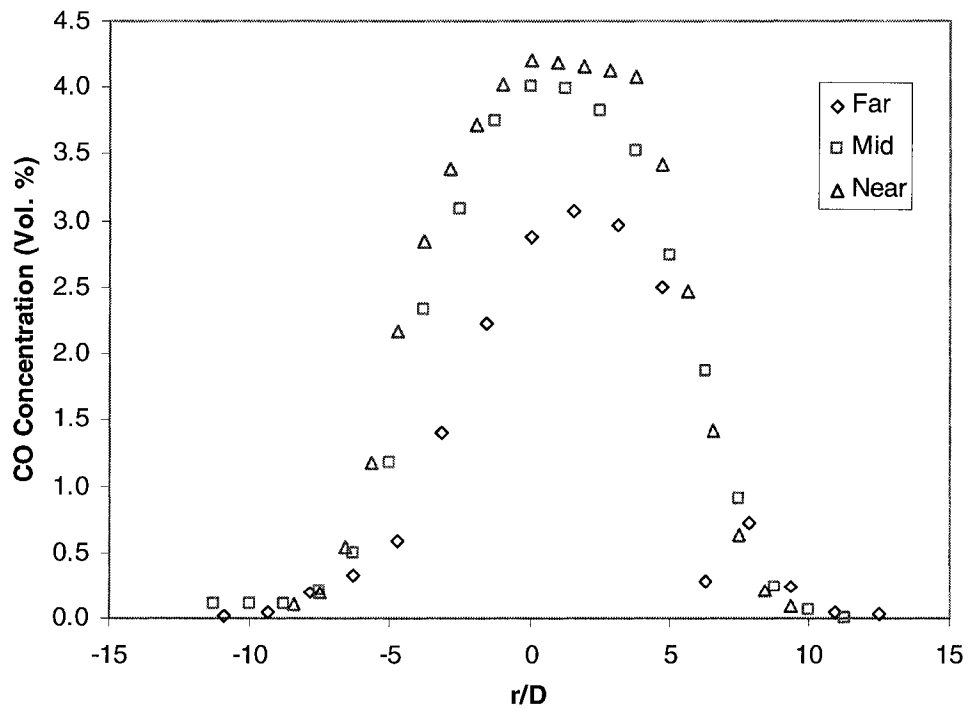


Figure 3.41b Radial CO Concentration Profiles on X Axis at Three Locations at 60% CFMFR at 2 m/s Cross-Flow. (Far: 75%, Mid: 50%, Near: 25% Flame Length) (D: Burner Diameter)

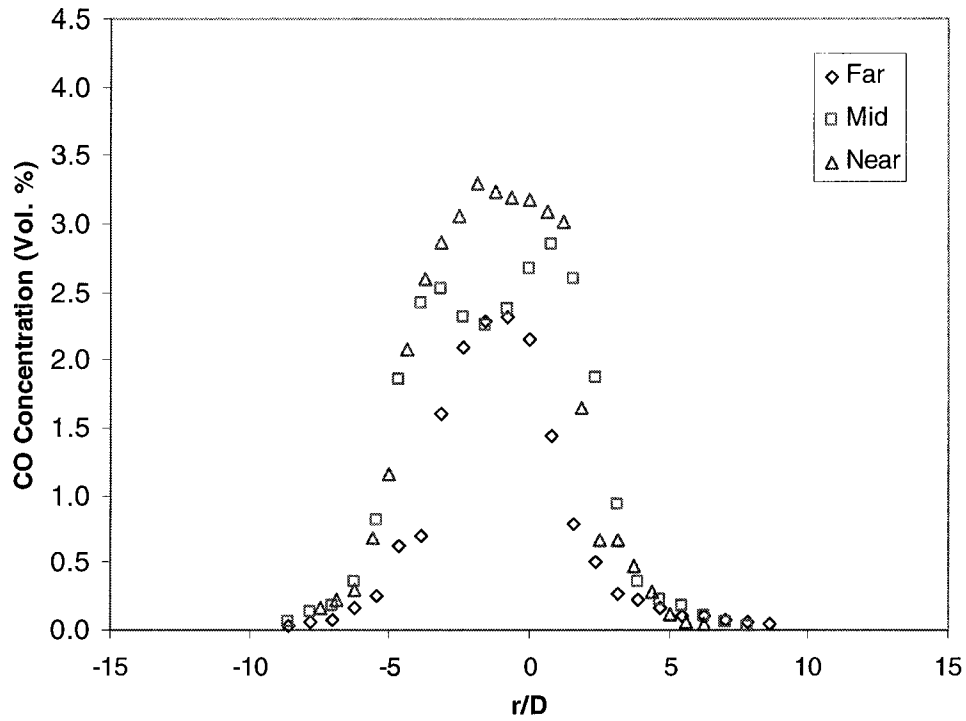


Figure 3.41c Radial CO Concentration Profiles on X Axis at Three Locations at 20% CFMFR at 2 m/s Cross-Flow. (Far: 75%, Mid: 50%, Near: 25% Flame Length) (D: Burner Diameter)

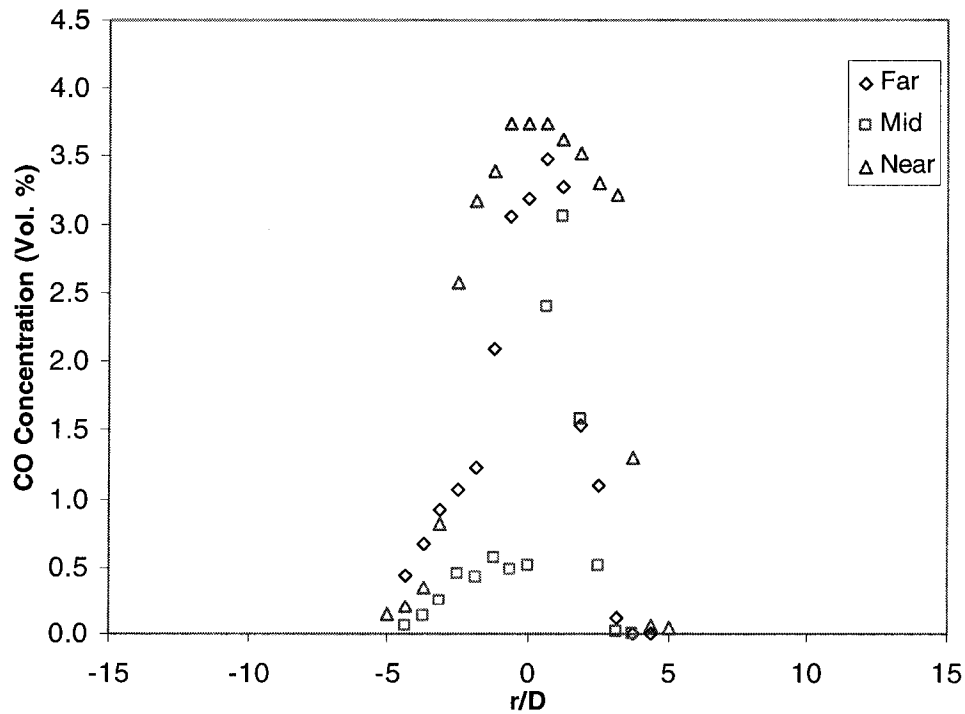


Figure 3.41d Radial CO Concentration Profiles on X Axis at Three Locations at 10% CFMFR at 2 m/s Cross-Flow. (Far: 75%, Mid: 50%, Near: 25% Flame Length) (D: Burner Diameter)

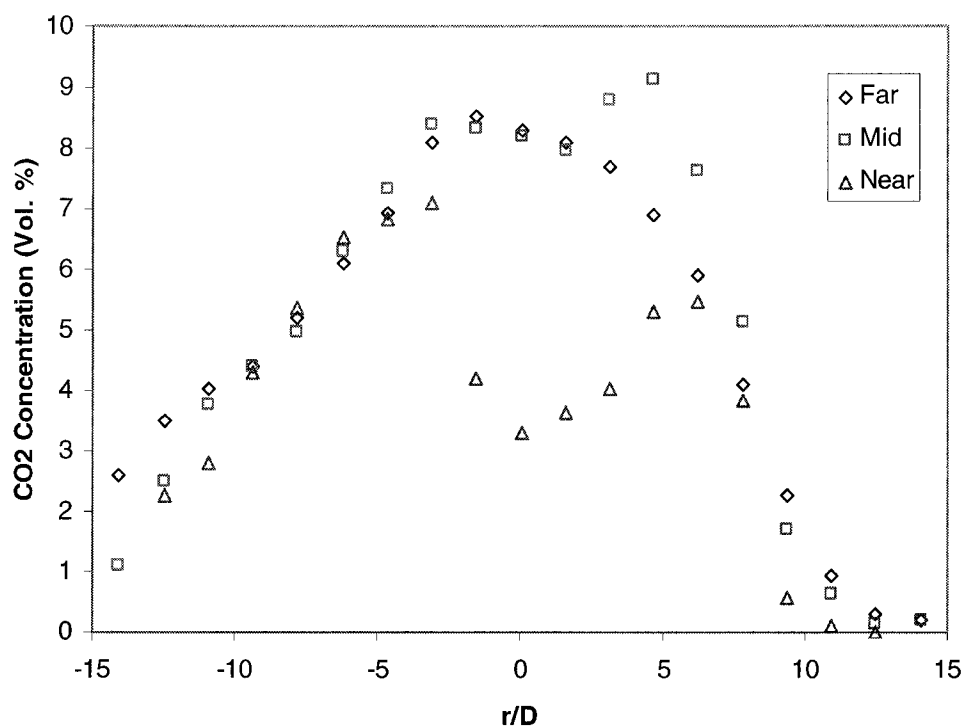


Figure 3.42a Radial CO₂ Concentration Profiles on X Axis at Three Locations at 100% CFMFR at 2 m/s Cross-Flow. (Far: 75%, Mid: 50%, Near: 25% Flame Length) (D: Burner Diameter)

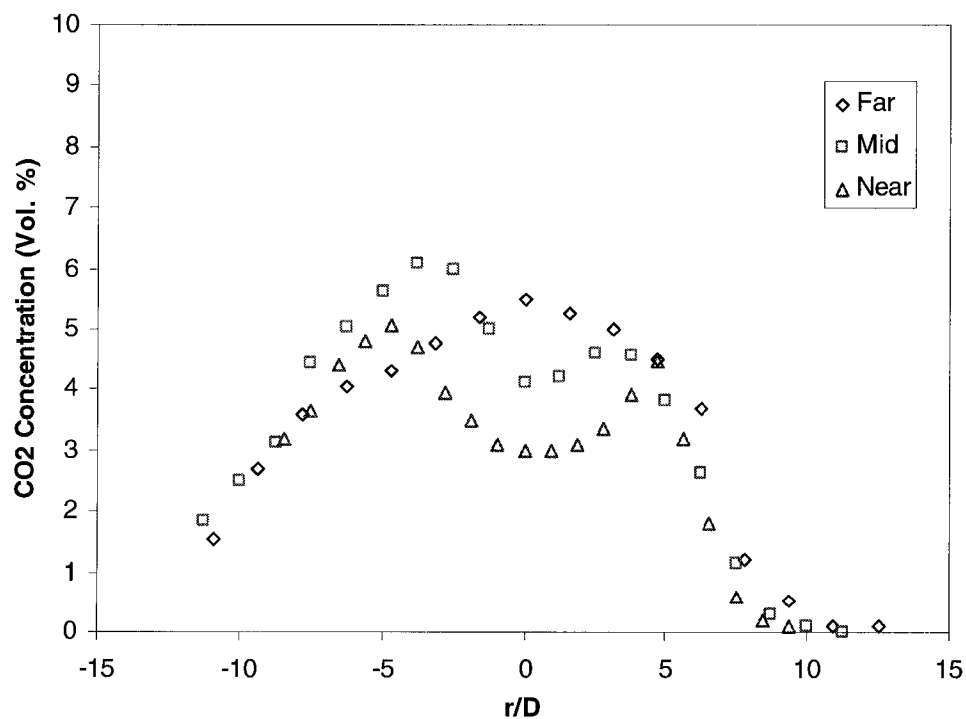


Figure 3.42b Radial CO₂ Concentration Profiles on X Axis at Three Locations at 60% CFMFR at 2 m/s Cross-Flow. (Far: 75%, Mid: 50%, Near: 25% Flame Length) (D: Burner Diameter)

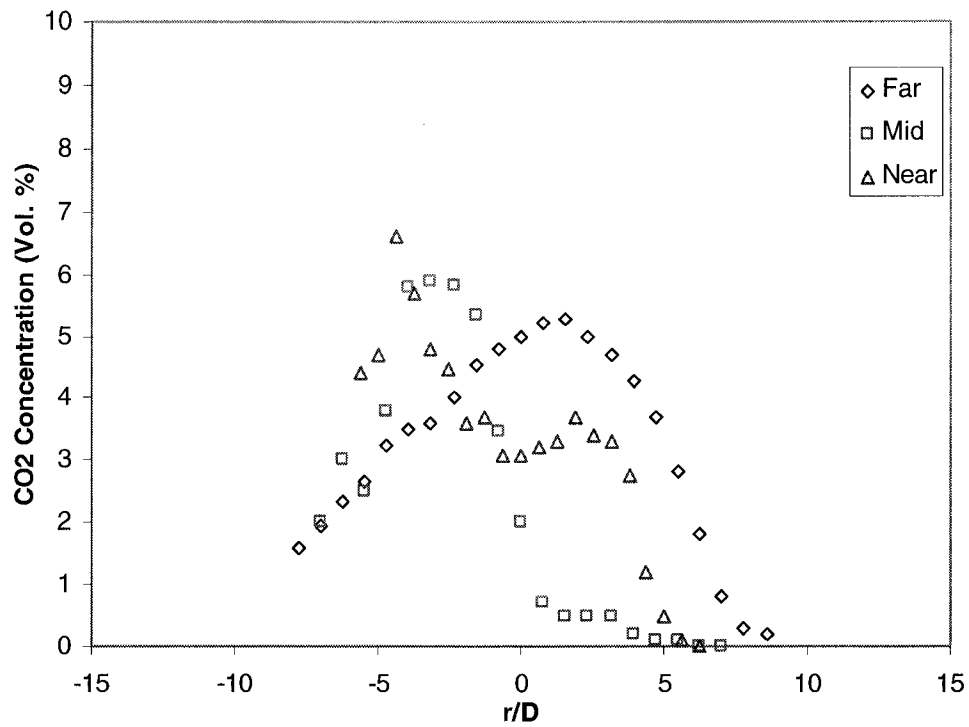


Figure 3.42c Radial CO₂ Concentration Profiles on X Axis at Three Locations at 20% CFMFR at 2 m/s Cross-Flow. (Far: 75%, Mid: 50%, Near: 25% Flame Length) (D: Burner Diameter)

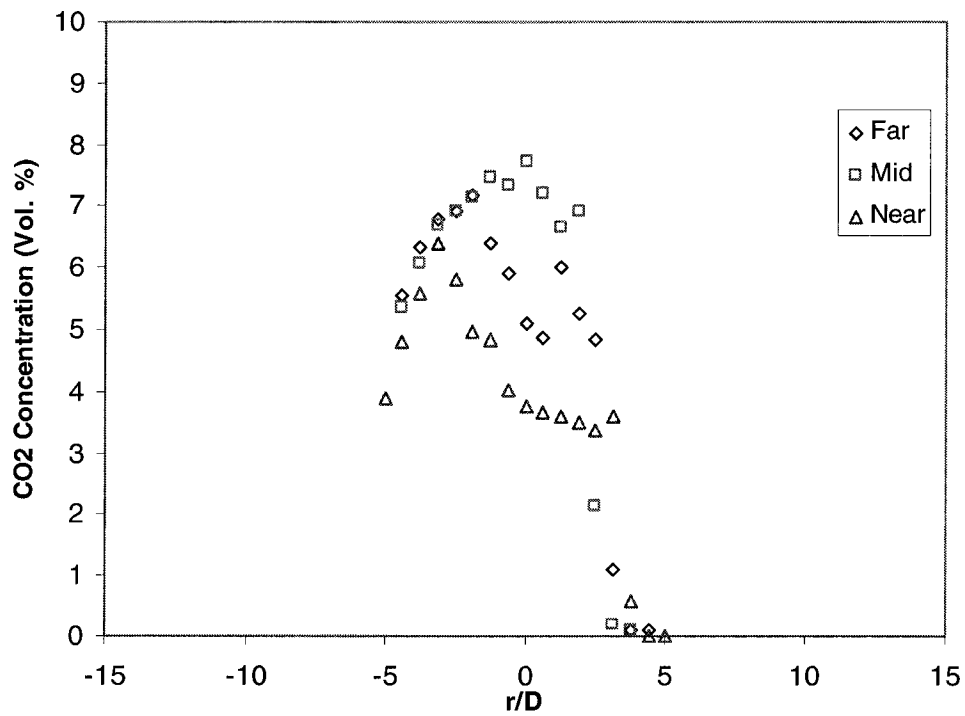


Figure 3.42d Radial CO₂ Concentration Profiles on X Axis at Three Locations at 10% CFMFR at 2 m/s Cross-Flow. (Far: 75%, Mid: 50%, Near: 25% Flame Length) (D: Burner Diameter)

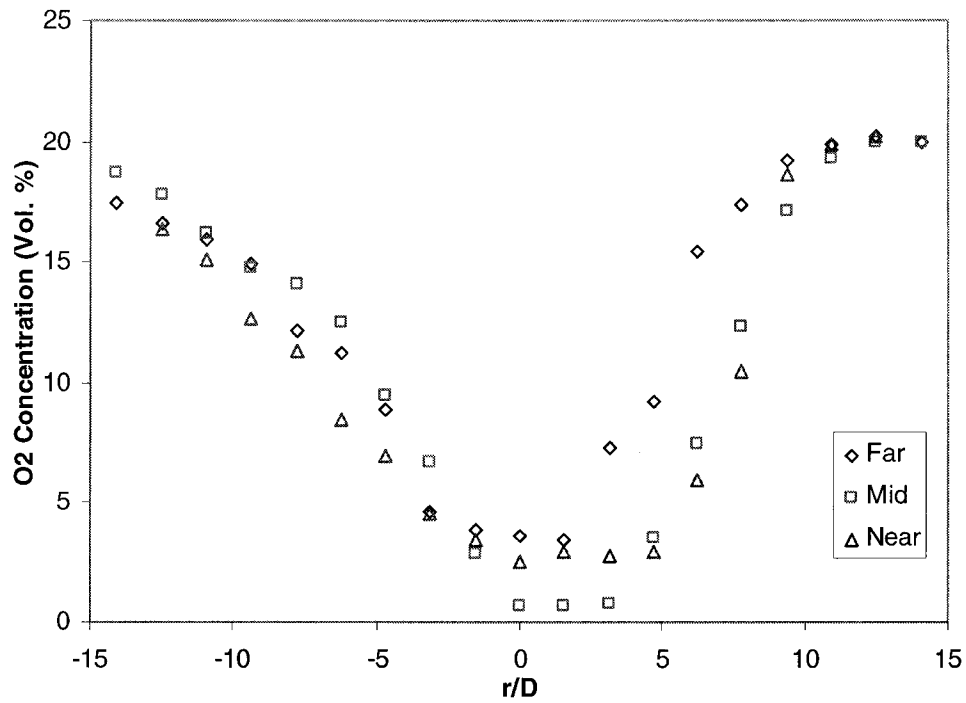


Figure 3.43a Radial O₂ Concentration Profiles on X Axis at Three Locations at 100% CFMFR at 2 m/s Cross-Flow. (Far: 75%, Mid: 50%, Near: 25% Flame Length) (D: Burner Diameter)

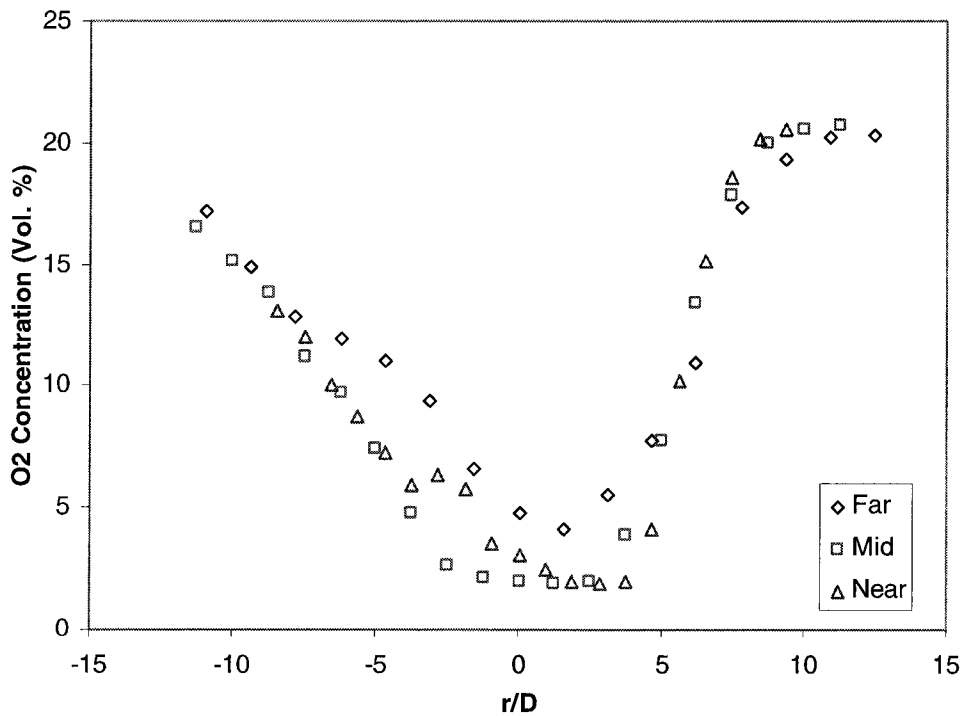


Figure 3.43b Radial O₂ Concentration Profiles on X Axis at Three Locations at 60% CFMFR at 2 m/s Cross-Flow. (Far: 75%, Mid: 50%, Near: 25% Flame Length) (D: Burner Diameter)

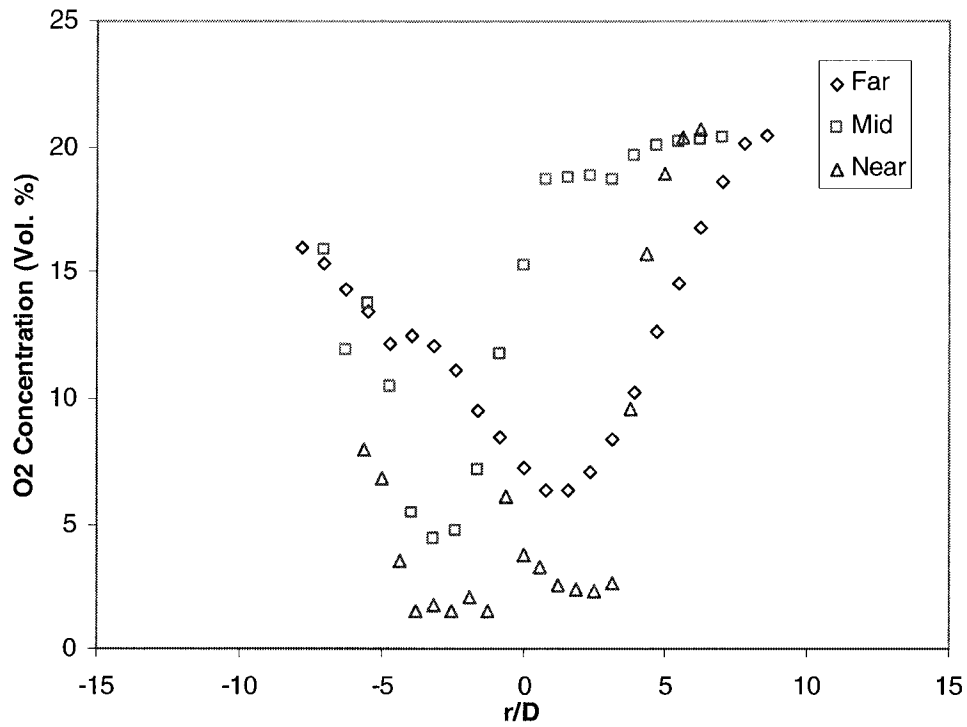


Figure 3.43c Radial O₂ Concentration Profiles on X Axis at Three Locations at 20% CFMFR at 2 m/s Cross-Flow. (Far: 75%, Mid: 50%, Near: 25% Flame Length) (D: Burner Diameter)

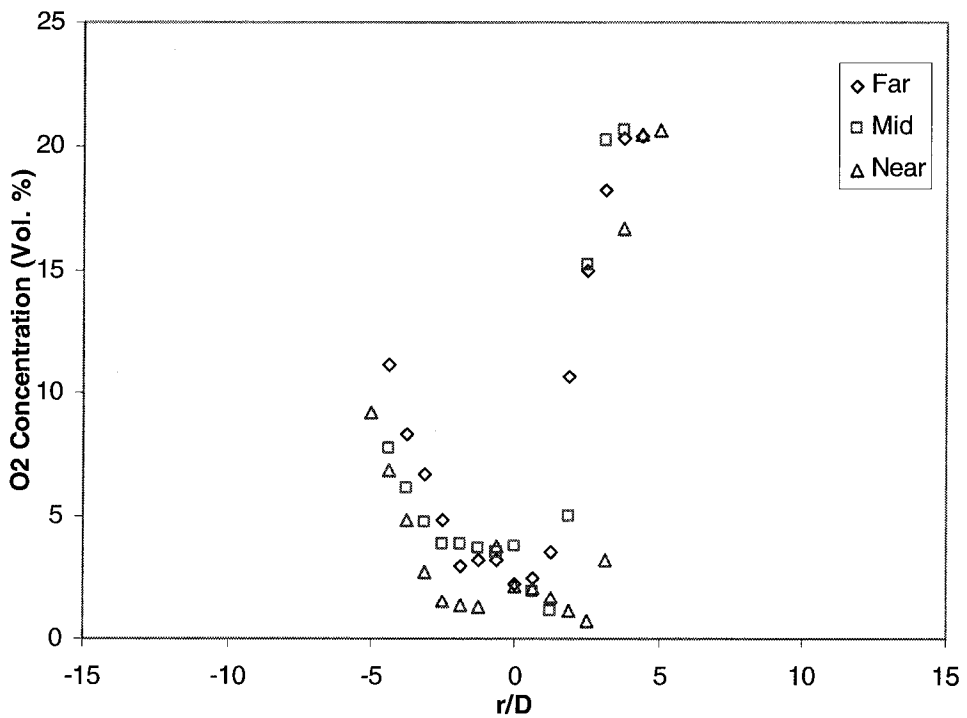


Figure 3.43d Radial O₂ Concentration Profiles on X Axis at Three Locations at 10% CFMFR at 2 m/s Cross-Flow. (Far: 75%, Mid: 50%, Near: 25% Flame Length) (D: Burner Diameter)

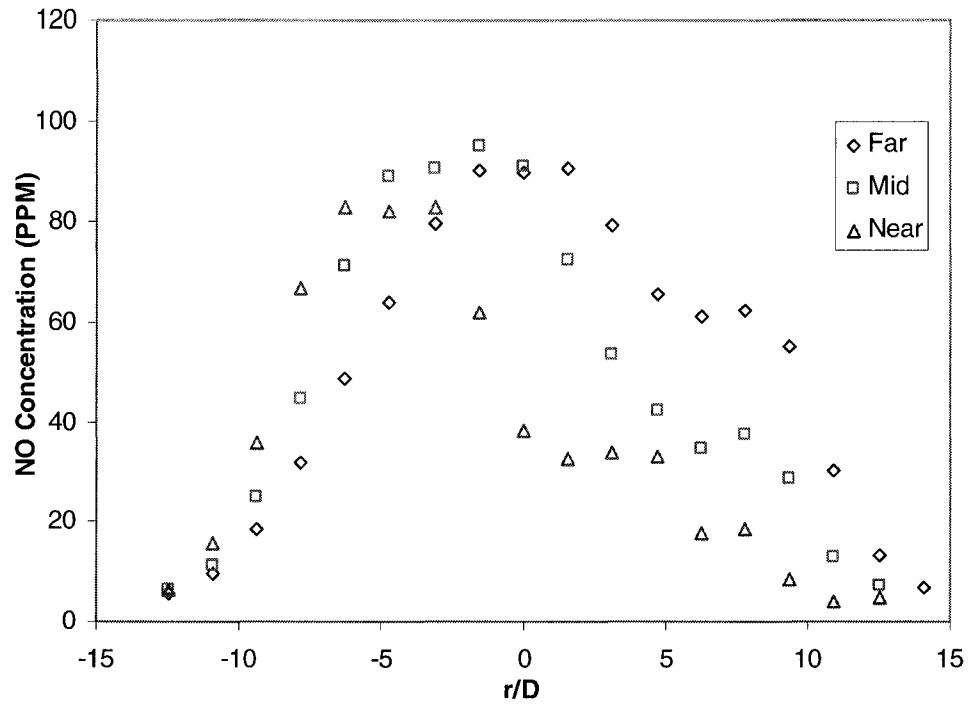


Figure 3.44a Radial NO Concentration Profiles on X Axis at Three Locations at 100% CFMFR at 3 m/s Cross-Flow. (Far: 75%, Mid: 50%, Near: 25% Flame Length) (D: Burner Diameter)

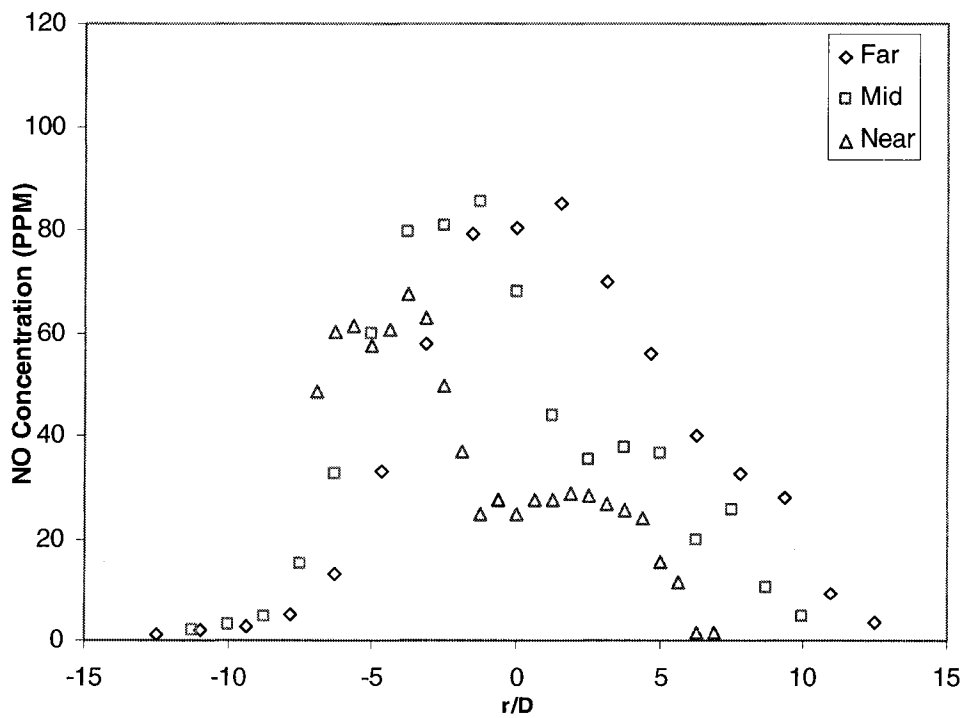


Figure 3.44b Radial NO Concentration Profiles on X Axis at Three Locations at 60% CFMFR at 3 m/s Cross-Flow. (Far: 75%, Mid: 50%, Near: 25% Flame Length) (D: Burner Diameter)

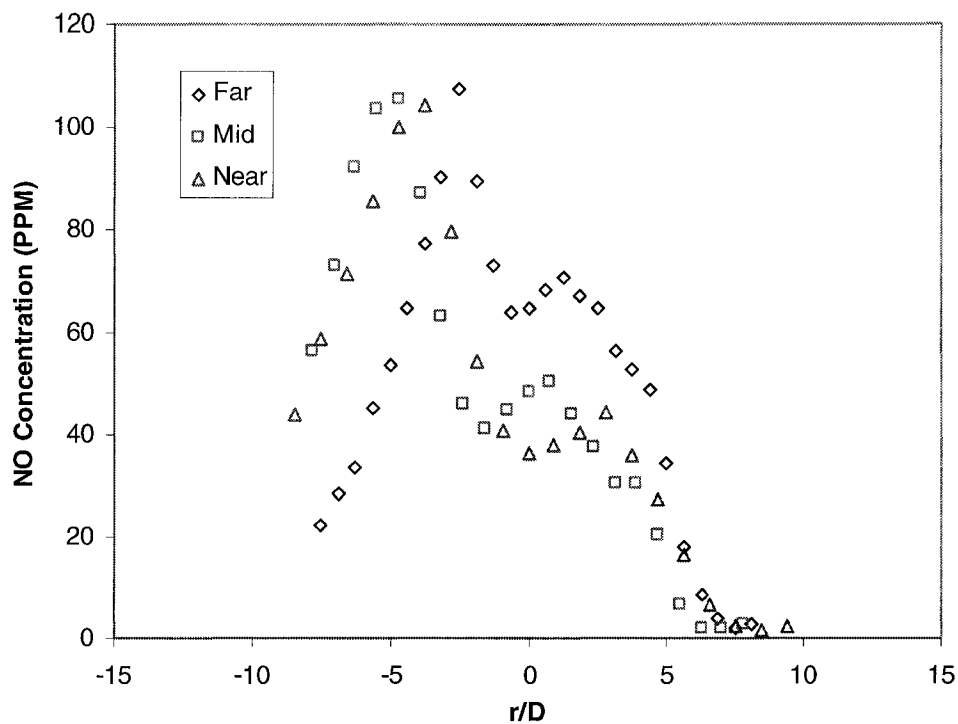


Figure 3.44c Radial NO Concentration Profiles on X Axis at Three Locations at 20% CFMFR at 3 m/s Cross-Flow. (Far: 75%, Mid: 50%, Near: 25% Flame Length) (D: Burner Diameter)

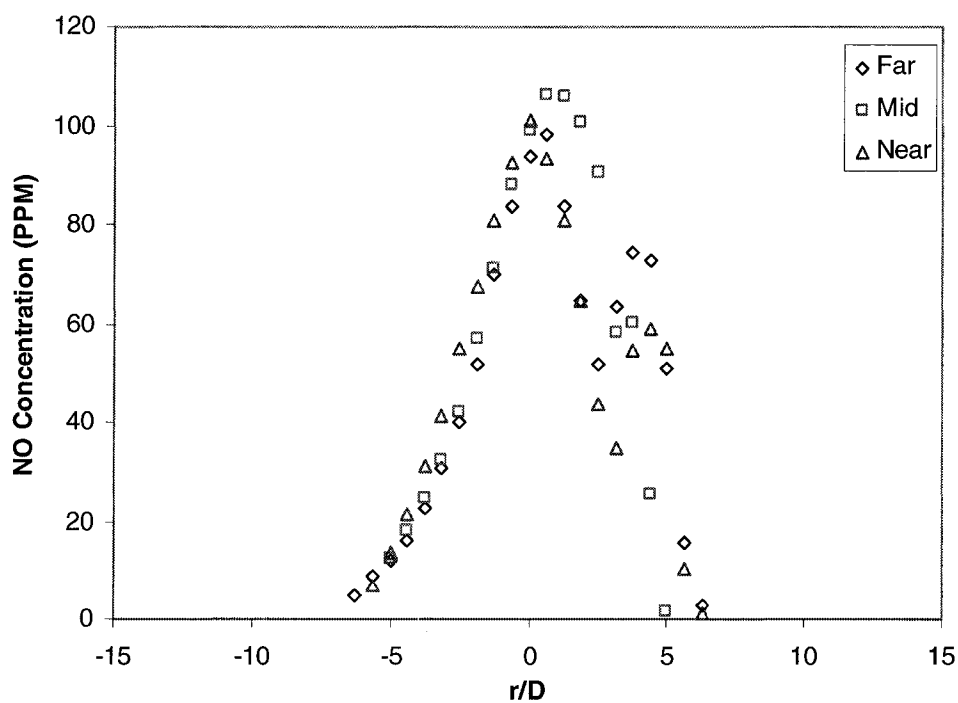


Figure 3.44d Radial NO Concentration Profiles on X Axis at Three Locations at 10% CFMFR at 3 m/s Cross-Flow. (Far: 75%, Mid: 50%, Near: 25% Flame Length) (D: Burner Diameter)

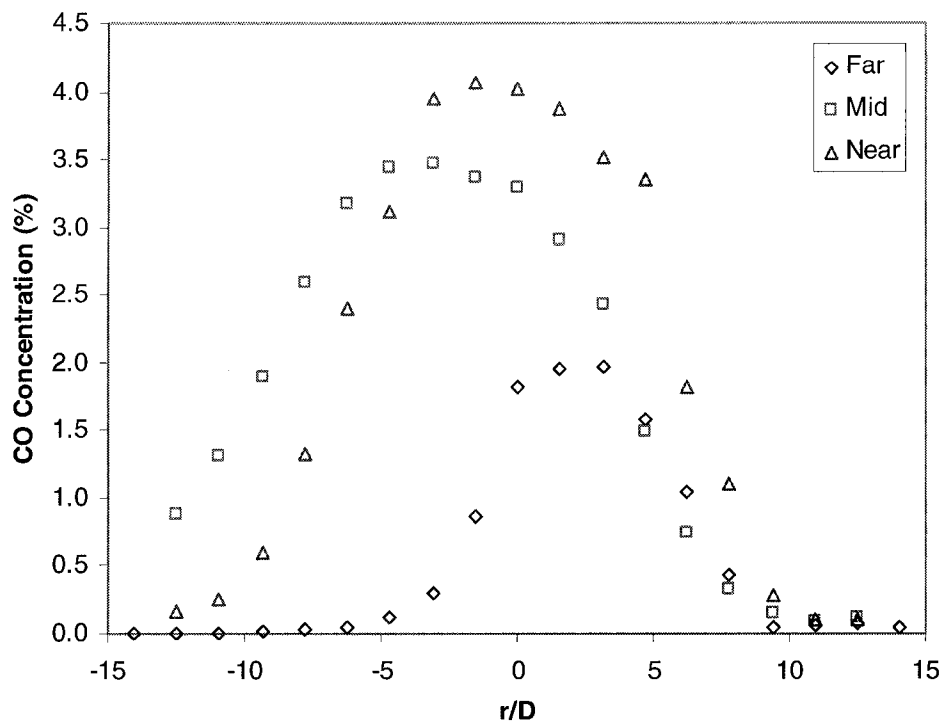


Figure 3.45a Radial CO Concentration Profiles on X Axis at Three Locations at 100% CFMFR at 3 m/s Cross-Flow. (Far: 75%, Mid: 50%, Near: 25% Flame Length) (D: Burner Diameter)

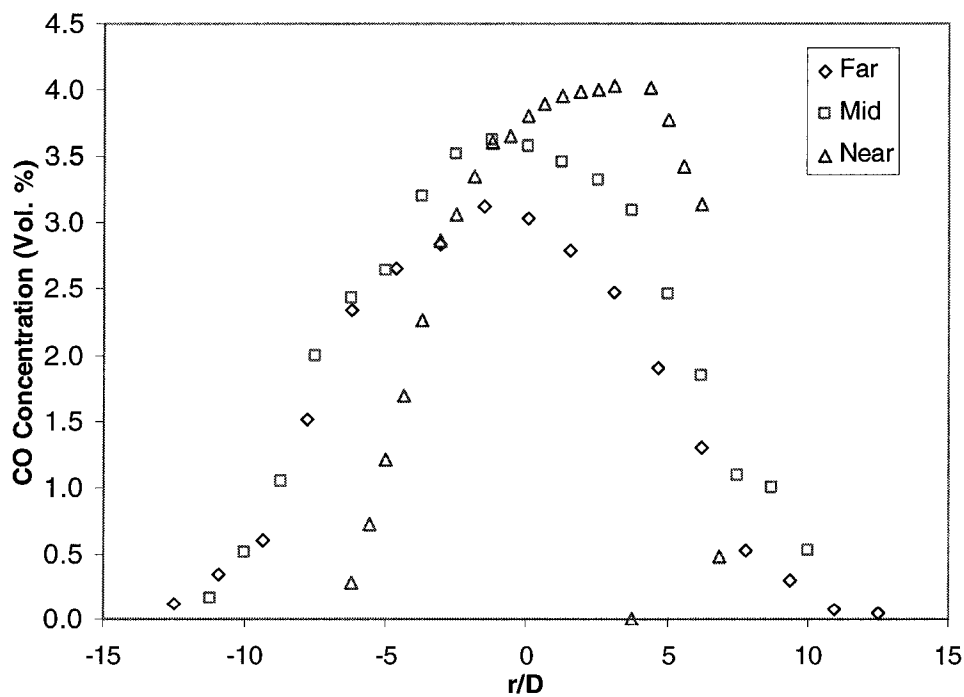


Figure 3.45b Radial CO Concentration Profiles on X Axis at Three Locations at 60% CFMFR at 3 m/s Cross-Flow. (Far: 75%, Mid: 50%, Near: 25% Flame Length) (D: Burner Diameter)

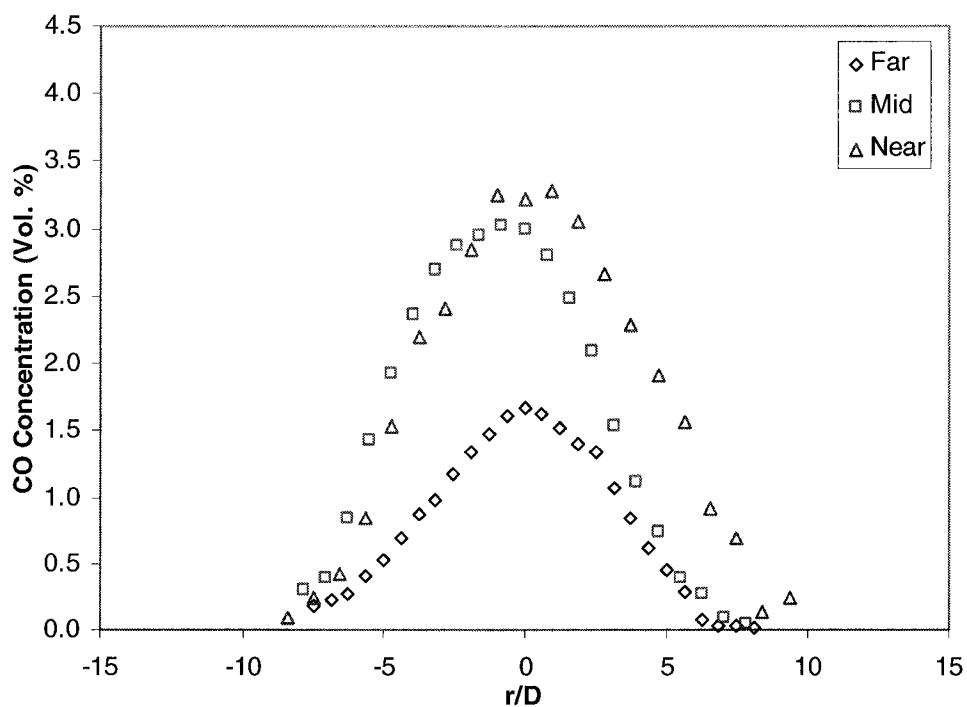


Figure 3.45c Radial CO Concentration Profiles on X Axis at Three Locations at 20% CFMFR at 3 m/s Cross-Flow. (Far: 75%, Mid: 50%, Near: 25% Flame Length) (D: Burner Diameter)

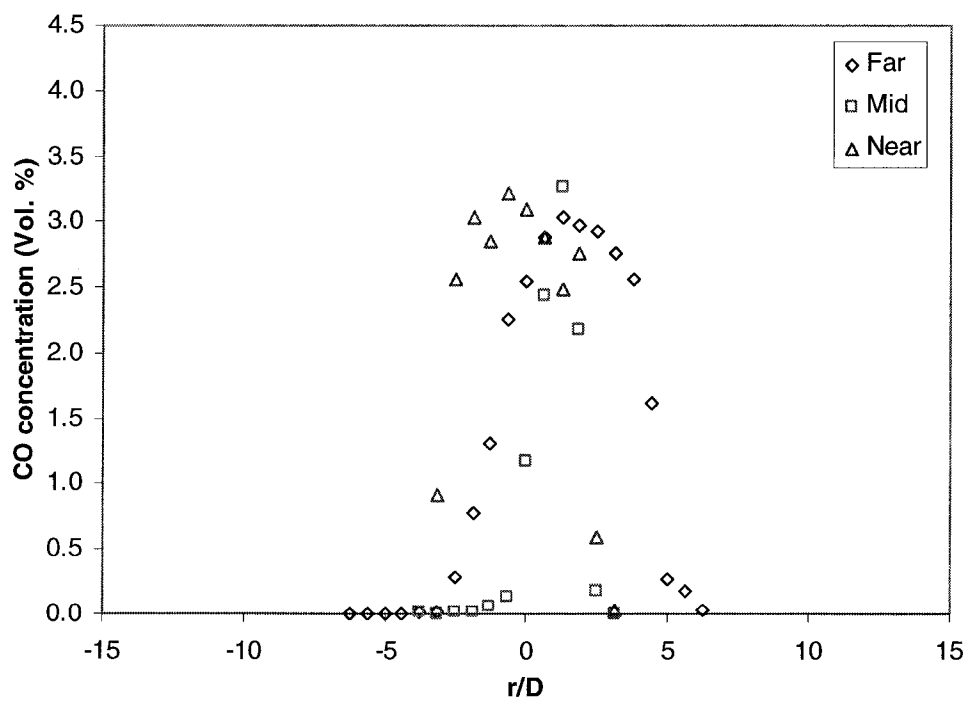


Figure 3.45d Radial CO Concentration Profiles on X Axis at Three Locations at 10% CFMFR at 3 m/s Cross-Flow. (Far: 75%, Mid: 50%, Near: 25% Flame Length) (D: Burner Diameter)

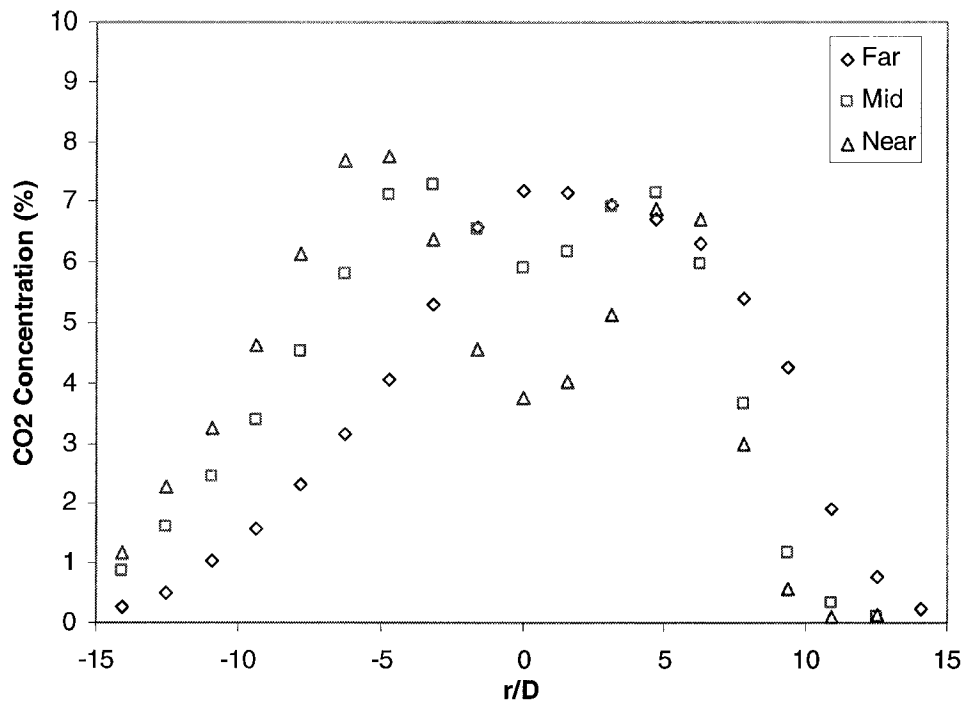


Figure 3.46a Radial CO₂ Concentration Profiles on X Axis at Three Locations at 100% CFMFR at 3 m/s Cross-Flow. (Far: 75%, Mid: 50%, Near: 25% Flame Length) (D: Burner Diameter)

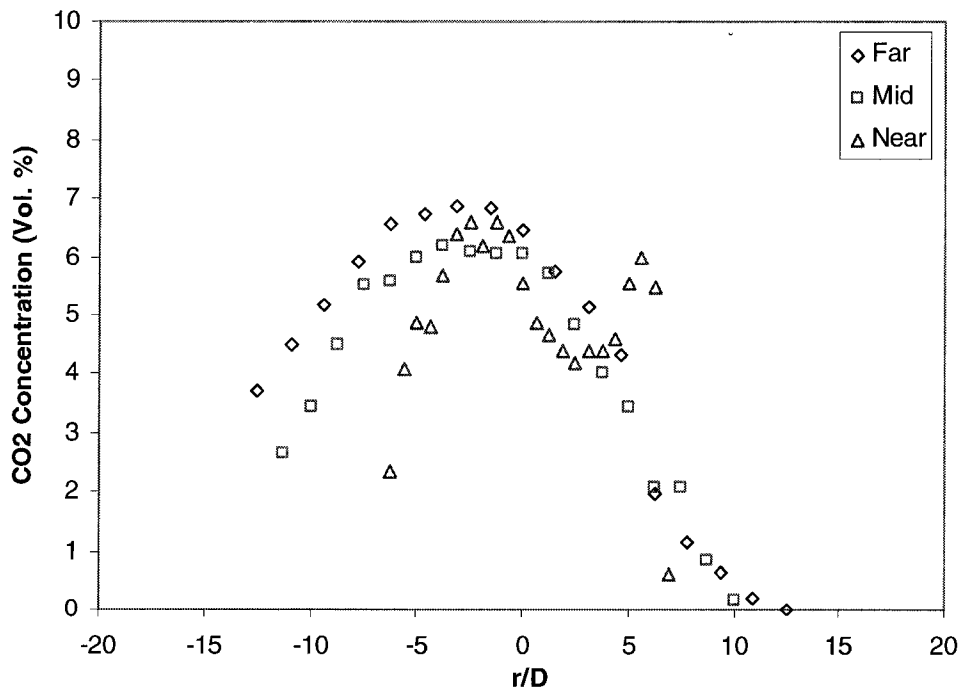


Figure 3.46b Radial CO₂ Concentration Profiles on X Axis at Three Locations at 60% CFMFR at 3 m/s Cross-Flow. (Far: 75%, Mid: 50%, Near: 25% Flame Length) (D: Burner Diameter)

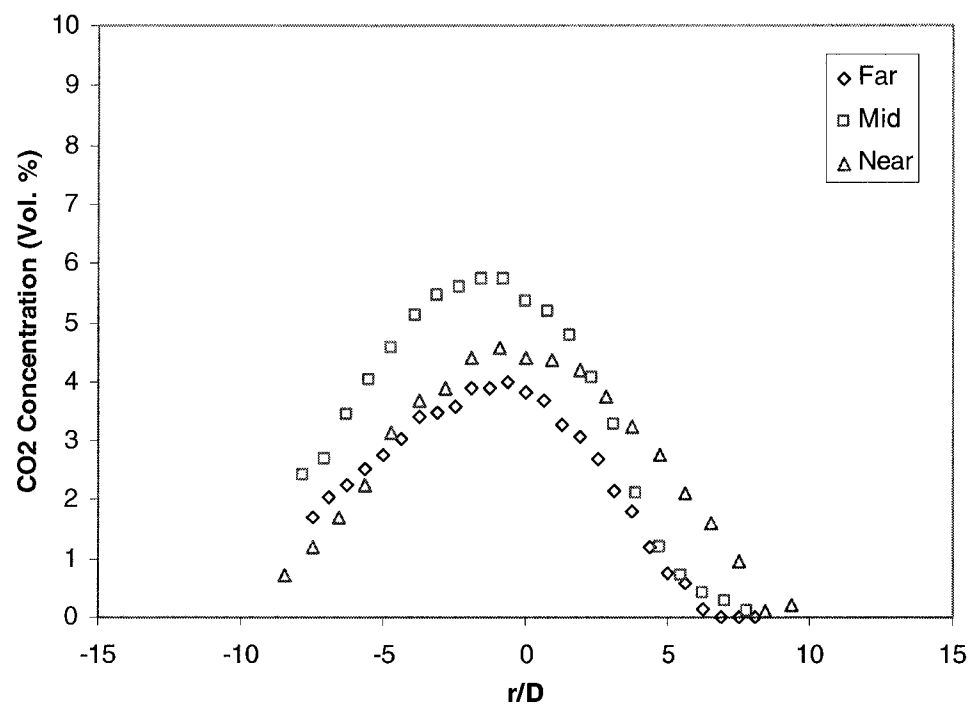


Figure 3.46c Radial CO₂ Concentration Profiles on X Axis at Three Locations at 20% CFMFR at 3 m/s Cross-Flow. (Far: 75%, Mid: 50%, Near: 25% Flame Length) (D: Burner Diameter)

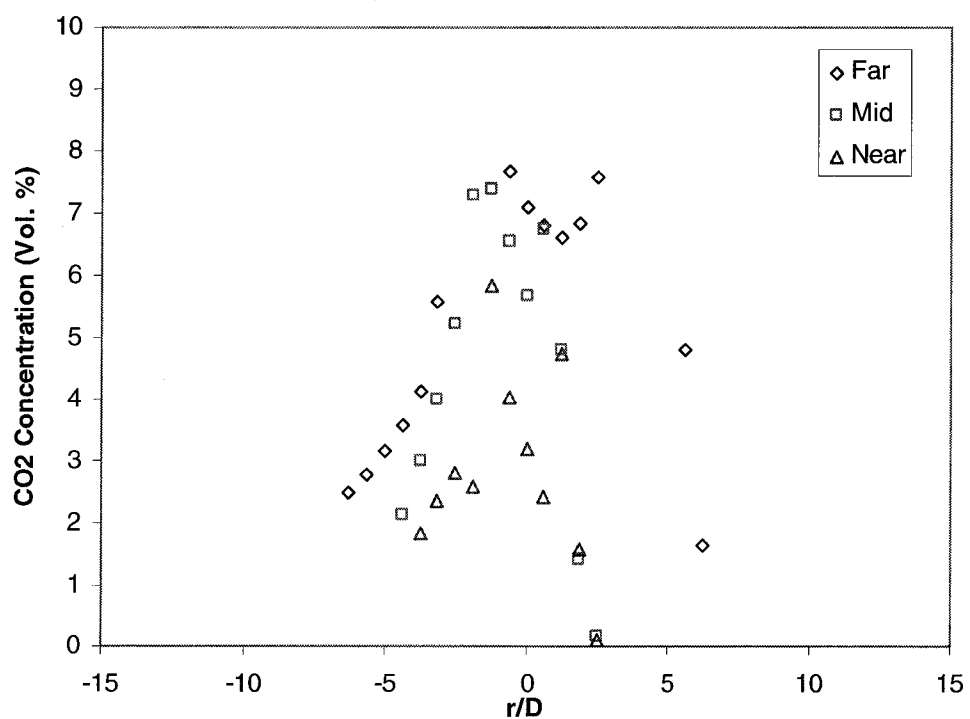


Figure 3.46d Radial CO₂ Concentration Profiles on X Axis at Three Locations at 10% CFMFR at 3 m/s Cross-Flow. (Far: 75%, Mid: 50%, Near: 25% Flame Length) (D: Burner Diameter)

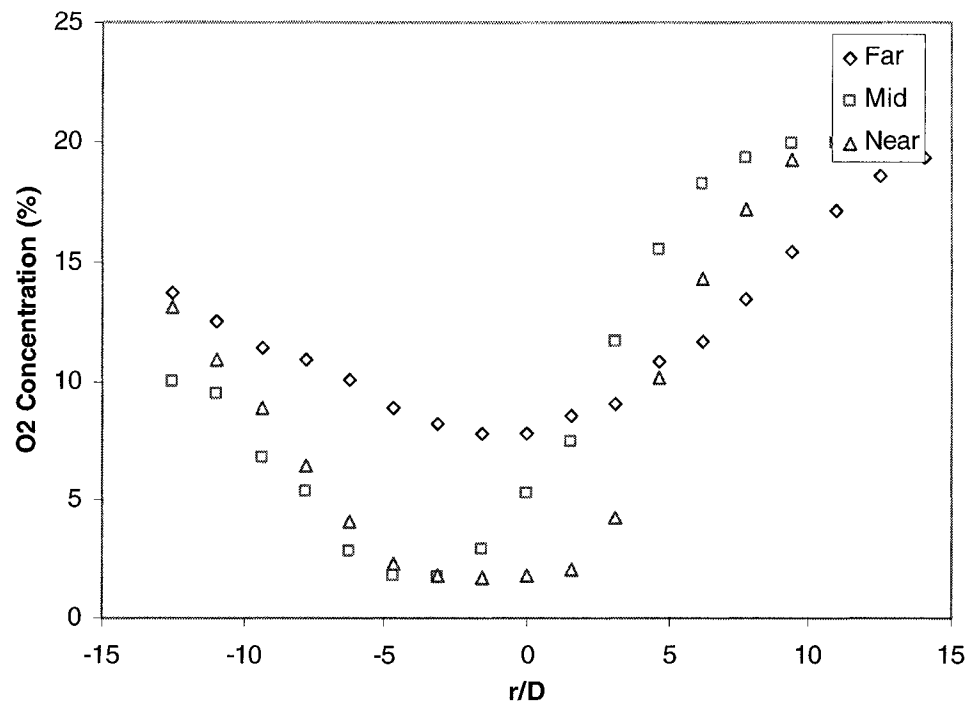


Figure 3.47a Radial O₂ Concentration Profiles on X Axis at Three Locations at 100% CFMFR at 3 m/s Cross-Flow. (Far: 75%, Mid: 50%, Near: 25% Flame Length) (D: Burner Diameter)

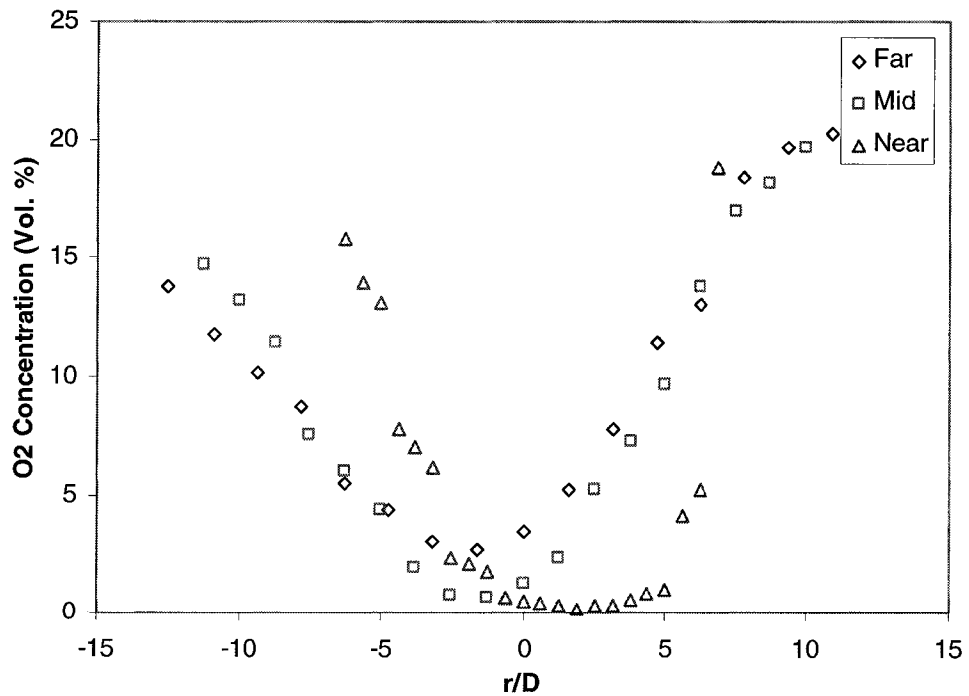


Figure 3.47b Radial O₂ Concentration Profiles on X Axis at Three Locations at 60% CFMFR at 3 m/s Cross-Flow. (Far: 75%, Mid: 50%, Near: 25% Flame Length) (D: Burner Diameter)

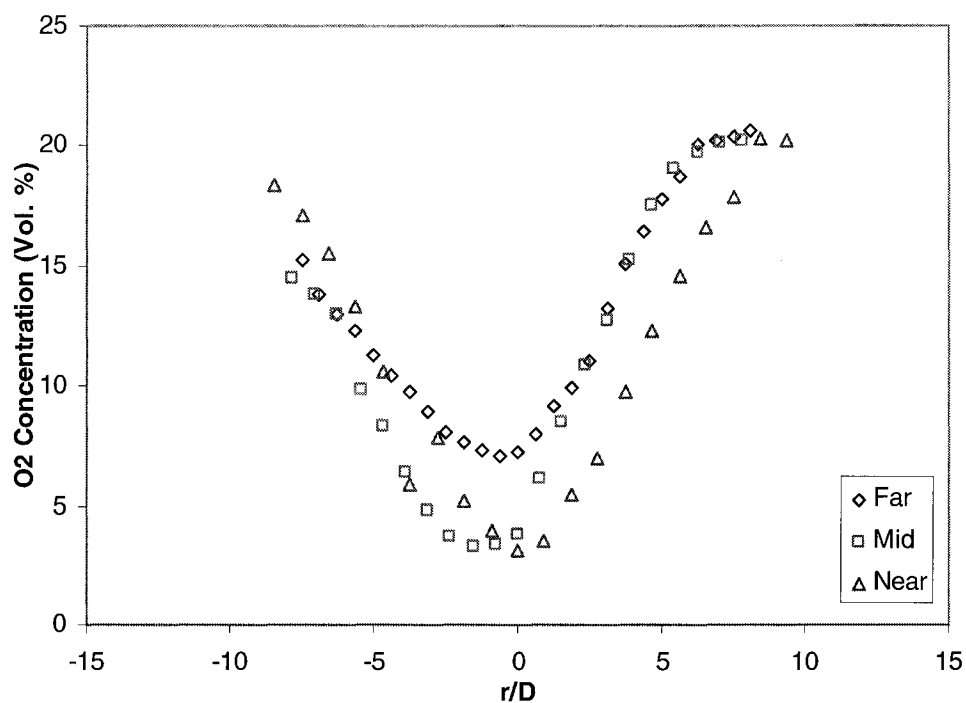


Figure 3.47c Radial O₂ Concentration Profiles on X Axis at Three Locations at 20% CFMFR at 3 m/s Cross-Flow. (Far: 75%, Mid: 50%, Near: 25% Flame Length) (D: Burner Diameter)

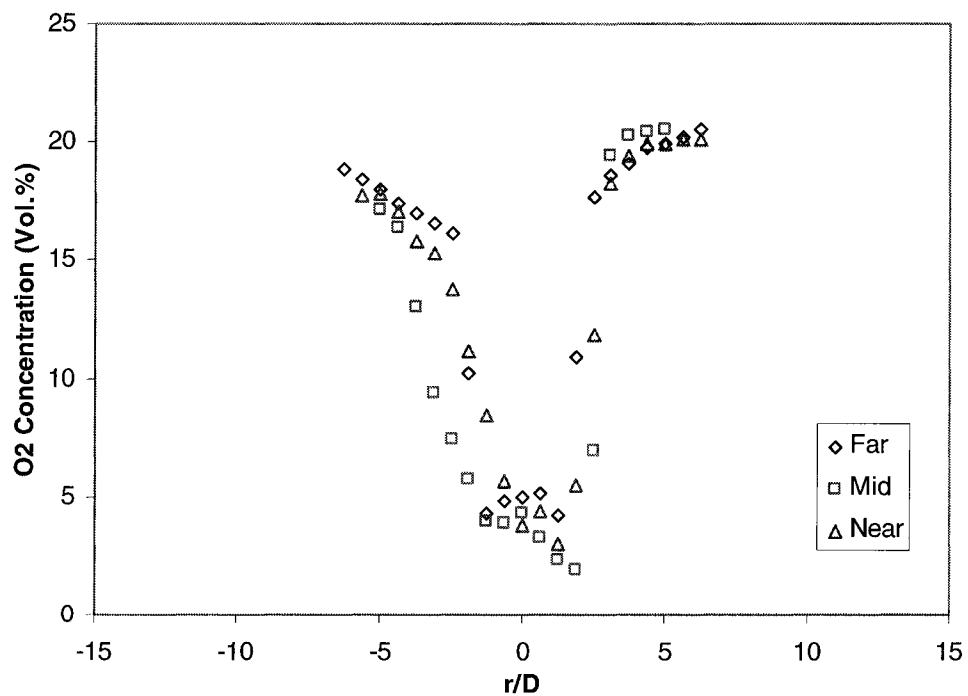


Figure 3.47d Radial O₂ Concentration Profiles on X Axis at Three Locations at 10% CFMFR at 3 m/s Cross-Flow. (Far: 75%, Mid: 50%, Near: 25% Flame Length) (D: Burner Diameter)

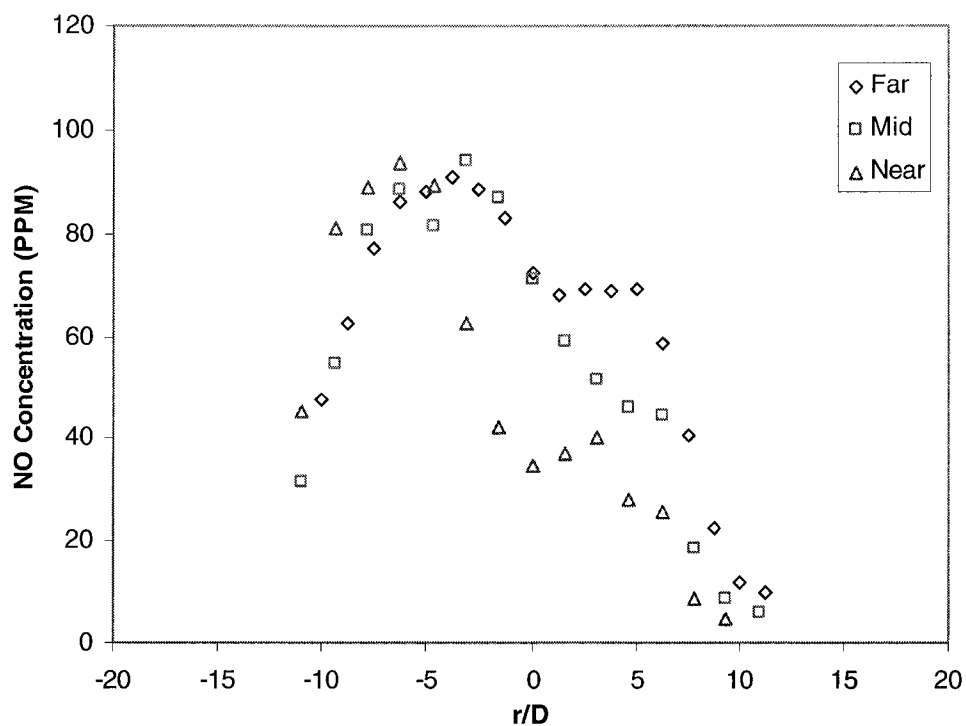


Figure 3.48a Radial NO Concentration Profiles on X Axis at Three Locations at 100% CFMFR at 4 m/s Cross-Flow. (Far: 75%, Mid: 50%, Near: 25% Flame

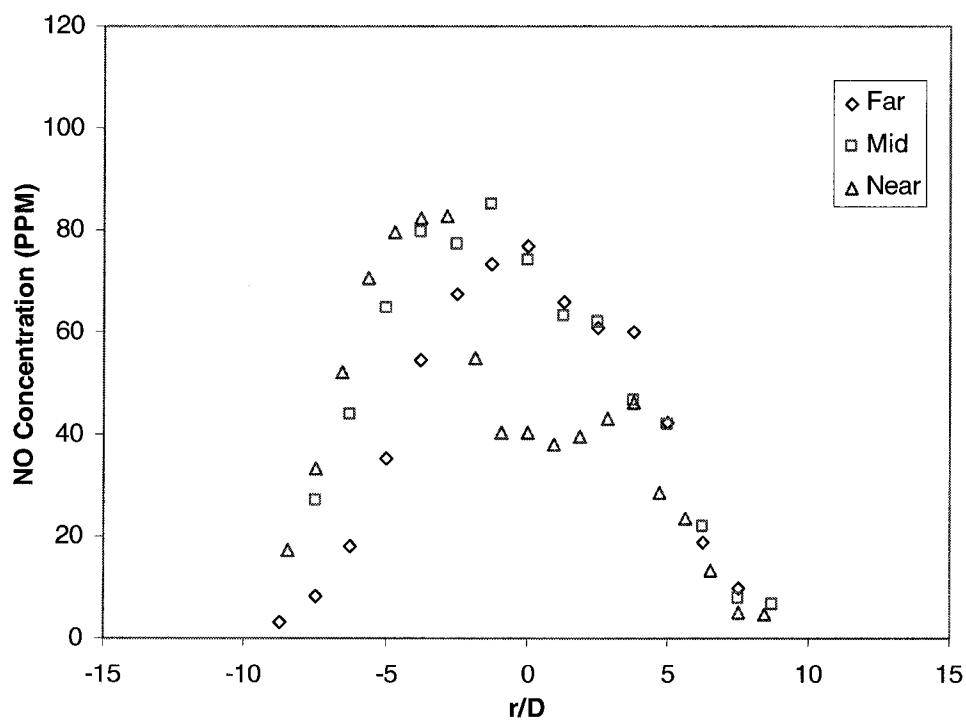


Figure 3.48b Radial NO Concentration Profiles on X Axis at Three Locations at 60% CFMFR at 4 m/s Cross-Flow. (Far: 75%, Mid: 50%, Near: 25% Flame Length) (D: Burner Diameter)

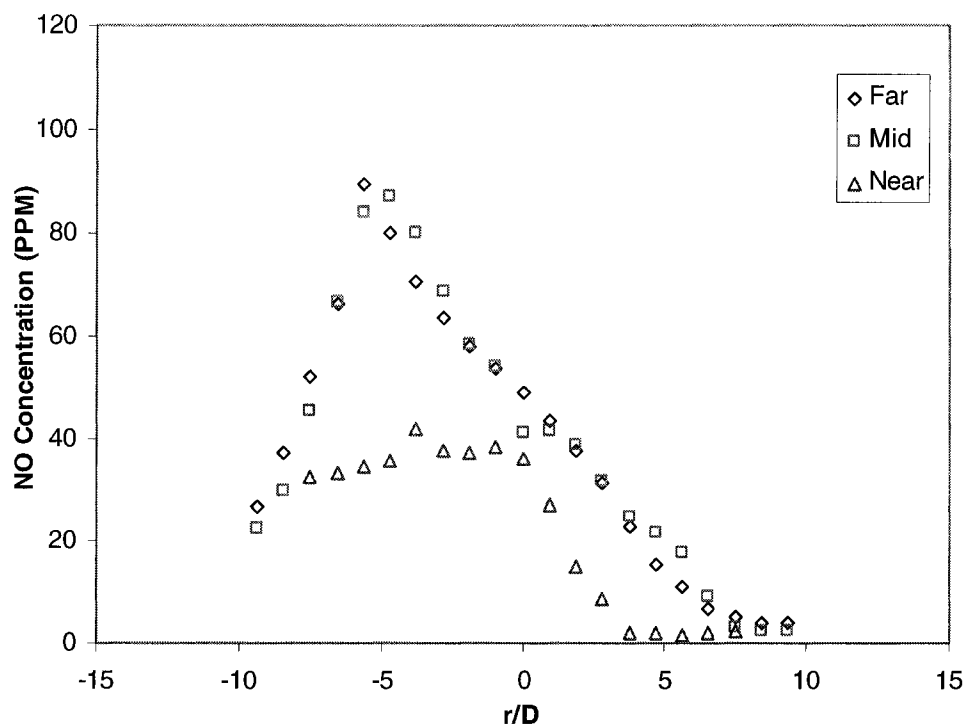


Figure 3.48c Radial NO Concentration Profiles on X Axis at Three Locations at 30% CFMFR at 4 m/s Cross-Flow. (Far: 75%, Mid: 50%, Near: 25% Flame Length) (D: Burner Diameter)

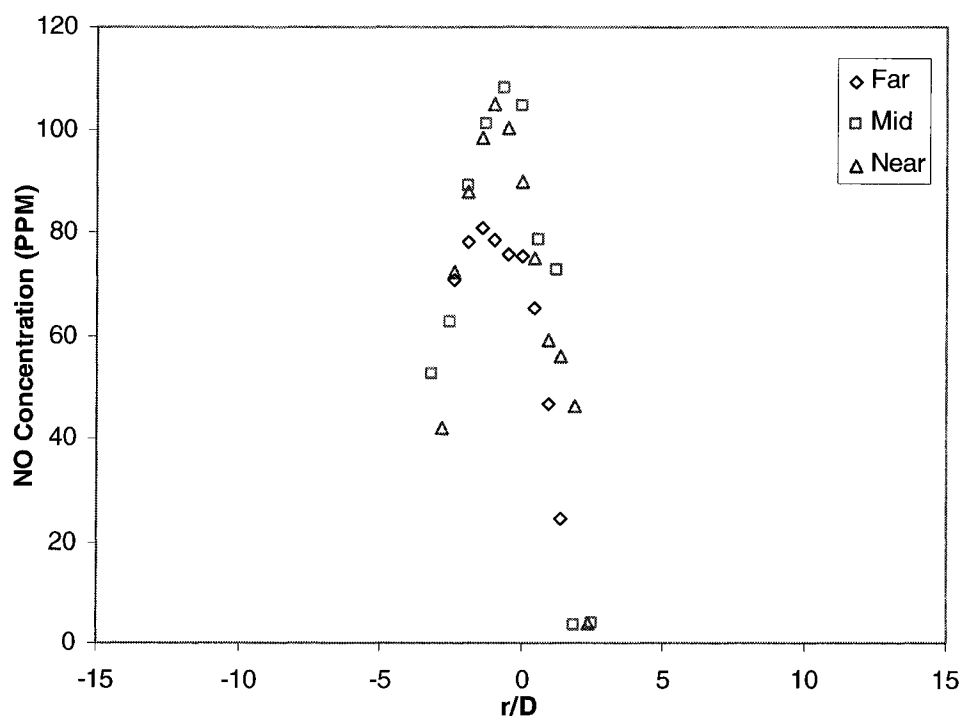


Figure 3.48d Radial NO Concentration Profiles on X Axis at Three Locations at 10% CFMFR at 4 m/s Cross-Flow. (Far: 75%, Mid: 50%, Near: 25% Flame Length) (D: Burner Diameter)

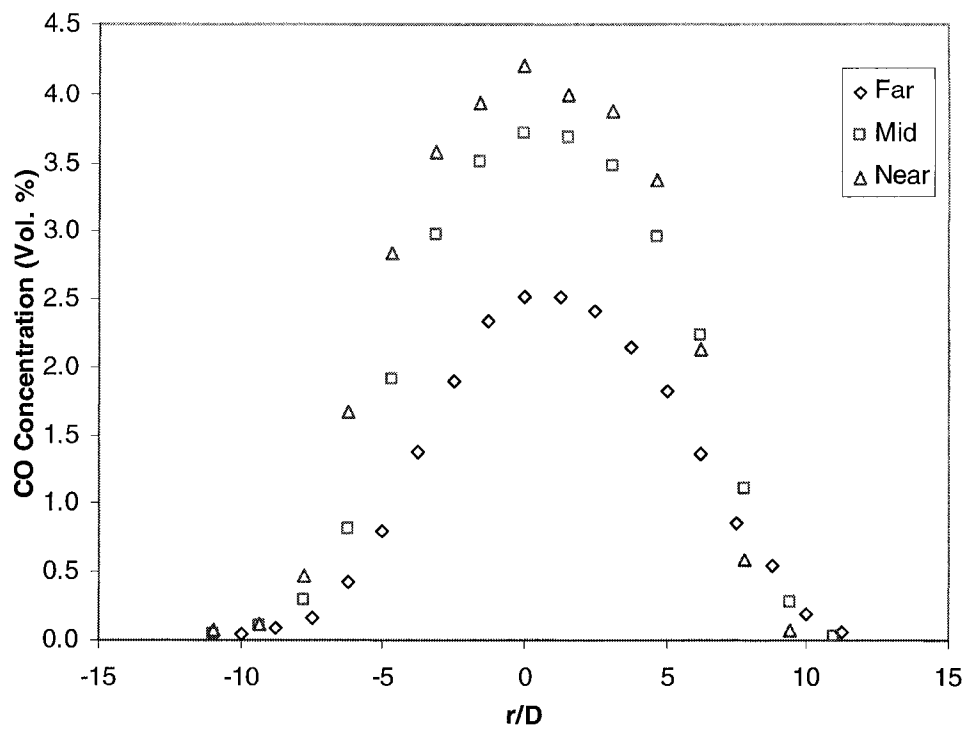


Figure 3.49a Radial CO Concentration Profiles on X Axis at Three Locations at 100% CFMFR at 4 m/s Cross-Flow. (Far: 75%, Mid: 50%, Near: 25% Flame Length) (D: Burner Diameter)

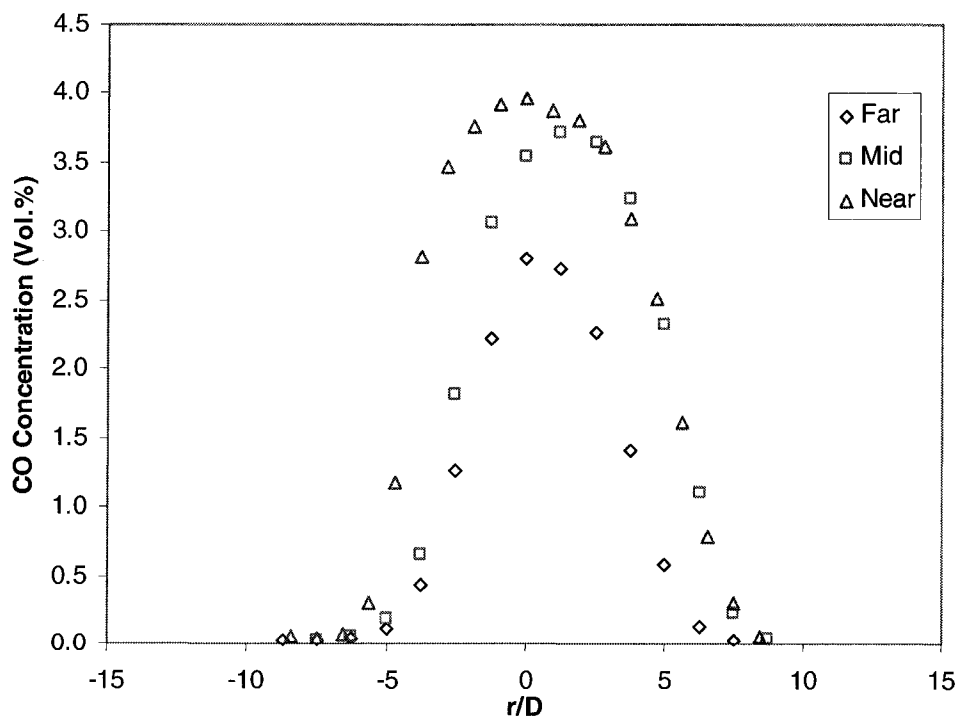


Figure 3.49b Radial CO Concentration Profiles on X Axis at Three Locations at 60% CFMFR at 4 m/s Cross-Flow. (Far: 75%, Mid: 50%, Near: 25% Flame Length) (D: Burner Diameter)

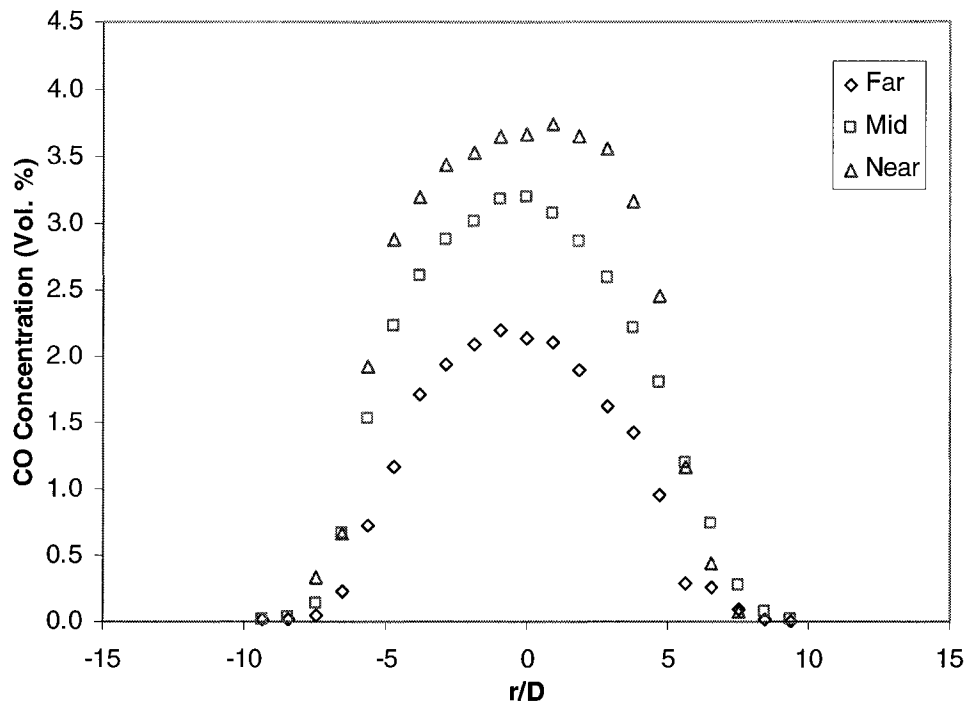


Figure 3.49c Radial CO Concentration Profiles on X Axis at Three Locations at 30% CFMFR at 4 m/s Cross-Flow. (Far: 75%, Mid: 50%, Near: 25% Flame Length) (D: Burner Diameter)

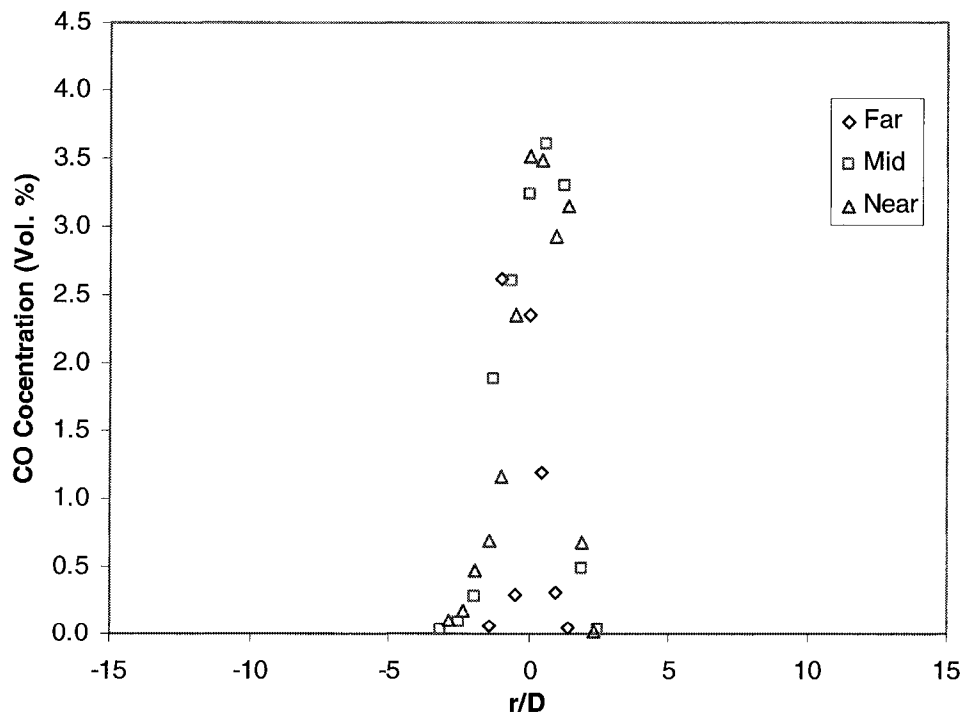


Figure 3.49d Radial CO Concentration Profiles on X Axis at Three Locations at 10% CFMFR at 4 m/s Cross-Flow. (Far: 75%, Mid: 50%, Near: 25% Flame Length) (D: Burner Diameter)

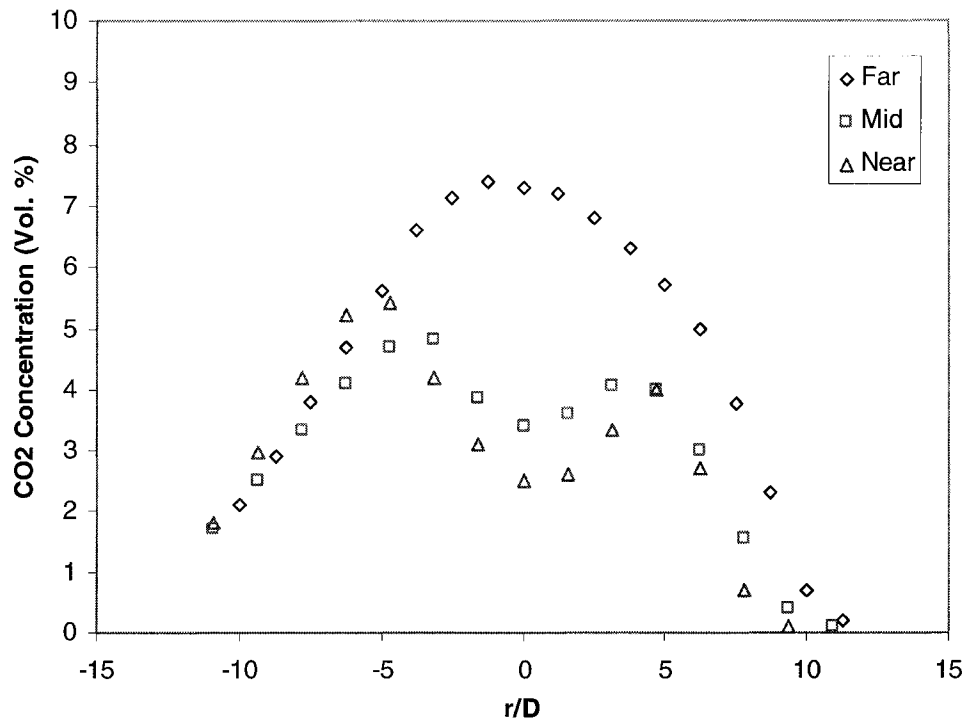


Figure 3.50a Radial CO₂ Concentration Profiles on X Axis at Three Locations at 100% CFMFR at 4 m/s Cross-Flow. (Far: 75%, Mid: 50%, Near: 25% Flame Length) (D: Burner Diameter)

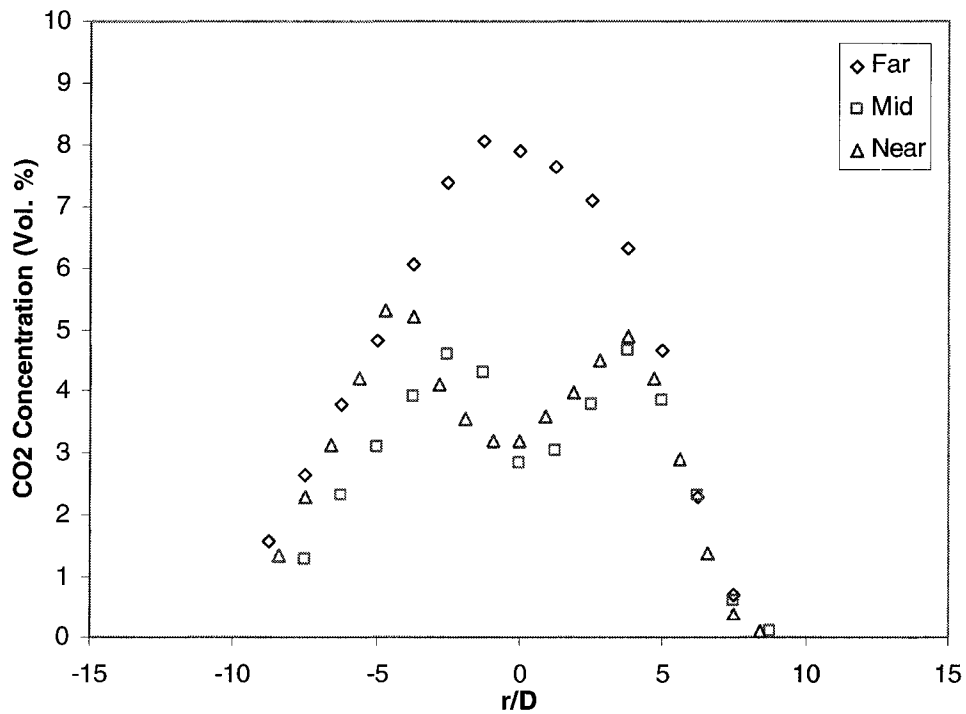


Figure 3.50b Radial CO₂ Concentration Profiles on X Axis at Three Locations at 60% CFMFR at 4 m/s Cross-Flow. (Far: 75%, Mid: 50%, Near: 25% Flame Length) (D: Burner Diameter)

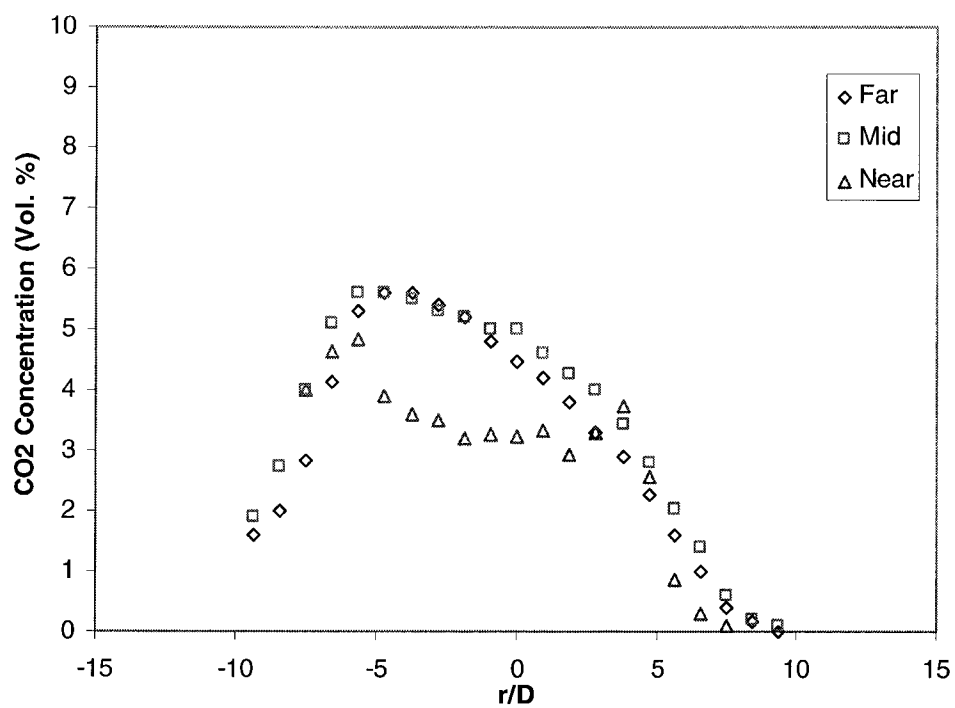


Figure 3.50c Radial CO₂ Concentration Profiles on X Axis at Three Locations at 30% CFMFR at 4 m/s Cross-Flow. (Far: 75%, Mid: 50%, Near: 25% Flame Length) (D: Burner Diameter)

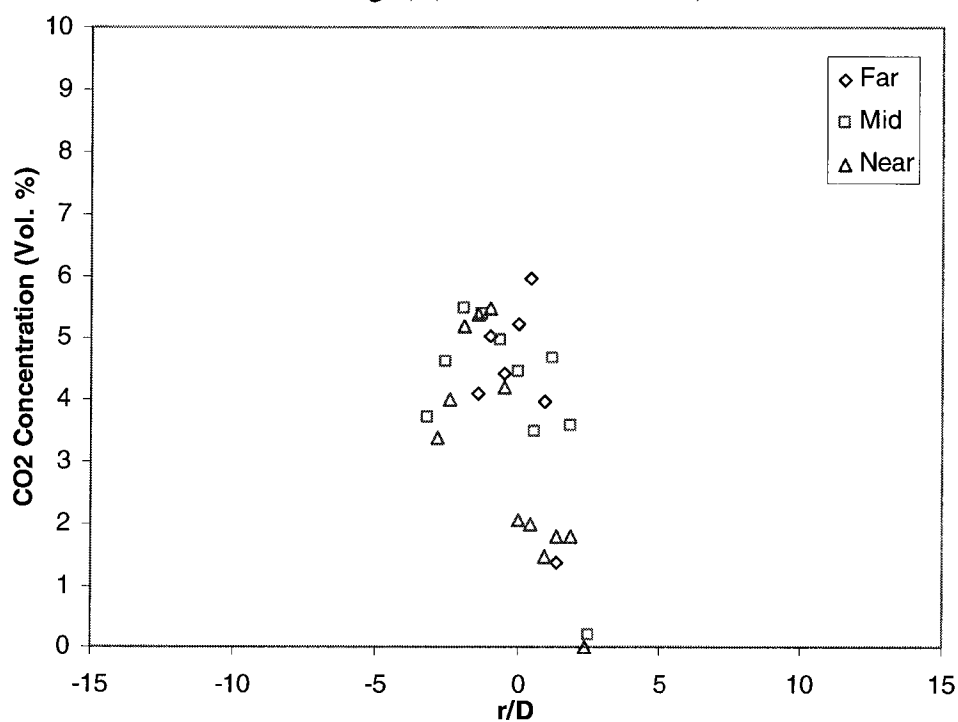


Figure 3.50d Radial CO₂ Concentration Profiles on X Axis at Three Locations at 10% CFMFR at 4 m/s Cross-Flow. (Far: 75%, Mid: 50%, Near: 25% Flame Length) (D: Burner Diameter)

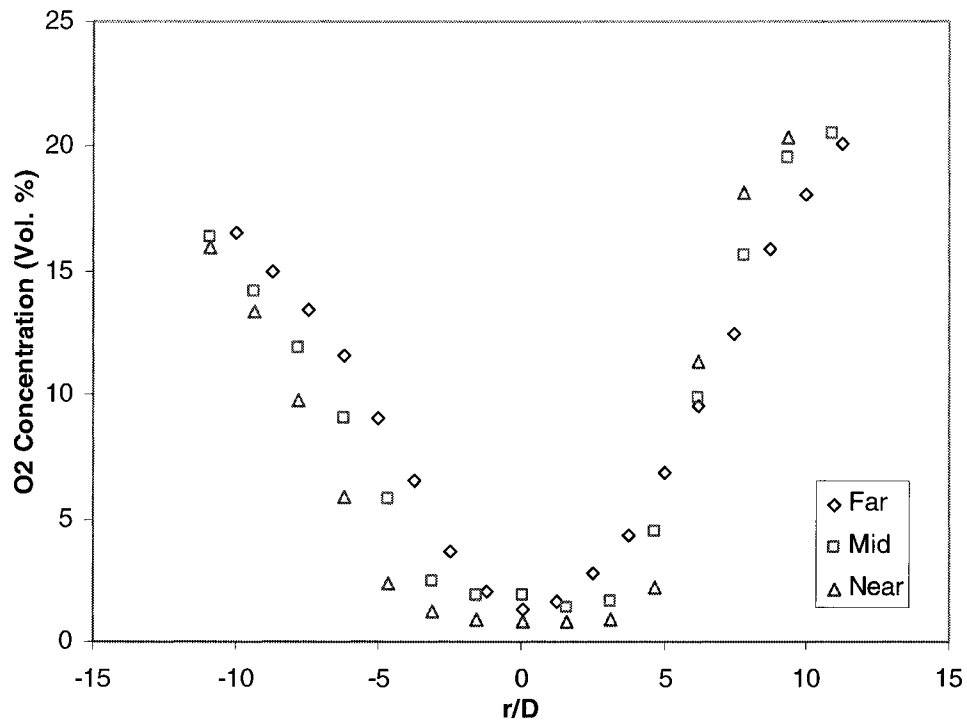


Figure 3.51a Radial O₂ Concentration Profiles on X Axis at Three Locations at CFMFR at 4 m/s Cross-Flow. (Far: 75%, Mid: 50%, Near: 25% Flame Length) (D: Burner Diameter)

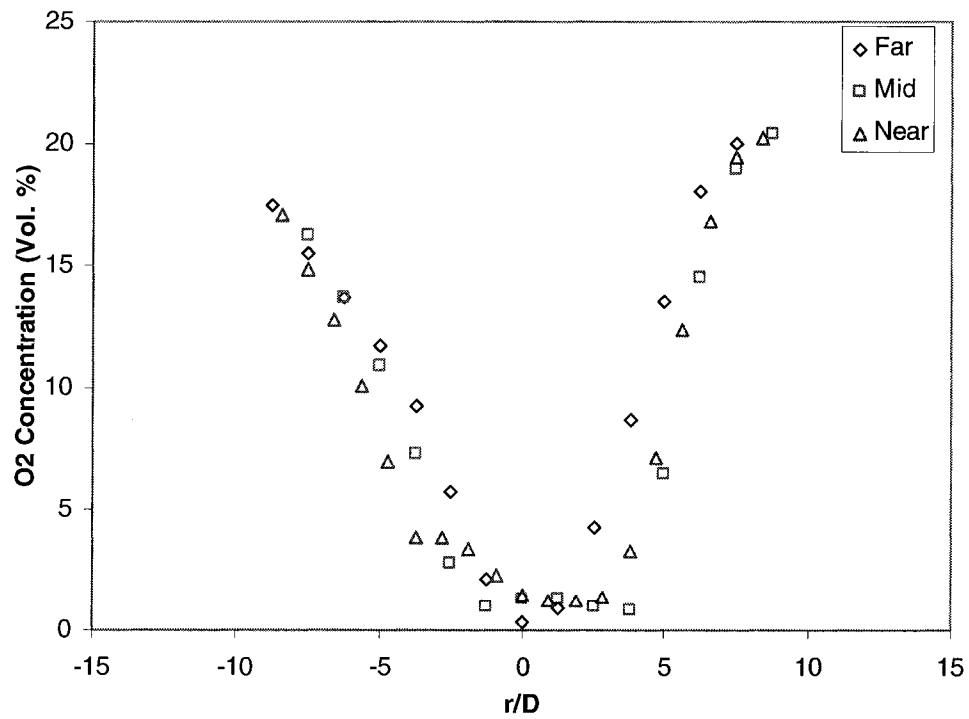


Figure 3.51b Radial O₂ Concentration Profiles on X Axis at Three Locations at 60% CFMFR at 4 m/s Cross-Flow. (Far: 75%, Mid: 50%, Near: 25% Flame Length) (D: Burner Diameter)

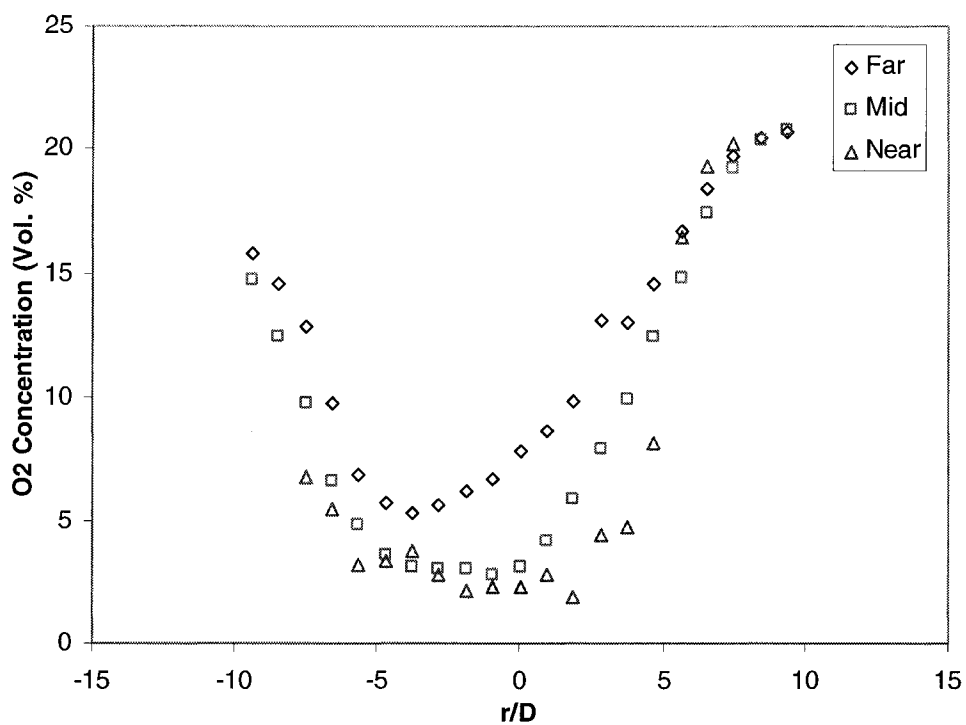


Figure 3.51c Radial O₂ Concentration Profiles on X Axis at Three Locations at 30% CFMFR at 4 m/s Cross-Flow. (Far: 75%, Mid: 50%, Near: 25% Flame Length) (D: Burner Diameter)

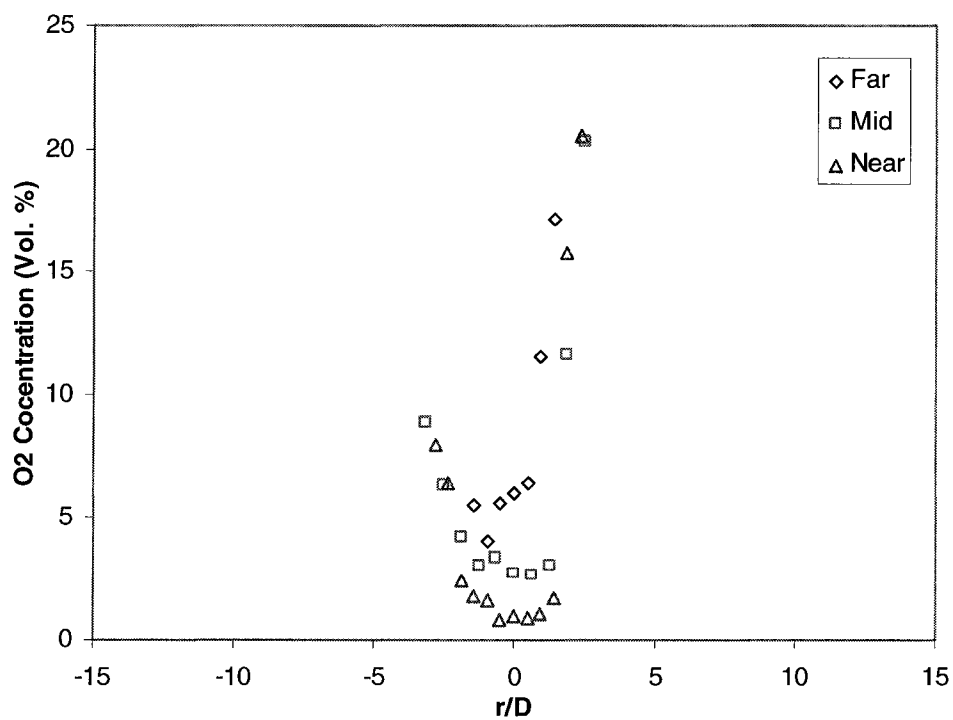


Figure 3.51d Radial O₂ Concentration Profiles on X Axis at Three Locations at 10% CFMFR at 4 m/s Cross-Flow. (Far: 75%, Mid: 50%, Near: 25% Flame Length) (D: Burner Diameter)

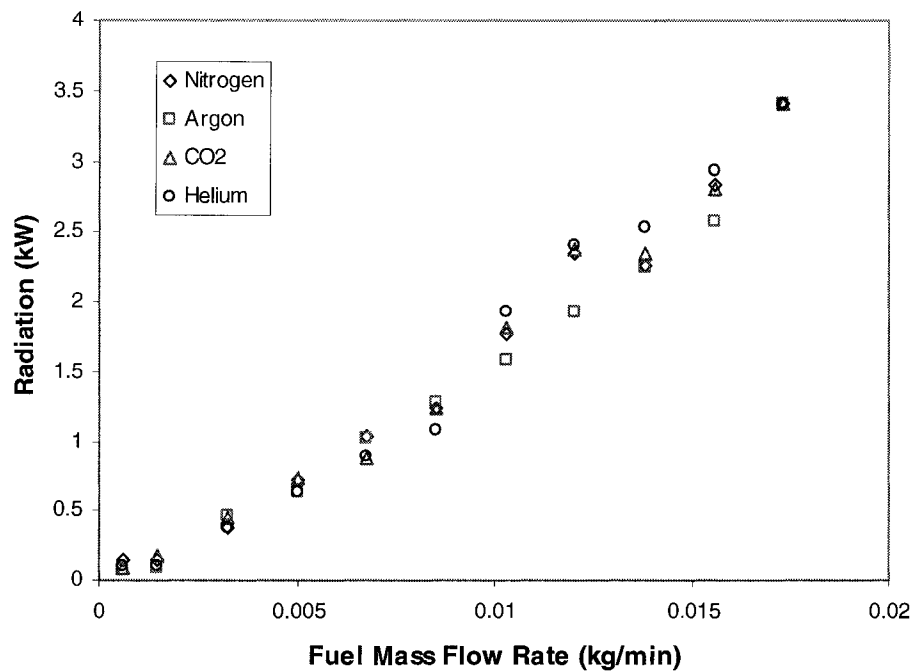


Figure 3.52 Flame Radiation for Different Inert Gases at Smoke Point

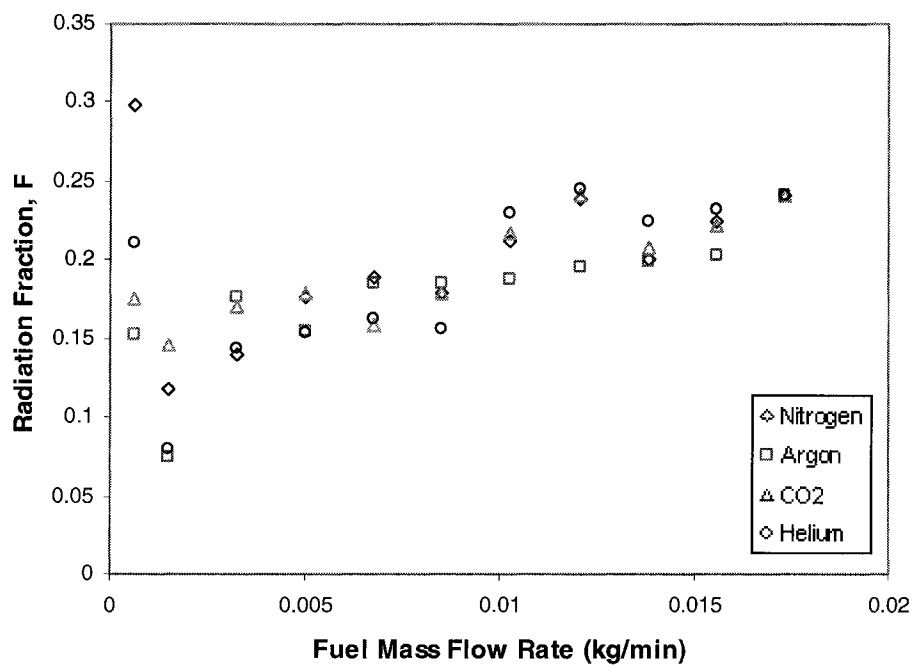


Figure 3.53 Flame Radiation Fraction for Different Inert Gases at Smoke Point

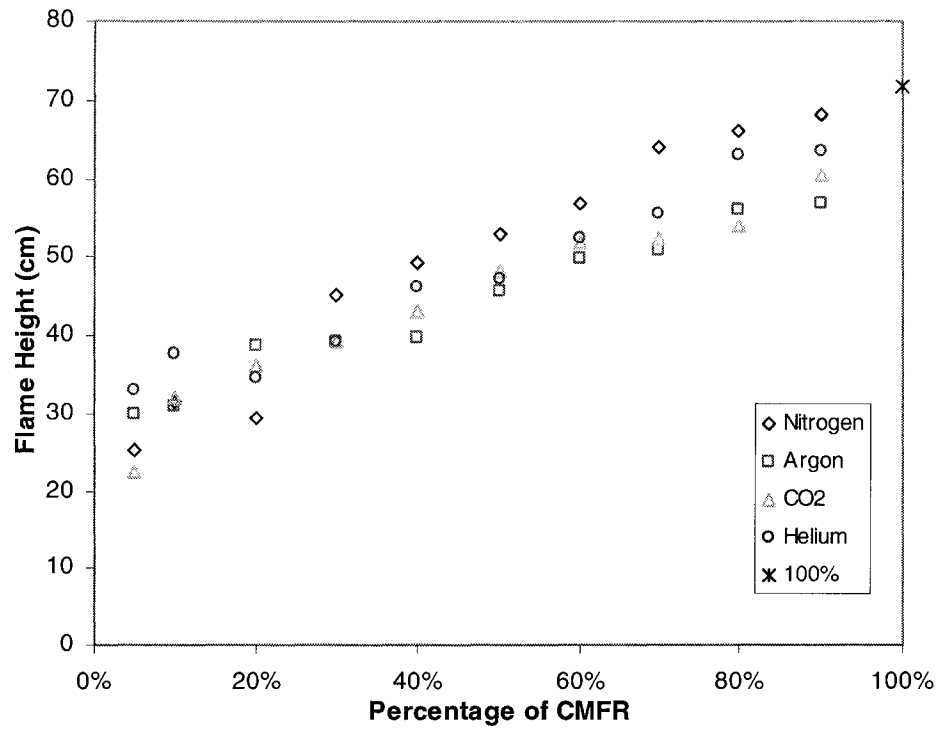


Figure 3.54a Flame Height for Different Inert Gases at Smoke Point

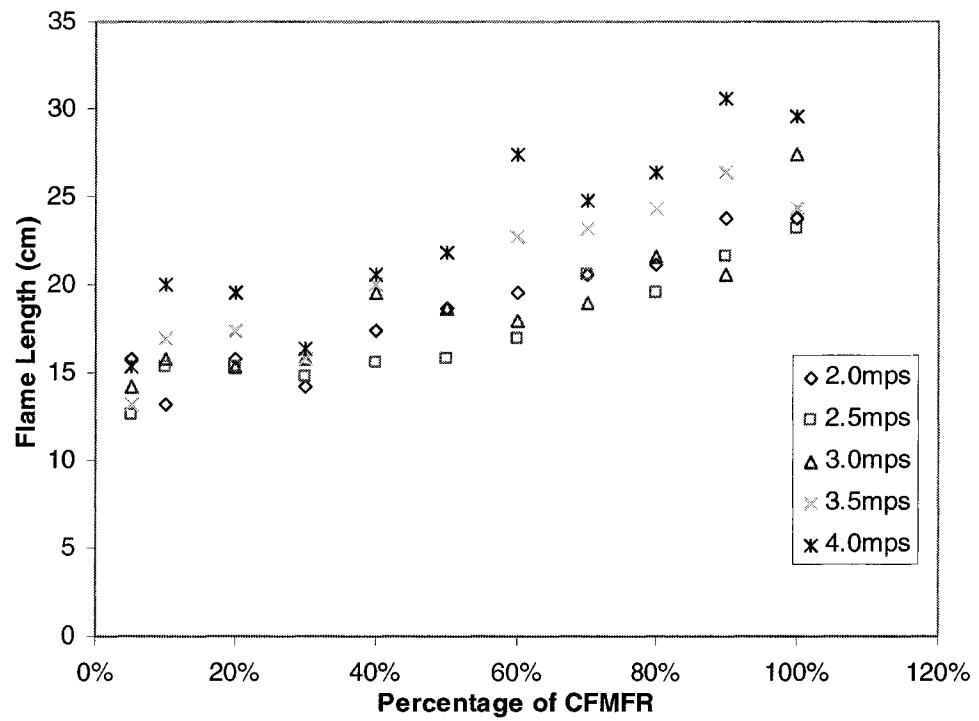


Figure 3.54b Flame Length for Different Cross-Flow Speed at Smoke Point

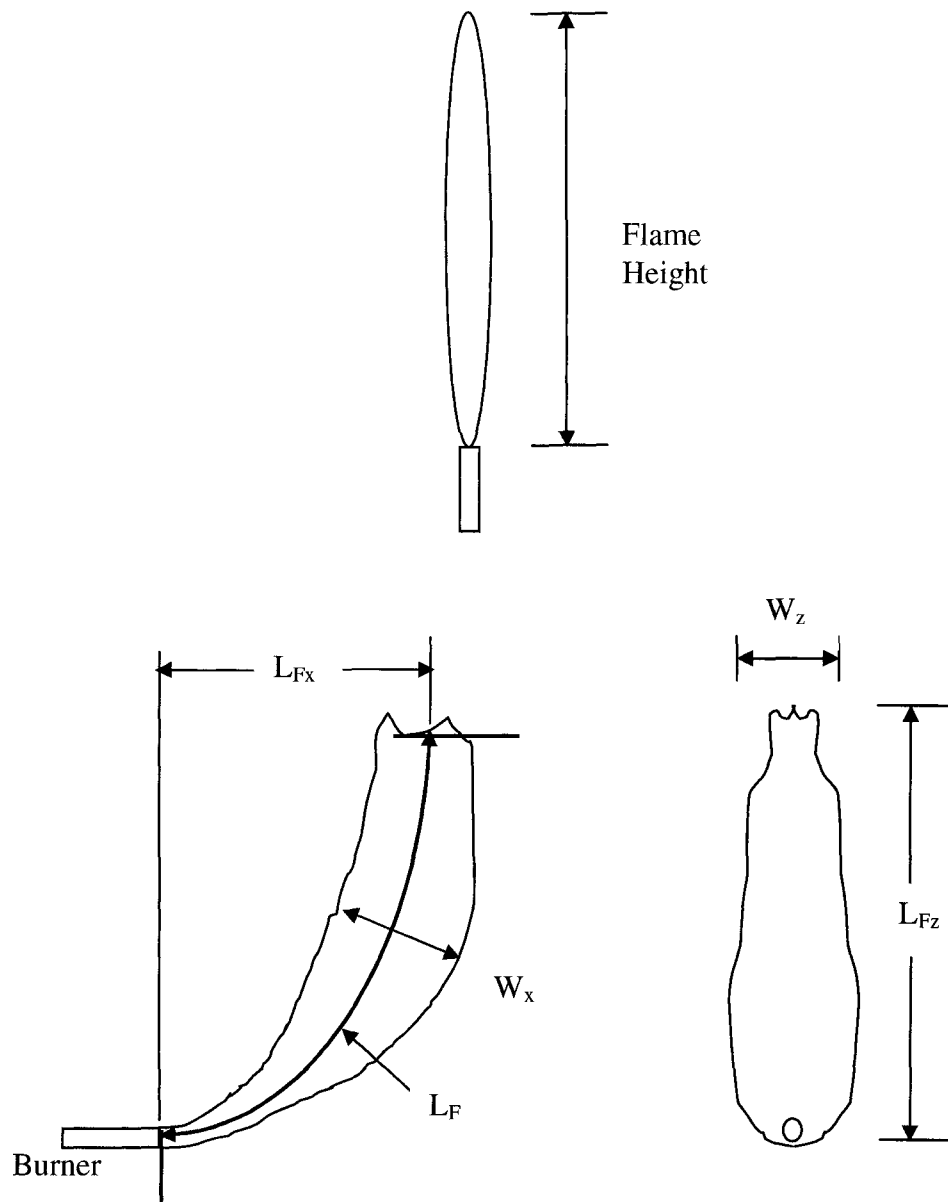


Figure 3.55 Definitions of Flame Height in Quiescent Environment and Flame Length and Width in Cross-Flow

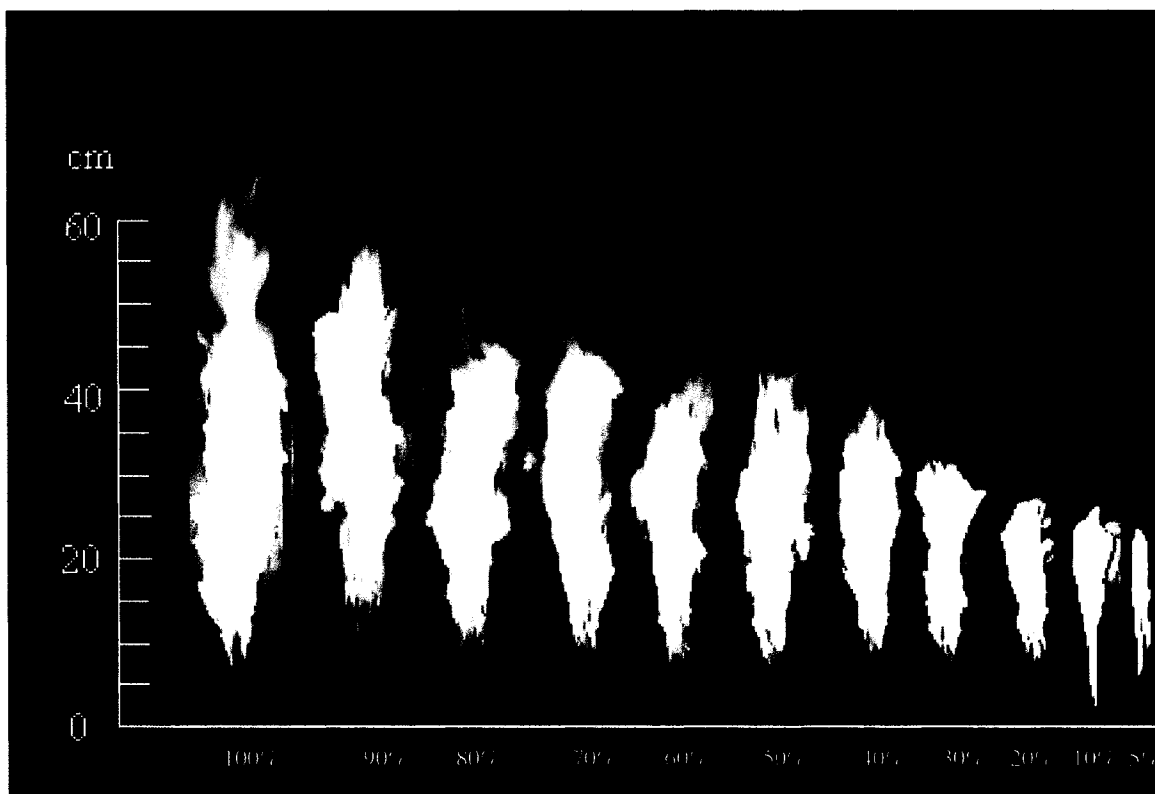


Figure 3.56a 100% CFMFR Flame and Nitrogen Inert Gas Dilution Flames Images

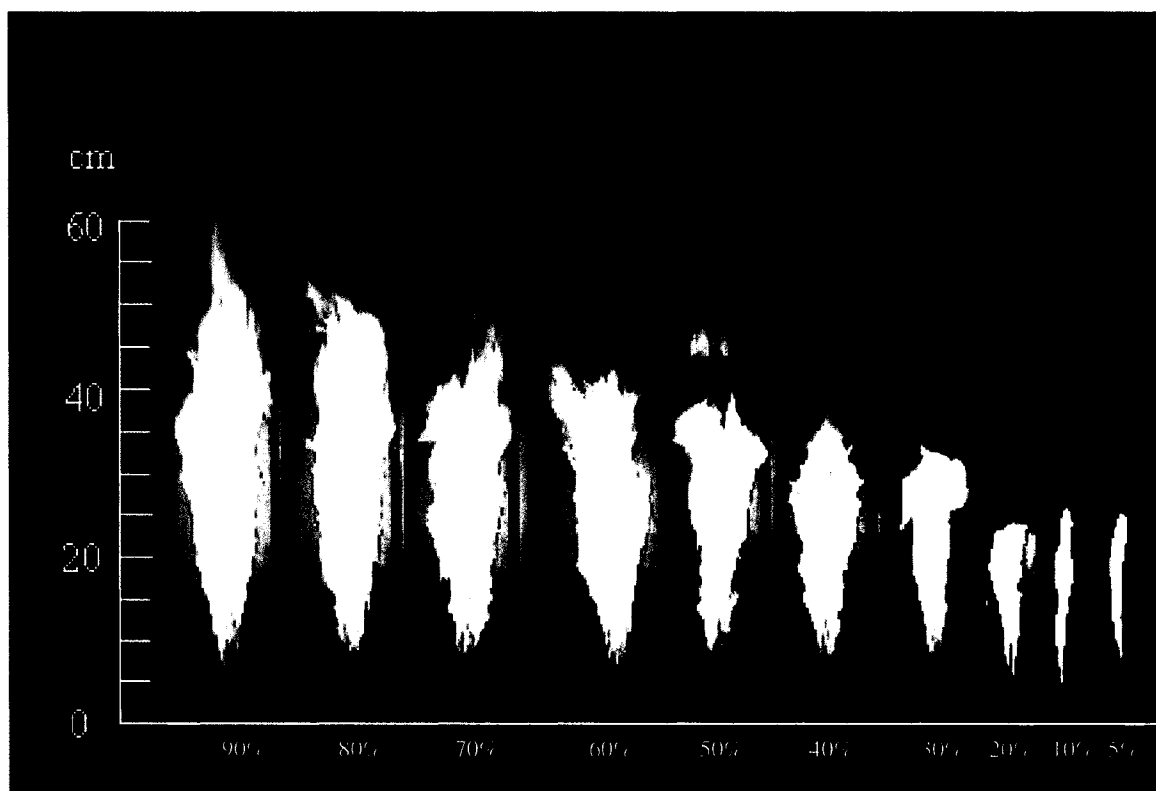


Figure 3.56b Argon Inert Gas Dilution Flames Images

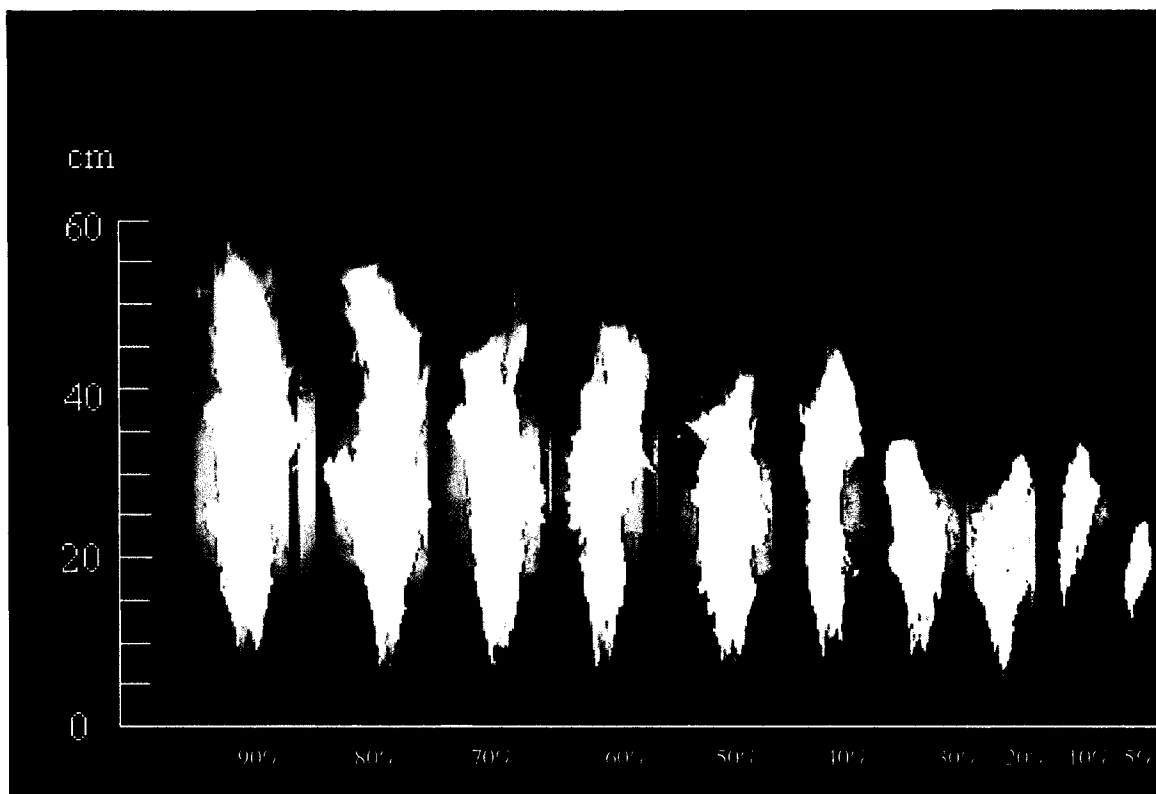


Figure 3.56c Carbon Dioxide Inert Gas Dilution Flames Images

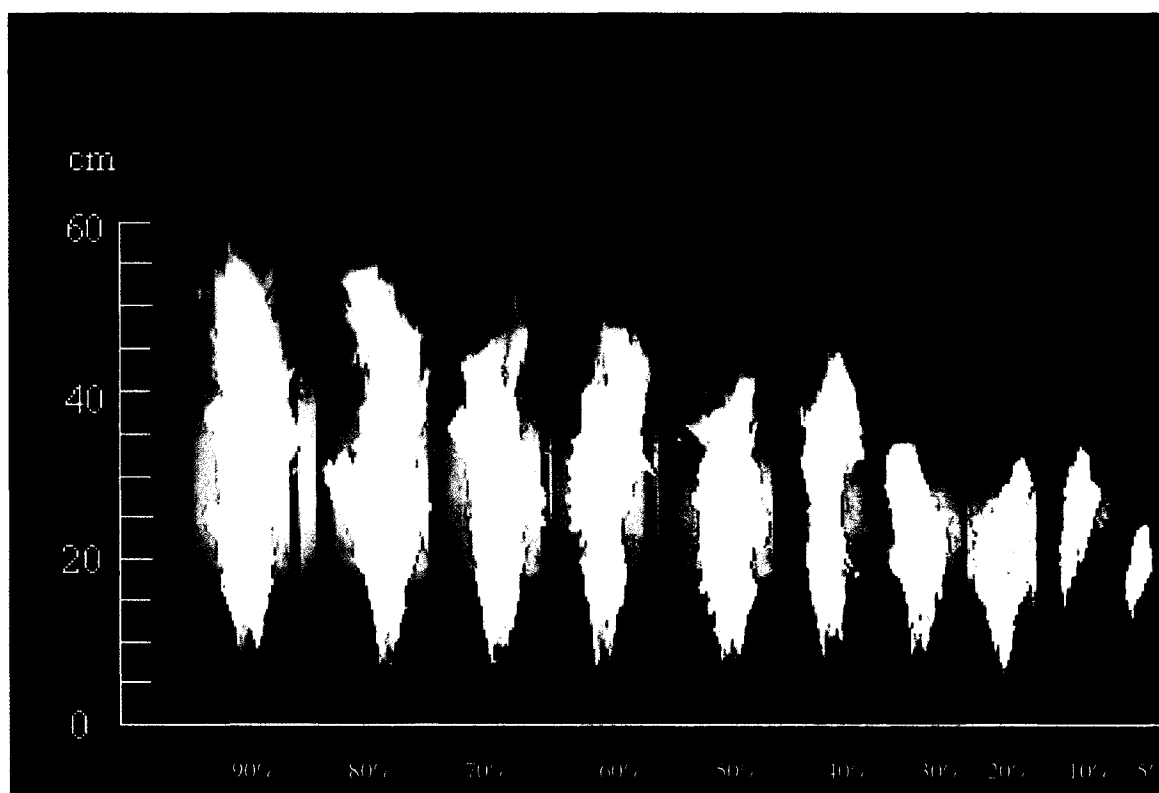
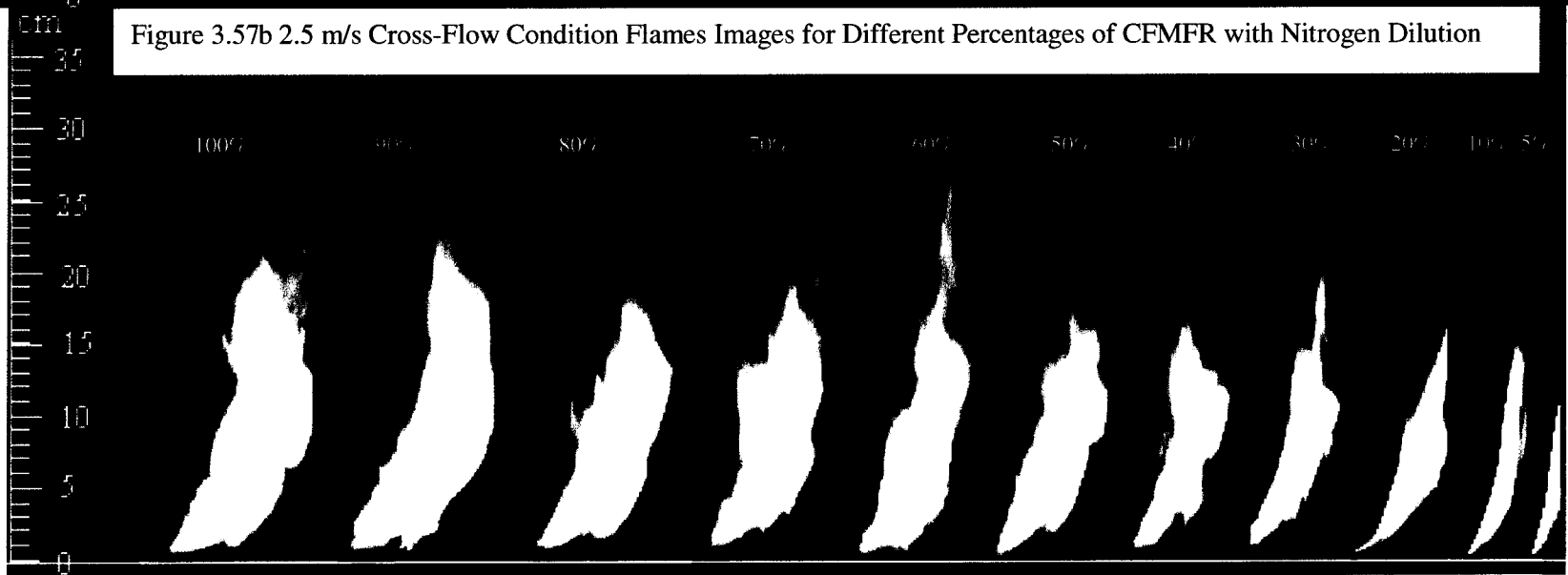
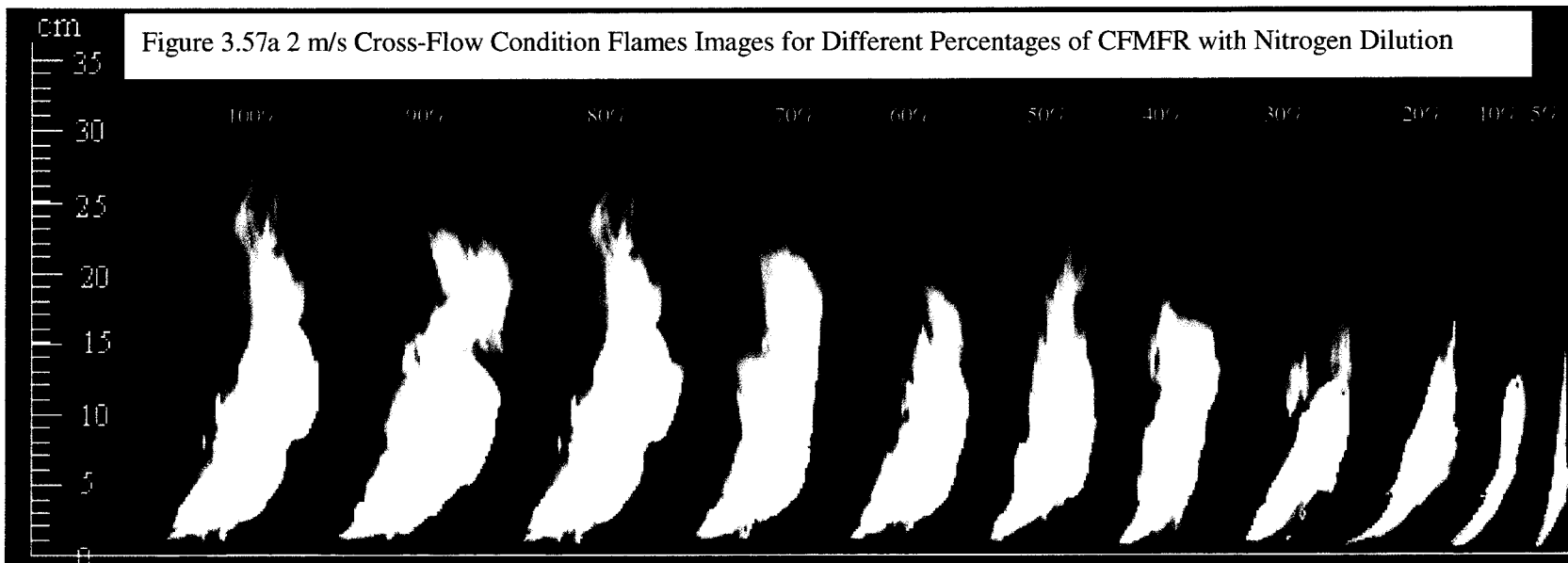
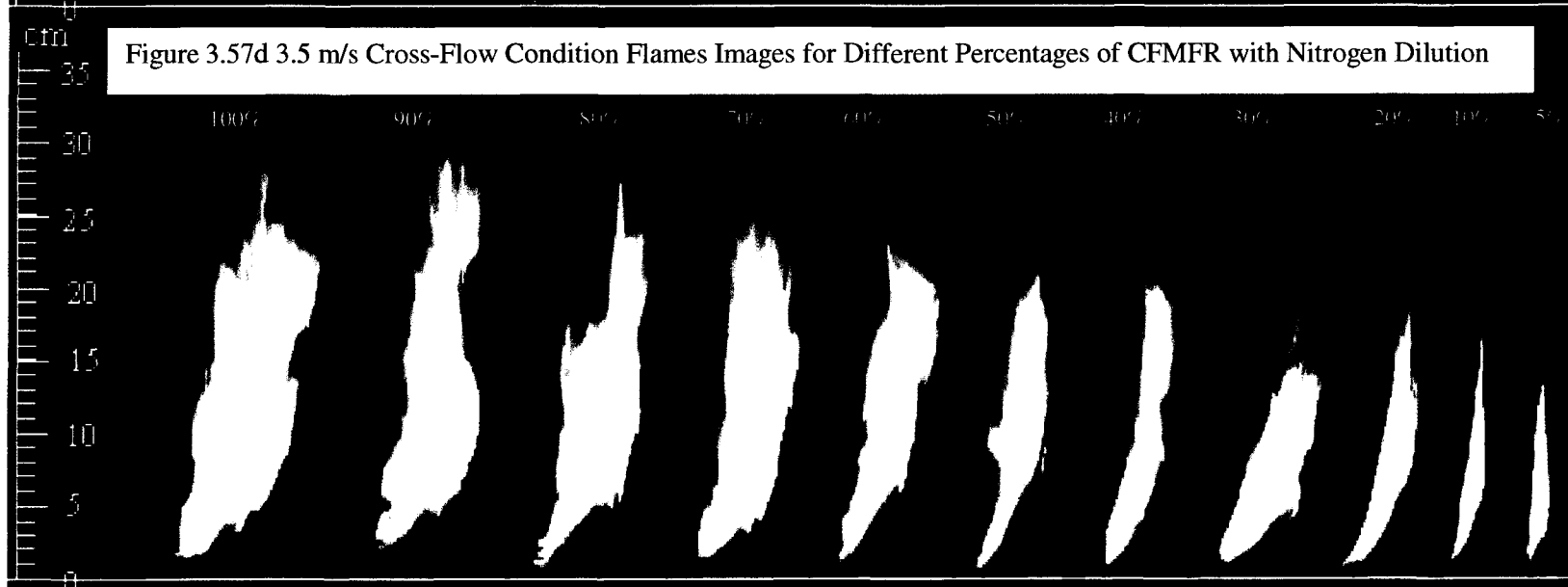
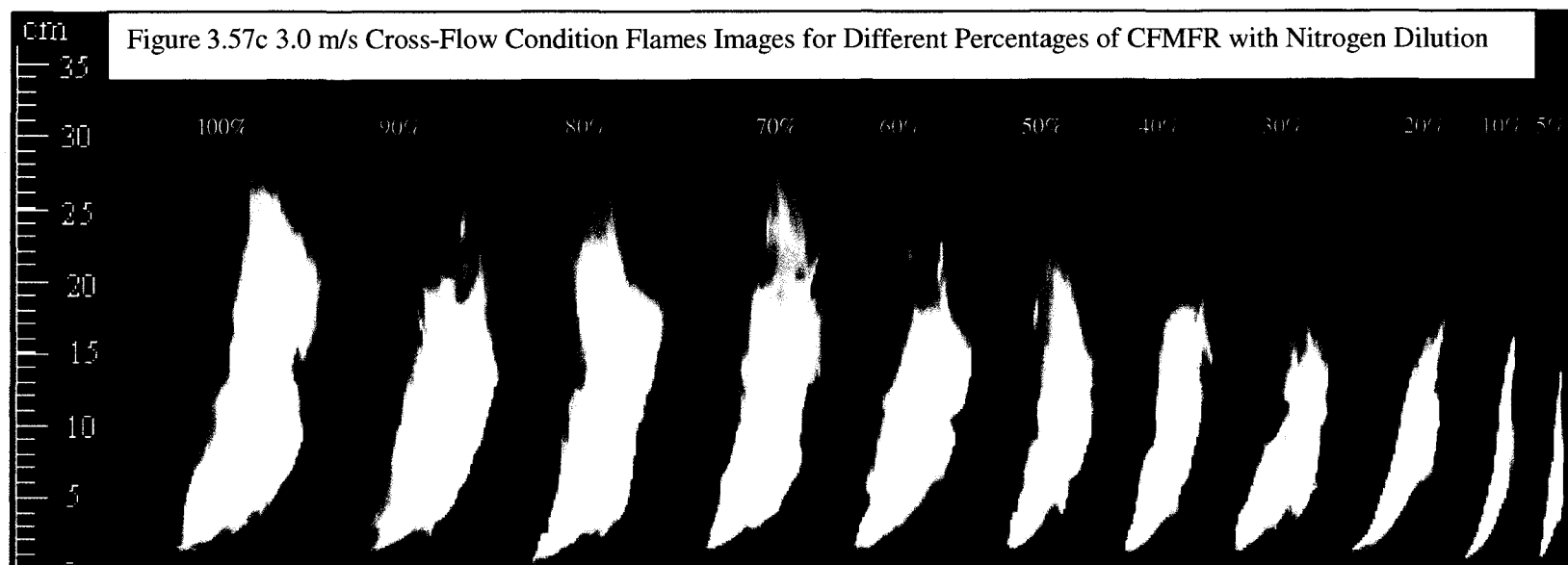


Figure 3.56d Helium Inert Gas Dilution Flames Images





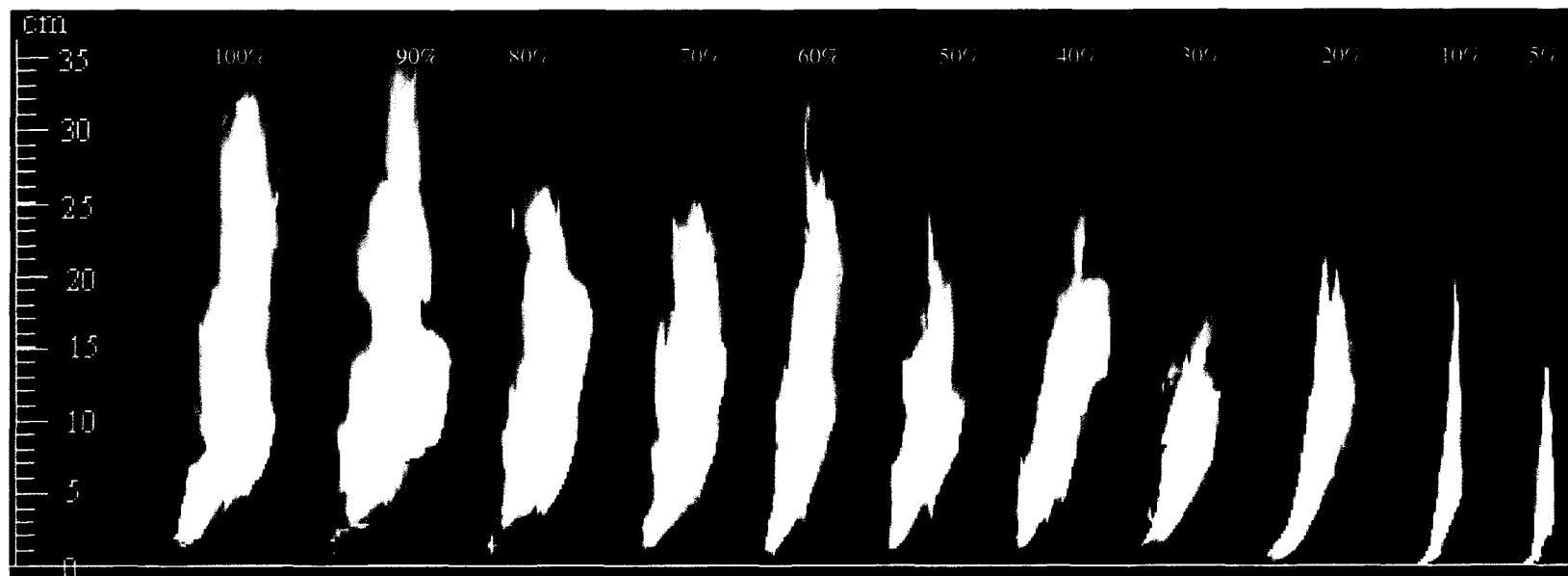


Figure 3.57e 4.0m/s Cross-Flow Condition Flames Images for Different Percentages of CFMFR with Nitrogen Dilution

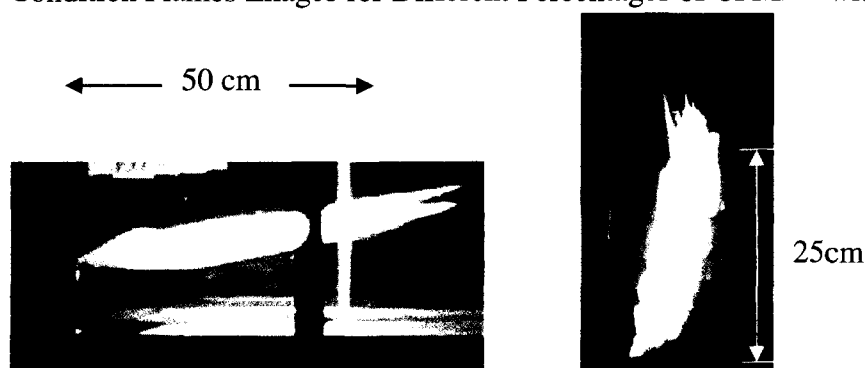


Figure 3.58 Flame Shape Comparison of Horizontal (at CFMFR and 4.02 m/s Cross-Flow) and Vertical (at CFMFR and 4.0 m/s Cross-Flow) Cross-Flow Flame

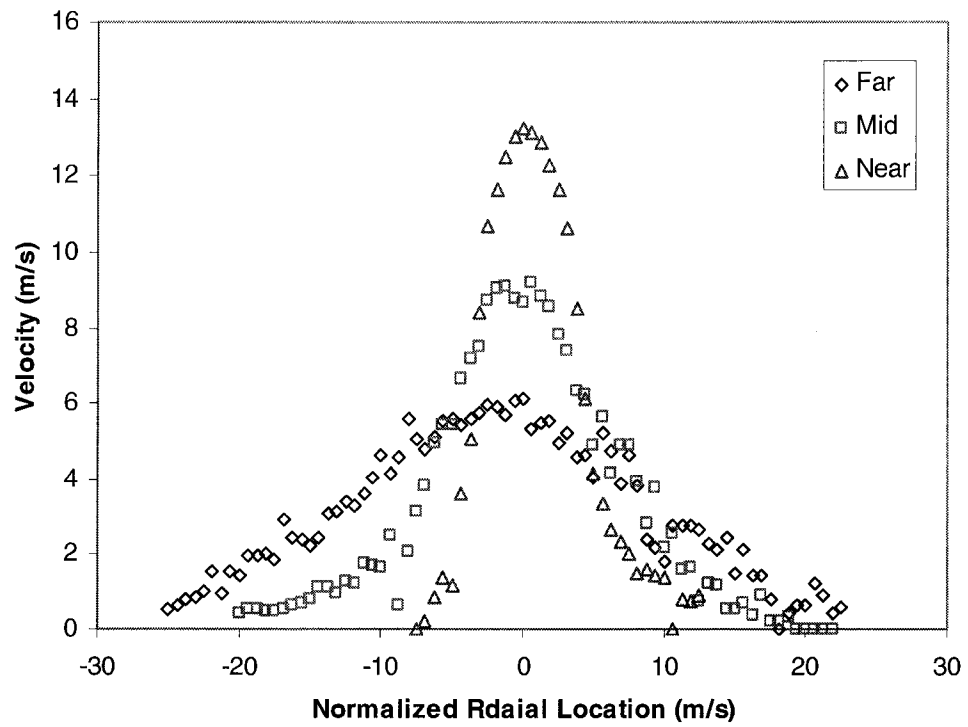


Figure 3.59a Radial Velocity Profiles at 100% CFMFR for Three Flame Heights (Far: 75%, Mid: 50%, Near: 25% Flame Height) (D: Burner Diameter)

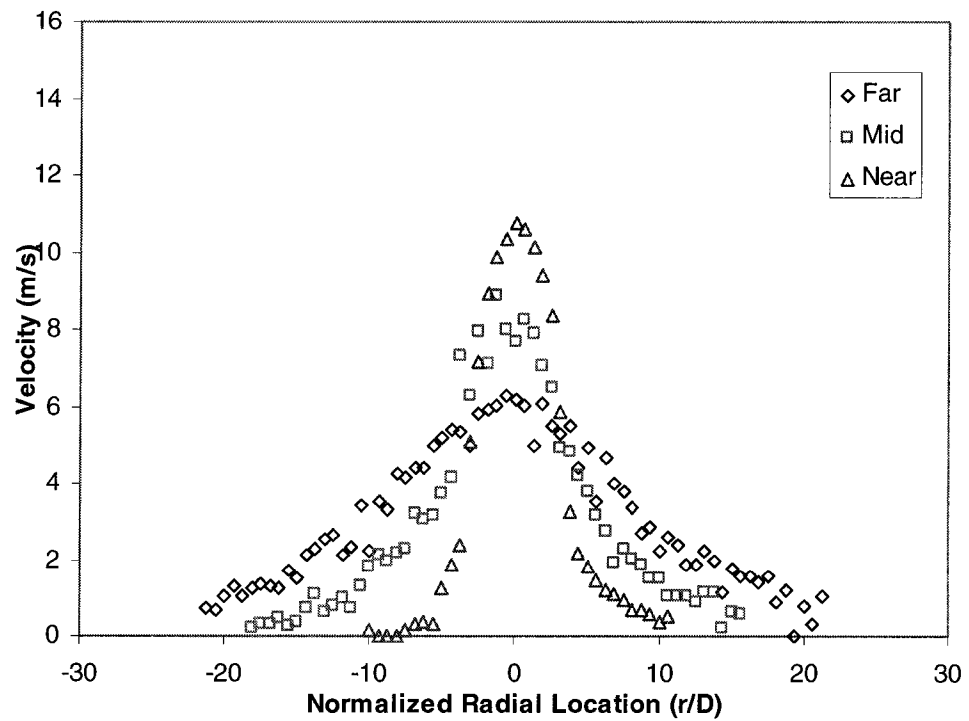


Figure 3.59b Radial Velocity Profiles at 60 % CFMFR for Three Flame Heights (Far: 75%, Mid: 50%, Near: 25% Flame Height) (D: Burner Diameter)

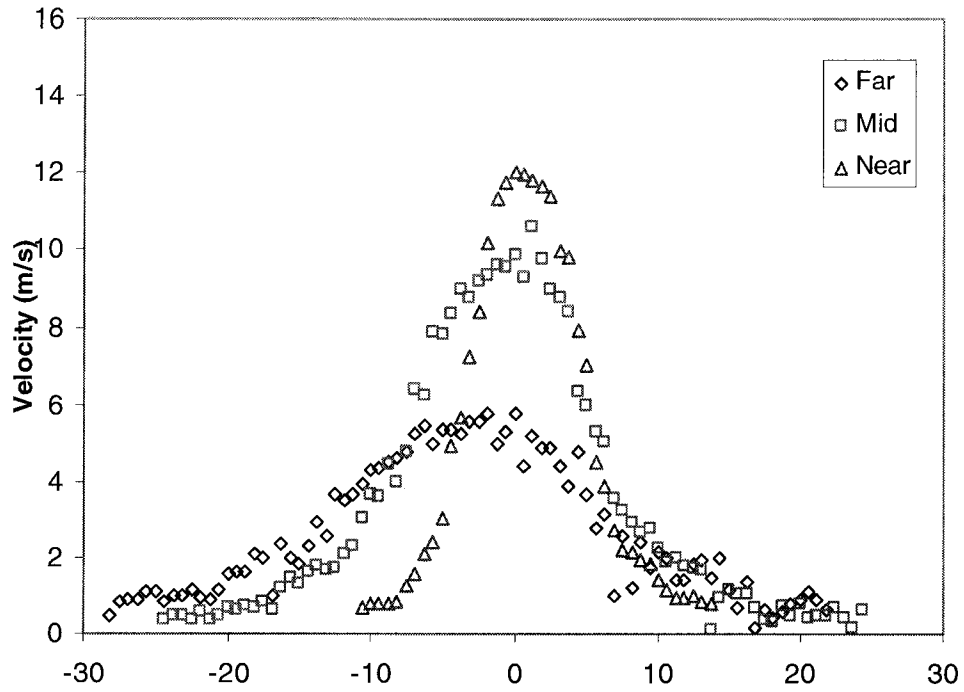


Figure 3.59c Radial Velocity Profiles at 30 % CFMFR for Three Flame Heights (Far: 75%, Mid: 50%, Near: 25% Flame Height) (D: Burner Diameter)

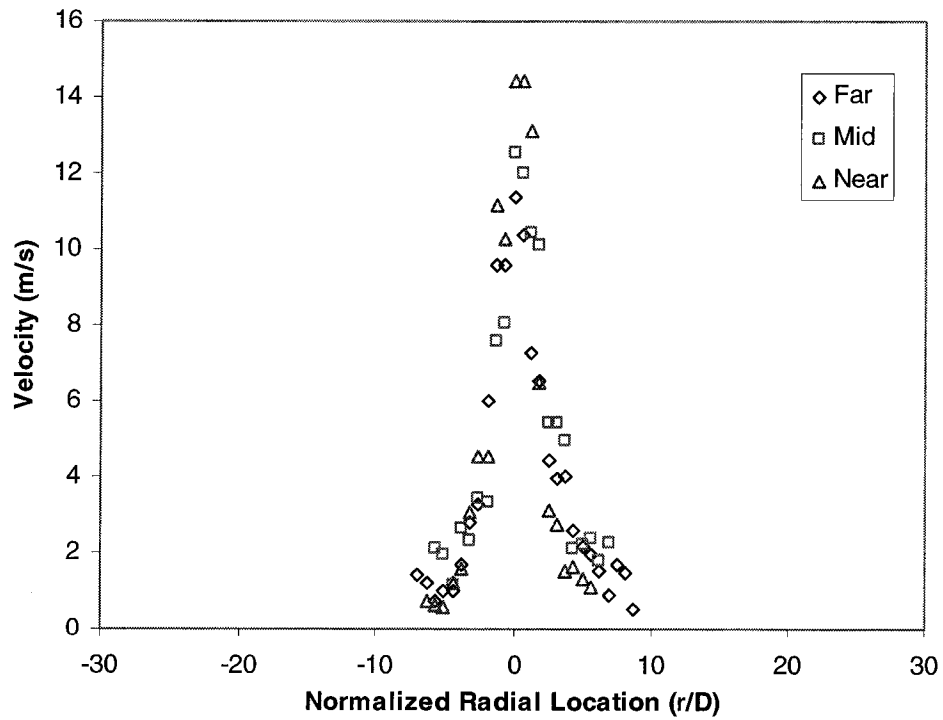


Figure 3.59d Radial Velocity Profiles at 10 % CFMFR for Three Flame Heights (Far: 75%, Mid: 50%, Near: 25% Flame Height) (D: Burner Diameter)

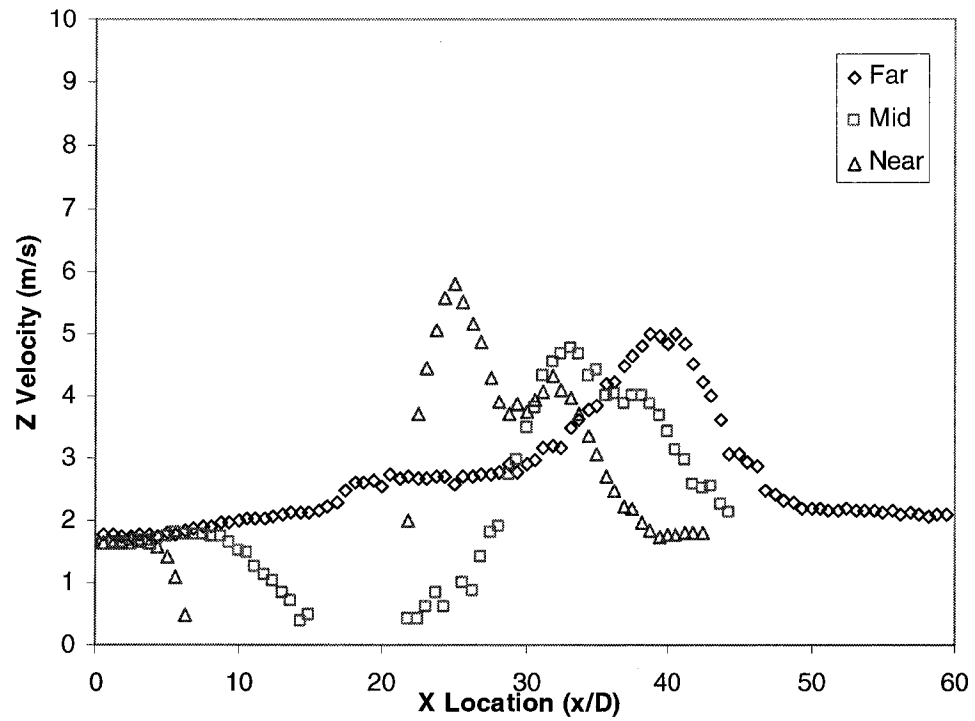


Figure 3.60a Z Velocity Profiles in X direction at 100% CFMFR at 2 m/s Cross-flow at Three Different Locations (Far 75%, Mid 50% and Near 25% of Flame Length)

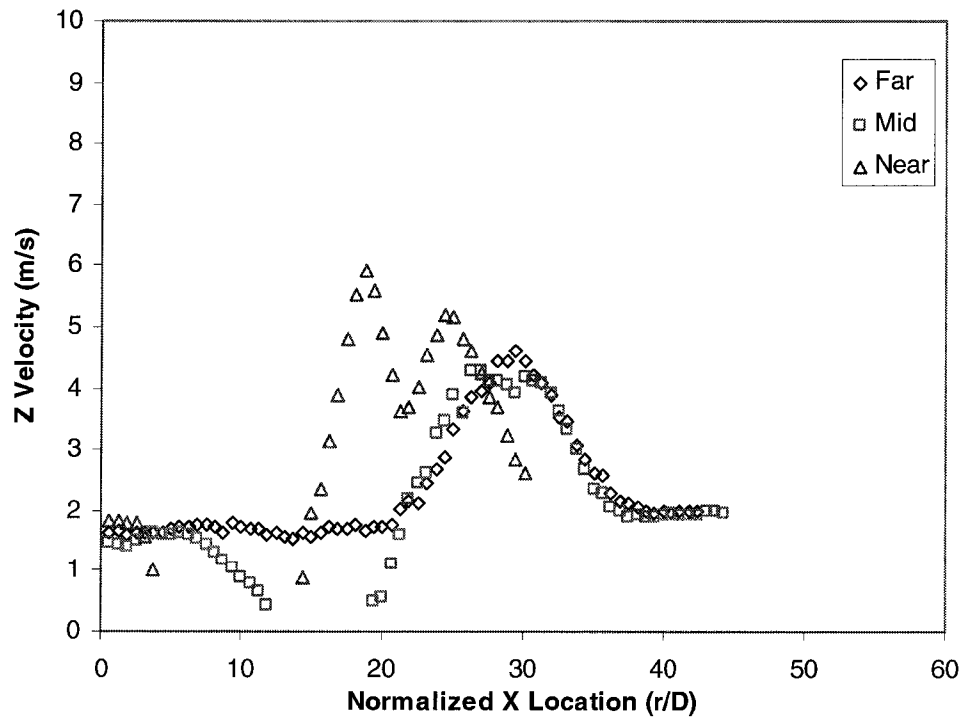


Figure 3.60b Z Velocity Profiles in X direction at 60% CFMFR at 2 m/s Cross-flow at Three Different Locations (Far 75%, Mid 50% and Near 25% of Flame Length)

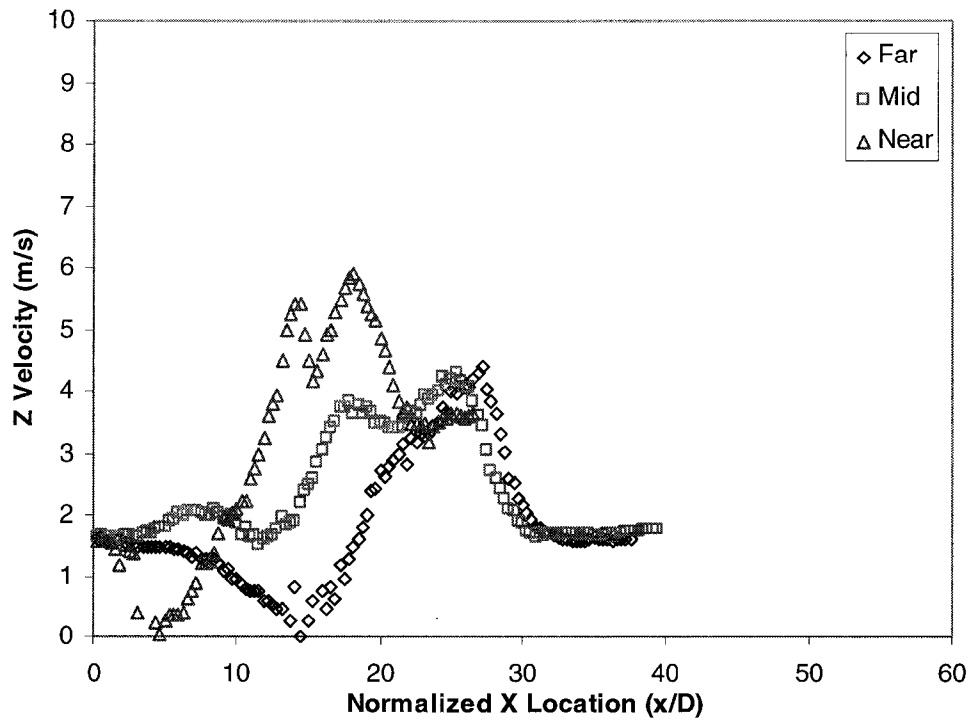


Figure 3.60c Z Velocity Profiles in X direction at 20% CFMFR at 2 m/s Cross-flow at Three Different Locations (Far 75%, Mid 50% and Near 25% of Flame Length)

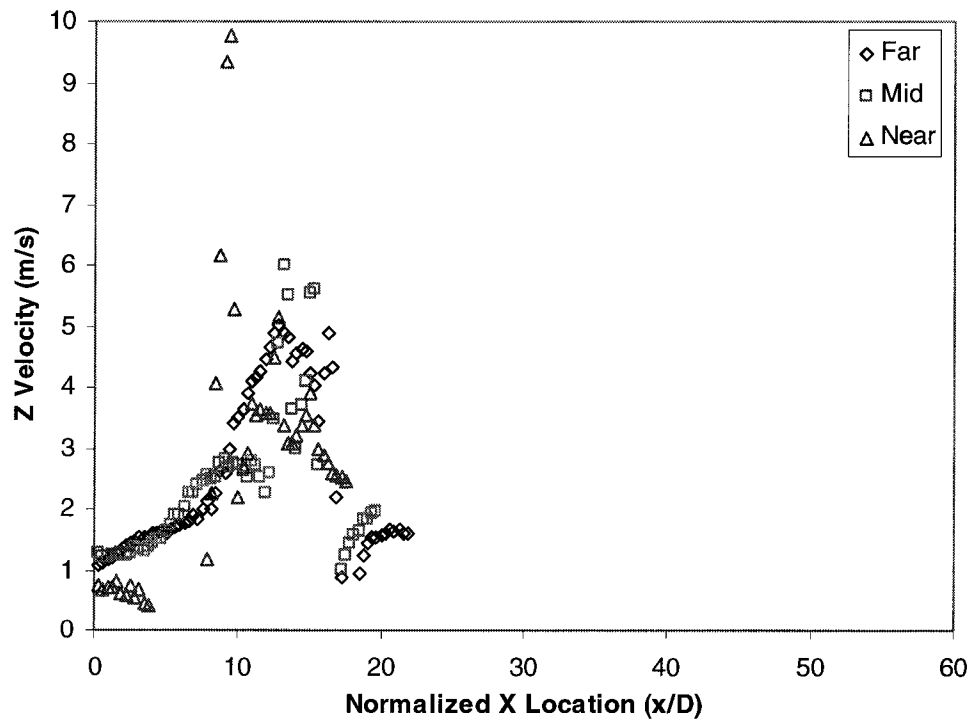


Figure 3.60d Z Velocity Profiles in X direction at 10% CFMFR at 2 m/s Cross-flow at Three Different Locations (Far 75%, Mid 50% and Near 25% of Flame Length)

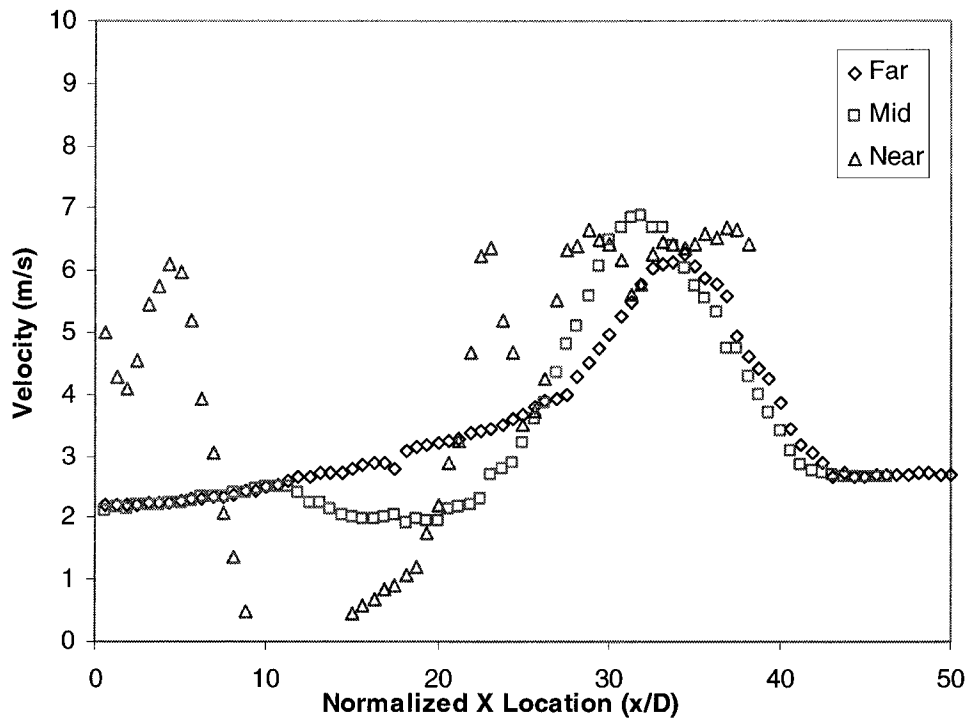


Figure 3.61a Z Velocity Profiles in X direction at 100% CFMFR at 3 m/s Cross-flow at Three Different Locations (Far 75%, Mid 50% and Near 25% of Flame Length)

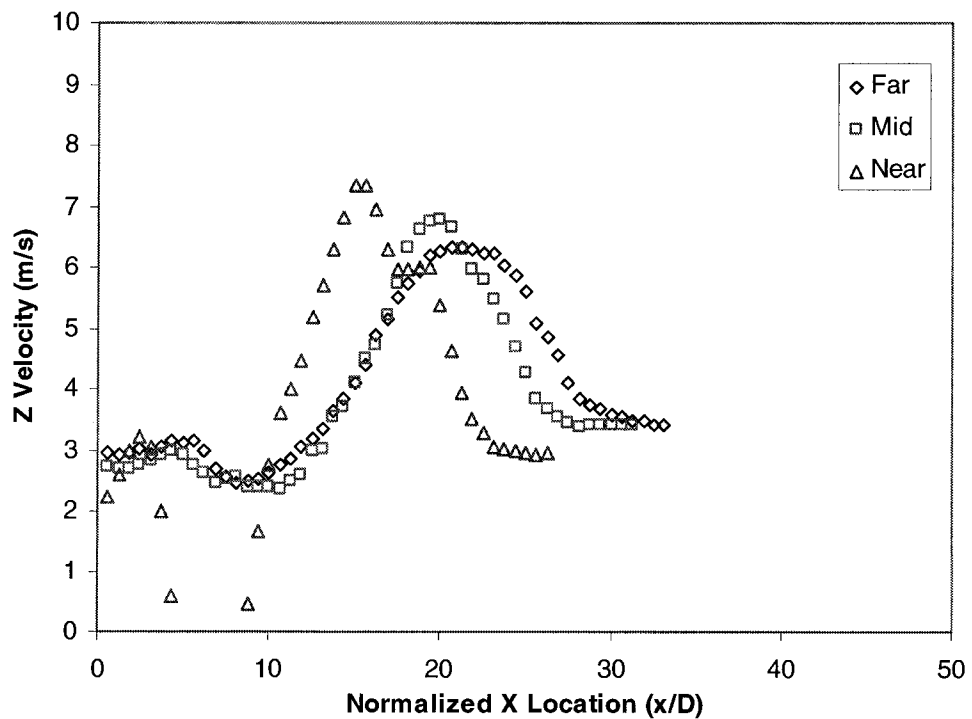


Figure 3.61b Z Velocity Profiles in X direction at 60% CFMFR at 3 m/s Cross-flow at Three Different Locations (Far 75%, Mid 50% and Near 25% of Flame Length)

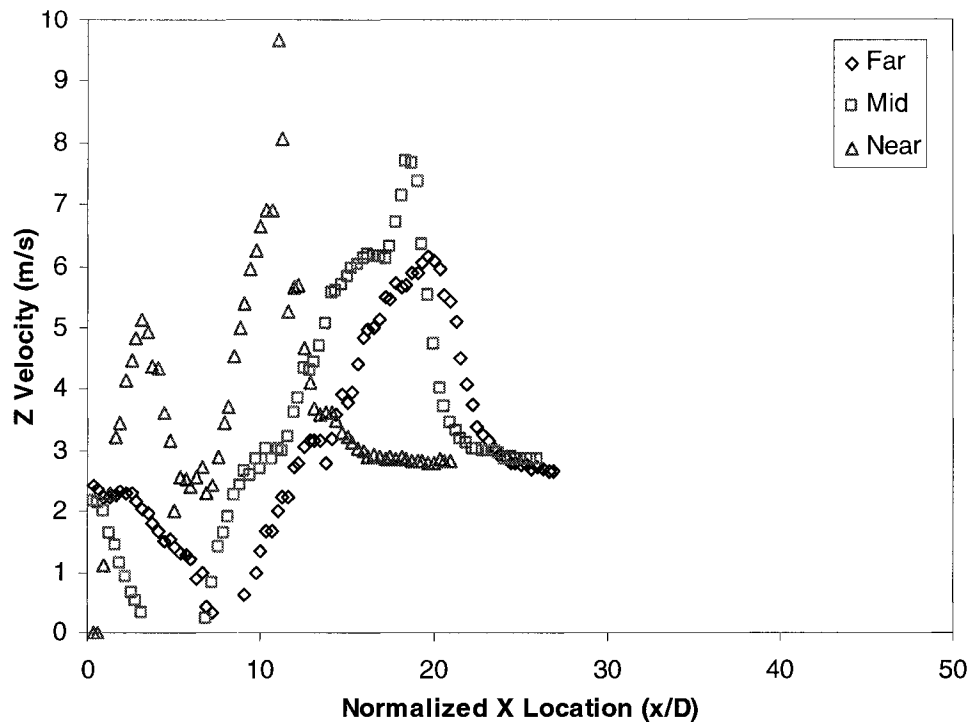


Figure 3.61c Z Velocity Profiles in X direction at 20% CFMFR at 3 m/s Cross-flow at Three Different Locations (Far 75%, Mid 50% and Near 25% of Flame Length)

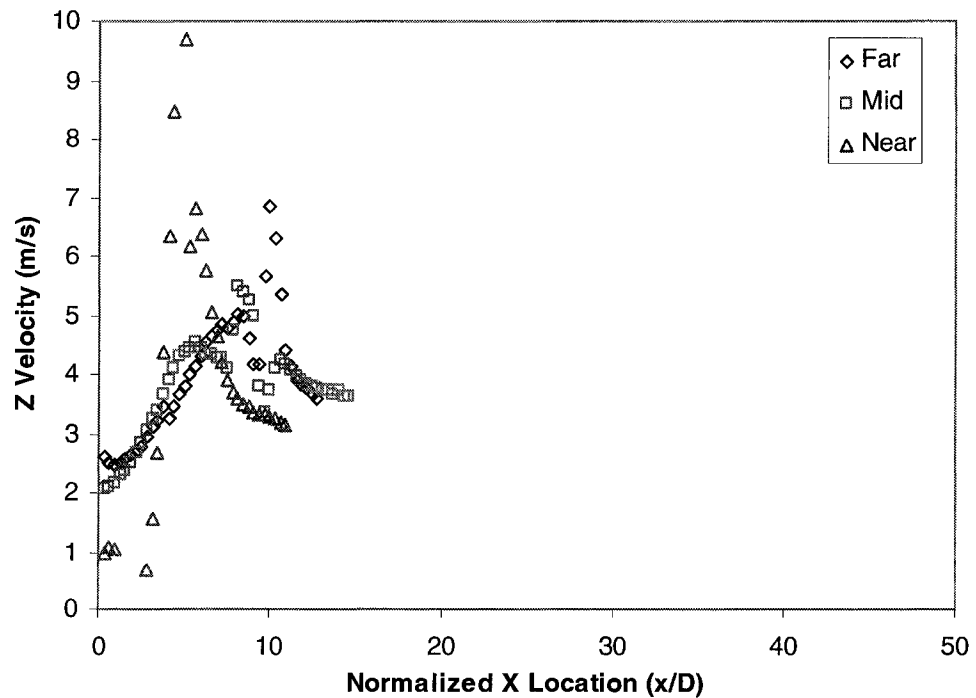


Figure 3.61d Z Velocity Profiles in X direction at 10% CFMFR at 3 m/s Cross-flow at Three Different Locations (Far 75%, Mid 50% and Near 25% of Flame Length)

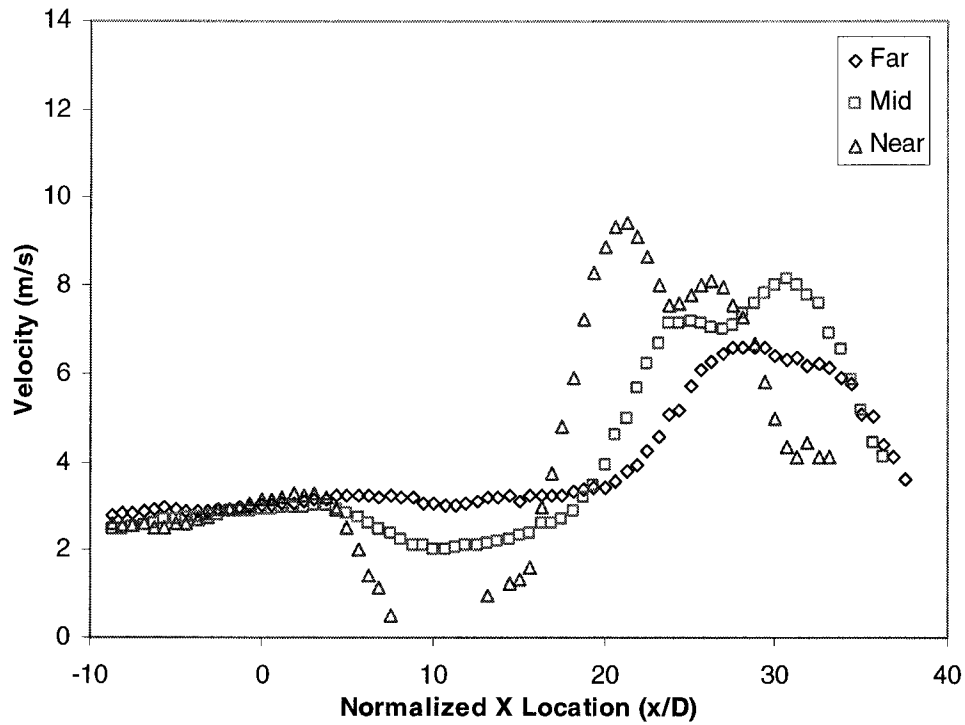


Figure 3.62a Z Velocity Profiles in X direction at 100% CFMFR at 4 m/s Cross-flow at Three Different Locations (Far 75%, Mid 50% and Near 25% of Flame Length)

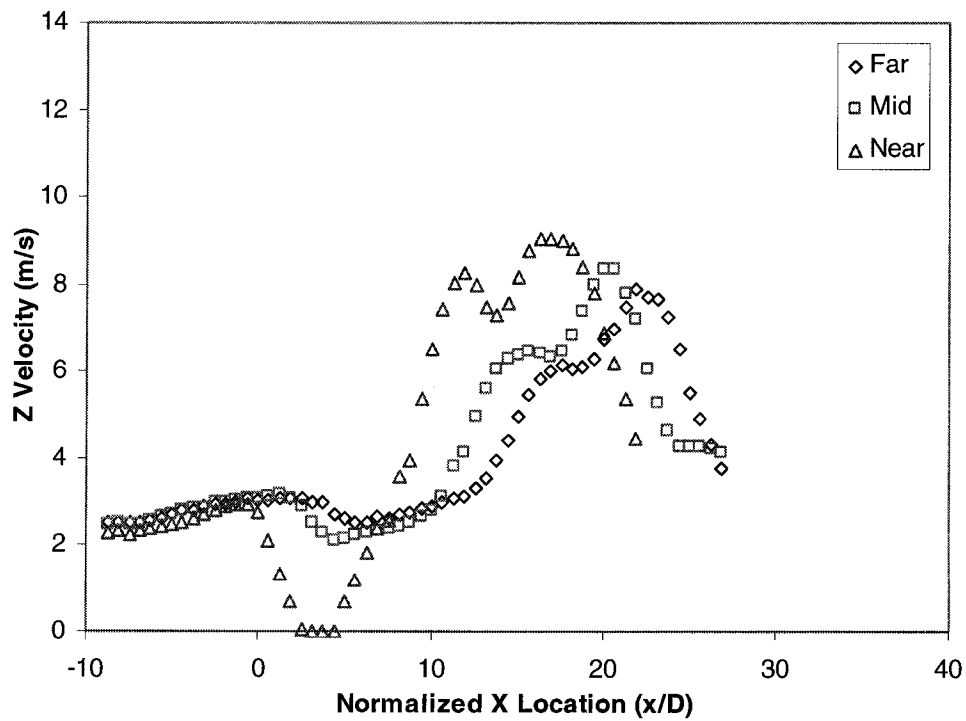


Figure 3.62b Z Velocity Profiles in X direction at 60% CFMFR at 4 m/s Cross-flow at Three Different Locations (Far 75%, Mid 50% and Near 25% of Flame Length)

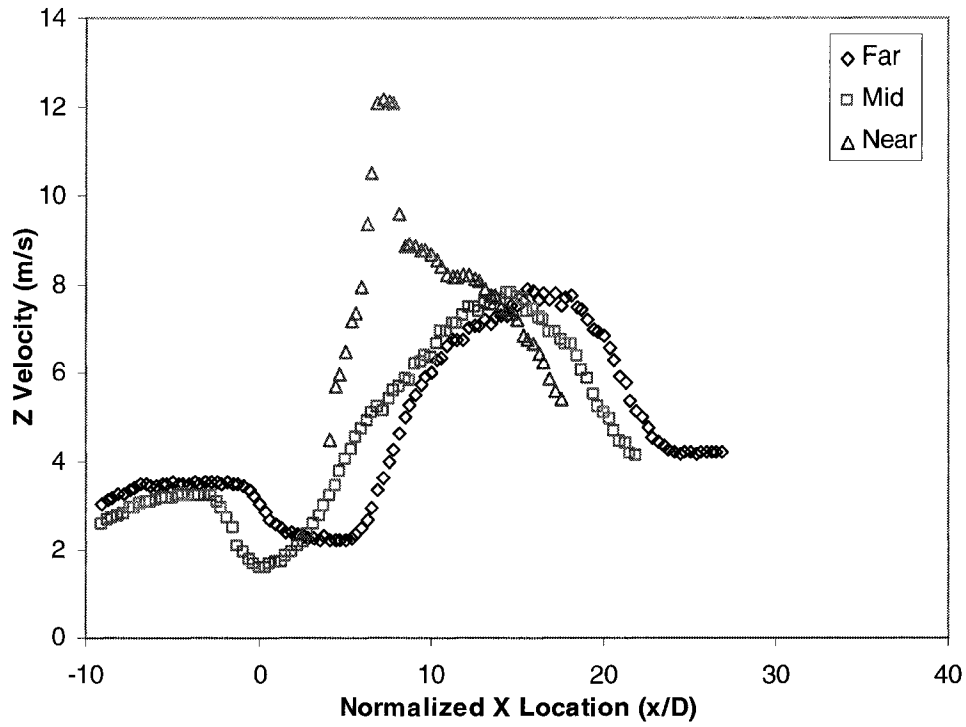


Figure 3.62c Z Velocity Profiles in X direction at 30% CFMFR at 4 m/s Cross-flow at Three Different Locations (Far 75%, Mid 50% and Near 25% of Flame Length)

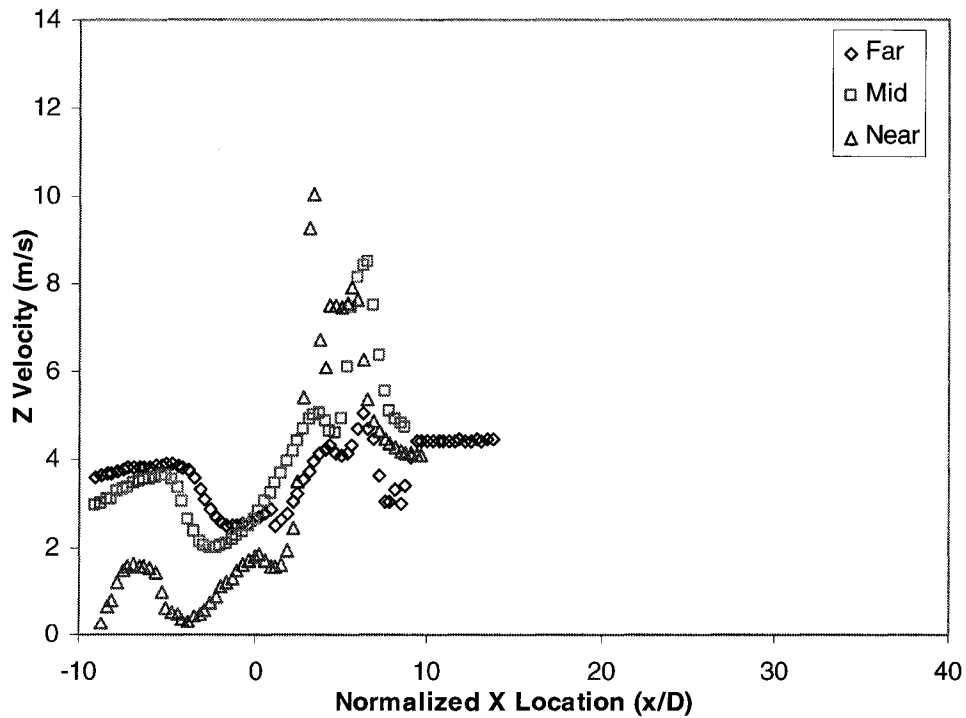


Figure 3.62d Z Velocity Profiles in X direction at 10% CFMFR at 4 m/s Cross-flow at Three Different Locations (Far 75%, Mid 50% and Near 25% of Flame Length)

Chapter IV

Laser Induced Incandescence Measurement

Nomenclature

a	Radius of particle
C_s	Specific heat of carbon, $1.90 \text{ J g}^{-1} \text{ K}^{-1}$ (Melton, 1984)
c	Speed of light
E_i	Laser irradiance
$e_{b,\lambda}$	Blackbody spectral emission power
f_v	Soot volume fraction
G_λ	Combination of spectral response function of the detector and its optics
h	Plank's constant
ΔH_v	Heat of vaporization, $7.78 \times 10^5 \text{ J/mol}$ (Melton, 1984)
k	Heat transfer coefficient, (air) $5.83 \times 10^{-5} (T/273)^{0.82} \text{ W cm}^{-1} \text{ K}^{-1}$ (Melton, 1984)
M	Carbon molar mass, 12 g/mol
M_λ^b	Blackbody spectral radiant existence
m	Mass
N	Number density of aggregates
N_p	Total number density
n_p	Number of primary particles per aggregate
$p(a)$	Probability density for a particle with radius a
R	Response function
T_o	Initial temperature

T_{∞} Temperature of the surrounding gases

t Time

Δt_L Temporal duration

Greek symbols:

$\bar{\epsilon}$ Mean emission coefficient

$\epsilon_{\lambda,p}$ Spectral emissivity

σ_{SB} Stefan-Boltzmann constant

ρ Density

ρ_s Solid carbon density, 2.26 g cm⁻¹ (Melton, 1984)

ρ_v Vapor density

β Fresnel reflectivity for spherical particle

λ_{em} Center of bandwidth

λ_{ex} Excitation wavelength

$\Delta\lambda$ Bandwidth

η_{abs} Absorption efficiency

Ω Collection solid angle of the detector

δ Absorption length parameter

δ_B Bulk absorption depth

4.1 Literature Survey on Laser Induced Incandescence (LII)

In the past, the incandescence signal was only considered as interference in pulse laser diagnostics (Eckbreth, 1996). However, recently, LII method has been studied by many researchers because of its simplicity and accuracy in facilitating soot concentration and size measurement. Most recent studies are listed in Table 4.1. Eckbreth (1996) started the pioneering studies of LII optical signal using Raman scattering diagnostics in flame. Melton (1984) developed a theoretical model to predict the behavior of LII. The model is described in the following section. Since then, many experimental and theoretical works have been carried out to understand this non-intrusive and simple method to measure in-flame soot concentration and particle size.

4.1.1 Introduction

According to Plank's law, an object that is heated up above 900 K emits visible radiation. Hence, if an object is heated to a temperature above 3000 K, all visible wavelengths are emitted with enough intensity that the object appears white-hot. The intensity of the electromagnetic radiation increases with the temperature of the object. The peak intensity falls more toward the shorter wavelengths. When a pulse of laser beam fires through the flame and it further heats up the soot far above the flame temperature, the soot particle will eventually incandesce in a broadband radiation, which is very intense in the visible spectrum.

Laser induced incandescence (LII) applies the mechanism of the heating of soot particles to a temperature above the surrounding gas temperature due to the absorption of laser energy, and the subsequent detection of the blackbody radiation (incandescence)

which corresponds to the elevated soot particle temperature. The spectrum of the emitted incandescence is broadband and is a strong function of the soot particle temperature.

The mechanism starts when a laser pulse as an energy source heats up a particle rapidly. This laser pulse represents an energy source in the energy balance equation. The soot particle absorbs the laser energy and causes the soot temperature to rise rapidly. The temperature of the soot particle is determined by taking into account the rate of laser energy absorption, soot vaporization, conductive heat transfer to the surrounding gas, and radiative heat loss through blackbody radiation. The heat sink terms in this phase are the conductive and radiative heat losses to the surrounding gas, and they are very small compared to the laser energy absorption rate. Subsequent to the laser pulse, the temperature gradually decreases due to conductive and radiative heat losses to the surrounding. The LII intensity or the blackbody radiation of a soot particle due to the laser heating has a dependence on the soot particle temperature, detection wavelength, and the laser fluence. LII emitted from a heated soot particle is fourth order dependent on the particle temperature. (Melton, 1984)

Vander Wal et al. (1999) verified a LII method by using transmission electron microscopy (TEM). Soot was sampled thermophoretically through analysis of TEM micrographs. TEM is an intrusive and time-intensive process (Vander Wal et al., 1999). The prediction of the soot particle was based on the temporal decay rate of the LII signal compared with TEM measurements. The conclusion was that LII could be used to predict the size of primary soot particles under certain conditions. There are two factors that can influence the signal. One is the flame temperature, because of its influence on the cooling rate of the particle and thus on the LII signal. The second factor is the cluster-

cluster aggregation. An aggregated structure could decrease the rate of cooling of individual primary particles through self-absorption of emitted thermal radiation and inhibition of conductive and convective cooling to the environment (Vander Wal et al., 1999).

Randy et al. (1995) did a study on the effects of laser heating on soot particles. It would be expected that the heating by the laser would remove the surface material of the soot, but their results showed that the soot particle appeared shell-like with a hollow structure or a porous material in the inner core. Their explanation was that the interior of the particle originated from the aggregation of polycyclic aromatic hydrocarbons (PAH), so it may contain a higher H/C ratio than the outer surface, which forms via an addition of C_2 fragments. This makes the outer layers resistant to laser ablation. Therefore, suitable laser heating may not alter the dimensions of the soot particle or the soot volume fraction.

To facilitate further discussion of the experimental techniques, the theoretical model that explains the heat transfer process of the soot particle by laser heating is provided. Some literature has developed the model to simulate the influence of different factors that have an effect on the LII signal, the soot concentration and the soot primary particle size. Though the LII signal is linearly proportional to the soot concentration, soot size, laser fluence or irradiance, laser and detection wavelength, and detection gate can influence the accuracy of the measurement.

4.1.2 Theoretical development

This section is the literature survey of some theoretical models that the literature has used to describe the LII process. The basic equation used is the energy balance of the soot particle during the laser heating. Although these models were not used in the current study, it is a good reference for understanding the soot heating process and the important factors that can influence the LII signal.

With the assumption of the soot particles as spherical in shape with a radius of a , the conservation of energy equation is

$$\eta_{abs}(a)\pi a^2 E_i - \kappa(T - T_\infty)4\pi a^2 + \frac{\Delta H_v}{M} \frac{dm}{dt} - \bar{\epsilon}(T)\sigma_{SB}(T^4 - T_\infty^4)4\pi a^2 - \frac{4\pi a^3}{3} \rho_c C_s \frac{dT}{dt} = 0$$

[4.1.1]

The first term is the laser energy absorbed per second (absorption efficiency, $\eta_{abs}(a)$; irradiance, E_i) the second term is the conductive heat transfer to the surrounding medium (heat transfer coefficient, κ ; temperature of the surrounding gases, T_∞) followed by energy expended in vaporization of the soot particle (heat of vaporization, ΔH_v ; carbon molar mass, M ; loss rate of mass, $\frac{dm}{dt}$). The fourth term is the blackbody or thermal radiation (mean emission coefficient, $\bar{\epsilon}(T)$; Stefan-Boltzmann constant, σ_{SB}) and finally the rate of internal energy rise (density, ρ ; specific heat of carbon, C_s). The constants in the above equation are also presented in Nomenclature (Melton, 1984; Schraml et al., 2000).

The continuity equation is written as

$$-\rho_c \frac{da}{dt} = \rho_v U_v \quad [4.1.2]$$

$$m = \frac{4}{3} \pi \rho_c a^3 \quad [4.1.3]$$

Where ρ_s is the solid carbon density, and ρ_v is the vapor density,

$$\rho_v = \frac{PM_v}{RT} \text{ and } U_v = \left(\frac{RT}{2M_v} \right)^{1/2} \text{ (Eckbreth, 1977)} \quad [4.1.4]$$

Where P is the vapor pressure of carbon, M_v is the molecular weight of vapor as 36 g/mol (Melton, 1984) and R is the gas constant.

By substituting the continuity equation and on simplification, the energy equation become

$$\eta_{abs}(a)E_i - k(T - T_\infty) + \frac{\Delta H_v}{M} 4\rho_v U_v - 4\bar{\epsilon}(T)\sigma_{SB}(T^4 - T_\infty^4) - \frac{4}{3}\rho_c C_s \frac{dT}{dt} = 0 \quad [4.1.5]$$

η_{abs} can be calculated using the results of Carter et al. (1965) in the ultraviolet region and the results of Lee and Tien (1981) in the visible region.

But the analytical approximation of η_{abs} for a $<\delta$ (Melton, 1984)

$$\eta_{abs} = a / \delta$$

$$\frac{1}{\delta} = \frac{2(2\pi)}{\lambda} \left[\frac{12n\beta^{-1}(l)}{an^2 j^2 - (n^2 - j^2 - 2)^2} \right] \quad [4.1.6]$$

$\beta(m)$ is the Fresnel reflectivity for a spherical particle, and $l = n - ij$ is the complex index of reflection. Here δ may be considered as an absorption length parameter in which the

$$\text{bulk absorption depth is } \delta_B = \frac{\lambda}{2(2\pi)j}. \quad [4.1.7]$$

In the limit of high laser power and maximum temperature ($\frac{dT}{dt} = 0$), where the radiation and the heat transfer to the surrounding medium terms become insignificant, and the energy equation becomes

$$\eta_{abs}(a)E_i + \frac{\Delta H_v}{M} 4\rho_v U_v \approx 0 \quad [4.1.8]$$

For $a < \delta$

$$a \frac{E_i}{\delta} - 1.22 \times 10^8 T^{1/2} \exp \left[23.9 \left(1 - \frac{3915}{T} \right) \right] \approx 0 \quad (\text{Melton, 1984}) \quad [4.1.9]$$

or

$$\frac{1}{T} \approx \frac{1}{3915} \left[1 - \frac{1}{23.9} \log \left(\frac{aE_i}{\delta} \right) \right] \quad (\text{Melton, 1984}) \quad [4.1.10]$$

The incandescence or the signal obtained from a distribution of particles according to Melton (1984) is

$$S(t, E_u, \lambda_{ex}, \lambda_{em}, \Delta\lambda) = \int_0^\infty N_p p(a) R(a, t, E_i, \lambda_{ex}, \lambda_{em}, \Delta\lambda) da \quad [4.1.11]$$

where R , is the response function as the incremental incandescent radiation received at time t in a bandwidth $\Delta\lambda$ centered at λ_{em} for excitation of a particle of radius a at wavelength λ_{em} with triangular laser pulse of peak intensity E_i and 10-nsec FWHM. $p(a)$ is the normalized probability density for a particle with radius a , and N_p is the total number density.

With the known values of $t, E_i, \lambda_{ex}, \lambda_{em}, \Delta\lambda$ from the experimental parameter and detected values, the detected signal at the moment of maximum temperature can be calculated to give

$$S \propto N_p a^x \quad [4.1.12]$$

$$\text{where } x = 3 + 154nm / \lambda_{em} \quad [4.1.13]$$

or it can be written as

$$S = C_1 N_p a^x \quad [4.1.14]$$

Where C_1 is the calibration constant, which can be obtained by calibrating the optical system on flames with a known volume fraction or by a data point acquired by an independent technique.

Mewes and Seitzman (1997) introduced two simplifications on their model for relation of soot size with the LII signal. First, the soot volume fraction can be described by three parameters, a , the radius of the particle, n_p , the number of primary particles per aggregate, and N is the number density of aggregates in the measurement volume. Hence, the soot volume fraction is defined as

$$f_v = \frac{4\pi}{3} N n_p a^3 \quad [4.1.15]$$

Second, the model of the LII measurement process was based on an energy balance for a single primary particle, rather than the soot aggregate.

$$S(t, T_\infty, T_o, E_i, \Delta t_L, \lambda_{em}) = \pi(2a)^2 \times \frac{\Omega}{4\pi} \int_{-\infty}^{\infty} G_\lambda(\lambda_{em}) \epsilon_{\lambda,p}[a(t)] e_{b,\lambda}[T(t)] d\lambda \quad [4.1.16]$$

Δt_L is the temporal duration. Ω is the collection solid angle of the detector and G_λ is the combination of spectral response function of the detector and its optics, nominally centered at detection wave length, λ_{em} . $\epsilon_{\lambda,p}[a(t)]$, spectral emissivity is a function of particle size and emission wavelength and it is equal to particle spectral absorptivity (Hofeldt, 1993). Blackbody spectral emission power, $e_{b,\lambda}[T(t)]$ is a function of particle

temperature. The particle initial temperature T_0 , in the model is assumed to have the same temperature as the local gas temperature, T_∞ . In practical situation, the soot particle temperature should be higher than the surrounding gas temperature because of chemical reaction on the particle. The higher particle temperature will slightly reduce the amount of energy required to vaporize the soot. But Mewes and Seitzman (1997) showed that effect did not significantly affect the results.

On the other hand, after the peak temperature, the thermal radiation term becomes significant. Schraml et al. (2000) expressed the thermal radiation term as,

$$4\pi a^2 \int \varepsilon(a, \lambda) M_\lambda^b(T, \lambda) d\lambda \quad [4.1.17]$$

instead of

$\bar{\varepsilon}(T) \sigma_{SB} (T^4 - T_\infty^4) 4\pi a^2$ (Melton, 1984, Schraml et al., 2000), which was described previously. The emission coefficient, $\varepsilon(a, \lambda)$ is a function of the particle radius, a and wavelength λ .

$$\varepsilon(a, \lambda) = \frac{2\pi a}{\lambda} E(l) \text{ where}$$

$$E(l) = -\text{Im} \left(\frac{l^2 - 1}{l^2 + 2} \right) \quad [4.1.18]$$

The blackbody spectral radiant existence $M_\lambda^b(T, \lambda)$ is

$$M_\lambda^b = \varepsilon(a, \lambda) \frac{2\pi h c^2}{\lambda} \frac{1}{\exp \left(\frac{hc}{\lambda k T} \right) - 1} \quad [4.1.19]$$

The energy equation shows that the particle cooling is essentially governed by the temperature gradient between the surrounding gas, T_∞ and particles, T . Hence, an accurate local gas temperature has to be included in the model calculation to provide an

accurate size measurement. Schraml et al. (2000) suggested the assumption of thermal equilibrium between the soot particles and the surrounding gas, and soot particle temperature before laser heating can be calculated by applying a simple inversion algorithm for axisymmetric flame. Although the soot surface temperature is higher than the surrounding gas due to chemical reaction at the surface, the temperature difference in most cases is small. Many researchers have observed this phenomenon by comparison of soot emission data to coherent anti-Stokes Raman spectroscopy (CARS) thermometry data (Hall and Bonczyk, 1990) or rapid insertion of thermocouples (De Iulilis et al., 1998).

To sum up the findings of the theoretical model, the vaporization term is more significant in affecting the LII signal in the initial part of the heating process than in other terms. However, after the soot particle is heated up to a maximum temperature $\frac{dT}{dt} = 0$ and the soot temperature starts to decrease, the heat loss due to thermal radiation and conduction becomes significant. Thus, the involvement of these two heat transfer terms causes the particle size to become very significant in influencing the LII signal. Heat conduction dominates the cooling mechanism after the laser decays. The conduction cooling is very sensitive to the particle diameter and local gas temperature. In the measurement of the soot concentration, the influence of the particle size always has to be avoided. Different soot particle with different dimensions cools at different rates. The larger soot particle cools faster than the smaller. Thus, the LII signal will be biased toward larger soot size if other heat transfer terms are involved. In the following section, there will be a more detailed description about choosing the proper gate size to avoid the influence of particle size and local gas temperature.

4.2 Experimental Techniques

In the past, the commonly used method for soot volume fraction measurement is the laser scattering/extinction method. The author found that this method works well for laminar flame and low turbulence flame. However, for a highly turbulent flame like TDFCF, the error margin is unsatisfactory. Furthermore, this method has low sensitivity to particle shape and particle composition. The second reason is the use of an ICCD camera to capture the LII signal making the measurement more efficient than current laser scattering/extinction method. With a camera, one-dimensional or two-dimensional data can be measured at one time. On the other hand, the scattering/extinction method is a point measurement, which is a very labor intensive process.

The important factors that can influence the LII signal are the laser fluence and the pulse width, the detection gate width and the timing, the detection wavelength, and laser wavelength. The calibration method is also very important in correlating the soot concentration and the LII signal.

4.2.1 Laser Fluence or Irradiance

There are two different ways that the literature defined the laser power used in generating the LII signal. Shaddix and Smyth (1996) claimed that the laser fluence (J/cm^2) is more accurate because it is the energy term that couples to the soot particle and not the power. For a short pulse laser (in nanoseconds), the energy conduction within the soot particle is over an order of magnitude faster than the laser pulse width. Once the particle is heated near or at its vaporization point during the laser pulse, the heat loss is

dominated by the vaporization rather than through conduction or radiation. On the other hand, Will et al. (1998) claimed that if longer laser pulse is used, the condition can be complicated because pulse lengths become similar with the time scale of the heat transfer process. Thus, irradiance (W/cm^2) provides a better picture for long pulse laser because the temporal behavior of the energy is important. In fact, for short pulse laser, the temporal behavior is also important because of the short temporal behavior of the vaporization term. For this study, the pulse width is 8 ns. Thus, the unit use is laser fluence. Anyway, both values can be easily calculated with the known pulse width laser power and beam size.

The LII signal is almost linearly dependent on the laser fluence at a low value of laser fluence. Then, the signal is relatively independent of the laser energy at the plateau region, which is around $0.2 \text{ J}/\text{cm}^2$ to $0.4 \text{ J}/\text{cm}^2$. Hence, the soot particle distribution has weak dependence on the laser fluence once this threshold has been reached. However, at a higher laser fluence, the LII signal decreases. For a laser fluence greater than $0.5 \text{ J}/\text{cm}^2$, the peak LII signal intensity begins to decrease but the temporal decay rate of the signal continues to increase (Ni et al., 1995; Vander Wal and Jensen, 1998). Dasch (1984), Ni et al. (1995), Witze et al. (2001) also found the plateau laser fluence to be $0.2 \text{ J}/\text{cm}^2$. In Table 4.1, many studies used the laser fluence around $0.2 \text{ J}/\text{cm}^2$ to $0.5 \text{ J}/\text{cm}^2$. However, Shaddix and Smyth (1996) determine that the threshold value for laser fluence should be $0.03 \text{ J}/\text{cm}^2$. Ni et al. (1995) determined that the minimum threshold fluence to generate a traceable LII signal is $0.06 \text{ J}/\text{cm}^2$. Optimum laser fluence should be applied to avoid too much saturation due to decrease of mean volume caused by high energy laser excessive

vaporization, and to avoid too much attenuation of incident laser across that flame due to lower laser fluence.

In the Mewes and Seitzman (1997) theoretical and experimental study, they found that the soot volume fraction measurements with low overall error required high laser intensity. High laser intensity reduced the sensitivity to the variation of soot temperature because all the soot is almost evenly heated to the vaporization point (3915 K vaporization temperature for graphite (Leider et al., 1973)).

In the current study, the highest LII signal was produced by a laser fluence around 0.37 J/cm^2 , which is within the range of values in most of the literature. The variation of laser fluence with relative LII signal is shown in Figure 4.1. The beam size for this study was 1 mm diameter. The beam size was measured through making a laser burn on Polaroid photo paper. From the burn pattern, the Gaussian profile of the laser was also observed. To avoid camera signal saturation by a high LII signal in a high soot concentration region, a lower fluence than the plateau was used. The laser fluence for all the LII measurement was 0.34 J/cm^2 .

4.2.2 Detection Gate and Timing

During a laser-heating event, the LII signal rises and reaches a maximum and then decays to a lower value. The rise and decay rate also depends on the laser fluence (Ni et al. 1995). At a high laser fluence (around 0.2 J/cm^2), the LII signal rises rapidly to a maximum (15 to 30 ns) and then decays at a slower rate. A faint LII signal is traceable even after 500 ns.

The temporal variation of the LII signal results because of the nature of the rise and decay of the signal. The decay of the signal reflects the cooling of the soot particles via conduction and convection heat transfer. Hence, it is very critical on the gate that the signal is captured. As mentioned in the above section (Literature Review – Theoretical Development), different cooling mechanisms play a significant role at different temporal locations. The initial part of the signal (around 0 to 30ns) is mostly due to the vaporization. Soon after that, the conduction and the radiation dominate the heat loss process. From the numerical calculation with the model mentioned above by Melton (1984), the comparison of the relative magnitude through various heat loss for a soot particle is shown in Figure 4.2 (Will et al., 1998).

There were three temporal methods in measuring the LII signal available in the literature. Prompt gate is taking a time average signal of a short duration (normally 25 ns to 50 ns gate width) gate; beginning from 0 s. Zero second is where the laser beam just starts penetrating into the flame. The second method is delayed gate method, which skips a short duration of the initial part of the signal (normally 25 ns to 50 ns) and time average the rest of the signal with a certain gate width. The third method is overall gate, which is basically the same as prompt gate method except it applies a long gate width (example, 500ns).

The prompt gate gives the lowest error (Mewes and Seitzman, 1997). It is the least biased (to soot dimension) because the dominant heat transfer term during and promptly after the laser pulse vaporization. Vaporization heat transfer term is not size dependent.

The advantage of using delayed gate was that it avoided the LIF signal of some species like C_2 and PAH. However, the delayed gate gives the greatest error because it is strongly influenced by the heat conduction from the particle to the surrounding gas. In the theory section, the conduction term in the energy equation shows its sensitivity to the particle diameter and local gas temperature.

The error for the overall gate is in between the prompt and delayed gate. It has the advantage of prompt gate, but on the other hand it also suffers the same setback by the conduction dependent LII decay.

Thus, to achieve highest accuracy results, a prompt LII signal was used in the study. Prompt gates of duration from 20ns to 50ns were attempted with the known results in order to search for the most appropriate gate that would give the best representation. A 30 ns gate was selected because it captured most of the rise period during the laser heating and it also avoided the influence of size dependent heat loss path because heat transfer through vaporization is more important in this period (observe Figure 4.2).

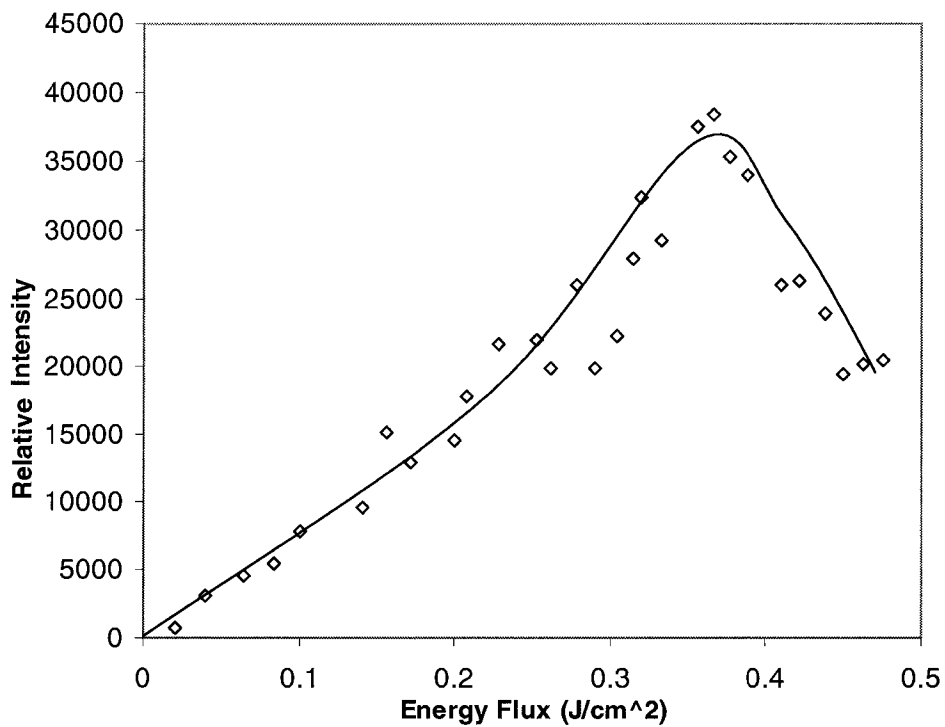


Figure 4.1 Effect of Laser Fluence on LII Signal

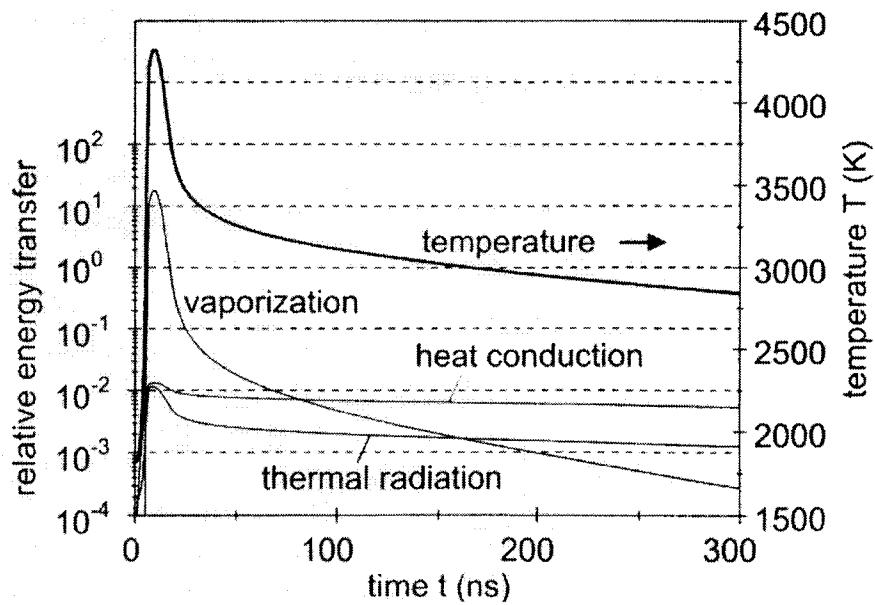


Figure 4.2 Comparison of Relative Heat Transfer of a Laser Heated Soot Particle Through Various Heat Transfer Path (Will et al., 1998)

4.2.3 Laser and Detection Wavelength

The soot absorption constant at a wavelength of 1064 nm is half that at 532 nm. The scaling factor of the absorption constant to the laser wavelength is about $1/\lambda$ (Habib and Vervisch, 1988). The laser with 532 nm and 1064 nm were the commonly used sources in LII study. In fact, 1064 nm is preferable because it is least likely to result in photochemical interference (Vander Wal, 1996). A 532 nm laser has the potential to produce C_2 in the vaporization process (Weiner, 1999)

The LII signal is of broadband distribution of incandescence and also LIF. At the vaporization temperature (3915K) or higher, the soot particles emit LII spectrum with a maximum at the visible wavelength and extend from the near infra-red region to the near ultraviolet. However, the interference of some other species may contaminate the LII signal especially at the peak LII signal region (wavelength). The LIF signal from C_2 swan band extends from ≈ 420 to 620 nm and it peaks at 516.5 nm. A short-pass dielectric 431nm filter was used for this study. Although it is in the C_2 swan band, the interference is small because it is at the minimum starting edge of the band. Most of the literature used a detection wavelength around 400 nm to 450nm. (Table 4.1)

The error caused by the size can be reduced if a longer detection wavelength is used. This is because at longer wavelength the emissivity variation between different particle diameters is small. Furthermore, different size particles have different temperatures; as a result they also have different blackbody term $e_{b,\lambda}(T)$ (Mewes and Seitzman, 1997).

Quay et al. (1994) used a laser probe of 1064 nm wavelength to produce LII signal. They found no significant difference of LII signal for wavelength of 500- and

700-nm because of the continuous nature of the LII spectrum in the visible wavelength. Although LII signal has a continuous spectrum in visible wavelength range, the interference from light scattering and PAH fluorescence will be expected near wavelength of 532 nm and above. Hence, the detection wavelength must be lower than 532 nm. Quay et. al (1994) used detection wavelength of LII signal at 400 nm.

In this study, 1064 nm laser generated from a Nd:YAG laser was used as the laser source. A 431 narrow band filter was installed prior to the ICCD camera.

4.2.4 Calibration Method

In order to know the relation of the LII signal to soot volume fraction, calibration was carried out with another independent method. Table 4.1 shows the different methods that were used for calibration of LII signal to soot volume fraction. They were extinction method, cavity ring down (Vander Wal, 1998), gravimetric (Vander Wal et al., 1996), soot generator (Jenkins et al., 2002) and TEM (Vander Wal and Jensen, 1998). Most studies refer to extinction method for calibration.

4.3 Experimental Setup

The schematic diagram of the experimental setup is shown in Figure 4.3 for quiescent condition and in Figure 4.4 for cross-flow condition. The Gaussian profile 1064 nm laser with pulse width of 8ns was generated by a Continuum NY 60B Nd:YAG laser which was operating under Q-switch condition. The specification of pulse width at FWHM was 8 to 9 ns. The laser beam was split by a 70%-30% beam splitter. The split signal was used for monitoring laser power variation. The laser power was measured by a

thermopile volume absorber detector (PHIR, model 30(150)A) with a digital power meter (NOVA, LaserStar series). Two 1064 nm mirrors mounted on the traverse mechanism were used to direct the beam into the flame. The traverse mechanism was able to move in two dimensions. A high power-focusing lens was used to focus the beam to a size close to 1 mm diameter at FWHM.

The detection setup was perpendicular to the beam path. Two pairs of lenses were used to zoom and to focus the image on to the ICCD (intensify charge couple device) camera. A 431 nm narrow band pass filter was installed prior to the ICCD camera to filter out other radiation. A Princeton Instrument ICCD-576E ICCD camera with an array size of 576×384 pixel was used to capture the image. A Princeton Instrument ST-138 High Performance camera controller controlled the camera operations, like data transfer and cooling operation. A Princeton Instrument PG-200 programmable camera gate and trigger was used to control the camera gate width, the delay duration and triggering. The ICCD camera was synchronized with the laser pulse. The trigger signal from the Stanford Research Instrument pulse generator was sent to the Nd:YAG laser and PG-200. The 10 Hz signals sent from the pulse generator were saturating the camera operation for full array imaging. As a result, to avoid the camera data saturation, and to speed up the camera data transfer, signal binning was applied. It was a reasonable approach because for the entire array, only the region of a line of LII signal was useful. Signal binning option allowed the camera to capture images at 10 Hz rate and it also allowed binning of the signal for the whole beam width (1mm). Since the laser and the camera were triggered at the same time, a delay was needed to take into account the time that was needed for the laser operation (the lamp, the Q-switch and delay between the two) and

electronic delay. The chronograph of the timing is shown in Figure 4.5. The period for the lamp flashing was 10 μ s. A period of delay was needed between lamp flashing and Q-switching. The length of the delay determined the laser power output. The sum of total laser operation length and the electronic delay was the delay imposed on the camera in order to capture the image specifically from the point the laser entered the flame to the point the gate close. The image data was sent to an image acquisition installed in a PC. The image was processed with a Princeton Instrument WinView or WinSpec imaging software. All the LII results presented were the average of 500 sets of data.

4.3.1 Calibration

Shaddix and Smyth (1996) used the laser-extinction method to calibrate LII signal. Their LII results were closely related to the soot concentration measured using the extinction method. Hence, in current study, the propane flame experiment of Shaddix and Smyth (1996) was repeated to calibrate the LII signal with their soot concentration profiles. The burner diameter for this experiment was 1.1 cm ID and surrounded by a 10.2 cm ID air annulus. The propane fuel velocity was 2.6 cm/s (2.57 cm³/s) and the co-flow air velocity was 8.66 cm/s (694 cm³/s). The propane calibration flame image is shown in Figure 4.8. The calibration was performed at 40mm height above burner (HAB). The result of the calibration is shown in Figure 4.9. The peak concentration point was used as the calibration point. The constant C in $f_n = CS'_n$ found from the calibration was 2.8×10^{-10} intensity/soot volume fraction. The unit of intensity is the measured LII signal intensity from the ICCD camera. The comparison shows that both results are almost identical except for the region very close to the center of the burner. The current

study results are slightly lower than Shaddix and Smyth (1996) data, but most of them are within the experimental uncertainty (error bar in Figure 4.9).

4.3.2 Signal Correction

Before soot concentration can be quantified from the signal and calibration constant, the LII signal trapping due to its extinction by the soot field in the flame between the laser beam and the detector has to be taken into account. The signal correction method proposed by Choi and Jensen (1998) and Bryce et al. (2000) was applied to correct the signal loss due to the attenuation along the path through the flame. The correction method basically is accomplished through a tomographic correction procedure. The Bryce et al. (2000) method not only performs LII signal trapping correction, but also calibrates the soot volume fraction by a single laser extinction measurement in the same path as the laser beam.

Figure 4.6 shows the simulated geometry used in the tomographic correction and the parameters used in the calculation. The correction was performed on half of the geometry because the domain was symmetrical. The signal S_n was stored in each pixel n for N total pixel. The principle of the correcting procedure was based on onion peeling or Abel inversion technique. The procedure of the correction started from the outer most ring and then applied the obtained value to correct the next ring. This procedure continued to the center.

The soot volume fraction of pixel n of a corrected signal, S'_n is defined as

$$f_n = CS'_n \quad [4.2.1]$$

where C is the calibrated constant wanted. The signal from the centerline travel through a ring m needs to be increased by an exponential factor to accommodate the Beer-Lambert absorption along a length, $L_{n,m}$.

$$S'_{n,m} = S'_{n,m-1} \exp\left(f_m \frac{K_\lambda}{\lambda} L_{n,m}\right) \quad [4.2.2]$$

Where the dimension is determined by geometry:

$$L_{n,m} = (r_m^2 - a_n^2)^{1/2} - L' \quad [4.2.3]$$

When $m=n$, $L' = 0$

$$\text{Else, } L' = (r_{m+1}^2 - a_n^2)^{1/2} \quad [4.2.4]$$

Where a_n is the adjacent distance, r_n is the radial distance and R_x is the scaling of width per pixel. The geometry used is shown in Figure 4.3.

$$a_n = R_x(N - n) \quad \text{and} \quad r_n = R_x[N - n + 1/2] \quad [4.2.5]$$

Since these dimensions are fixed in space and are not affected by the signal, these dimensional calculations are not included in the iterative process in the program (refer to the flow chart, Figure 4.7).

In this experiment the detection wavelength, λ is 431 nm, and this is substituted into the dimensionless soot extinction constant, K_λ .

$$K_\lambda = \frac{36\pi\eta_\lambda\kappa_\lambda}{(\eta_\lambda^2 + \kappa_\lambda^2 + 2)^2 + 4\eta_\lambda^2\kappa_\lambda^2} \quad [4.2.6]$$

Where η_λ is the real part and κ_λ is the imaginary part of the refractive index, the commonly used values are $\eta_\lambda=1.58$ and $\kappa_\lambda=0.58$ for detection wavelength around 400 nm. For extinction calculation, He-Ne laser with wavelength of 633 nm, $\eta_\lambda=1.80$ and $\kappa_\lambda=0.58$ (Chang and Charalampopoulos, 1990).

Substituting equation 4.2.1 into 4.2.2, for left half circle (LHC)

$$S'_n = S'_n \exp\left(\frac{K_{trap} C}{\lambda} \sum_{m=n}^{m=1} S'_m L_{n,m}\right) \quad [4.2.7a]$$

and right half circle (RHC)

$$S'_{2N-n} = S'_{2N-n} \exp\left(\frac{K_{trap} C}{\lambda} \sum_{m=n}^{m=1} S'_{2N-m} L_{n,m}\right) \quad [4.2.7b]$$

$$\left(\frac{I}{I_o}\right)_{pre} = \exp\left(\frac{K_{ext} C d}{\lambda} \sum_{n=1}^{2N-1} S'_n\right) \quad [4.2.8]$$

K_{ext} is the dimensionless soot extinct coefficient for He-Ne and K_{trap} is the extinct coefficient for the detected trapped signal. The unknown values of S'_m on the left hand side (LHS) of equation 4.2.7a and S'_{2N-m} of equation 4.2.7b have to be determined iteratively. First, S_n is substituted for S'_m and S'_{2N-m} into Equation 4.2.7a and b for the first round of iteration. Then, after the first iteration, S'_n and S'_{2N-n} on the right hand side (RHS) were reconstituted into the S'_m and S'_{2N-m} LHS of the equations. The calculation of equation 4.2.7 a and b continues until the difference of the old and new values is less than the convergence criterion.

Calibration constant C (equation 4.2.1) is iterated through the comparison of the predicted and the measured extinction value. Equation 4.2.8 is the prediction of the extinction across the flame, and it was calculated after the convergence of all values of S'_n . This predicted extinction value, $(I/I_o)_{pre}$ is compared with the measured extinction value, $(I/I_o)_{msr}$. The iteration process for the C begins with a guess value. The first guess value can be calculated from the known soot concentration data (Shaddix and Symth, 1996) and the measured signal. The iteration process of C proceeds until the difference of $(I/I_o)_{pre}$ (equation 4.2.8) and $(I/I_o)_{msr}$ is less than the convergence criterion.

The FORTRAN code for the signal correction is presented in the Appendix I. The experimental setup was basically the same as in the LII measurement, except a He-Ne laser was used for extinction measurement, and the schematic of the experimental setup is shown in Figure 4.3.

Figures 4.9 and 4.10 show the results for the corrected value and the original data. The difference between the corrected and uncorrected results is small. Figure 4.11 shows the difference in percentage for Figure 4.10 (result from 100% CFMFR at 30cm HAB [height above burner]). The maximum difference is around 3.38%, which is smaller than the uncertainty of the results, 7.9%. The difference after the correction is still within the experimental uncertainty, so it is insignificant. As a result, all the soot concentration results were not corrected.

The experimental uncertainty for the soot concentration measurement was calculated from the peak LII signal reading of the 50% flame length of the 60% CFMFR flame at 3 m/s cross-flow result, and it is about ± 0.02 ppm or $\pm 5.2\%$ of the average value (0.393 ppm).

4.4 Results and Discussion

4.4.1 Quiescent Condition

Figure 4.13 is the 2D axial tomographic view of the soot concentration results for 100%, 60%, 30% and 10% CFMFR. The results were collected with one cm step size along the flame axis. At lower flame location, the data were collected for the whole flame width. For flame heights above 20cm, only half of the flame of 100%, 60% and 30%

CFMFR data were collected because the flame widths were out of the range of the CCD array.

The results show that soot concentrations were highest at around 50-60% of the flame height for the 100%, 60%, and 30% CFMFR flame, but for the 10% CFMFR flame, it is located around 80% of the flame height (Figure 3.54). Although the 100% CFMFR flame has higher carbon content, the 60% CFMFR flame has higher soot concentration than the 100% CFMFR flame in this high soot concentration region (or soot growth zone). The length for this high soot concentration region or the soot growth zone of 60% CFMFR (~6cm) flame was longer than in the 100% CFMFR (~2 to 3cm) flame. The longer length shows that the residence time for soot growth was longer for 60% CFMFR flame. Longer soot growth residence time caused more soot formation. For that reason, 60% CFMFR flame had higher soot concentration than 100% CFMFR flame. Higher turbulence intensity of 100% CFMFR flame may increase the oxidation rate of small soot particles before they enter the soot growth zone. Consequently, there was less soot in the soot growth region for 100% CFMFR flame than at 60%. Furthermore, the soot oxidation zone (which is after the soot growth zone) for 60% CFMFR flame was shorter than in the 100% CFMFR flame. The 60% CFMFR flame appeared shorter because it had less initial momentum than the 100% CFMFR flame (compare the jet exit Reynolds number in Figure 3.14). This meant that the 60% CFMFR flame had less time to burn-off the soot particles that came out from the soot growth zone. From these two observations, it is apparent that momentum effect was dominating the soot formation and burn-off process for these two flames.

The higher in-flame soot concentration increased the radiative heat loss. The 100% and 60% CFMFR flame temperature results in Figure 3.24a and b show that the temperature level in 100% CFMFR flame was overall higher than in the 60% CFMFR flame. On the other hand, although the 30% CFMFR flame has a higher fuel flow rate than the 10% CFMFR flame, the higher soot concentration, which caused higher radiative heat loss in the 30% CFMFR flame, may have off-set the flame temperature raise. For that reason, both 30% and 10% CFMFR flame temperatures were similar in magnitude.

For 30% and 10% CFMFR flame conditions, the observation is opposite that shown in 100% and 60% CFMFR flames. 10% CFMFR flame appeared to have less soot concentration than 30% CFMFR flame. The length of the soot growth zone (soot concentration ~1.8 to 2.0 ppm) for 30% CFMFR flame was approximately 6 cm, and for 10% CFMFR flame was 2 cm. On the other hand, the region of soot concentration of 0.8 to 1.2 ppm or the soot oxidation zone for 10% CFMFR flame was longer than that in the 30% CFMFR flame. This observation is also contrary to that observed in 100% and 60% CFMFR flame behavior. Apparently, the reduction of mixing rate from the 30% to 10% CFMFR caused the increase of the residence time for soot oxidation. Furthermore, the 30% CFMFR flame has higher carbon content than the 10% CFMFR. Higher fuel content or C/O in the flame increases the production of radicals and PAH, which are the essential species for soot formation. Compared with 100% and 60% CFMFR flames, the low mixing rate caused the soot particles to continue to agglomerate and react with other PAH in the soot inception zone (before the soot growth zone) and increased the residence time for soot formation. Also, the higher in-flame soot concentration of the 60% CFMFR flame has caused a higher heat loss through soot radiation. The phenomenon is evident

from the temperature results in Figure 3.24b, where the 60% CFMFR flame has a lower temperature compared with the 100% CFMFR flame (Figure 3.24a).

From the above observation, the soot formation and oxidation are not only determined by the local temperature, but also by the local effective C/O ratio, the local hydrocarbon concentrations, and the residence time of the particle, both in the soot forming the region and oxidation region (Wagner, 1978).

4.4.2 Cross-Flow Condition

Figure 4.14s to 16 (a to d) show the tomographic plot of soot concentration on the x-y plane at three locations. Figure 4.12 shows the locations where the measurements were taken. The laser was fired in x direction and it was traversed in y direction with a step size of 1 or 2 mm (depending on the flame size) to cover half of the flame x-y plane cross section. All these figures are mirrored images at $y=0$. Figure 4.17 to 19 (a to d) show the relative PLII (Planer Laser Induced Incandescence) signal on the x-z plane.

X-Y Plane Results

Most x-y plane tomographic plots of the soot concentration show a kidney shape; which is in agreement with the previous study (Gollahalli et al., 1975). This kidney shape was caused by the CVP (counter rotating vortex pair), which was extensively discussed in Chapter III. Figure 4.14 and 15, a and b (10% and 20% CFMFR) at 25% and 50% of flame length, show high soot concentration at the center of each wing. Figure 3.32 shows that fuel jet and the cross-flow cause the rolling and folding that leads to the CVP. Hence, higher air entrainment was at the center of the flame on $y=0$, where air entered from the –

x direction through the rolling and folding process. Due to low oxidizers (both OH and O₂) concentration in the wings, the soot particles formed and grew in that region. In these two figures (4.14 and 4.15), the 2 m/s cross-flow flames have higher soot than the 3 m/s flame. The higher cross-flow velocity of the 3 m/s increased the air entrainment (through CVP and other means) and subsequently increased the soot oxidation rate.

Although the 4 m/s cross-flow results in Figure 4.16, a and b, show that the kidney structures are still vaguely present, the points of the highest soot concentration are not located inside the wings. The reason is that the flames at 4 m/s cross-flow have changed their structure to co-flow-like flame. This change of the flame structure has also been observed in the previous cross-flow flame study (Goh, 1999). In Figure 4.14a, the highest soot concentration is located at the center of the flame instead of in the wings. This is very similar to the quiescent condition flames (Figure 4.13). Furthermore, the soot concentration of the 4 m/s cross-flow, 10% CFMFR flame was higher compared to soot concentration in the 2 and 3 m/s cross-flow flames. Especially at 50% and 75% of the flame length, the soot concentration in 4 m/s cross-flow flame was 1.5 to 3 times higher than in the 2 and 3 m/s cross-flow flames. The non-monotonic soot concentration versus the cross-flow speed relation was also observed in Goh's (1999) study. This non-monotonic relation was mainly caused by the transformation of flame structure, which was discussed in Chapter 3, section 3.3.5.

The soot concentration results of 10% CFMFR flames (Figure 4.14a, 4.15a, and 4.16a) show the highest soot concentration was located at around 50% flame length for 2 m/s cross-flow results; at 3 m/s cross-flow condition, the highest soot concentration was located at around 50% and 75% of the flame length; at 4m/s cross-flow condition, the

highest soot concentration was located at around 75% of the flame length. The 20% CFMFR, 2 m/s and 3 m/s cross-flow flames, have the highest soot concentration located at around 50% of the flame length, but at 4 m/s cross-flow, the highest soot concentration was located at around 75% of the flame length. At 4 m/s cross-flow, all the percentages of CFMFR conditions have the highest soot concentration located at or close to 75% of the flame length. The change of flame structure due to the increase of the cross-flow velocity has increased the flame residence time, which was substantiated by the flame length results in Chapter III (Figure 3.55). The increase of the residence time has allowed the soot to generate for a longer period of time and has shifted the soot generation zone upstream.

For most of the momentum-controlled region (60% and 100% CFMFR), the soot concentration results for all the cross-flow at 25%, 50% and 75% flame length, show a kidney-shaped structure in Figures 4.14, 15, 16, c and d. The 60% and 100% CFMFR flame results for the 4 m/s cross-flow show a relatively smaller cross-section than the 2 and 3 m/s cross-flow flame. The change of structure can be observed from the flame images in Figure 3.57e. The 4 m/s flames appeared to be narrower and longer than the rest of the lower cross-flow flames. The explanation of this phenomenon is given in Chapter III. The soot concentration results of the 4 m/s, 60% CFMFR flame (for the three flame locations) are about four to eight times higher than the 2 and 3 m/s cross-flow results. On the other hand, at 100% CFMFR, all the soot concentration in the three cross-flows have almost the same range of soot concentration.

The 100% CFMFR flame has a higher soot concentration than the 60% CFMFR flame for the 2 and 3 m/s cross-flow, except for one case at 25% flame length for the 3

m/s cross-flow flame, where the 100% CFMFR flame has slightly lower soot concentration than the 60% CFMFR flame. On the contrary, the 4 m/s cross-flow results and the quiescent condition results show otherwise. This is also another indication that at the 4 m/s highly turbulent cross-flow, the flames behave like in a quiescent condition, and cross-flow has less effect on the flame than at the 2 and 3 m/s cross-flow. However, the 10% CFMFR flame has higher soot concentration than the 30% CFMFR flame for the 4 m/s cross-flow; this is different from the quiescent condition results, where the 10% CFMFR flame has lower soot concentration than 30% CFMFR flame, but it is consistent with the rest of the cross-flow conditions results. The difference of maximum soot concentration between the 10% CFMFR and 20% CFMFR flames for the 2 m/s cross-flow (Figure 4.14 a and b) is about 2 ppm at 50% and 75% flame length, and it is about 3 ppm at 25% flame length. The differences are about twice or more from 20% CFMFR to 10% CFMFR (4 ppm for 10% CFMFR and 1 to 2 ppm for 20% CFMFR). The 3 m/s cross-flow results (Figure 4.15 a and b) show that the difference is also 2 ppm, but the magnitude between 20% CFMFR and 10% CFMFR is three times higher for 25% and 75% flame length, and 1.5 times higher for 50% flame length (4 ppm for 10% CFMFR and 2 ppm for 20% CFMFR). The results show that the difference of maximum soot concentration between the 30% CFMFR and 10% CFMFR at the 4 m/s cross-flow (Figure 4.16 and b) is 2 ppm at 25% flame length, 5 ppm at 50% flame length and 10 ppm at 75% flame length; the magnitude between 30% CFMFR and 10% CFMFR is three times higher for 25% and six times higher for 50% and 75% flame length [3 ppm (25% FL), 6 ppm (50% FL), and 12 ppm (75% FL) for 10% CFMFR and 1 ppm (25% FL and 50% FL) and 2 ppm (75% FL) for 30% CFMFR]. These findings show that the

increase of cross-flow caused the increase in maximum soot concentration difference between the 10% and 20% CFMFR flame at 2 and 3 m/s cross-flow, and the difference between the 10% and 30% CFMFR at 4 m/s cross-flow. As mention in Chapter III, the 20% CFMFR flame and the 30% CFMFR flame are at the transition point between the chemically controlled region and the momentum-controlled region. The soot concentration in this region is reduced with the increase of cross-flow speed.

To summarize the above findings, the soot concentrations vary in a small magnitude with the increase of the cross-flow velocity for 100% CFMFR flames. For 60% CFMFR flames, the soot concentrations decrease slightly (10 to 20%) from 2 to 3 m/s cross-flow, but increase significantly (three to seven times) from 3 to 4 m/s cross-flow. For the transition point (20% CFMFR for 2 and 3 m/s cross flow, and 30% for 4 m/s cross-flow), the results show that the overall soot concentration decreased a little from 2 to 3 m/s (especially at 75% flame length), and maintained about the same magnitude from 3 to 4 m/s (besides the change of the location of high soot concentration from 50% flame length to 75% flame length). The 10% CFMFR flame results show that the overall soot concentration drops slightly from 2 to 3 m/s cross-flow (besides the change of the location of high soot concentration from 50% flame length to 75% flame length), but it increases tremendously from 3 to 4 m/s cross-flow. The general trend for all the cross-flow conditions is that the overall soot concentration decreases with the increase of CFMFR. The percentage difference of the soot concentration between CFMFR increases with the increase of cross-flow velocity.

X-Z Plane PLII Results

Figures 4.17 to 4.19, a to d, show the x-z plane PLII images. All these results are relative LII signals. These images were put together in a mosaic form as discussed in the previous section. The burner is located at $x=0$ and $z=0$ in all these figures. The $z = 0$ to 1 cm measurement was skipped because for all cases (except 4 m/s 10% CFMFR flame), the LII signal for that region was very small due to low soot concentration.

The 10% CFMFR flames for all the cross-flow conditions appear laminar. Hence, the soot concentration distribution for the three 10% CFMFR flames (Figure 4.16a, 4.17a, and 4.18a) appears smoother than the rest of the higher CFMFR flames. The 10% CFMFR results for 2 and 3 m/s cross-flow (Figure 4.16a and 4.17a) show that the soot concentration is highest at around $z = 6$ to 7 cm. In 4 m/s cross-flow flame (Figure 4.19a), the highest soot concentration is located above 8.5 cm (the domain of PLII measurement), and it is located at around 75% (Figure 4.16a) of the flame length, which is about 15 cm. There are two findings that can be observed from these results. First, the flame bends more toward the $-x$ direction with the increase of cross-flow velocity, which is caused by the decrease of momentum flux ratio. Secondly, the increase of cross-flow also increases the width (in x) of the soot distribution, which is caused by the change of flame structure that is discussed in Chapter III.

The results of the 20% CFMFR flame at 2 m/s (Figure 4.17b) show the soot is distributed along the flame and a larger concentration is located at around $z = 7$ to 8 cm. However, the 20% CFMFR flame at 3 m/s cross-flow (Figure 4.18b) shows that the soot is concentrated around 4 to 5.5 cm along the z -axis and in the 4 m/s cross-flow flame (Figure 4.19b) shows it is located at 6 to 7 cm along the z -axis. These observations

confirmed the results in Figure 4.14b, 4.15b, and 4.16b, where the soot concentration is highest at 75 % of the flame length for 2 m/s cross-flow flame, 50% of the flame length for 3 m/s cross-flow flame, and 75% for the flame length for 4 m/s cross-flow flame.

Although the 10% CFMFR flame results show that the soot concentration distribution increases in width (x direction) with the increase of cross-flow velocity, the 60% and the 100% CFMFR results (Figure 4.17 to 4.19, c and d) show the opposite behavior. Comparing 2 and 4 m/s cross-flow results, we notice that the 4 m/s cross-flow flame bends more along the cross-flow direction and its width is also smaller.

4.5 Conclusion

The quiescent flame result shows that the overall rank of the magnitude of soot concentration with respect to percentage CFMFR provides a means to distinguish the regions of momentum and chemically dominant region. The 60% CFMFR flame had a higher soot concentration than the 100% CFMFR flame because the 100% CFMFR flame had a higher mixing rate. However, the 10% CFMFR flame had less soot concentration than the 30% CFMFR flame. The reason for this phenomenon was the change of residence time. Hence, it can be concluded that the 10% CFMFR flame lies in the a chemically-dominated region, whereas the 60% CFMFR flame lies in the momentum-dominated region.

The cross-flow velocity versus the flame soot concentration relation shows a non-monotonic behavior. The overall soot concentration decreases with the increase of cross-flow velocity from 2 to 3 m/s. However, the increase of cross-flow velocity from 3 to 4 m/s increases the soot concentration. This phenomenon was mainly attributed by the

change of flame structure at higher cross-flow velocities. The increase of cross-flow velocity from 2 to 3 m/s increased the flame-air mixing rate through the intensifying the CVP structure. On the other hand, the increase of cross-flow velocity from 3 to 4 m/s changed the flame configuration to more like a co-flow flame.

The quiescent and the 4 m/s cross-flow flames results show that the 60% CFMFR flame had higher soot concentration than the 100% CFMFR flame. However, the 2 and 3 m/s cross-flow flames results show that the 100% CFMFR flame had higher soot concentration than the 60% flame. Which is another evidence that the 4 m/s cross-flow was behaving like a quiescent or co-flow flame.

Generally, all the cross-flow flames show a decrease of overall soot concentration with the increase of CFMFR. The difference in percentage of the peak soot concentration increases with the increase of cross-flow velocity.

Table 4.1 Literature on Applications of LII for Soot Concentration Measurement

Author	Fuel	Burner Size	Laser wavelength	Detection wavelength	Power	Gate	Pulse	Calibration	Soot size
B. Quay et. al 1994	Ethylene	11.1 mm (fuel) 101.6mm (air)	532 & 1064nm	400nm	0.12MW/cm ²	10ns	7ns	Extinction	Yes
T. Ni et. al 1995	Ethylene	10.1mm (fuel) 100.2 mm (air)	532nm	450nm	0.27J/cm ²	18ns	7ns		Yes
C .R. Shaddix et. al 1994	Methane	10.1mm (fuel) 100.2 mm (air)	560nm	300-480nm	7*10 ⁸ W/cm ²	100ns		Extinction	
C .R. Shaddix and K. C. Smyth 1996	Methane Propane Ethylene	10.1mm (fuel) 100.2 mm (air)	560.3nm	450nm (threshold) (threshold)0.03 J/cm ² (used)5.0J/cm ²	6*10 ⁶ W/cm ²	45ns	5ns	Extinction	Yes
R. L. Vander Wal 1996	Ethylene	10.5mm fuel 101mm air	1064nm	400-450nm	30MW/cm ²	100ns	10ns		
R. L. Vander Wal et. al 1998	Acetylene air mixed	10.5mm fuel 101mm air	Dual 1064nm	400-450nm(threshold)	0.36J/cm ²	50ns			
R. L. Vander Wal 1998	Methane	10.5mm fuel 101mm air	1064nm	405-415nm 590-610nm	0.25J/cm ²	50ns		Cavity ring down CRD	No
R. L. Vander Wal and K. A. Jensen 1998	Ethylene	10.5mm fuel 101mm air	1064nm	400-450nm	0.5J/cm ²	50ns		Extinction	Yes
R. L. Vander Wal and D. L. Dietrich 1994	Droplet combustion		1064nm	1064nm	400-450 nm	1 x 10 ⁷ w/cm ²			No

Author	Fuel	Burner Size	Laser wavelength	Detection wavelength	Power	Gate	Pulse	Calibration	Soot size
R. L. Vander Wal et. al 1996	Ethylene	McKenna burner	1064nm	450nm and 550nm	29MW/cm ² 57MW/cm ²	250ns		Gravimetric	Yes
R. L. Vander Wal et. al 1999	Methane Ethane Ethylene Acetylene	10.5mm fuel 101mm air	1064nm	300 and 600nm	0.25J/cm ²	50ns		TEM	No
S. Will et. al 1996	Ethylene	13mm	532nm	532nm	100MW/cm ²	20ns	8ns	Extinction	Yes
S. Will et. al 1998	Ethylene	13mm	532nm	450nm	50-150MW/cm ²	10ns	8ns	Extinction	Yes
S. Schraml et. al 2000	Ethylene	13mm	532nm	532nm	5*10 ⁷ W/cm ²	4ns	8ns	Extinction	Yes
D. Bryce et. al 2000	Diesel	10mm (fuel) 100mm (air)	532nm	368-423nm	10J/cm ²	30ns			
M. Braun-Unkhoff et. al 1998	Premixed Ethylene	8mm	532nm	450nm		100ns	8ns	Extinction	No
H. Geitlinger et. al 1998	C ₂ H ₂	2mm 16mm	532nm	430nm	35mJ	250ns	10ns	Extinction	No
B. Mews and J. M. Seitzman 1997	Ethylene		532nm	400nm	100MW/cm ²	50ns	7ns	Extinction	Yes

Author	Fuel	Burner Size	Laser wavelength	Detection wavelength	Power	Gate	Pulse	Calibration	Soot size
J. Hult et. al 2002	Ethylene	1.7mm	532nm	<450nm	0.3J/cm ²	10ns		Extinction	No
B. Axelsson et. al 2001	Premixed Ethylene	Flat Flame Burner	1064nm	400 & 470 nm	0.6J/cm ²	40ns		Extinction	Yes
McManus et. al 1997	Ethylene	Flat flame	532nm		10*6W/cm ²	20ns	30ns	Extinction	No
D. Woiki et. al 2000	C2H2	Shock tube	1064nm	633nm	43mJ		15ns	Extinction	Yes
P. O. Witze et. al 2001	Propane	50 mm(fuel) 75mm (air)	532nm	570nm up (threshold)	0.2J/cm ²			Extinction	No
T. P. Jenkins et. al 2002	Gas Turbine Combustor		1064nm			50ns		Soot generator	No
M. Brown and T. Meyer 2002	Gas Turbine Combustor		532nm	500nm up	100-600J/pulse			None	No

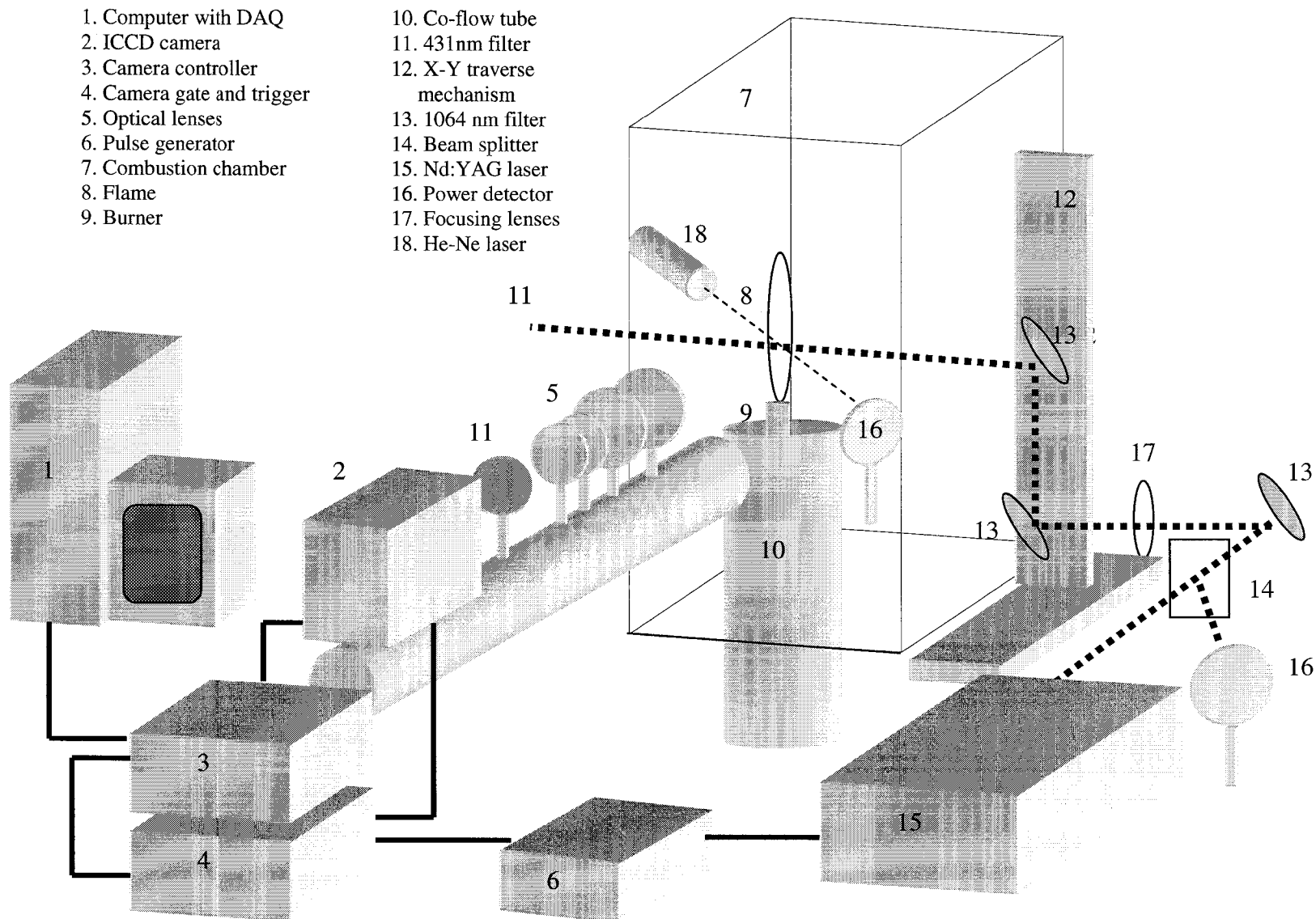
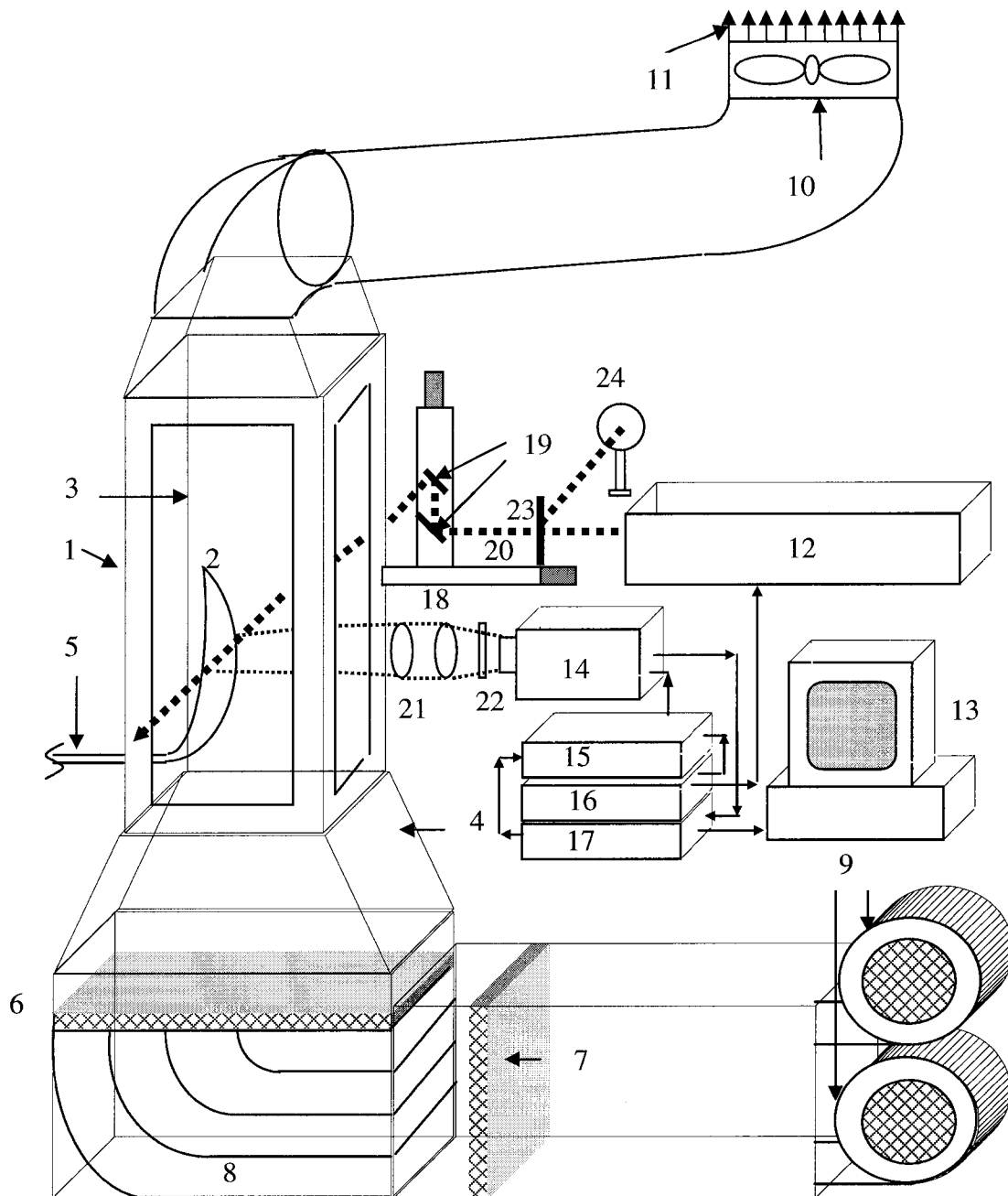


Figure 4.3 Experimental Setup for LII Measurement at Quiescent Condition



- | | |
|----------------------------|---|
| 1. Test section | 13. Computer and DAQ system |
| 2. Flame | 14. ICCD camera |
| 3. 3 tempered glass window | 15. Camera gate controller |
| 4. Contraction | 16. Stanford Instrument Pulse Generator |
| 5. Fuel and mixture supply | 17. Camera imaging system |
| 6. Single layer filter | 18. Traverse mechanism |
| 7. Two layers filter | 19. Turning mirrors |
| 8. Turning ducts | 20. Laser |
| 9. Blowers | 21. Focusing lens |
| 10. Suction fan | 22. 431 nm narrow band filter |
| 11. Exhaust to atmosphere | 23. 70%-30% beam splitter |
| 12. Nd-YAG laser | 24. Thermopile volume absorber detector |

Figure 4.4 Schematic of LII Measurement Setup for Cross-flow Condition

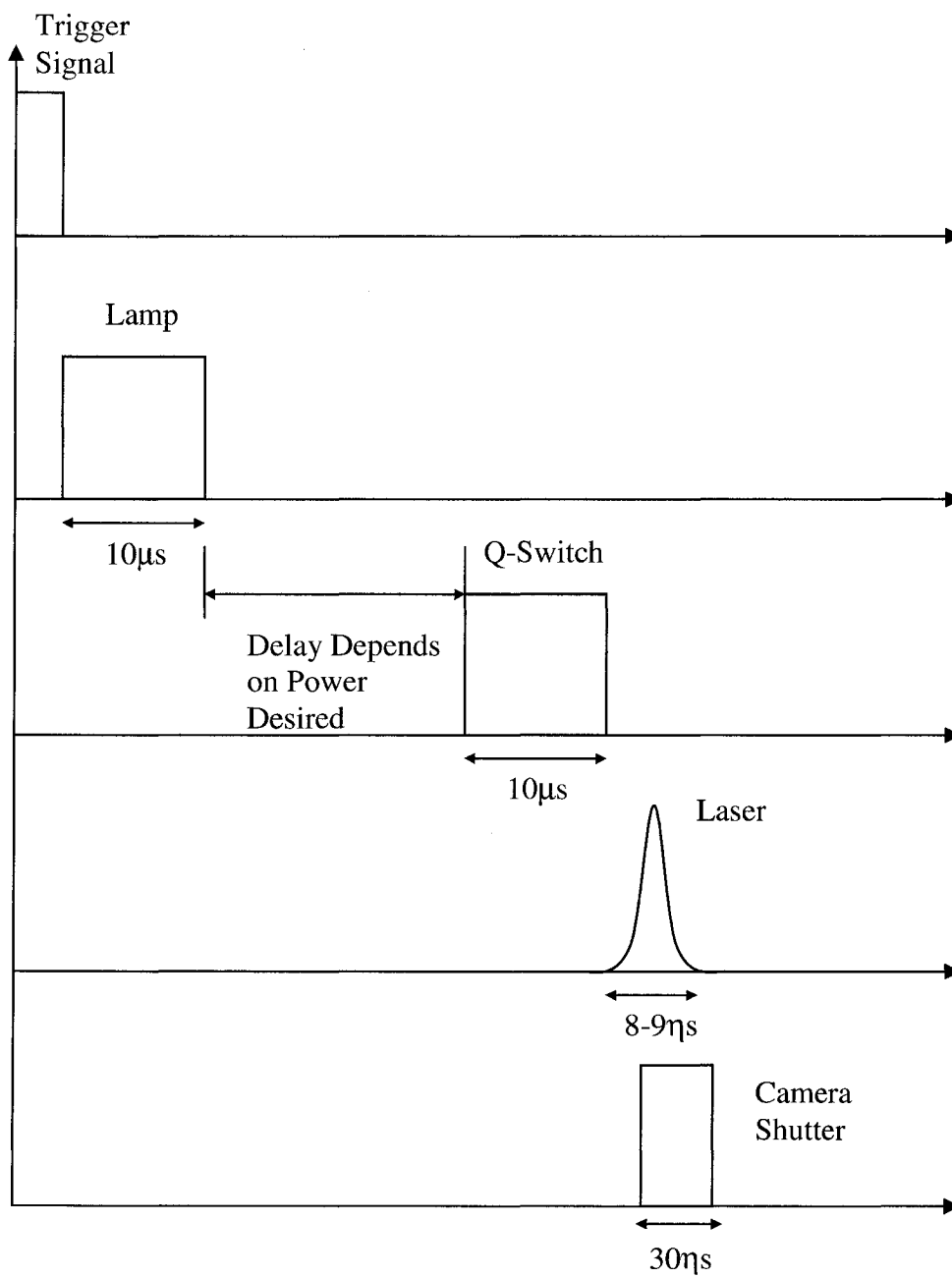


Figure 4.5 Laser and Camera Chronological Chart

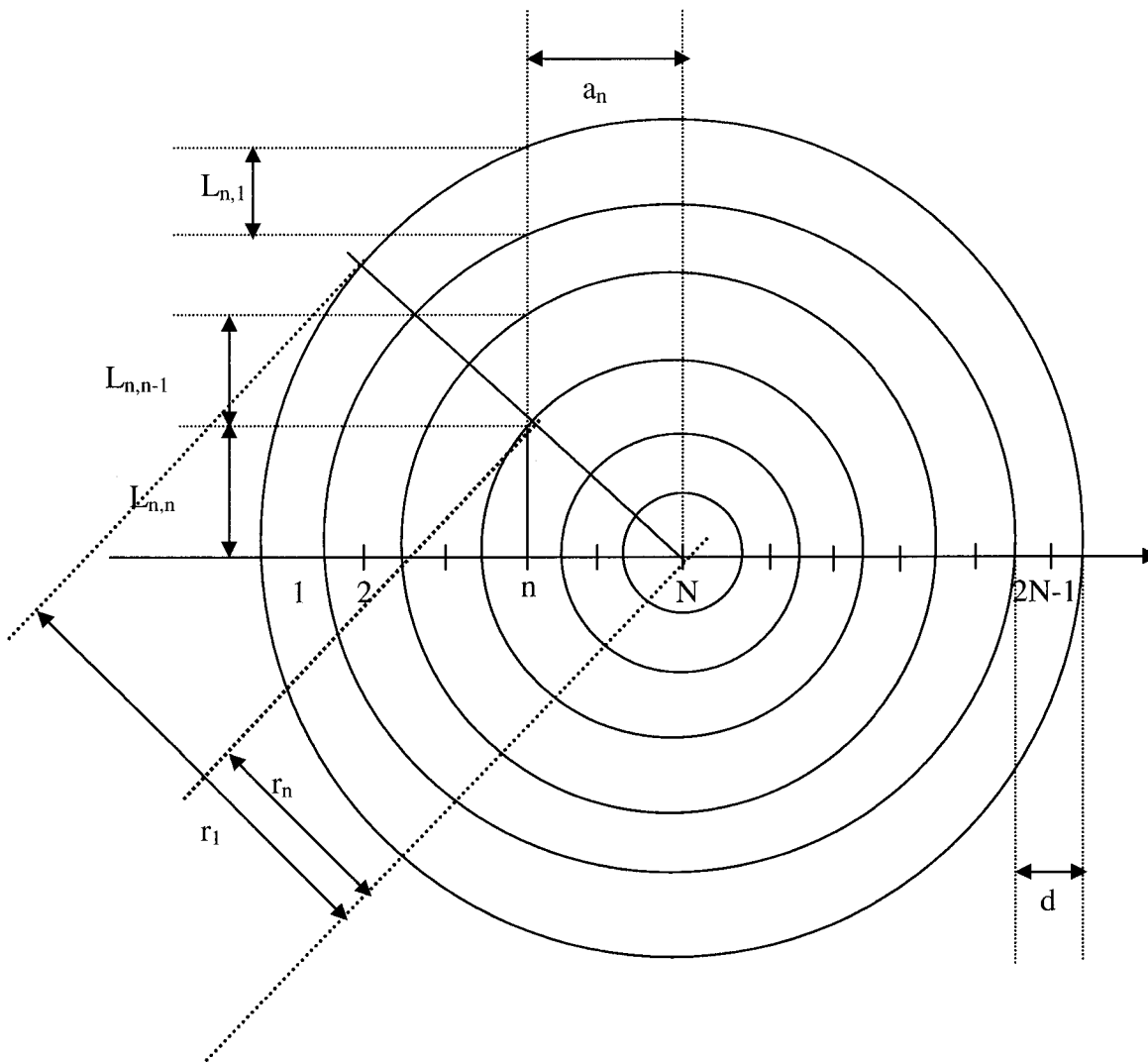
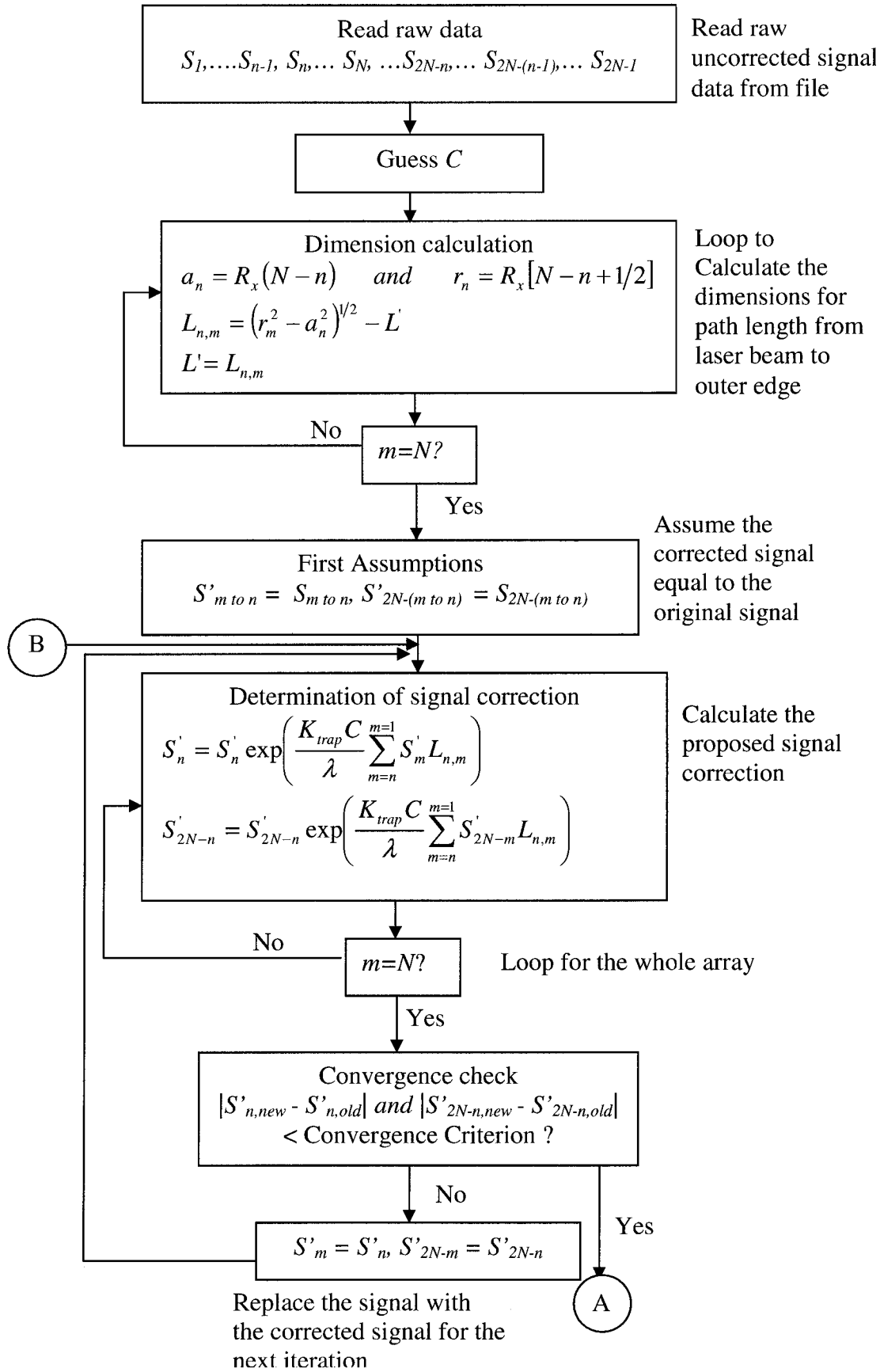


Figure 4.6 Geometry of the Tomographic Correction



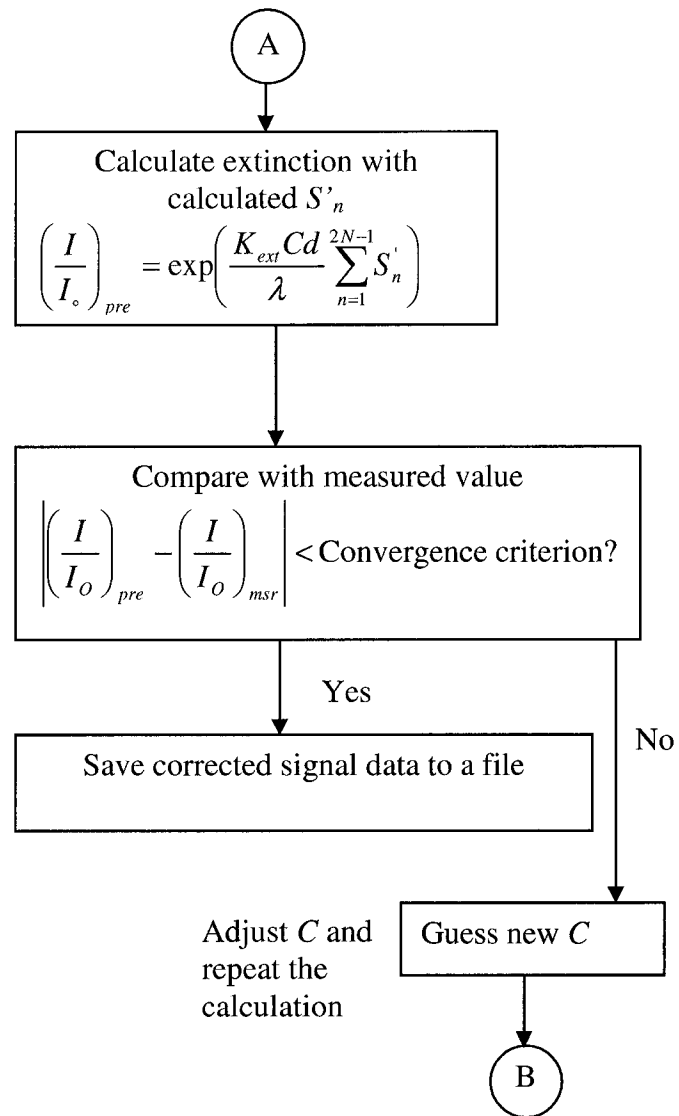


Figure 4.7 Flow Chart for Signal Correction

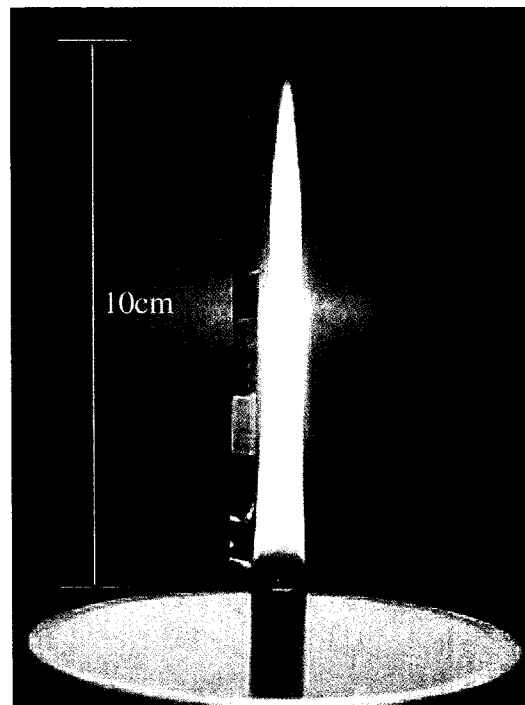


Figure 4.8 Propane Calibration Flame

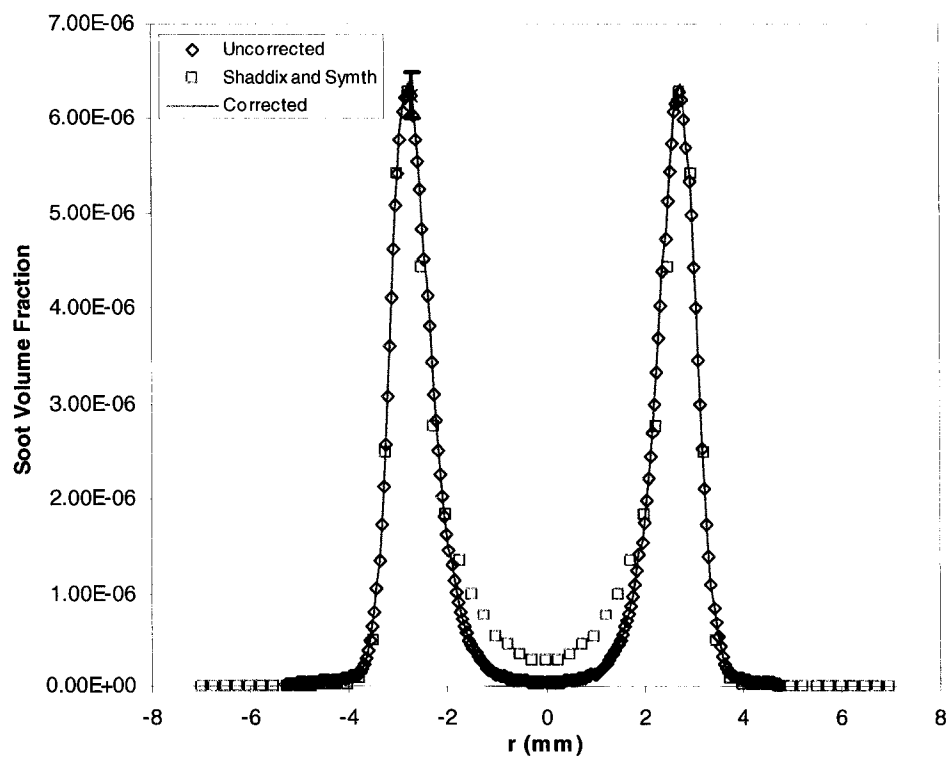


Figure 4.9 Corrected and Uncorrected Results and Shaddix and Symth Results (1996)

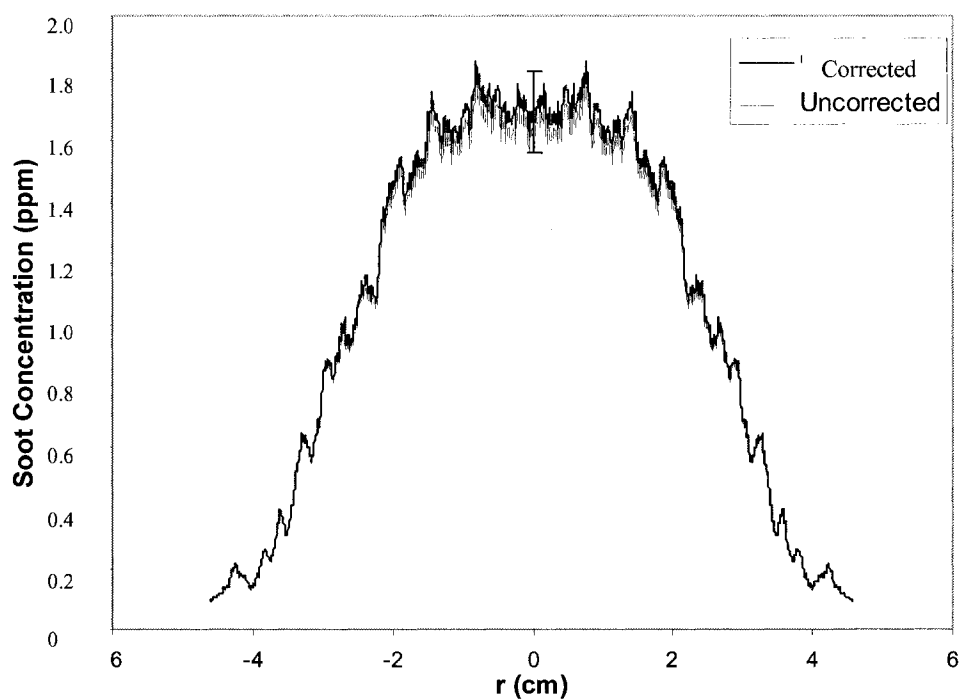


Figure 4.10 Corrected and Uncorrected Results for Quiescent Flame at 100% CFMFR at 30cm HAB (Height Above Burner)

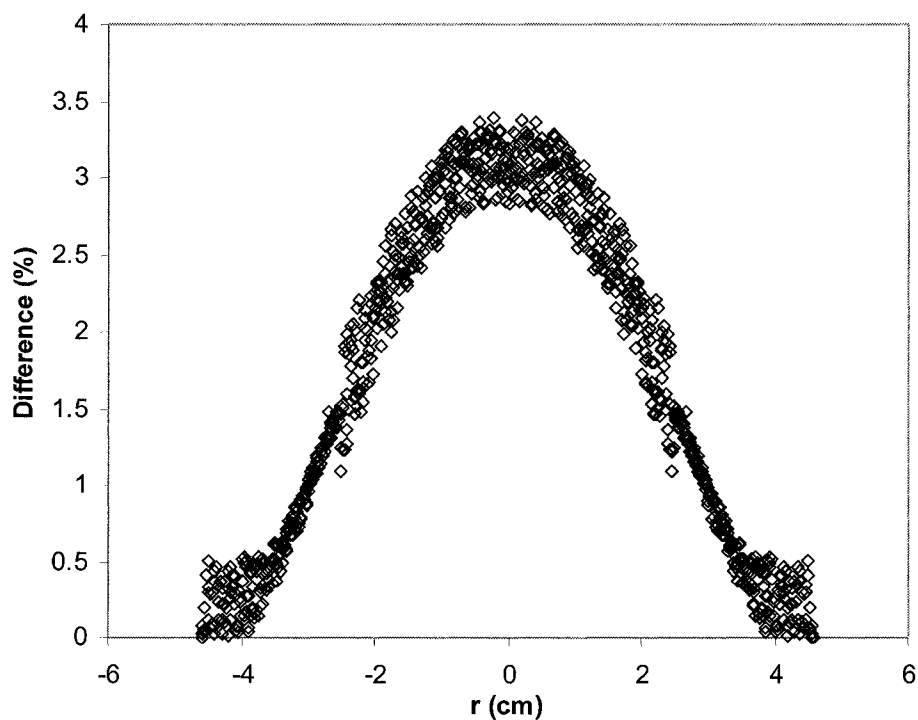


Figure 4.11 The Difference in Percentage of Corrected and Uncorrected Result for Quiescent Flames at 100% CFMFR at 30cm HAB (Height Above Burner)

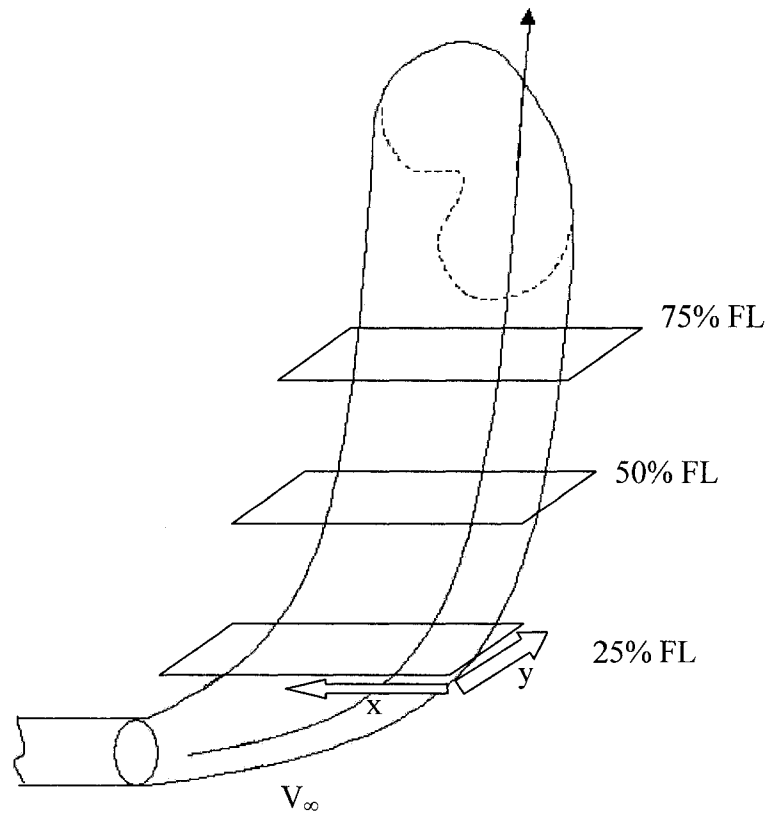


Figure 4.12 Schematic Diagram Showing the Slice of measurement Taken at Three Flame Locations in Cross-Flow (FL= flame length)

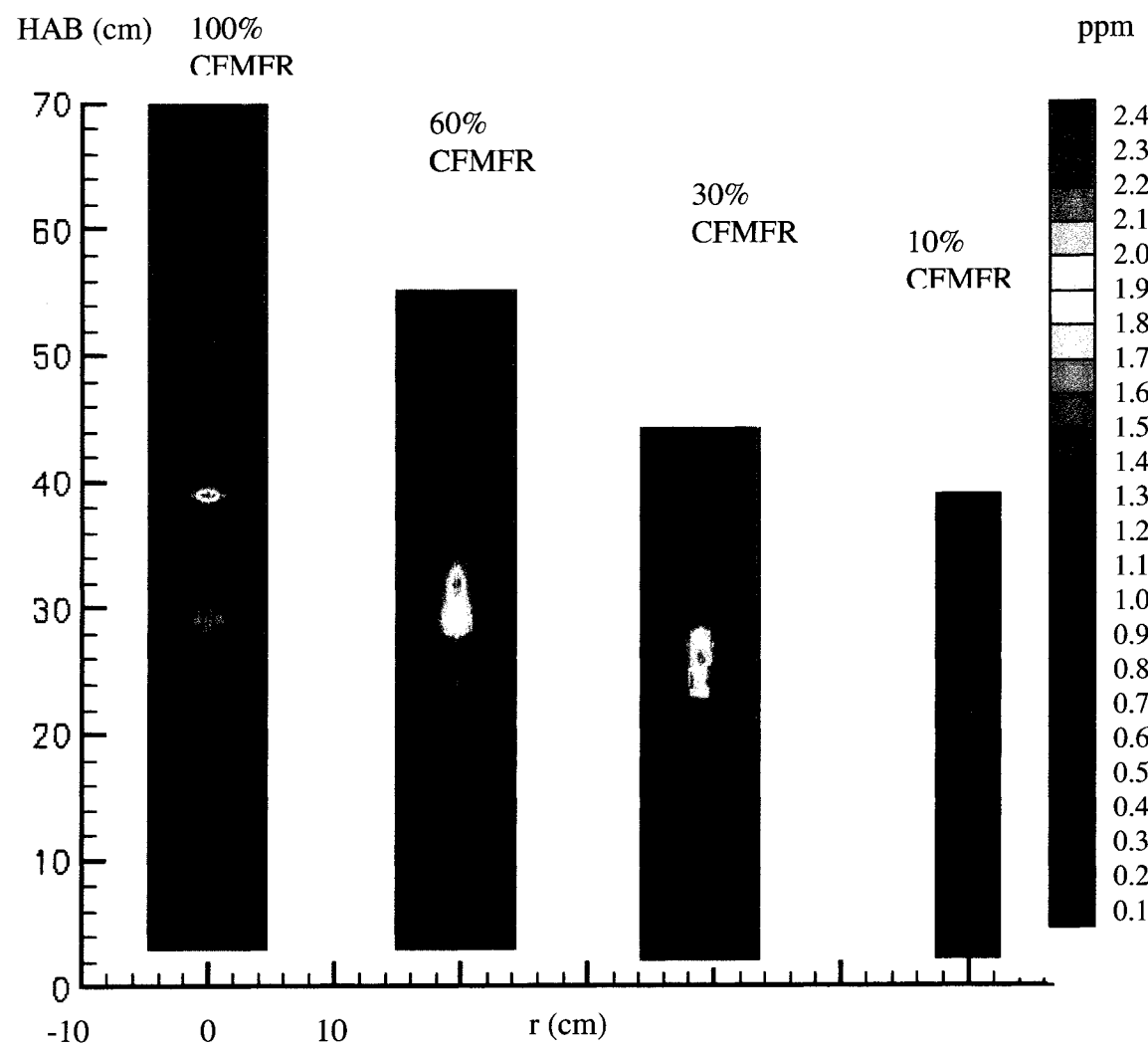


Figure 4.13 2-D View of Soot Concentration Profiles

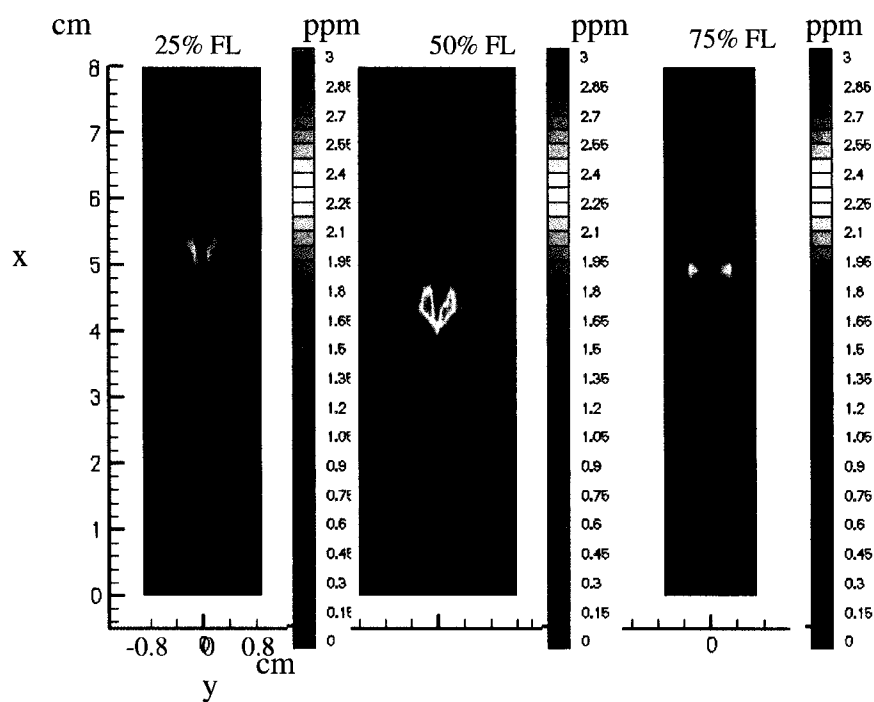


Figure 4.14a Tomographic Plot of Soot Concentration at Three Flame Locations for 10% CFMFR Flame at 2.0 m/s Cross-Flow

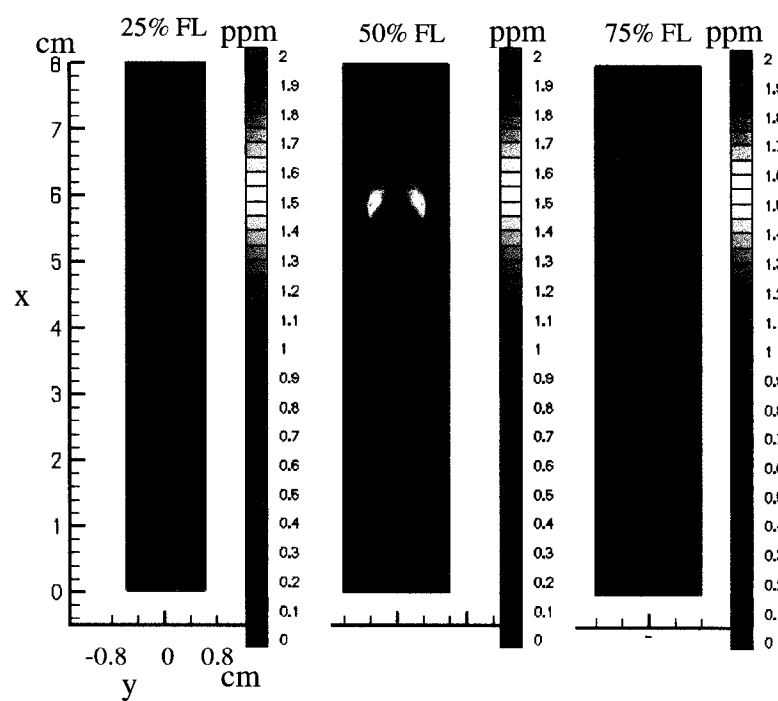


Figure 4.14b Tomographic Plot of Soot Concentration at Three Flame Locations for 20% CFMFR Flame at 2.0 m/s Cross-Flow

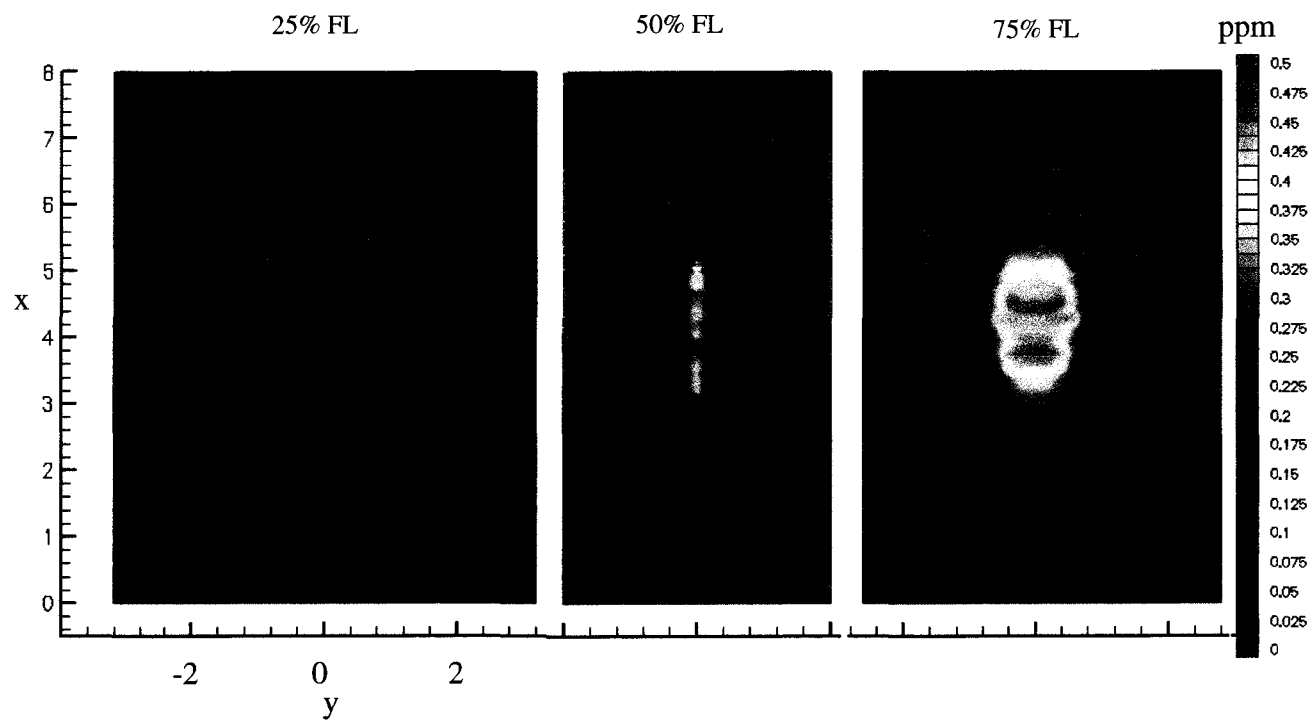


Figure 4.14c Tomographic Plot of Soot Concentration at Three Flame Locations for 60% CFMFR Flame at 2.0 m/s Cross-Flow

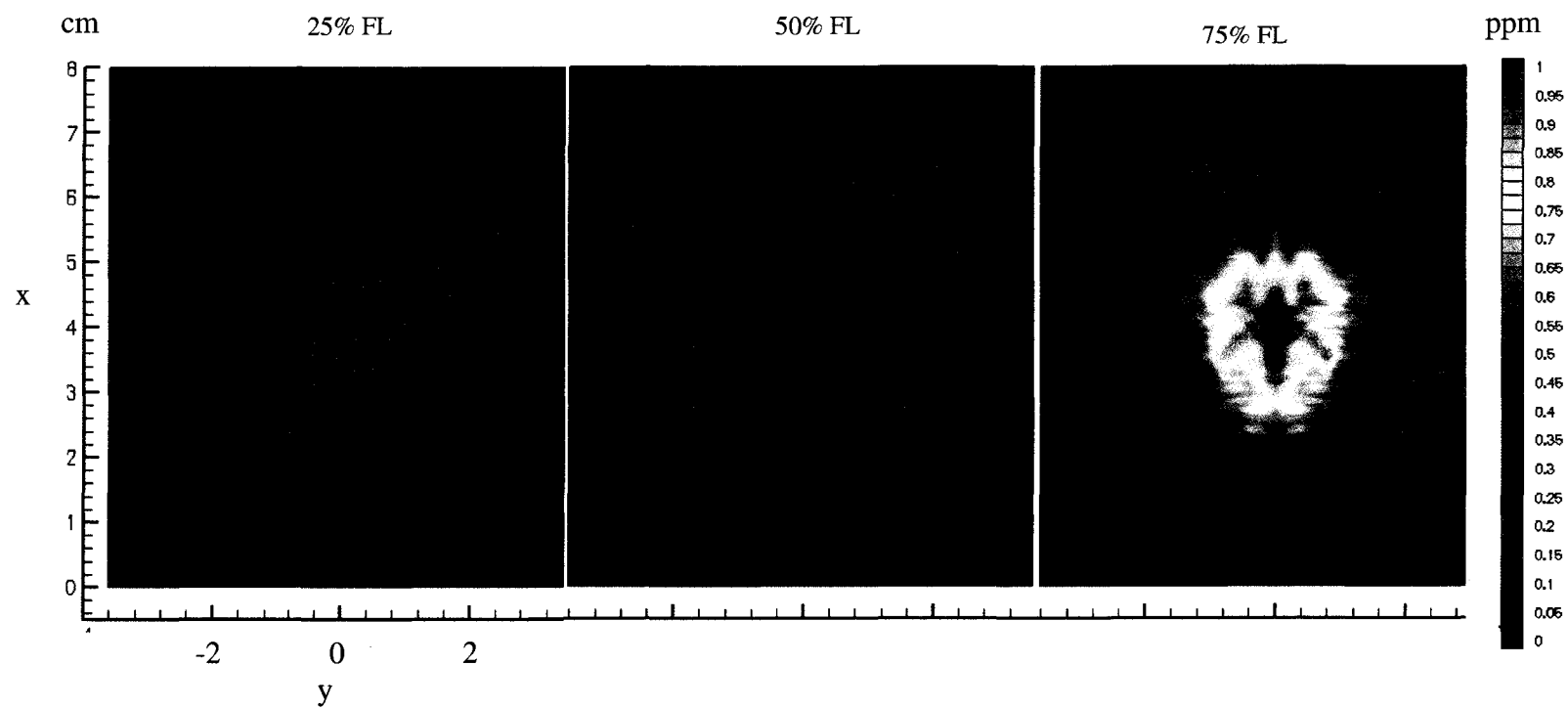


Figure 4.14d Tomographic Plot of Soot Concentration at Three Flame Locations for 100% CFMFR Flame at 2.0 m/s Cross-Flow

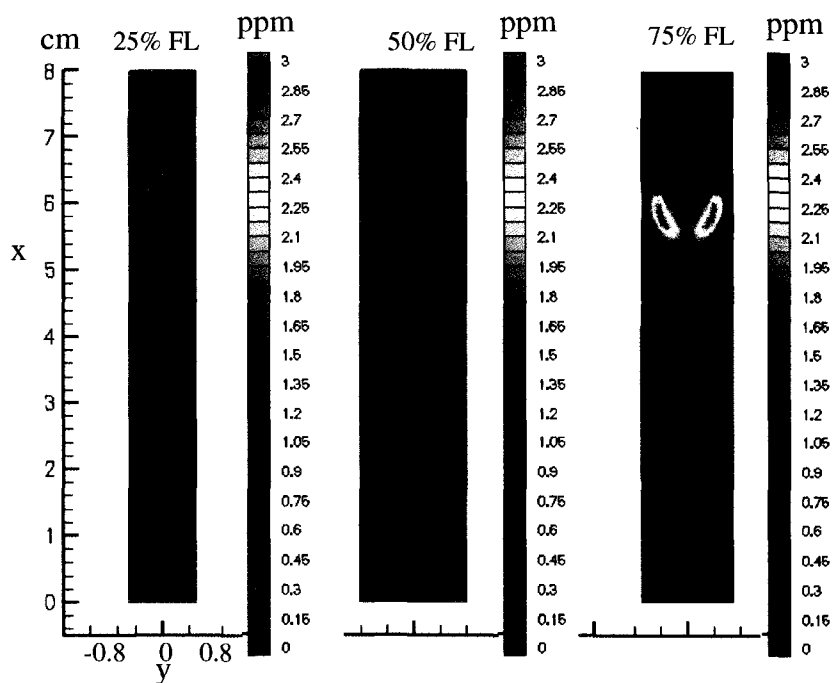


Figure 4.15a Tomographic Plot of Soot Concentration at Three Flame Locations for 10% CFMFR Flame at 3.0 m/s Cross-Flow

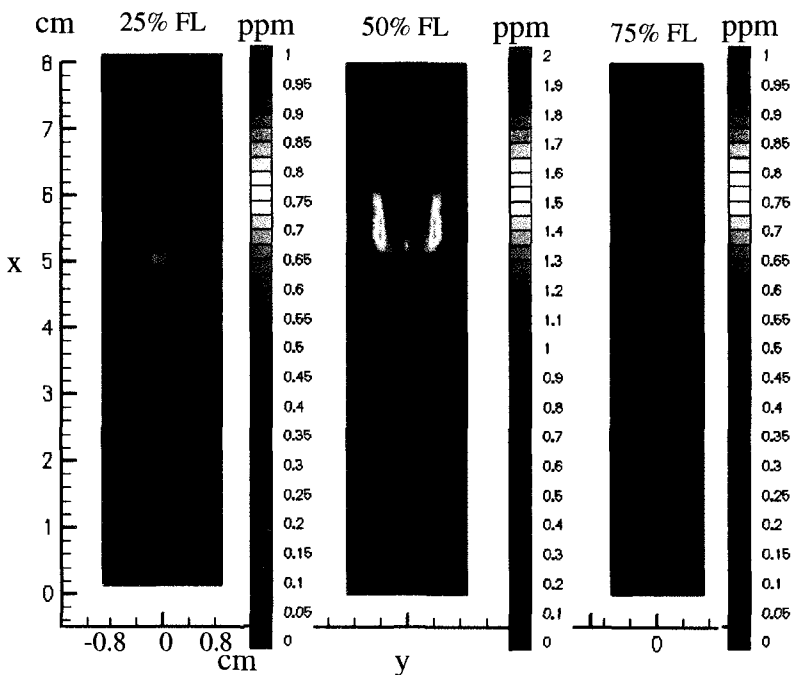


Figure 4.15b Tomographic Plot of Soot Concentration at Three Flame Locations for 20% CFMFR Flame at 3.0 m/s Cross-Flow

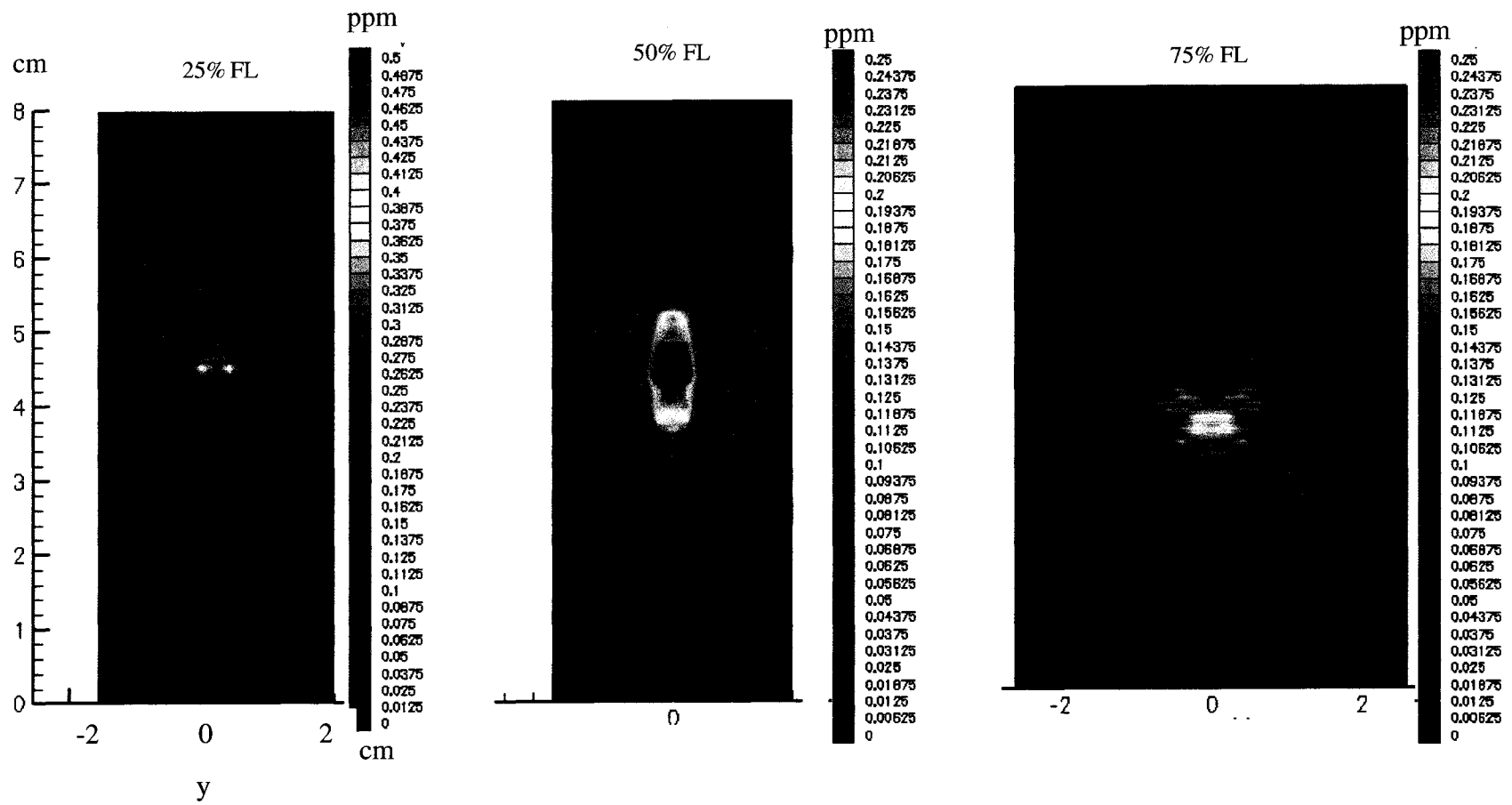


Figure 4.15c Tomographic Plot of Soot Concentration at Three Flame Locations for 60% CFMFR Flame at 3.0 m/s Cross-Flow

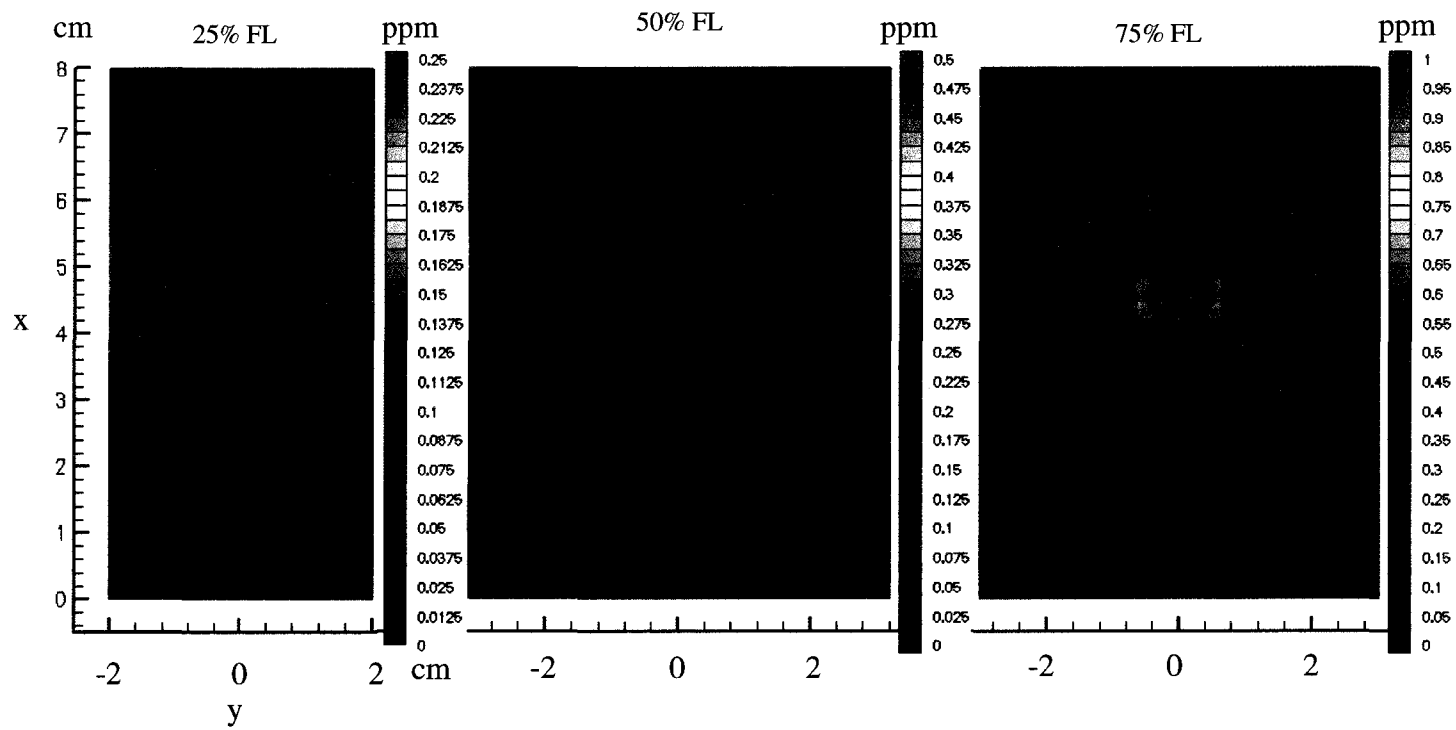


Figure 4.15d Tomographic Plot of Soot Concentration at Three Flame Locations for 100% CFMFR Flame at 3.0 m/s Cross-Flow

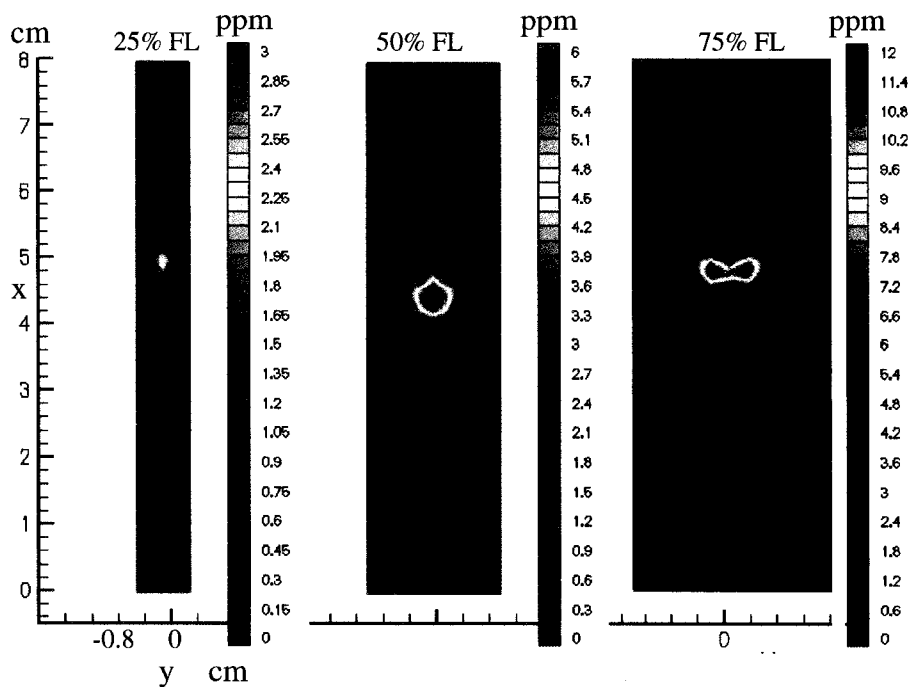


Figure 4.16a Tomographic Plot of Soot Concentration at Three Flame Locations for 10% CFMFR Flame at 4.0 m/s Cross-Flow

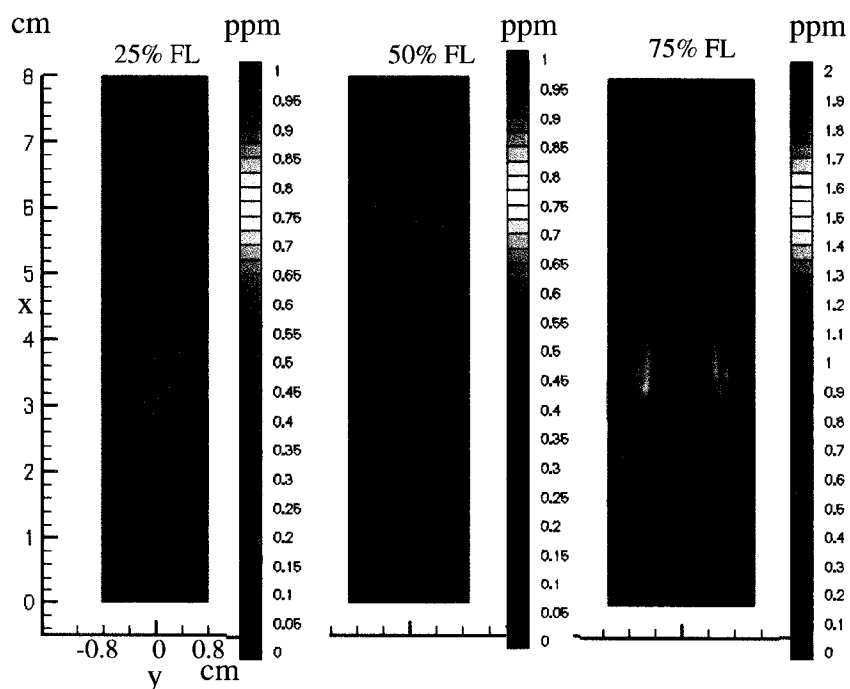


Figure 4.16b Tomographic Plot of Soot Concentration at Three Flame Locations for 30% CFMFR Flame at 4.0 m/s Cross-Flow

NOTE TO USERS

Page(s) missing in number only; text follows. Page(s) were scanned as received.

211

This reproduction is the best copy available.

UMI[®]

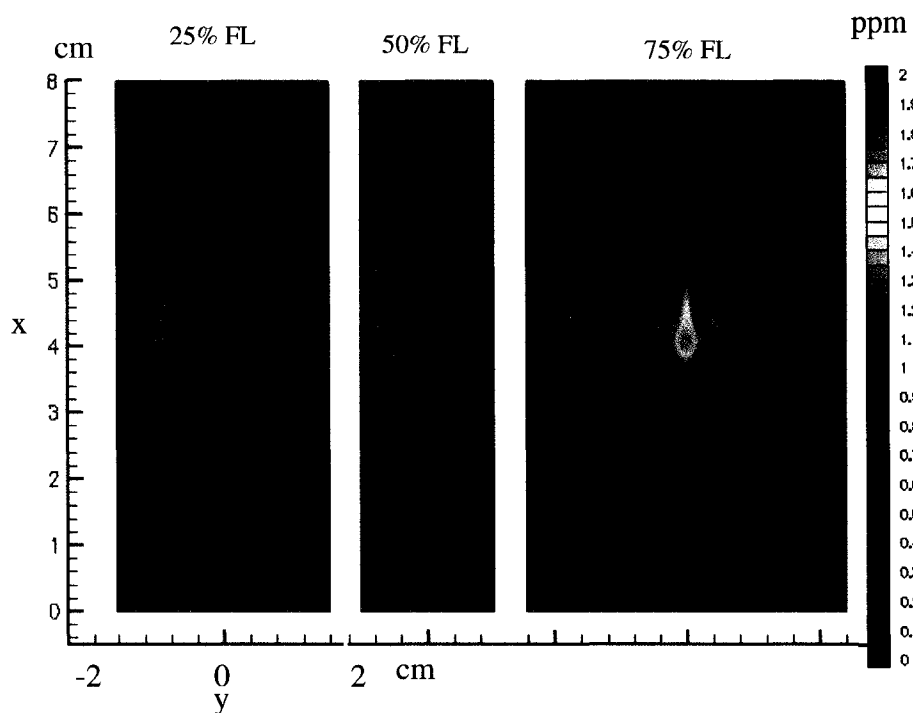


Figure 4.16c Tomographic Plot of Soot Concentration at Three Flame Locations for 60% CFMFR Flame at 4.0 m/s Cross-Flow

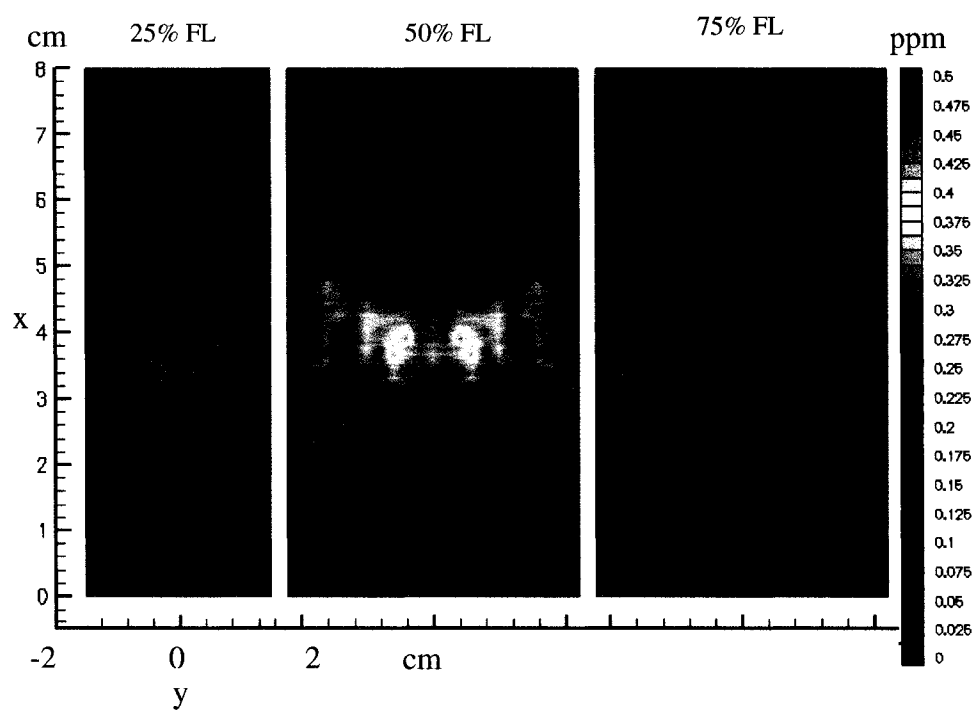


Figure 4.16d Tomographic Plot of Soot Concentration at Three Flame Locations for 100% CFMFR Flame at 4.0 m/s Cross-Flow

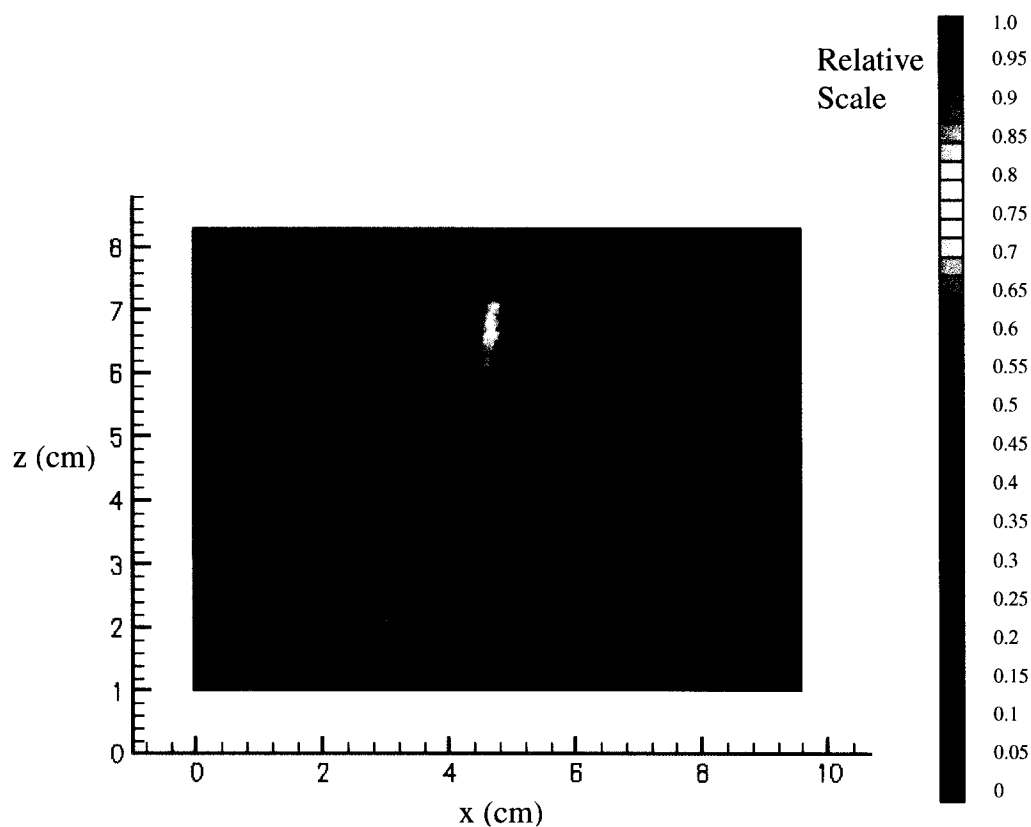


Figure 4.17a PLII for 10% CFMFR Flame at 2 m/s Cross-Flow in x-z Plane

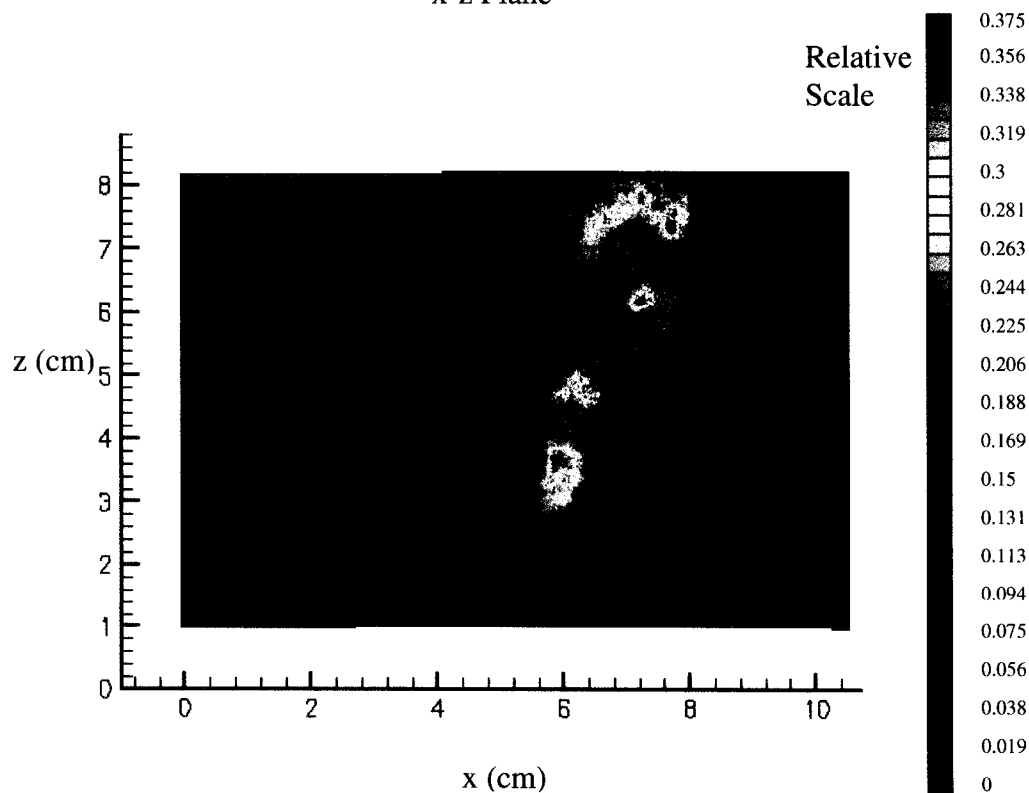


Figure 4.17b PLII for 20% CFMFR Flame at 2 m/s Cross-Flow in x-z Plane

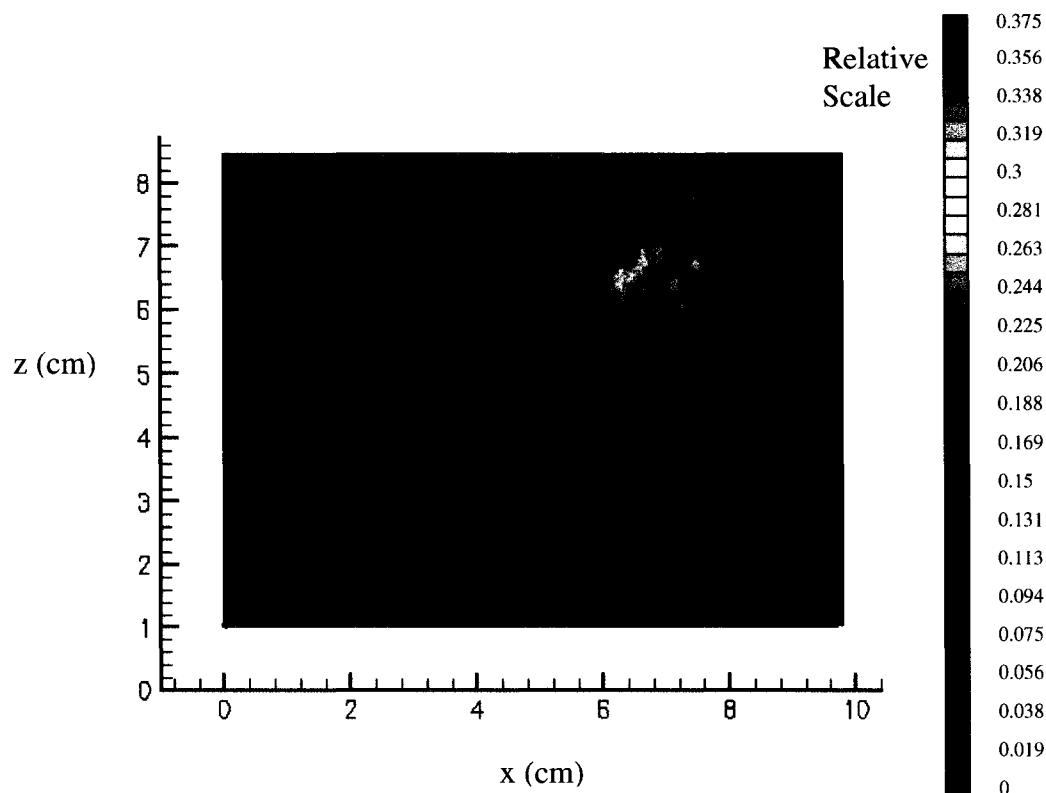


Figure 4.17c PLII for 60% CFMFR Flame at 2 m/s Cross-Flow in x-z Plane

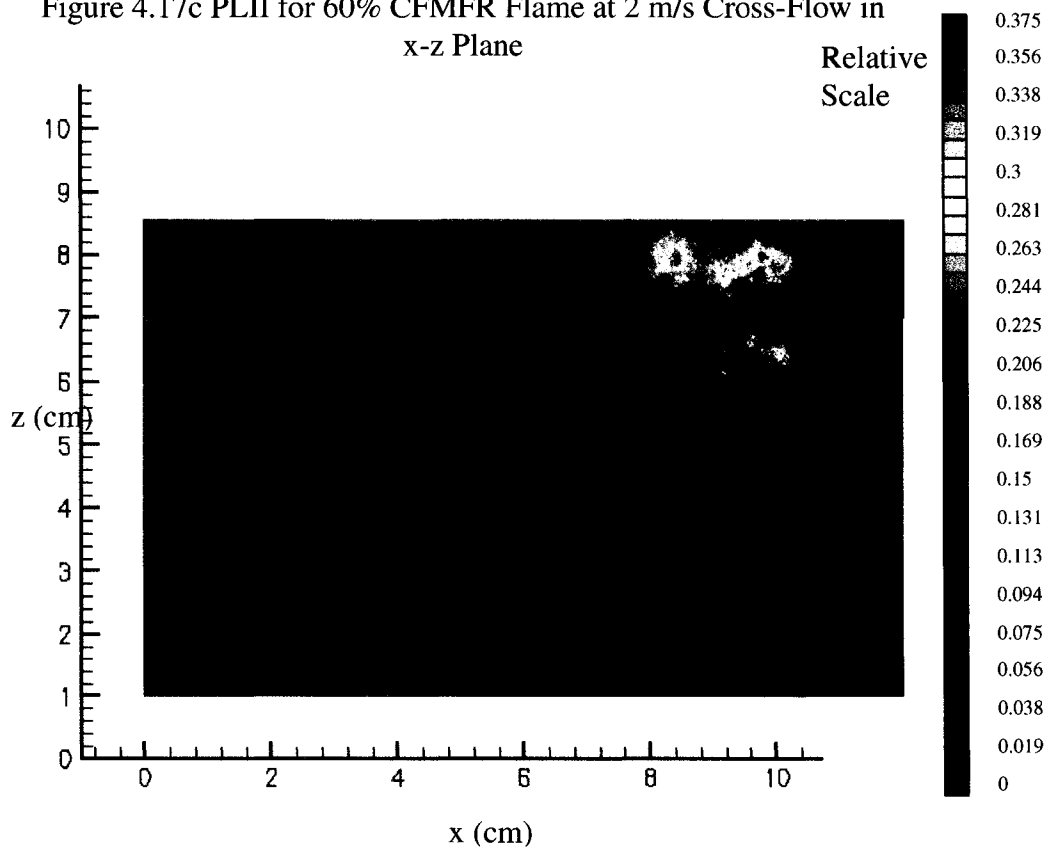


Figure 4.17d PLII for 100% CFMFR Flame at 2 m/s Cross-Flow in x-z Plane

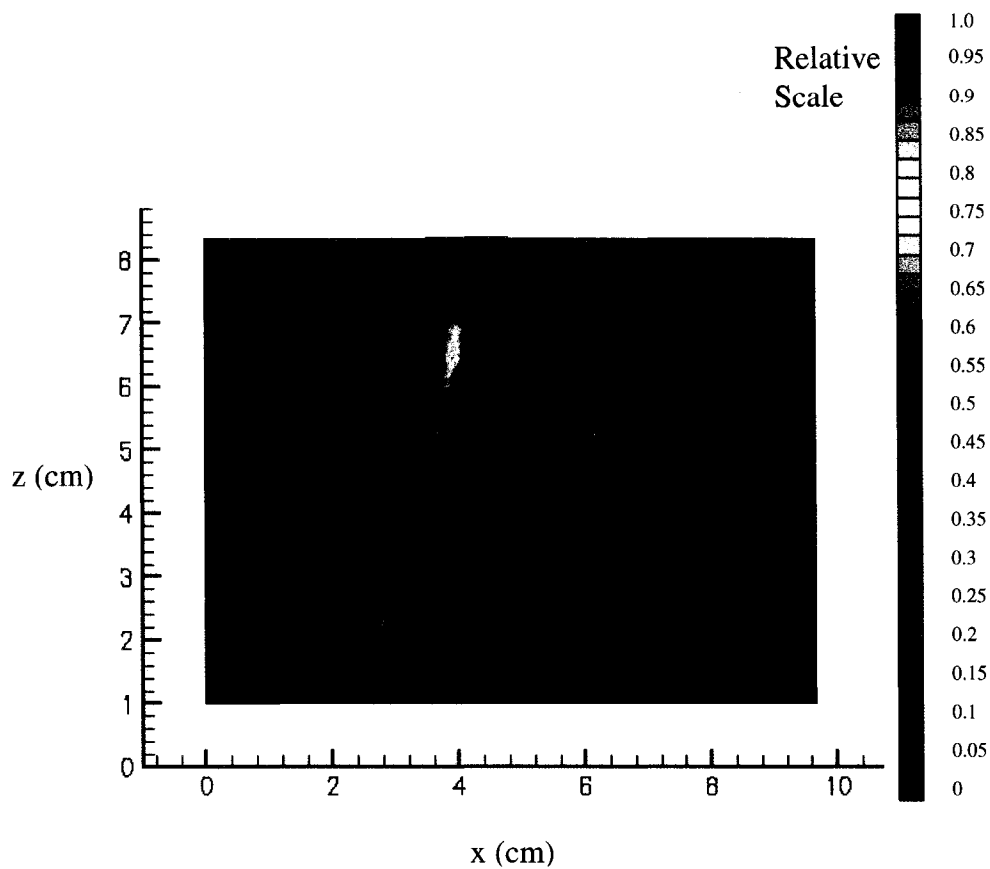


Figure 4.18a PLII for 10% CFMFR Flame at 3 m/s Cross-Flow in x-z Plane

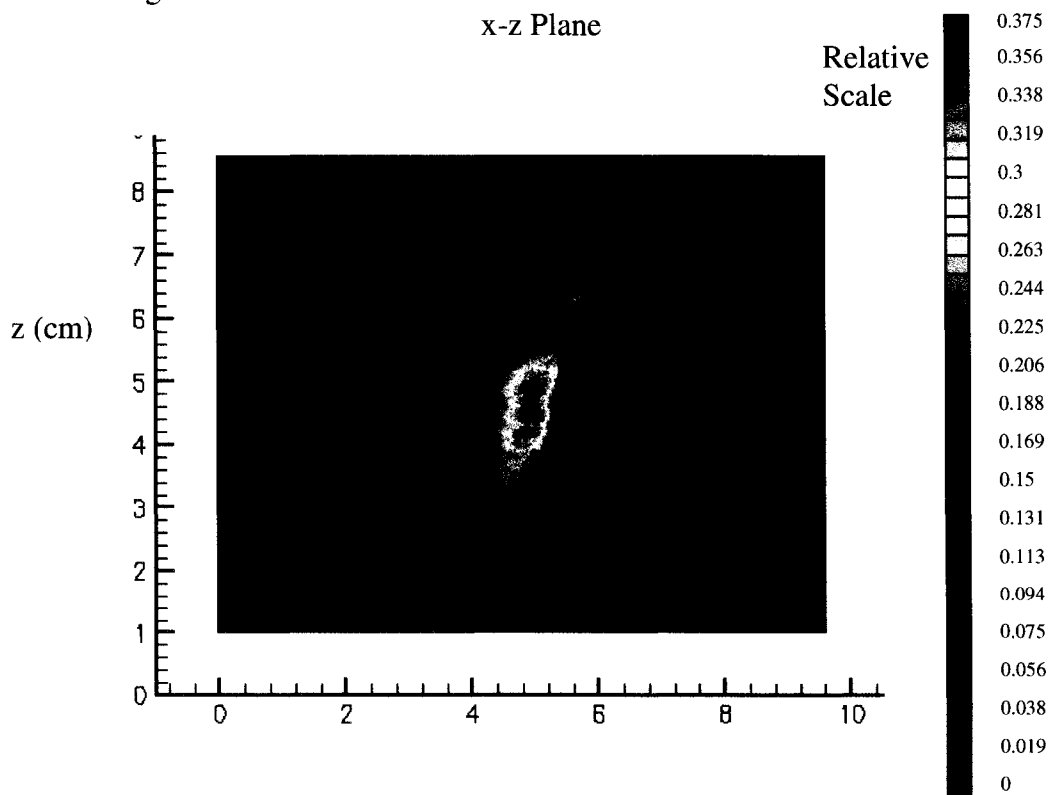


Figure 4.18b PLII for 20% CFMFR Flame at 3 m/s Cross-Flow in x-z Plane

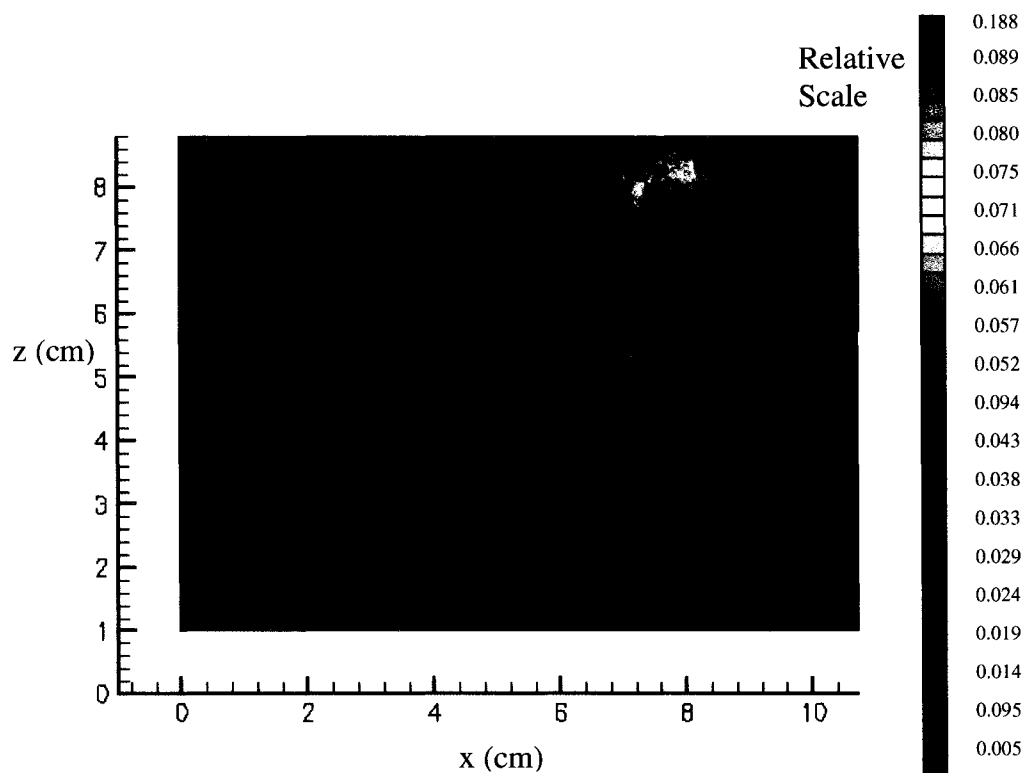


Figure 4.18c PLII for 60% CFMFR Flame at 3 m/s Cross-Flow in x-z Plane

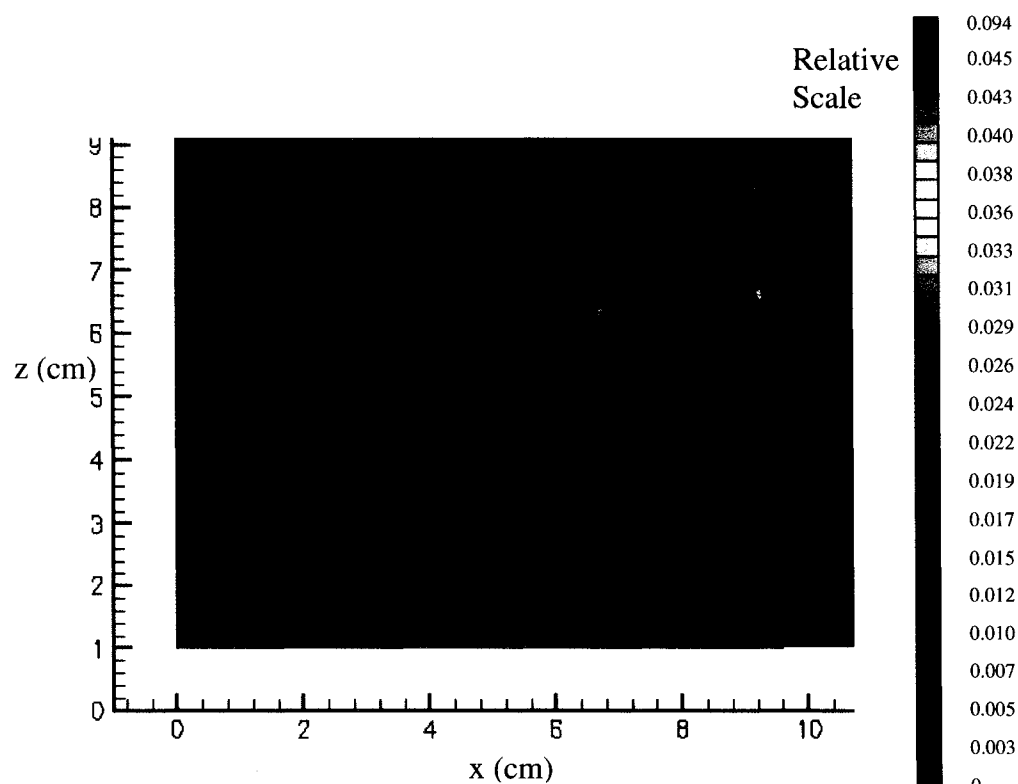


Figure 4.18d PLII for 100% CFMFR Flame at 3 m/s Cross-Flow in x-z Plane

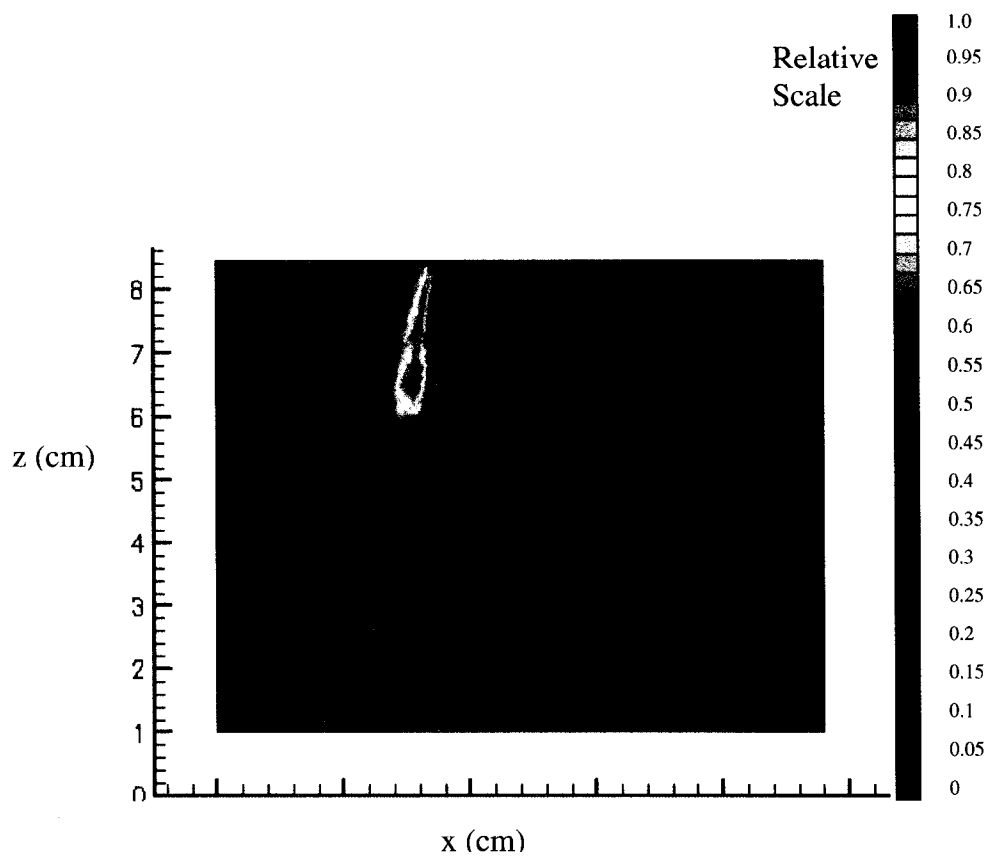


Figure 4.19a PLII for 10% CFMFR Flame at 4 m/s Cross-Flow in x-z Plane

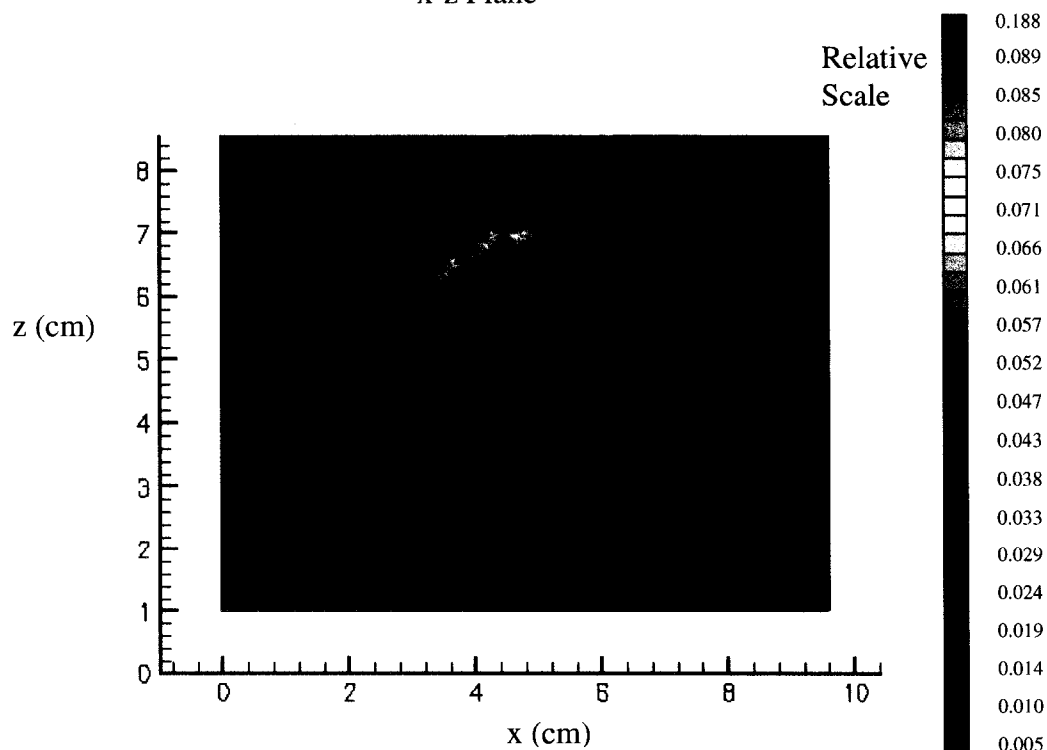


Figure 4.19b PLII for 30% CFMFR Flame at 4 m/s Cross-Flow in x-z Plane

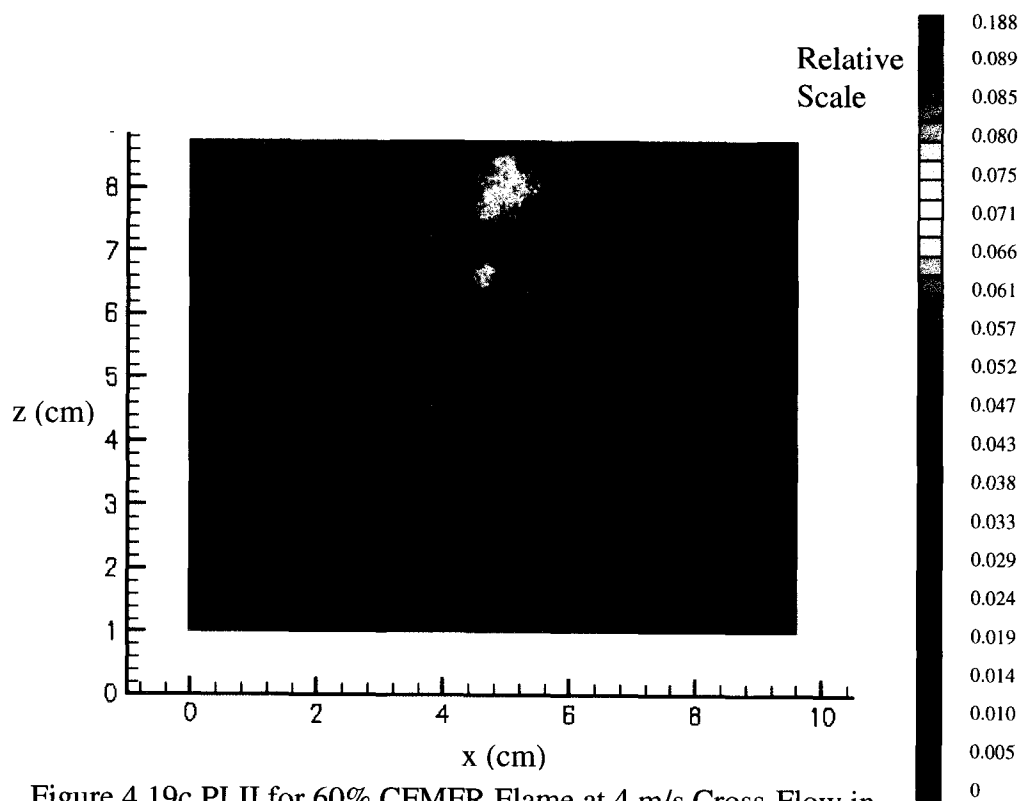


Figure 4.19c PLII for 60% CFMFR Flame at 4 m/s Cross-Flow in x-z Plane

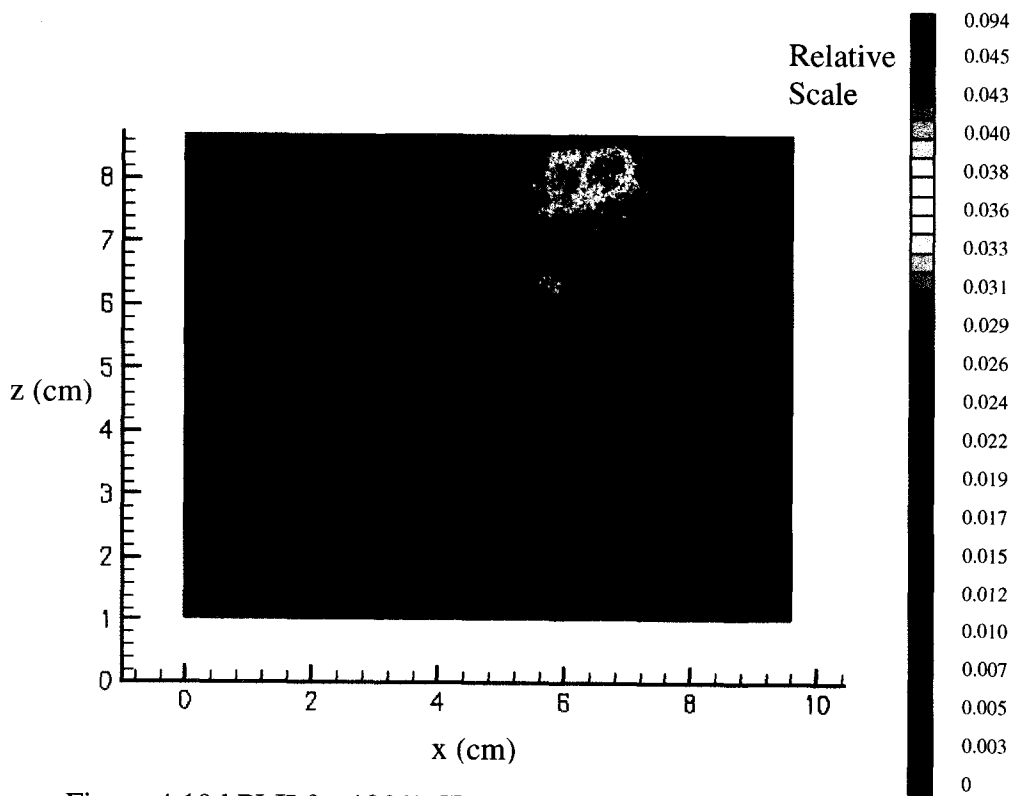


Figure 4.19d PLII for 100% CFMFR Flame at 4 m/s Cross-Flow in x-z Plane

Chapter V

Laser Induced Fluorescence Measurement

Nomenclature

A_{12}	Einstein spontaneous emission
B_{ge}	Einstein B coefficient
C_{exp}	Experimental constant from the optics and the detection setup
C_{SV}	Stern-Volmer coefficient
c	Speed of light
I_L	Incident of the laser beam
h	Plank's constant
l_{flame}	Flame length
n_A	Total number of photon lost
n_e	Number of photons emitted in a laser beam
n_{pe}	Detected LIF signal
P	Rate of predissociation of excited molecules
Q_C	Rate of collisional quenching
S	Rate of stimulated emission by the intense laser beam
T	Temperature

Greek symbols

ν_{ge}	Transition frequency
χ_o	Mole fraction of the probe species
η	Quantum efficiency or the detection efficiency

η_D	Detection efficiency
η_T	Transmission efficiency
Δl	Beam path
$\Delta\nu$	Absorption bandwidth
β_{ge}	Boltzman fraction
σ_{ge}	Absorption cross section
Ω	Collection solid angle

Subscript

g	Ground state
e	Excited state
i	Collider species,
x	Measured species

5.1 Introduction

One of the most developed resonant techniques is Laser-induced fluorescence (LIF). The purpose of LIF is to find out the population density of selected quantum states and the thermodynamic properties of the test medium. A specific narrow band laser is used to selectively excite the atom or molecule to a specific vibrational and electronic level from its original state. The fluorescence emission from the population of the excited species is proportional to the total density of the population of probed species at the ground state. In a typical LIF experiment, the energy state of the subjected species is illustrated in Figure 5.1. A narrowband laser source with photon energy $h\nu_{ge}$ matches the

energy difference between the ground state g and the excited state e . The excited species may spontaneously undergo relaxation to any of the lower states, which are represented by 1 to 3 (although in a real case it may involve tens or even hundreds of energy levels) in Figure 5.1, by emitting a photon. However, the species may lose its energy or remove from the upper state through dissociation, ionization, stimulated emission, or collisional quenching. Ionization process occurred when the provided energy is sufficiently high, then the molecule may lose electrons and become ionized. Stimulated emission occurs when the molecule collides with a photon and it is forced to release its energy. Collisional quenching is the exchange of energy through collision with another object. Since every transition is unique, the LIF process can be modeled as an isolated radiative interaction consisting of a separated two-level system (Laufer, 1996).

OH radical is a very good indicator for the flame reaction zone, where temperature is highest. In this study, OH radical is also used as an indicator for the chemical (kinetic) and the momentum (diffusion) dominance of the soot oxidation. Besides molecular O_2 oxidation of soot particle, other molecule species are also very important in the process of soot oxidation, such as H_2O , CO_2 , and NO (Tesner, 1967). Other studies also found that OH radical is the major soot oxidant (Mulcahy and Young, 1975). Garo, et al. (1990) in their laminar flame study found that in the zone where solid carbon disappears, OH radical decreases, and O_2 dominates the soot oxidation process.

5.2 Experimental Techniques

The laser equipment used for LIF and PLIF measurement consisted of a Quanta-Ray GCR 250 pulse Nd:YAG laser, a Quanta-Ray MOPO-730 Optical Parametric

Oscillator (OPO) with Frequency Double Option (FDO). GCR 250 provided a pumped laser beam at 355 nm to OPO. An adjustment of OPO crystal angle provided tuning of the laser for various wavelengths. MOPO-730 with FDO has a tunability range of 190 nm to 2000 nm. The OPO crystal used in MOPO-730 is Type I phase-matched Beta Barium Borate (BBO), which is a nonlinear gain medium. The gain of an OPO system is derived from the nonlinear interaction between an intense optical wave and crystal having a large nonlinear polarizability coefficient. The OPO used in this experiment was a coupled dual oscillator system where a high energy power oscillator was injection-seeded with the narrow output from a master oscillator. This enabled the coupled oscillator system to produce a narrow bandwidth, high-energy, coherent radiation. The precise orientation of the crystals for various specific wavelengths was controlled by a MOPO controller.

The output laser from the OPO was focused on a 570 mm focal length fused silica best-form laser-focusing lens. Along the laser beam, a beam splitter deflected 50% of the output beam to a pyroelectric power meter to monitor the incident beam energy. The continuous monitoring of the incident beam was used to normalize the measurements for accounting for pulse-to-pulse power variations. The fluorescence signal was collected at right angle to the incident beam using a Princeton Instruments Model ICCD-576-G/RB-E Intensified Charge Coupled Device (ICCD) camera. A focusing lens was placed in front of the camera to focus the image on the ICCD array. A narrow band filter for each specific fluorescence signal was placed prior to entry of the camera to reduce the stray incident radiation and to increase signal-to-noise ratio. The data collection method was the same as in the LII method. The schematic diagram of LIF measurement setup is shown in Figure 5.2.

For OH measurement, a frequency-doubled output (285.265nm) of the OPO was used to induce fluorescence (Battles, et. al. 1994). At this wavelength, OH was pumped at the $Q_1(6)$ transition in the OH $A^2\Sigma \leftarrow X^2\Pi$ system of the (1,0) band and the fluorescence from the (1,1) band was collected (Hanson, 1986). For all the measurements, a beam size with diameter of 1 mm was used.

The turning mirror, beam splitter and pyroelectric power meter were mounted on a traverse mechanism. On the detection side, the ICCD camera along with the focusing lenses and the narrow band pass filter were mounted on a similar traverse mechanism for horizontal movement, and vertical movement was enabled by raising the height of the stand. The optical arrangement was traversed along the height of the flames to measure the axial concentration profiles of the radicals for quiescent condition flames and planar laser induced fluorescence (PLIF) measurement for cross-flow flames.

Planar Laser Induced Fluorescence (PLIF) images were collected in a similar fashion as in the LIF method. The difference was that PLIF experimental setup applied a laser sheet, rather than a single laser beam. The laser sheet created a 2-D field of radical fluorescence. A cylindrical lens was mounted after the last turning mirror to generate the laser sheet. Due to the Gaussian nature of the laser beam, the sheet generated was also Gaussian. Hence, if the full sheet is used, the PLIF images will be misrepresented with higher intensity at the center of the sheet. In order to reduce the effect of the Gaussian distribution, a slit was placed after the cylindrical lens to limit the sheet length to 2 cm and the sheet width of 1.5 mm at the center of the flame. In quiescent condition flames, PLIF images were captured from burner tip to about 60% of flame length. In cross-flow flame, the PLIF images were captured up to 8.5cm from the burner, which was about half

of the 100% CFMFR flame length for all cross-flow conditions. The PLIF results presented were the composite images of a number of PLIF images. The results are presented as normalized signal intensity, which gives a qualitative representation.

This 2-D fluorescence field was then captured by an ICCD camera. This image was acquired and processed with a data-acquisition computer using WinSpec software. For all flame conditions, both the resonance and the off-resonance (explained in next paragraph), a total of fifty images were collected and were averaged.

LII signal interference can be significant in a high soot concentration region. Figure 5.3 shows the signal of both LII signal and OH signal. In order to isolate the interference signal of LII and other species, a second set of data was obtained with an off-resonance frequency (285.285 nm) laser. The OH signal was the result of the subtraction of the signal at the resonance frequency and the signal of the off-resonance frequency. With this method, both LIF and PLIF results presented below are isolated from LII and other species interference.

5.2.1 OH Quantification

For a diffusion flame in atmospheric condition, only 3 out of 1000 excited OH radicals lose energy through fluorescence, and the rest of the molecules lose their energy through collisional quenching with ambient gases (Tamura et. al 1998). The domination of LIF quantum yield by the collisional quenching can be avoided through advanced experimental setup. For instance, a short and prompt electronic gate to detect the fluorescence promptly after the laser pulse before significant quenching happened. However, this method only works for low-pressure combustion. Another method is the

direct measurement of the fluorescence decay rate. Nevertheless, this method requires a pico-second experimental technique, which is not commonly applied. The method applied an excitation of a predissociating transition where the predissociation is much faster than the collisional quenching. This method also suffered a setback by the experimental complications (Tamura et. al 1998). The commonly used method for OH and other radicals measurement using LIF is the direct calculation or estimation of the quenching rate at the location of the measurement to determine the quantum yield. This method required the knowledge of quenching rate and concentration of species involved. Beside that, this method is relatively less complicated and more feasible. The concentration and the local flame temperature can be obtained from the numerical results.

There are four basic requirements that must be satisfied to achieve the quantification of the fluorescence of a species. First, the emission spectrum of the species must be known. Secondly, a tunable laser source is required to provide the wavelength to excite the species. Thirdly, it is required to know the rate of radiative decay of the excited species. This is because the fluorescence power is proportional to this rate. The fourth requirement is that the loss due to dissociation, ionization, and collisional quenching has to be taken into account (Eckbreth, 1998)

5.2.2 Spectroscopic Modeling

In Laufer (1996), the LIF signal can be quantified with following expression

$$n_{pe} = C_{exp} \times n_A \times C_{SV} \quad [5.2.1]$$

The total number of photons lost (or absorbed by the species) by the incident laser beam by absorption while traveling through a sample element of length of Δl , which is the flame width the laser traveled in the experiment is

$$n_A = \frac{I_L}{h\nu_{ge}} \chi_o \beta_{ge} \sigma_{ge} \Delta l \quad [5.2.2]$$

Hence, n_A is the number of photons which is equal to the number of molecules excited along Δl of the laser beam, I_L is the incident of the laser beam, σ_{ge} is the absorption cross section, h is the Plank's constant, is the transition frequency, χ_o is the mole fraction of the probe species. The population density is represented by β_{ge} , the Boltzman fraction, which is the fraction of χ_g/χ_o , of the tested species that is in the probe state. The subscribed g and e are for ground state and excited state.

As mentioned in the introduction section, in the application of LIF, the energy lost is not limited to spontaneous emission. Collisional quenching, dissociation, ionization and stimulated emission are also very important, especially in ambient diffusion flame, collisional quenching is very important. Stern-Volmer coefficient is an expression for the measured yield of LIF process. The coefficient is defined bellow (Laufer. 1996),

$$C_{SV} = \frac{A_{21}}{A_{21} + P + Q_C + S} \quad [5.2.3]$$

A_{12} is the Einstein spontaneous emission for a specific transition. P is the rate of predissociation of excited molecules. Stimulated emission by the intense incident beam may further deplete the excited state at a rate of S (saturation). Q_C is the rate of collisional quenching. The multiplication of the number of excited molecules, n_A by SV is the number of emitted photons. The number of photons emitted in a laser beam volume of a slice of Δl is n_e .

$$n_e = n_A \times C_{SV} = \frac{I_L}{h\nu_{ge}} \chi_o \beta_{ge} \sigma_{ge} \Delta l \frac{A_{21}}{A_{21} + P + Q_C + S} \quad [5.2.4]$$

Most of the emitted photons are unable to be detected because of the loss through the optical components like the aperture size, the filter or the camera and the detector quantum efficiency. C_{exp} is the experimental constant from the optics and the detection setup.

$$C_{exp} = \left(\frac{\Omega}{4\pi} \eta_T \eta_D \right) \quad [5.2.5]$$

Ω is the collection solid angle, η_T is the transmission efficiency of the filter, η_D is the quantum efficiency or the detection efficiency of the camera. This quantum efficiency is a quantum mechanical property of the photocathode that specifies the fraction of the conversion incident photons into electrons through photoelectric effect.

Hence, the final expression for the detectable signal in photoelectrons is (Laufer, 1996),

$$n_{pe} = \left(\frac{\Omega}{4\pi} \eta_T \eta_D \right) \frac{I_L}{h\nu_{ge}} n_o \beta_{ge} \sigma_{ge} \Delta l \frac{A_{21}}{A_{21} + P + Q_C + S} \quad [5.2.6]$$

The absorption coefficient is defined as

$$\sigma_{ge} = \frac{B_{ge} h\nu_{ge}}{c\Delta\nu} \quad [5.2.7]$$

where B_{ge} is Einstein B coefficient, which is an absorption coefficient. c is the speed of light and $\Delta\nu$ is the absorption bandwidth. In the linear regime, predissociation and saturation effect is trivial. Hence, P and S is very small compare to A_{21} and Q_c , so they are assume zero in the calculation (Hanson et al., 1990, Eckbreth, 1996).

OH Collisional Quenching Calculation

Since there are many species involved in the collisional quenching, the rate of collisional quenching Q_C is expressed as the summation of the collider species, i mole fraction with the rate of quenching of measured species, x with the collider species, q_{ix} (Garland and Crosley, 1986).

$$Q_C = \sum_i n_i q_{ix} \quad [5.2.8]$$

Quenching rate of OH as studied extensively by Paul et al. (1994a) and Tamura et al. (1998). Both studies result in cross sections for OH-A- state quenching, σ_∞ are shown in Table 5.1. With the parameters a_i and σ_∞ for each species and the temperature from the numerical results, the quenching rate for each collider can be calculated by following formulation (Tamura et. al 1998).

$$q_{ix} = a_i \sigma_q T^{0.5} \quad [5.2.9]$$

The empirical relation for the temperature dependence of the cross section for OH quenching is expressed below with the constants, a_i for each species listed in Table 5.1 (in unit of $10^{-13} \text{ cm}^3 \text{ s}^{-1}$).

$$\sigma_q = \sigma_{Q_\infty} \exp\left(\frac{\varepsilon}{kT}\right) \quad [5.2.10]$$

This expression is the application for a wide range of flame temperatures.

The quantification modeling was performed with the above method. Tamura et al. (1998) OH collisional quenching parameters were used in the calculation, since both Tamura et al. (1998) and Paul et al. (1994a) parameters do not make a significant difference in OH concentration results. The concentrations of the quenching species and the temperature were taken from the numerical results (Chapter VI). Choudhuri's (2000)

study shows that the OH concentration calculated using the measured (Raman measurement) and the computed (local equilibrium model) quenching species concentration do not have a significant difference (within the uncertainty). The uncertainty for the OH concentration measurement was calculated from the peak LIF fluorescence reading of the 60% CFMFR flame at 3 m/s cross-flow result, and it is about $\pm 2.43 \times 10^{-6}$ mole/m³ or ± 5.8 % of the average value (4.23×10^{-5} mole/m³).

5.3 Results and Discussions

The results presented below will discuss importance of the OH and the O₂ in oxidizing the soot particle. The discussion will focus on substantiating the characterization of the chemically and momentum domination regions in the flame. In a diffusion flame, OH radical is reaction rate dependent; on the other hand, O₂ is diffusion rate dependent. Hence, the comparison of the OH and O₂ domination of soot oxidation in the flame provides an evident of the analogy of the chemical and momentum dominance of the flame. However, the reaction rates of OH and O₂ are very different. OH radical is more reactive than the O₂ molecule in soot oxidation process (Fenimore and Jones, 1967; Mulcahy and Young, 1975). Neoh et al. (1984) study showed that OH radical is more important than O₂ in the soot oxidation process in an atmospheric pressure flame at temperature range of 1580 to 1860K and in the O₂ mole fraction range of 10^{-5} to 0.05.

Quiescent Condition

The OH concentration in the flame at quiescent condition is shown in Figure 5.4. These axial tomographic plots of the measurement were made at one-centimeter increments along the axial direction of the flame. The 10% CFMFR flame result is

presented on a different scale, which is thirty times higher than the 30%, 60%, and 100% CFMFR flame results. The OH concentration shows dual peaks along most parts of the lower section of the flames. On the contrary, the turbulent flame soot concentration result at the quiescent condition (Figure 4.13) exhibits two-peak behavior only in the region close to the burner. However, in a laminar flame, the dual-peak structure of soot concentration is still visible at a height above 50% of the flame length.

The OH concentration in the 10% CFMFR flame was significantly higher than in the other CFMFR flames. This may be mainly due to the fact that the 10% CFMFR flame is a laminar flame. In the momentum-dominated region, the 60% CFMFR flame OH concentration result shows a higher value than the 100% CFMFR flame. The results show that the 10% CFMFR flame has its peak at around 15 cm ($x/l_{flame} = 0.48$) of the flame length, 30% CFMFR flame OH concentration peak was at 17.5 cm ($x/l_{flame} = 0.39$), and 60% and 100% CFMFR flame OH concentration peak were at around 33 cm ($x/l_{flame} = 0.58$) and 18 cm ($x/l_{flame} = 0.25$).

Figure 5.4 shows that the OH radical concentration (with the scale provided) extends up to about 80% of the flame length for 30% CFMFR flame, 65% and 27% of the flame length for 60% and 70% CFMFR flame. The 10% CFMFR flame result shows that the OH concentration extends further than 80% of the flame length if the result is plotted on the same scale as the 30%, 60%, and 100% CFMFR flame results. This observation shows that the OH influence on the soot oxidation extends further downstream of the flame for the low CFMFR flame. In other words, OH radical dominates the soot oxidation in the chemical-dominated flame. The oxidation of soot by the O_2 molecule may come into play at the very end of the flame for the chemical-dominated flame, which

agrees with laminar flame studies by Neoh et al. (1984) and Garo et al. (1990). For a laminar diffusion flame, the OH continues to dominate the soot oxidation process until the O_2 concentration is sufficiently high. Oxygen (O_2) is intrinsically less reactive than OH radical, so the O_2 molecule is able to penetrate deeper into pores in the soot particles or open spaces within the aggregates. This effect increases the internal burning in the soot particle. The combination of the internal oxidation of the soot particle (by O_2) and the surface regression caused by the external oxidation (by OH) leads to the breakup of the soot particle. The breakup occurs only after 80% of the initial mass had been oxidized (Neoh et al., 1984 and Garo et al., 1990). Figure 4.13 also shows that the high soot concentration for the 10% CFMFR flame is located around 80% of the flame length. Hence, slightly further downstream of this region, the soot particles may start the breakup process. This discussion also provides an argument that the significant of O_2 oxidation of the soot particle is located slightly upstream of this region. Figure 3.33d shows that at 25% and 50% of the flame height, the O_2 concentration at the center of the flame is 2.5% and 5.5% respectively; and at 75% of the flame length, the in-flame O_2 concentration is slightly above 10%. According to Neoh et al. (1984), OH dominates the soot oxidation process in region with O_2 mole fraction of 0.001% and 5%. The region of 50% to 75% of the flame length is the transition of OH to O_2 dominance of the soot oxidation process. Hence, the OH radical dominated most part soot oxidation process of the 10% CFMFR flame.

To further substantiate this argument, the soot concentration and the OH concentration of the flames were plotted radially in the same figure for half of the flame (Figure 5.5 and 5.6, a and b). These figures show the comparison of the OH and the soot

concentration for 10% and 60% CFMFR flames, each from the chemically and momentum dominated regions, at 25% and 50% of the flame height. The results show that the OH concentration in the 10% CFMFR flame is at the outer rim of the soot concentration for both the 25% and 50% of the flame length, which agrees with many OH concentration results for a laminar flame (Puri et al., 1992; Smyth et al., 1997). The OH concentration and the soot layer overlapping region is where the active soot oxidation occurred (Smyth et al., 1997). The 60% CFMFR flame result shows the same characteristic at the 25% flame length. However, at the 50% of the flame length, the OH concentration and the soot concentration do not show the same characteristics. At this location, the result shows the soot concentration has the peak at the flame center and the OH concentration still maintains a dual-peak profile. Though the OH peak is not as significant as the one at the 25% flame length and the 10% CFMFR flame results. In fact, the soot concentration at this location is almost the inverse of the in-flame O_2 concentration. The comparison of the soot and the O_2 concentration of the 60% CFMFR flame at 50% flame length is shown in Figure 5.6c. Furthermore, as discussed earlier, the soot layer and the OH concentration overlapping region is not present in this result, which means that the OH radical oxidation of soot in this flame location is not as significant as in the 25% flame length and the 10% CFMFR flame. Hence, at this region, the O_2 dominated the oxidation of soot particle rather than the OH radical.

According to Kent and Wagner (1984), the difference between a laminar flame and a turbulent flame at the region close to the burner is that the soot generation or oxidation is kinetically controlled for a laminar flame but it is diffusion control for a turbulent flame. At the high soot concentration region, both the laminar and the turbulent

flames are diffusion controlled by oxygen containing species (Kent and Wagner, 1984). In this study, the oxygen containing species for the 10% CFMFR flame is OH radical and the 60% CFMFR flame is O₂ molecule. Soot particle in the 60% CFMFR flame has to compete with CO for OH radicals. The 60% CFMFR flame has a lower flame temperature at the 50% flame length and was mainly due to the high soot concentration. Soot particle radiative heat loss reduces the flame temperature, which enhances CO formation by reducing its oxidation rate (Puri et al. 1992). This is the reason that at 50% flame length of the 60% CFMFR flame, the CO concentration was higher (Figure 3.31b) than the 10% CFMFR flame results (Figure 3.31d). Higher CO concentration reduced the availability of OH radical to react with soot particle, which increased the importance of O₂ molecule in soot oxidation.

Cross-Flow Condition

Figures 5.7, 5.8, and 5.9 show the tomographic plots of OH concentration on the x-y plane. The OH measurements were done in a similar fashion as in the LII measurement in Chapter IV. However, only the 25% flame height plane was measured, because above that height, the OH concentration was scarce. From the observation in the PLIF results (Figure 5.13, 14, 15), the OH concentration beyond 30% of the flame height for a highly turbulent flame is hardly detectable. Most of the OH concentration profiles also exhibit a kidney or a horseshoe shaped structure. Most of these results show a high OH concentration at the outer rim and the center of the flame. These were the areas of active reaction, where O₂ from the air reacts with the hydrocarbon. The high OH

concentration at the center was mainly due to the CVP (counter rotating vortex pair) effect, which enhanced the mixing and reaction rate (as discussed in Chapter III).

From the results of the 10% CFMFR flames, the 4m/s cross-flow flame has the highest OH concentration than the rest of the cross-flow flames. Chapter III results (Figure 3.22a to k) show that the 4 m/s cross-flow flame required higher amount of hydrogen (for 10% CFMFR flame, 4 m/s cross-flow flame has 61% by mass more than the one at 2 m/s cross-flow) to attach the flame than other lower cross-flow velocities flame. Hence, the higher amount of hydrogen input caused the increase of OH concentration for the 10% CFMFR flame at 4 m/s cross-flow. Although the 10% CFMFR flame in 3 m/s cross-flow also had higher hydrogen input (than 2m/s), its result does not show a higher OH increase. This was mainly due to that the 3 m/s cross-flow flame has better mixing than the 2 and 4 m/s cross-flow condition. The increase of cross-flow from 2 to 3 m/s increased the CVP effect. However, from 3 to 4 m/s, the change of the flame structure (from cross-flow to co-flow like structure) has reversed the effect. Hence, the strong dilution from the surrounding air of the 3 m/s cross-flow flame was the main cause for the lower measured OH concentration. This phenomenon has also been observed in the LII results. The soot concentration results for the 10% CFMFR flame at 3 m/s cross-flow is the lowest compare to the other two cross-flow velocities. Also, from the in-flame O₂ concentration results, the 10% CFMFR flame at 3 m/s cross-flow (Figure 3.47d) has the highest O₂ concentration then the 2 and 4 m/s cross-flow results (Figure 3.47d and 3.51d). However, this phenomenon is only observable in laminar flame results (10% CFMFR), and it is not obvious for turbulent flame results. The main reason is that the OH

concentration is very small compared with other species, and at highly mixing conditions, the difference maybe too small to be traceable.

The results in 20% CFMFR flame at 2 m/s cross-flow are very similar (in size and OH distribution) to the ones in 3 m/s cross-flow, although magnitude wise, the 2m/s cross-flow flame had a slightly higher OH concentration. The results of soot concentration distribution for these two flames are also very similar (in size and distribution) (Figure 4.14b and 4.15b). Hence, from this observation, it can be concluded that the soot and the OH distribution are related to each other. The OH distribution in these two flames shows a low OH concentration in the region between the two peaks on the $y=0$ axis. The absence of OH concentration is clearer in the 3 m/s results (Figure 5.8). This phenomenon was due to the high soot concentration and the CVP effect (which will be discussed after the next paragraph) at this region. The transition point (from chemical to momentum) for the 4 m/s cross-flow is 30% CFMFR (higher fuel flow rate). As a result, the OH distribution at the transition point for the 4 m/s cross-flow was wider than in the other two cross-flow flames. Figure 5.9 also shows a void at the middle of the flame. The soot distribution results for this flame condition (Figure 4.16b) shows a high soot concentration at this OH void region.

The 60% and 100% CFMFR flames at 2 m/s cross-flow had the overall highest OH concentration, and then followed by 3 m/s and 4 m/s cross-flow flame. Although in these three flames OH distributions look different, the horseshoe shape distribution to some extent is still visible. From the comparison of the soot concentration distribution and the OH distribution, most of the cases show that at the high soot concentration region show a low OH concentration. For instance, the soot concentration distribution results of

the 60% CFMFR flame at 2 m/s cross-flow (Figure 4.14) shows a high soot concentration in the wing-like region and a void of soot concentration at the middle of the flame. Then, the OH concentration in Figure 5.7 also shows a wing like structure, however it is opposite to that shown in Figure 4.14. Figure 5.7 shows that the 100% CFMFR flame at 2 m/s cross-flow had a higher OH concentration at the upper part (in x direction) of the flame, instead of a horseshow shape like the other two 100% CFMFR flames (Figure 5.8 and 5.9). This can be explained by observing the soot concentration distribution of this flame at 25% of the flame length in Figure 4.14d. Figure 4.14d shows the high soot concentration located at the lower part of the flame and the soot distribution extends up (in x direction) like a wing shape. Figure 5.7 shows the OH concentration distribution had a void like a wing shape and it had a low OH concentration at the lower part (in x direction) of the flame.

The OH concentration distributions for all the 10% CFMFR flame results show a relatively similar trend. All the results show a horseshoe shape at the outer rim and a high OH concentration at the center of the flame ($y=0$). At the center of the flame ($y=0$), all the 10% CFMFR flames show a dual-peak. The OH concentration distribution at $y=0$ is plotted in Figure 5.10 to 12, a and b. These figures show the comparison of the soot concentration and the OH concentration for 10% and 60% CFMFR, each from the chemically and momentum dominated regions at 25% of the flame length at three cross-flow conditions. All these figures show a dual peak structure (or vaguely in some cases) at $y=0$ axis. These figures also show that the higher peak is on the left side of the flame. Compared to the temperature results in Chapter III, the temperature profiles shows higher temperature on the left peak (Figure 3.25 to 3.27, a to d). The reason behind this

phenomenon was the higher mixing rate on the left side of the flame due the curving characteristic of the CVP. The details were discussed in Chapter III. The higher mixing rate on the left side of the flame caused the increase of reaction rate, which led to higher OH concentration on the left side. Similar to the quiescent condition results, most of these soot-OH concentration comparison results show soot concentration peak between the OH peaks. The most distinguishable difference between the quiescent and the cross-flow results is that the cross-flow soot concentration has only a single peak, except in the case of 60% CFMFR flame at 2m/s cross-flow, which has scattered dual peaks. The quiescent flame soot concentration had a dual peak at 25% of the flame length. The reason for the difference is that the quiescent and the cross-flow flame have different mixing mechanisms. Generally, the quiescent flame mixing is mainly due to the shearing effect of the jet and the surrounding air. However, besides shearing effect of the jet and the surrounding air, the cross-flow flame mixing also influenced by the CVP and the recirculation effect from the burner. Hence, a cross-flow has flame higher mixing rate than a quiescent condition flame. The higher mixing rate in a cross-flow flame brings the peaks closer and combines them into one peak. For a 60% CFMFR flame, the mixing rate for the flame at 2 m/s cross-flow is lower than the one in 3 m/s cross-flow. As a result, Figure 5.10b soot concentration profile shows dual peak soot, whereas other 60% CFMFR flame results show only one peak. Again, as mentioned in the quiescent section, the overlapping region between the high soot concentration region and the OH concentration peaks is where the active soot oxidation takes place.

Hence, from all these comparisons and observations, at the 25% flame length region, both the chemical and momentum-dominated flames behaved like the observation

made in the quiescent condition flame. At this region, the OH radical dominated the flame soot particle oxidation process.

The OH concentration profile of 50% of the flame length could not be measured due to low signal to noise ratio. However, the qualitative OH concentration profile (in x direction) can be predicted from the temperature results because, the OH concentration indicates the reaction zone. Hence, the peak temperature region is a good indication of high OH concentration. The temperature results in Chapter III show that all the chemical-dominated flames at low CFMFR (for all cross-flow) show a sharp dual peak structure at 50% of the flame length primary due to gas-phase dominant interface combustion. However, the momentum dominated flame (high CFMFR) temperature profiles (for all cross-flow) do not show a significant peak temperature due to the dominance of the heterogeneous combustion of soot and turbulence. Hence, from these temperature profiles, the same conclusion drawn in the quiescent condition can be applied here. O₂ oxidation (or diffusion rate) dominated the oxidation process for the momentum-dominated flame. Table 5.2 summarized the OH and O₂ dominance on soot oxidation at 25% and 50% flame length. Momentum flux ratio, R is provided for the cross-flow condition flames.

PLIF and Incorporate Discussion with Results in Chapter III and IV

Figure 5.13 to 15, a to d show the PLIF images in the similar fashion that shown in Chapter IV. The PLIF images were taken in different slices and the results presented here are the result of the mosaic of the all the slices. All the results are the relative OH-LIF florescence signal after the subtraction from the non-resonance signal.

From these PLIF results, the 2 m/s cross-flow flame results show a high OH concentration at the region around $z=6$ to 8 cm, except for the 20% CFMFR flame. However, the 3 m/s and the 4 m/s cross-flow flame results show the high OH concentration is located at the region around $z=3$ to 4 cm for 10%, 20% (3m/s), 30% (4m/s), and 60% CFMFR; at 100% CFMFR flame, the high OH concentration is located at $z=7$ to 8 cm region. The non-monotonic relation of the cross-flow and the oxidation rate is again apparent in the PLIF result, especially in the 10% CFMFR results. The result shows that the 10% CFMFR flame at the 2 m/s cross-flow had the high OH concentration region located at around $z=7$ cm. However, the 3m/s cross-flow result shows that the 10% CFMFR flame has peak around 3 cm, but for 4 m/s cross-flow condition, it is located at around 3.5 cm. The high OH concentration indicates the region of the high reaction rate. The 2 m/s cross-flow flame high reaction region was further downstream than the 3m/s cross-flow flame. However, at 4 m/s cross-flow, the effect of increase the cross-flow shows otherwise. In higher CFMFR flames, the non-monotonic cross-flow velocity effect is also apparent, except for a few cases.

While comparing these PLIF results with the PLII results in Chapter IV (Figures 4.17 to 4.19 a to d), for most cases, we see that the high OH concentration region is either at the region slightly upstream or at about the same location of the high soot concentration region. This phenomenon is expected because a smoke point flame is a highly sooting flame, beyond the high soot region, there should not be many OH radicals left in the flame.

5.4 Conclusion

From the perspective of the OH and O₂ oxidation of the soot particles, the distinction of the chemically and momentum dominated region is clearly drawn. The comparison of the OH concentration and the soot concentration shows that at all flame conditions (all CFMFR and cross-flow condition) at the 25% flame length region, OH radical dominated the soot oxidation process. However, at 50% of the flame length, OH dominates the oxidation of soot particle for the chemically-dominated flame; on the other hand, O₂ dominated the oxidation of soot particles for the momentum-dominated flame.

There is a non-monotonic relation for the cross-flow velocity with the flame oxidation process. The comparison of the OH concentration and the soot concentration for different cross-flow velocity shows that the increase of cross-flow velocity from 2 to 3 m/s increases the overall oxidation rate of the flame. However, the increase of cross-flow velocity from 3 to 4 m/s shows that the overall oxidation rate was decreased due to the change of flame structure from cross-flow flame to a co-flow-like flame.

Table 5.1 OH Collisional Quenching Parameters

Collider	$\sigma_{Q\infty}$ (Å ²)		ϵ/k (K)	a X10 ⁻¹³ cm ³ s ⁻¹
	Paul et al.	Tamura et al.		
N ₂	0.351	0.4	624	4.47
O ₂	8	8	243	4.37
H ₂ O	17.87	20	434	4.92
H ₂	4.24	4.5	224	10.88
CO ₂	11.87	11	488	4.16
CO	12.3	12	397	4.47
CH ₄	13.68	11	320	5.07
H	14.29	14.5	84	15.00
OH	14	20	384	4.99

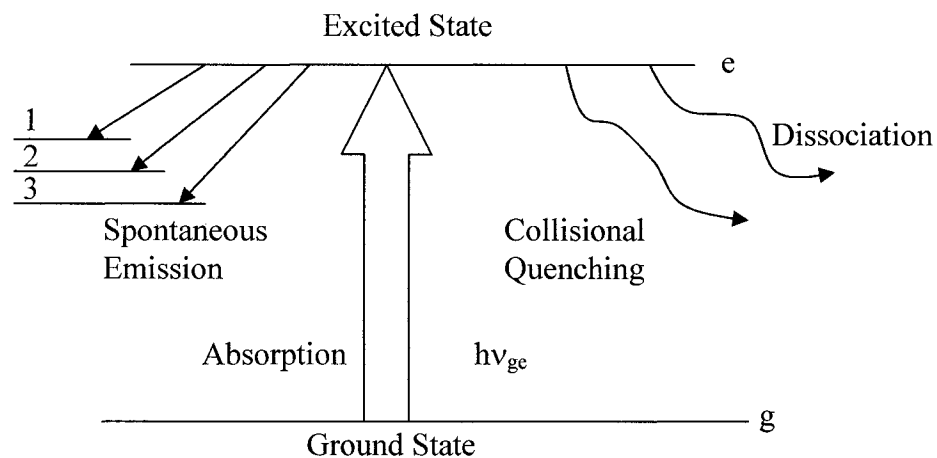
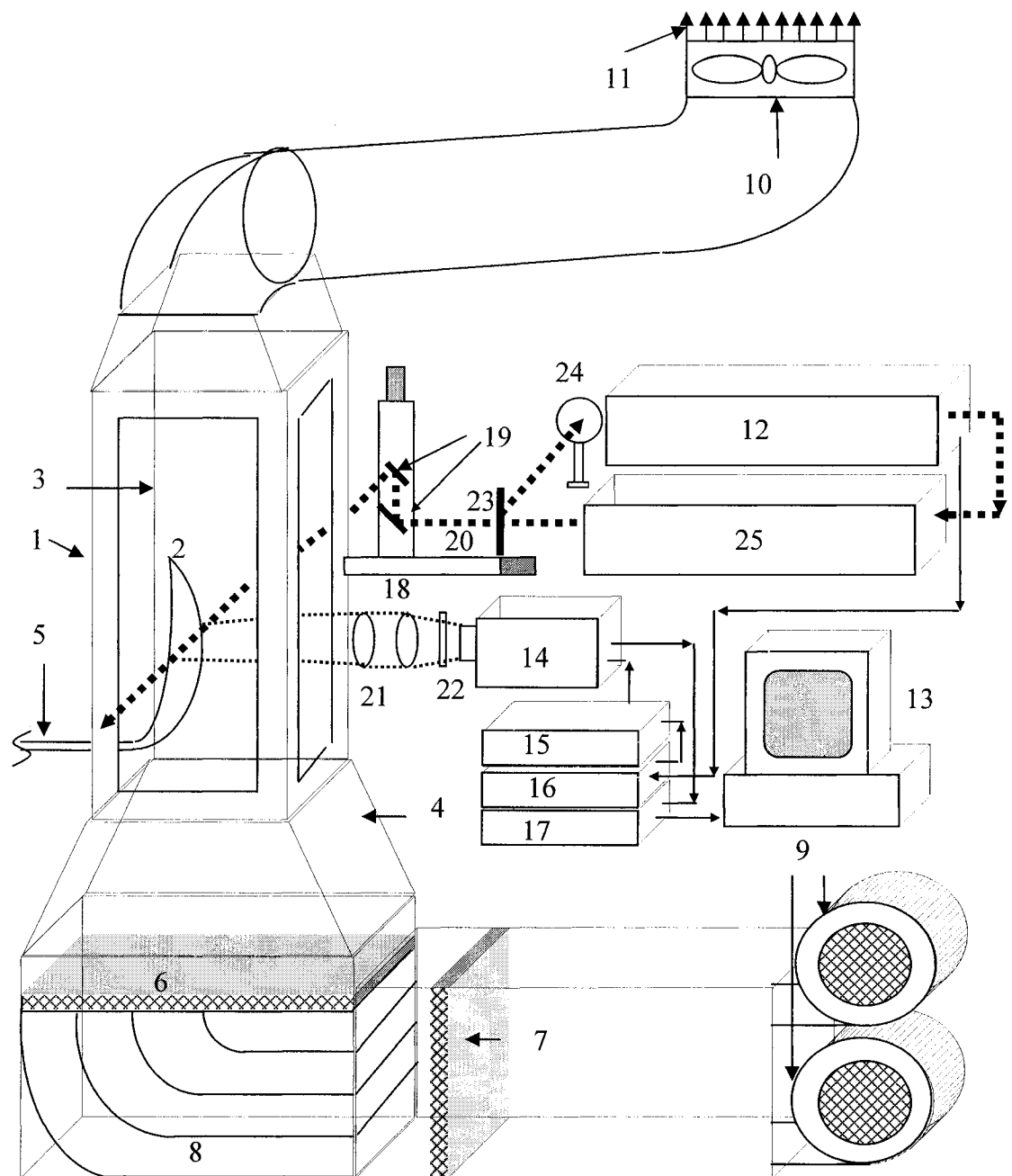


Figure 5.1 Quantum Excitation

Table 5.2 Summery of the OH and O₂ Dominance Effect

	R (Momentum Flux ratio)	Soot Oxidant Dominant Flame Location	
		25% L _{flame}	50% L _{flame}
Quiescent			
10% CFMFR	-	OH	OH
60% CFMFR	-	OH	O ₂
Cross-Flow			
2 m/s			
10% CFMFR	6.36	OH	OH
60% CFMFR	64.79	OH	O ₂
3 m/s			
10% CFMFR	2.49	OH	OH
60% CFMFR	29.97	OH	O ₂
4 m/s			
10% CFMFR	1.20	OH	OH
60% CFMFR	13.27	OH	O ₂



- | | |
|-----------------------------|---|
| 1. Test section | 14. ICCD camera |
| 2. Flame | 15. Camera gate controller |
| 3. 3 tempered glass window | 16. Stanford Instrument Pulse Generator |
| 4. Contraction | 17. Camera imaging system |
| 5. Fuel and mixture supply | 18. Traverse mechanism |
| 6. Single layer filter | 19. Silver turning mirrors |
| 7. Two layers filter | 20. Laser |
| 8. Turning ducts | 21. Focusing lens |
| 9. Blowers | 22. Narrow band pass filter |
| 10. Suction fan | 23. Beam splitter |
| 11. Exhaust to atmosphere | 24. Thermopile volume absorber detector |
| 12. Nd-YAG laser | 25. MOPO with FDO |
| 13. Computer and DAQ system | |

Figure 5.2 Schematic of LIF and PLIF Measurement Setup

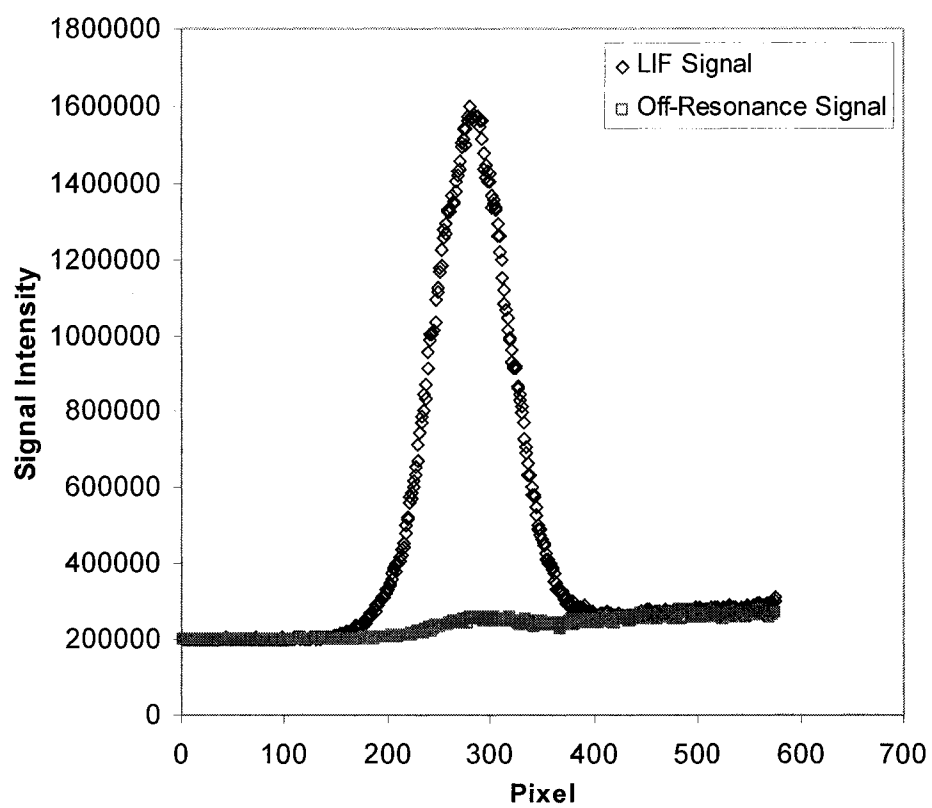


Figure 5.3 Comparison of LIF Signal and Off-Resonance Signal

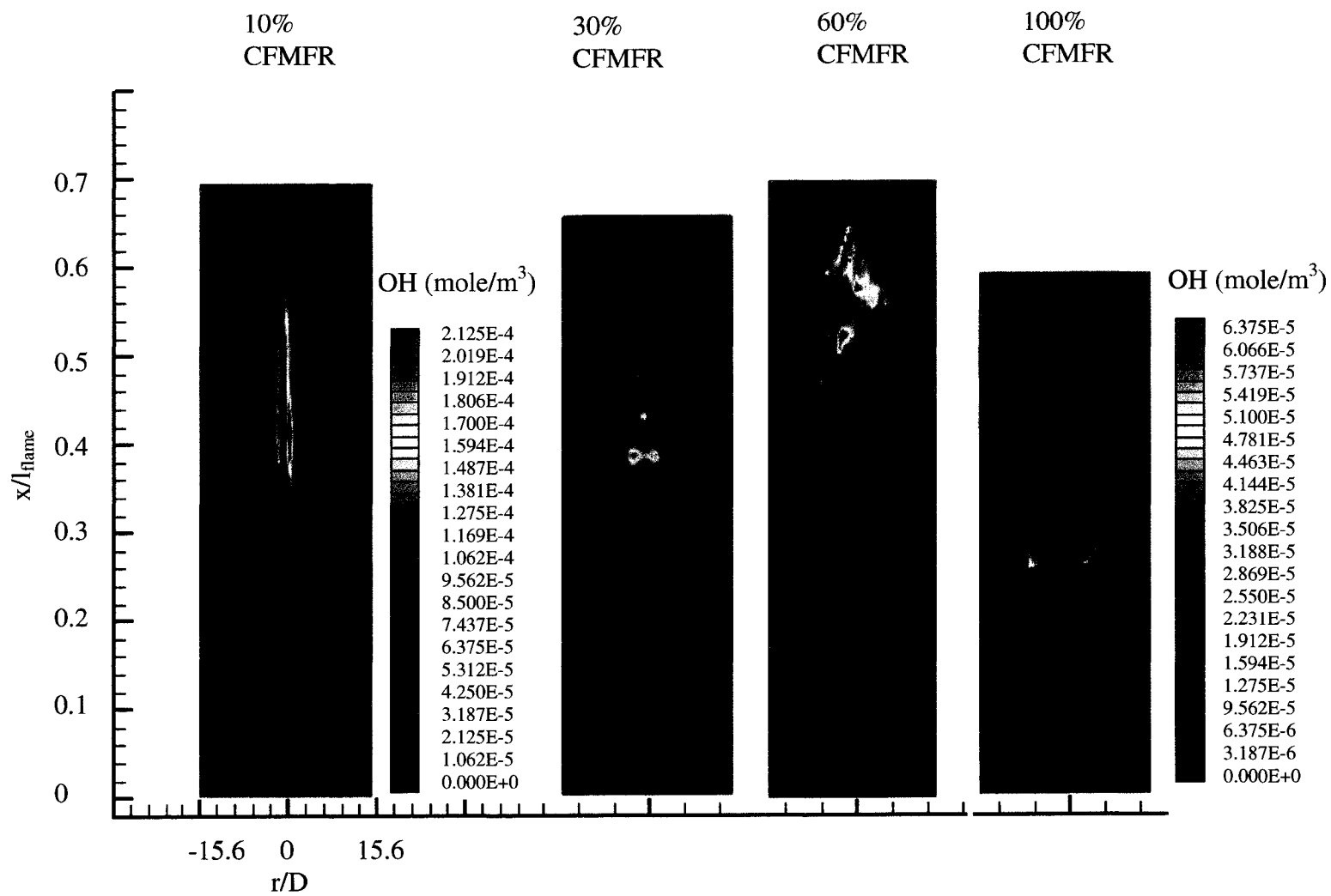


Figure 5.4 OH Concentration of Quiescent Condition Flames at Four Different CFMFR

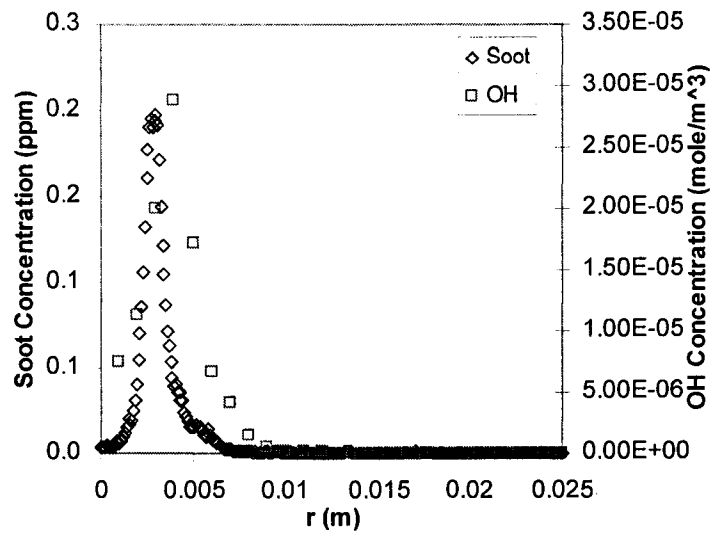


Figure 5.5a Radial Soot and OH Concentration Profiles for 10% CFMFR Flames at 25% Flame Length

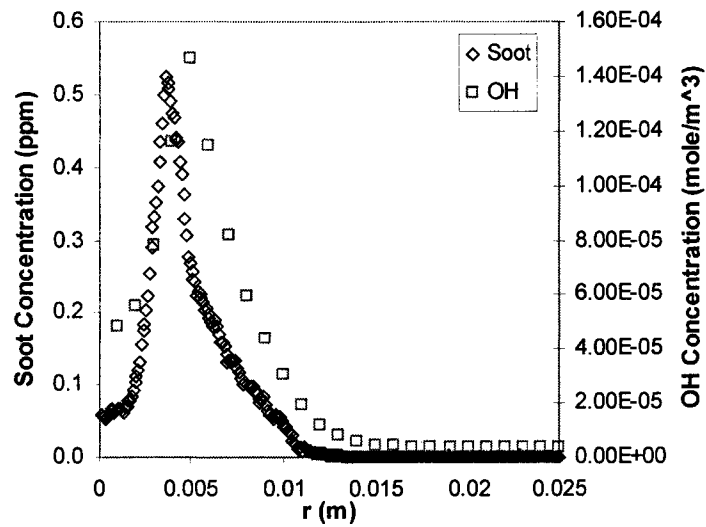


Figure 5.5b Radial Soot and OH Concentration Profiles for 10% CFMFR Flames at 50% Flame Length

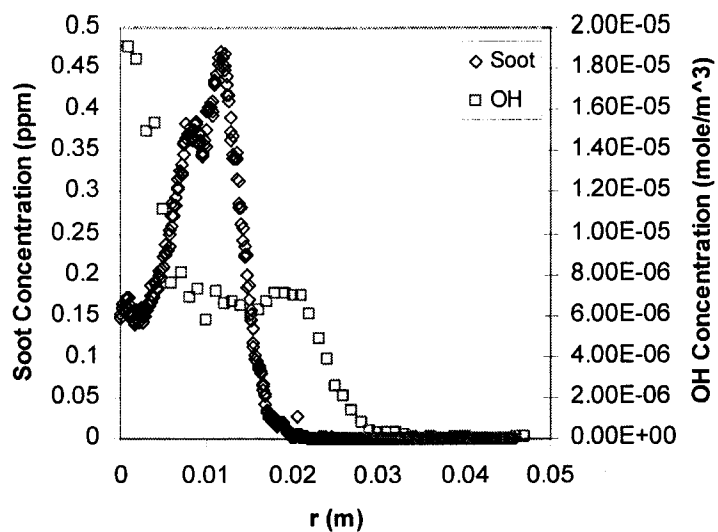


Figure 5.6a Radial Soot and OH Concentration Profiles for 60% CFMFR Flames at 25% Flame Length

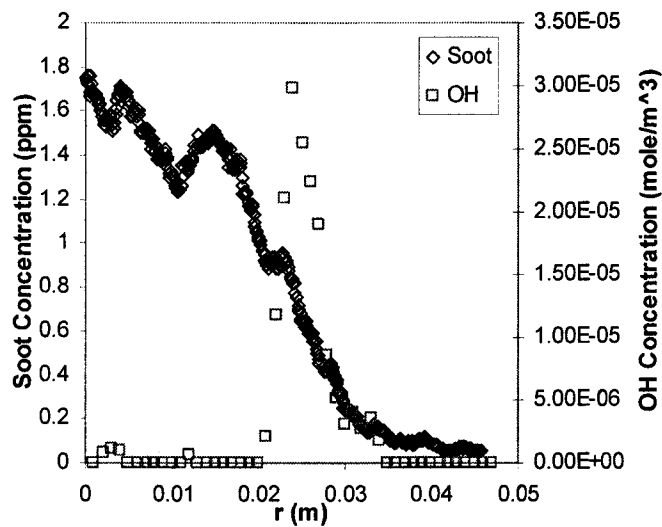


Figure 5.6b Radial Soot and OH Concentration Profiles for 60% CFMFR Flames at 50% Flame Length

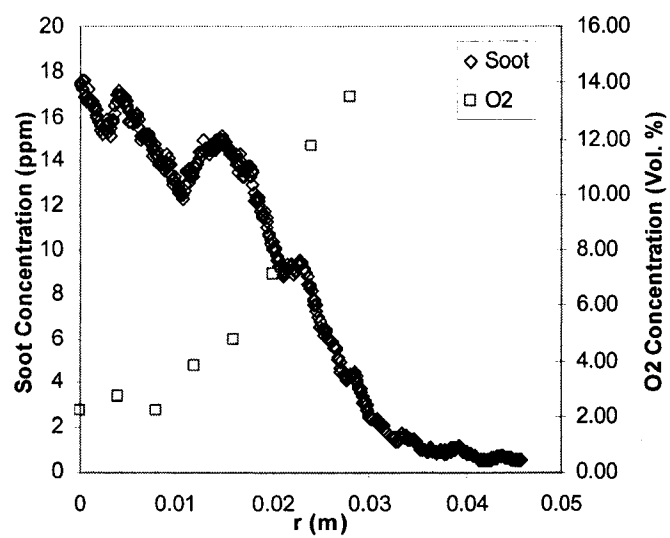


Figure 5.6c Radial Soot and O₂ Concentration Profiles for 60% CFMFR Flames at 50% Flame Length

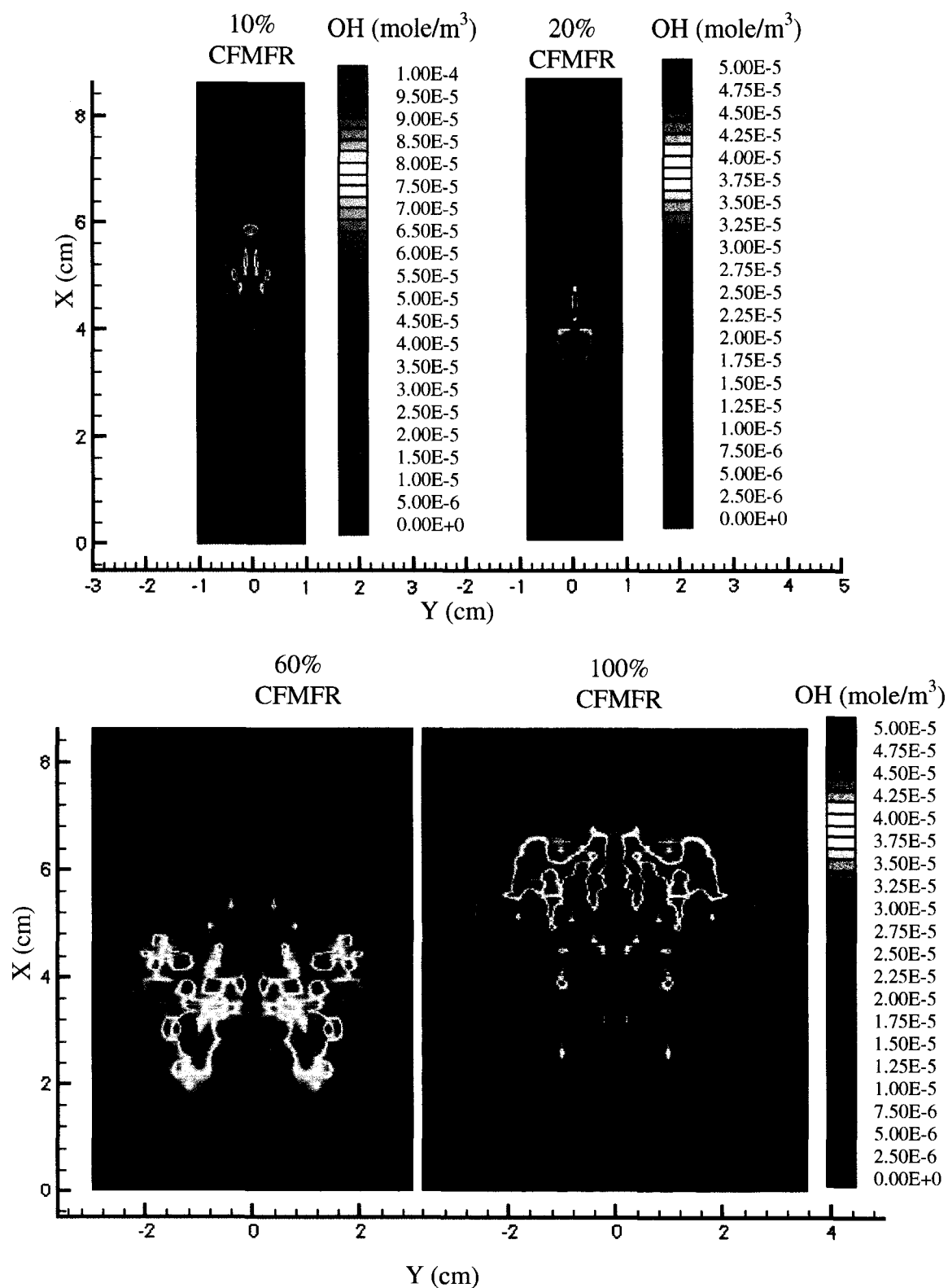


Figure 5.7 X-Y Plane OH Molar Concentration at 25% Flame Length at 2 m/s Cross-Flow for 10%, 20%, 60% and 100% CFMFR Flame

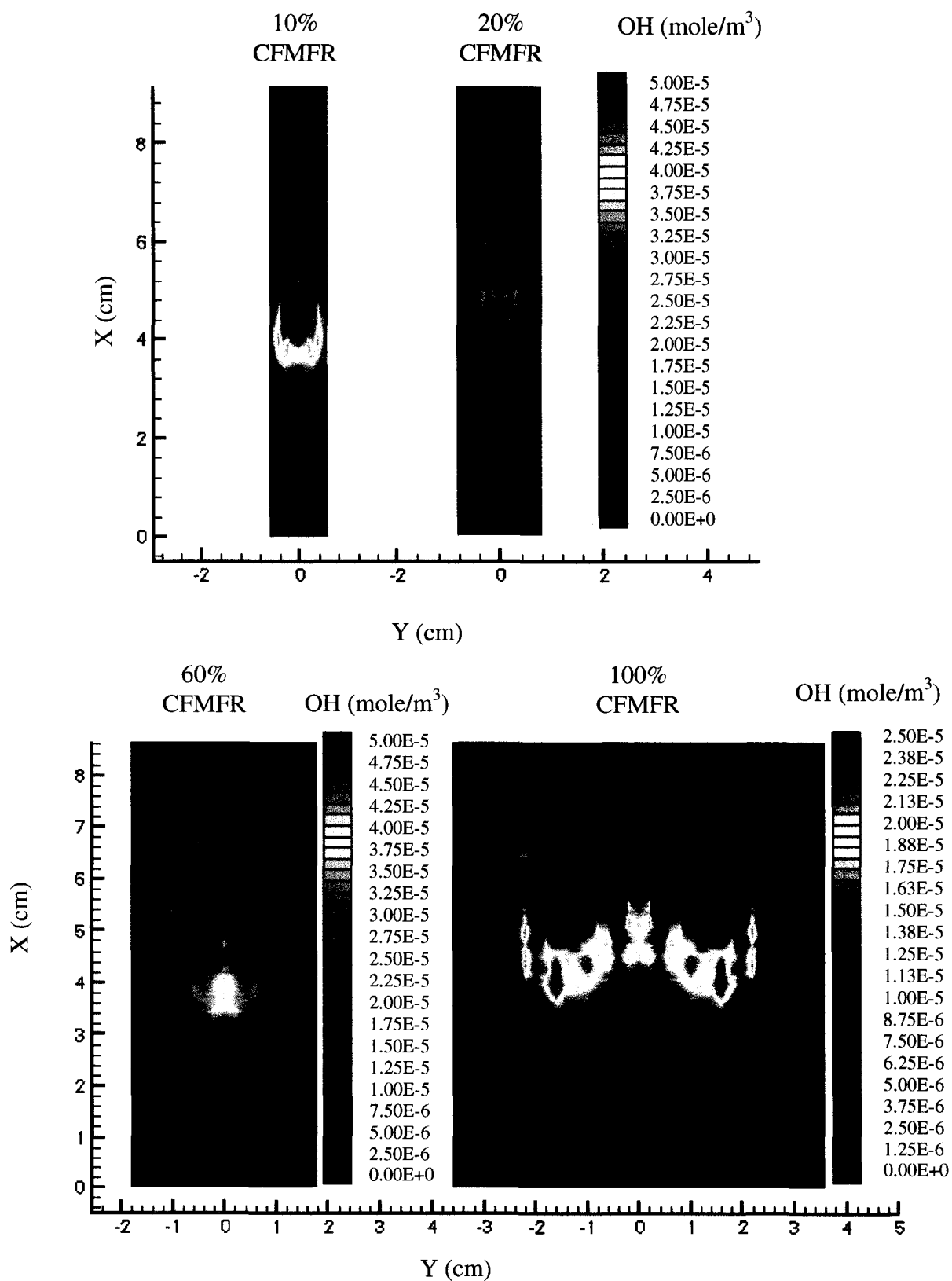


Figure 5.8 X-Y Plane OH Molar Concentration at 25% Flame Length at 3 m/s Cross-Flow for 10%, 20%, 60% and 100% CFMFR Flame

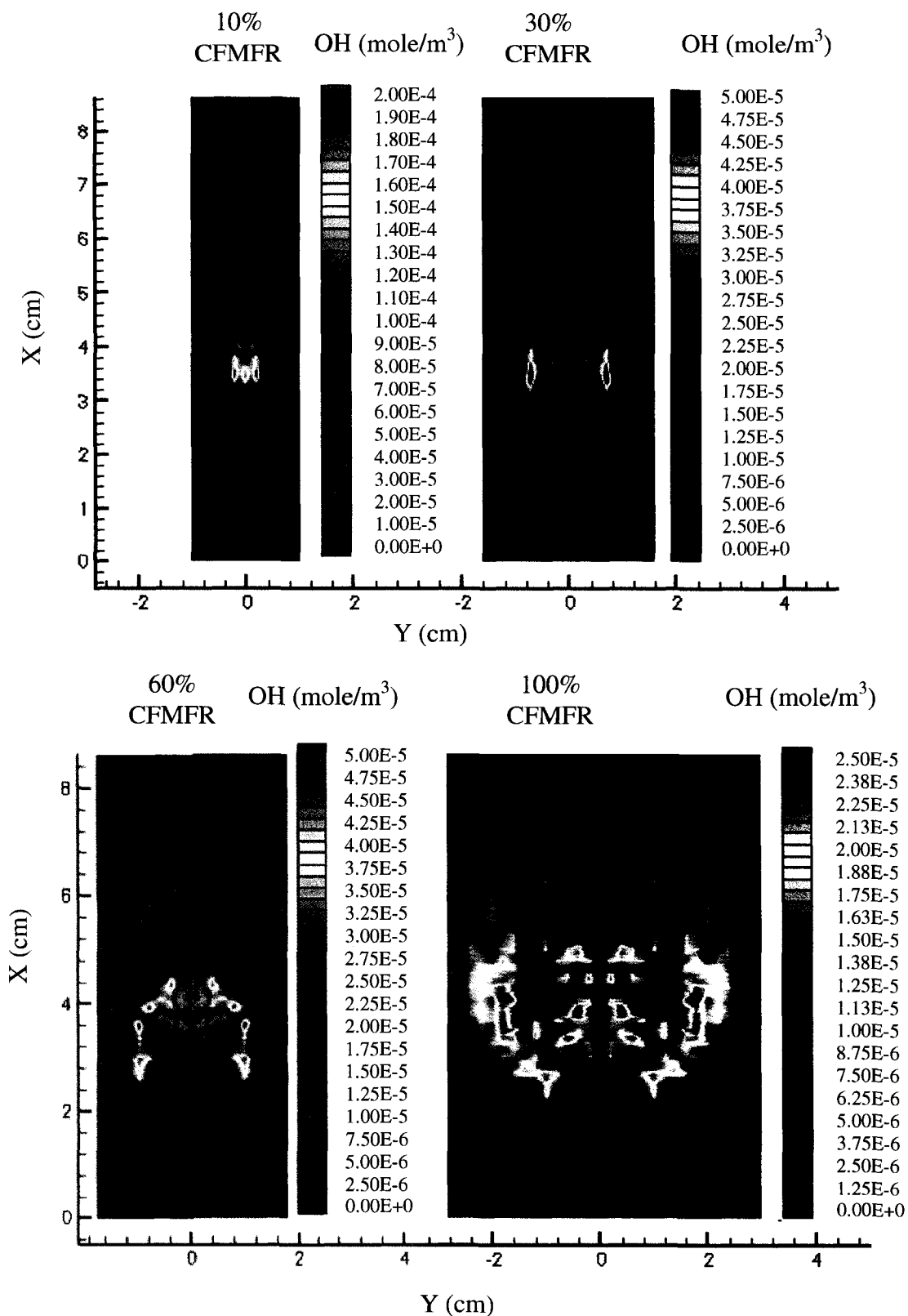


Figure 5.9 X-Y Plane OH Molar Concentration at 25% Flame Length at 4 m/s Cross-Flow for 10%, 20%, 60% and 100% CFMFR Flame

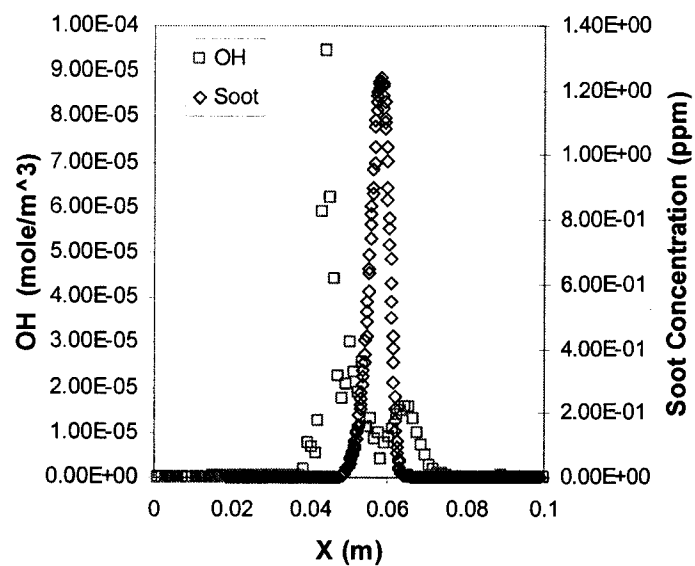


Fig 5.10a Soot and OH Concentration Profiles for 10% CFMFR Flame in 2m/s Cross-Flow at 25% Flame Length

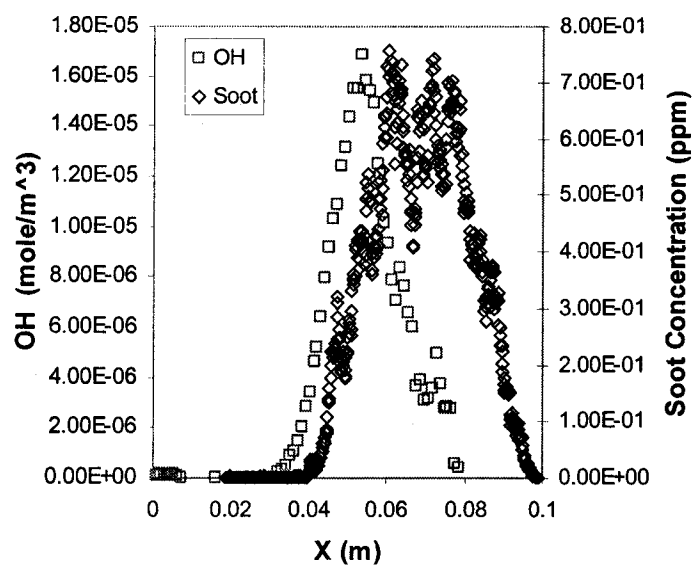


Fig 5.10b Soot and OH Concentration Profiles for 60% CFMFR Flame in 2m/s Cross-Flow at 25% Flame Length

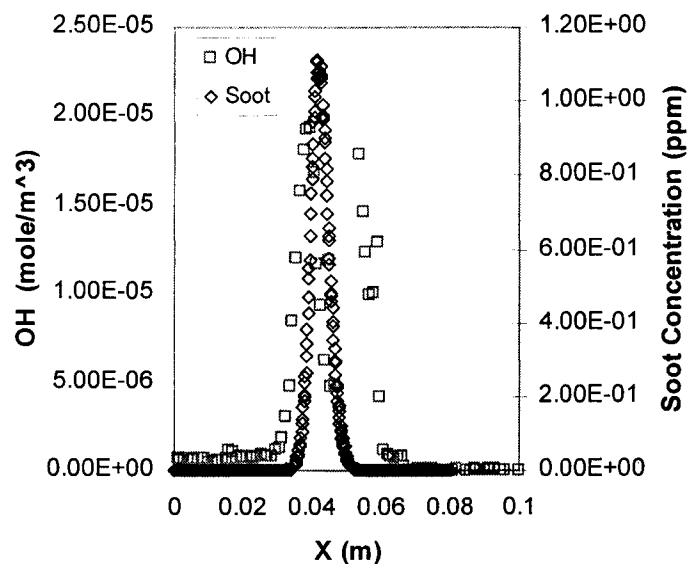


Fig 5.11a Soot and OH Concentration Profiles for 10% CFMFR Flame in 3m/s Cross-Flow at 25% Flame Length

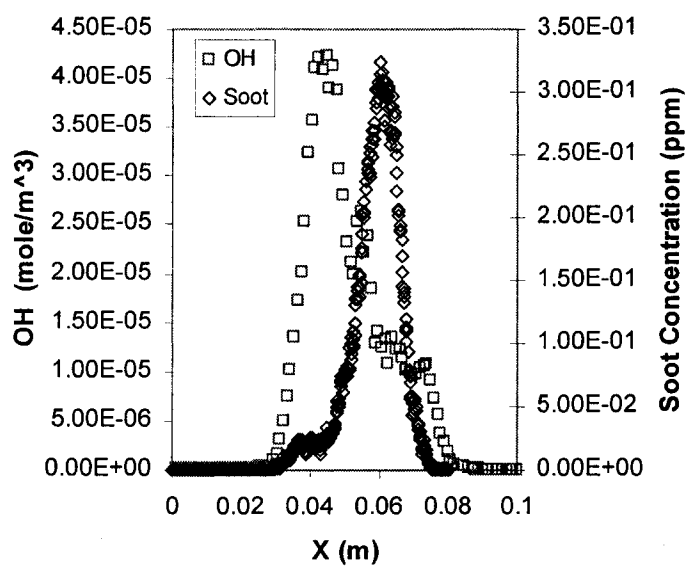


Fig 5.11b Soot and OH Concentration Profiles for 60% CFMFR Flame in 3m/s Cross-Flow at 25% Flame Length

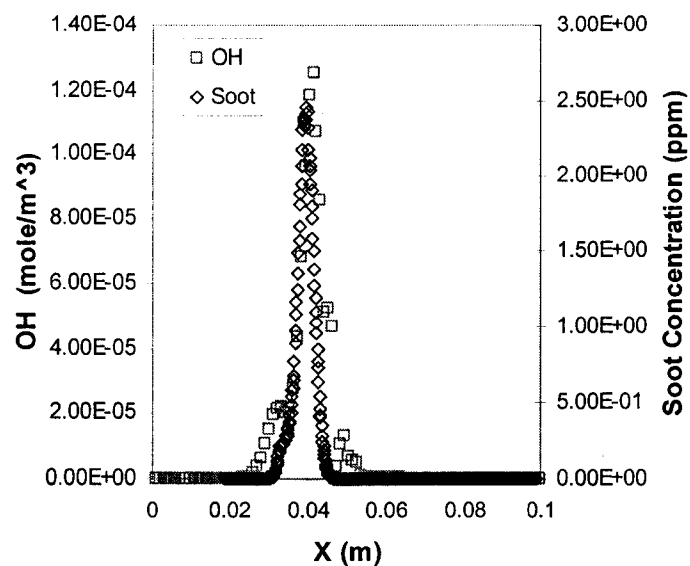


Fig 5.12a Soot and OH Concentration Profiles for 10% CFMFR Flame in 4m/s Cross-Flow at 25% Flame Length

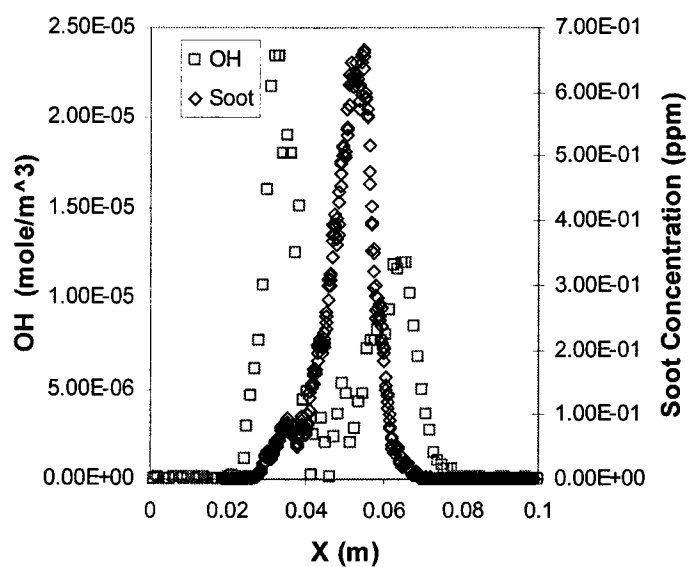


Fig 5.12b Soot and OH Concentration Profiles for 60% CFMFR Flame in 4m/s Cross-Flow at 25% Flame Length

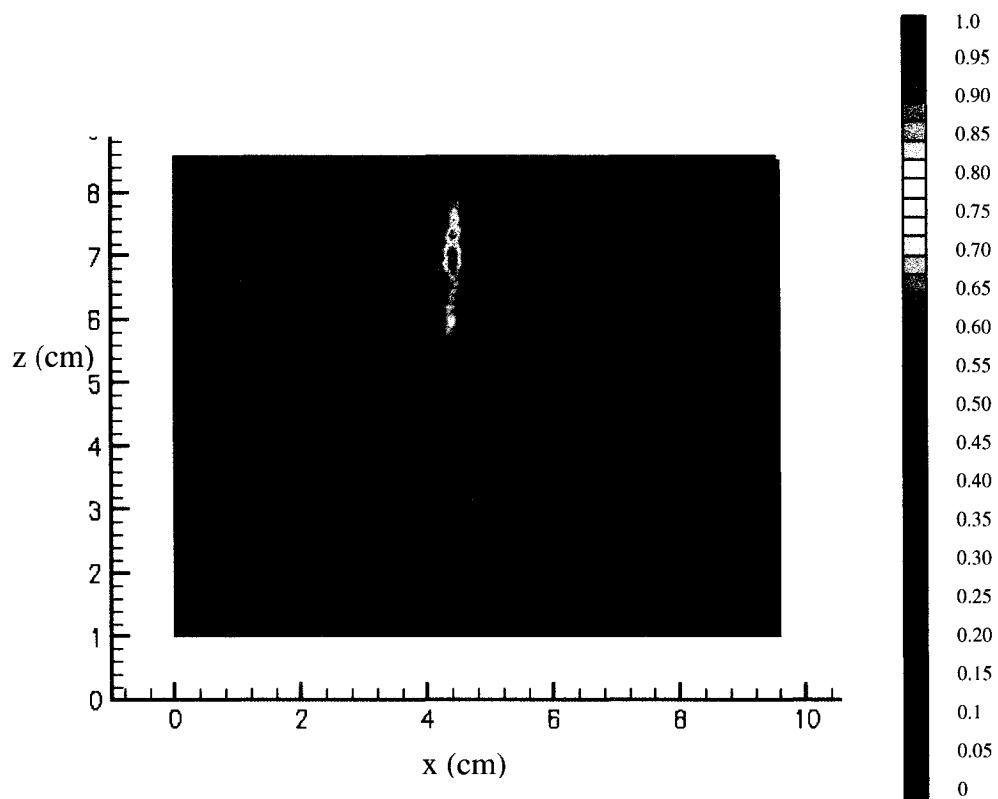


Figure 5.13a OH PLIF Image for 10% CFMFR at 2 m/s cross-flow

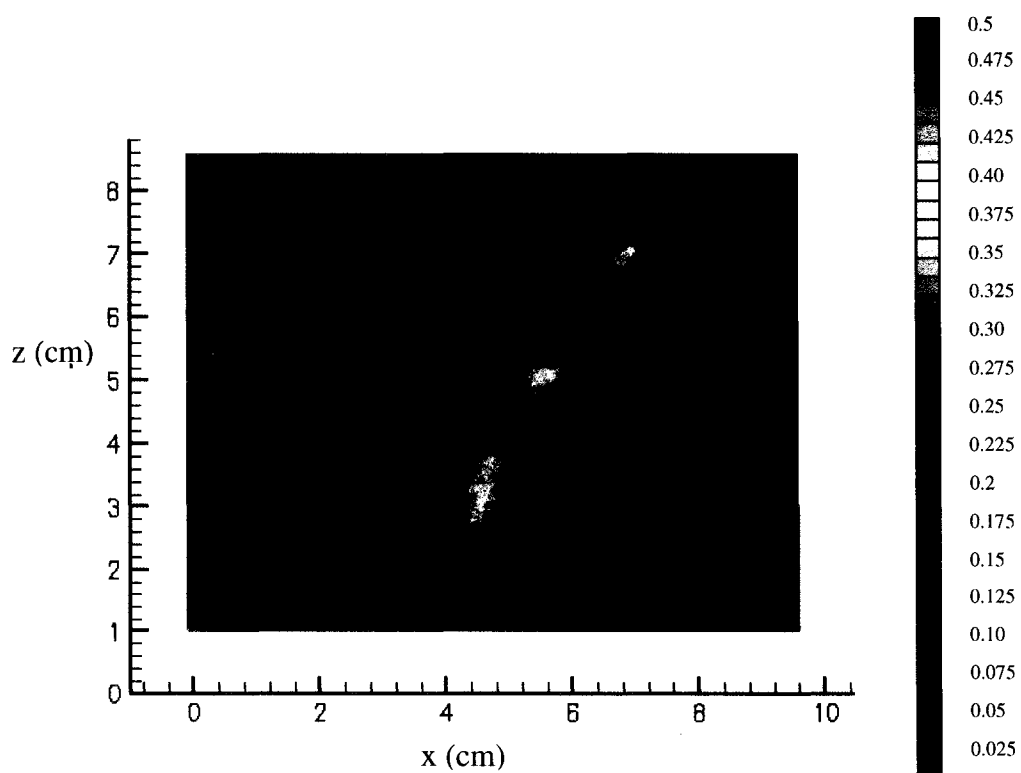


Figure 5.13b OH PLIF Image for 20% CFMFR at 2 m/s cross-flow

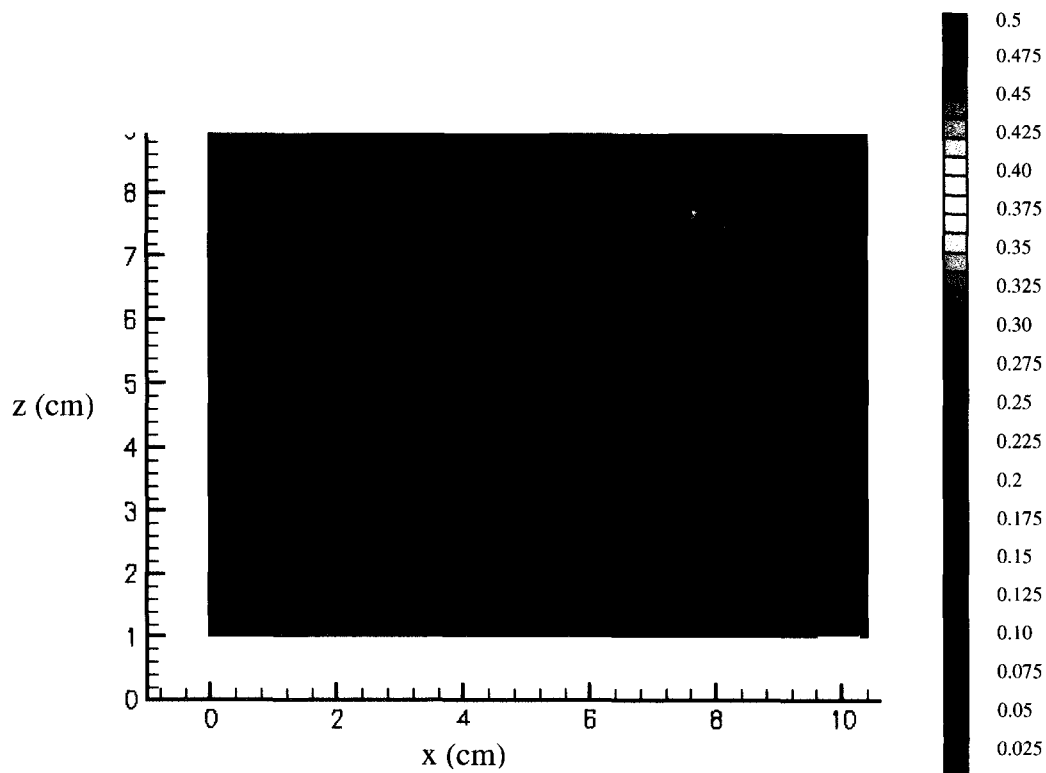


Figure 5.13c OH PLIF Image for 60% CFMFR at 2 m/s cross-flow

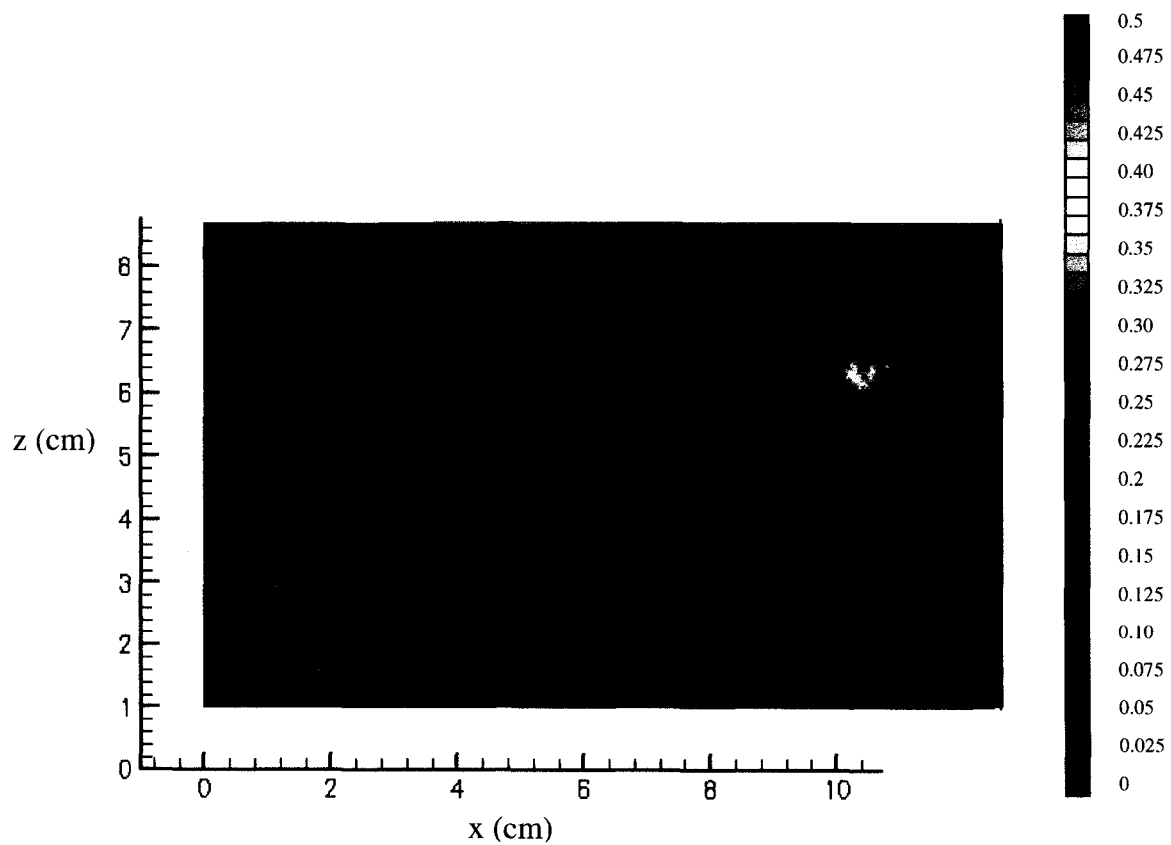


Figure 5.13d OH PLIF Image for 100% CFMFR at 2 m/s cross-flow

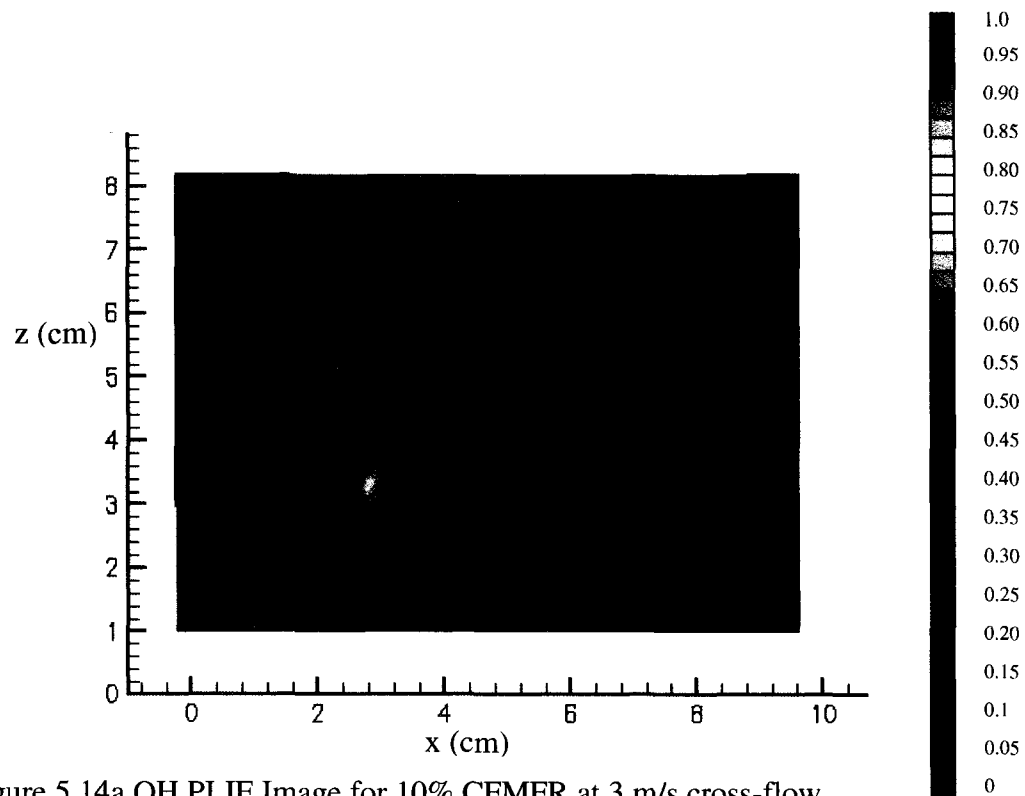


Figure 5.14a OH PLIF Image for 10% CFMFR at 3 m/s cross-flow

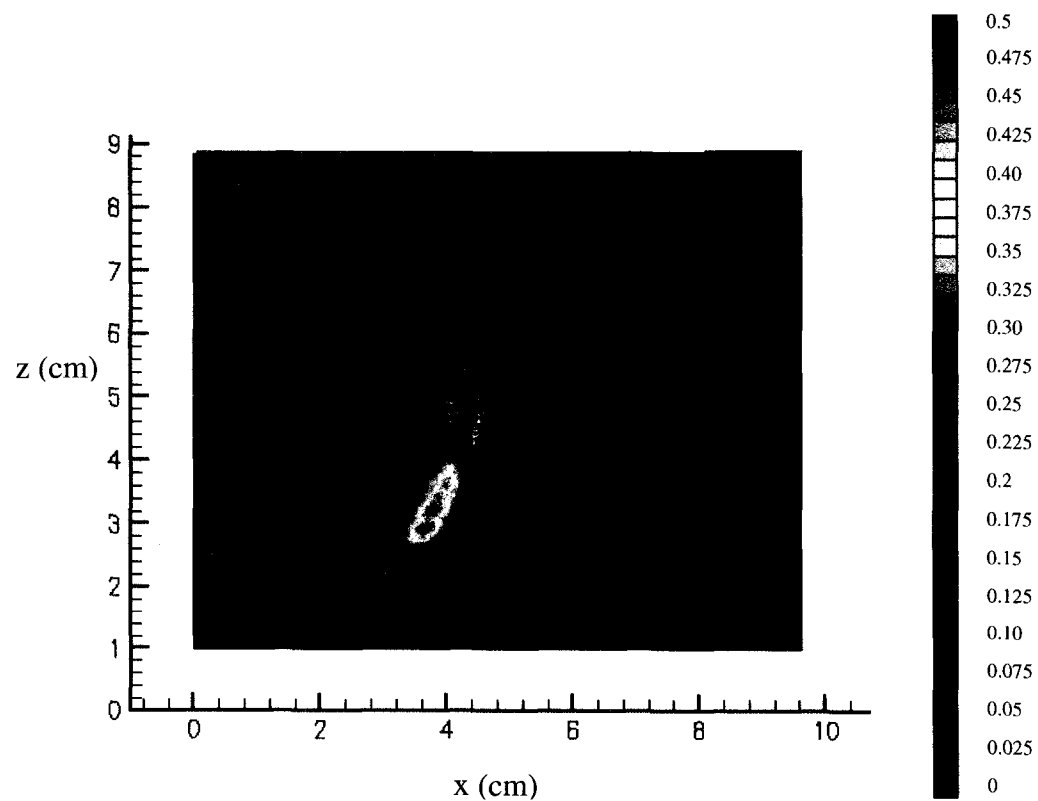


Figure 5.14b OH PLIF Image for 20% CFMFR at 3 m/s cross-flow

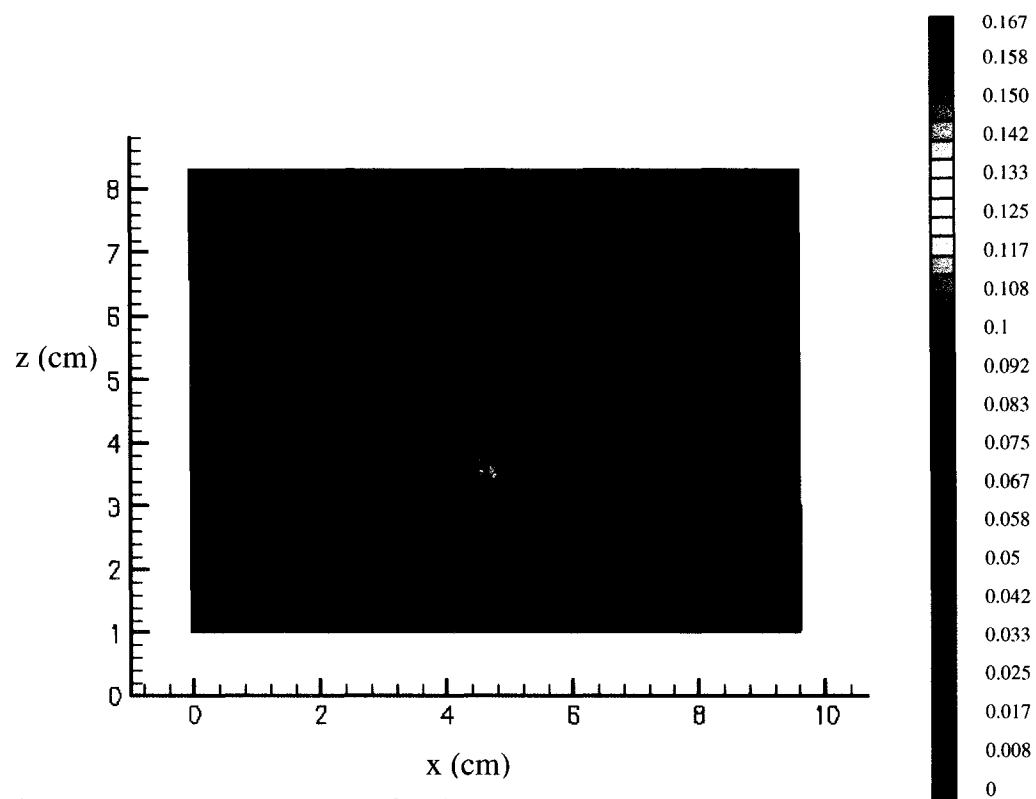


Figure 5.14c OH PLIF Image for 60% CFMFR at 3 m/s cross-flow

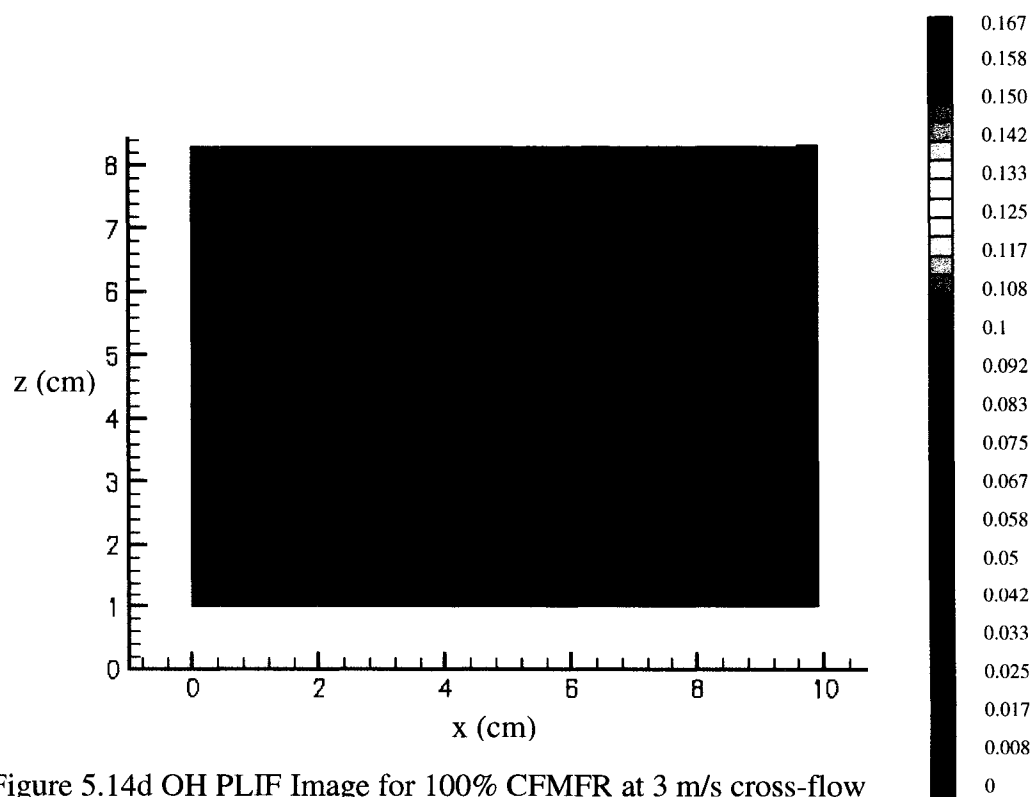


Figure 5.14d OH PLIF Image for 100% CFMFR at 3 m/s cross-flow

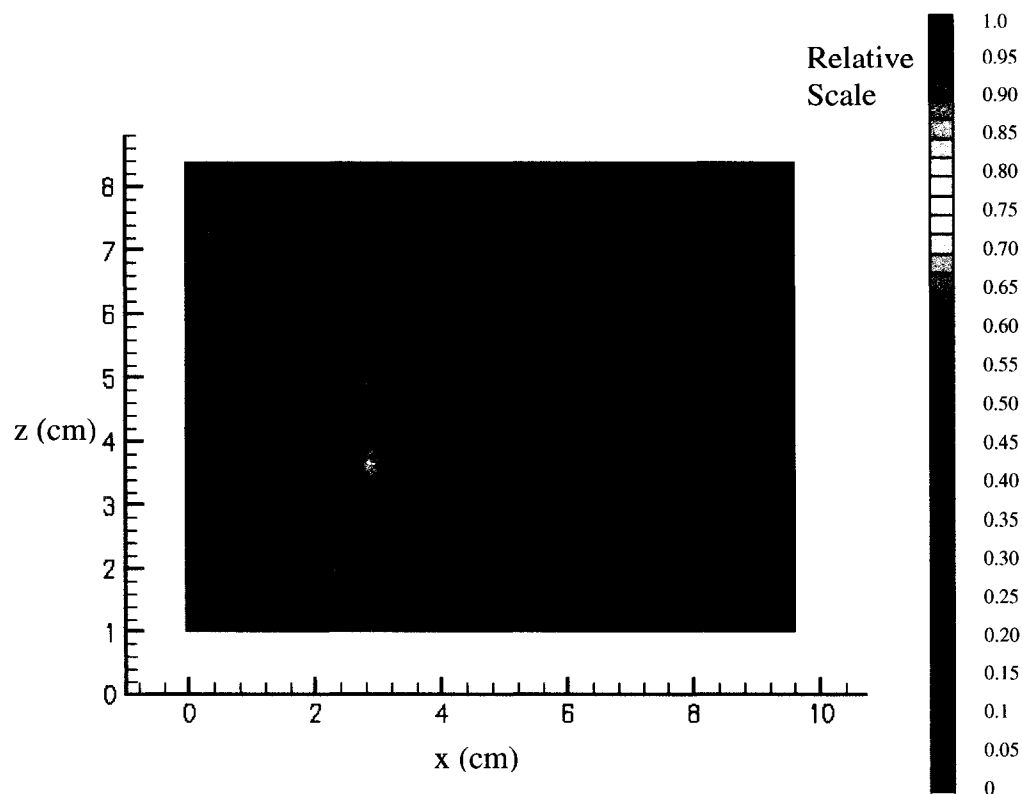


Figure 5.15a OH PLIF Image for 10% CFMFR at 4 m/s cross-flow

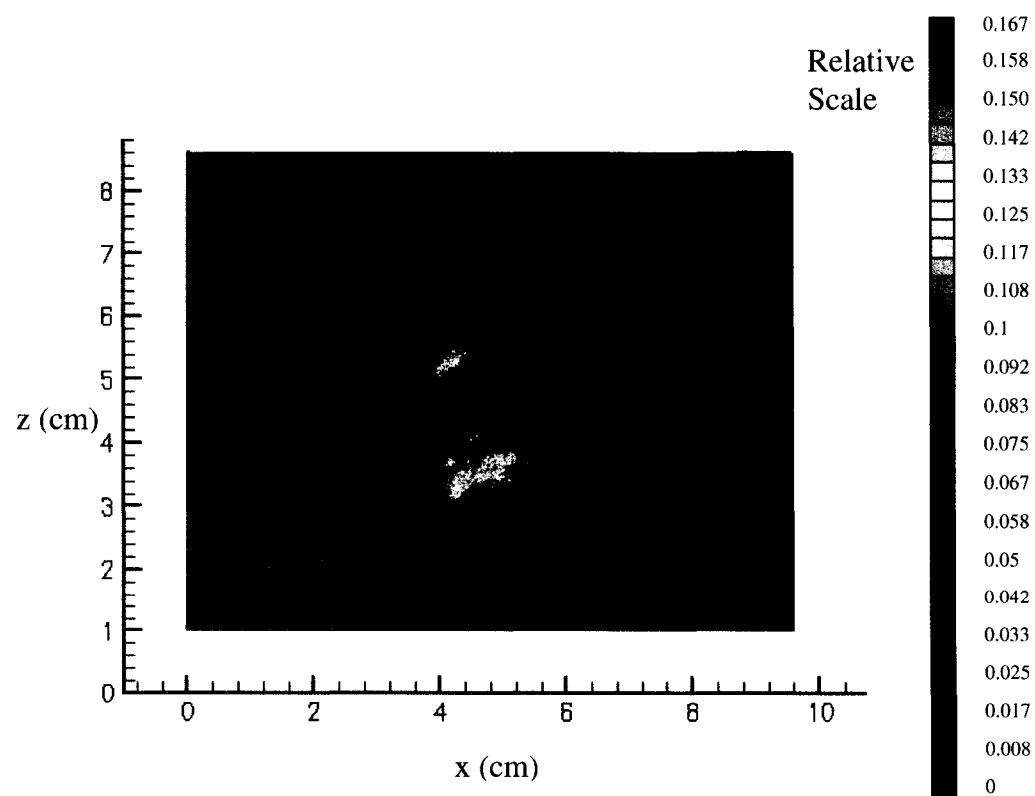


Figure 5.15b OH PLIF Image for 30% CFMFR at 4 m/s cross-flow

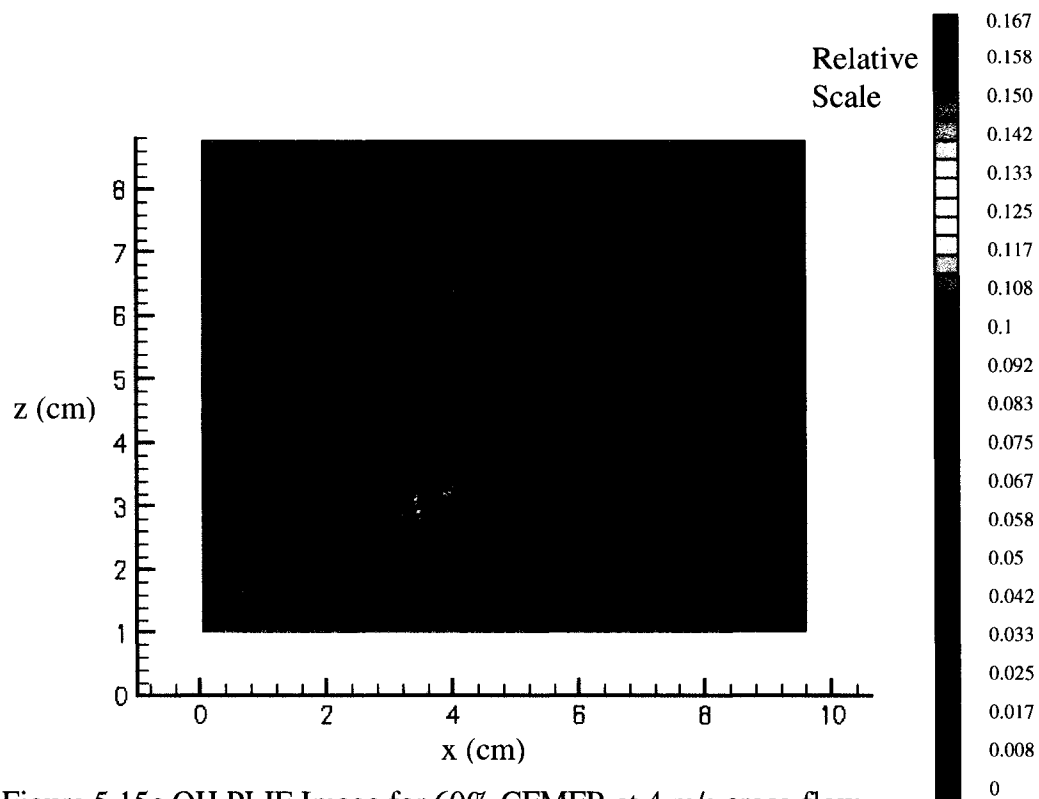


Figure 5.15c OH PLIF Image for 60% CFMFR at 4 m/s cross-flow

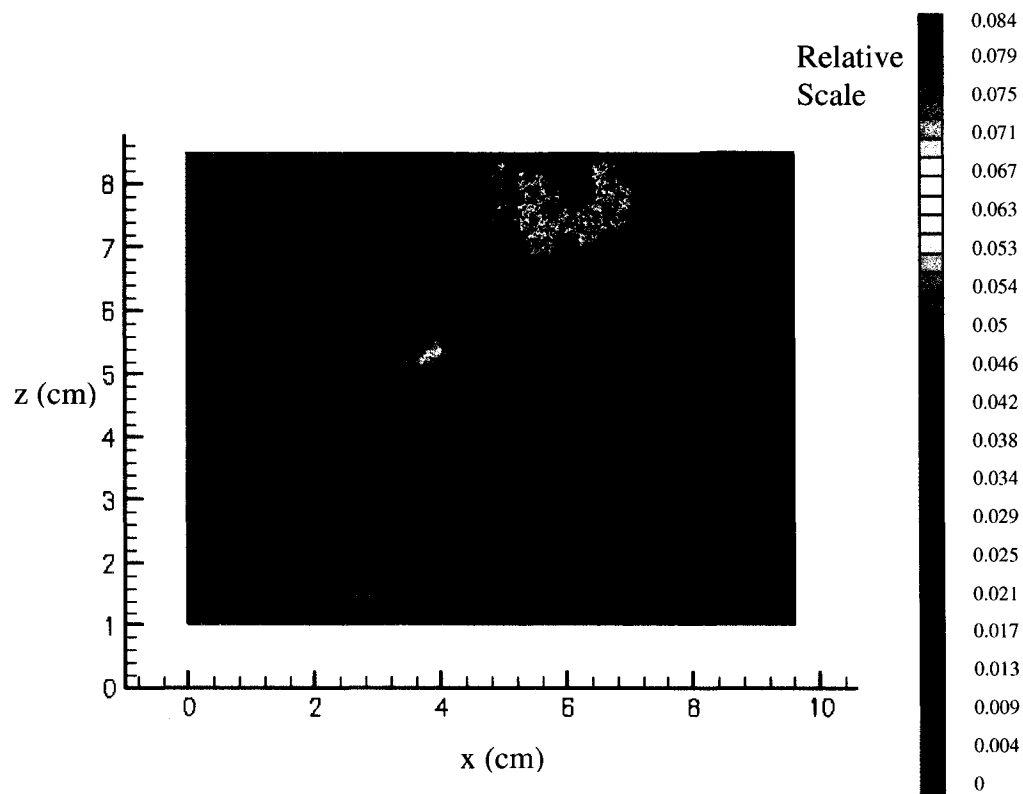


Figure 5.15d OH PLIF Image for 100% CFMFR at 4 m/s cross-flow

Chapter VI

Computational Analysis

Nomenclature

E	Total energy
f	Mixture fraction
f'	Mixture fraction variance
\vec{g}	Gravitational acceleration
K_k	Generation of turbulence kinetic energy due to the mean velocity gradients
K_b	Generation of turbulence kinetic energy due to buoyancy
κ_{eff}	Effective thermal conductivity
P	Static pressure
Pr_t	Turbulent Prandtl number
r	Air-to-fuel ratio on a mass basis
S_r	Source of energy due to chemical reaction
T	Temperature
u	Velocity
u_j	Jet velocity
u_∞	Cross-flow velocity
w	z-velocity
Y_α	Elemental mass fraction for some element
ε	Dissipation rate
κ	Kinetic energy

σ_k	Turbulent Prandtl numbers for κ
σ_ε	Turbulent Prandtl numbers for ε
ϕ	Equivalence ratio
$\bar{\tau}$	Stress tensor term
ρ_∞	Ambient density
ρ_j	Jet gas density
μ_t	Turbulent viscosity

6.1 Introduction

A 2-D modeling was used for computation of the quiescent flame because the flame is an axisymmetric structure. However, the cross-flow flame required a 3-D modeling because the flame is non-axisymmetric. The 3-D domain dimension is based on the half of the test section of the wind tunnel with the symmetry plane at x-z plane. A standard k- ε model was used to compute the flow, and an equilibrium mixture fraction/PDF Model was used to compute the reaction.

6.2 Continuity and Momentum Equations

In this study, the computational fluid dynamics code “FLUENT” was used to solve conservation equations for mass and momentum. For flows involving heat transfer or compressibility, an additional equation for energy conservation was solved. For flows involving species mixing or reactions, a species conservation equation was solved. The

combustion model solved conservation equations for the mixture fraction and its variance. Additional transport equations were solved for turbulence.

The continuity equation was expressed as

$$\frac{\partial \rho}{\partial t} + \nabla \cdot (\rho \vec{v}) = 0 \quad [6.2.1]$$

and the momentum equation was

$$\frac{\partial}{\partial t}(\rho \vec{v}) + \nabla \cdot (\rho \vec{v} \vec{v}) = -\nabla P + \nabla \cdot (\vec{\tau}) + \rho \vec{g} \quad [6.2.2]$$

where P was the static pressure and $\vec{\tau}$ is the stress tensor term. $\rho \vec{g}$ was the gravitational body force. In this study, the gravity was only in the Z direction.

6.2.1 The Standard k-ε Model

Besides the continuity, momentum and energy equations were solved, and additional equations were solved to take turbulence into account. Two-equation models were used in this study, in which the solution of two separate transport equations allowed the turbulent velocity and length scales to be independently determined. The Launder and Spalding (Launder and Spalding, 1972) standard k-ε model was applied in the study. This model was a semi-empirical model with commonly acceptable empirical constants listed in equation 6.2.13.

6.2.2 Transport Equations for the Standard k-ε Model

The following two transport equations calculate the turbulence kinetic energy k , and the dissipation rate, ϵ .

$$\frac{\partial}{\partial t}(\rho\kappa) + \frac{\partial}{\partial x_i}(\rho\kappa u_i) = \frac{\partial}{\partial x_j} \left[\left(\mu + \frac{\mu_t}{\sigma_\kappa} \right) \frac{\partial \kappa}{\partial x_j} \right] + K_k + K_b - \rho\epsilon \quad [6.2.3]$$

$$\frac{\partial}{\partial t}(\rho\epsilon) + \frac{\partial}{\partial x_i}(\rho\epsilon u_i) = \frac{\partial}{\partial x_j} \left[\left(\mu + \frac{\mu}{\sigma_\epsilon} \right) \frac{\partial \epsilon}{\partial x_j} \right] + C_{1\epsilon} \frac{\epsilon}{\kappa} (K_k + K_{3\epsilon} K_b) - C_{2\epsilon} \rho \frac{\epsilon^2}{\kappa} \quad [6.2.4]$$

In the above equations, K_k is the generation of turbulence kinetic energy due to the mean velocity gradients. The formulation for production of turbulence kinetic energy, K_k is shown in Equation 6.2.6. K_b is the generation of turbulence kinetic energy due to buoyancy, calculated as described in 6.2.10. $C_{1\epsilon}$ $C_{2\epsilon}$ $C_{3\epsilon}$ are constants listed in 6.2.13. σ_κ and σ_ϵ are the turbulent Prandtl numbers for κ and ϵ .

$$K_k = -\rho \overline{u'_i u'_j} \frac{\partial u_j}{\partial x_i} \quad [6.2.5]$$

To evaluate K_k in a manner consistent with the Boussinesq hypothesis,

$$K_k = \mu_t S^2 \quad [6.2.6]$$

where S is the modulus of the mean rate-of-strain tensor, defined as

$$S \equiv \sqrt{2S_{ij}S_{ij}} \quad [6.2.7]$$

6.2.3 Effects of Buoyancy on Turbulence in the k-ε Models

Due to the temperature gradient in the flow, the k-ε models in FLUENT account for the generation of k due to buoyancy (K_b in Equations 6.2.5), and the corresponding contribution to the production of ϵ in Equations 6.2.4.

$$K_b = \beta g \frac{\mu_t}{Pr_t} \frac{\partial T}{\partial x_i} \quad [6.2.8]$$

Pr_t is the turbulent Prandtl number for energy and g is the component of the gravitational vector in the z direction. The value for Pr_t is set to 0.85.

$$\beta = -\frac{1}{\rho} \left(\frac{\partial \rho}{\partial T} \right)_p \quad [6.2.9]$$

For ideal gases, Equation 6.2.6 reduces to

$$K_b = -g \frac{\mu_t}{\rho \text{Pr}_t} \frac{\partial \rho}{\partial x_i} \quad [6.1.10]$$

Buoyancy only occurs in z direction. Thus, $C_{3\varepsilon}$ was used to ensure that (Henkes et. al, 1991):

$$C_{3\varepsilon} = \tanh \left| \frac{w}{u_i} \right| \quad [6.2.11]$$

w is the z-velocity (parallel to gravity) and u_i is the other two velocity components respectively. Hence, $C_{3\varepsilon}$ only equals to one when the flow is parallel to z direction and it is zero when the flow is in the other two directions.

6.2.4 Modeling the Turbulent Viscosity

The turbulent viscosity is defined by combining k and ε . (Launder and Spalding, 1974)

$$\mu_t = \rho C_\mu \frac{\kappa^2}{\varepsilon} \quad [6.2.12]$$

The following are the commonly used model constants $C_{1\varepsilon}$, $C_{2\varepsilon}$, C_μ , σ_k and σ_ε (Launder and Spalding, 1974, Peters 2000):

$$C_{1\varepsilon} = 1.44$$

$$C_{2\varepsilon} = 1.92$$

$$C_\mu = 0.09$$

$$\sigma_k = 1.0$$

$$\sigma_\varepsilon = 1.3 \quad [6.2.13]$$

The constants in 6.2.13 have been determined from experiments with air and water for fundamental turbulent shear flows. They have been found to work fairly well for a wide range of wall-plane jet and mixing layers. Unfortunately, there are no exact constants for $C_{2\varepsilon}$ and C_μ for the current study; they are both functions of the flow. However, the variations are small, and the values given in 6.2.11 are nearly always applicable for most problems. (Launder and Spalding, 1974) Furthermore, FLUENT only allows input of constants for $C_{2\varepsilon}$ and C_μ .

6.3 Energy Equation

The energy equation is defined as

$$\frac{\partial}{\partial t}(\rho E) + \frac{\partial}{\partial x_i} [u_i (\rho E + P)] = \frac{\partial}{\partial x_j} \left(\kappa_{eff} \frac{\partial T}{\partial x_j} \right) + S_r \quad [6.3.1]$$

The effective thermal conductivity is given by

$$\kappa_{eff} = \kappa + \frac{c_p \mu_t}{Pr_t} \quad [6.3.1]$$

The value of the turbulent Prandtl number in this study is 0.85, which is a commonly used number in combustion problems. S_r is the source of energy due to chemical reaction, which is defined below

$$S_r = - \sum_i \left(\frac{h_j}{M_i} + \int_{T_{ref_i}}^T c_{p_i} dT \right) R_i \quad [6.3.1]$$

h_j and R_i are the enthalpy of formation and the volumetric rate of creation of species i .

6.4 Equilibrium Mixture Fraction/PDF Model

The non-premixed modeling approach involves the solution of transport equations for one or two conserved scalars (the mixture fractions). Equations for individual species are not solved. Instead, species concentrations are derived from the predicted mixture fraction fields. The thermochemistry calculations are preprocessed in prePDF and tabulated for look-up in FLUENT. Interaction of turbulence and chemistry is accounted for with a probability density function (PDF). Flow Chart 6.1a and b show the calculation process.

6.4.1 Advantages of the Non-Premixed Approach

The PDF modeling for non-premixed combustion has been proven well for the simulation of turbulent diffusion flames with fast chemistry. This model is able to accommodate intermediate (radical) species prediction, dissociation effects, and rigorous turbulence-chemistry coupling. This method is computationally efficient; the solution of a large number of species transport equations is not required.

6.4.2 Definition of the Mixture Fraction

Since this is a turbulent combustion study, the molecular transport is less important than the turbulent transport. Hence, the mixture fraction method holds good because all the species share the same diffusion coefficient. Mixture fraction is defined as the mass fraction of both burnt and unburnt fuel stream elements. In fact, it is the elemental mass fraction that originated from the fuel stream. The mixture fraction is written in terms of the atomic mass fraction as (Sivathanu and Faeth, 1990)

$$f = \frac{Y_\alpha - Y_{\alpha,air}}{Y_{\alpha,F} - Y_{\alpha,air}} \quad [6.4.1]$$

Y_α is the elemental mass fraction for some element, α . The subscript *air* and *F* represent the value at the air stream inlet and the value at the fuel stream inlet, correspondingly. If the diffusion coefficients for all species are equal, then the equation 6.4.1 is identical for all elements, and the mixture fraction definition is unique. This mass fraction includes all elements from the fuel stream, including inert species N_2 that is mixed with the fuel.

6.4.3 Transport Equations for the Mixture Fraction

The species equations were reduced to a single equation for the mixture fraction, f because of the assumption of equal diffusivity for all species. The assumption of equal diffusivity is generally acceptable for turbulent flows where turbulent convection overwhelms molecular diffusion, though it is problematic for laminar flows. f is a conserved quantity. The mean (time-averaged) mixture fraction equation is (Jones and Whitelaw, 1982)

$$\frac{\partial}{\partial t}(\rho \bar{f}) + \nabla \cdot (\rho \bar{v} f) = \nabla \cdot \left(\frac{\mu_t}{\sigma_t} \nabla \bar{f} \right) \quad [6.4.2]$$

Also, the mean mixture fraction variance,

$$\frac{\partial}{\partial t} \left(\rho \overline{f'^2} \right) + \nabla \cdot \left(\rho \bar{v} \overline{f'^2} \right) = \nabla \cdot \left(\frac{\mu_t}{\sigma_t} \nabla \overline{f'^2} \right) + C_g \mu_t (\nabla^2 \bar{f}) - C_{dp} \frac{\epsilon}{K} \overline{f'^2} \quad [6.4.3]$$

$$f' = f - \bar{f} \quad [6.4.4]$$

$$\sigma_t = 0.85$$

$$C_g = 2.86$$

$$C_d = 2.0 \quad [6.4.5]$$

The mixture fraction modeling approach is capable of reducing the chemistry model to one conserved mixture fractions. With adiabatic condition assumption, all the thermochemical scalars (species mass fraction, density, and temperature) are uniquely related to the mixture fraction. At each location in the flow field, the instantaneous mixture fraction value was used to compute the instantaneous values of individual species mole fractions, density, and temperature. ψ_i was used to represent the instantaneous species mass fraction, density, or temperature,

$$\psi_i = \psi_i(f, H^*) \quad [6.4.6]$$

$$H^* = \sum_i m_i H_i = \sum_i m_j \left[\int_{T_{ref,i}}^T c_{p,i} dT + h_i^o(T_{ref,i}) \right] \quad [6.4.7]$$

The ψ_i relation with the temperature, species mass fraction and density depends on the chemistry model used. In this study, the equilibrium model was selected to perform the calculation.

6.5 Equilibrium Model

The equilibrium model assumes that the chemistry is rapid enough for chemical equilibrium to always exist at the molecular level. This model was used to calculate the flame temperature and the mole fraction of the products species. With the computed mixture fraction (f), the individual species mole fractions were calculated using an algorithm based on the minimization of Gibbs free energy. (Kuo, 1986) The information of the detailed kinetic data (eg. CHEMKIN data) is not required in this model. Furthermore, it can also predict the formation of intermediate species.

6.5.1 Derivation of Mean Scalar Values from the Instantaneous Mixture Fraction

The probability density function $p(f)$, describing the temporal fluctuations of f in the turbulent flow, has the very beneficial property that it can be used to compute time-averaged values of variables that depend on f . Time-averaged values of species mole fractions and temperature can be computed (in adiabatic systems) as

$$\bar{\psi}_i = \int p(f) \psi_i(f) df$$

[6. 5. 1]

A presumed β -function was used to compute the probability density function. The β -function has been broadly applied for the computation of probability distribution of the mixture fraction in many turbulent mixing and turbulent diffusion combustion models in the literature (Landenfeld et al., 2002; Liu et al., 2002).

$$p(f) = \frac{f^{\alpha-1} (1-f)^{\beta-1}}{\int f^{\alpha-1} (1-f)^{\beta-1} df} \quad [6.5.2]$$

$$\alpha = \bar{f} \left[\frac{\bar{f}(1-\bar{f})}{\bar{f}'^2} - 1 \right] \quad [6.5.3]$$

$$\beta = (1-\bar{f}) \left[\frac{\bar{f}(1-\bar{f})}{\bar{f}'^2} - 1 \right] \quad [6.5.4]$$

With the assumption of adiabatic condition, all the thermochemical scalars (species mass fraction, density, and temperature) are uniquely related to the mixture fraction. At each location in the flow field, the instantaneous mixture fraction value was used to compute

the instantaneous values of individual species mass fractions, density, and temperature. An equilibrium chemistry model, which assumed a rapid reaction, was used to calculate the flame temperature and the products species. With the computed mixture fraction, f , the individual species mole fractions were calculated using an algorithm based on the minimization of Gibbs free energy. (Kuo, 1986) The reactant species from the fuel stream and the oxidizer stream were C_3H_6 , H_2 , air (21% O_2 and 79% N_2 by volume) and the additional N_2 from the fuel dilution. The presumed products species were CO_2 , CO , H_2O (gas and liquid), C , CH , O , H , and OH .

6.6 Computational Facility

A computational fluid dynamics software, FLUENT was used to perform the numerical analysis for this study. The software IDEAS was used to generate the 3-D domain for cross-flow flame computation. Gambit grid generation software was used to generate the 2-D domain for quiescent flame computation. A Pentium IV 1.8 GHz workstation was used for the computation.

6.7 Boundary Conditions

Figures 6.3a and 6.4 show the definition of the boundary condition of the domain for both the cross-flow and the quiescent computation. The 3-D domain was modeled exactly as the (half of) test section of the combustion wind tunnel. The value of the cross-flow velocity and the jet exit velocity and fuel properties were all taken from Chapter III. The entire boundaries were well defined except for the outlet of the domain. The test section outlet was defined as the outflow plane, where the diffusion flux normal to the

exit plane is defined as zero. The condition of the outflow plane was extrapolated from the domain and has no effect on the upstream flow. The extrapolation was performed in the manner that is consistent with the fully developed flow.

6.8 Grid Generation and Validation

The flame symmetry plane is at the x-z plane. Hence, a three-dimensional domain with half of the test section (x-z symmetry plane) was created. Several different grid sizes were selected to perform on a benchmark problem. The domain that has the finest grid size, has the most efficient computation time, and produced the most accurate result was selected for the computation of the problem. A benchmark problem was selected from Goh and Gollahalli (2000) cross-flow flame study. The grid was generated on IDEAS grid generation software. Several different grid sizes were tried on a benchmark problem. Five different grid sizes for the 3-D domain were tried, and their sizes are shown in Table 6.1. The comparison of the axial temperature solution with different grid sizes is shown in Figure 6.1a. Grid E was selected for the computation because further refining the grid (grid A to D) did not make a significant difference in the result. However, further coarsening grid caused a gridding problem at the burner exit region. The software had a problem generate grid at that coarsen value. After the solution was converged, the grids were further refined. The grid refinement process was based on the temperature solution. The grids with the temperature gradient of 0.02 (dT/dV) and above were refined. Temperature gradients of 0.02 and above were selected because refinement of grid of any gradient that was lower than 0.02 produced insignificant changes in the result. The results of the comparison is shown in Figure 6.2 and Table 6.2 listed the size of the domain. The

number of grids involved in the refinement is inversely proportional to the temperature gradient selected. Thus, the highest temperature gradient that produced insignificant changes was selected to avoid an increase of unnecessary grids in the domain. After the grid refinement, the computation was continued until the solution was converged. Figure 6.3b shows the domain of x-z symmetry plane for 100% CFMFR condition after grid refinement. This grid refinement process was performed using the FLUENT grid adaptation function.

The comparison of the solution from the model with the benchmark problem is shown in Figure 6.1b. All the computational results match relatively well with the benchmark experimental results.

6.9 Converging Criteria

At the end of each iteration, the residual sum for each of the conserved variables is computed and stored. The solution converges when the residuals reach a certain value.

6.9.1 Definition of Residuals

After discretization, the conservation equation for a general variable ϕ at a cell P is defined as

$$a_P \phi_P = \sum_{nb} a_{nb} \phi_{nb} + b \quad [6.9.1]$$

The coefficients a_P and a_{nb} are the center coefficient and the influence coefficients for the neighboring cells. b is the contribution of the constant part of the source term S_c in $S=S_c+S_{P\phi}$ and of the boundary conditions. In Equation 6.9.1, a_P is defined as

$$a_P = \sum_{nb} a_{nb} - S_P \quad [6.9.2]$$

The residual is defined as the imbalance in Equation 6.9.1 totaled over all the computational cells P .

$$R^\phi = \sum_{cellsP} \left| \sum_{nb} a_{nb} \phi_{nb} + b - a_P \phi_P \right| \quad [6.9.3]$$

It is easier to judge the convergence with a scale residual. The residual was scaled using a scaling factor representative of the flow rate through the domain. The scaled residual is defined as

$$R^\phi = \frac{\sum_{cellsP} \left| \sum_{nb} a_{nb} \phi_{nb} + b - a_P \phi_P \right|}{\sum_{cellsP} |a_P \phi_P|} \quad [6.9.4]$$

For example, the momentum equations denominator term $a_P \phi_P$ is replaced by $a_P v_P$, where v_P is the magnitude of the velocity at cell P .

To check for convergence, the comparison of current iteration with the previous was calculated through the normalization of the residual. Normalization of the residual was calculated by dividing the current iteration residual by the maximum residual value after 5 iterations

$$\bar{R}^\phi = \frac{R_{iteration\ N}^C}{R_{iteration\ 5}^C} \quad [6.9.5]$$

The defined normalized residuals for all the parameters are given in Table 6.3.

6.10 2-D Modeling

The modeling for the quiescent condition flame was a simplified version of the 3-D modeling that was discussed above. The formulation and the theory can be referred from the FLUENT 6.0 manual (FLUENT, 2001).

6.11 Results and Discussion

The results for the quiescent condition flame are presented in Figures 6.5 to 6.8 for 10%, 30%, 60%, and 100% CFMFR flames. The model described above performed relatively well for the highly turbulent flames. The comparability of the numerical and the experimental results improves as the turbulence intensity increases. The 10% CFMFR flame was a laminar flame (refer to Figure 3.56a). Since the model is based on turbulent flow, none of results (temperature and species) in the 10% CFMFR flame condition, Figure 6.5 d, 6.6b, 6.7b, and 6.8b show a good match. Hence, the flame results of this condition (10% CFMFR) in the cross-flow condition will not be presented. Since the numerical results do not add on to further discussion to the main objective of this study, the laminar case results will not be discussed in this chapter. The main objective of the numerical study is to find the most appropriate model that is able to simulate the flame for a practical application. The common application of cross-flow flame is normally in a turbulent condition. The most appropriate application for this study is flare, which is a highly turbulent flame. Hence, the current model provides a relatively good representation and a basis for the application purpose. Overall the model gives a good basis for future study. A number of recommendations for the improvement of the model will be given in Chapter VII.

6.11.1 Quiescent Condition Flame

The numerical temperature results showed that the flames were narrower than the experimental results. This observation was mainly caused by the assumption of rapid reaction in the equilibrium model. In the Sivathanu and Faeth (1990) study, the numerical temperature data based on the equilibrium model departed from the experimental results

when the stoichiometric ratio was not close or equal to unity. Hence, the numerical results in this study were closely matched to the experimental results at high flame temperature region, where the flame stoichiometry was close to unity. At the region of 75% flame length, the numerical temperature results were lower than the one in experimental. Other than the numerical flame being narrower than the experimental, it was also shorter than the experimental flame. Hence, the 75% of the visible flame length in the experimental was not the 75% flame length for the numerical. Since the physical flame length from the experimental result were applied for numerical (for the location of 25%, 50% and 75% of flame height), most of the results shown were slight displaced downstream, especially at the 75% flame length location. The quiescent flame temperature results showed that the temperature matched well with the experimental results as long as the flame was in low soot concentration and high turbulence intensity. Figure 6.5a shows that the temperature profile of the computation results for the 100% CFMFR matched well with the experimental results for all three flame height locations.

The 60% CFMFR computational results in Figure 6.5b show that the flame temperature profile at 50% of the flame height was higher and narrower than the experimental profile. The difference was mainly because the equilibrium model did not take into account of soot particle growth and buildup, although the model took into account the solid carbon formation. The soot concentration results in Chapter IV (Figure 4.13) showed that the soot concentration for the 60% CFMFR was highest at 50% flame length location. Furthermore, the model assumed an adiabatic flame condition. As a result, the radiative heat loss by the soot particles in the experimental flame was not accounted for in the computation, which resulted in higher computed flame temperature

in high soot regions. The overestimation of the temperature caused the overestimation of CO_2 (Figure 6.7a) at 25% and 50% of the flame length. At 75% of the flame length, the computed CO_2 is lower than the experimental result. The reason was explained above.

At 75% of the flame height, all flame conditions (including the cross-flow flames) showed a lower temperature than the experimental. In a turbulent diffusion flame, the soot particle dominated the oxidation process at this region. Furthermore, the smoke point flame had significantly higher soot concentration than a non-smoking flame. Hence, the computed temperature results at this region were lower than the experimental results.

The O_2 results for the 100%, 60% and the 30% CFMFR case matched well within the experimental results (Figure 6.6a and 6.6b), especially at the 25% and 50% flame height region. The concentration of O_2 in the numerical calculation was more diffusion dependent, rather than temperature dependent likes the CO and CO_2 . Hence, the O_2 concentration results were well matched with the experimental results.

The numerical results of CO concentration in Figures 6.8a and b show an overestimation of CO concentration at high equivalence ratios and high soot concentration regions (25% and 50% of the flame height). This phenomenon was also observed in the Sivathanu and Faeth study (1990). At the higher equivalence ratio region, finite rate chemistry is more significant than equilibrium prediction (Sivathanu and Faeth, 1990). Again, the nature of high soot concentration of the flame also affected the correlation of the model in this region. There were four species in the products that contain carbon. Since, the model did account for soot in the flame, there was an excess of carbon in carbon-contained species.

6.11.2 Cross-Flow Condition Flame

Figures 6.9a to 6.9e show the x-z plane temperature profiles on the symmetry plane for the cross-flow conditions of 2, 2.5, 3, 3.5 and 4 m/s. Figures 6.10 to 6.24 show the comparison of the numerical and experimental results of temperature, O₂, CO₂, CO and OH (only on selected conditions) in x direction for three flame locations. Figure 6.25 to 6.28 (a and b) show the temperature profiles in x-y plane at three flame locations for 60% and 100% CFMFR at 2, 3, and 4 m/s cross-flow conditions.

Figures 6.9 a to e show the temperature profiles of the 100% (a), 60% (b) and 20% (c) CFMFR flame at 2 to 3 m/s cross-flow, but it was 30% CFMFR instead of 20% (c) for 3.5 and 4 m/s cross-flow cases. These temperature profiles showed that the increase of cross-flow velocity caused the flame to become narrow and bend more toward the x direction. The experimental results showed a non-monotonic relation of the flame length (Figure 3.54b), and the cross-flow velocity that was mentioned in the previous chapter, especially in the 60% CFMFR flame. The 60% CFMFR flame results showed a decrease of flame length from the cross-flow velocity of 3.0 m/s to 3.5 m/s (Figures 6.9c and 6.9d). However, from the cross-flow velocity of 3.5 to 4 m/s (Figure 6.9d and 6.9e), the flame length showed an increase. The change of flame length for the 100% CFMFR case is not significant. The 20% CFMFR flame also showed a decrease of flame length from the cross-flow of 2.5 to 3 m/s (Figure 6.9b and 6.9c). The computational results of the 30% CFMFR flame results at 3.5 and 4 m/s (Figure 6.9d and 6.9e) cross-flow showed an increase of flame length. All the observations were consistent with the behavior of the experimental flame length results shown in Figure 3.54b.

Besides the non-monotonic relation, two observations shown in the experimental section were also seen here in the numerical results. First, the temperature profile showed a higher temperature at the side closer to the burner, which had also been observed in the experimental section. Secondly, the change of flame structure from a cross-flow to a co-flow like structure was also apparent in the numerical results. The temperature peaks became closer together and the temperature difference became smaller as the cross-flow increases, and it behaved almost like a co-flow condition flame. The comparison of the numerical and the experimental results at the three cross-flow velocities is presented in the following section.

The comparison of the temperature results (Figures 6.10 to 6.12) showed that the experimental 100% CFMFR flame tilted more in x direction than the numerical results. This was because at a higher momentum flux ratio flame, the flame tilted further toward positive x direction along the flame length. Numerical flame was not long enough to show the significant tilting. The numerical flame was shorter because the computation did not take account of the soot oxidation. Soot oxidation required long residence time, which caused the flame to be longer than the computational flame. Table 6.4 shows the numerical. The numerical flame length was obtained from the temperature results with the assumption that visible flame ceases when the soot ceases to oxidize at temperatures below 1300 (Kent and Wagner, 1984). The discrepancy between the numerical and the experimental results increased with the decrease of turbulence intensity, which was also the case for CO₂ and CO calculation.

The numerical results of O₂ concentration (Figures 6.13, 6.17 and 6.21) were in a good agreement with the experimental results, except for some cases at 75% flame length

of the 20% CFMFR flame at 2 and 3 m/s cross-flow and the 30% CFMFR flame at 4 m/s cross-flow. Again, the results showed that the numerical flames are slightly narrower than the experimental flames.

Figure 6.14, 6.18, and 6.22 show the CO₂ concentration results. Both the numerical and the experimental results exhibited a double peak structure at 25% and 50% flame length regions. These peaks were related to the stoichiometry of the flame. The peaks were located at the region close to stoichiometric. On the other hand, at 75% flame length region, the results showed only one peak. The experimental result showed that a single peak at the 75% flame length region was mainly due to the fact that soot concentration was high at the flame core, and the dominance of the heterogeneous combustion of soot, and the mixing effect. However, the computational flame did not take account of soot oxidation, so the single peak phenomenon in the computation is only due to the mixing effect. The CO₂ concentration in the 75% flame length region was higher than in the 50% region, and the 25% region had the lowest CO₂ concentration. This was because CO₂ produced upstream was carried downstream along the flame. 100% CFMFR CO₂ numerical results were relatively well related to the experimental results, especially at 25% and 50% flame length region in both 3 and 4 m/s cross-flow flames. At 75% flame length region, the computational result underestimated the CO₂ concentration. The reason for this was the same as the reason for the wider experimental flame. The assumption of a rapid reaction may have shortened the duration for the actual reaction process. Furthermore, the high soot concentration in the smoke point flame also caused a problem. Soot required a longer time to be oxidized compared to other smaller molecules. Since, the computational model did not take account of soot oxidation, the

computational flame was shorter and narrower. The 60% CFMFR CO_2 concentration results at 2 and 3 m/s cross-flow were very well related to the experimental results, though the experimental flame was slightly wider than the computational. The experimental CO_2 concentration in 60% CFMFR flame at 4 m/s cross-flow was higher than the computational results. The reason behind this might due to the higher soot concentration (Figure 4.16c) in this flame compared to the other two cross-flow condition (2 and 3 m/s) flames. The computational CO_2 concentration results of the 20% CFMFR flame at 2 and 3 m/s cross-flow and the 30% CFMFR flame at 4 m/s cross-flow flame matched relatively well with the experimental results, though the experimental flame was also slightly wider. Besides the comparison of the experimental and the numerical results, there was another interesting observation from the comparison of the 100% CFMFR flame for the three cross-flow results. The comparison shows that the CO_2 concentration profile of the 100% CFMFR flame in 4 m/s cross-flow (Figure 6.22) had a shape like a quiescent condition flame. This again confirmed of the result of non-monotonic relation discussed in the previous chapters.

Figures 6.15, 6.19, and 6.23 show that the numerical and experimental flames have the peak of CO concentration at or close to the center of the flames. The concentration profiles of CO had a bell shape or a slightly skewed bell shape. For both flame conditions, the 25% flame length region had the highest CO concentration followed by the 50% region and then the 75% region. The reason for this behavior was mainly due to the availability of the O_2 in the flame. The numerical results overestimate the CO concentration at the fuel rich region (middle of the flame), which has also been observed by Sivathanu and Faeth (1990). The CO concentration only agrees in the region

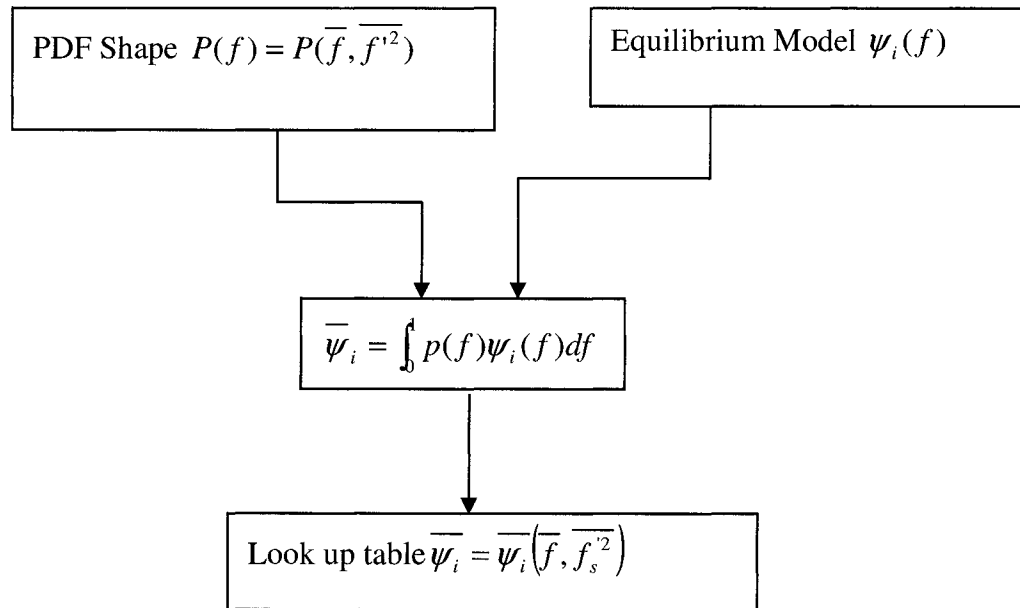
where the equivalence ratio is close to unity, which is located at the flame front. The equilibrium model over predicted the CO concentration several times more than the experimental value at the high equivalence ratio region. At a higher equivalence ratio region, finite rate chemistry is more significant than an equilibrium prediction. High soot concentration present in the flame may also affect the correlation of the model in this region (Sivathanu and Faeth, 1990).

The OH concentration profiles in the x direction at 25% of the flame length of the 60% CFMFR flame at 2, 3 and 4 m/s cross-flow are shown in Figures 6.16, 6.20 and 6.24. The numerical and the experimental results exhibited a dual peak structure. However, the equilibrium model failed to predict the OH concentration up to a satisfactory level. The reason may be that the finite rate reaction was more significant for OH radicals than other stable species like CO₂ or O₂.

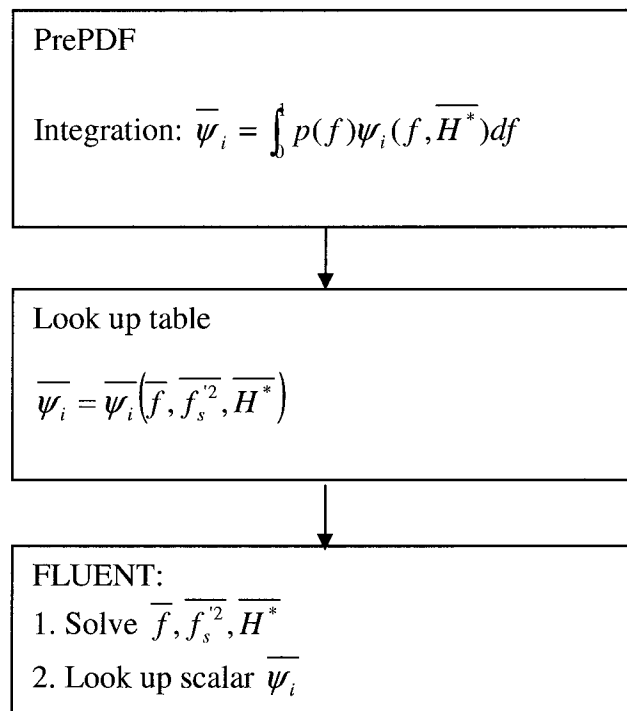
6.12 Conclusion

In conclusion, the standard κ - ϵ turbulent model and the mixture fraction method with the equilibrium model were reasonably satisfactory in predicting qualitatively the structure of the smoke point turbulent diffusion flame in cross-flow and quiescent conditions. However, this method cannot be applied to the laminar flame case. From the comparison, the experimental and numerical temperature and O₂ concentration profiles had shown a good agreement in most cases. The CO₂ concentration comparison was relatively good for a highly turbulent flame condition, though in some cases the high soot concentration in the experimental flame caused a discrepancy between the experimental and the computational results. All the results showed that the numerical flame was shorter

and narrower than the experimental flame. This was mainly due to the rapid reaction assumption and the presence of soot in the experimental flame. Soot particles normally required a longer time to be oxidized than other smaller molecules. Due to the significance of the finite rate reaction and the presence of soot in the flame, the equilibrium model did not serve well for CO concentration prediction at high equivalence ratio regions, and it was also the case for OH concentration prediction.



Flow Chart 6.1a Logical Dependence of Averaged Scalars
on $\psi_i(f)$, f , f'^2 and the Equilibrium Model



Flow Chart 6.1b Separation of Computational Tasks Between FLUENT and prePDF for a Single-Mixture-Fraction Case

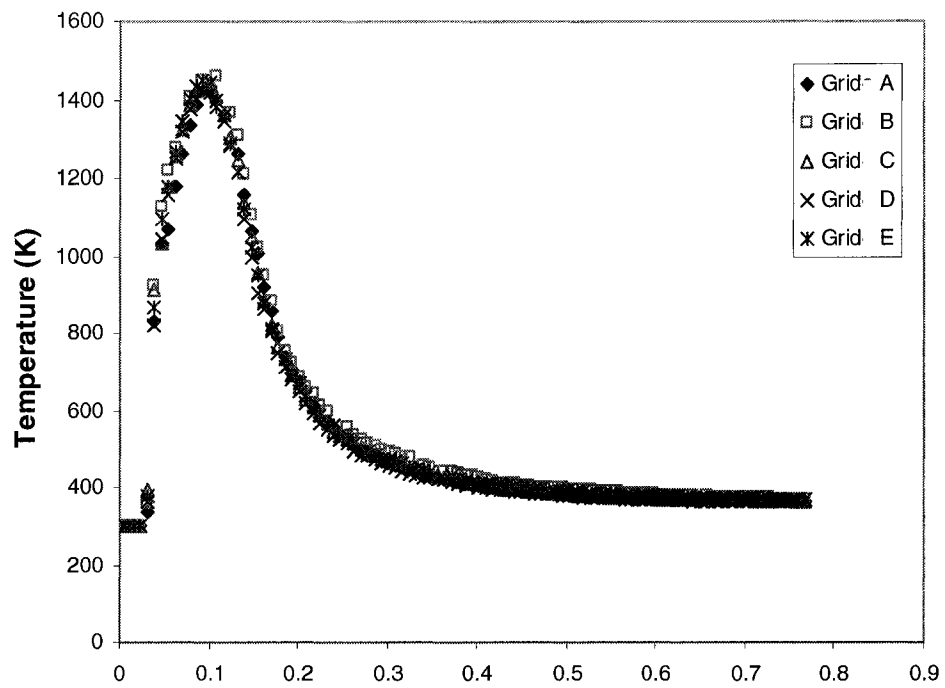


Figure 6.1a Temperature Results Comparison of Different Grid Sizes for a Benchmark Solution at a Line at Symmetry Plane.

Table 6.1 Grid Information for Different Grid Configuration

Grid	Cells	Faces	Nodes
A	198608	411673	40729
B	202952	420860	41727
C	233434	483964	47923
D	288075	596879	58922
E	100279	208596	20977

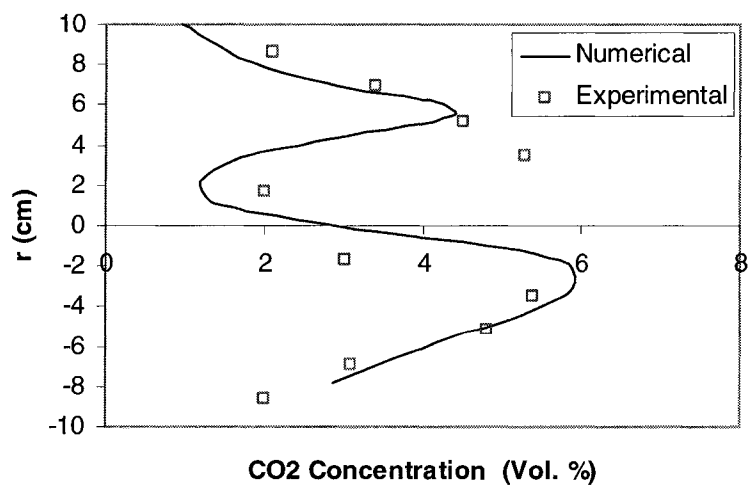
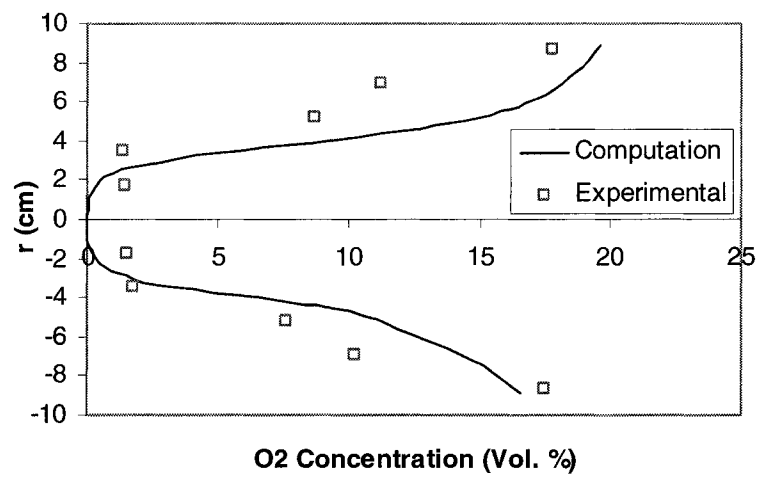
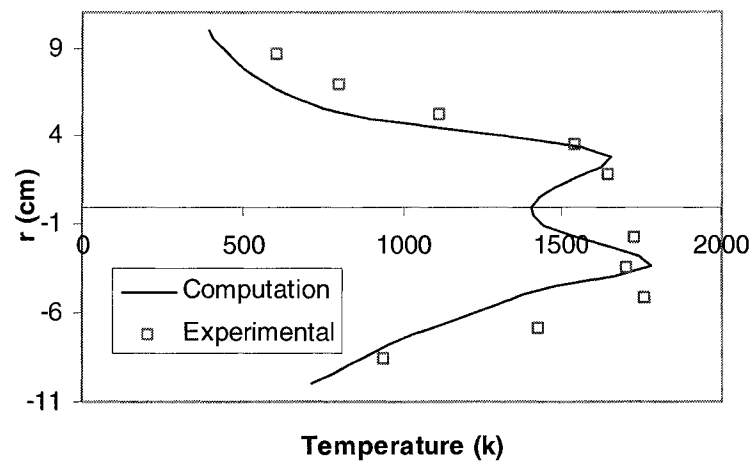


Figure 6.1b Comparison of Benchmark Problem and Solution From the Model

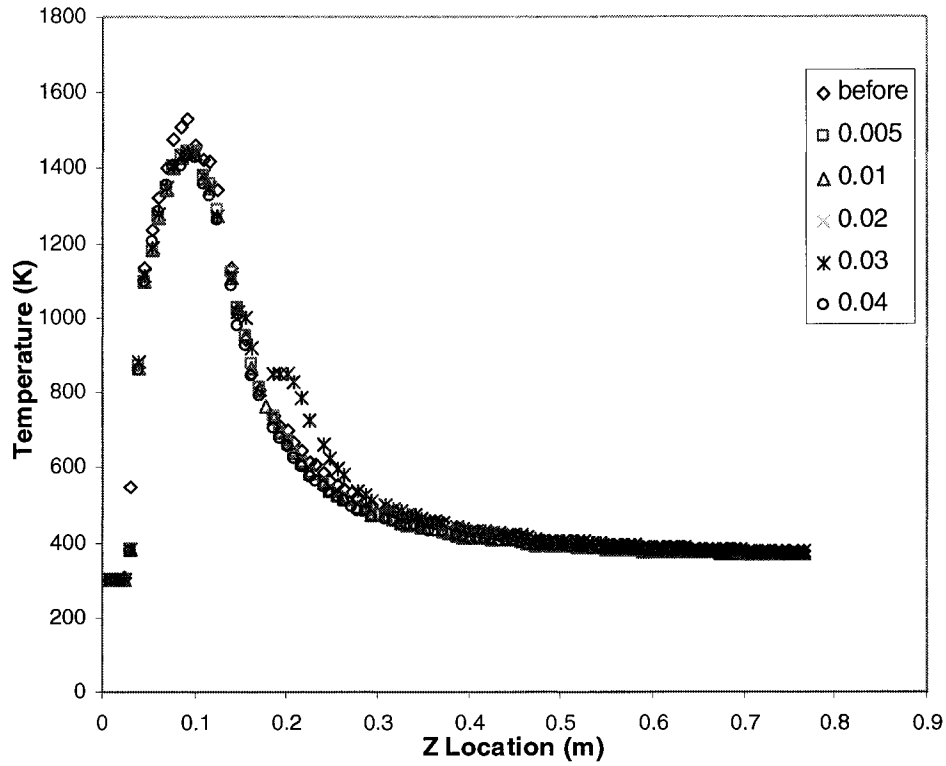


Figure 6.2 Temperature Results Comparison for Different Grid Sizes After Grid Adaptation with Different Temperature Gradients for a Benchmark Solution at a Line On Symmetry Plane.

Table 6.2 Grid Information for Different Grid Configuration with Different Temperature Gradient

Temperature Gradient	Cells	Faces	Nodes
Before	100279	208596	20977
0.005	392326	835011	87382
0.01	317650	681117	73776
0.02	243401	523592	58306
0.03	202430	434981	48645
0.04	175809	377233	42235

Table 6.3 Converging Criteria

	Residual
Continuity	1.00E-05
x-velocity	1.00E-06
y-velocity	1.00E-06
z-velocity	1.00E-06
<i>k</i>	1.00E-05
epsilon	1.00E-05
<i>f</i> _{mean}	1.00E-05
<i>f</i> _{variance}	1.00E-05

Table 6.4 Numerical Flame Lengths

Cross-Flow Velocity m/s	CFMFR	Numerical Flame Length (cm)
Quiescent	100%	44
	60%	32.7
	30%	23.2
2	100%	20.2
	60%	14.2
	20%	7.3
3	100%	20.5
	60%	14.5
	20%	6.5
4	100%	19.6
	60%	13.2
	30%	9.5

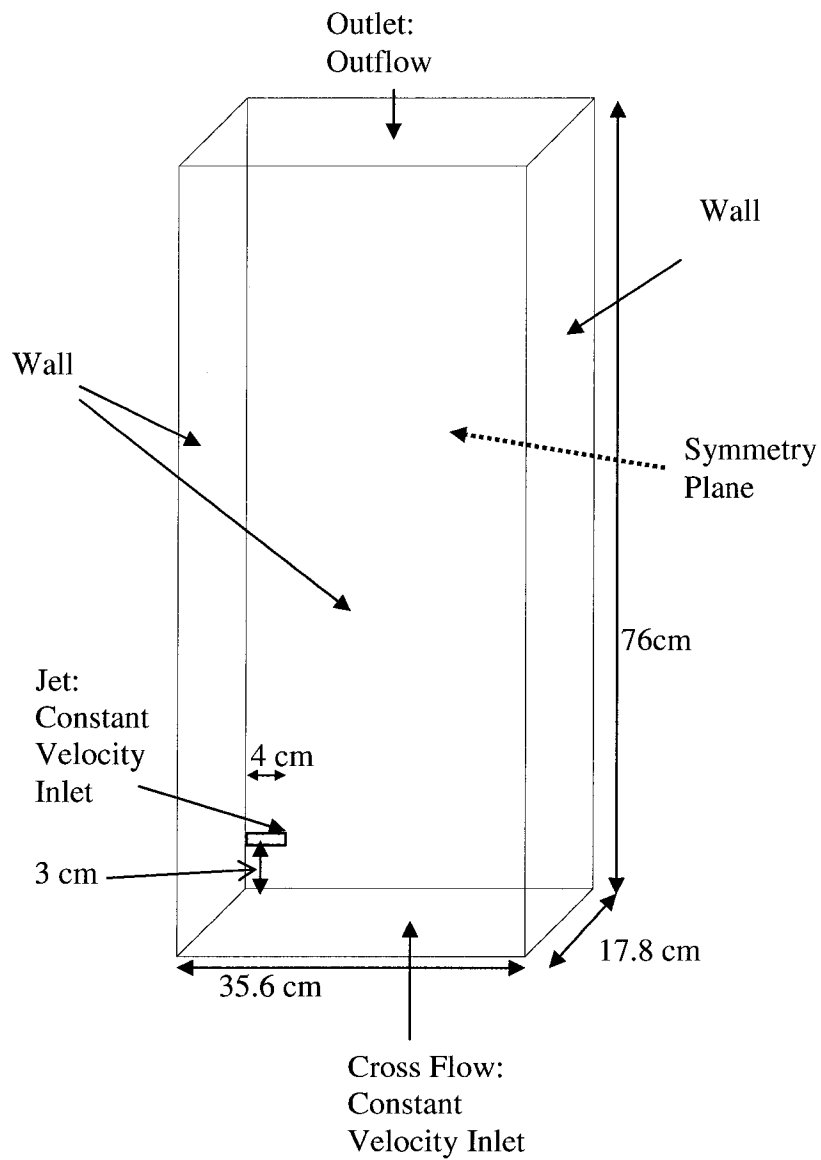


Figure 6.3a Boundary Conditions and Dimensions of the Domain.

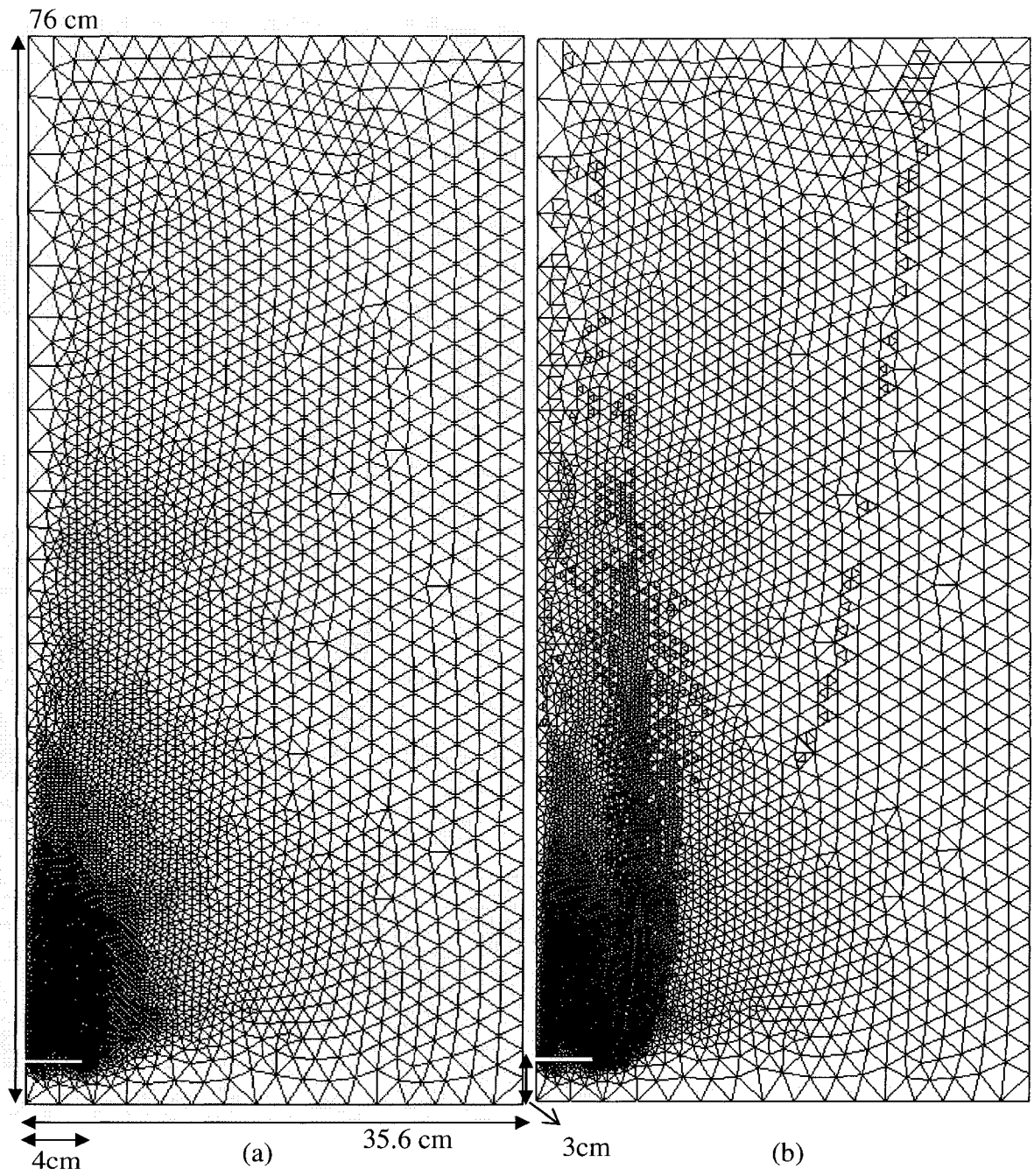


Figure 6.3b Initial Before Grid Adaptation for All Cases (a), and Grid for 100% CFMFR After grid Adaptation at the Symmetry Plane

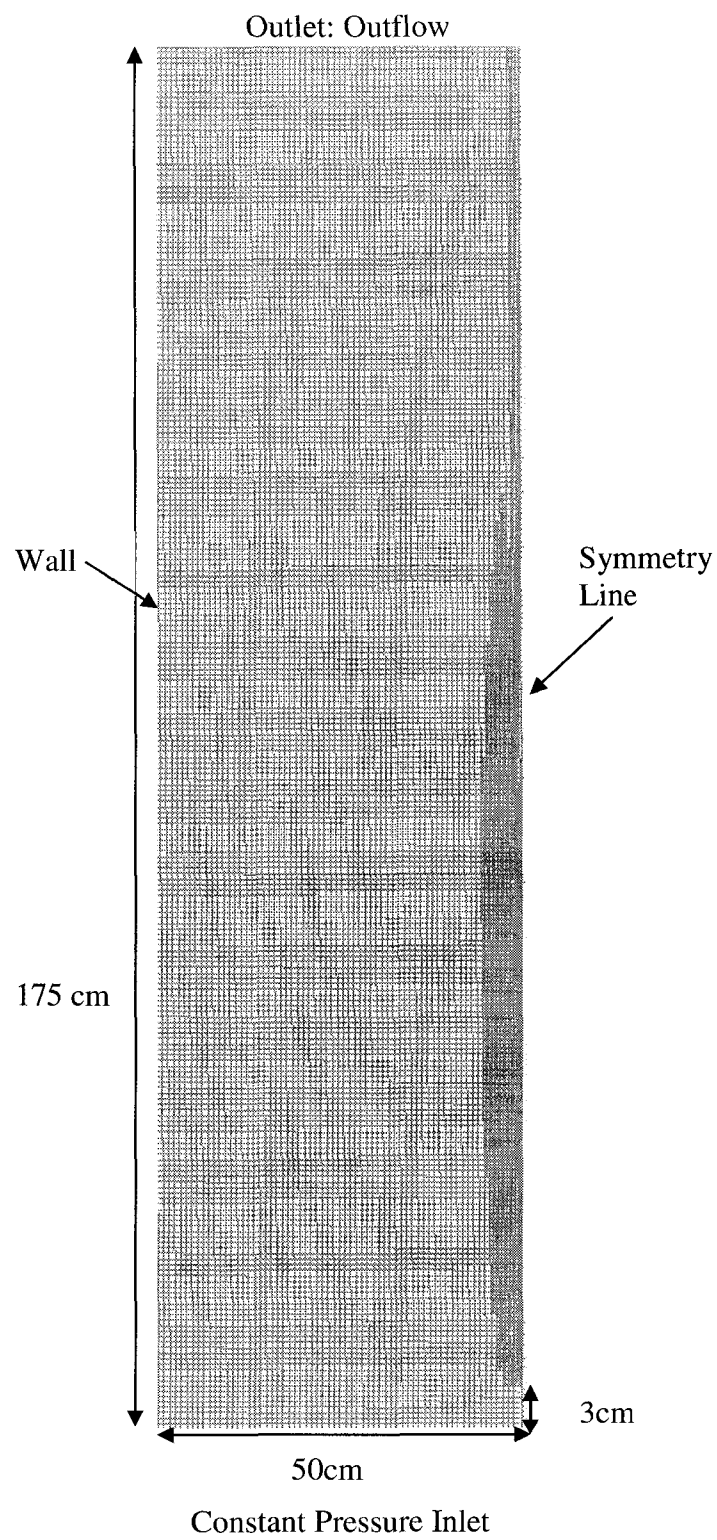
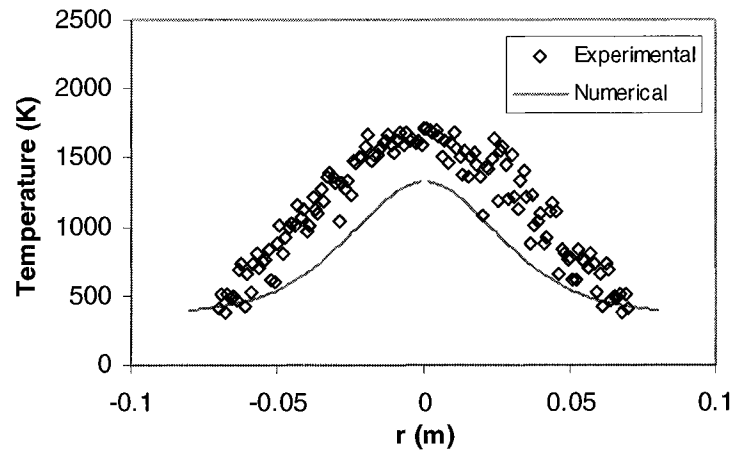
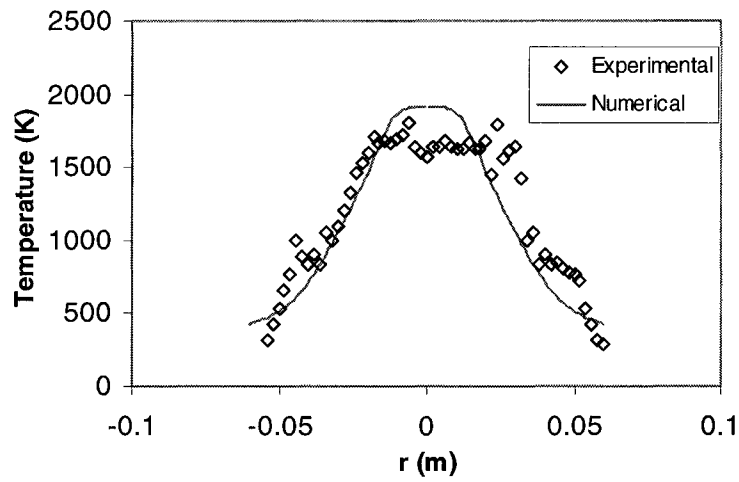


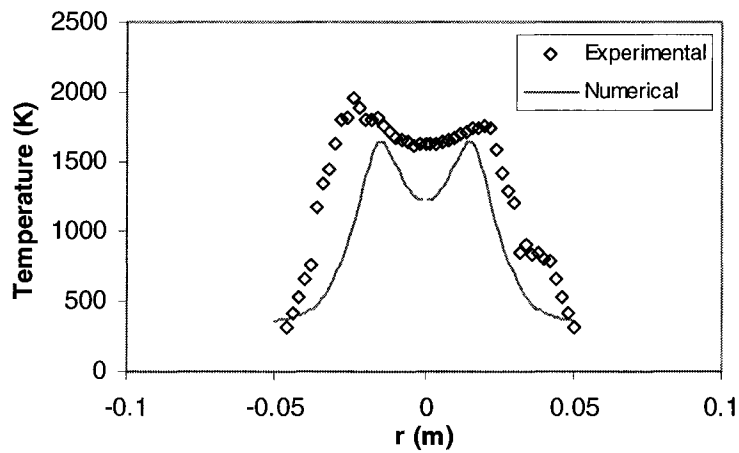
Figure 6.4 After Adaptation Grid for 100% CFMFR Quiescent Flame Study in 2-D



A

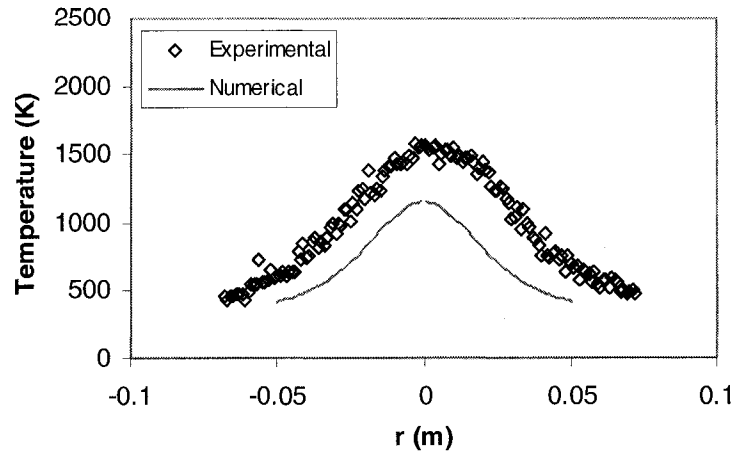


B

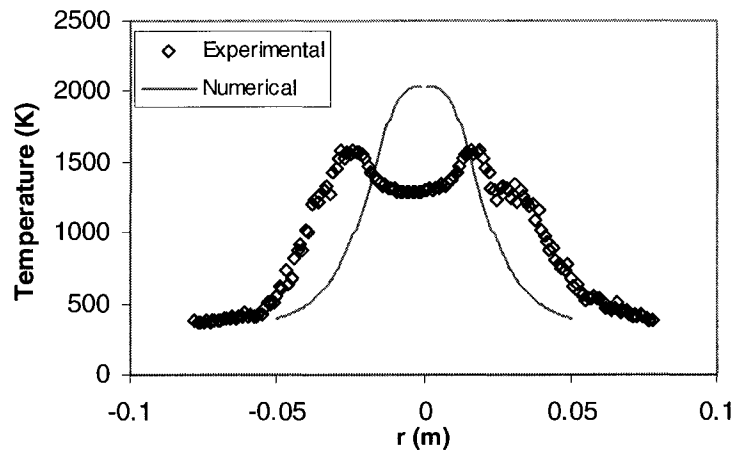


C

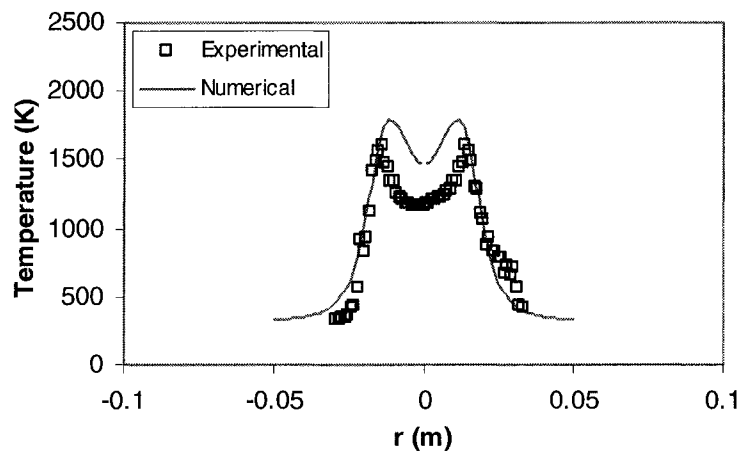
Figure 6.5a Comparison Results of Flame Temperature for Both Numerical and Experimental for 100% CFMFR Flame in Quiescent Condition at Three Flame Locations (A) 75%, (B) 50%, and (C) 25% of Flame Length



A

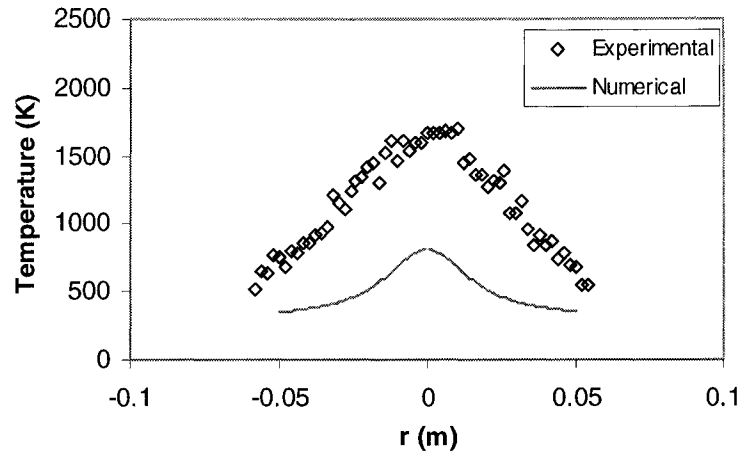


B

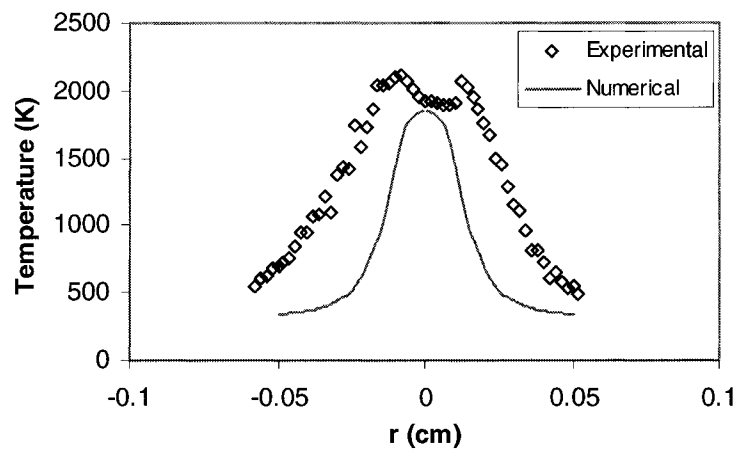


C

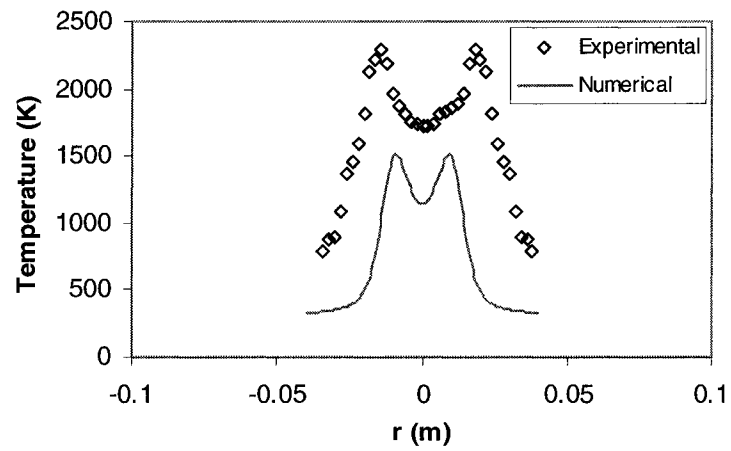
Figure 6.5b Comparison Results of Flame Temperature for Both Numerical and Experimental for 60%CFMFR Flame in Quiescent Condition at Three Flame Locations (A) 75%, (B) 50%, and (C) 25% of Flame Length



A

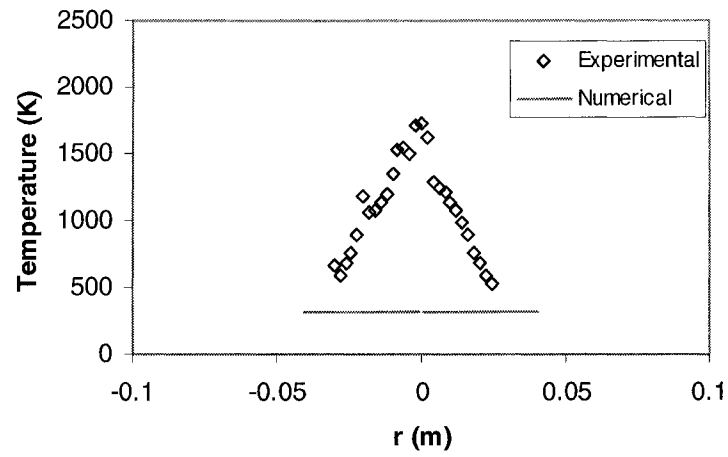


B

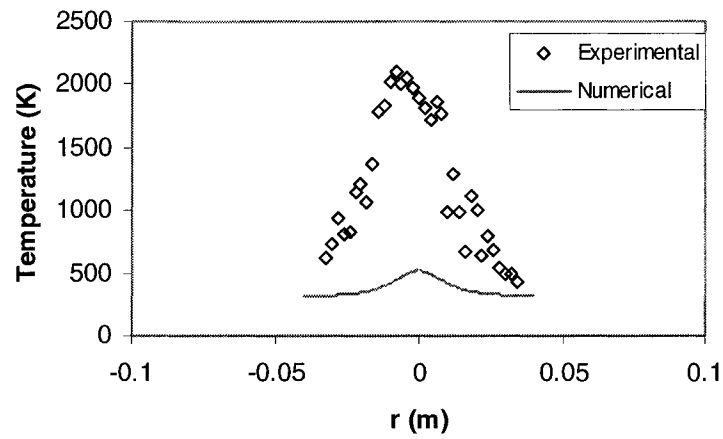


C

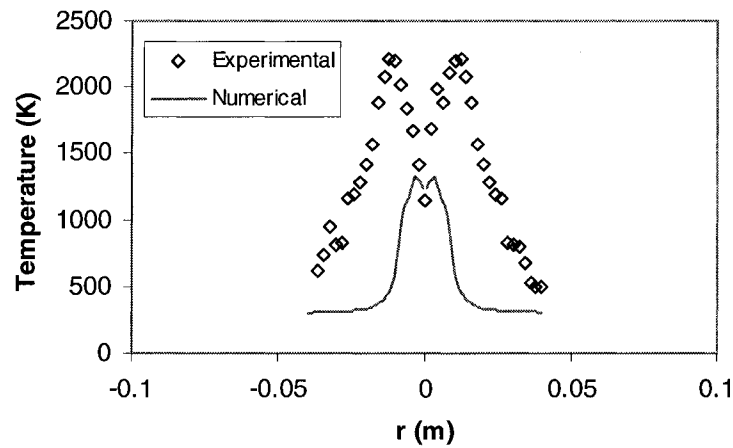
Figure 6.5c Comparison Results of Flame Temperature for Both Numerical and Experimental for 30%CFMFR Flame in Quiescent Condition at Three Flame Locations (A) 75%, (B) 50%, and (C) 25% of Flame Length



A

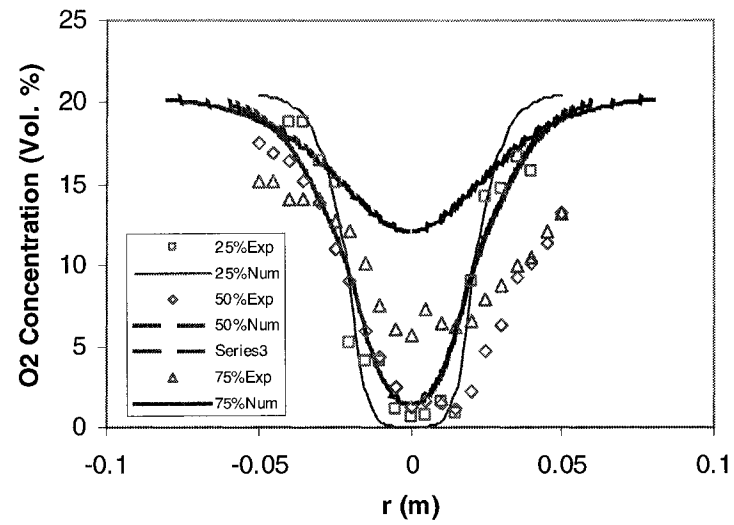


B

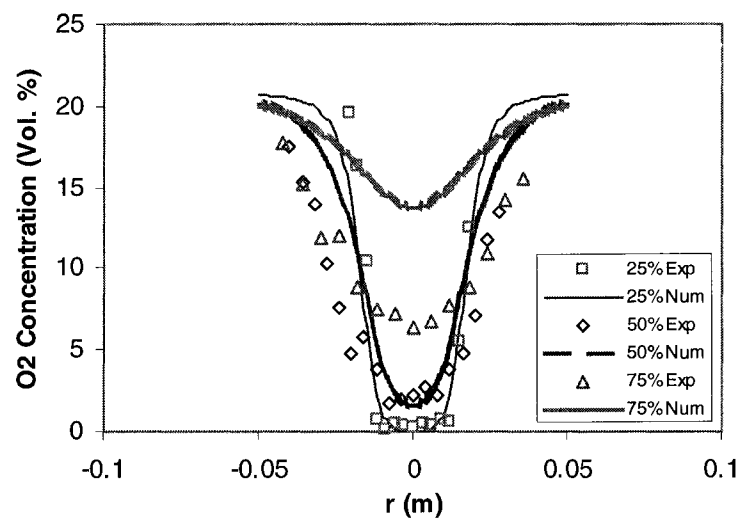


C

Figure 6.5d Comparison Results of Flame Temperature for Both Numerical and Experimental for 10% CFMFR Flame in Quiescent Condition at Three Flame Locations (A) 75%, (B) 50%, and (C) 25% of Flame Length

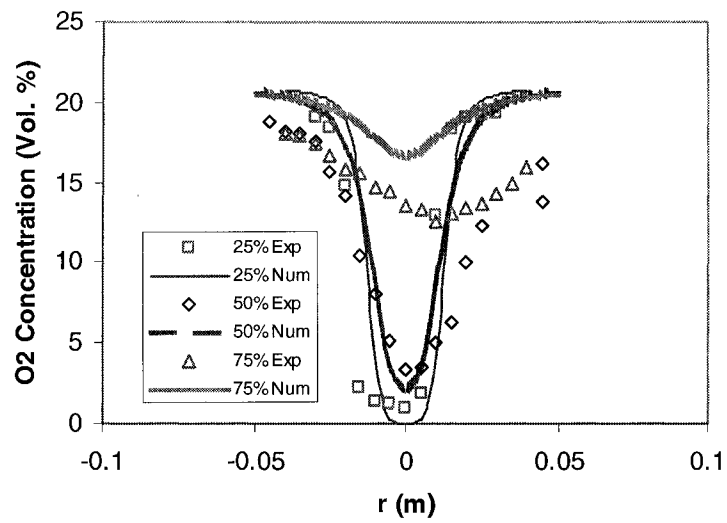


A

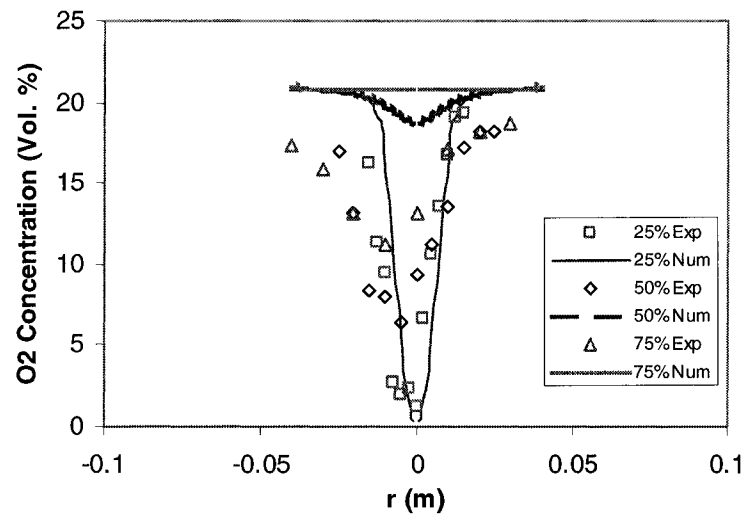


B

Figure 6.6a Comparison Results of Flame O₂ Volumetric Concentration for both Numerical and Experimental in (A) 100% and (B) 60% CFMFR Flame in Quiescent Condition

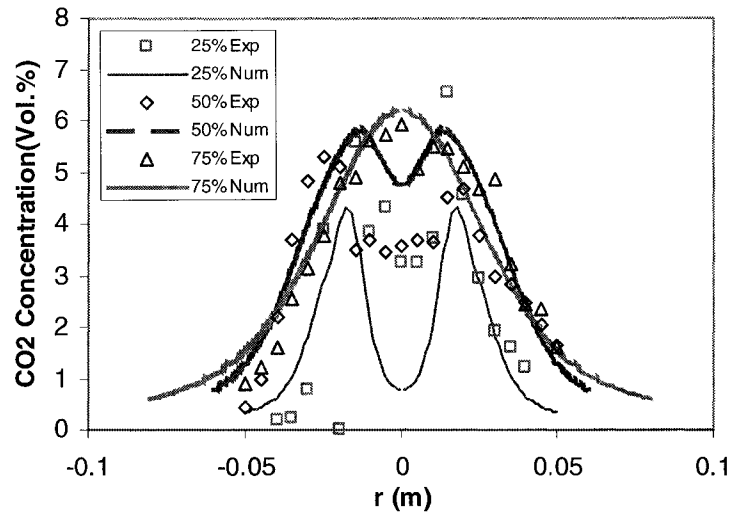


C

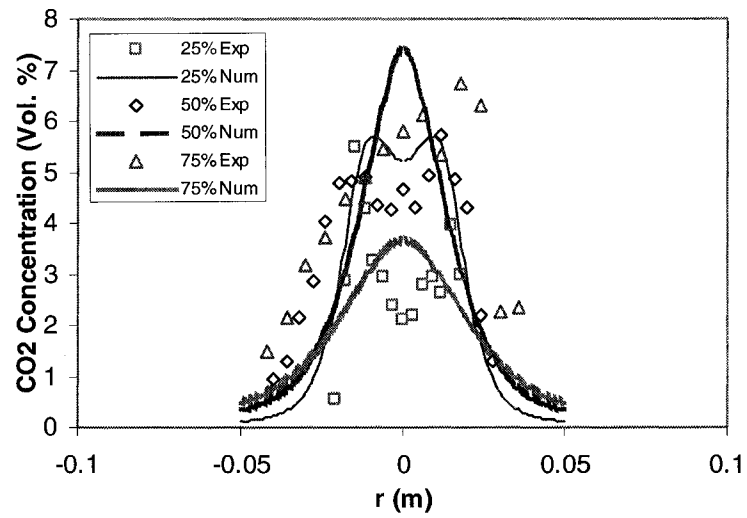


D

Figure 6.6b Comparison Results of Flame O₂ Volumetric Concentration for both Numerical and Experimental in (C) 30% and (D) 10% CFMFR Flame in Quiescent Condition

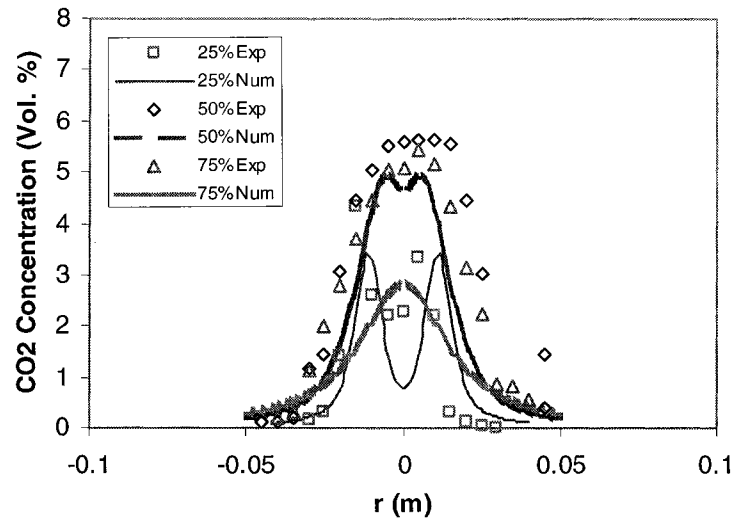


A

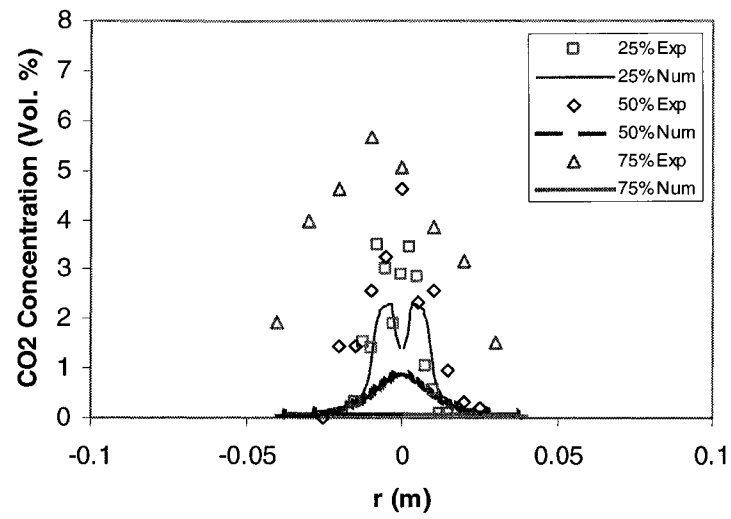


B

Figure 6.7a Comparison Results of Flame CO₂ Volumetric Concentration for both Numerical and Experimental in (A) 100% and (B) 60% CFMFR Flame in Quiescent Condition

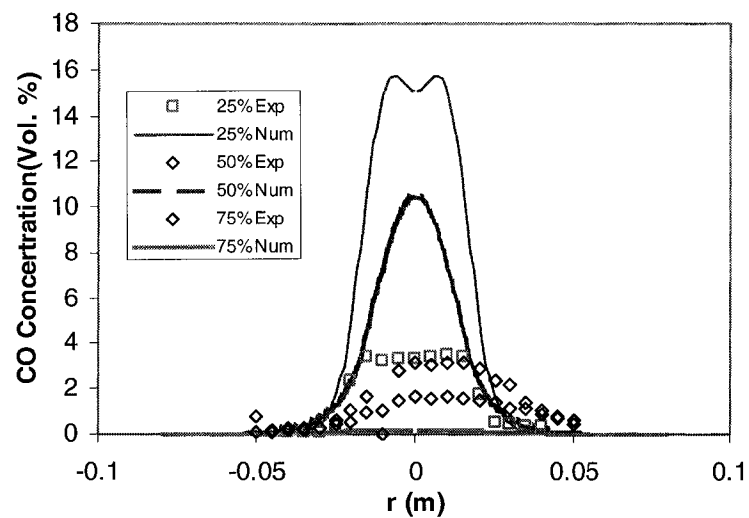


C

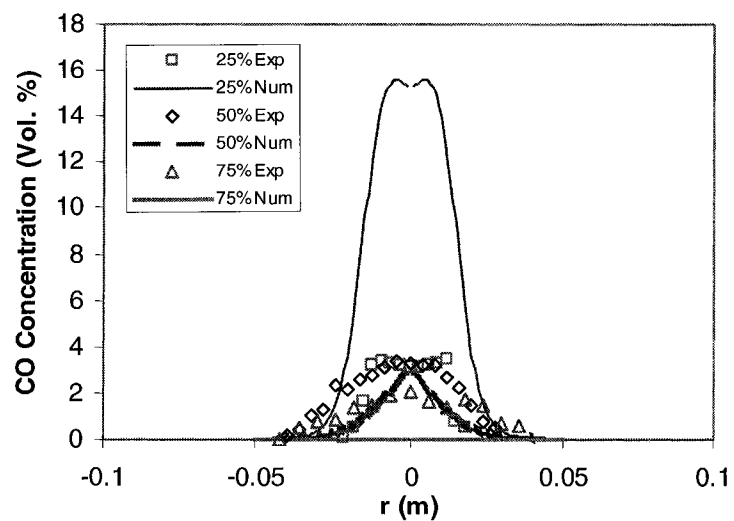


D

Figure 6.7b Comparison Results of Flame CO₂ Volumetric Concentration for both Numerical and Experimental in (C) 30% and (D) 10% CFMFR Flame in Quiescent Condition

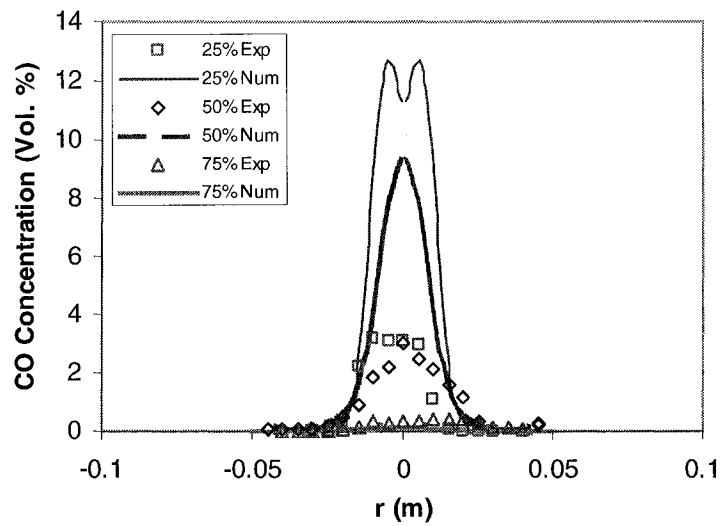


A

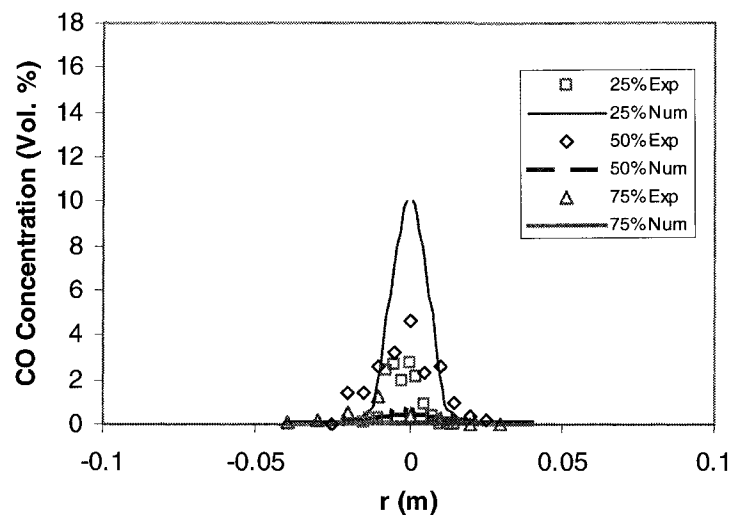


B

Figure 6.8a Comparison Results of Flame CO Volumetric Concentration for both Numerical and Experimental in (A) 100% and (B) 60% CFMFR Flame in Quiescent Condition



C



D

Figure 6.8b Comparison Results of Flame CO Volumetric Concentration for both Numerical and Experimental in (C) 30% and (D) 10% CFMFR Flame in Quiescent Condition

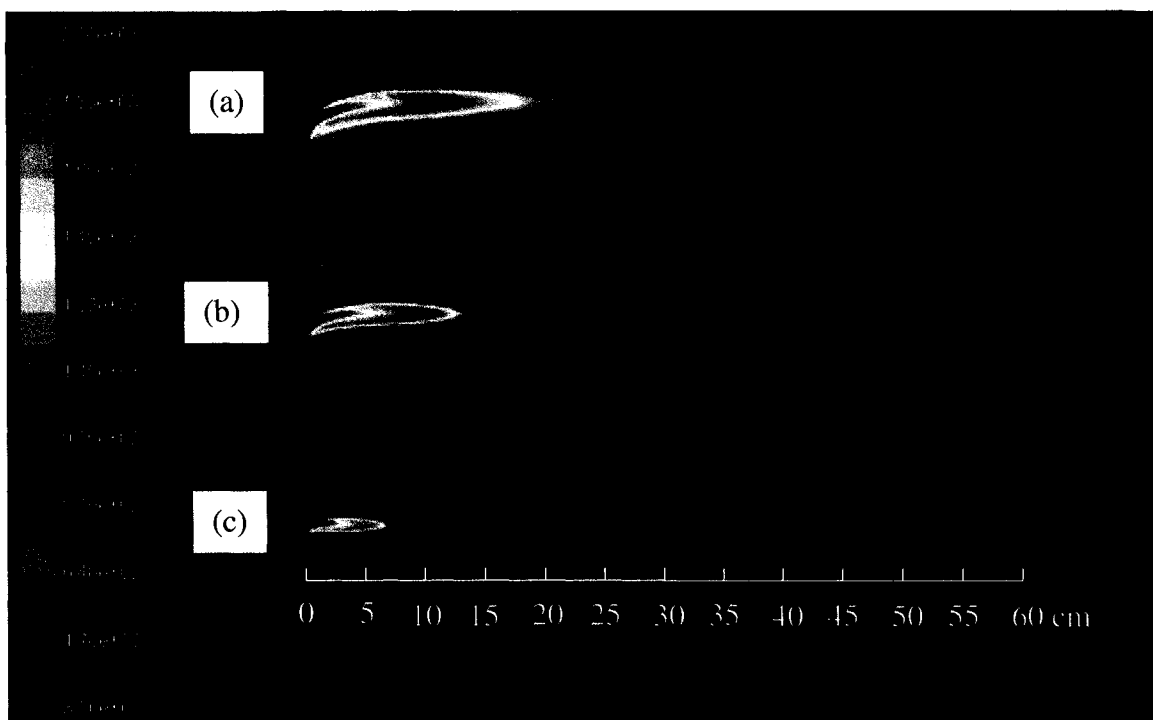


Figure 6.9a X-Z Plane Temperature Profile at 2 m/s Cross-Flow Condition for 100% (a), 60% (b), and 20% (c) CFMFR

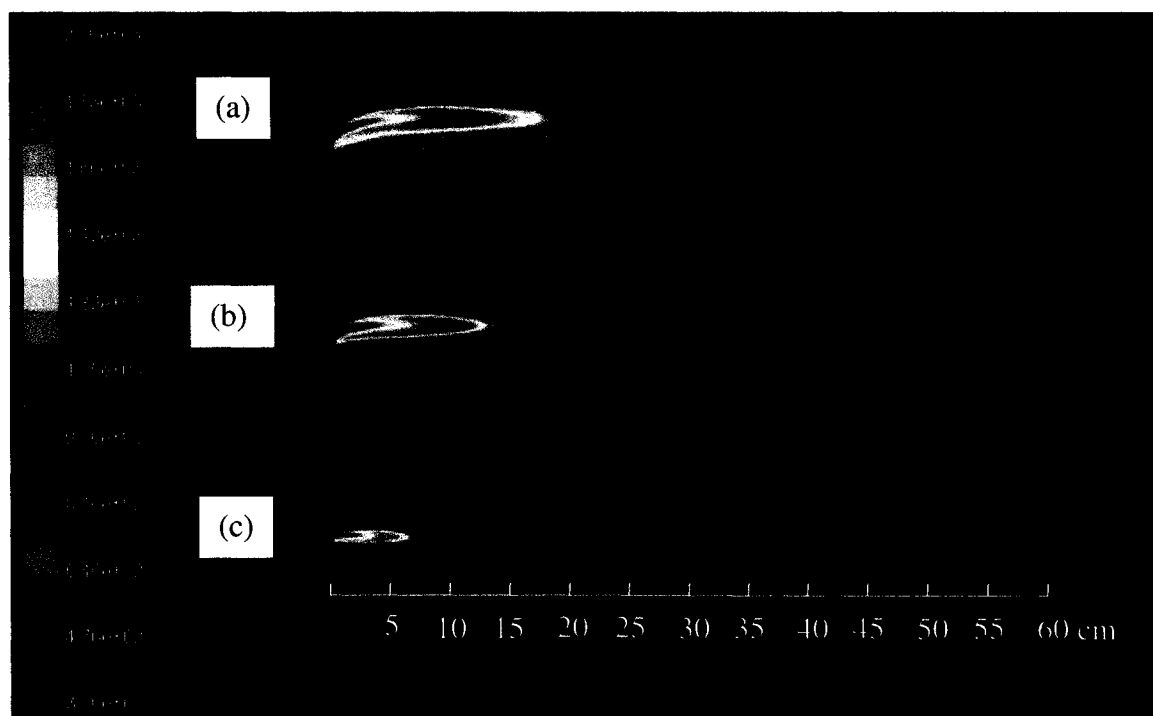


Figure 6.9b X-Z Plane Temperature Profile at 2.5 m/s Cross-Flow Condition for 100% (a), 60% (b), and 20% (c) CFMFR

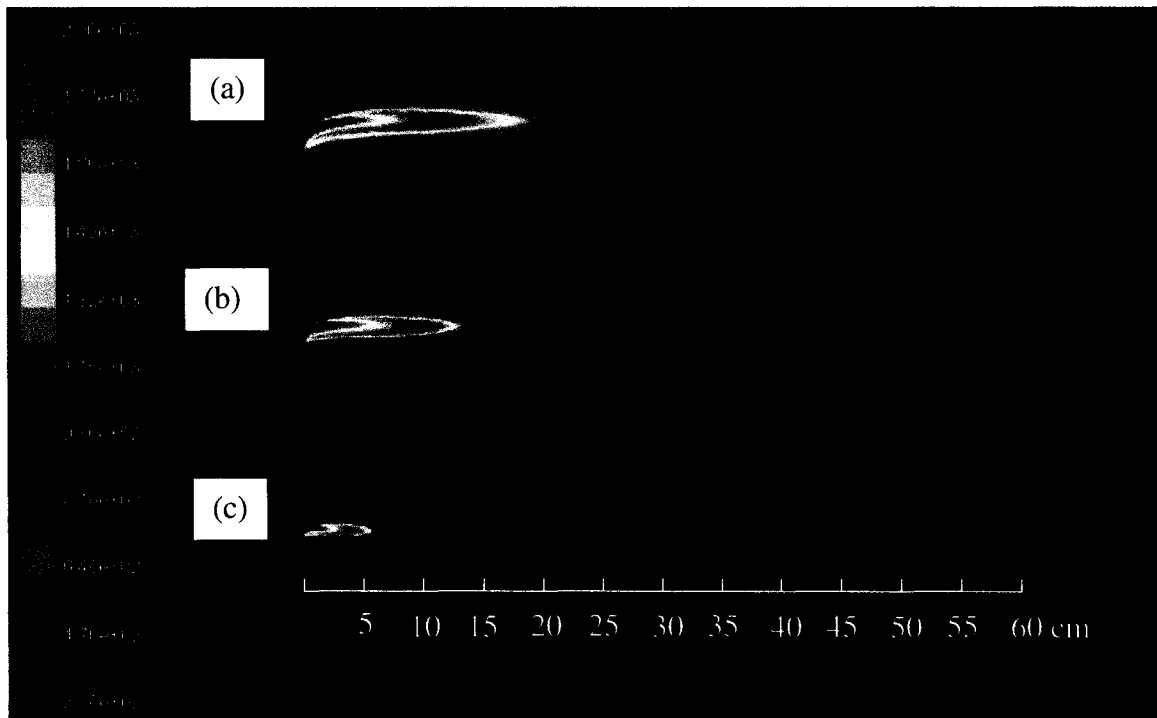


Figure 6.9c X-Z Plane Temperature Profile at 3 m/s Cross-Flow Condition for 100% (a), 60% (b), and 20% (c) CFMFR

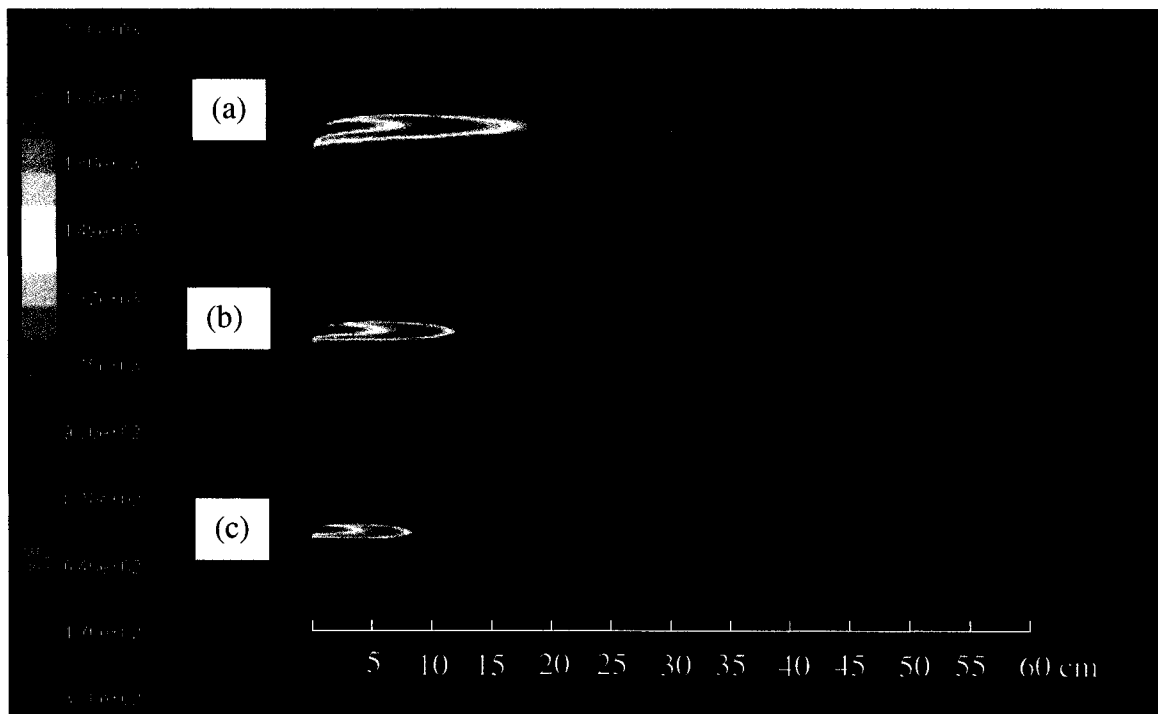


Figure 6.9d X-Z Plane Temperature Profile at 3.5 m/s Cross-Flow Condition for 100% (a), 60% (b), and 30% (c) CFMFR

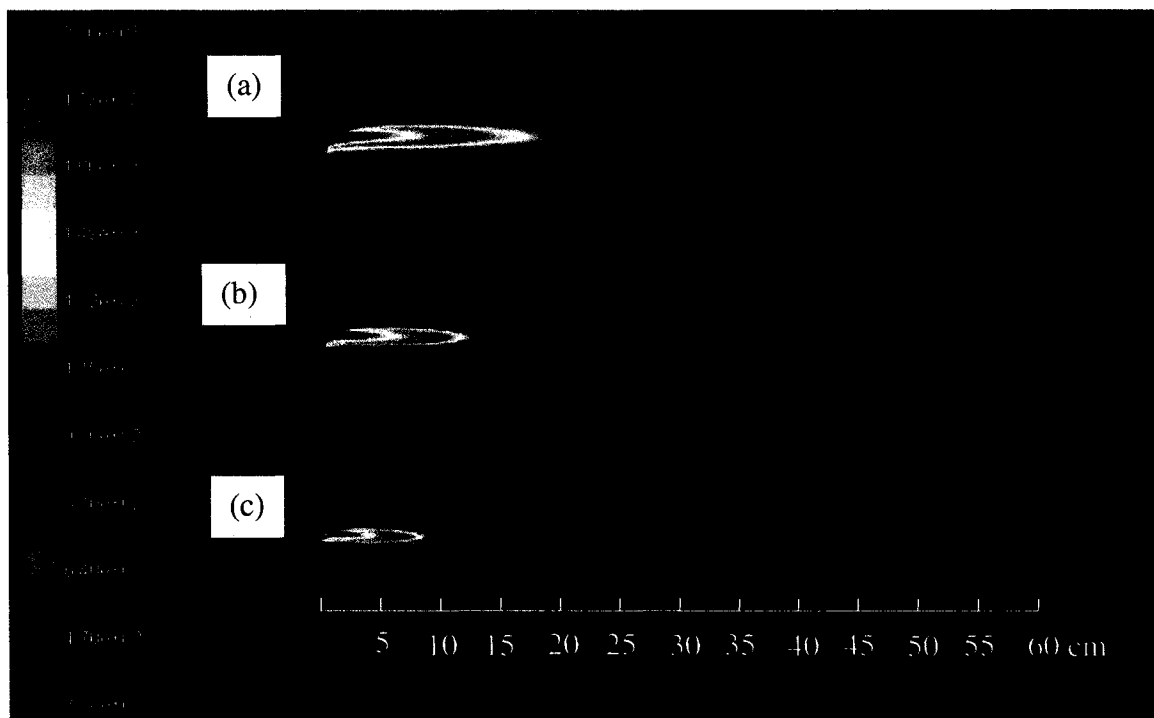
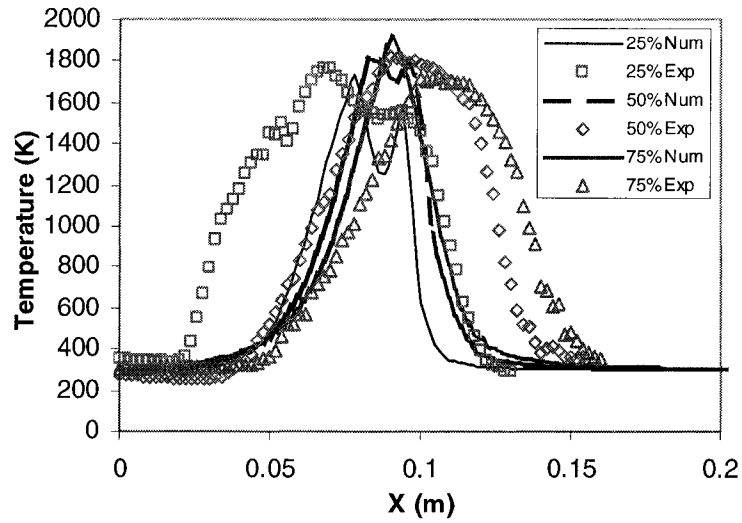
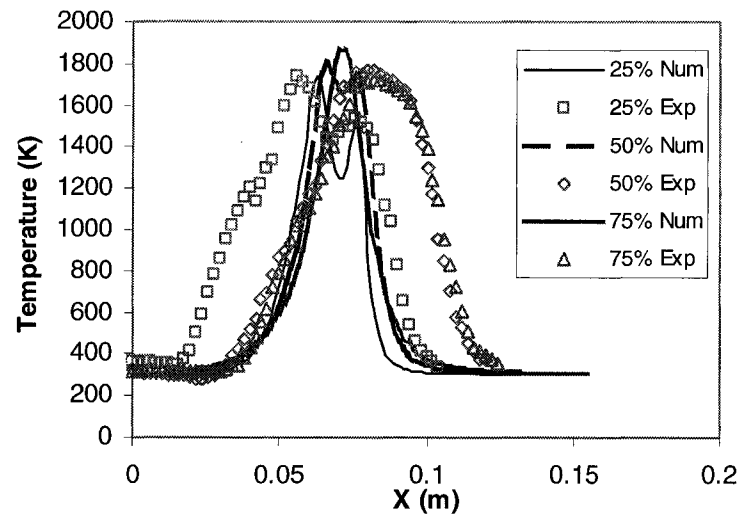


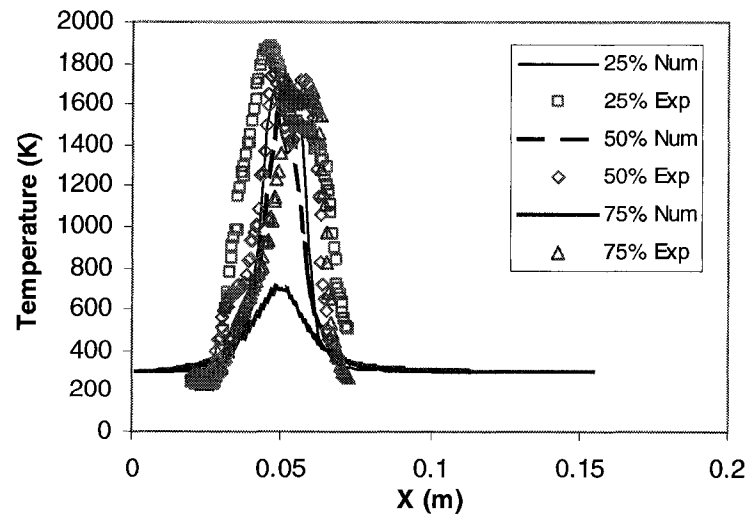
Figure 6.9e X-Z Plane Temperature Profile at 4 m/s Cross-Flow Condition for 100% (a), 60% (b), and 30% (c) CFMFR



A

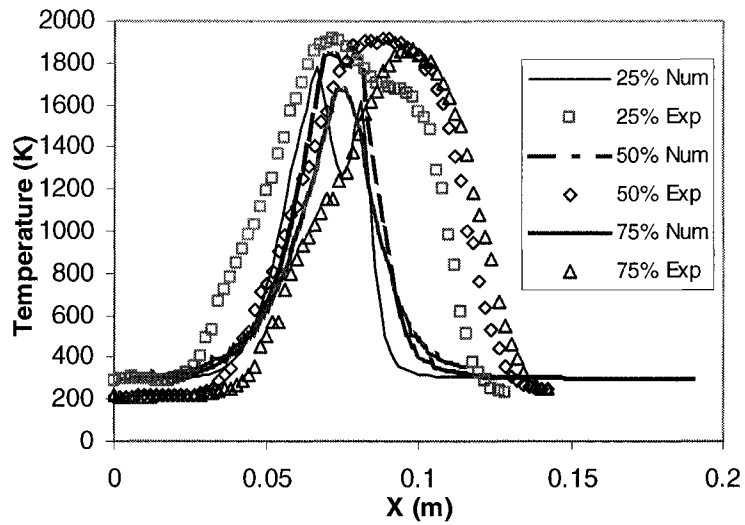


B

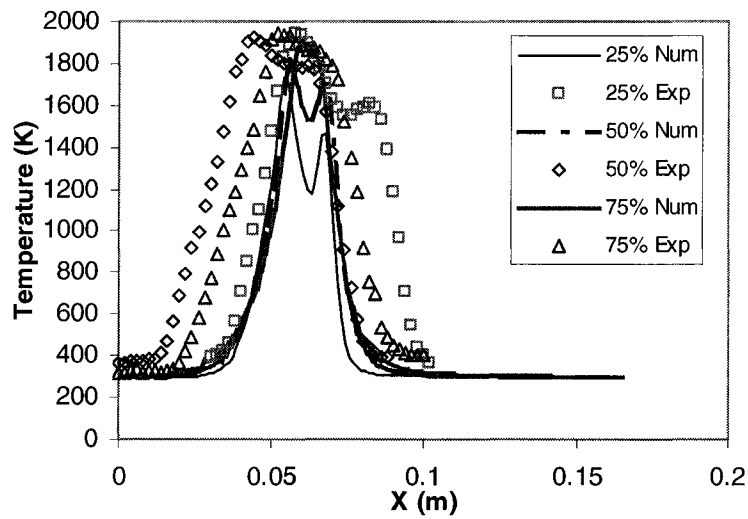


C

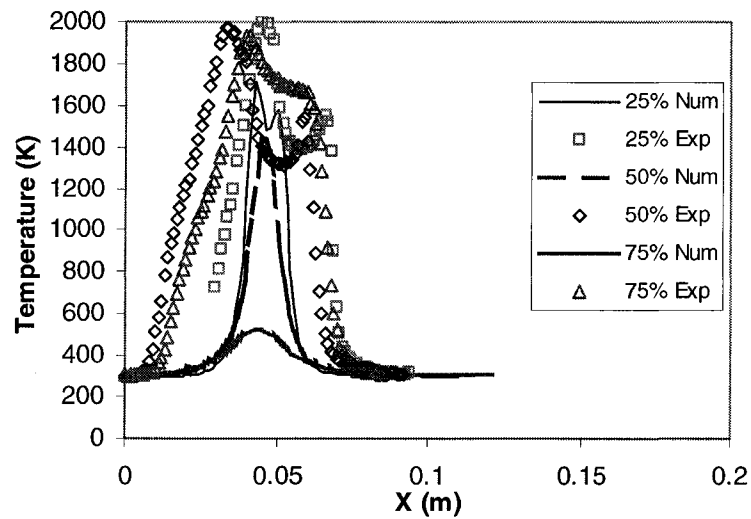
Figure 6.10 Comparison of In-Flame Temperature for Model and Experimental Results At 2.0m/s Cross-Flow at the Three Flame Locations (25%, 50%, and 75% of Flame Length) for (A)100%, (B) 60%, and (C) 20% CFMFR.



A

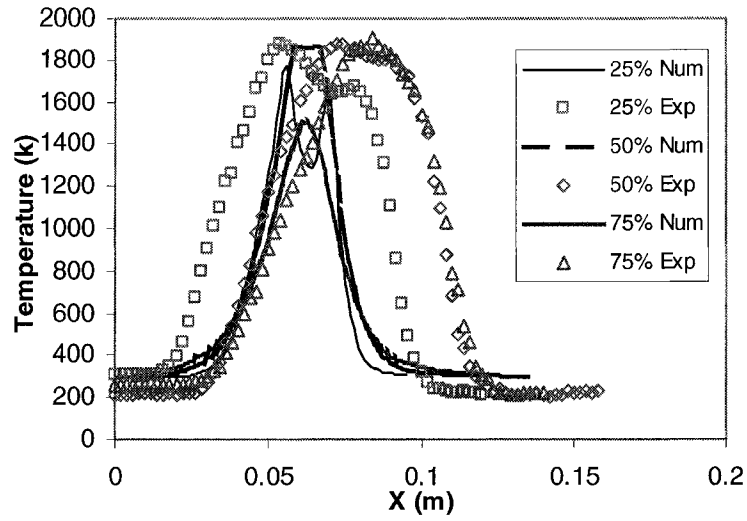


B

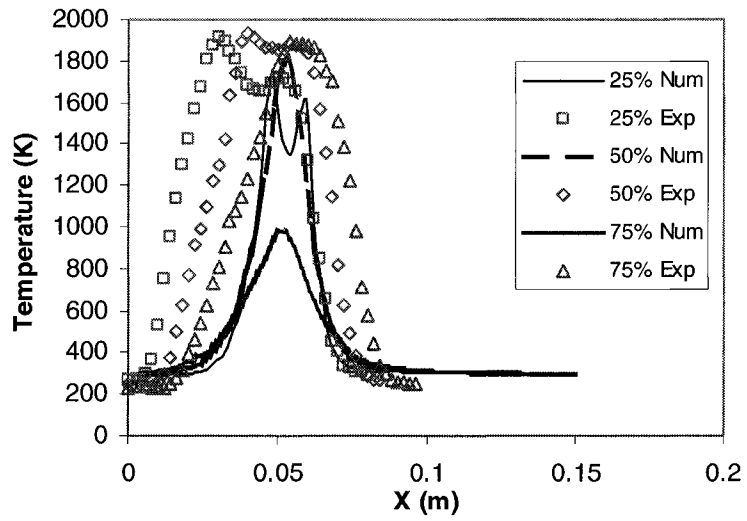


C

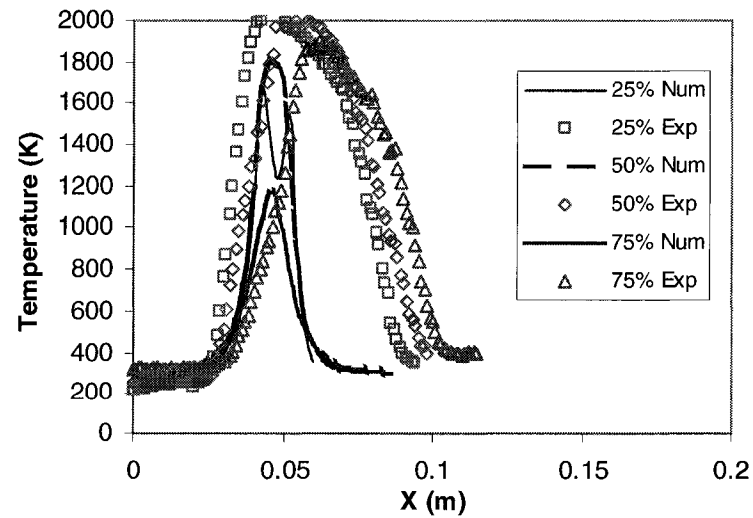
Figure 6.11 Comparison of In-Flame Temperature for Model and Experimental Results At 3.0m/s Cross-Flow at the Three Flame Locations (25%, 50%, and 75% of Flame Length) for (A) 100%, (B) 60%, and (C) 20% CFMFR.



A

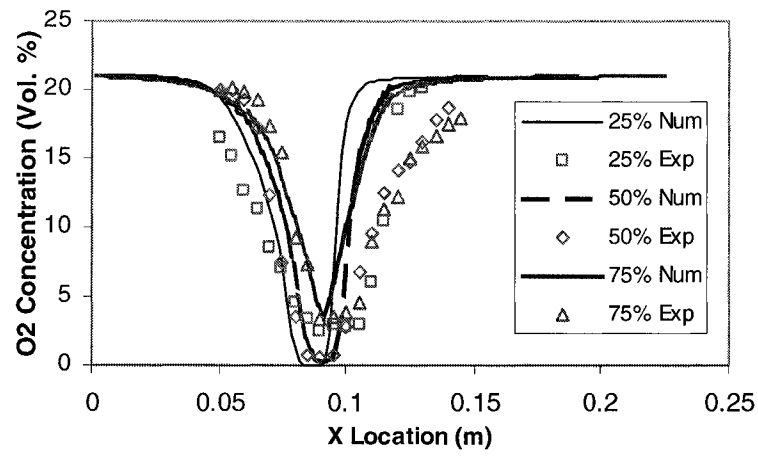


B

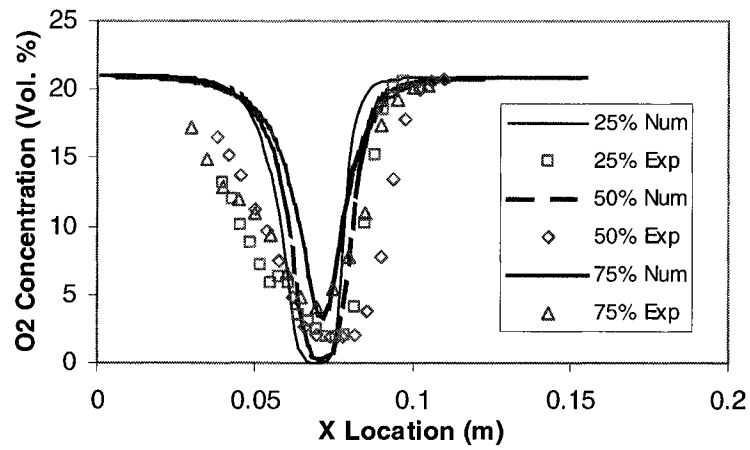


C

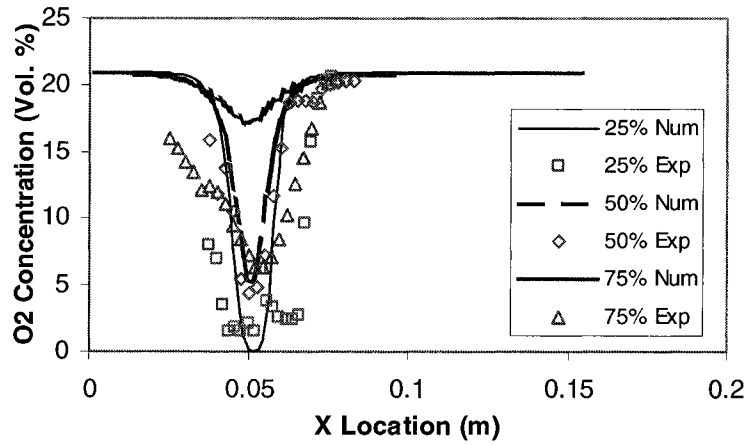
Figure 6.12 Comparison of In-Flame Temperature for Model and Experimental Results At 4.0m/s Cross-Flow at the Three Flame Locations (25%, 50%, and 75% of Flame Length) for (A)100%, (B) 60%, and (C) 30% CFMFR.



A

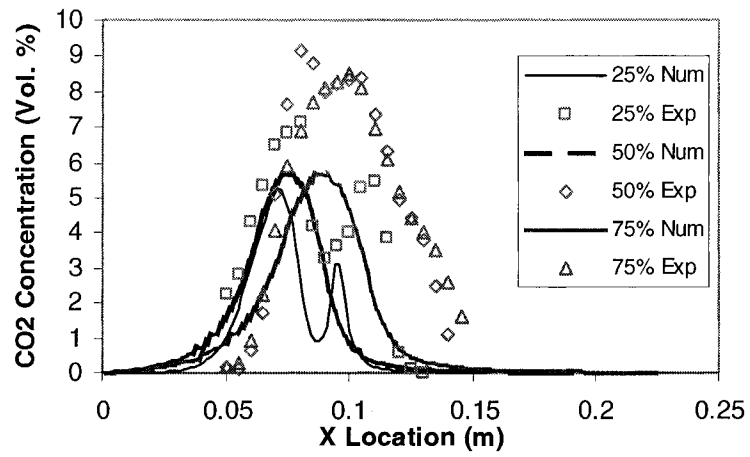


B

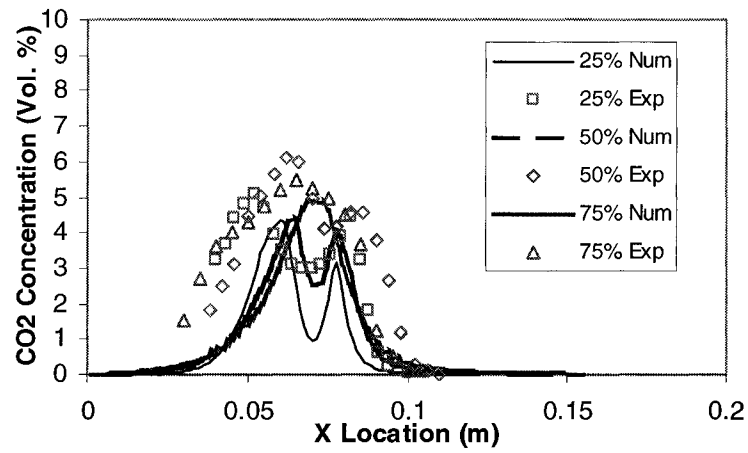


C

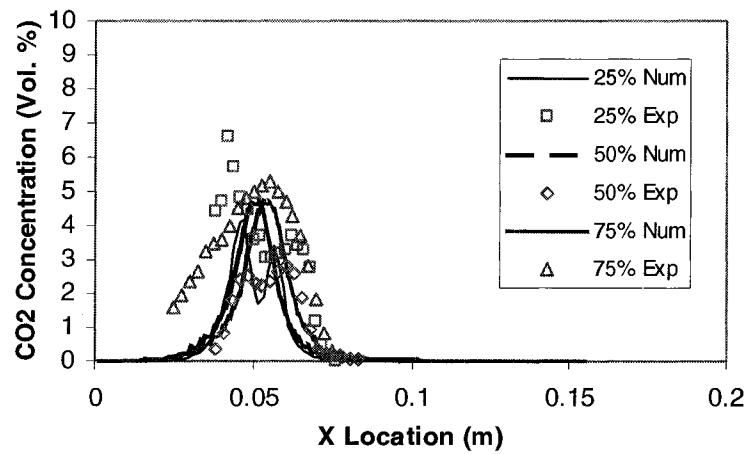
Figure 6.13 Comparison of In-Flame O₂ Concentration for Model and Experimental Results At 2.0m/s Cross-Flow at the Three Flame Locations (25%, 50%, and 75% of Flame Length) for (A) 100%, (B) 60%, and (C) 20% CFMFR.



A

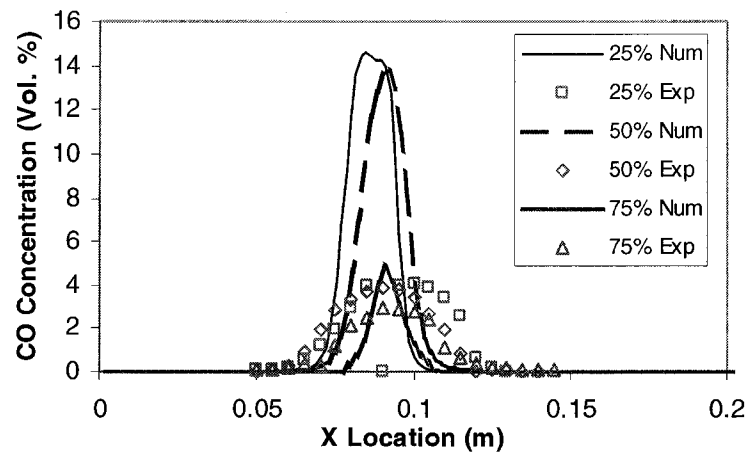


B

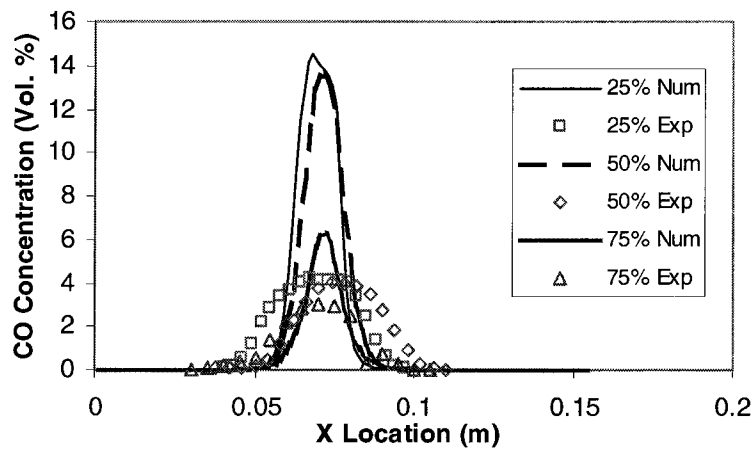


C

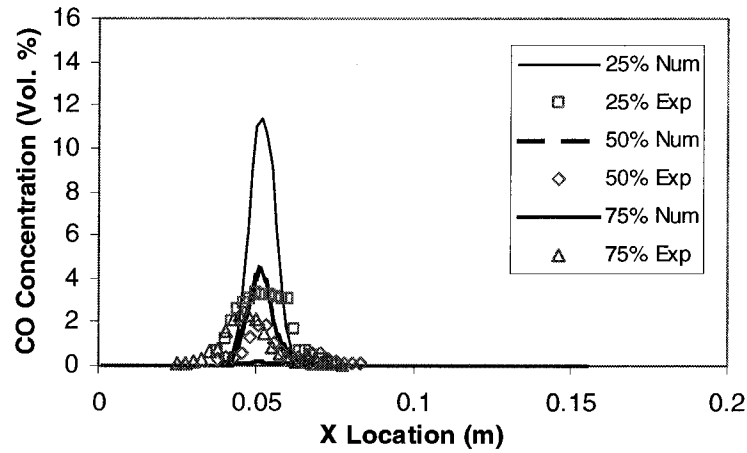
Figure 6.14 Comparison of In-Flame CO₂ Concentration for Model and Experimental Results At 2.0m/s Cross-Flow at the Three Flame Locations (25%, 50%, and 75% of Flame Length) for (A) 100%, (B) 60%, and (C) 20% CFMFR.



A



B



C

Figure 6.15 Comparison of In-Flame CO Concentration for Model and Experimental Results At 2.0m/s Cross-Flow at the Three Flame Locations (25%, 50%, and 75% of Flame Length) for (A) 100%, (B) 60%, and (C) 20% CFMFR.

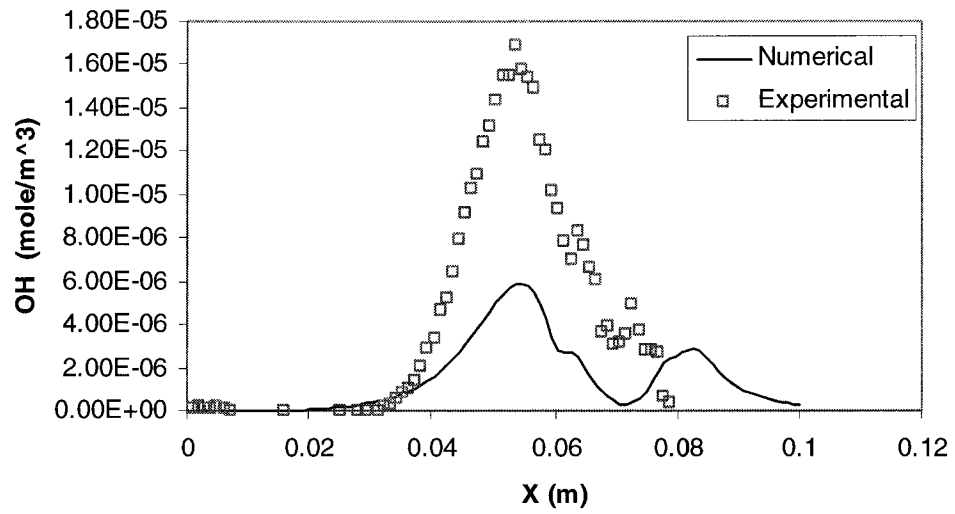
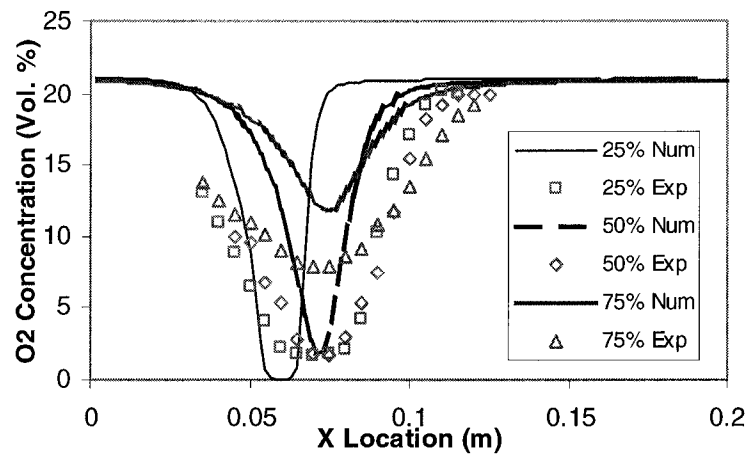
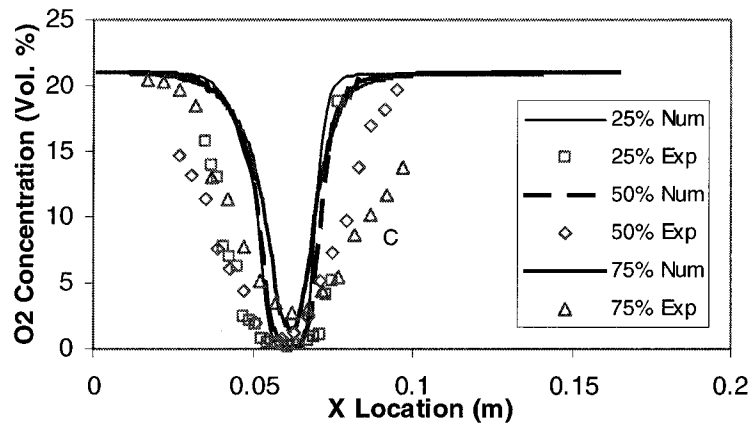


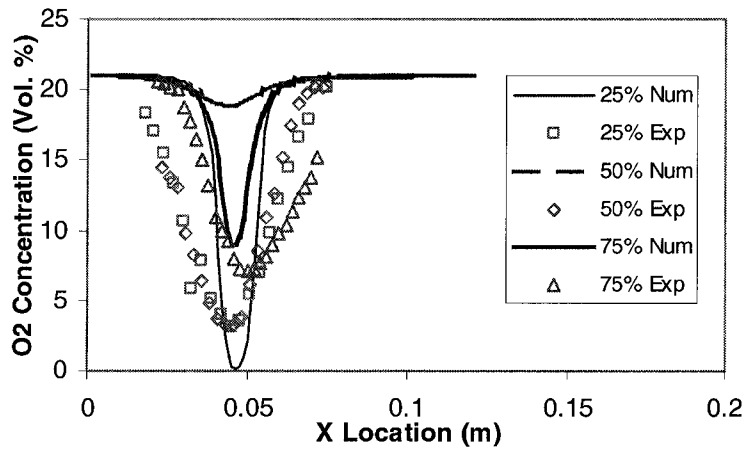
Figure 6.16 Comparison of In-Flame OH Concentration for Model and Experimental Results At 2.0m/s Cross-Flow, 60% CFMFR, 25% of the Flame Length.



A

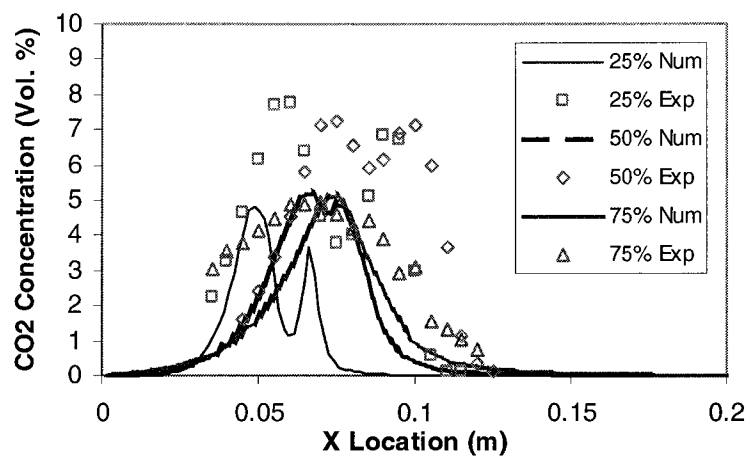


B

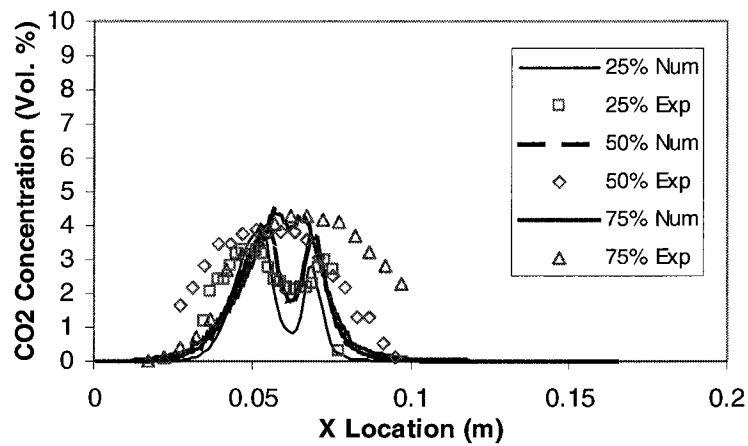


C

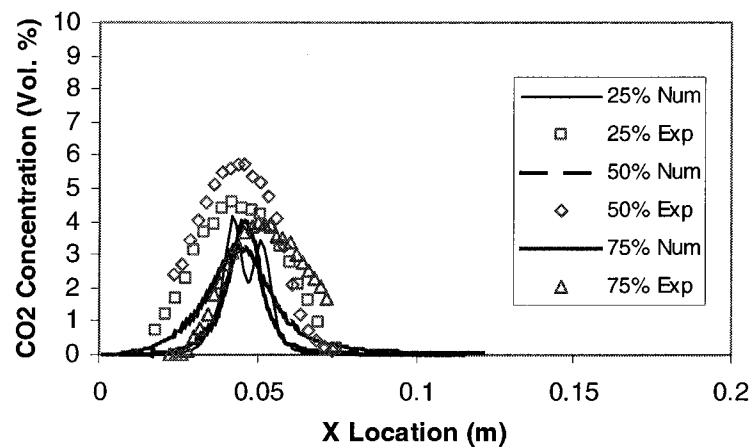
Figure 6.17 Comparison of In-Flame O_2 Concentration for Model and Experimental Results At 3.0m/s Cross-Flow at the Three Flame Locations (25%, 50%, and 75% of Flame Length) for (A) 100%, (B) 60%, and (C) 20% CFMFR.



A

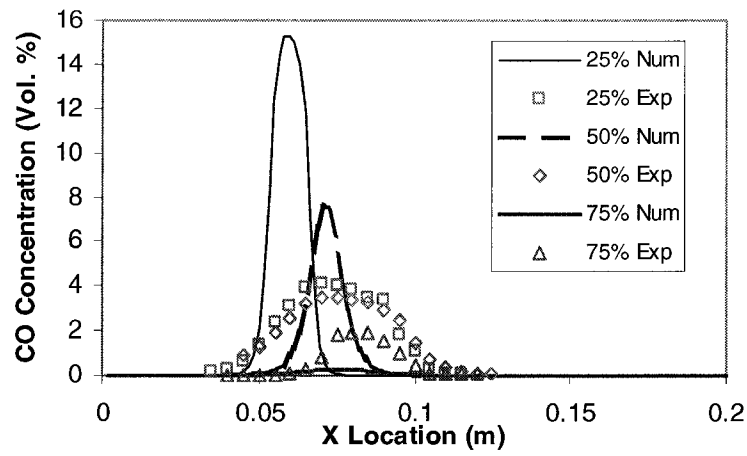


B

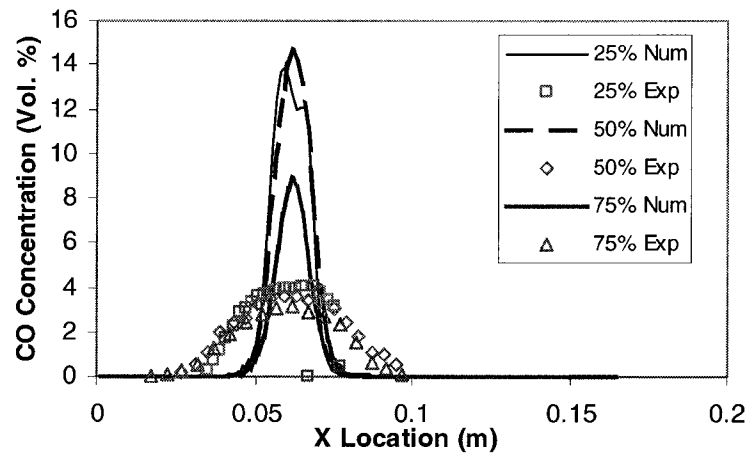


C

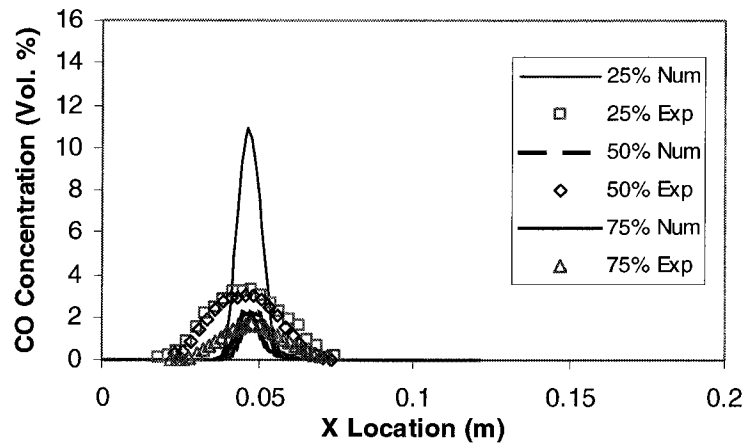
Figure 6.18 Comparison of In-Flame CO₂ Concentration for Model and Experimental Results At 3.0m/s Cross-Flow at the Three Flame Locations (25%, 50%, and 75% of Flame Length) for (A) 100%, (B) 60%, and (C) 20% CFMFR.



A



B



C

Figure 6.19 Comparison of In-Flame CO Concentration for Model and Experimental Results At 3.0m/s Cross-Flow at the Three Flame Locations (25%, 50%, and 75% of Flame Length) for (A) 100%, (B) 60%, and (C) 20% CFMFR.

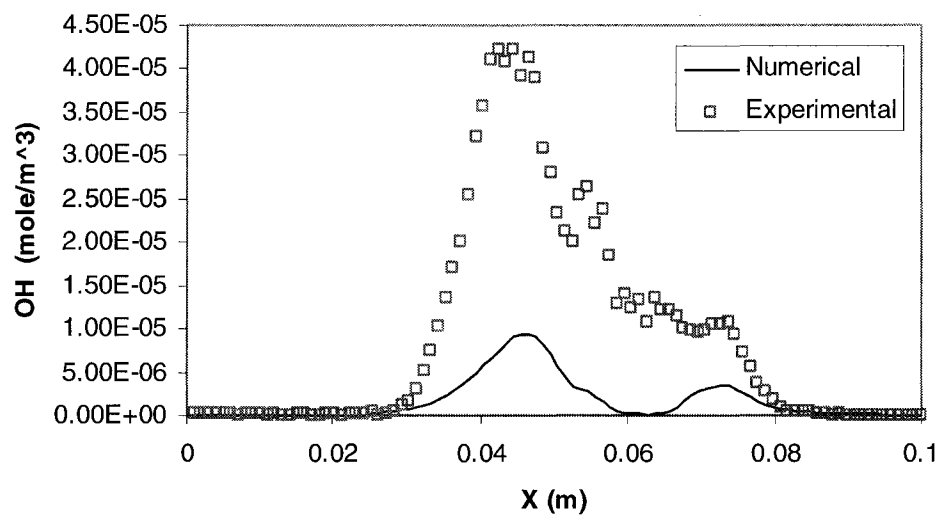
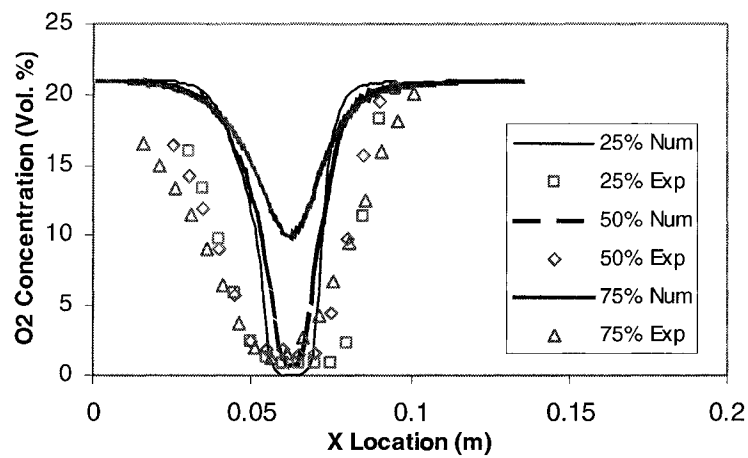
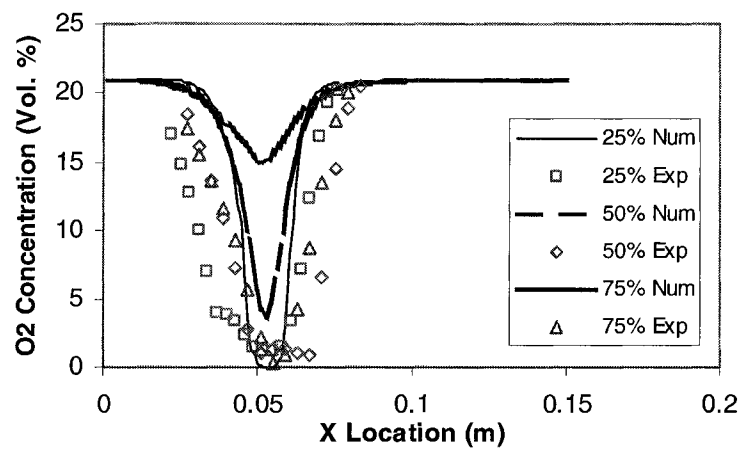


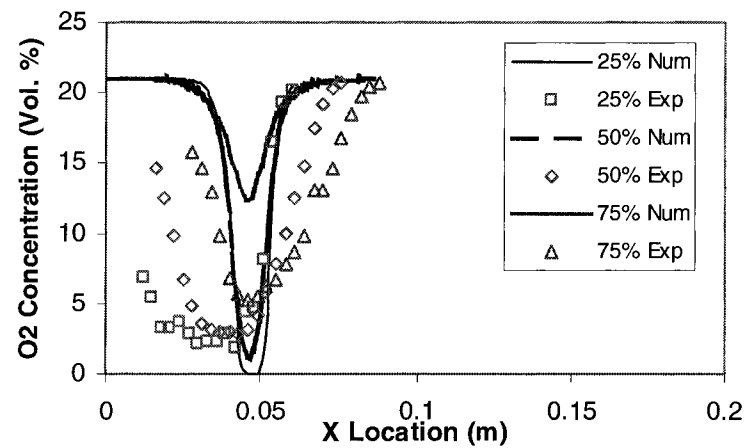
Figure 6.20 Comparison of In-Flame OH Concentration for Model and Experimental Results At 3.0m/s Cross-Flow, 60% CFMFR, at 25% of the Flame Length.



A

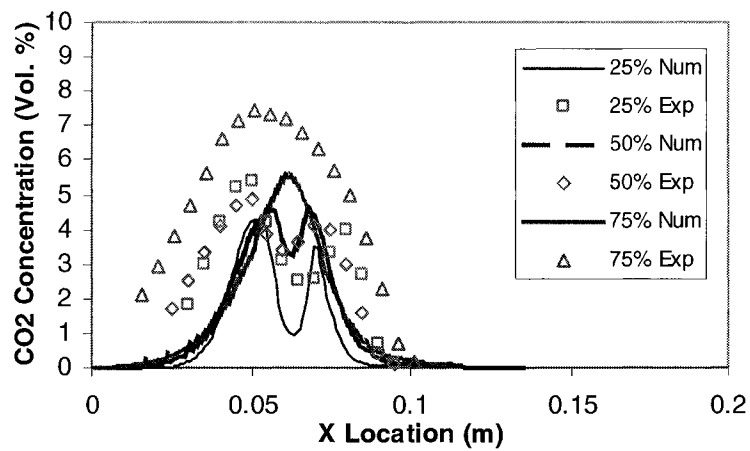


B

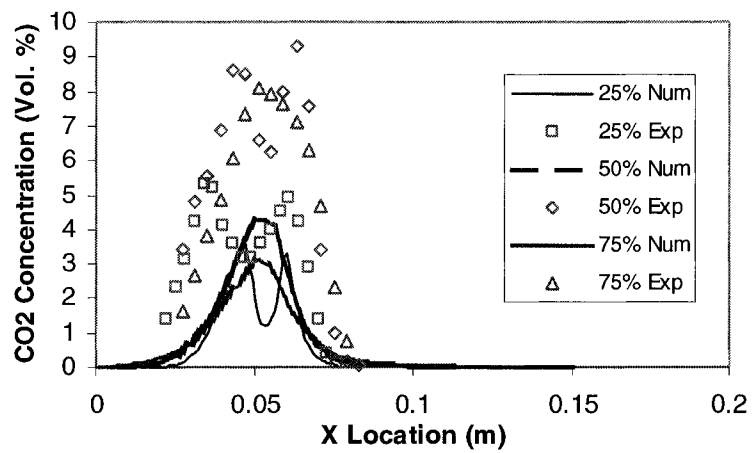


C

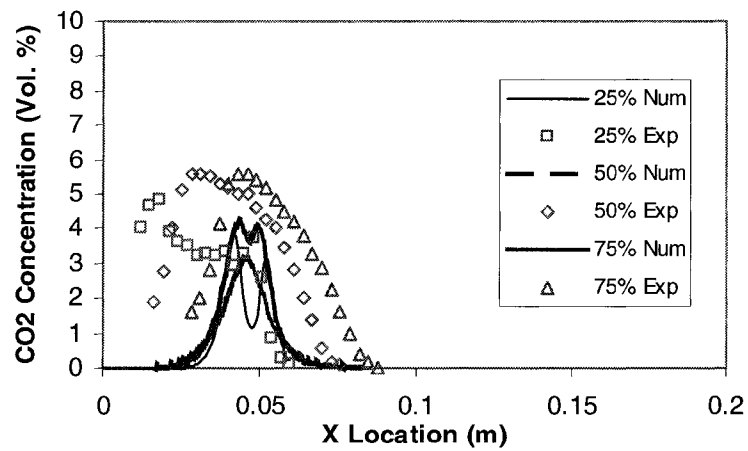
Figure 6.21 Comparison of In-Flame O₂ Concentration for Model and Experimental Results At 4.0m/s Cross-Flow at the Three Flame Locations (25%, 50%, and 75% of Flame Length) for (A) 100%, (B) 60%, and (C) 30% CFMFR.



A

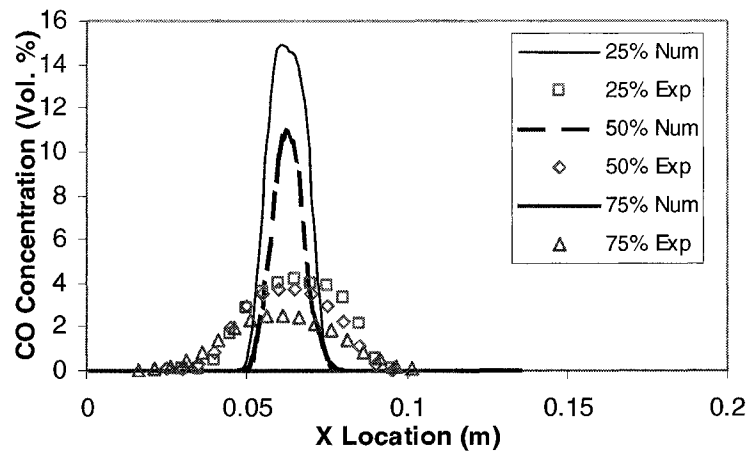


B

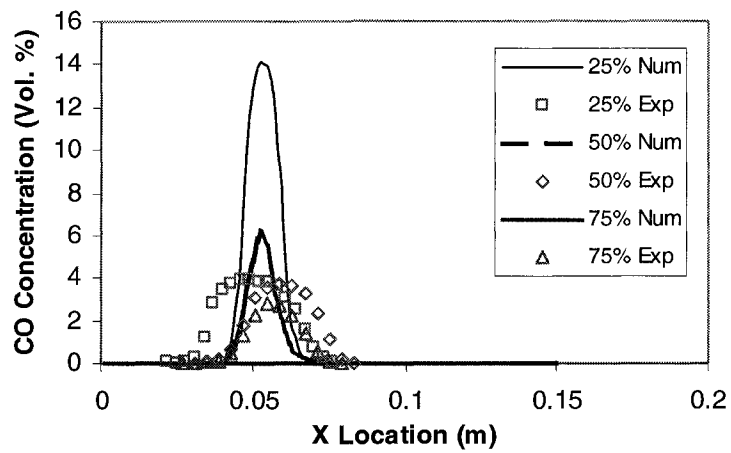


C

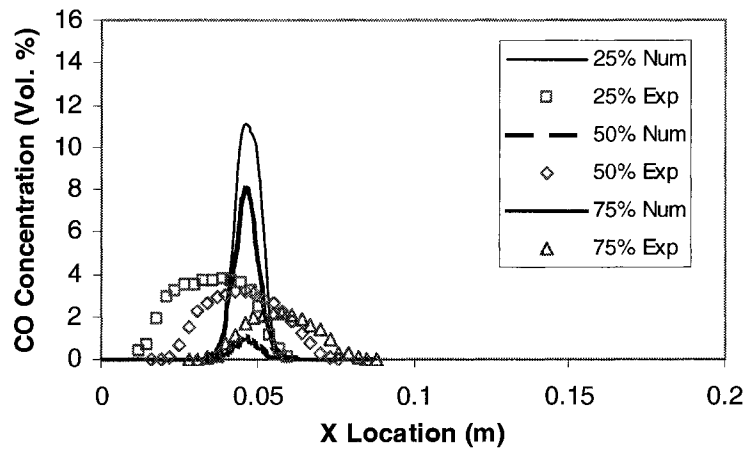
Figure 6.22 Comparison of In-Flame CO_2 Concentration for Model and Experimental Results At 4.0m/s Cross-Flow at the Three Flame Locations (25%, 50%, and 75% of Flame Length) for (A) 100%, (B) 60%, and (C) 30% CFMFR.



A



B



C

Figure 6.23 Comparison of In-Flame CO Concentration for Model and Experimental Results At 4.0m/s Cross-Flow at the Three Flame Locations (25%, 50%, and 75% of Flame Length) for (A) 100%, (B) 60%, and (C) 30% CFMFR.

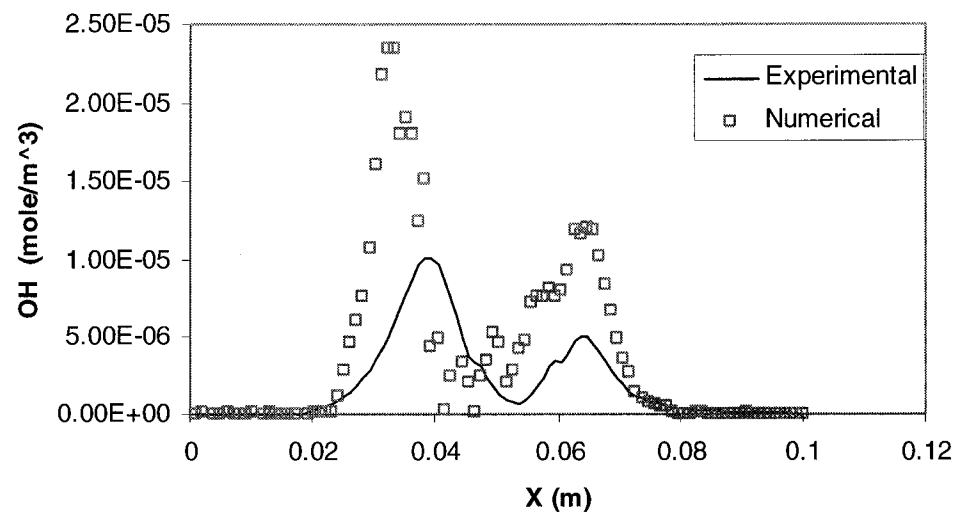


Figure 6.24 Comparison of In-Flame CO Concentration for Model and Experimental Results At 4.0m/s Cross-Flow, 60% CFMFR, at 25% of the Flame Length.

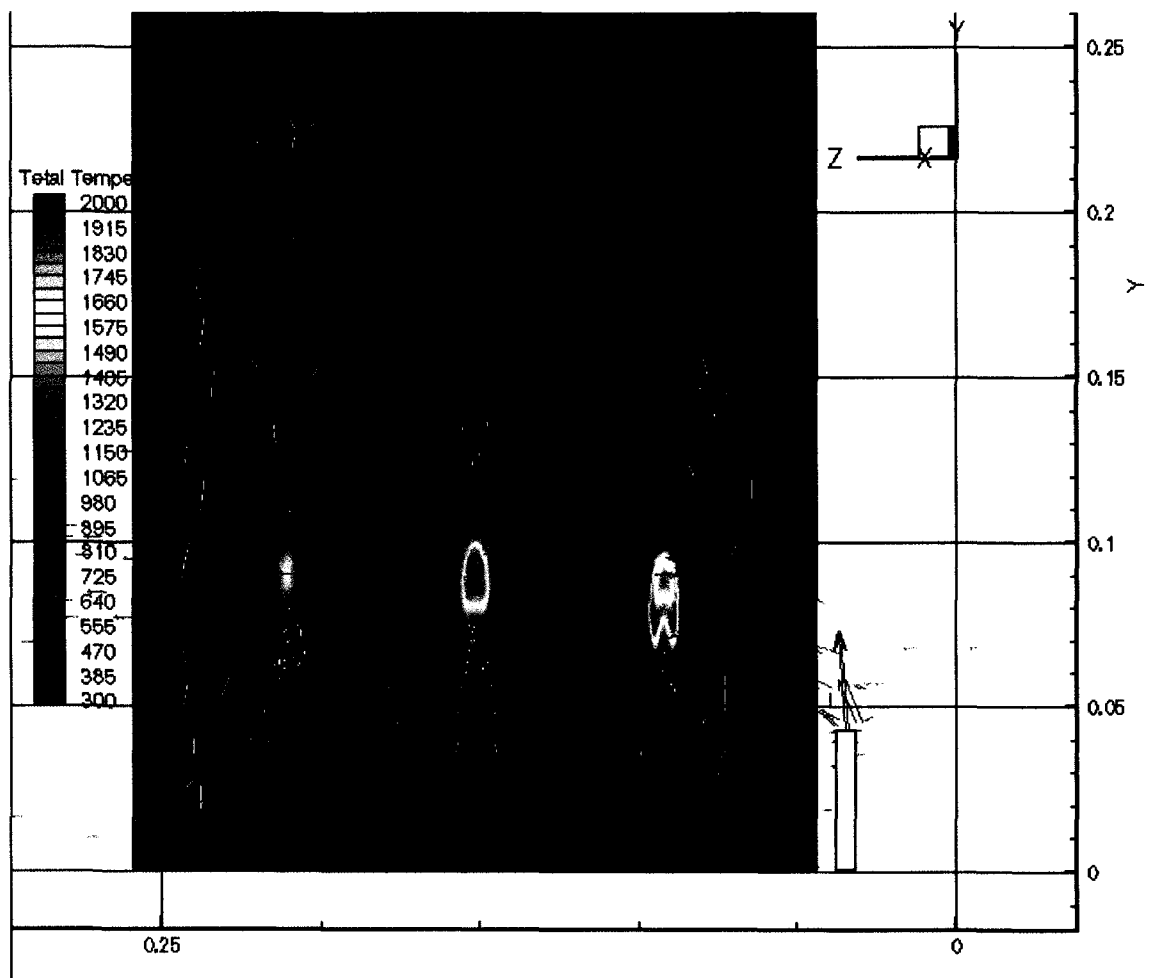


Figure 6.25 3-D Plot of 100% CFMFR Flame at 2 m/s Cross-Flow

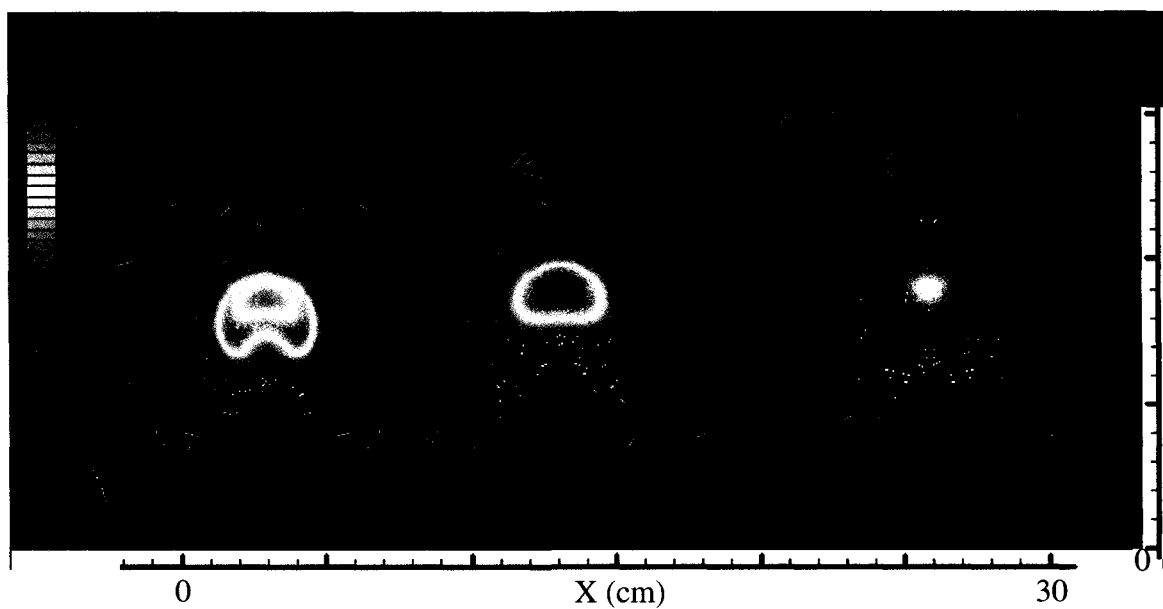


Figure 6.26a 100% CFMFR Flame x-y Plane Temperature Profiles at 2 m/s Cross-Flow for Three Flame Locations

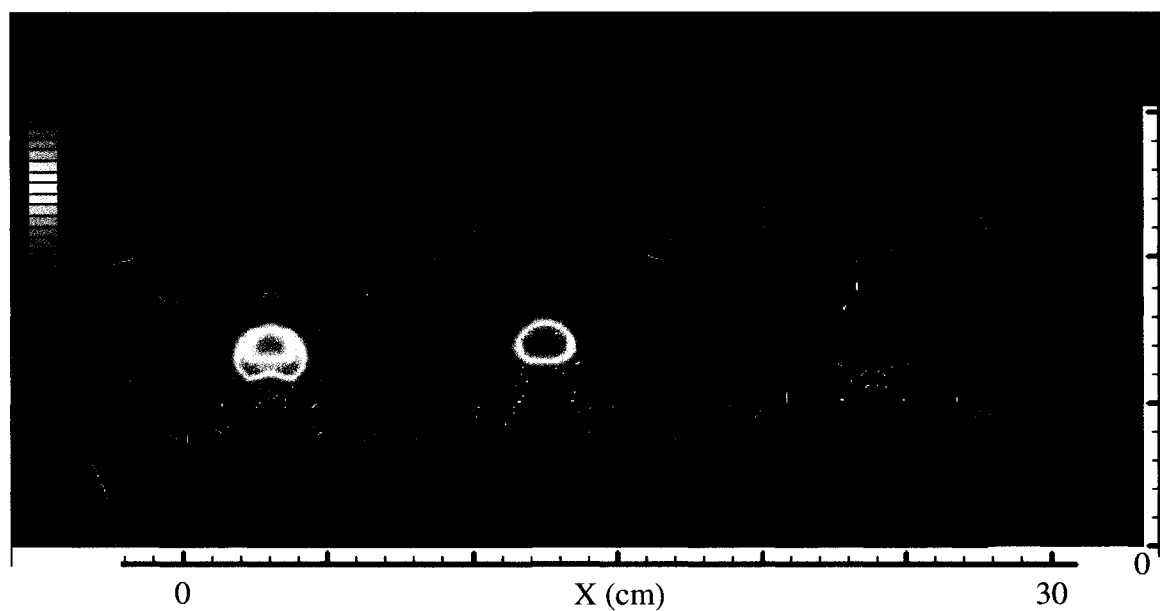


Figure 6.26b 60% CFMFR Flame x-y Plane Temperature Profiles at 2 m/s Cross-Flow for Three Flame Locations

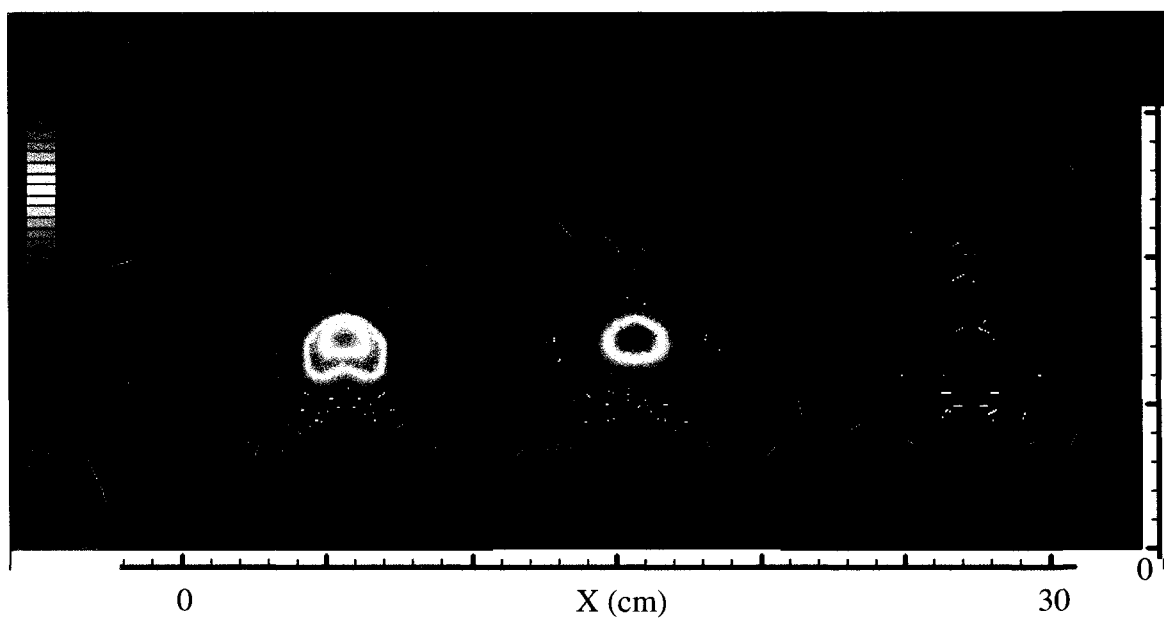


Figure 6.27a 100% CFMFR Flame x-y Plane Temperature Profiles at 3 m/s Cross-Flow for Three Flame Locations

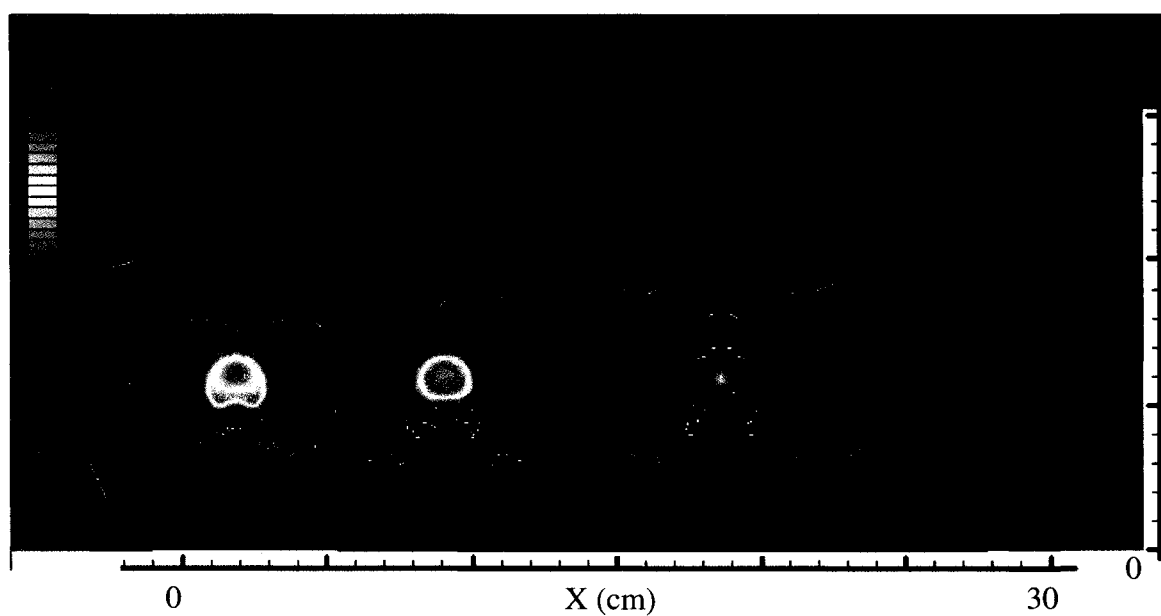


Figure 6.27b 60% CFMFR Flame x-y Plane Temperature Profiles at 3 m/s Cross-Flow for Three Flame Locations

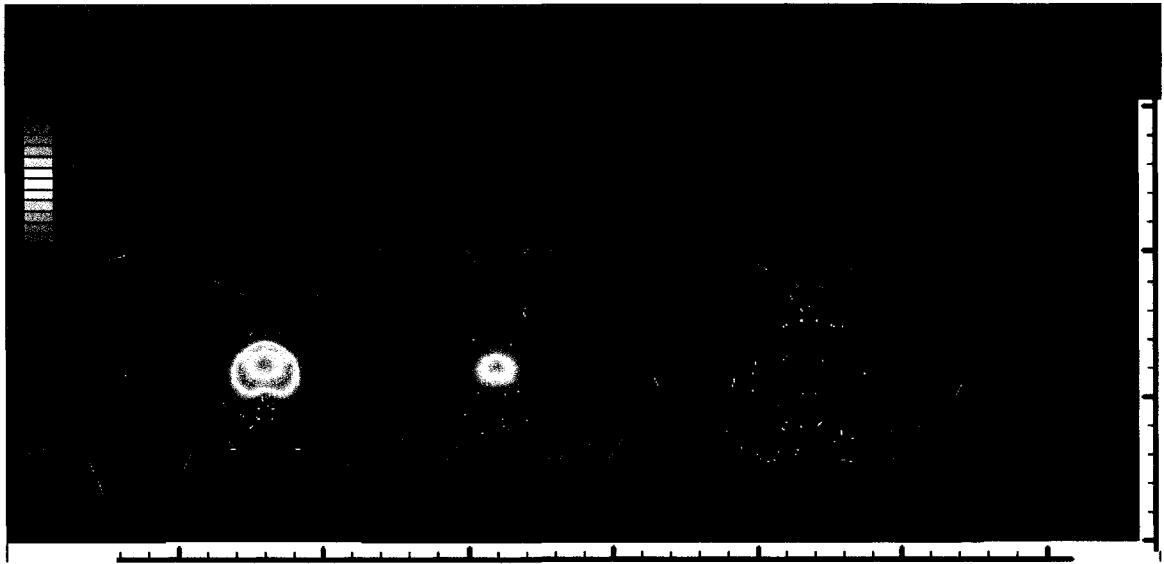


Figure 6.28a 100% CFMFR Flame x-y Plane Temperature Profiles at 4 m/s Cross-Flow for Three Flame Locations

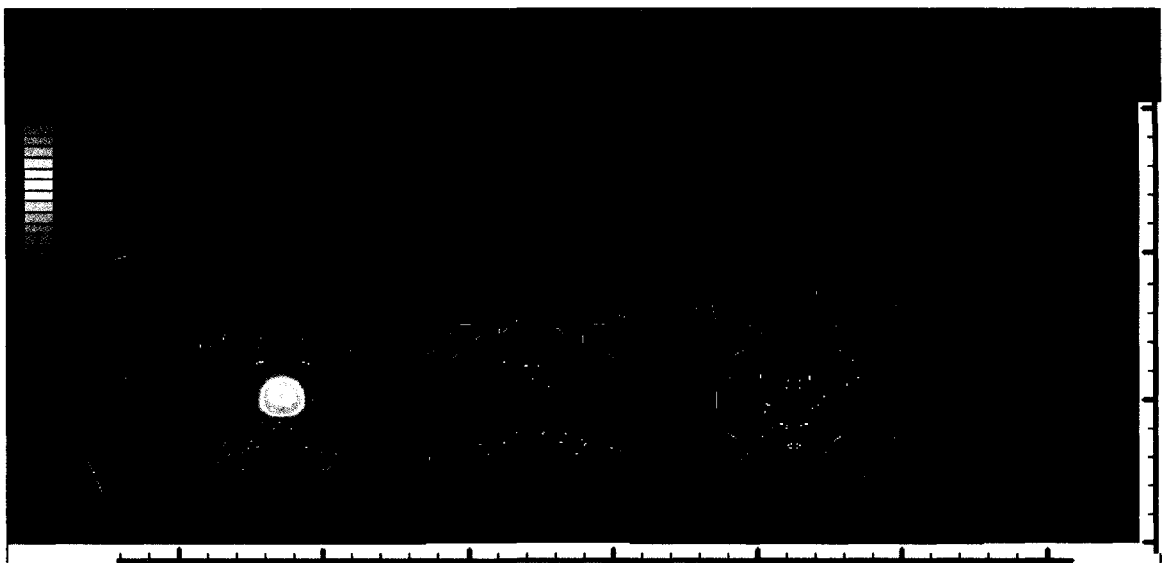


Figure 6.28b 60% CFMFR Flame x-y Plane Temperature Profiles at 4 m/s Cross-Flow for Three Flame Locations

Chapter VII

Overall Discussion, Conclusions and Recommendations

7.1 Chemical and Momentum Effect

The temperature results in Chapter III show a conspicuous dual peak structure in the 25% and the 50% flame length regions for the chemically-dominated and the transition flames, which are at 10% and 20% CFMFR for the 2 and 3 m/s cross-flow and 10% and 30% CFMFR for the 4 m/s cross-flow. However, in the momentum-dominated flames, which are the 60% and 100% CFMFR flames, the dual peak structure does not exist. It is well known that the reaction zone in the laminar diffusion flames is clearly defined by the twin peaks. This indicates that the chemically-dominated flames was similar to laminar diffusion flames and the heat release and reaction process were dominated by chemical reaction rate rather than by the an diffusion rate from the surroundings. In the momentum-dominated flames, the reaction zone is not as sharp as in the chemically-dominated flame due to strong entrainment and diffusion from the surroundings, which are similar to a turbulent diffusion flame. The same observation can also be made from the in-flame CO₂ and NO concentration profiles.

The quiescent flames soot concentration profiles presented in Chapter IV show that the reduction of the jet flow rate from 100% to 60% CFMFR, which was accompanied by a reduction in turbulence intensity, increased the overall soot concentration. Hence, it can be concluded that the momentum decrease dominated the soot oxidation rate in these two flames. However, the comparison of the 30% and 10%

CFMFR flames showed that the overall flame soot concentration was lower for the 10% CFMFR flame. Hence, the chemical effect dominated the 10% CFMFR flame. The decrease of mixing rate caused by the decrease of flow rate from 30% to 10% CFMFR showed the opposite behavior accompanying the decrease from 100% to 60% CFMFR; in this case, the mixing rate decrease led to the overall decrease of soot concentration. Hence, the momentum and mixing effects were not dominant in the 10% CFMFR flame, where as the opposite was true in the 60% CFMFR flame.

The comparison of the importance of OH and the O₂ on soot oxidation presented in Chapter V shows the reason for the division of the chemically and momentum dominate region. In a chemically dominated flame, the OH radical dominates the soot oxidation process for the entire the flame. However, the momentum dominated flame shows OH oxidation of soot only up to (or slightly above) 25% of the flame length and the rest of the flame O₂ dominated the soot oxidation. Since OH is chemical reaction rate dependent and O₂ is diffusion rate dependent, the distinct between the chemical and momentum effect was clearly shown.

7.2 Cross-Flow Effect

The results in Chapter III show the first sign of the non-monotonic relation of the flame length and the cross-flow velocity. The flame length decreased with the increase of the cross-flow velocity from 2 to 3 m/s. However, the flame length increased when the cross-flow velocity was increased from 3.5 to 4 m/s. These higher cross-flow velocity flames (3.5 and 4 m/s) started to behave like a co-flow flame, which caused the decrease of the mixing rate, and the increase of the residence time and the flame length.

The results from Chapter III, IV and V were incorporated in the following discussion to further understand of this behavior in depth. The discussions were categorized into three separate regions; the momentum-dominated region, the transition region, and the chemically-dominated region.

7.2.1 Momentum-Dominated Region Flame (60% and 100% CFMFR Flame)

The comparison of the relative LIF signal for the 60% and 100% CFMFR flames at different cross-flow velocities shows that the OH concentration dropped with the increase of cross-flow velocity. This was due to the non-monotonic relation mentioned in the previous paragraph. The increase of cross-flow velocity from 2 to 3 m/s increased the soot oxidation rate in the 25% flame length region. The results presented in Chapter III, Figure 3.42b and 3.46b (60% CFMFR), 3.42a and 3.46a (100% CFMFR) show that the CO₂ concentration at 25% of the flame length was higher at 3 m/s than at 2 m/s cross-flow velocity. The higher OH concentration present in this region (Figure 5.10b and 5.11b, 60% CFMFR; Figure 5.8, 100% CFMFR) in the 3 m/s cross-flow flame oxidized higher amount of soot precursors than in the 2 m/s cross-flow flame before more soot particles could be formed or travel downstream. Furthermore, at 25% of the flame length, the 3 m/s cross-flow flame behaved more like a partially premixed flame because it had significantly lower CO concentration (Figure 3.45b, 60% CFMFR; Figure 3.45a, 100%CFMFR) and higher flame temperature (Figure 3.26b, 60% CFMFR; Figure 3.26a, 100% CFMFR) than in the 2 m/s cross-flow flame (Figure 3.41b and 3.25b, 60% CFMFR; Figure 3.41a and 3.25a, 100% CFMFR).

When the cross-flow velocity was increased from 3 to 4 m/s, the change of the flame structure (to co-flow-like) caused the 100% CFMFR flame at 4 m/s cross-flow to have higher CO (Figure 3.45a and 3.49a) due to decreased air entrainment. However, in the 60% CFMFR flames, CO concentration magnitudes are about the same at both cross-flow velocities (3 and 4 m/s). The 100% and 60% CFMFR flames at 4 m/s cross-flow show lower CO₂ concentration (Figure 3.46b and 3.50b, 60% CFMFR; Figure 3.46a and 3.50a, 100% CFMFR) at the 25% and 50% of the flame length than in the flame in 3 m/s cross-flow. This shows that the 4 m/s cross-flow flame had a lower oxidation rate than the 3 m/s cross-flow flame.

7.2.2 Transition Region Flame (20% CFMFR Flames for 2 and 3 m/s Cross-Flow and 30% CFMFR for 4 m/s Cross-Flow)

The CO concentration at 25% and 50% flame length shows that the 20% CFMFR flame at 2 and 3 m/s cross-flow had almost the same magnitude at the corresponding location. The soot concentration profiles show that the 20% CFMFR flame at 2 and 3 m/s cross flow velocities (figure 4.14b and 4.15b) had a comparable amount of soot concentration at corresponding location. However, at the 75% flame length, the 3m/s cross-flow flame had a significantly lower CO concentration than 2 m/s. In this flame region, the 2 m/s cross-flow flame had a higher soot concentration than the 3 m/s cross-flow flame. The higher soot concentration at 75% flame length in the 2 m/s cross-flow flame is the main reason for higher CO concentration. The transition point for the 4 m/s cross-flow was 30% CFMFR, which had a higher fuel flow rate than the other two cross-flow cases (2 m/s and 3 m/s). From the comparison, the 4 m/s cross-flow flame had

higher CO concentration than the 2 and 3 m/s cross-flow flames for all flame location, except for the 25% flame length, where all the CO concentration results are comparable. Beside the reason that the 4 m/s flame at this CFMFR had higher fuel flow rate, the low mixing rate (due flame acting like that in a co-flow) might also be a cause of the higher CO production rate.

The CO₂ concentrations of the 2 and 4 m/s cross-flow flames were comparable. Overall, the 3 m/s cross-flow flame CO₂ concentration was also comparable with 2 and 4 m/s cross-flow flames except at the 75% flame length, where the CO₂ concentration in 3 m/s cross-flow flame was lower; and all these profiles did not exhibit a dual-peak structure. The low CO₂ concentration of the 3 m/s cross-flow flame at 75% flame length might be due low oxidation rate because the soot concentration in this region was significantly low compared to that at the other two cross-flow velocities (since soot oxidation dominate the reaction at this region, Figure 4.14b, 15b, 16b).

The overall flame temperature in the 2 m/s cross-flow flame was lower than in the 3 m/s cross-flow flame. This might be mainly due to the reason that the 2 m/s cross-flow flame had higher soot radiative heat loss, because it had higher in-flame soot concentration than the 3 m/s cross-flow flame. The 4m/s cross-flow flame had higher flame temperature the 3 m/s cross flow flame at 25% and 50% flame length, because at these two regions, the 4 m/s cross-flow flame had a low soot concentration than in the 3 m/s cross-flow. However, at the 75% flame length, the 4 m/s cross-flow flame had a lower flame temperature than in the 3 m/s cross-flow because of its higher soot concentration at this region.

7.2.3 Chemical-dominant region (10% CFMFR Flame)

In Chapter IV, the soot distribution profile in the 4 m/s cross-flow flame shows that the soot was concentrated at the center of the flame rather like in a wing structure, which was seen in soot concentration profiles at the other two cross-flow velocities. This phenomenon indicated that the 4 m/s cross-flow flame behaved more like a co-flow flame.

Although the 4 m/s cross-flow flame soot concentration (Figure 4.16a) was higher than the flames at other two cross-flow velocities (Figures 4.14a and 4.15a), the temperature of this flame (Figure 3.27d) was not significantly lower than that in the flame at the other cross-flow velocities (Figures 3.25d and 3.26d). Since the 4 m/s cross-flow flame behaved more like a co-flow flame, the flame cross-flow-air mixing rate was lower than in the other flames. The lower mixing rate of the 4 m/s cross-flow flame was not diluted keenly and maintained most of the high temperature gases in the flame (like a co-flow flame). However, the high radiative heat loss due to high in-flame soot concentration offset the flame temperature, which caused it to have a comparable flame temperature with the other two flames. However, at 2 and 3 m/s cross-flow velocities the temperature was different. The 2 m/s cross flame had an overall lower temperature than the 3 m/s cross-flow flame. The reason was that the 2 m/s cross-flow flame had a higher soot concentration, which resulted in a higher soot radiative heat loss. As mentioned in Chapter III, the flame temperature profile in the 4 m/s cross-flow was narrower than the other two cross-flow flames. The 3 m/s cross-flow flame temperature profile is the widest among the three flames, which meant that it had the highest mixing rate. The non-

monotonic behavior with distance from the burner was again observed in these temperature profiles characteristic.

The order of comparison of CO concentration in the three cross-flow flames (Figures 3.41d, 3.45d, 3.49d) was essentially the same as the soot concentration results presented in Chapter IV, which was expected for a diffusion flame. Overall, the 4 m/s cross-flow flame had the highest CO concentration followed by the 2 m/s cross-flow flame, than the flame in the 3 m/s cross-flow. In a laminar flame, the increase of soot radiative heat loss (due to higher soot concentration) causes the increase of CO concentration in the flame, which is due to low OH production rate and oxidation rate of CO (Garo et al., 1990). All the CO and soot concentration results showed a peak at the center of the flame, which was expected because CO was one of the main products of soot oxidation.

The CO₂ concentration profiles (Figure 3.42d, 3.46d and 3.50d) showed that the 2 and 3 m/s cross-flow flames had comparable results except at the 75% flame length region, where the 3 m/s cross-flow flame had a higher CO₂ concentration. The 4 m/s cross-flow flame had the lowest CO₂ concentration compared with the other two flames. The high soot and CO concentration, and low CO₂ concentration showed that the 4 m/s cross-flow flame was least effective among the three flames in terms of complete combustion.

7.3 Computation Modeling

The standard κ - ϵ turbulent model and the mixture fraction method with the equilibrium model were reasonably satisfactory in predicting the smoke point turbulent

diffusion flame in a cross-flow and a quiescent condition. The model failed to predict the laminar flame. Hence, the laminar flame computational results were discarded.

In all turbulence flame cases, the computational and the experimental temperature and O_2 concentration results showed a good agreement in most cases. At a highly turbulent flame condition, the CO_2 concentration comparison was relatively good, though in the high soot concentration region, the discrepancy between the experimental and the computational results was significant. The numerical flame was shorter and narrower than the experimental flame for all cases. The main reason was due to the assumption of the rapid reaction and the present of soot in the experimental flame. The present of the soot particle and the lower oxidation rate of the soot particle than other molecules in the experimental flame also caused the discrepancy between the experimental and the computational results. The significant of finite rate reaction and the presence of soot in the flame caused the failure of the equilibrium model in predicting the CO and OH concentration at high equivalence ratio region.

Recommendations for Future Computational Work

It is recommended that the multi-steps reaction model over the PDF model for a laminar flame computation. Then, the individual species diffusion rate will be taken into account. Multi-steps reaction model can also be tried on the turbulence flame to resolve the OH radicals. However, the present of soot in the experimental flame cannot be predicted even in the multi-steps reaction model. An advance soot modeling is recommended for smoke point condition flames computation. The soot modeling has been study by many researches. One of the most commonly use model is the single-step

Khan and Greeves (1974) model, which predict the rate of soot formation with a simple empirical rate. The two-step Tesner (1971) model is a more complicated model, which predicts the formation of nuclei particles with soot formation on the nuclei. Both of these soot formation models are empirically based (Magnussen and Hjertager, 1976); they are only approximate models for the soot formation process in combustion systems. Normally, these models are used in a post-processing, and they have nothing to do with the detail combustion process. The soot formation chemistry and physical process are very complex, which is still studied by many researchers. Hence, the incorporate soot chemistry modeling into the multi-step reaction modeling posted a great challenge.

7.4 Experimental Recommendations

This study only reveals the part of soot oxidation process. In order to complete the whole picture, the soot production part need to come into the picture. In Chapter II, the PAH (polycyclic aromatic hydrocarbon) is one of the important key players in the soot production process. Hence PAH measurement is recommended in the future study. PAH was not measured in this study because there were two technical problems raised during the attempt process. The first problem was the MOPO had problem attaining two of the specific wavelengths for a PAH excitation (283.5 nm, 560.3 nm, 488 nm (Symth et. al, 1997)). Secondly, the noise of the LII signal interfered with the PAH fluorescence signal. There are many different types of PAH in the flame, but the population of each type is small in the flame. The laser can only excite a certain type of PAH, but not all the PAH. Hence, the signal to noise ratio was very low because the PAH fluorescence signal was very weak compared with the LII signal. To overcome these problems, a specific

wavelength that can excite the PAH with highest population has to be generated in order to obtain higher the signal to noise ratio. This required the understanding of the nature of the propylene smoke point flame chemistry.

References

- Axelsson, B., Collin, R. and Bengtsson, P. E. (2001), "Laser Induced Incandescence for Soot Particle Size and Volume Fraction Measurement Using On-line Extinction Calibration," *Applied Physics B*, Vol. 72, pp. 367-372.
- Axelbaum, R. L. and Law, C. K. (1990), "Soot Formation and Inert Addition in Diffusion Flames," *Twenty-Third Symposium (International) on Combustion*, pp. 1517-1523.
- Axelbaum, R. L., Law, C. K., and Flower, W. L. (1988), "Preferential Diffusion and Concentration Modification in Sooting Counterflow Diffusion Flames," *Twenty-Second Symposium (International) on Combustion*, pp.379-386.
- Bandaru, R. V., and Turns, S. R. (2000), "Turbulent Jet Flames in a Crossflow: Effects of Some Jet, Crossflow, and Pilot-Flame Parameters in Emissions," *Combustion and Flames*, Vol. 121, pp. 137-151.
- Battles, B. E., Seitzman, J. M., and Hanson, R. K. (1994), "Quantitative Planar Laser Induced Fluorescence Imaging of Radical Species in High Pressure Flames," AIAA 94-0229, 32nd *Aerospace Sciences Meeting and Exhibit*, Reno, NV.
- Bockhorn, H. (1994), "A Short Introduction to the Problem – Structure of the Flowing Parts," Soot Formation in Combustion, Bockhorn, H. (Editor), Springer-Verlag, Berlin, pp. 4-7.
- Benson, S. W. (1983), Comments in Longwell, J. P. (1983), "The Formation of Polycyclic Aromatic Hydrocarbons by Combustion," *Nineteenth Symposium (International) on Combustion*, pp.1350.
- Boedeker, L. R., and Dobbs, G. M. (1987), "CARS Temperature Measurements in Annular Soot Zones of Axisymmetric Laminar Diffusion Flames," *Chemical and Physical Processes in Combustion*, Chemical and Physical Processes in Combustion: Fall Technical Meeting, 1987, San Juan Bautista, PR.
- Braun-Unkhouff, M. Chrysostomou, A., Frank, P., Gutheil, E., Lückerrath, R., and Stricker, W. (1998), "Experimental and Numerical Study on Soot Formation in Laminar High-Pressure flames," *Twenty-Seventh Symposium (International) on Combustion*, pp. 1565-1572.
- Broadwell, J. E. and Breidenthal, R. E., 1984 "Structure and Mixing of a Transverse Jet in Incompressible Flow," *Journal of Fluid Mechanics*, Vol. 148, pp. 405-412.
- Brown, M. and Myer, T. (2002), "Laser-Induced Incandescence Measurements in the Reaction Zone of a Model Gas Turbine Combustor," 40th *Aerospace Science Meeting & Exhibit*, 14-17 January, 2002, Reno, Nevada, Paper no. AIAA2002-0393.

Bryce, D. J., Ladommatos, N., and Zhao, H (2000), "Quantitative Investigation of Soot Distribution by Laser-Induced Incandescence," *Applied Optics*, Vol.: 39, No. 27, pp. 5012-5022.

Brzustowski, T. A. (1976), "Flaring in the Energy Industry," *Progress in Energy Combustion Science*, Vol. 2, pp. 129-141.

Brzustowski, T.A., Gollahalli, S. R. and Sullivan, H. F., 1975 "Experimental Studies on Hydrocarbon Turbulent Diffusion Flames in Cross-Wind," *Proceeding in Second European Combustion Symposium*, Combustion Institute, pp. 7.16-744.

Carter, J. G., Huebner, R. H., Hamm, R. N., and Birkhoff, R. D. (1965), "Optical Properties of Graphite in the Region of 1100 to 3000 Å," *Physical Review*, Vol. 137, No. 2, pp. A639-A461.

Cavaliere, A., Barbella, R., Ciajolo, A., D'Anna, A., and Ragucci, R. (1994) "Fuel and Soot Oxidation in Diesel-Like Condition," *Twenty-Fifth Symposium (International) on Combustion*, The Combustion Institute, PA, pp. 167-174.

Chang, H. and Charalampopoulos, T. T. (1990), "Determination of the Wavelength Dependence of Refractive Indices of Flame Soot," *Proc. R. Soc. London Ser. A*, Vol. 430, pp 577-591. (Reference from Bryce et al., 2000)

Choi, M. Y. and Jensen, K. A. (1998), "Calibration and Correction of Laser-Induced Incandescence for soot Volume Fraction Measurements," *Combustion and Flames*, Vol. 112, pp. 485-491.

Choudhuri, A. R. (2000) An Experimental and Numerical Investigation on Hydrogen-Hydrocarbon Composite Fuel Combustion, Published PhD. Thesis, University of Oklahoma, Norman, Oklahoma.

Crittenden, B. D. and Long, R. (1973), "Formation of Polycyclic Aromatics in Rich Premixed Acetylene and Ethylene Flames," *Combustion and Flame*, Vol. 20, n 3, pp. 359-368.

Dalzell, W. H., William, G. C., and Hottel, H. C (1970), "Light-Scattering Method for Soot Concentration Measurement," *Combustion and Flame*, Vol. 14, pp. 161-169.

Dasch, C. J. (1984), "Continues-Wave Probe Laser Investigation of Laser Vaporization of Small Soot Particles in a Flame," *Applied Optics*, Vol.: 23, No. 13, pp. 2209-2215.

De Iulilis, S., Barbini, M., Benecchi, S. Cignoli, F., and Zizak, G. (1998), "Determination of the Soot Volume Fraction in an Ethylene Diffusion Flame by Multiwavelength Analysis of Soot Radation," *Combustion and Flame*, Vol. 115, pp. 253-261.

Du, Z., Sarofim, A. F., and Long Well, J. P. (1990), "Activation Energy in Temperature-Programmed Desorption: Modeling and Application to the Soot-Oxygen System," *Energy Fuel*, Vol. 4, pp. 296-302.

Eckbreth, A. C. (1998), Laser Diagnostics for Combustion Temperature and Species, 2nd ed, Gordon and Breach Publishers, Amsterdam, The Netherlands.

Eckbreth, A. C. (1996), Laser Diagnostics for Combustion Temperature and Species Combustion Science and Technology, pp.184-186.

Fenimore, C. P., and Jones, G. W. (1967), "Oxidation of Soot by Hydroxyl Radicals," *Journal of Physical Chemistry*, Vol. 71, No. 3, pp.593-597.

FLUENT Version 6.0 manual, Fluent Inc, 2001.

Fric, T. F. and Roshko, A. (1994), "Vortical Structure in the Wake of a Transverse Jet," *Journal of Fluid Mechanics*, Vol. 279, pp. 1-47.

Garo, A., Prado, G., and Lahaye, J. (1990), "Chemical Aspect of Soot Particle Oxidation in a Laminar Methane- Air Diffusion Flame," *Combustion and Flames*, Vol. 79, pp. 226-233.

Garland, N. L., and Crosley, D. R. (1986), "On the collisional quenching of Electronically Excited OH, NH and CH in Flames," *Twenty-First Symposium (International) on Combustion*, The Combustion Institute, PA, pp.1693-1702.

Geitlinger, H., Streibei, TH., Suntz, R. and Bockhorn, H. (1998), "Two-Dimensional Imaging of Soot Volume Fraction, Particle Number Densities, and Particle Radii in Laminar and turbulent Diffusion Flames," *Twenty-Seven Symposium (International) on Combustion*, pp. 1613-1621.

Glassman, I. (1988), "Soot Formation in Combustion Process," *Twenty-Second Symposium (International) on Combustion*, pp. 295-311.

Glassman I. and Yaccarino, P. (1980), "The Effect of Oxygen Concentration on Sooting Diffusion Flames," *Combustion Science and Technology*. Vol. 24, pp. 107-114.

Glassman, I. and Yaccarino, P. (1981), "The Temperature Effect in Sooting Diffusion Flames," *Eighteenth Symposium (International) on Combustion*, pp. 1175-1183.

Goh, S. F. 1999 Experimental Studies of Diffusion Flame Smoke Point in Quiescent and Cross-Flow Environments, Published M. S. Thesis, University of Oklahoma, Norman, Oklahoma.

Goh, S. F. and Gollahalli, S. R. (2000), "Pilot Flame Effects on Gas Jet Flames in Crossflow," *Journal of Propulsion and Power*, Vol. 18, pp.1068-1075.

Goh, S. F., Kusadomi, S., and Gollahalli, S. R. (2001), "Effects of Cross-wind on Smoke-Point Flow Rate of Nitrogen-Diluted Hydrocarbon Fuels," International Power Generation Conference, New Orleans, LA, June 4-7, 2001, Paper No. JPGC2001/FACT-19097.

Goh, S. F., Kusadomi, S., and Gollahalli, S. R. (2002), "Effects of Cross-Wind on the Structure of Nitrogen-Diluted Propylene Flame at the Smoke Point Flow Rate," Sixth Asia Pacific International Symposium on Combustion and Energy Utilization, Kuala Lumpur, Malaysia, May 20-22, 2002.

Gollahalli, S. R., Brzutowski, T. A., and Sullivan, H. F. (1975), "Characteristic of a Turbulent Propane Diffusion Flame in a Cross-Wind," *Transactions of the Canadian Society for Mechanical Engineer*, Vol. 3, No. 4, pp. 205-214.

Habib, Z. G. and Vervisch, P. (1988), "On the Reflective Index of Soot and Their Application to Heat Flux Calculation," *Combustion Science and Technology*, Vol. 59, pp. 261-274.

Hanson, R. K. (1986), "Combustion Diagnostics: Planer Image Techniques," *Twenty-First Symposium (International) on Combustion*, The Combustion Institute, PA, pp.1677-1691.

Hanson, R. K., Seitzman, J. M., and Paul, P. H. (1990), "Planer Laser Fluorescence Imaging of Combustion Gases," *Applied Physics B*, Vol. 50, pp. 414-454.

Hall, R. J., and Bonczyk, P. A. (1990), "Sooting Flame Thermometry Using Emission/Absorption Tomography," *Applied Optics*, Vol.: 29, pp. 4590-4598.

Harris, S. J. and Weiner, A. M. (1984), "Soot Particle Growth in Premixed Toluene/Ethylene Flames," *Combustion Science and Technology*, Vol. 38, pp. 75-87.

Harris, S. J., Weiner, A. M., and Ashcraft, C. C. (1986), "Soot Particle Inception Kinetics in Premixed Ethylene Flames," *Combustion and Flame*, Vol. 64, pp. 65-81.

Henkes, R. A. W. M., Van der Flugt, F. F., and Hoogendoorn, C. J., (1991), "Natural Convection Flow in a Square Cavity Calculated with Low-Reynolds-Number Turbulence Models," *International Journal of Heat Mass Transfer*, Vol. 34, pp. 1543-1557.

Hofeldt, D. L. (1993), "Real-Time Soot Concentration Measurement Technique for Engine Exhaust Stream," SAE Paper 930079, pp. 45-57.

Howard, J. B. (1990), "Carbon Addition and Oxidation Reaction in Heterogeneous Combustion and Soot Formation," *Twenty-Third Symposium (International) on Combustion*, pp. 1107-1127.

- Homann, K. H. and Wagner, H. G. (1967), "Some New Aspect of the Mechanism of Carbon Formation in Premixed Flames," *Eleventh Symposium (International) on Combustion*, pp. 371-379.
- Hult, J., Omrane, A., Nygren, J., Kaminski, C. F. and Axelsson, B. (2002), "Quantitative Three-Dimensional Imaging of Soot Volume Fraction in Turbulent Non-Premixed Flames," *Experimental in Fluids*, Vol. 33, pp. 265-269.
- Jenkins, T. P., Bartholomew, J. L., DeBarber, P. A., Yang, P., Seitzmen, J. M., and Howard, R. P. (2002), "Laser Induced Incandescence fir Soot Concentration Measurements in Turbine Engine Exhaust," *40th Aerospace Science Meeting & Exhibit*, 14-17 January, 2002, Reno, Nevada, Paper no. AIAA2002-0828.
- Jones, W. P. and Whitelaw, J. H. (1982), "Calculation Methods for Reacting Turbulent Flows: A Review," *Combustion and Flame*, Vol. 48, pp. 1-26.
- Khan, I. M. and Greeves, G. (1974), "A Method for Calculating the Formation and Combustion of Soot in Diesel Engines," In N. H. Afgan and J. M. Beer, editors, Heat Transfer in Flames, chapter 25. Scripta, Washington DC, 1974.
- Kelso, R. M., Lim, T. T. and Perry, A. E. (1996), "An Experimental Study of Round Jets in Cross-Flow," *Journal of Fluid Mechanics*, Vol. 306, pp. 111-144.
- Kent, J. H. and Wagner, H.G. (1984), "Why Do Diffusion Flames Emit Smoke?" *Combustion Science and Technology*, Vol. 41, pp. 245-269.
- Kern, R. D., Wu, C. H., Yong, J. N., Pamidimukkala, K. M., and Singh, H. J. (1988) "Correlation of Benzene Production with Soot Yield Measurements as Determined From Fuel Pyrolyses," *Symposium on Advances in Soot Chemistry*, pp. 454-457.
- Köylü, Ü. Ö and Faeth, G. M. (1991), "Carbon Monoxide and Soot Emission from Liquid Fueled Buoyant Turbulent Diffusion Flames," *Combustion and Flames*, Vol. 87, pp. 61.
- Kuo, K. K. Y. (1986), *Principles of Combustion*, John Wiley and Sons, New York.
- Kusadome, S. (1999), "Structure of Gas Diffusion Flames Near Smoke Point." M.S. Thesis, School of Aerospace and Mechanical Engineering, The University of Oklahoma. Norman, Oklahoma, pp. 52-58.
- Landenfeld, T., Sadiki, A., and Janicka, J. (2002), "A Turbulent-Chemistry Interaction Model Based on a Multivariate Presumed Beta-PDF Method for Turbulent Flames," *Flow, Turbulence and Combustion*, Vol 68: pp. 111-135.
- Laufer, G. (1996), Introduction to Optics and Lasers in Engineering, Cambridge University Press, New York.

Launder, B. E. and Spalding, D. B. (1972), Lectures in Mathematical Models of Turbulence, Academic Press, London, England.

Launder, B. E. and Spalding, D. B. (1974), "The Numerical Computation of Turbulent Flows," *Computer Methods in Applied Mechanics and Engineering*, Vol. 3, pp. 269-289.

Leider, H. R., Kuckovian, O. H., and Young, D. A. (1973), "Thermodynamic Properties of Carbon up to the Critical Point," *Carbon*, Vol. 11, pp. 555.

Lee, S. C. and Tien, C. L. (1981), "Optical Constants of Soot in Hydrocarbon Flames" *Eighteenth Symposium (International) on Combustion*, The Combustion Institute, PA, pp. 1159-1166.

Leider, H. R., Kuckovian, O. H., and Young, D. A. (1973), "Thermodynamic Properties of Carbon up to the Critical Point," *Carbon*, Vol. 11, No.5, pp. 555-563.

Liu, F., Guo, H., Smallwood, G. J., Gulder, O. L., Matovic, M.D. (2002), "A robust and accurate algorithm of the β -pdf integration and its application to turbulent methane-air diffusion combustion in a gas turbine combustor simulator," *International Journal of Thermal Sciences*, Vol. 41, No. 8, pp. 763-772.

Macadam, S., Be r, J. M, and Sarofin, A. F. (1996), "Soot Surface Growth by Polycyclic Aromatic Hydrocarbon and Acetylene Addition," *Twenty-Sixth Symposium (International) on Combustion*, The Combustion Institute, PA, pp. 1415-1425.

Magnussen, B. F. (1975), "Investigation into the Behavior of Soot in a Turbulent Free C₂H₂ Flame," *Fifteenth Symposium (International) on Combustion*, The Combustion Institute, PA, pp. 1415-1425.

Magnussen, B. F. and Hjertager, B. H. (1976), "On mathematical models of turbulent combustion with special emphasis on soot formation and combustion," *Sixteenth Symposium (International) on Combustion*, The Combustion Institute, PA.

Marcucilli, F., Gilot, P., Chambrion, P., and Ehrburger, P., (1994) "Experimental and Theoretical Study of Diesel Soot Reactivity," *Twenty-Fifth Symposium (International) on Combustion*, The Combustion Institute, PA, pp. 619-626.

McKinnon, T. J. and Howard, J. B. (1992), "The Role of PAH and Acetylene in Soot Nucleation and Growth," *Twenty-Fourth Symposium (International) on Combustion*, The Combustion Institute, PA, pp. 965-971.

McManus, K. R., Allen, M. G., and Rawlins, W. T. (1997), "Quantitative Detection and Imaging of Soot Particles by Laser Induced Incandescence," *35th Aerospace Science Meeting & Exhibit*, 14-17 January, 1997, Reno, Nevada, Paper no. AIAA1997-0117.

- Melton, L. A., (1984), "Soot Diagnostic based on Laser Heating," *Applied Optics*, Vol. 23, No. 13, pp. 2201-2208.
- Mewes, B. and Seitzman, J. M. (1997), "Soot Volume Fraction and Particle Size Measurement with Laser Induced Incandescence," *Applied Optics*, Vol.: 33, No. 3, pp. 709-717.
- Megaridis, C. M. and Dobbins, R. A. (1989), "Comparison of Soot Growth and Oxidation in Smoking and Non-Smoking Ethylene Diffusion Flame," *Combustion Science and Technology*, Vol. 66, pp. 1-6.
- Miller, F. J., Gardner, D. E., Graham, J. A., Lee Jr, R. E., Wilson, W. E., and Bachmann, J. D., (1979) "Size Considerations for Establishing a Standard for Inhalable Particle," *Journal of Air Pollution Association*, Vol. 29, pp. 610-615.
- Millikan, R. C. (1962), "Non-equilibrium Soot Formation in Premixed Flames," *Journal of Physical Chemistry*, Vol. 66, No.5, pp. 794-799.
- Mulcahy, M. F. R. and Young, B. C. (1975), "The Reaction of Hydroxyl Radicals with Carbon at 298 K," *Carbon*, Vol. 13, pp. 115-124.
- Neoh, K. G., Howard, J. B., and Sarofim, A. F. (1984), "Effect of Oxidation on the Physical Structure of Soot," *Twenty Symposium (International) on Combustion*, The Combustion Institute, PA, pp. 951-957.
- Ni, T., Pinson, J. A., Gupta, S., and Santoro, R. J. (1995), "Two-Dimensional Imaging of Soot Volume Fraction by Use of Laser Induced Incandescence," *Applied Optics*, Vol.: 34, No. 30, pp. 7083-7091.
- Palmer, H. B. and Cullis, H. F. (1965), "The Chemistry and Physics of Carbon," Vol. 1, pp. 204, Marcel Dekker, New York, 1965. Sited from: (Glassman, I (1988) "Soot Formation in Combustion Process," *Twenty-Second Symposium (International) on Combustion*, pp. 295-311.
- Paul, P. H., Carter, C. D., and Gray, J. A. (1994a), Sandia National Laboratories Report No. SAND 94-8244.
- Paul, P. H., Gary, J. A., and Durant, J. L. (1994b), "Collisional Quenching Corrections for Laser-Induced Florescence Measurements of NO $A^2\Sigma^+$," *AIAA Journal*, Vol. 32, No. 8, 1670-1675.
- Peters, Norbert (2000), *Turbulent Combustion* Cambridge University Press, Cambridge, UK, pp.12-13.
- Puri, R., Moser, M., Santoro, and Smyth, K. C. (1992), "Laser- Induced Fluorescence Measurement of OH Concentrations in the Oxidation Region of Laminar, Hydrocarbon

Diffusion Flames,” *Twenty-Fourth Symposium (International) on Combustion*, The Combustion Institute, PA, pp.1015-1022.

Prefferle, L. D., Bermudez, G., and Boyle, J. (1994), “Benzene and Higher Hydrocarbon Formation During Allen Pyrolysis,” *Soot Formation in Combustion*, Bockhorn, H. (Editor), Springer-Verlag, Berlin, pp. 25-49.

Quay, B., Lee, T. -W., Ni, T., and Santoro, R. J. (1994), “Spatially Resolved Measurement of Soot Volume Fraction Using Laser-Induced Incandescence,” *Combustion and Flame*, Vol. 97, pp. 384-392.

Randy L. V. W, Choi, M. Y., and Lee, K-O, (1995), “The effects of Rapid Heating of Soot: Implication When Using Laser-Induced Incandescence for Soot Diagnostics,” *Combustion and Flame*, Vol. 102, pp. 200-204.

Richter, H. and Howard, J. B. (2000), “Formation of Polycyclic Aromatic Hydrocarbon and Their Growth to Soot – a Review of Chemical Reaction Pathways,” *Progress in Energy and Combustion Science*, Vol. 26, pp. 565-608.

Roper, F.G. (1977), “Prediction of Laminar Jet Diffusion Flame Size Part 1 Theoretical Model,” *Combustion and Flame*, Vol. 29, pp. 219-226.

Roper, F.G., Smith, C., and Cunningham, A. C. (1977), “Prediction of Laminar Jet Diffusion Flame Size Part 2 Experimental Model,” *Combustion and Flame*, Vol. 29, pp. 227-234.

Roper, F.G. (1984), “Soot Escape from Diffusion Flames: A Comparison of Recent Work in This Field,” *Combustion Science and Technology*. Vol. 40, pp. 323-329.

Roper, F. G. and Smith, C. and Smith. C.A. (1979), “Soot Escape from Laminar Air-Starved Hydrocarbon Flames,” *Combustion and Flame*, Vol. 36, pp.125-138.

Roth, P., Eckhardt, T., Franz, B., and Patschull, J. (1998), “H₂O₂-assited Regeneration of Diesel Particulate Traps at Typical Exhaust Gas Temperatures,” *Combustion and Flame*, Vol. 115, pp. 28-37.

Santoro, R. J., Semerjian, H. G., and Dobbins, R. A. (1983), “Soot Particle Measurement in Diffusion Flames,” *Combustion and Flame*, Vol. 51, pp. 203-218.

Santoro, R. J. and Richardson T. F. (1994), “Concentration and Temperature Effects in Soot Formation in Diffusion Flames,” *Soot Formation in Combustion*. New York: Springer-Verlag Berlin Heidelberg, pp. 221-238.

Schug, K. P., Manheumer-Timnat, Y., Yaccarino, P., and Glassman, I. (1980), “Sooting Behaviour of Gaseous Hydrocarbon Diffusion Flames and the Influence of Additives,” *Combustion Science and Technology*, Vol. 22, pp. 235-250.

Schraml, S., Dankers, S., Bader, K. Will, S., and Leipertz, A. (2000), "Soot Temperature Measurements and Implication Time-Resolved Laser-Induced Incandescence (TIRE-LII)," *Combustion and Flames*, Vol. 120, pp. 439-450.

Seitzman, J. M. and Hansin, R. K. (1993), "Comparison of Excitation Techniques for Quantitative Fluorescence Imaging of Reaction Flows," *AIAA Journal*, Vol. 31, No. 3, pp.513-519.

Shaddix, C. R., Harrington, J. E., and Smyth, K. C. (1994), "Quantitative Measurements of Enhanced Soot Production in a Flickering Methane / Air Diffusion Flame," *Combustion and Flames*, Vol. 99, pp. 723-732.

Shaddix, C. R. and Smyth, K. C. (1996), "Laser-Induced Incandescence Measurement of Soot Production in Steady and Flickering Methane, Propane, and Ethylene Diffusion Flames," *Combustion and Flames*, Vol. 107, pp. 418-452.

Sivathanu, Y. R. and Faeth, G. M. (1990), "Generalized State Relationships for Scalar Properties in Non-Premixed Hydrocarbon/Air Flames," *Combustion and Flame*, Vol. 82, pp. 211-230.

Smith, S. H. and Mungal, M. G. (1998), "Mixing, Structure and Scaling of the Jet in Crossflow," *Journal of Fluid Mechanics*, Vol. 357, pp. 83-122.

Smyth, K. C., Shaddix, C. R., and Everest, D. A. (1997), "Aspect of Soot dynamics as Reveal by Measurements of Broadband Florescence and Flame Luminosity in Flickering Diffusion Flames," *Combustion and Flames*, Vol. 111, pp. 185-207.

Stanmore, B. R., Brilhac, J. F., and Gilot, P. (2001), "The Oxidation of Soot: a Review of Experiments, Mechanism and Models," *Carbon*, Vol. 39, pp. 2247-2268.

Smyth, K. C., and Miller, J. H. (1987), "Chemistry of Molecule Growth Process in Flames," *Science*, Vol. 236, pp. 1540-1546.

Smyth, K. C., Miller, J. H., Dorfman, R. C., Mallard, W. G, and Santoro, R. J. (1985), "Soot Inception in a Methane/Air Diffusion Flames As Characterized by Detailed Species Profiles," *Combustion and Flame*, Vol. 62, pp. 157-181.

Smyth, K. K., Shaddix, C. R., and Everest, D. A. (1997), "Aspect of Soot dynamics as Revealed by Measurement of Boardband Fluorescence and Flame Luminosity in Flickering Diffusion Flames," *Combustion and Flame*, Vol. 111p. 185-207.

Sunderland, P. B. and Feath, G. M. (1996), "Soot Formation in Hydrocarbon/Air Laminar Jet Diffusion Flames," *Combustion and Flame*, Vol. 105, pp. 132.

Sunderland, P. B., Koylu, U. O., and Faeth, G. M. (1995), "Soot Formation in Weakly Buoyant Acetylene-Fuel Laminar Jet Diffusion Flames Burning in Air," *Combustion and Flame*, Vol. 100 pp. 310-322.

Tamura, M., Berg, P. A., Harrington, J. E., Luque, J., Jeffries, J. B., Smith, G. P., and Crosley, D. R. (1998), "Collisional Quenching of CH(A), OH(A), and NO(A) in Low Pressure Hydrocarbon Flames," *Combustion and Flames*, Vol. 114, pp. 502-514.

Tesner, P. A., Snegiriova, T. D., and Knorre, V. G. (1971), "Kinetics of Dispersed Carbon Formation," *Combustion and Flame*, Vol. 17, pp. 253-260.

Tesner, P. A. and Tsibulevsky, A. M. (1967), "Kinetic of Dispersed Carbon Gasification in Diffusion Flames of Hydrocarbons," *Combustion and Flames*, Vol. 11, pp. 227-233.

Turns, S. R. (1996), An Introduction to Combustion. New York: McGraw-Hill, Inc. pp. 291-293, 428.

Ubhayakar, S. K. (1976), "Burning Characteristic of a Spherical Particle Reacting with Ambient Oxidizing Gas at Its Surface," *Combustion and Flame*, Vol. 26, pp. 23-34.

Vander Wal, R. L. (1996), "Soot Precursor Material: Spatial Location via Simultaneous LIF-LII Imaging and Characterization via TEM," *Proceeding of 1996 Technical Meeting of the Central States Section of the Combustion Institute*.

Vander Wal, R. L. (1996), "Laser-Induced Incandescence: Detection Issues," *Applied Optics*, Vol.: 35, No. 33, pp. 6548-6559.

Vander Wal, R. L. (1998), "Calibration and Comparison of Laser-Induced Incandescence with Cavity Ring-Down," *Twenty-Seven Symposium (International) on Combustion*, pp. 59-67.

Vander Wal, R. L. and Dietrich, D. L. (1994), "Laser-Induced Incandescence Applied to Droplet Combustion," *Applied Optics*, Vol.: 34, No. 6, pp. 1103-1107.

Vander Wal, R. L. and Jensen, K. A. (1998), "Laser-Induced Incandescence: Excitation Intensity," *Applied Optics*, Vol.: 37, No. 9, pp. 1607-1616.

Vander Wal, R. L., Ticich, T. M., and Stephens, A. B. (1999), "Can Soot Primary Particle Size be Determined Using Laser Induced Incandescence," *Combustion and Flame*. Vol. 116, pp. 291-296.

Vander Wal, R. L., Zhou, A. and Choi, M. Y. (1996), "Laser-Induced Incandescence Calibration via Gravimetric Sampling," *Combustion and Flames*, Vol. 105, pp. 462-470.

Wagner, H. Gg. (1978), "Soot Formation in Combustion," *Seventeenth Symposium (International) on Combustion*, The Combustion Institute, PA, pp. 3-19.

Walker, P. L., Austin, L. G., and Nandi, S. P. in: Walker, P. L., editor (1966), Chemistry and Physics of Carbon, Vols. 1 and 2, New York: Marcel Decker.

Watson, K. A., Lyons, K. M., Donbar, J. M., Carter, C.D. (2000), "Simultaneous Rayleigh imaging and CH-PLIF measurements in a lifted jet diffusion flame," *Combustion and Flames*, Vol. 123, pp. 252-265.

Weiner, R. T. (1999) An analytical and Quantitative Analysis of the Laser-Induced Incandescence of Soot, PhD. Thesis, Georgia Institute of Technology, Georgia, pp. 65.

Will, S., Schraml, S. Bader, K. and Leipertz, A. (1998), "Performance Characteristic of Soot Primary Particle Size Measurements by Time-Resolved Laser-Induced Incandescence," *Applied Optics*, Vol.: 37, No. 24, pp. 5647-5658.

Will, S., Schraml, S. and Leipertz, A. (1996), "Comprehensive Two-Dimensional Soot Diagnostics Based on Laser-Induced Incandescence (LII)," *Twenty-Six Symposium (International) on Combustion*, pp. 2277-2284.

Witze P. O., Hochgreb, S., Kayes, D., Michelsen, H. A., and Shaddix, C. R. (2001), "Time-Resolved Laser-Induced and Laser-Scattering Measurements in a Propane Diffusion Flame,," *Applied Optics*, Vol. 40, No.15, pp. 2443-2451.

Woiki, D., Geisen, A., and Roth, P. (2000), "Time-Resolved Laser-Induced Incandescence for Soot Particle Sizing During Acetylene Pyrolysis Behind Shock Waves," *Proceeding of the Combustion Institute*, Vol. 28, pp. 2531-2537.

Wylen, G. V, Sontag, R., and Borgnakke, C. (1994), Fundamental of Classical Thermodynamics. New York, John Wiley & Sons, Inc. pp. 753-754.

Xu, X. and Pacey, P.D. (2001), "Interactions between acetylene and carbon nanotubes at 893 and 1019 K," *Carbon*, Vol. 39, no. 12, 1839-1847.

Zizak, G., Lanauze, J. A., and Winefordner, J. D. (1986), "An Experimental Study of the Excited State Rotational Population of OH in Flames Using Laser Induced Fluorescence," *Combustion and Flames*, Vol. 65, pp. 203-214.

Appendix I

LII Signal Correction Program

Below is the FORTRAN program that was used to correct the LII signal (Chaper IV, section 4.4.3).

```
PARAMETER (IN=108)
DOUBLE PRECISION S(2*IN),Sp(2*IN),L(2*in,2*IN)
DOUBLE PRECISION a(2*IN),r(2*IN),sum1, sum2,m,Lpold
DOUBLE PRECISION LAMDA,C,pi,nlamda,klamda,P,Lp,Ktrap,Kext,CONVER
DOUBLE PRECISION DIPIO,nlamdE,klamdE,lamdE,IPIOP,IPIOPM,SpL,SpR
INTEGER n,e,f,h,j,q

RN=108.0

pi=22.0/7.0
* Signal Taping: Detection for Nd:YAG of LII
  nlamda=1.58
  klamda=0.75
  lamda=0.00431
* Extinction measurement: Detection for He-Ne
  nlamdE=1.8
  klamdE=0.58
  lamdE=0.00633
* Convergence critirion
  CONVER=1.0E-10
* Pixal ratio (pixal/mm)
  PXrtio=22.5
* Initial reset
  j=0
  e=0
  P=0.0
  Lp=0.0
  SUM1=0.0
  SUM2=0.0
  SUM3=0.0
  DIPIO=1.0
* DIFIPI=0.0
  IPIOPM=.907011
* Guess C
  C=1.0/3.57E9
* C=1.326E-8
* C=1.0/3.64901E8
  Cd=1.326E-8

* Coefficient of signal traping and extinction
  Ktrap=(36.0*pi*nlamda*klamda)/((nlamda**2.0-klamda**2.0+2.0)
$ **2.0+4.0*(nlamda**2.0)*(klamda**2.0))
  Kext=(36.0*pi*nlamdE*klamdE)/((nlamdE**2.0-klamdE**2.0+2.0)
$ **2.0+4.0*(nlamdE**2.0)*(klamdE**2.0))

* Read from raw data
  OPEN (UNIT=5, FILE='SIGNAL.DAT',STATUS='UNKNOWN')
  DO 60 n=1,2*in-1
    READ(5,*) S(n)
60  CONTINUE
  n=0

* Calculation for a, r and L
  DO 10 n=1,IN
    P=P+1.0
```

```

a(n)=(RN-P)/PXrtio

DO 20 m=n,1,-1
r(m)=(RN-m+0.5)/PXrtio
IF (m.EQ.n) THEN
Lp=0.0
ENDIF
L(n,m)=((r(m)**2.0-a(n)**2.0)**0.5)-Lp
L(n,2*IN-m)=((r(m)**2.0-a(n)**2.0)**0.5)-Lp

Lpold=Lp
Lp=L(n,m)+Lpold
20 CONTINUE
10 CONTINUE
REWIND 5
n=0

* Set all initial signal to data value
DO 70 n=1,2*IN-1
Sp(n)=S(n)
70 CONTINUE
n=0

* Calculation for signal correction
* Do-loop for Calculation of Sp(n)
DO 40 n=1,IN

h=2*IN-n

* Do-loop for summation
47 DO 50 f=1,n
e=2*IN-f
SUM1=SUM1+Sp(f)*L(n,f)
SUM2=SUM2+Sp(e)*L(n,e)

50 CONTINUE
SpL=Sp(n)
SpR=Sp(h)
Sp(n)=S(n)*dEXP((Ktrap*C/lamda)*SUM1)
Sp(h)=S(h)*dEXP((Ktrap*C/lamda)*SUM2)

* Reset SUM1 and SUM2 before next loop
SUM1=0.0
SUM2=0.0

* Convergence check
IF ((DABS((Sp(n)-SpL)).GT.CONVER).AND.
$ (Dabs((Sp(h)-SpR)).GT.CONVER)) GOTO 47
40 CONTINUE
DO 80 j=1,2*IN-1
SUM3=SUM3+Sp(j)
80 CONTINUE
d=7.0
IPIOP=EXP(-Kext*C/(lamdE*PXrtio)*SUM3)
DIPIO=IPIOP/IPIOPM
print*, IPIOP,DIPIO

* Output data of corrected signal
OPEN (UNIT=7, FILE='OUTPUT.DAT',STATUS='UNKNOWN')
DO 90 q=1,2*IN-1
WRITE(7,*) Sp(q)
90 CONTINUE

END

```

Appendix II

Uncertainty Calculation

There are two categories that related to the uncertainty of a measurement, they are the precision or random error, $P_{\bar{x}}$, and bias or fixed error, B. The random error is depends on the sample size, which can be calculated statistically from the sample. However, the calculation of bias error of the result needs the knowledge of the properties and the measurement method (example: least count of the instrument) of all the components used in the calculation.

$$\omega = \sqrt{(P_{\bar{x}}^2 + B^2)}$$

$$P_{\bar{x}} = t_{\alpha/2} S$$

For a population, n of 10 and at 95% confidence, $t_{\alpha/2}$ is equal to 2.262. S is the standard deviation, and it is defined as

$$S = \sqrt{\frac{\sum_{i=1}^n (x_i - \bar{x})^2}{n-1}}$$

The bias error was assumed to be constant for all cases for the particular type of measurement. Which is reasonable because the same instrument was used through out the measurement. Since the present study is most comparative, it is reasonable to neglect bias error in the uncertainty calculation. In order to estimate the random error, at selected condition, the measurement was repeated ten times. The following is a sample of the measurement of the CFMFR at quiescent condition. The readings were the reading from the scale of a calibrated flowmeter. The average reading was converted into volume flow

rate with the flowmeter calibration equation, then multiplied by density to get mass flow rate.

Trial	Reading
1	19.6
2	19.6
3	19.8
4	19.8
5	19.8
6	19.7
7	19.8
8	19.8
9	19.9
10	19.8
Average, \bar{x}	19.76
Convert \bar{x} into Volume and Mass Flow Rate	
Volume Flow (l/min)	10.13
Mass Flow (kg/min)	0.0173

S of measurement	0.0966
P_x of measurement	0.0691
Convert P_x into Volume and Mass Flow Rate	
Volume Flow (l/min)	0.0360
Mass Flow (kg/min)	6.16E-05
% error of mean value	0.355

The table above shows that the estimated uncertainty of CFMFR at 95% confidence interval is 0.06 $\mu\text{g}/\text{min}$, which is 0.36% of the mean value.

Appendix III

Sample Calculation

Emission Index Calculation

$$EI_{NOx} = \left(\frac{\chi_{NOx}}{\chi_{CO} + \chi_{CO_2}} \right) \left(\frac{x MW_{NOx}}{MW_{fuel}} \right)$$

$$\chi_{NOx} = 17.98 \text{ ppm}$$

$$\chi_{NOx} = 74 \text{ ppm}$$

$$\chi_{NOx} = 2.84\%$$

Number of mole of carbon in a mole of fuel, $x = 3$

Molecular weight of NO_x , $MW_{NOx} = 30 \text{ g/mol}$

Molecular weight of C_3H_6 , $MW_{NOx} = 42.08 \text{ g/mol}$

$$EI_{NOx} = \left(\frac{17.8 \times 10^{-6}}{74 \times 10^{-6} + 0.0284} \right) \left(\frac{3 \times 30}{42.08} \right) \times 1000 \frac{g}{kg} = 1.34 \frac{g}{kg}$$

Soot Concentration Calculation

Signal intensity for 500 shots = 2337820

Background signal intensity for 300 shots = 128615

Calibration constant = 2.80×10^{-10} intensity/ppm of soot

Local soot concentration = $(2337820/500 - 128615/300) \times 2.80 \times 10^{-10} = 1.19 \text{ ppm}$

LIF Sample Calculation

The LIF signal can be quantified with following expression

$$n_{pe} = C_{\text{exp}} \times n_A \times C_{SV}$$

$$n_A = \frac{I_L}{h\nu_{ge}} \chi_o \beta_{ge} \sigma_{ge} \Delta l$$

$$C_{SV} = \frac{A_{21}}{A_{21} + P + Q_C + S}$$

$$n_e = n_A \times C_{SV} = \frac{I_L}{h\nu_{ge}} \chi_o \beta_{ge} \sigma_{ge} \Delta l \frac{A_{21}}{A_{21} + P + Q_C + S}$$

$$C_{\text{exp}} = \left(\frac{\Omega}{4\pi} \eta_T \eta_D \right)$$

$$A_{21} = 474800 \text{ s}^{-1} \quad (\text{Holtzclaw et al., 1993})$$

$$P = 0 \text{ s}^{-1} \quad (\text{Hanson et al., 1990, Eckbreth, 1996})$$

$$S = 0 \text{ s}^{-1} \quad (\text{Hanson et al., 1990, Eckbreth, 1996})$$

$$B_{ge} = 3.46 \times 10^{15} \text{ m}^3 \text{ s}^{-2} \text{ J}^{-1} (\text{Laufer, 1996})$$

$$\Omega = 0.00427 \text{ Sr} \quad I_L = 450 \text{ }\mu\text{J} \quad \beta_{ge} = 0.023 (\text{Laufer, 1996})$$

$$h = 6.63 \times 10^{-34} \text{ Js} \quad \Delta l = 1.67 \times 10^{-4} \text{ m} \quad \lambda = 285.265 \text{ nm}$$

$$c = 2.997 \times 10^8 \text{ m/s} \quad \Delta\nu = 1.8 \times 10^{10} \text{ Hz}$$

$$\nu_{ge} = c/\lambda = 2.997 \times 10^8 \text{ m/s} / 285.265 \text{ nm} = 1.05 \times 10^{15} \text{ Hz}$$

$$\eta_T = \text{Focusing lens efficiency} = 0.96$$

$$\eta_D = \text{Filter efficiency} \times \text{camera efficiency} = 0.13 \times 0.13$$

$$C_{\text{exp}} = \left(\frac{\Omega}{4\pi} \eta_T \eta_D \right) = \left(\frac{0.00427}{4\pi} 0.96 \times 0.13 \times 0.13 \right) = 5.51 \times 10^{-6}$$

$$\sigma_{ge} = \frac{B_{ge} h \nu_{ge}}{c \Delta \nu} = \frac{3.46 \times 10^{15} m^3 s^{-2} J^{-1} \times 6.63 \times 10^{-34} Js \times 1.05 \times 10^{15} s^{-1}}{2.997 \times 10^8 ms^{-1} \times 1.8 \times 10^{10} s^{-1}} = 4.46 \times 10^{-22} m^2$$

$$Q_C = \sum_i n_i q_{ix}$$

$$q_{ix} = a_i \sigma_q T^{0.5}$$

$$\sigma_q = \sigma_{Q_\infty} \exp\left(\frac{\varepsilon}{kT}\right)$$

Refer to Table 5.1 for the constant on above equation

$$\sigma_{qN_2} = 0.4 \exp\left(\frac{624}{1187.44}\right) = 0.677$$

$$\sigma_{qO_2} = 8 \exp\left(\frac{243}{1187.44}\right) = 9.82$$

$$\sigma_{qCO_2} = 11 \exp\left(\frac{488}{1187.44}\right) = 16.59$$

$$\sigma_{qCO} = 12 \exp\left(\frac{397}{1187.44}\right) = 16.76$$

$$\sigma_{qH_2O} = 20 \exp\left(\frac{434}{1187.44}\right) = 28.82$$

$$\sigma_{qH} = 14.5 \exp\left(\frac{84}{1187.44}\right) = 15.6$$

$$\sigma_{qOH} = 20 \exp\left(\frac{384}{1187.44}\right) = 27.64$$

$$\sigma_{qH_2} = 4.5 \exp\left(\frac{224}{1187.44}\right) = 5.43$$

$$n_{ix} q_{ix} = n_{ix} a_i \sigma_q T^{0.5}$$

N_{ix} is in molarity (mole/liter), which is the unit export out from FLUENT for each quenching species. N_{ix} is then multiplied by Avogadro number, A_v to get it into the unit of number of molecule.

$$n_{ix} = N_{ix} A_v$$

$$\begin{aligned} n_{N_2} q_{N_2} &= 3.21 \times 10^{-6} \frac{\text{mole}}{l} \times 1000 \frac{l}{m^3} \times 6.02 \times 10^{23} \frac{\text{atom}}{\text{mole}} \times 4.47 \times 10^{-13} \frac{cm^3}{s} \times 10^{-6} \frac{m^3}{cm^3} \\ &\times 0.677 \times 1187 k^{0.5} = 2.02 \times 10^4 \end{aligned}$$

$$n_{O_2} q_{O_2} = 1.68 \times 10^{-9} \frac{\text{mole}}{l} \times 1000 \frac{l}{m^3} \times 6.02 \times 10^{23} \frac{\text{atom}}{\text{mole}} \times 4.37 \times 10^{-13} \frac{cm^3}{s} \times 10^{-6} \frac{m^3}{cm^3}$$

$$\times 9.82 \times 1187 k^{0.5} \times 10^{-6} \frac{m^3}{cm^3} = 1.49 \times 10^2$$

$$n_{CO_2} q_{CO_2} = 9.12 \times 10^{-8} \frac{mole}{l} \times 1000 \frac{l}{m^3} \times 6.02 \times 10^{23} \frac{atom}{mole} \times 4.16 \times 10^{-13} \frac{cm^3}{s} \times 10^{-6} \frac{m^3}{cm^3}$$

$$\times 16.59 \times 1187 k^{0.5} = 1.31 \times 10^4$$

$$n_{CO} q_{CO} = 8.15 \times 10^{-15} \frac{mole}{l} \times 1000 \frac{l}{m^3} \times 6.02 \times 10^{23} \frac{atom}{mole} \times 4.47 \times 10^{-13} \frac{cm^3}{s} \times 10^{-6} \frac{m^3}{cm^3}$$

$$\times 16.76 \times 1187 k^{0.5} = 1.26 \times 10^{-3}$$

$$n_{H_2O} q_{H_2O} = 1.19 \times 10^{-7} \frac{mole}{l} \times 1000 \frac{l}{m^3} \times 6.02 \times 10^{23} \frac{atom}{mole} \times 4.92 \times 10^{-13} \frac{cm^3}{s} \times 10^{-6} \frac{m^3}{cm^3}$$

$$\times 28.82 \times 1187 k^{0.5} = 3.51 \times 10^4$$

$$n_H q_H = 2.42 \times 10^{-10} \frac{mole}{l} \times 1000 \frac{l}{m^3} \times 6.02 \times 10^{23} \frac{atom}{mole} \times 15.0 \times 10^{-13} \frac{cm^3}{s} \times 10^{-6} \frac{m^3}{cm^3}$$

$$\times 15.6 \times 1187 k^{0.5} = 1.17 \times 10^2$$

$$n_{OH} q_{OH} = 9.70 \times 10^{-19} \frac{mole}{l} \times 1000 \frac{l}{m^3} \times 6.02 \times 10^{23} \frac{atom}{mole} \times 4.99 \times 10^{-13} \frac{cm^3}{s} \times 10^{-6} \frac{m^3}{cm^3}$$

$$\times 27.64 \times 1187 k^{0.5} = 2.78 \times 10^{-7}$$

$$n_{H_2} q_{H_2} = 2.10 \times 10^{-6} \frac{mole}{l} \times 1000 \frac{l}{m^3} \times 6.02 \times 10^{23} \frac{atom}{mole} \times 10.88 \times 10^{-13} \frac{cm^3}{s} \times 10^{-6} \frac{m^3}{cm^3}$$

$$\times 5.43 \times 1187 k^{0.5} = 2.58 \times 10^5$$

$$Q_C = \sum_i n_i q_{ix} = 2.02 \times 10^4 + 1.49 \times 10^2 + 1.31 \times 10^4 + 1.26 \times 10^{-3} + 3.51 \times 10^4$$

$$+ 1.17 \times 10^2 + 2.78 \times 10^{-7} + 2.58 \times 10^5 = 3.27 \times 10^5$$

$$C_{SV} = \frac{A_{21}}{A_{21} + P + Q_C + S} = \frac{474800 s^{-1}}{474800 s^{-1} + 0 + 3.27 \times 10^5 + 0} = 0.592$$

Camera intensity = 3573.416 count

$$n_{pe} = \text{Camera intensity} / \text{camera calibration (intensity count to photon count)}$$

$$= \frac{3573.416 \text{ intensity}}{96 \text{ intensity/photon}} = 37.22 \text{ photon}$$

$$n_{pe} = C_{\text{exp}} \times n_A \times C_{SV}$$

$$n_A = \frac{n_{pe}}{C_{\text{exp}} \times C_{SV}} = \frac{37.22}{5.51 \times 10^{-6} \times 0.592} = 1.14 \times 10^7 \text{ photon}$$

$$n_A = \frac{I_L}{h\nu_{ge}} \chi_o \beta_{ge} \sigma_{ge} \Delta l$$

$$\chi_o = \frac{n_A h\nu_{ge}}{I_L \beta_{ge} \sigma_{ge} \Delta l} \frac{1}{A_v} \text{ in the unit of mole/m}^3$$

$$= \frac{1.14 \times 10^7 \times 6.63 \times 10^{-34} \text{ Js} \times 1.05 \times 10^{15} \text{ s}^{-1}}{4.05 \times 10^{-4} \text{ J} \times 0.023 \times 4.47 \times 10^{-22} \text{ m}^2 \times 1.67 \times 10^{-4} \text{ m}} \frac{1}{6.02 \times 10^{23} \frac{1}{\text{mole}}}$$

$$= 1.90 \times 10^{-8} \text{ mole/m}^3$$